Dating, isotope fingerprinting and metallogenic role of alkali metasomatism in Fe and Mn-rich rocks of the Northern Cape, South Africa

PAPADOPOULOS VLASSIS
Matriculation Number:

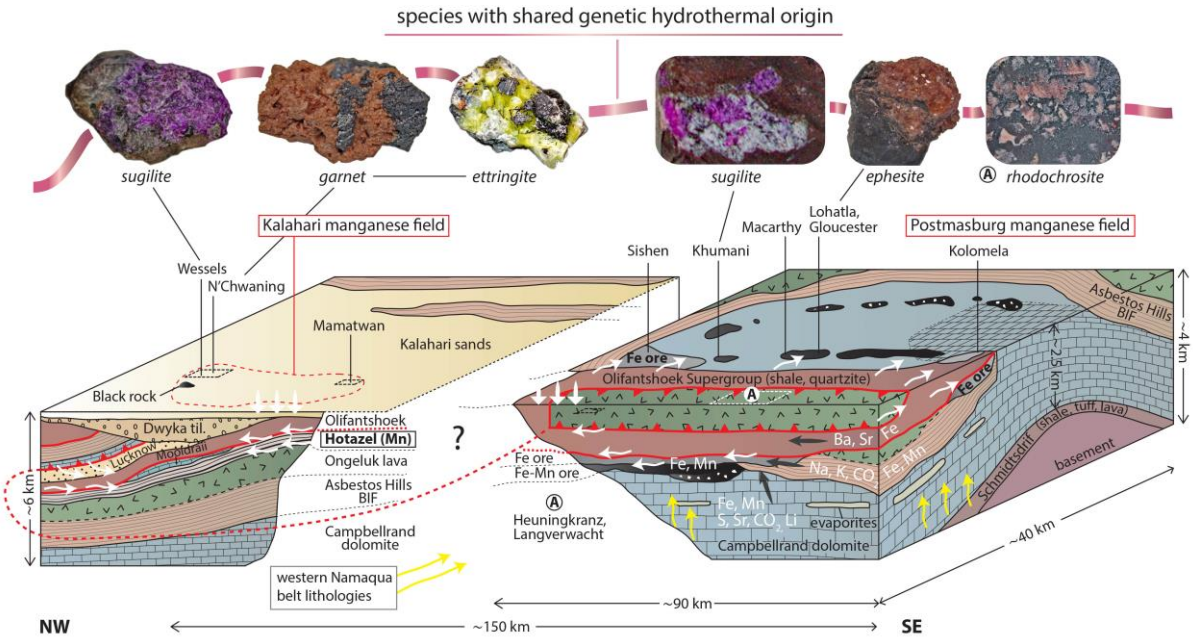

A Thesis submitted for the degree of Doctor of Philosophy

College of Science and Engineering, University of Glasgow.

Supervisors: Prof Darren Mark, Prof Adrian Boyce (SUERC), Prof Harilaos Tsikos (Un. of Patras)

Submitted: June 2022

Resubmitted: May 2023

Declaration of Originality

This study is a result of research carried out between July 2017 and June 2023, at the Scottish Universities Environmental Research Centre (SUERC), University of Glasgow, under the supervision of Professors Darren Mark, Adrian Boyce (SUERC) and Harilaos Tsikos (University of Patras, formerly at Rhodes University of South Africa).

I here certify that the following work is my own work and that all scientific borrowings have been properly acknowledged and referenced. The copyright of this thesis rests with the author. I declare that no portion of the work referred to in the thesis has been submitted in support of an application for another degree or qualification of this or any other university or other institute of learning. This thesis has been produced in accordance with the University of Glasgow's Code of Good Practice in Research.

Signature: _____

Vlassis Papadopoulos

Always advocating solidarity
I dedicate this thesis
to all those who in good faith
Agreed to spent three weeks of their lives
in 2020 To flatten the earth

Acknowledgments

Phantoms permeate this thesis. Genuinely, veraciously, factually and in the long run, who is to be acknowledged for this and any similar piece of work? Contemplating of the onerous moments, the exhilarating ones, flashes of pleasant interactions with people in the labs, around coffee tables, restaurant tables, in front of screens, in the open, in the phenomenal Scotland, moments seeking for company, seeking for pieces of scientific or plainly common-sense edges to hold onto, for peace of mind when madness escalated to new world highs in 2020, I can genuinely acknowledge that a thesis is a piece of team work, and the pieces lie within and around oneself, stretch to many years. Even before the turning point, before the most pervasive, in plain view admission that science is conformity, compliance with the abortive system blindly followed by almost everyone, acceptance that after acceptance of the ludicrous there is no more ludicrous, no more, not even room to think of acceptance, consent that all is 'normal', even before all that, before corporate and legacy media misinformation became admittedly scientific thinking among even my closest circles, walking and breathing in the era when censorship was not that overwhelming, prior to all that, when people would prefer a fleshy colour for their hands instead or red one and would bother slightly more wiping out foreign hemoglobin, back then, well, back in the little better, I'd realized that identifying and acknowledging, in keeping with academic tradition, people that molded this thesis through shaping me would be an utterly challenging task.

The events of the last couple of years made this task more labyrinthine, more thorny for me, but most importantly became synonym with the necessity for buttressing my deep-rooted morality, accepting duty and gathering essential backbone to articulate acknowledgements suited to the quality of scientific research I so stubbornly attempted to approach, even if failed in some aspects. Deviating from the routine, the cause I suppose begs for an answer. Well, not for my sleepless nights, nor the post-traumatic stress, not any absurd form of vengeance. Just to keep my ethos breathing, ensure morality survives, undertake even a small action for the future of our children. The latter though, indispensable. Remembering the story. Memorizing 'them' for them, the young ones, retelling the story, reciting the moral lessons and my truth to future generations. Invoking anamnestic responses

to not forget that some out there, the overwhelming majority, let our children break. Which brings me in front of my broken mental mirror, where I repeatedly watch my soul asking 'and so who, who merits above all your acknowledgements and does the turn matters?'

Indeed, it does. I genuinely feel that many should be acknowledged, for different reasons and besides the wretched drops seeped out of my soul in the above paragraphs. But if I could thank just a single person in the whole world, that would be undoubtedly Giannis Karampitsos, my former teacher of film direction. He retained his ethos in the most passionate way I've seen in my life, he shared his truth and stood his ground similarly, and oh dear, he clasped my spirit like a loving mother's hand. He is the only genuine 'rebelled' man I know, one that rebelled, remained in that state and will continue to do so. From here on, the list indistinguishably encompasses all those who in one way or the other, during the last couple of years, did not integrated into the only appropriate reality, remained parts of something incomplete, resisted completion of totalitarianism. Names on that list are not significant, at least not more than their actions and despite my different points of view with some of them, they all deserve a sincere thank you from me, for constantly reminding me to 'stay sane'. Off the top of my head thank you Ivor Cummins, Martin Kulldorff, Sunetra Gupta, Jay Bhattacharya, people signing the Great Barrington Declaration, John Ioannidis, Gabor Erdosi, Clare Craig, Gordan Lauc, Mattias Desmet, Beda Stadler, Michael Levitt, Paul Mason, Laura Dodsworth, Nick Hudson, Peter Castleden, Ian McGorian, Todd Kenyon, Bret Weinstein, Heather Heying, Neil Oliver, Geert Vanden Bossche, Dan Astin-Gregory, Robert Malone, David Bell, Sebastian Rushworht, Dimitrios Kouvelas, Konstantinos Pharsalinos, Grigoris Petrakos, Michalis Mytakidis (B.D. Foxmoor) and many many more who I forget. A huge debt of gratitude to the crazy, the brilliant, the fools, the gifted and the troubled, the ones refusing shampoo for brainwash, turning down coercion and mandates, the ones taught to avoid indoctrination.

Now let's not forget our souls. Our solidarity and treating our wounds with love. I won't forget anyone that made my research journey possible, interesting, enjoyable and unforgettable. My friend and supervisor Harilaos Tsikos. Hari steps into the story way before the inauguration of this project and persuades me to carry out this path. He dexterously picks up one the finest marble blocks from a Greek island (location hidden) and chooses me as the

sculptor for one of his most beloved ideas, a vision distilled by his expertise and great talent. He then visits the workroom regularly, smiling, advising, whatever the weather outside and inside the workroom, sharing unconditionally and presidentially wisdom. It's really impossible to forget any of my interactions with him, whatever the physical distance. In fact, Hari is responsible for a series of circumstances and choices that had led to my current life. Words just feel weak and feeble to describe my unreserved appreciation for him. am also more than convinced that my supervisors Adrian Boyce and Darren Mark did all they could to make my time at SUERC the best possible experience. They had been genuinely friendly and I wish I could have spent more time with them both inside and outside the scientific sphere, something that would have been greatly facilitated if circumstances were different. They are both remarkable people and I will always carry memories from that time in my future life. Thank you sincerely both for trusting me with this project, letting me experiment in the fancy labs, providing all the necessary help and having a positive attitude. There have been rough patches, but it is you both along with Hari that worked in the background and did it magnificently to make all that possible for me, so, you will always have my honest gratitude. Also, I think I will not be able to shake off the regret I feel about not trying to form more memories with Darren and Adrian.

Then it is you. And you are top of the list my forever partner Danae Apeiranthiti. And there is no space for you here, because you've impregnated every pore of this document and myself with your melancholic exuberance, always in the summer light of winter and shouting 'purpose'. Thank you. Ευχαριστώ (Efcharistó) for our son Hector. Lucky me, I couldn't have asked for a better family. And I mean you my friend Stratis, as you are intimate part of it as well. We are fused in the same crucible, we are music and games, we are perpetual walks and eternal nights, we are dialogue, we are love. That's how it has been and will always be, so there was not going to be a thesis without you. Keeping the rest short, I pay a heartfelt tribute to the rest of my family, especially my dear mother who has tried so hard to understand me the past few years and been there for me and my loving sister, to whom I am indebted to for her constant love and care in the past 34 years or so. Also, my belated thanks to Agis Goumas, another special friend there.

Finally, I am grateful that I met and worked with a series of people during these years, many of who have kindly offered their help and support, without which the project would have never been in its current form. Hoping I am not forgetting someone, big thanks to Alison McDonald, Alex McDonald, Terry Donnelly, Ross Dymock, Anne Kelly, Vinnie Gallagher, Ryan Ickert, Tracey Mark, Dan Barfod, Derek Hamilton and Rona McGill. Lastly, Assmang is thanked for providing imperative financial support and PRIMOR for the so much needed team spirit.

Abstract

The Northern Cape Province of South Africa is host to some of the largest deposits of iron and manganese metal in the world, contained in two separate districts, namely the Kalahari (KMF) and Postmasburg Manganese fields (PMF). The current thesis attempts to shed light on the chronicle of the complex epigenetic history of the two ore fields by focusing on the previously underexamined recurring theme of gangue alkali-rich assemblages, contained in and flanking a series of Fe and Mn orebodies. The principal outcomes of this study not only (a) set constrains on the characteristics, origin, sources, timing and relationship of alkali mineralization between the KMF and PMF, but also (b) challenge current ore genetic models by exploring the role of regional "alkali flooding" as a shared mechanism in the formation or at least hydrothermal upgrade of the deposits, (c) are beneficial for future exploration for new orebodies in the study and other prospective areas and (d) improve our knowledge of fluid circulation in sedimentary basins.

Extended abstract

Prevailing models place a clear dichotomy between the KMF and PMF, with the first having been locally enriched by hydrothermal alkali fluids of unknown origin during the Namaqua orogeny (1.2-1.0 Ga), whereas deposits of the latter, stretching as far as ca. 140 km to the south, interpreted as having formed between 2.2 and 2.0 Ga by a range of palaeo-weathering processes, involving karst- and fresh-water sedimentation. Solid evidence for alkali metasomatism has also been documented from the PMF, where a series of comparable and apparently younger (ca. 650-600 Ma) associations from relatively new exploration drill-cores greatly motivated the current study. A suite of new in situ UV laser $^{40}Ar/^{39}Ar$ dated samples comprising muscovite, paragonite, phlogopite, potassic magnesio-arfvedsonite, hyalophane and ephesite provides concrete evidence for a single wide-scale regional hydrothermal event, genetically linked to the 1.2- 1.0 Ga Namaqua orogeny, and renders the Northern Cape deposits as the best age-constrained among all alkali-bearing Mn/Fe districts worldwide. Moreover, these data refine the temporal extent of hydrothermal activity,

suggesting a long-lived (ca. 100 Ma) and likely bimodal character (pulses at ca. 1180-1130 Ma and 1090-1060 Ma), that is further evidenced by textural and paragenetic data, and is probably linked to distinct periods of orogenic activity and associated distal granitoid emplacement.

Regional barite mineralization inextricably linked with alkali associations displays a remarkably homogeneous sulfur isotopic signature (24.9 ± 2.5 ‰, 1σ, n =93) and highly radiogenic $^{87}Sr/^{86}Sr$ ratios (0.71238 - 0.73818), furnishing proof for a common origin by fluids derived from deeper parts of the basin, clastic sediments overlying orebodies and/or more distal lithologies, that also infiltrated and dissolved ancient (2.5 Ga) now-vanished evaporites in the Campbellrand carbonate sequence, marked by a signal of bacterial sulfate reduction produced in a restricted basin during evaporite formation.

Measured and calculated $\delta^{18}O$ (+3 to +8 ‰) and δD (-29 to -63‰) values from diverse ore-gangue mineralogy from both fields (for e.g., aegirine, sugilite, ephesite, natrolite, garnet, hyalophane, mica, etc.) in conjunction with geochronological, petrographic and existing geotectonic information suggest that infiltrating fluids can be safely characterized as saline basinal brines, largely comparable with fluids recovered from oilfields and associated with Mississippi Valley-type (MVT) Pb-Zn deposits. Striking uniformity in $\delta^{18}O$ values of gangue silicates, for example between average sugilite (KMF): +11.7 ± 1.1 ‰ and ephesite (PMF): +11.8 ± 0.3 ‰, is attributed to large water to rock mass ratio and fluid buffering during mineral precipitation, despite documented fluid-rock interactions, fractionation mechanisms, fluid mixing and subsequent events of precipitation or isotopic exchange with fluids, all further imprinting their signature on the isotopic values of minerals such as armbrusterite, arfvedsonite, lithiophorite, berthierine and other hydrous phases characterized by considerably lighter δD ratios and larger ranges in $\delta^{18}O$ values. Oxygen isotopic fingerprinting further allows to forensically differentiate between early calc-silicate precipitation in the KMF, characterized by heavier $\delta^{18}O_{FLUID}$ values on average (5.3 ± 1.4 ‰) from main and later stages (0.2 ± 2.8 ‰), during which original fluids evolved and were possibly diluted after mixing with meteoric water. $\delta^{18}O$ measurements of garnet-hematite, garnet-hausmannite and aegirine-natrolite pairs suggest realistic temperatures of formation for both fields (175°, 120°, 200° and 215°C), being broadly in agreement with previous fluid inclusion work from

the KMF. Contrastingly, similar estimates from ephesite and diaspore (PMF) suggest that the two previously regarded products of the same diagenetic/metamorphic system have not been formed coevally and/or not in isotopic equilibrium, which stresses the need for elucidating individual alteration histories within the broader regional hydrothermal metasomatism.

Exhaustive investigation of combined in situ $^{40}Ar/^{39}Ar$ data and textural observations reveals a series of important findings asserting that caution should be exercised when dating complex and fine-grained lithologies. These include: (1) identification of distinct episodes of sugilite formation in the KMF, (2) late-stage alteration involving amphibole veining in the same district, (3) an episode of reheating causing partial to complete thermal resetting of sugilite and K-felspar and coevally forming lipuite (ca. 650 Ma), (4) high $^{40}Ar/^{39}Ar$ age heterogeneity of different sample domains being only microns apart, (5) 'old' Pre-Namaqua age data from sample matrix domains (ca. 1700-1500 Ma) being broadly comparable with integrated step-heating ephesite $^{40}Ar/^{39}Ar$ ages (ca. 1500-1600 Ma), and falling within the timeframe of intrusive activity in the outer terranes of the Namaqua Province. The two most important geotectonic implications of this study are that: (a) the age similarity between the current suite of Neoproterozoic ages (ca. 650-600 Ma) from both fields and the timespan of Pan-African orogeny in the wider area vindicate previous suggestions that the former are a far-field response to the distal Pan-African compressional tectonics and (b) by virtue of the abundant new Namaqua radioisotopic ages on the edge of the Kaapvaal Craton, Kheis Province, i.e., eastern Namaqua front, should be better regarded as another tectonic zone within the extensive Namaqua Province.

Mineralogical diversity in the PMF is much higher than previously recognized, with forty-two species reported from a single locality, most of them for the first time, comprising thoroughly intergrown assemblages of hyalophane-celsian, grossular, Mn-carbonates, diaspore, apophyllite, hollandite, coronadite, As-tokyoite, As-bearing apatite and hematite, unidentified Ba- and Mn-rich silicates, as well as traces of rare species such as macedonite, pyrobelonite and tamaite. The ephesite-bearing Fe/Mn ores further encompass barian goyazite, pyrophanite, barian muscovite, ferrihollandite and gamagarite, emphasizing the coexistence of Na, Li, Al, Ba and V in the hydrothermal fluids. Alteration processes permeated

intergranular porosity and all sorts of discontinuities and repeatedly reworked the host lithologies, as evidenced by complex zoned parageneses, cross-cutting veins, vugs, replacement metasomatic textures of microconcretions or former minerals, colloform textures, overprints and diverse breccias, all comprising Na-, K-, Ba- and CO_3-bearing hydrothermal mineral associations. The origin of certain (alkali-bearing) layered mica may be related with detrital, diagenetic/metamorphic processes and/or textural control from interbedded or overlying shale units. Gangue mineral formation such as that of sugilite or ephesite involved external fluid introduction of elements (Na, K, Li, Al) and reaction(s) with components of the host rocks (Si, Al, Fe, Mn), while crystallization of the latter occurred ca. 700 Ma later than previously suggested, i.e., Namaqua instead of Kheis orogeny.

Mobilization of ore metals at the hand specimen scale is deduced to have occurred in the PMF through (a) scavenging by alkali gangues and transportation prior to their precipitation (for e.g., Mn-bearing assemblages in conglomeratic iron ore) and (b) formation of hydrothermal/metasomatic oxide generations such as replacement-related braunite, vein- and breccia-related hematite, minor braunite (II), partridgeite, and hausmannite, the extent and origin of the later requiring further examination. The critical source of Li in the fluid(s) is elusive but may be dominated by dissolution of Type II continental evaporites. Reconnaissance whole-rock lithium data reveal high Li abundances (up to 1 wt. % in ephesite ores), controlled apart from ephesite and lithiophorite by high content (up to 35 wt. %) of Li-rich (0.3-0.4 wt. %) muscovite and paragonite in ferromanganese ore, something that suggests an evaluation of the economic lithium potential in the area.

Evidence stemming from this study give no definitive answer as to whether hydrothermal metasomatic fluids were imperative for concentration of metals and the current ore grade, but emphasize the multiple and craton-wide complex epigenetic fluid events that are entrenched in the texturally diverse lithologies of the Northern Cape and furthermore urge that ore genesis should not be confined in a verry narrow timeframe (ca. 2.2-2.0 Ga) that does not account for regional tectonics. New findings demonstrate that hydrothermal activity in the Northern Cape is a fertile research topic and moreover constitute a stepping stone for new models that will focus on the possible synergy between residual/sedimentary and epigenetic tectonometamorphic/ hydrothermal processes.

Full list of minerals addressed in the thesis (n=160)

acmite	$NaFe^{3+}Si_2O_6$
aegirine	$NaFe^{3+}Si_2O_6$
albite	$Na(AlSi_3O_8)$
alexkuznetsovite-(La)	$La_2Mn(CO_3)(Si_2O_7)$
alunite	$KAl_3(SO_4)_2(OH)_6$
amesite	$Mg_2Al(AlSiO_5)(OH)_4$
analcime	$NaAlSi_2O_6H_2O$
anatase	TiO_2
andalusite	Al_2SiO_5
andradite	$Ca_3Fe^{3+}{}_2(SiO_4)_3$
anhydrite	$CaSO_4$
ankerite	$Ca(Fe^{2+},Mg)(CO_3)_2$
apatite	$Ca_5(PO_4)_3(F,Cl,OH)$
(hydroxy)apophyllite	$KCa_4(Si_8O_{20})(OH,F)8H_2O$
APS (alumino-phosphate-sulfate)	$SrAl_3[PO_4,SO_4]OH_6)$ $(REEAl_3(PO_4)2OH_6)$ $SrAl_3(PO_4)(PO_3OH)(OH)_6$
aragonite	$CaCO_3$
arfvedsonite (Mg)	$NaNa_2(Mg_4Fe^{2+})Si_8O_{22}(OH)_2$
armbrusterite	$K_5Na_7Mn_{15}[(Si_9O_{22})_4](OH)_{10}4H_2O$
As-apatite	$Ca_5(As,PO_4)_3(F,Cl,OH)$
As-hematite	Fe_2O_3 (As)
As-tokyoite	$Ba_2Mn^{3+}(As,VO_4)_2(OH)$
augite	$(Ca,Na)(Mg,Fe,Al,Ti)(Si,Al)_2O_6$
banalsite	$Na_2BaAl_4Si_4O_{16}$
barian goyazite	$BaAl_3(PO_4)_2(OH)_5H_2O$
barian muscovite	$(Ba,K)Al_2(AlSi_3O_{10})(OH)_2$
barite	$BaSO_4$
barytocalcite	$BaCa(CO_3)_2$
berthierine	$(Fe^{2+},Fe^{3+},Al)_3(Si,Al)_2O_5(OH)_4$
bixbyite	$Mn^{3+}{}_2O_3$
boehmite	γ-AlO(OH)
braunite (I)	$Mn^{2+}Mn^{3+}{}_6(SiO_4)O_8$
braunite (II)	$CaMn^{3+}{}_{14}(SiO_4)O_{20}$
brucite	$Mg(OH)_2$
bultfonteinite	$Ca_2(HSiO_4)FH_2O$
calcite	$CaCO_3$
celadonite	$K(MgFe^{3+})(Si_4O_{10})(OH)_2$
celestine	$SrSO_4$
celsian	$Ba(Al_2Si_2O_8)$
chalcocite	Cu_2S
chalcopyrite	$CuFeS_2$
charlesite	$Ca_2(HSiO_4)FH_2O$
chernovite (Y)	$Y(AsO_4)$
chlorite (clinochlore-chamosite)	$Mg_5Al(AlSi_3O1_0)(OH)_8$ $(Fe^{2+})_5Al(Si,Al)_4O_{10}(OH,O)_8$
chrysoberyl	$BeAl_2O_4$
coronadite	$Pb(Mn^{4+}{}_6Mn^{3+}{}_2)O_{16}$

corundum	Al_2O_3
crocidolite	$Na_2Fe^{2+}{}_3Fe^{3+}{}_2Si_8O_{22}(OH)_2$
cryptomelane	$K(Mn^{4+}{}_7Mn^{3+)}O_{16}$
datolite	$CaB(SiO_4)(OH)$
diaspore	$AlO(OH)$
diopside	$CaMgSi_2O_6$
dolomite	$CaMg(CO_3)_2$
effenbergerite	$BaCuSi_4O_{10}$
ephesite	$NaLiAl_{2(}Al_2Si_2O_{10})(OH)_2$
epidote	$Ca_2Al_2(Fe^{3+,}Al)(SiO_4)(Si_2O_7)O(OH)$
ettringite	$Ca_6Al_2(SO_4)_3(OH)_{12}26H_2O$
fermorite (V)	$Ca_5(As,VO_4)_3OH$
ferrihollandite	$Ba(Mn^{4+}{}_6Fe^{3+}{}_2)O_{16}$
florencite (Ce)	$CeAl_3(PO_4)_2(OH)_6$
fluorapatite	$Ca_5(PO_4)3F$
fluorite	CaF_2
gamagarite	$Ba_2Fe^{3+(}VO_4)2(OH)$
ganophyllite	$(K,Na,Ca)_2Mn_8(Si,Al)_{12}(O,OH)_{32}8H_2O$
gatehouseite	$Mn^{2+}{}_5(PO_4)_2(OH)_4$
gaudefroyite	$Ca_4Mn^{3+}{}_{2\text{-}3}(BO_3)_3(CO_3)(O,OH)_3$
gibbsite	$Al(OH)_3$
glaucochroite	$CaMn^{2+}SiO_4$
glauconite	$(K,Na)(Fe^{3+,}Al,Mg)_2(Si,Al)_4O_{10}(OH)_2$
goethite	$\alpha\text{-}Fe^{3+}O(OH)$
gowerite	$Ca[B_5O_8(OH)][B(OH)_3]3H_2O$
grossular	$Ca_3Al_2(SiO_4)_3$
gypsum	$CaSO_42H_2O$
gypsum	$CaSO_42H_2O$
halite	$NaCl$
hausmannite	$Mn^{2+}Mn^{3+}{}_2O_4$
hectorite	$Na_{0.3}(Mg,Li)_3Si_4O_{10}(OH)_2)$
hematite	Fe_2O_3
hennomartinite	$SrMn^{3+}{}_2(Si_2O_7)(OH)_2H_2O$
hollandite	$Ba(Mn^{4+}{}_6Mn^{3+}{}_2)O_{16}$
hyalophane	$(K,Ba)Al(Si,Al)Si_2O_8$
illite	$(K,H_3O)(Al,Mg,Fe)_2(Si,Al)_4O_{10}[(OH)_2,(H_2O)]$
ilmenite	$Fe^{2+}TiO_3$
inesite	$Ca_2(Mn,Fe)_7Si_{10}O_{28}(OH)_2\,5H_2O$
inyoite	$Ca(H_4B_3O_7)(OH)4H_2O$
jacobsite	$Mn^{2+}Fe^{3+}{}_2O_4$
kaolinite	$Al_2(Si_2O_5)(OH)_4$
kentrolite	$Pb_2Mn^{3+}{}_2(Si_2O_7)O_2$
k-feldspar	$KAlSi_3O_8$
kornite	$Na(CaNa)Fe^{2+}{}_4(Al,Fe^{3+})Si_7AlO_{22}(OH)_2$
kutnohorite	$CaMn^{2+(}CO_3)_2$
lavinskyite	$K(LiCu)Cu_6(Si_4O_{11})_2(OH)_4$
leakeite (K-Mn)	$KNa_2(Mg,Mn^{3+,}Fe^{3+},Li)_5Si_8O_{22}(OH)_2$
lepidolite	$K(Li,Al)_3(Al,Si,Rb)_4O_{10}(F,OH)_2$

lipuite	$KNa_8Mn^{3+}{}_5Mg_{0.5}[Si_{12}O_{30}(OH)_4](PO_4)O_2(OH)_24H_2O$
lithiophorite	$(Al,Li)MnO_2(OH)_2$
macedonite	$PbTiO_3$
magnesite	$MgCO_3$
magnetite	$Fe^{2+}Fe^{3+}{}_2O_4$
manganite	$Mn^{3+}O(OH)$
manganomelane	$Mn^{4+}O_2$
margarite	$CaAl_2(Al_2Si_2O_{10})(OH)_2$
martite	Fe_2O_3
muscovite	$KAl_2(AlSi_3O_{10})(OH)_2$
namansilite	$NaMn^{3+}Si_2O_6$
natrolite	$Na_2Al_2Si_3O_{10}2H_2O$
nchwaningite	$Mn^{2+}{}_2(SiO_3)(OH)_2H_2O$
noélbensonite	$BaMn^{3+}{}_2(Si_2O_7)(OH)_2H_2O$
norrishite	$KLiMn^{3+}{}_2(Si_4O_{10})O_2$
olmiite	$CaMn^{2+}[SiO_3(OH)](OH)$
osumilite	$(K,Na)(Fe^{2+},Mg)_2(Al,Fe^{3+})_3(Si,Al)_{12}O_{30}$
oyelite	$Ca_{10}Si_8B_2O_{29}12.5H_2O$
paragonite	$NaAl_2(AlSi_3O_{10})(OH)_2$
pargasite	$NaCa_2(Mg_4Al)(Si_6Al_2)O_{22}(OH)_2$
partridgeite	$a\text{-}Mn_2O_3$
pectolite	$NaCa_2Si_3O_8(OH)$
phlogopite	$KMg_3(AlSi_3O_{10})(OH)_2$
piemontite	$Ca_2(Al,Mn^{3+},Fe^{3+})_3(SiO_4)(Si_2O_7)O(OH)$
prehnite	$Ca_2Al(AlSi_3O_{10})(OH)_2$
pyrite	FeS_2
pyrobelonite	$PbMn^{2+}(VO_4)(OH)$
pyrolusite	MnO_2
pyrophanite	$Mn^{2+}TiO_3$
pyrophyllite	$Al_2Si_4O_{10}(OH)_2$
quartz	SiO_2
rhodochrosite	$MnCO_3$
rhodonite	$CaMn_3Mn[Si_5O_{15}]$
richterite	$Na(NaCa)Mg_5(Si_8O_{22})(OH)_2$
riebeckite	$[Na_2][Fe^{2+}3Fe^{3+}{}_2]Si_8O_{22}(OH)_2$
roedderite	$KNaMg_2(Mg_3Si_{12})O_{30}$
romanechite	$(Ba,H_2O)_2(Mn^{4+},Mn^{3+})_5O_{10}$
rutile	TiO_2
saponite	$Ca_{0.25}(Mg,Fe)_3((Si,Al)_4O_{10})(OH)_2nH_2O$
scottyite	$BaCu_2Si_2O_7$
serandite	$NaMn^{2+}{}_2Si_3O_8(OH)$
shigaite	$Mn_6Al_3(OH)_{18}[Na(H_2O)_6](SO_4)_26H_2O$
siderite	$FeCO_3$
specularite	Fe_2O_3
spessartine	$Mn^{2+}{}_3Al_2(SiO_4)_3$
spodumene	$LiAl(SiO_3)_2$
stevensite	$(Ca_{0.5},Na)_{0.33}(Mg,Fe^{2+})_3Si_4O_{10}(OH)_2n(H_2O)$
strontianite	$SrCO_3$
sturmanite	$Ca_6Fe^{3+}{}_2(SO_4)_{2.5}[B(OH)_4](OH)_{12}25H_2O$

sugilite	$KNa_2Fe^{3+}{}_2(Li_3Si_{12})O_{30}$
svanbergite	$SrAl_3(PO_4)(SO_4)(OH)_6$
tamaite	$(Ca,K,Ba,Na)_{3\text{-}4}Mn_{24}(Si,Al)_{40}(O,OH)_{112}21H_2O$
tephroite	$Mn^{2+}{}_2SiO4$
thaumasite	$Ca_3(SO_4)[Si(OH)_6](CO_3)12H_2O$
todorokite	$(Na,Ca,K,Ba,Sr)_{1\text{-}x}(Mn,Mg,Al)_6O_{12}3\text{-}4H_2O$
topaz	$Al_2(SiO_4)(F,OH)_2$
tourmaline (schorl)	$NaFe^{2+}{}_3Al_6(BO_3)_3Si_6O_{18}(OH)_4$
vesuvianite	$Ca_{10}Mg_2Al_4(SiO_4)_5(Si_2O_7)_2(OH)_4$
vonbezingite	$Ca_6Cu_3(SO_4)_3(OH)_{12}2H_2O$
wesselsite	$SrCuSi_4O_{10}$
witherite	$BaCO_3$
wollastonite	$Ca_3(Si_3O_9)$
xenotime	$Y(PO_4)$
xonotlite	$Ca_6(Si_6O_{17})(OH)_2$
yttrialite	$(Y,Th)_2Si_2O_7$
zinnwaldite	$KLi_2Fe_2{}^{2+}Al(Al_2Si_2O_{10})(OH)_2$
zircon	$ZrSiO_4$

Table of contents

PART THREE - Postmasburg Manganese field (PMF)

Chapter 1

Introduction

1. Scope

South Africa is one of the richest countries in mineral resources and a key global producer of iron and manganese. The Northern Cape in particular, is renowned for its exceptional wealth of economic deposits of both these commodities, that have resulted from an interplay between its unusual lithotype associations and a series of prolonged geological events. The nature of the ores varies from biochemical/sedimentary to epigenetic, the latter comprising modified supergene and replacement-type hydrothermal ores (Gutzmer and Beukes; 1995, Beukes et al; 2003). This thesis focuses exclusively on epigenetic processes that have influenced the two large ore districts in the area, namely the Kalahari Manganese Field (KMF) and the Postmasburg Manganese Field (PMF).

Localized hydrothermal activity related to alkali metasomatic fronts of unknown origin has been recognized to have upgraded the giant sedimentary manganese deposits of the KMF (Cairncross and Beukes; 2013), resulting in a high-grade ore which maintains all profitable extraction today. The same event(s) has produced a rare diversity of more than 200 gangue minerals. To date, ores of the PMF stretching up to ca. 150 km south of KMF, are largely believed to have escaped hydrothermal fluid circulation and the widely accepted models attribute genesis of iron ores to surficial lateritic weathering (Beukes et al; 2003) and that of manganese ores to residual karst-related and fresh-water accumulation (Plehwe-Leisen; 1985, Gutzmer and Beukes; 1996b). Therefore, the potential of a genetic relationship between the two ore districts involving upgrade mechanisms related to alkali metasomatic fluids, has been suggested by researchers (e.g., de Villiers; 1983) but not further explored in detail, despite the existence of comparable gangue alkali (Na, K, Ca, Ba, Li) mineralogical signatures regionally (Moore et al; 2011, Costin et al; 2015, Fairey et al; 2019).

The aforementioned alkalis form the research theme of this thesis. In particular, this work concentrates for the first time on alkali metasomatic signals on a regional scale with an aim to document their characteristics, decipher how mineralizing fluids originated, identify fluid sources and cast light on the geodynamic evolution of the region by providing time constraints of fluid-flow events. Critical gaps in our knowledge, questionable hypotheses and inconsistencies exist in the current ore genetic models regarding the PMF, with the relationship between alkali mineralization and ore formation being at the forefront. Ways are sought to get to the heart of the above matters.

This study has primarily an academic nature that can be summarized as research on improvement of our understanding on low-temperature hydrothermal systems and migration of palaeo-fluids in Precambrian sedimentary basins. However, the current work extends also to avenues of applied research, in the sense that both Fe and Mn are significant industrial metals used in steel alloys and any involvement of the studied hydrothermal system(s) to ore formation may be beneficial towards future prospecting in this and other related areas worldwide. Recent ore discoveries made in the past decade or so in the PMF by drill-core exploration programs attest to high prospectivity of Fe/Mn ores in unexplored parts, particularly to the west of the type-locality deposits. Therefore, better characterization of their geology, genesis and alteration history may provide better plans for future drill targets and selective mining. Future depletion of high-grade Mn ores and new metallurgical processing for the extraction of both Mn and Fe from high-iron manganese ores (Yu et al; 2019), such as that of PMF, may resuscitate mining in the area.

2. Geological framework

2.1 Regional Geology

The iron and manganese deposits of the Northern Cape in South Africa, which form the subject of this thesis are considered to be among the largest resources in the world and have been of great interest to researchers and explorers since the 1800s (Astrup and Tsikos; 1998, Cairncross and Beukes; 2013). The prodigious amounts of the metals iron and manganese in this area come in the form of ancient pristine rocks and deposits but also

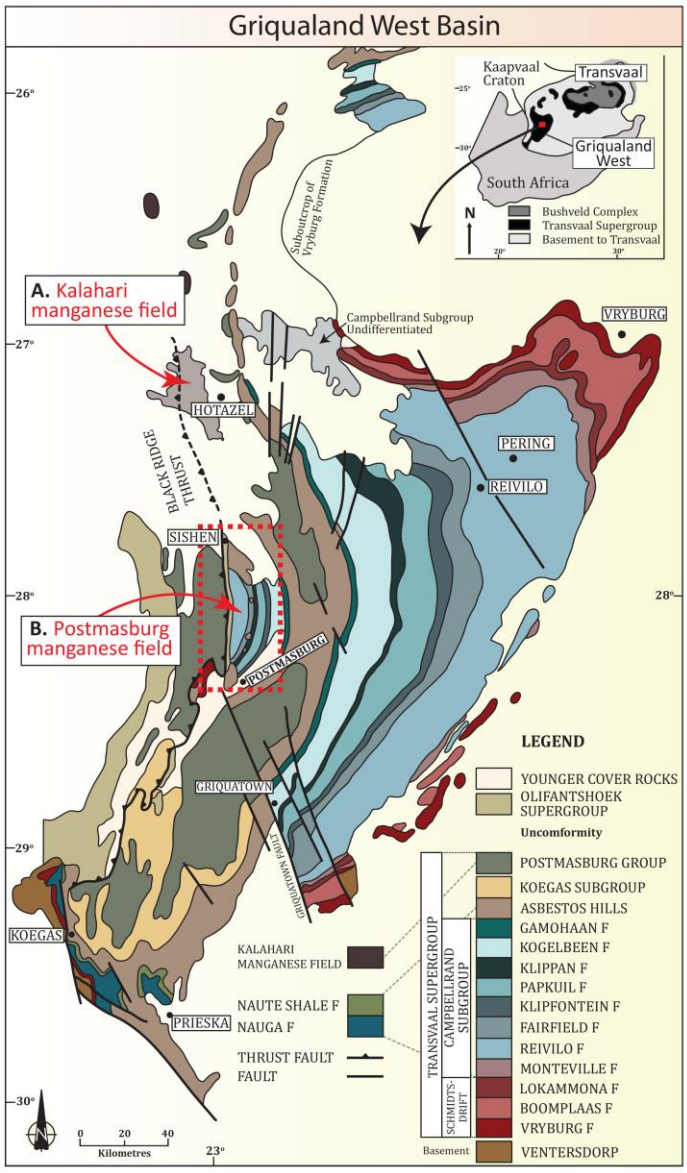

Figure 1. Regional map showing distribution of the Kalahari and Postmasburg Manganese fields in the Griqualand West basin and major stratigraphic units of the Transvaal Supergroup (see also Figure 2). Inset: Distribution of the Griqualand West and Transvaal basins on the Kaapvaal Craton. Modified after Beukes; 1983 and Cairncross and Beukes; 2013.

mineralized occurrences formed by long-lasting and complex interactions. These deposits are hosted in the Griqualand basin situated on the border of the Kaapvaal Craton and are subdivided into two economically important districts that are separated by a hiatus of ca. 40 km, namely the Kalahari Manganese field (KMF) in the north and the Postmasburg Manganese field in the south (Figure 1). The giant KMF is the world's single largest resource of manganese, accounting for more than 70 percent of global manganese resources (ca. 13.500 Mt estimated reserves), a small portion of which occurring in high-grade ore class (max ca. 60 % Mn) (Nel et al; 1986, Gutzmer; 1996, Cannon, Kimball, and Corathers; 2017). Therefore, it comes as no

surprise that exploration and mining has largely ceased in the smaller individual manganese orebodies of the PMF, which further display irregular size and shape as well as often unfavorable composition for market purposes, at least before recent advancements. On the other hand, the latter ore district is host to some of the largest BIF-hosted high-grade (> 60 wt.% Fe) iron deposits worldwide (Friese and Alchin; 2007), concentrated as strata-bound bodies around a regional unconformity and exploited chiefly at the large mines situated at the northern (Sishen, Khumani) and southern part (Beeshoek, Kolomela) of the PMF.

All regarded lithologies in this study are hosted by two major stratigraphic entities, the Transvaal Supergroup and the overlying Olifantshoek Supergroup. These rocks are preserved within the Kaapvaal Craton, an Archean geotectonic unit which covers an area of roughly 1.200 km^2 (Beukes; 1986) and is composed of some of the oldest continental lithosphere on Earth. The Neoarchaean-Palaeoproterozoic Transvaal Supergroup was deposited on the Kaapvaal Craton in a single sedimentary basin between ca. 2.65 and 2.05 Ga (Tsikos et al; 2003), but is now contained in two preserved structural basins with excellent correlated strata, the Griqualand West basin (Northern Cape) and the Transvaal basin (Figure 1, inset). Only the stratigraphy of the Transvaal Supergroup in the Griqualand West Basin is dealt here in detail.

The Transvaal Supergroup in the Northern Cape Province is a several kilometre-thick succession, represented by a mix of sediments deposited in mainly shallow marine environments (carbonates, iron formations, clastics, and glacial deposits) and volcanics, that is further subdivided into two major Groups, namely the Ghaap and the Postmasburg Group (Tsikos et al; 2003). A thorough appraisal of the literature has led to the production of the stratigraphic column seen in Figure 2. The older Ghaap Group, which forms the base of the Transvaal Supergroup is in turn comprises four subgroups, the Schmidtsdrift, Campbellrand, Asbestos Hills, and Koegas Subgroups (Beukes; 1983). Schmidtsdrif Subgroup which consists of fluvial, shallow marine, intertidal arenites and platform carbonates unconformably overlies the ca. 2.7 Ga volcanic rocks of the basement Ventersdorp Supergroup (Beukes; 1986). Schmidtsdrif Subgroup is conformably overlain by the 1600-1700 metre thick Campbellrand Subgroup, which represents an extensive carbonate platform, divided into two facies associations, the Ghaap Plateau Facies and the Prieska Facies (Beukes; 1987). These are

separated from each other by a syn-sedimentary hinge known as the Griquatown growth fault (Figure 1). The Ghaap Plateau facies is further subdivided into eight laterally persistent formations which comprise chiefly stromatolitic dolomites with minor limestone chert and shales (Beukes; 1987).

Depositional environment for this extensive platform, laterally correlated to the Malmani Subgroup of the Transvaal basin, range laterally from supratidal and shallow marine environments (Malmani Subgroup), to shelf margin, slope and basin environments (Campbellrand Subgroup, Sumner and Grotzinger; 2004). According to the latter authors, this carbonate sequence has experienced only partial dolomitization and silicification, leaving much of the primary limestone pristine. The deposition of the platform is constrained by the lowermost dolomitic and oolitic Monteville and the capping, evaporite-bearing Gamohaan Formation (Gandin and Wright; 2007) between 2.555 ± 5 and 2.521 ± 3 Ma (Sumner and Bowring; 1996, Altermann and Nelson; 1998). Among the eight formations, only the Reivilo and the Fairfield Formations are known to be hosts to the manganese of the PMF. One of the basal Members of the chert-free Reivilo Formation (Ulco) comprises giant domal bioherms which host about 2-3 wt.% MnO (Altermann and Siegfried; 1997, Beukes; 1987). In contrast, the chert-bearing Fairfield formation consists of columnar and domal stromatolites, fenestral dolomites with chert replacements, fenestral mats and dolomite-clast breccia in a shale matrix, but similarly contains on average of 1-3 wt. % MnO and along with the aforementioned Formation are thought to be key sources of manganese to the PMF ore bodies (Plehwe-Leisen and Klemm; 1995, Gutzmer and Beukes; 1996a). This is illustrated in Figure 2 and discussed later on.

Subsequent major marine transgression facilitated the deposition of the ca. 1 km thick Asbestos Hills Subgroup that conformably overlies the Campbellrand Subgroup and is divided into the ca. 2.465 Ma microbanded Kuruman and the ca. 2.432 Ma clastic-textured Griquatown Iron Formations. (Beukes; 1983, Trendall et al; 1990, Pickard et al; 2003). The pristine iron-formations consist mainly of quartz, magnetite, ankerite, siderite, greenalite, stilpnomelane, minnesotaite and riebeckite (Beukes and Klein; 1990) and protrude as a range of hills that can be traced for ca. 400 km N-S in the Northern Cape. Oxidized and mineralized counterparts of these two BIF formations consist of hematite and quartz, are preserved locally

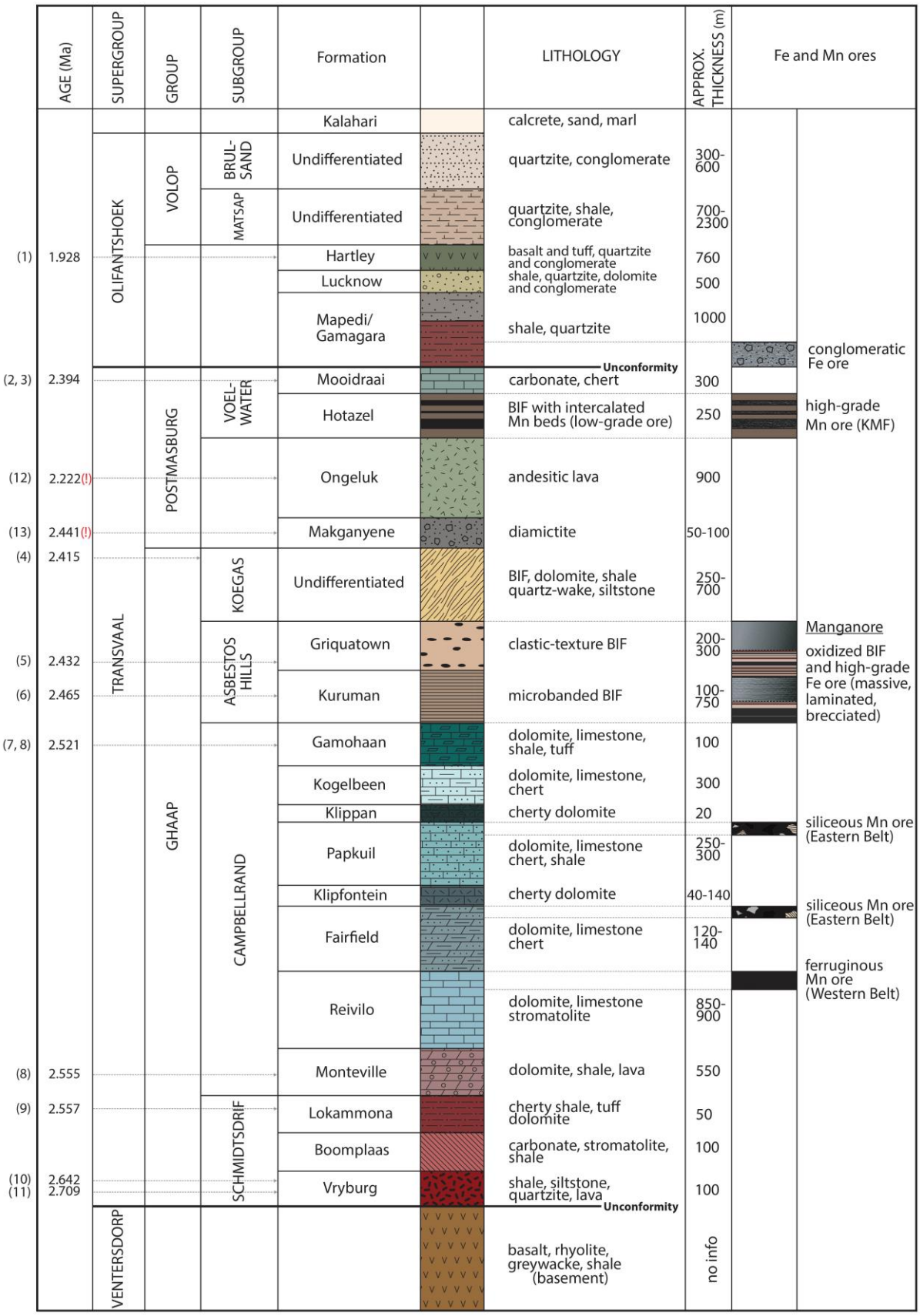

Figure 2. The lithostratigraphy of the Transvaal Supergroup in Griqualand West, illustrating also distribution of Fe-Mn ores and their relationship with protore or precursor lithologies. Inspired by figures found in Gutzmer; 1996 and Dorland; 1999. References for radiometric ages on next page.

Figure 2. (previous page) References for ages:

(1) Cornell et al; 1998 (Pb-Pb on zircons from a porphyry sample)
(2, 3) Bau et al; 1999 (Pb-Pb whole-rock), Fairey et al; 2013 (U-Pb) [2392 ± 23 Ma, whole-rock age]
(4) Kirschvink et al; 2000 (Pb-Pb)
(5) Trendall et al; 1990 (U-Pb zircon) [tuff layer at the base of Griquatown]
(6) Pickard et al; 2003 (U-Pb zircon) [intercalated tuffaceous mudrocks]
(7, 8) Sumner and Bowring; 1996 (U-Pb zircon) [ash-fall tuffs], Altermann and Nelson; 1998 (U-Pb) [2516 ± 4 Ma for Gamohaan and 2.555 ± 19 Ma]
(9) Jahn et al; 1990 (Pb-Pb dolomite whole-rock)
(10) Walraven and Martini; 1995 (single zircon Pb-evaporation) [volcanics]
(11) Armstrong et al; 1991 (U-Pb zircon) [felsic tuffs]
(12) Cornell et al; 1996 (Pb-Pb whole-rock)
(13) Fairey et al; 2013 (Pb-Pb whole-rock) [2444 ± 200 Ma, large uncertainty]

as large isolated blocks slumped into palaeo-sinkhole structures developed in dolomite units of the Campbellrand Subgroup under a solution collapse unconformity and host high-grade massive, brecciated and laminated iron ore (Van Schalkwyk and Beukes; 1986). The last unit of the Ghaap Group is the Koegas Subgroup which comprises siliciclastics and iron formations, although it is restricted to the southern parts of the Northern Cape Province, effectively south of the Griquatown growth fault (Beukes; 1983, 1986).

The conformable transition between the Ghaap Group and the overlying Postmasburg Group is evidenced by glacial diamictite beds of the lower stratigraphic member of the Postmasburg Group, i.e., the Makganyene Formation, commonly found interbedded with the upper parts of the Koegas Subgroup (shales, sandstones and minor BIF) (Moore et al; 2001, Polteau et al; 2006). A contention over the nature of the Ghaap-Postmasburg transition existed until recently, with Beukes (1986) supporting the existence of a regional unconformity between the two, attributed to a period of uplift and erosion, an interpretation further used to strengthen the ca. 2.22 Ga age of the Ongeluk Formation, the volcanic sequence overlying the Makganyene diamictite (Cornell et al; 1996). However, apart from the existing textural evidence, the previous interpretation can be safely abandoned in view of absolute detrital zircon ages obtained from the Makganyene Formation (Moore et al; 2012), Pb-Pb carbonate dating (2.39 Ga) of the carbonate Mooidraai Formation at the very top of the Postmasburg Group (Fairey et al; 2013), as well as recent re-dating of the Ongeluk Formation itself (Gumsley et al; 2017).

The Makganyene Formation is overlain by subaqueously deposited continental flood-type basaltic andesites and pillow lavas of the Ongeluk Formation (Cornell et al; 1996), showing a stratigraphic thickness of ca. 900 metres. Conformably overlying the Ongeluk Formation is the economically significant Palaeoproterozoic Lake Superior-type Hotazel Iron-Formation, which comprises three sedimentary manganese units interbedded with iron-formation (ca. 250 m) and constitutes the dominant succession in what is broadly known as the Kalahari Manganese Field (Tsikos and Moore; 1997). Several post-depositional alteration events have affected the primary sedimentary ore beds and have significantly increased the ore-grade (Gutzmer; 1996, Gutzmer and Beukes; 1996b) (Figure 2). The stratigraphy of the Postmasburg Group is terminated by the Mooidraai Formation, a succession of largely limestones with lesser dolomitizes in the southern parts of the KMF (Fairey et al; 2013).

The Transvaal Supergroup and the basal shale units of the overlying Olifantshoek Supergroup, known as the Mapedi/Gamagara Formation, are believed to be divided by a major low-angle regional angular unconformity, which marks a lengthy era of non-deposition and synchronous erosion (Grobbelaar et al; 1995, Yamaguchi and Ohmoto; 2006). This feature has been attributed a major metallogenic role in the literature. Specifically, is thought to control all primary ore formation in the PMF, including BIF-hosted iron ores and dolomite-hosted manganese orebodies (as means of ore enrichment and accumulation during palaeo-lateritic weathering) (Gutzmer and Beukes; 1996a, Beukes et al; 2003) and subsequent hydrothermal upgrading (as a later fluid conduit) of the KMF ores (Tsikos et al; 2003) and possibly certain PMF deposits (Moore et al; 2011, Fairey et al; 2019). The basal part of the Olifantshoek Supergroup consists of shales and quartzites and is commonly encountered in boreholes, directly overlying or interlayered with iron and manganese ores in the wider area.

The Transvaal Supergroup strata have been deformed during several extensive and compressional events that have affected the Griqualand West basin (Friese and Alchin; 2007). The first of the these, is believed to have been a major E-W compressive event (ca. 2.2-2.1 Ga Kalahari orogeny: Alchin et al; 2008) which induced uplift, erosion, large-scale folding and inversion of certain strata, as well as formation of a prominent structural feature in the area known as the Maremane dome. This double plunging anticlinal structure dips gently at less than 10^{o} in a northerly, easterly and southeasterly direction and is defined by carbonates of

the Campbellrand Subgroup cropping out in its core, fringed by conformably overlying iron-formations of the Asbestos Hills Subgroup (Figures 3 and 4). The above stratigraphic configuration is believed to have facilitated the development of the aforementioned Transvaal-Olifantshoek regional unconformity during a period of at least 200 Ma, through erosion of the folded and exposed strata and subsequent deposition of the sediments of the Olifantshoek Supergroup. As illustrated in Figure 3, iron mineralization is particularly prolific in the northern and southern extremities of this dome whereas manganese orebodies occur in two belts along an ca. 65 km long, N-S transect across the dome, referred to as the Western and Eastern Belts. This division has been made on the basis of textural characteristics, bulk chemical and mineralogical compositions and differences associated with the envisaged setting of their genesis (Plehwe-Leisen and Klemm; 1995, Gutzmer and Beukes; 1996a), but the existence of mixed ore-types and other inconsistencies with the above classification later discussed in this thesis do not support existing classifications (Fairey et al; 2019).

Further deformation of the Transvaal Supergroup strata in the western portion of the Griqualand West basin was later caused by accretion of new crust to the western margin of the Kaapvaal Craton during the Kheis Orogeny (1.83-1.73 Ga) (Cornell et al; 1988) a N-S striking belt that caused shearing along the contact with the Olifantshoek Supergroup, crustal shortening, imbrication, thin-skinned thrusting of the Transvaal over the Olifantshoek Supergroup and strata duplications (Beukes and Smit; 1987, Grobbelaar et al; 1995). Eastward movements during this event were largely accommodated by the Blackridge thrust fault system (Figure 3). The initiation of the Blackridge Fault system during the Kheis Orogeny was disputed by Altermann and Hälbich (1990, 1991), who postulated it was established much later and attributed folding of the Transvaal strata to the ca. 1.35-1.0 Ga Namaqua orogeny (Altermann and Siegfried; 1997, Moen; 2006). The latter is a local expression of the global Grenville Orogeny (Cornell et al; 2006) and is suggested to have reactivated several normal faults and produced eastward-directed faults, superimposed on higher-order structures.

Much dispute exists over the existence and timing of Kheis orogeny in the area, which has been also regarded as an early phase of the Mesoproterozoic evolution of the Namaqua orogenic belt (Moen; 1999, Eglinton; 2006). This matter is discussed in more detail later in this thesis. A clear manifestation of the Namaqua orogeny in the Northern Cape Province is

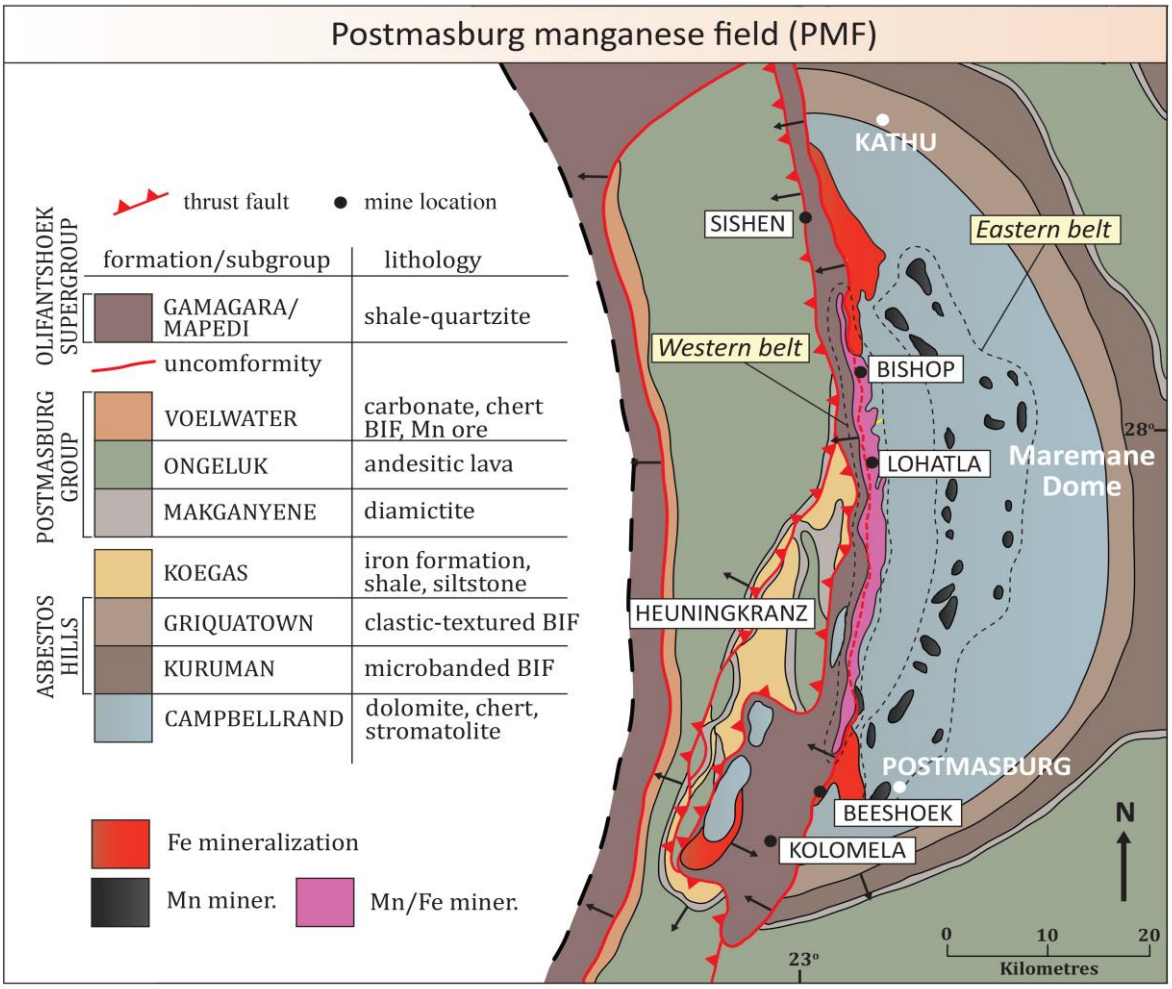

Figure 3. Geological map of the PMF, showing the stratigraphic configuration of the Transvaal and Olifantshoek Supergroups in the Maremane dome region, broad extent of the Transvaal-Olifantshoek unconformity and Blackridge Thrust fault system. Also emphasized is the distribution of the different Fe-Mn lithotypes in the area. Modified after Plehwe-Leisen; 1995 and Moore et al; 2011.

the hydrothermal upgrade of the northernmost part of the KMF at ca. 1050 Ma (Gnos et al; 2003). Regional metamorphism in the region has never exceeded temperatures of about 170ºC and pressures of 2 kbar, i.e., sub-greenschist grade (Holland and Beukes; 1990).

2.2 Ore genesis in the Northern Cape

The Northern Cape Province displays a relatively flat topography interrupted only by few hills, while natural outcrops are limited and most of the terrain, especially in the Kalahari Manganese field, is covered by Cenozoic sands and calcretes of the Kalahari Formation. The area brims with surface and underground mines exploiting a series of important Fe and Mn

deposits which extend over a distance of some 140 km from Postmasburg to Black rock in the north.

Postmasburg Manganese field (PMF)

Exploitation of iron ore in the PMF is currently taking place at the thick, large and laterally continuous BIF-hosted deposits (Sishen and Kolomela mines) delineating the southern and western margins of the Maremane dome (Figures 4 and 5), whereas ore occurrences in other parts of the dome are in the form of numerous, small, isolated ore bodies, spreading over a large area (Carney and Mienie; 2003). An important iron-rich lithology forming part of the commercial iron ore in the region is a type of clastic/detrital deposit, characterized by hematite-rich matrix and variably enriched iron-formation pebbles (Van Schalkwyk and Beukes; 1986). This entity is known as Doornfontein Conglomerate and essentially develops as allochthonous deposition at the base of the Mapedi/Gamagara Formation from reworking of eroded BIF during the major erosional period associated with the development of the Transvaal/Olifantshoek unconformity (Gutzmer and Beukes; 1996a). Some of the historically major manganese mines in the area are the Lohatla, Glosam and Bishop mines (Figure 3), although mining in the area is taking place only on a small-scale today after cessation of most operations in 1989 (Gutzmer; 1996), as a result of the success of mining in the giant neighboring KMF. The most comprehensive and widely accepted model about the origin of both Fe and Mn ores to date, interpret the palaeoenvironment of ore formation in the Maremane dome as laying above sea level over protracted lengths of time and as a consequence exposing the rocks of the dome to intense chemical and physical erosion.

Manganese ores are intimately associated with the underlying dolomites and are subdivided into two distinct types, namely Eastern Belt or siliceous-type and Western Belt ore ferruginous-type deposits. Detailed descriptions on these ores and their postulated genetic models can be found in Plehwe-Leisen and Klemm (1995) and Gutzmer and Beukes (1996a, 1997b) and the following are based on these studies. Central to these models is the widespread karstification of the Campbellrand Subgroup dolomites and consequent

formation of sinkhole structures, at the base of which a manganese-rich residual wad, i.e., unconsolidated sediment comprising manganese oxides and hydroxides, was accumulated.

The siliceous ores of the Eastern Belt (Figures 4 and 5) were formed from manganese sourced from leaching of chert-rich manganiferous (1-3 wt. % MnO) dolomites of the Fairfield Formation, accumulated together with silicified dolomite and insoluble remnant chert-fragments, altogether composing a residual karst breccia known as the Wolhaarkop breccia. The massive matrix of this breccia is composed of quartz, hematite and braunite whereas bixbyite and pyrolusite are mentioned to be present in smaller quantities. Crude layering may also characterize this ore-type and has been interpreted to be inherited from the dissolved chert-rich dolostones. Transition zones between chert breccia and manganese ore bodies are characterized as gradual and high-grade manganese lenses and pods are reported to be dominant at the basal part of the breccia and in contact with the underlying dolomites. Thin hematite-rich illitic shale beds and laminated manganiferous clay intercalations are also mentioned and the iron content of the ores show significant variation stratigraphically, generally increasing towards the top as it transitions into the Manganore Iron Formation. The cave systems hosting these ores are believed to have formed below lithified banded iron-formation of the Asbestos Hills Subgroup, which however subsequently slumped into the developing cave system (forming the so-called Manganore Iron Formation) as dissolution continued its downward progression, a process facilitating iron-ore enrichment and locally forming inverted stratigraphy. A simplified stratigraphy is show in Figure 5. Later diagenesis and low-grade metamorphism led to recrystallization of residual manganese wad to the braunite-partridgeite (iron-poor Mn_2O_3) assemblages mined at present day. Crosscutting veins and replacements of chert fragments from coarse barite and globular hematite are attributed to syn- or post-metamorphic fluid flow.

The Western Belt type-ores are more ferruginous in nature, are confined in the central part of the Maremane dome and have been formed in a similar fashion, from dissolution of carbonates of the chert-free and manganiferous (2-3 wt. % MnO) Reivilo Formation. Their origin though comprises certain differences in comparison to the Eastern Belt ores and is somewhat is somewhat more ambiguous, even among researchers presenting the prevailing models (Plehwe-Leisen and Klemm; 1995, Gutzmer and Beukes; 1996a). These ores are not

associated with any residual karstic breccia, but instead show a more direct stratigraphic association with the Mapedi/Gamagara shale of the basal Olifantshoek Supergroup.

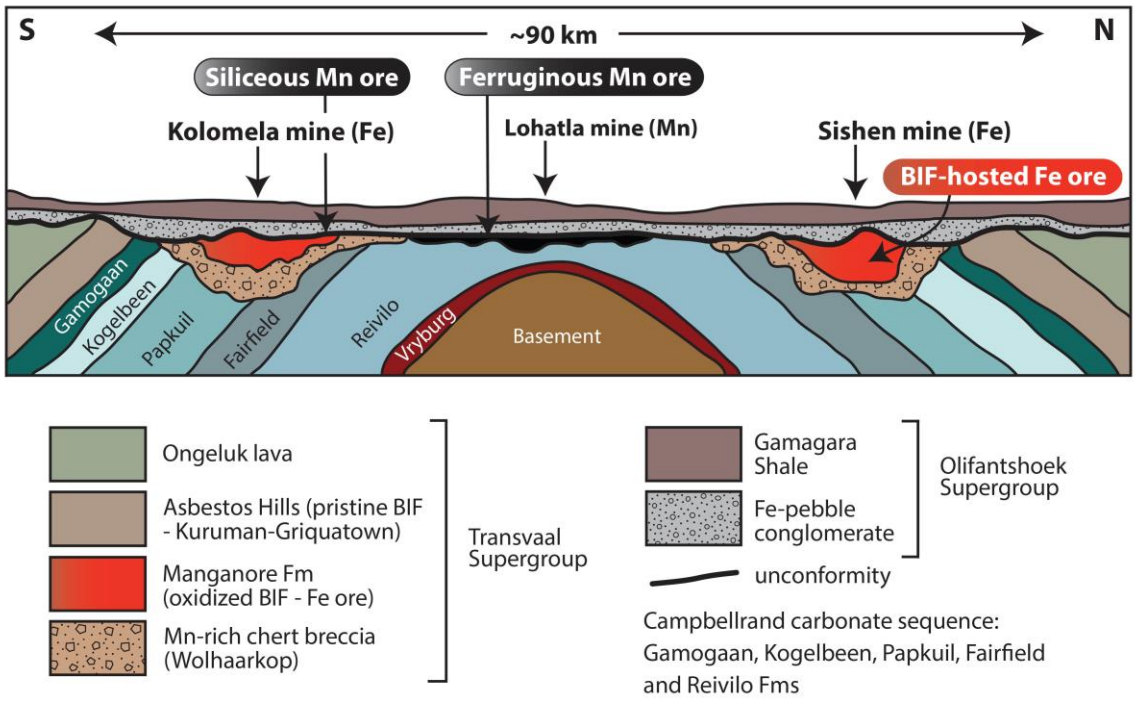

Figure 4. N-S schematic cross-section through the Maremane Dome, emphasizing associated manganese and iron ore deposits, the genesis of which is tied to supergene enrichment during the development of a regional angular unconformity. The latter is seen transecting different rock types owing to the deformed and tilted nature of the Transvaal Supergroup strata. Modified after Smith and Beukes; 2016.

In particular, the hanging wall of these ores may consist of the aforementioned Doornfontein conglomerate unit of the Gamagara Formation (Figure 5), with the contact between the two characterized as gradational and conformable. Where the Doornfontein conglomerates are absent, iron-rich and aluminous shales develop interbedded and conformably on top of the ores. Texturally, these ores are well-layered and towards the top of the sequence they may exhibit a distinct shaly parting. Ore minerals are similar to the Eastern Belt, but Al- and Li-rich silicates and oxides (ephesite, amesite, diaspore, lithiophorite) are commonly mentioned as gangue constituents in the ore genetic models and their formation is attributed to post-depositional reworking and burial diagenesis/metamorphism (Gutzmer and Beukes; 1996a) or even during initial ore accumulation (Plehwe-Leisen and

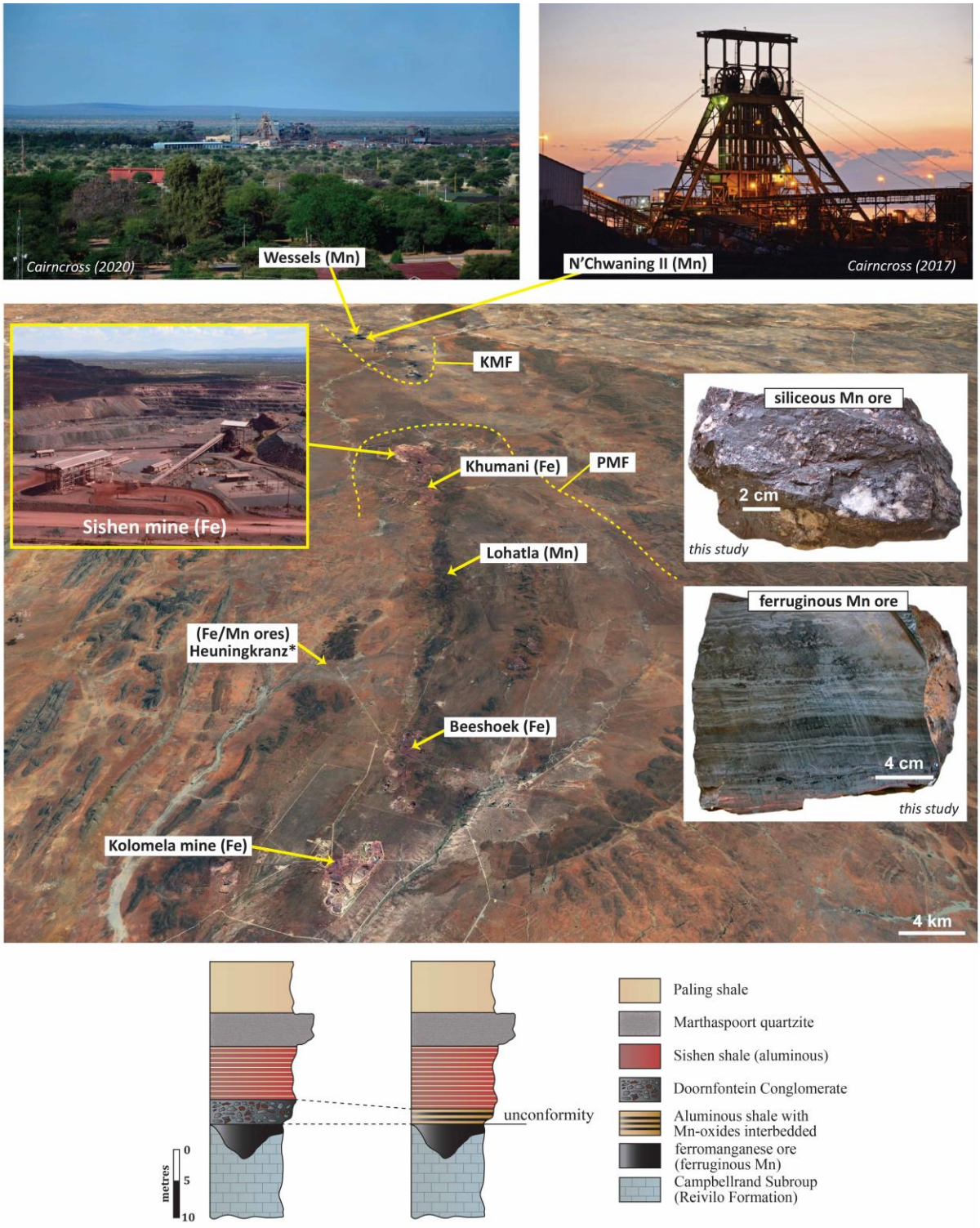

Figure 5. Google earth map showing major iron and manganese mines in the study area. Simplified stratigraphic profiles and characteristic samples for the siliceous (Eastern Belt) and ferruginous (Western Belt) ore types are also displayed. *Major focus in this thesis is given on exploration drillcores at Heuningkranz locality (wider Kolomela region).

Klemm; 1995), at least as regards species such as lithiophorite. The high Al content, association with overlying shales and sedimentary bedding have been taken as evidence of

lateritic provenance and deposition under surficial fresh-water karstic conditions. Plehwe-Leisen and Klemm (1995) further identified a second type of ferruginous ore located higher up in the stratigraphy, being finely layered, intercalated with shales and more iron-rich, which interpreted as having been precipitated from sea water after the transgression of the Transvaal Sea. Similar to the Eastern Belt, ferruginous ores have undergone recrystallization and modification through burial processes that formed the present mineralogy. Another textural type formed locally during these processes is the coarse-grained massive to vuggy bixbyite-rich ore mentioned by (Gutzmer and Beukes; 1996a). Recent supergene enrichment has altered the Western Belt type-ores to comprise romanechite, pyrolusite and cryptomelane.

Aside from the prevailing supergene ore genetic model presented above, other researchers have published opposing viewpoints with respect to ore genesis of the Western Belt Mn ores of the PMF. One of the early theories was that these ores are of replacive origin and specifically have occurred from metasomatic replacement reactions against precursor sedimentary clay material by manganese oxides by virtue of hydrothermal manganiferous circulating fluids (Hall; 1926, Nel; 1929). De Villiers (1994) placed emphasis on hydrothermal textures and the presence of bixbyite, ephesite, jacobsite, acmite (aegirine) and albite to suggest that suggested that manganese was leached from dolomites by hydrothermal fluid of magmatic origin, given the presence of lithium, sodium, boron and chlorine in the ores. Although this scenario was later dismissed by the same author (De Villiers; 1960) on the premise of no such magmatic thermal source in the area, the idea of transportation of manganese brought into solution and then deposited elsewhere apart from the base of the Wolhaarkop breccia was retained. A sedimentary origin, whereby ore deposition occurs before that of the Olifantshoek clastic sediments has also been postulated (Schneiderhöhn; 1931, Button; 1986).

Some authors who focused on gangue alkali mineralogy and temperatures of ore formation (Boardman; 1964, De Villers; 1983, 1992) have noted the mineralogical similarities between the KMF and PMF and in view of their close geographic association speculated genetic links, although this concept has apparently received little confirmation and no further proof has been presented since then. More recent work has exploited the metasomatic

effects on these ores and the highly complex alkali assemblages (see later section 1.2.3) to propose that the involved hydrothermal system may have acted as metal upgrading mechanism against an original low-Mn protolith and re-emphasized the possibility of a regional-scale system exploring large-scale fluid conduits (Moore et al; 2011, Costin et al; 2015 and Fairey et al; 2019).

In this thesis, sampling and focus on the manganese ores of the PMF is chiefly placed on a number of revisited drillcores, originally studied by the abovementioned authors and occurring closer to the Blackridge Thrust Fault, somewhat 10-20 km to the west of the type-locality ores (Heuningkranz-wider Kolomela region) (Figure 5). As mentioned above, the subdivision of the PMF ores into Western and Eastern Belt type has not much to offer in the broad sense since the ores in the wider area do not follow this strict classification and attached characteristics. Therefore, the only **subdivision regarding the manganese PMF ores** hereon is that between the ones studied so far in the s.s. Maremane dome (termed as Eastern Maremane dome or EMD) and the deposits discovered and studied more recently, further to the west of the former, in an area named here as Western Maremane dome (WMD). This is an informal and purely geographic subdivision made here to facilitate comparisons between findings from older and newer studies.

According to the most comprehensive and widely accepted model about the **origin of the iron ores** on the Maremane dome (Van Schalkwyk and Beukes; 1986, Beukes et al; 2003), iron enrichment in the area is associated with exposure and prolonged weathering of the Asbestos Hills BIF under lateritic conditions. Slumping of BIF into karstic depressions within the Campbellrand dolomites during this long period of oxidation and erosion is regarded as pivotal to ore upgrade (Figure 4). Supergene hematite ores characterized as massive, laminated or brecciated, all preserving to a lesser or greater extent textures of the unmineralized BIF (Papadopoulos; 2016), are primarily concentrated near the top of the Asbestos Hills Subgroup as stratabound bodies, within the locally known, oxidized Manganore iron formation. While the deposits generally straddle the BIF-Gamagara contact, they are not limited to it, since BIF intersections are found between ore and Gamagara/Mapedi shales (Basson et al; 2018).

Supporting evidence for the supergene origin of the iron ores are regarded to be the palaeomagnetic results indicating humid tropical environment during the perceived time of ore formation (Evans et al; 2001), preservation of hematite pisolites within the lower Gamagara Formation and light oxygen isotopic signatures of bulk hematite from the ore, interpreted to indicate involvement of meteoric water at the time of mineralization (Gutzmer et al; 2006). However, recent studies have started recognizing the importance of the protracted tectonic history of the ores (Basson et al; 2017, 2018), the superimposed hydrothermal activity on BIF, iron ore (Papadopoulos; 2016) and overlying shales (Land et al; 2017), thus championing the role of hypogene metasomatic fluid flow along impermeable lithological boundaries in ore genesis.

Kalahari Manganese field (KMF)

Mineralization in the KMF occurs as three biochemical/sedimentary manganese units deposited along with the interbedded pristine BIF of the Hotazel Formation. Among these three units consisting mainly of finely laminated braunite, hematite and kutnohorite, the lowermost is the most voluminous (generally 20-25 thick), but can reach a maximum thickness of about 50 metres in the pristine ores (Gutzmer; 1996). The transitions between iron-formation and manganese ore are gradational and are characterized by a very fine-grained hematite- and carbonate-rich lithology referred to as hematite lutite (Kleyenstüber; 1985). Within this stratigraphic succession two broad classes or types occur: low grade (30-38 wt. % Mn) and carbonate-rich (kutnohorite, Mn-calcite) braunite ore and high grade (38-62 wt. % Mn), carbonate-poor and oxide-rich (hausmannite, bixbyite) braunite II ore. All profitable extraction takes place from the southernmost (Mamatwan, Gloria mines) and northernmost (Wessels, N'Chwaning mines) areas of the KMF, which host low- and high-grade ore respectively (Figure 6). Open cast mining has proved feasible for the thick and large low-grade ore reserves, whereas the elevated grades of the high-grade ore class, permit exploitation via underground operations situated 300 metres below the surface (Wessels mine) despite its markedly lower thickness (generally 4-8 metres) (Tsikos; 1999).

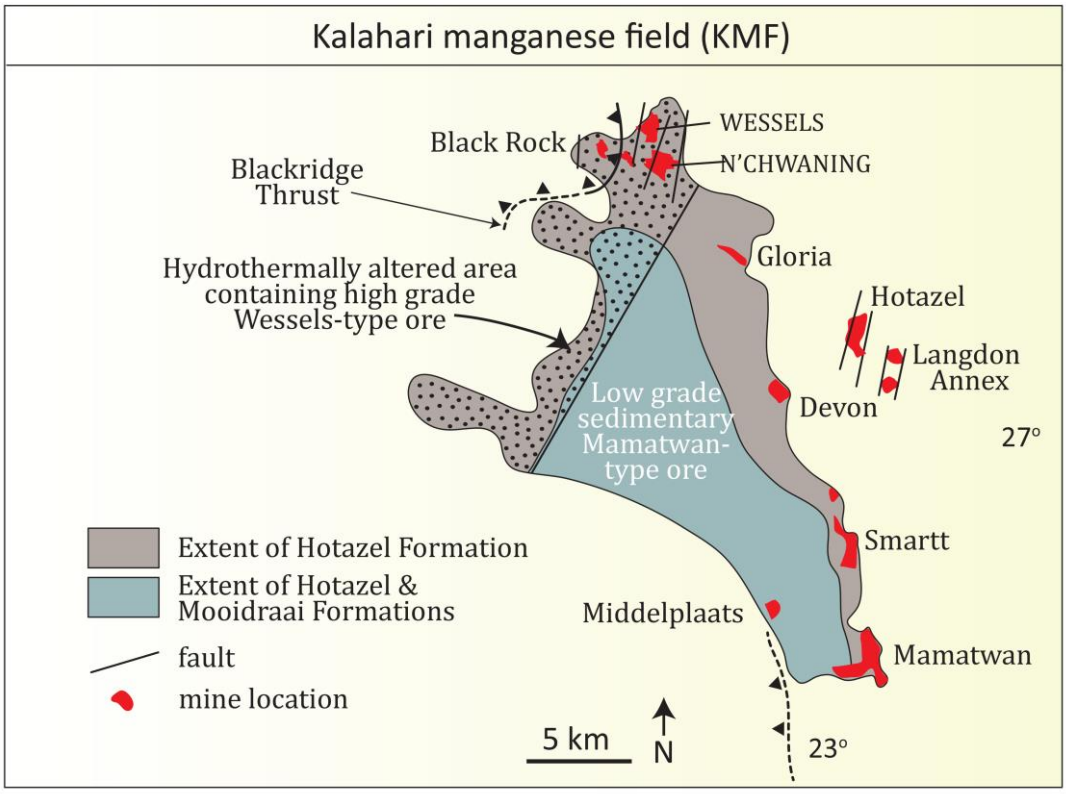

Figure 6. Locality map of the KMF showing the distribution of low- and high-grade Mn ore, localities of major manganese mines, important structural features and geographic extent of lithostratigraphic units overlying the Hotazel Formation. Modified after Tsikos and Moore; 2005.

High grade varieties have resulted from several post-depositional alteration events, of which the most important is the so-called Wessels event (Kleyenstüber; 1985, Beukes et al; 1995, Gutzmer and Beukes; 1995). According to the previous authors, high-grade Wessels-type ore formed through processes of structurally-controlled hydrothermal upgrade from low-grade (Mamatwan-type) ore, restricted to the structurally disturbed northwestern part of the KMF. Systems of normal faults are believed to have acted as feeders for hydrothermal fluids that infiltrated and laterally altered primary ore by leaching of CO_2 from pristine carbonates, removing significant SiO_2 from braunite and reprecipitating manganese as coarse-grained oxides and silicates [hausmannite, bixbyite, braunite II (silica deficient)]. Characteristics zonations and ore-grades next to the faults are also documented in the above publications. The most precise available age for this hydrothermal event is that of gangue sugilite (1049.1 ± 5.9 Ma) from Gnos et al (2003) which ties ore-upgrade to the Namaqua orogeny. Regarding temperatures of the involved fluids there is a lack of agreement depending on the author (from <200 to > 400: Dixon; 1985, Miyano and Beukes; 1987, Lüders

et al; 1999), whereas their ultimate origin remains unknown. From a mineralogical standpoint, the Wessels alteration event is very important, since a profusion of very attractive and rare mineralogical specimens accompanied ore-upgrade processes (Cairncross and Beukes; 2013). These same minerals attest to the alkali and particularly sodic-rich nature of these pervasive and highly saline hydrothermal fluids involved in ore-upgrade (Dixon; 1989, Tsikos et al; 2003, Tsikos and Moore; 2005).

2.3 Overview of alkali metasomatism in the Northern Cape

The recurring theme in the study area is a profusion of alkali minerals and other rare species hosted by different ore-types and associated lithologies. Kalahari Manganese field has received extensive attention with respect to its gangue mineralogical content (Cairncross and Beukes; 2013), probably even more than the ore-upgrade mechanisms responsible for the production of this mineralogical wealth. On the other hand, gangue mineralogy in the Postmasburg Manganese field has only been recently emphasized through studies focusing on alkali-rich ore occurrences and presenting new and uncommon mineral discoveries (Moore et al; 2011, Costin et al; 2015, Fairey et al; 2019). Overall, according to all previous research, it can be stated that mineralogical assemblages of metasomatic nature hosting Na, K, Ba, Ca, Sr and Li are pervasive in diverse ores of the PMF, but stratigraphically restricted in zones of alkali metasomatic enrichment influencing ores and flanking lithologies. Mineral diversity is apparently variable and akin to analogous assemblages from other Mn ores (e.g., Ashley, 1986) is controlled significantly by the chemistry of the hydrothermal fluid but also by the composition of the host rock. Concerning variability, the same goes for alkali abundances, which for the most part remain elusive. A distinct difference exists in the character of the mineralogy, in that PMF alkali metasomatism is chiefly represented by intergranular microscopic crystals associated with the ores, whereas its nature in the KMF is mostly that of coarse crystalline minerals developing in underground fissures and pockets.

Kalahari Manganese field (KMF)

KMF is globally renowned among mineral collectors for its suite of unusual ore and gangue minerals. Some 150 minerals (Cairncross and Beukes, 2013), probably counting up to more than 200 considering all latest studies presenting new species, have been discovered in

the mines from which hydrothermally enriched high-grade ore is being extracted. Comprehensive paragenetic descriptions and lists of minerals can be found in Gutzmer and Beukes; 1996b, Gutzmer and Cairncross; 2002 and Cairncross and Beukes, 2013. The large number of oxides, hydroxides, hydrous silicates (hennomartinite, natrolite, thaumasite, hydroxyl-apophyllite, inesite, oyelite), calc-silicates (usually Mn-bearing) and other silicates (aegirine, banalsite, andradite, datolite, glaucochroite, serandite-pectolite, sugilite, norrishite, tephroite), carbonates (rhodochrosite, kutnohorite, gaudefroyite), sulfates (barite, ettringite, shigaite, sturmanite) and borates is characterized by an abundance in alkali content such as Na, K, Ca, Mg, Ba, Sr, and Li. The remarkable mineralogy has been explained as a result of the fortuitous combination of an original Fe-, Mn- and Ca-rich rock succession and alkaline hydrothermal fluid infiltration (Miyano and Beukes; 1987, Gutzmer and Beukes; 1996b) but it would also seem to be due to physiochemical conditions and evolution of fluids during interactions with the host rock and/or mixing with meteoric water, as well as a consequence of a long-lasting alteration history, probably reaching until recent times as regards phases resulting from supergene processes (Gutzmer et al; 2012, Vafeas et al; 2018).

However, the bulk of the typifying minerals such as the rare sugilite-bearing calc-silicate assemblages are regarded to be cogenetic to manganese ore upgrade (ca. 1.1-1.0 Ga) and their formation has been associated with introduction of Na and K by a hydrothermal fluid which moved along normal faults and lithological boundaries, induced ore-upgrade and precipitated diverse gangue mineralogy during different stages of alteration (Gutzmer and Beukes; 1995, 1996b). Testament to Na introduction is the conspicuous absence of Na-bearing minerals in the Hotazel Formation, except from the local occurrence of the so-considered late diagenetic riebeckite disseminations in BIF chert bands (Tsikos and Moore; 1997). Formation of aegirine in the area has been also studied by Tsikos and Moore (2005) who have postulated that aegirine is developed by the reaction of a highly saline fluid with quartz and hematite constituents of the protolith, in a similar way to other studied environments (Fortey and Michie; 1978).

This unique mining region has produced some of the finest and visually appealing minerals specimens in the world, which overall comprise a kaleidoscope of colour, as epitomized by a selection of specimens sampled during this study (Figure 7). In particular,

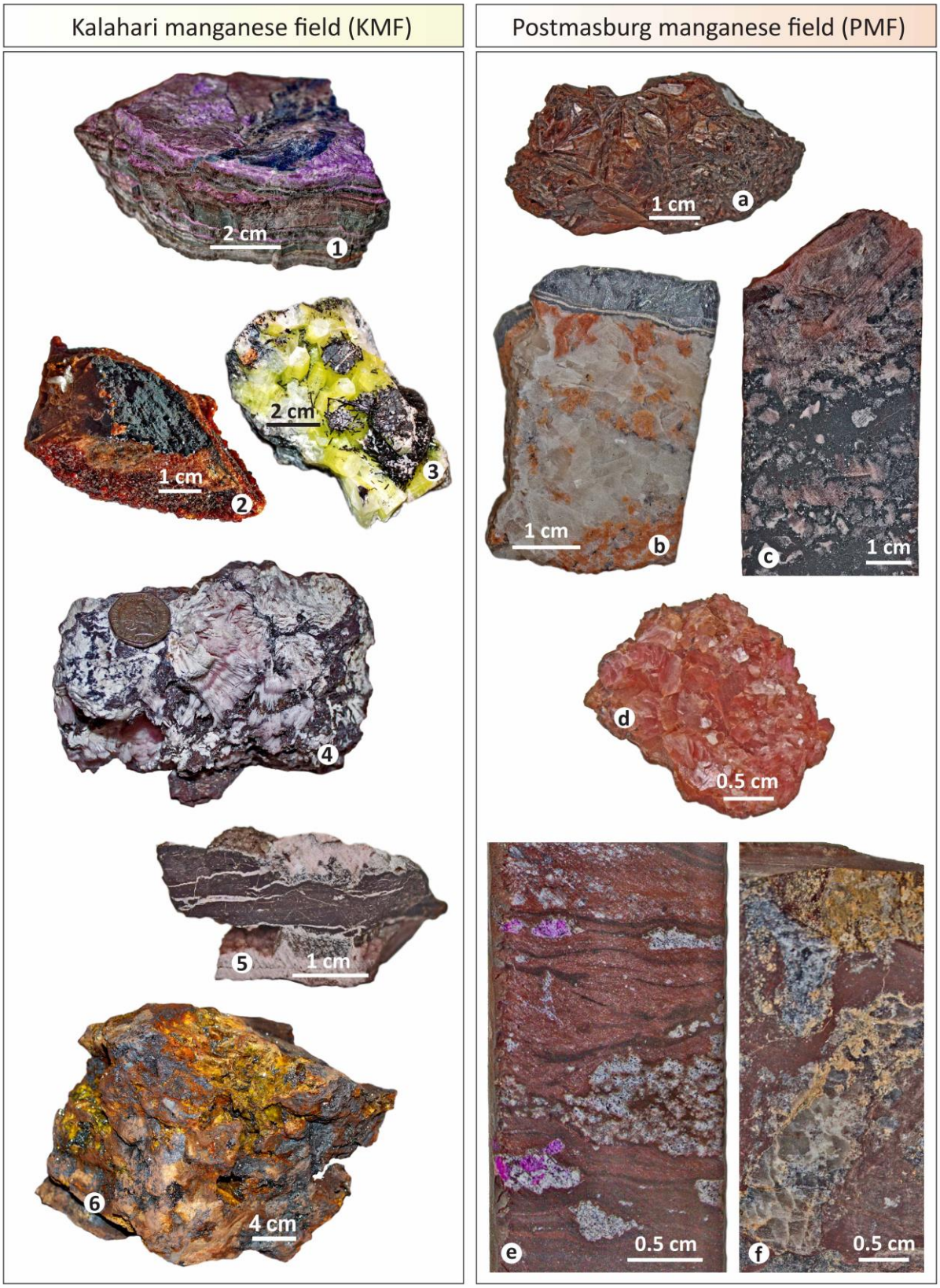

Figure 7. Representative photos of alkali-rich and other gangue mineral assemblages from the KMF and PMF used in this study. (1) Banded sugilite and blue amphibole (2) Red garnet with barite and hematite (3) Ettringite (sulfate)-barite association (4) Kutnohorite and pectolite (calc-silicate) (5) Rhodochrosite showing bedding-parallel feeding veins (6) Pocket comprising sturmanite (sulfate) (a) Laths of diaspore (b) Calcite and k-feldspar coated by specular hematite (c) Rhodochrosite and barite in ferruginized quartzite (d) Prismatic red-pink ephesite (Li-rich mica) (e) Vugs of sugilite and calc-silicates. (f) Armbrusterite (alkali Mn-silicate) and barite vugs

KMF has produced some of the best-known examples of rhodochrosite, ettringite, shigaite, sugilite and hematite among others (Figure 7.1, 7.3). Noteworthily, Wessels and N'Chwaning mines that exploit the high-grade ore from the lowermost mineralized unit, account for 122 and 197 valid mineral species of which tens are type-locality species including the minerals Wesselsite [$SrCuSi_4O_{10}$] and Nchwaningite [$Mn_2^{2+}SiO_3(OH)_2H_2O$] (Cairncross; 2017b, 2020). Gangue assemblages in these mines line cavities in the host rock, fill large cracks and vugs or dissolution hollows referred to as pockets by miners, typically in the Mn ore footwall or hanging wall. However, the existence of abundant feeding channels parallel to sedimentary layering, immediately below mineralization pockets (Figure 7.5), highlights a layer-parallel character to the metasomatism. For example, sugilite, a mineral that has attracted substantial interest over the years as gem material, has been reported to occur as layers or seams that spread laterally along conceivably compositional suitable layers that if grouped together reach lengths of more or less 15 consecutive metres and show thicknesses of ca. 15 centimetres (Dixon; 1985, 1988, Shigley et al; 1987).

Postmasburg Manganese field (PMF)

Alkali minerals in the PMF, such as the common aegirine and albite or the rare Ba-Mn vanadate gamagarite have been reported already since the 40s (de Villiers; 1943b, 1944). However, apart from a handful of silicates (barian muscovite, amesite), Li-bearing minerals (ephesite, lithiophorite), barite and diaspore (de Villiers; 1945, Gutzmer and Beukes; 1996a) (Figure 7a, 7d), there had been no publications mentioning any alkali-bearing or other gangue mineral phase from these ores. Cairncross (2017) refers to the PMF as the poorer relative to its northerly neighbor (KMF), emphasizing only the exceptional occurrences of diaspore and gamagarite from the Glosam, Gloucester and Lohatla mines. The presence of barite, albite and aegirine is barely even mentioned in the ore genetic models of the PMF ores and is broadly attributed to syn- or post-metamorphic fluid flow during the 1.8-.17 Ga Kheis orogeny (Gutzmer and Beukes; 1996a).

However, according to publications of the last decade or so, at least certain localities from the PMF so far, seem to host many more alkali-rich and rare species than previously reported, therefore bearing much more resemblance to the KMF. Specifically, within the

brecciated footwall of conglomeratic iron ore (Wolhaarkop breccia) at Bruce mine (Khumani), a complex assemblage of minerals has been described including aegirine, albite, serandite, barite, witherite, strontianite, norrishite, armbrusterite and the first report of sugilite from the PMF (Moore et al; 2011), overall underlying the presence of Na, K, Ba, Sr and Li in the mineralizing fluids (Figure 7e). Research on the ferromanganese ores and Wolhaarkop breccia from the Western Maremane dome (WMD-Heuningkranz locality) has also uncovered a hydrothermal event introducing similar elements to the rocks and has further documented the occurrence of a multitude of Ba-bearing phases (barite, witherite, barytocalcite, noélbensonite) and rare Mn-rich silicates (e.g., armbrusterite: Figure 7f), sometimes containing As and V (tokyoite, As-rich tokyoite), elements apparently related to the same alkali fluids (Fairey; 2013, 2019, Costin et al; 2015). Comparable geochemical signals recorded from conglomeratic iron ore and underlying ferromanganese ore in drillcores nearby, have pointed to alkali brines being responsible for formation of the Na- (albite, natrolite, serandite) and Ba-rich reported species (barite, hollandite, banalsite, hyalophane) (Bursey; 2018). Moreover, barite, sulfates (gypsum, celestine), tourmaline, berthierine and muscovite have been documented from oxidized BIF and iron ore in the wider Kolomela area and have been attributed to an external fluid source of alkaline nature (Papadopoulos; 2016).

Age constraints on sugilite and k-feldspar from two of the above localities showing alkali enrichments (Bruce mine and Heuningkranz) suggest fluid infiltration taking place at 620 ± 3 Ma and 614 ± 50 Ma respectively (Moore et al; 2011, Fairey et al; 2019), ages that are distinctly different from the alkali assemblages in the KMF. Traditionally, the possibility of hydrothermal activity in the area has not been much regarded, as a consequence of the established view for ancient supergene ore-forming processes. In that sense, specularite (coarse-grained hematite) mineralization in iron ore, being also ubiquitous along with ochre in underground caverns in the farm of Doornfontein, north-west of Postmasburg (Cairncross; 2011), has been identified as a late-stage event (Beukes et al; 2003) and not given much attention. More recently, the ferruginous Gamagara shales overlying ore mineralization have been regarded as hydrothermally altered by fluids rich in fluorine and HFSE elements (Land et al; 2017).

3. Research aims

This research has been prompted from all the foregoing recent studies in the PMF, that focused on exploration drillcore material and revealed a series of evidence supporting hydrothermal fluid flow of unknown origin and timing that is apparently different to the age of hydrothermal alkali gangues in the KMF. These unresolved issues along with the possibility of alkali-rich fluids migrating along regional conduits during major geological events to produce comparable metasomatic assemblages in the two large mineralization districts (e.g., Tsikos and Moore; 2005, Moore et al; 2011), even during different times, demands further attention. The current basin-wide research intends to place emphasis for the first time on the use of isotopes as tracers of fluid sources and pathways and furthermore as means of dating mineralization events. Major aims can be summarized as:

- Investigation of the relationship of alkali metasomatism between Kalahari and Postmasburg Manganese fields
- Characterization of fluid sources, chemistry, temperatures, pathways and clarification of fluid-rock interactions and stages of mineralization
- Setting age constraints on alkali metasomatism from different localities and possibly link the former to existing geological events
- Contribution to our understanding of ore-forming processes in the Northern Cape by elucidating the metallogenic implications of alkali metasomatism in the history of the manganese and iron ores

The latter had not been a primary research question from the inauguration of this project and research was not structured to directly address the possibility of alkali metasomatism being a critical ore formation or upgrade mechanism. However, any new findings towards that direction can be beneficial for future exploitation of the PMF manganese ores which may not be particularly large tonnage or high-grade but in most cases are easily mineable. Lastly, another indirect but important aim of this thesis is to improve our knowledge of fluid circulation in sedimentary basins by investigating what is considered to be a good and intriguing type area for this type of study.

4. Thesis organization

Individual chapters for this thesis have been written in a format that is more suitable for publication. This is in line with the Glasgow university policy. In spite of most chapters being fairly long and comprising extended discussions with exhaustive literature surveys, under the current format, chapters can be adapted for publication with relative ease either by removal of whole sections or by splitting bigger chapters into two parts. For example, chapter 5 can serve as the basis for one manuscript focusing on petrographic/geochemical characteristics and ore genesis and another one centering on the geochronological signals and geotectonic implications.

Each chapter can be read as a standalone. This results in minor overlap with respect to presentation of methodology and regional geological context but repetition in background information can be also evident in separate introduction and discussion sections, since this study is composed of distinct but interlinked parts. Moreover, this thesis has been restructured several times throughout the course of research and data collection and the current manner of presentation, i.e., chapter focus on localities, is regarded as preferable not only for publications but also for driving the narration within a framework of such complex and rich datasets and associated interpretations.

As regards the length of the current thesis, it is partly attributed to the profusion of obtained data (a lot of which were not included, see also Synthesis) and to the requirement for exhaustive analysis, detailed comments and interpretations, arising from the nature and original character of this approach on the research subject. Certain parts comprising literature surveys, such as the review on the Palaeoproterozoic ocean sulfur isotopic composition (chapter 2) or the geotectonic framework of the Kheis and Namaqua orogenies (chapter 5) could have been included in the Appendix but are again regarded as valuable for the reader in their current position. The seven chapter of this thesis are outlined below (next page).

Chapter 1 *Introduction*

Outline: This chapter introduces the concept of alkali metasomatism in the Fe and Mn rocks of the Northern Cape in the context of regional geology and important remaining questions regarding their origin. Thesis outline and major aims are stated.

Chapter 2: *Mineralogical, isotopic (S, Sr) and Ar-Ar geochronological investigation of barite mineralization in the Kalahari and Postmasburg Fe-Mn fields as proxy of regional-scale alkali metasomatism. Insights into the fluid(s) sources, alteration and the Precambrian Ocean.*

Outline: This first big chapter integrates detailed petrological, stable isotope and geochronological data to support a major link between the KMF and PMF. Fluid sources and formation mechanisms of barite in both districts are discussed extensively in terms of isotope fingerprinting and exhaustive comparisons with data from relevant literature. A significant portion of the chapter is dedicated to the sulfur isotopic composition of the Palaeoproterozoic ocean and potential relationship of the Northern Cape barite to the former.

Chapter 3: *New textural, isotopic and in situ $^{40}Ar/^{39}Ar$ age constraints on the origin, nature and duration of Mn-ore hydrothermal enrichment in the Kalahari manganese field, South Africa.*

Outline: This chapter is a revisited study of the hydrothermal ore-upgrade of the KMF (Wessels event) by means of $^{40}Ar/^{39}Ar$ geochronology and stable isotopes on gangue phases. A refinement of the previously documented event is presented, as well as intriguing new findings regarding the origin and evolution of the involved hydrothermal fluids.

Chapter 4: *In situ multiphase $^{40}Ar/^{39}Ar$ dating of sugilite and 5 coexisting minerals reveals fluid-induced ^{40}Ar loss owing to a newly emerging regional Neoproterozoic event that resets gangue associations of the hydrothermally upgraded Kalahari Manganese field, South Africa.*

Outline: This is essentially an $^{40}Ar/^{39}Ar$ geochronological study focusing on a single sample from Wessels which holds a breadth of important information among its six distinct potassium-bearing minerals. Implications on sugilite dating are emphasized and previous ages from the PMF are discussed in the context of a newly proposed tectonic event in the Northern Cape of South Africa.

Chapter 5: *Petrographic, $^{40}Ar/^{39}Ar$ geochronological and stable isotopic evidence for hydrothermal metasomatism of the Postmasburg manganese field during the Namaqua orogeny. Constraints on Fe-Mn mineralization along the western margin of the Kaapvaal Craton, South Africa.*

Outline: Petrographic, stable isotopic and geochronological data on alkali gangue mineralogy hosted by the ferromanganese ores of the Western Maremane dome are used to elucidate the origin, timing, characteristics of alteration fluids and interactions with the host lithologies. A new model emphasizing similarities with Mississippi Valley-type Pb-Zn deposits is presented and the geotectonic framework of the Northern Cape Province is scrutinized in view of new findings.

Chapter 6: *The ephesite-rich ferromanganese ores of Postmasburg Manganese Field. Insights into their origin and metasomatic processes through petrography, O-H isotopes, whole-rock Li geochemistry and geochronology documenting the easternmost arm of the Namaqua orogeny on the Kaapvaal Craton of South Africa.*

Outline: The type-locality ferromanganese ores of the PMF are revisited in this chapter and great focus is placed on the presence and origin of ephesite and Al-rich minerals. Discrepancies with the current models, revealed from ephesite dating, stable and textural evidence, as well as from surveying existing literature are discussed in detail and new data on Li content and mineralogical control in the PMF ores are presented.

Chapter 7: *Synthesis and extensive synopsis*

Outline: This chapter brings together all major findings of this thesis, mainly by presenting all evidence supporting a common epigenetic history between the KMF and PMF and making comparisons between different localities. This chapter also serves as an extensive synopsis of the whole thesis that can be read as a standalone and thus some repetition is expected. Recommendations for future work are also made and a separate second part presents supplementary ideas for future research in the form of preliminary reports of data not previously included in the main body of the thesis.

Appendix is available as a separate pdf file.

5. Workplan

The major challenge presented by the ores of the Northern Cape and particularly that of the PMF, is the extremely fine-grained size and intricately mixed assemblages shown by both ore and alkali minerals, the latter forming the main focus in this study. Another testament to the difficulty of studying these ores is the fact that polished thin sections are virtually opaque under transmitted light, which hinders most attempts for identification of gangue mineral phases, which in most instances are also rare and unique species. Finally, lack of outcrop-scale observations is a common matter in this geological setting and further hampers interpretations.

Combined use of isotopic tools, many of which employed in these ores for the first time, is expected to see through the mineralogical and textural complexities and reveal important information on different aspects of their origin. In view of the fact that small grain size and mixed mineralogy are challenges that cannot be easily circumvented by sample preparation methods for subsequent stable isotopic analysis, SEM/EDS techniques are central at all times, both for identification of potential targets for isotopic investigation (subsampling) as well as interpretations of isotopic results. Conducted lab work for this study comprises light stable isotopes (S, O and H), stable $^{87}Sr/^{86}Sr$ isotopes, $^{40}Ar/^{39}Ar$ laser in situ and laser fusion step-heating dating and lesser whole-rock geochemistry (Figure 8). All of the above challenges are complemented by the lack of relevant stable and radiogenic isotopic results from the study area and in the wider literature in general, at least with respect to the unique mineralogy. The latter renders interpretations difficult and require exhaustive discussions that call for patience from the reader.

Figure 8. Stable isotopic and geochronological tools used in this study, central to which is exhaustive petrographic examination with SEM/EDS techniques, in order to provide a robust context for subsampling and interpretations of isotopic results.

PART ONE

Barite mineralization in the Northern Cape

Chapter 2

Mineralogical, isotopic (S, Sr) and Ar-Ar geochronological investigation of barite mineralization in the Kalahari and Postmasburg Fe-Mn fields as proxy of regional-scale alkali metasomatism. Insights into the fluid(s) sources, alteration and the Precambrian Ocean.

Abstract

Barite is a sparsely developed but omnipresent admixture in various Fe/Mn-rich lithologies of the Northern Cape that has been so far overlooked in ore genetic and mineralogical studies. Coarse-grained occurrences in the Kalahari Manganese field (KMF) have been regarded as a gangue product of the ca. 1.1 Ga hydrothermal Mn-ore upgrade, whereas lenses and veins in the Postmasburg Manganese field (PMF) have been tentatively related to syn- or post-ore metamorphic fluid flow between 1.9 and 1.8 Ga and more recently to Neoproterozoic (ca. 600 Ma) metasomatic processes. Likewise, origin and timing of any hydrothermal fluid flow event in the area is largely unknown, owing to continuous emphasis on ancient supergene ore genetic models for the PMF deposits and lack of focus on existing hydrothermal gangue mineralogy and application of stable isotopic and geochronological techniques. Extensive regional-scale investigation validates the consistent association of barite with alkali-rich assemblages, documents the widespread occurrence of texturally diverse and replacive barite in different ore lithologies and reveals a very homogeneous sulfur isotopic signature ($\delta^{34}S$=24.9 ± 2.5‰, n=93) from different ore-types across the entire metallogenic province. Furthermore, $^{40}Ar/^{39}Ar$ age similarity between micas syngenetic with barite (1137 ± 2, 1129 ± 4 and 1067 ± 8 Ma, 2σ), corroborate large-scale synchronous hydrothermal fluid flow, making this the first study to clearly demonstrate a genetic link between the previously unrelated KMF and PMF with respect to epigenetic metasomatic processes of common origin, being further related to the 1.2-1.0 tectonic event of the Namaqua orogeny. Highly radiogenic $^{87}Sr/^{86}Sr$ values of barite and carbonates (0.71056-

0.73818, avg. = 0.7187 ± 0.0062, n=35) support mixed Ba/Sr derivation, mainly from the Olifantshoek sediments but also from the Campbellrand stratigraphy and possibly granitoids and other lithologies of the Namaqua metamorphic belt. Most barite formed by mixing of these Sr/Ba-rich fluids with sulfate derived from a seawater source, which promotes previous indications for ca. 2.5 Ga extensive evaporite beds in the Campbellrand platform. An in-depth survey of the sulfur isotopic seawater evolution during the Archean-Palaeoproterozoic and a comprehensive revised sulfur isotopic age curve, suggest that epigenetic barite in the Northern Cape serves as a palaeo-environmental indicator for bacterial sulfate reduction occurring in a more restricted basin, during a complex transition period with fluctuations in atmospheric oxygen levels and in oxidative sulfur cycle. Therefore, $\delta^{34}S$ values cannot be directly extrapolated to the contemporaneous Archean Ocean. Ore-forming role of hydrothermal activity in the PMF is still largely unexplored but our new observations for regional hydrothermal activity do not fit in the current models for metallogenesis and further highlight that a critical part of the evolution of the Fe/Mn ores is linked to processes that may have acted as mechanisms of ore-enrichment.

1.Introduction

Barite ($BaSO_4$) is a mineral frequently associated with hydrothermal systems of diverse geological settings and metalliferous deposits. Its chemical isotopic composition and widespread occurrence in magmatic, metamorphic, sedimentary basinal fluids and oceanic water have allowed its extensive study with a view to establishing the nature and sources of fluids (Johnson et al; 2004, Kontak et al; 2006), discerning mineralization processes (Staude et al; 2011) and reconstructing tectonic settings and ore genetic models (Lange et al; 1983, Maynard et al; 1995).

From an isotopic point of view, barite is particularly well-suited for tracer studies, since its $\delta^{34}S$ isotopic composition can be invaluable in the identification of sulfate sources, while significant amounts of Sr incorporated in its crystal lattice coupled with negligible rubidium content (Hofmann and Baumann; 1984), have made possible the use of $^{87}Sr/^{86}Sr$ barite ratios as a measure of the strontium isotopic composition of the mineralizing fluids. The great potential of barite in illuminating mineralization processes is evident and of

particular importance in non-magmatic systems, such as in Mississippi Valley-type (MVT) Pb-Zn deposits (Pfaff et al; 2010), epigenetic vein and karst barite deposits (Valenza et al; 2000), stratiform, and other types (Fe-Ba, F-Ba) of fault-controlled vein mineralization (Kesler and Jones; 1980, Barbieri et al; 1984), where often other isotopic tracer techniques are limited or laborious. However, this potential has not been yet explored in Precambrian iron and manganese mineralization, which has been associated with epigenetic hydrothermal activity (Gnos et al; 2003, Blake et al; 2011, Beukes et al; 2016).

Barite in the Northern Cape of South Africa is mostly known from Kalahari Manganese field (KMF), where it forms part of the staggering gangue mineralogy accompanying the hydrothermal upgrade of the giant primary sedimentary manganese deposits (Gutzmer and Beukes; 1996b). Fluids responsible for its deposition during ore-enrichment are suggested to have been saline and alkali-bearing (Lüders et al; 1999) but their origin remains unknown. In the Postmasburg Fe and Mn ores, stretching as far as 140 km to the south of the KMF, the occurrence of barite is underexamined. This extends to ore-zone gangue mineralogy which is regarded to be poorer to that seen in KMF (Cairncross; 2017) and largely remains elusive due to its complex and fine-grained nature. Limited earlier reports of barite veins and lenses generally cross-cutting lithologies or replacing components of the ores, attribute it to syn- or post-metamorphic hydrothermal fluid flow (De Villiers; 1960, Gutzmer and Beukes; 1996a). More recent studies focusing on hydrothermal activity affecting the ores, document its association with alkali (Na, K, Ca, Ba, Li) enrichments and assign it to a late-alteration stage (Moore et al; 2011, Fairey et al; 2019). From the above is unclear if barite represents one or more, related or not mineralization events in the wider region.

Here, we present a systematic and regional comparative petrographic study of barite from variable lithologies and apply S and Sr geochemical fingerprinting to deduce the possible sources of its components, mechanisms of formation and role in the broader geological evolution of mineralization in the area. We further attempt to get age constraints on syngenetic micas by means of in situ $^{40}Ar/^{39}Ar$ dating to further assist comparisons between different deposits from both mineralization districts (KMF and PMF) and illuminate the origin of hydrothermal activity. An exceptional correlation between isotopic and geochronological

data from the studied localities establishes a link between the two ore fields and calls for similar isotope reservoirs and comparable depositional mechanisms during a shared large-scale event. All of the former are discussed in depth, with particular emphasis placed on local distinctive paragenetic and isotopic features, as wells as on the possible implications of barite mineralization in the ore genetic models and evolution of the ancient ocean.

2. Geological framework

All studied barite occurrences lie within two separate metallogenic provinces situated in the Griqualand West basin, the Postmasburg manganese field (PMF) in the south and the Kalahari manganese filed in the north (KMF) (Figure 1A-1C). These provinces delineate the western margin of the Kaapvaal Craton and host either giant manganese ore bodies (KMF) or significant iron reserves and lesser manganese deposits (PMF). All significant ore reserves are hosted by a several km thick sequence of Palaeoproterozoic rocks that belong to the Transvaal Supergroup (Ghaap and Postmasburg Groups), a dominantly sedimentary succession, mostly comprising shallow marine carbonates and iron-formation and lesser clastic rocks and andesitic lavas (Tsikos and Moore; 1997). The stratigraphy of the Transvaal is truncated by a regional unconformity and is then overlain by the Olifantshoek Supergroup, of which the basal Mapedi unit comprises shales, red beds and quartzites (Beukes et al; 2003). Both the Transvaal and Olifantshoek sequences have undergone thin-skinned deformation and displacement of lithological units within the sequences during the 1.9-18 Ga Kheis and 1.2-1.0 Ga Namaqua orogeny (Cornell et al; 1998, Beukes and Smith 1987).

The iron and manganese-rich entities of the PMF are believed to have been formed largely by laterization during the development of the Transvaal-Olifantshoek unconformity (Gutzmer and Beukes; 1996a, Beukes et al; 2003). Pivotal to the enrichment processes are regarded to have been a local anticline (Maremane dome) and palaeo-sinkholes/karstic lakes in which slumped iron-formation (Asbestos Hills BIF) was upgraded into high-grade (> 65 wt. % Fe) hematite ore and dissolution of Fe/Mn carbonates resulted into residual ore accumulation of a siliceous braunite-rich (Eastern belt) and ferruginous braunite-hematite-bixbyite (Western belt) Mn ore-type (Figure 1B). Mixed types and recently reported hydrothermal overprints involving alkali minerals have highlighted the need for revision of

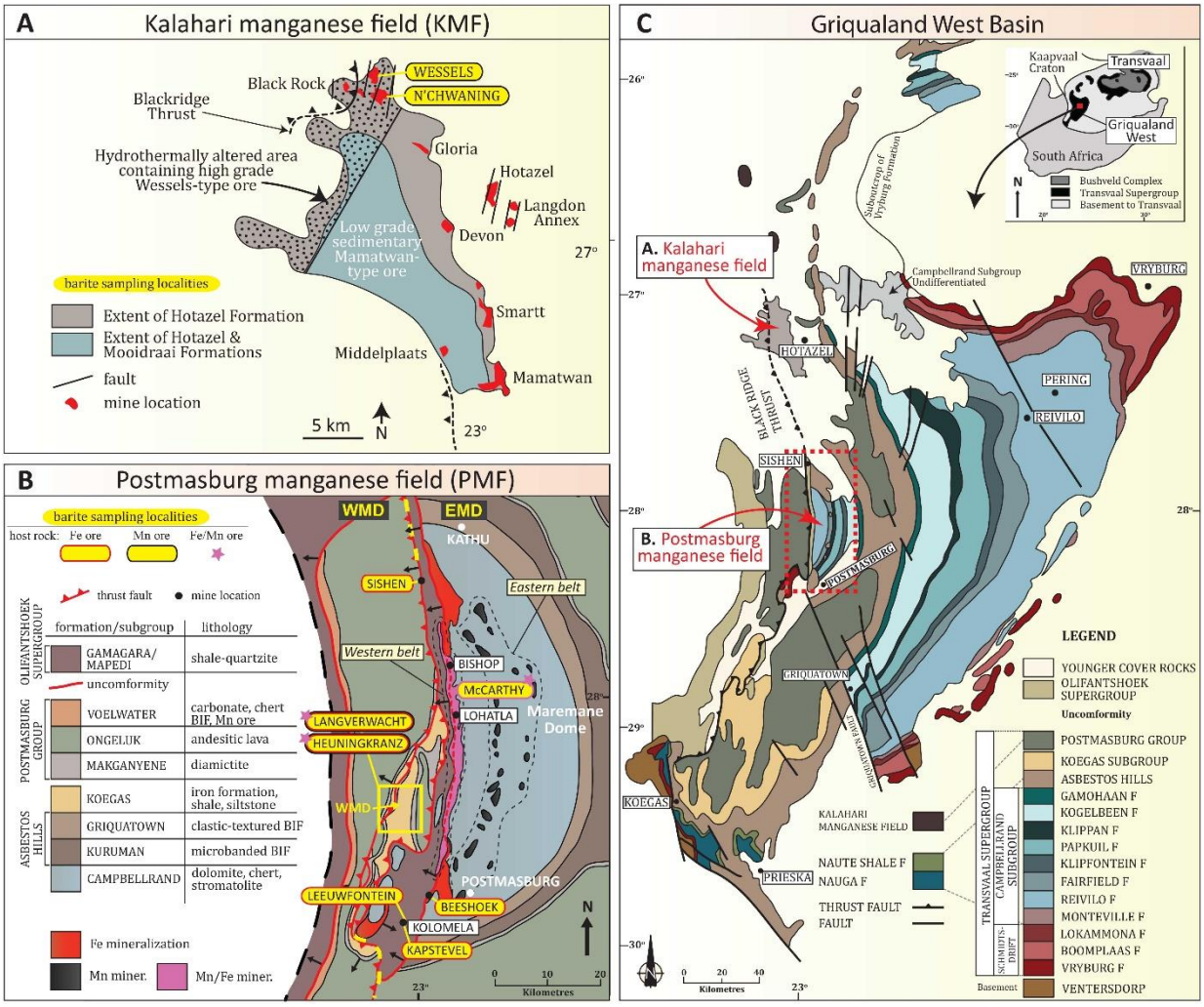

Figure 2. Map of the Griqualand West basin of the Northern Cape (C), distribution of major lithostratigraphic units and regional structures and approximate extent of the Kalahari (KMF) and Postmasburg (PMF) Manganese fields. (A & B) Enlarged views of the two ore fields showing distribution of major Fe and Mn mines, their crude classification into Eastern/Western belt and Eastern/Western Maremane dome (see text) and barite sampling localities for this study (yellow). Maps modified after Tsikos and Moore; 2005, Moore et al; 2001 and Cairncross and Beukes; 2013.

the former classification of the PMF manganese ores (Moore et al; 2011, Costin et al; 2015, Fairey et al; 2019). Here, a geographical division of the ores into the Eastern Maremane dome (EMD-type locality) and Western Maremane dome (WMD), the latter comprising ores anomalously-rich in alkalis and closer to the Blackridge Thrust system, is preferred. Being the first to focus on gangue mineralogy, the previous researchers report barite vugs, inclusions and replacement textures associated with rare Ba-silicates, Ba-feldspars, Ba-carbonates and generally sodic calc-silicates assemblages including sugilite, a rare Li-bearing species found abundantly in the KMF. Age constraints on the broader alkali metasomatism suggest a Neoproterozoic (ca. 600 Ma) age, which although not directly addressed, is also presumed for

barite. Earlier mentions of barite in the PMF as veins or lenses occurring along the contact of dolomites with the manganese orebodies have been tentatively attributed to Kheis (1.9-1.8 Ga) orogeny (Gutzmer and Beukes; 1996a). Much of the commercial iron ores in the Western belt of the EMD derive from the so-called Doornfontein conglomerate, a considered clastic detrital deposit, formed by erosion and reworking of enriched BIF during a transgressive period that was followed by deposition of the Olifantshoek Supergroup (Beukes; 1983). Conglomeratic iron ore, rich in alkalis and being stratigraphically equivalent to the Doornfontein Member, also occurs locally in the WMD and overlies ferromanganese deposits (Bursey; 2018). However, this formation may be absent in drillcores displaying thick, oxidized and hydrothermally altered iron-formation and associated iron ore, followed upwards by the Gamagara/Mapedi shales of the Olifantshoek Supergroup (Papadopoulos; 2016).

Manganese mineralization in the KMF lies in close geographic vicinity, after a hiatus of about 45 km (Figure 1C) and is hosted by the Voëlwater Subgroup (iron-formation, carbonates) and consists of three sedimentary manganese ore beds intercalated with iron-formation of the Hotazel Formation (Tsikos and Moore; 1997). Structurally-controlled hydrothermal enrichment of the northern part of the KMF (Figure 1A) during the 1.2-1.0 Ga Namaqua orogeny (Beukes et al; 2016) has led to the development of a very high-grade ore (45-60 wt. % Mn) and a profusion of gangue minerals rich in alkali elements. Among these assemblages, coarse-grained barite, Sr-barite and barian celestine usually crystallizes together with hematite, garnet, Mn oxides, carbonates and uncommon borates and sulfates (Gutzmer and Beukes; 1996b). Barite is very seldom directly addressed, while a lot of barite associations involving sulfates (for e.g., sturmanite, ettringite) and gaudefroyite are believed to post-date formation of the oxides in the ore.

3. Sampling and analytical techniques

More than a hundred samples containing barite from both ore districts were petrographically and isotopically examined in this study. Barite abundance in the area is variable, generally low and difficult to identify. Therefore, sampling was informed by previously studied and new drillcores showing anomalously high barium (and/or other alkalis) concentrations and encompassing a range of iron- and manganese-rich end-members.

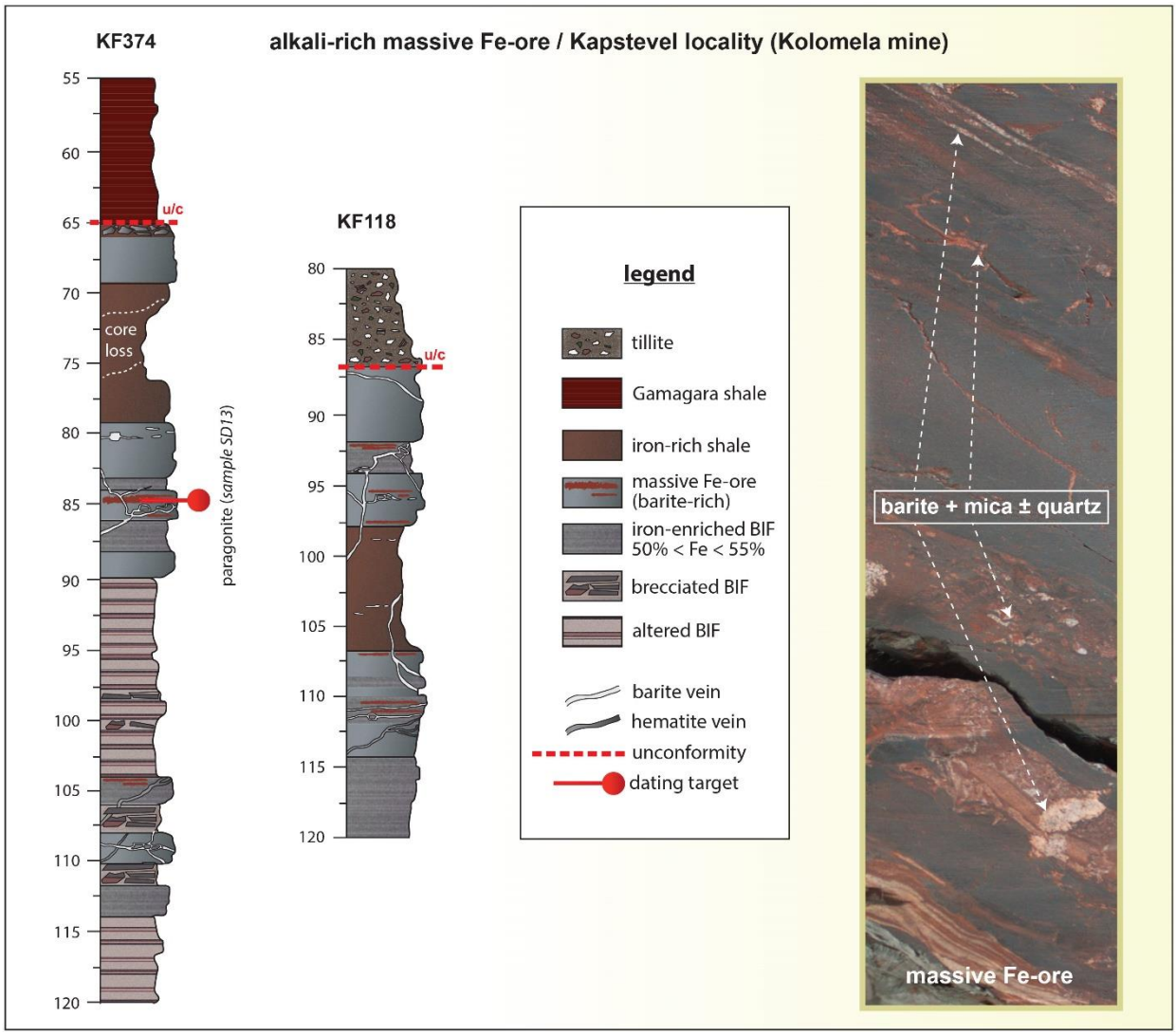

Figure 2A. Stratigraphic logs of drill cores from the large (159.3 Mt) Kolomela mine (Kapstevel locality), which constitutes a major sampling site for barite in this study (left) and representative iron ore sample with interlayered barite-mica horizons. Note the close relationship between shales and iron ore.

Regarding the PMF, samples derive primarily from nine drill cores, three from the Kapstevel locality (KF 118, KF 138 and KF 374: Kolomela mine) and the other six (SLT015, SLT017, SLT018, SLG02B, SLG537 and SLG017A) from the Heuningkranz and Langverwacht localities of the WMD (Figure 1B). Details regarding drillcores and sample depths can be found in the Appendix II, along with barite isotopic results (see also chapter 5 later on for drillcore stratigraphy). In addition, coarse barite crystal aggregates and veins hosted by Fe- and Mn-ore from another four localities (Beeshoek, Leeuwfontein, McCarthy, Sishen) were included in the sample suite. Among the selected PMF localities in which barite is relatively prominent, Kapstevel displays the higher abundances and the more easily recognizable barite at the hand specimen scale. Two representative drillcores from the former studied locality (Figure 2A),

comprise intercalations of altered and brecciated BIF, iron-enriched (50-55 wt. % Fe) BIF, massive Na/Ba-rich iron ore and brown ferruginous shales, unconformable overlain by the Gamagara shales of the Olifantshoek Supergroup or green to light brown tillite with BIF and igneous rock fragments. Barite fracture-fillings, pods and veins are particularly conspicuous in the iron-enriched intersections, the latter seen intercalated with both shale and oxidized BIF material. Veins consisting of specular hematite also traverse the unit. Reddish or yellowish-white, silicate- and barite-rich bedding-parallel layers can be commonly observed in the iron ore (Figure 2A, right side) and are usually interconnected with fractures of similar appearance, discordant to bedding.

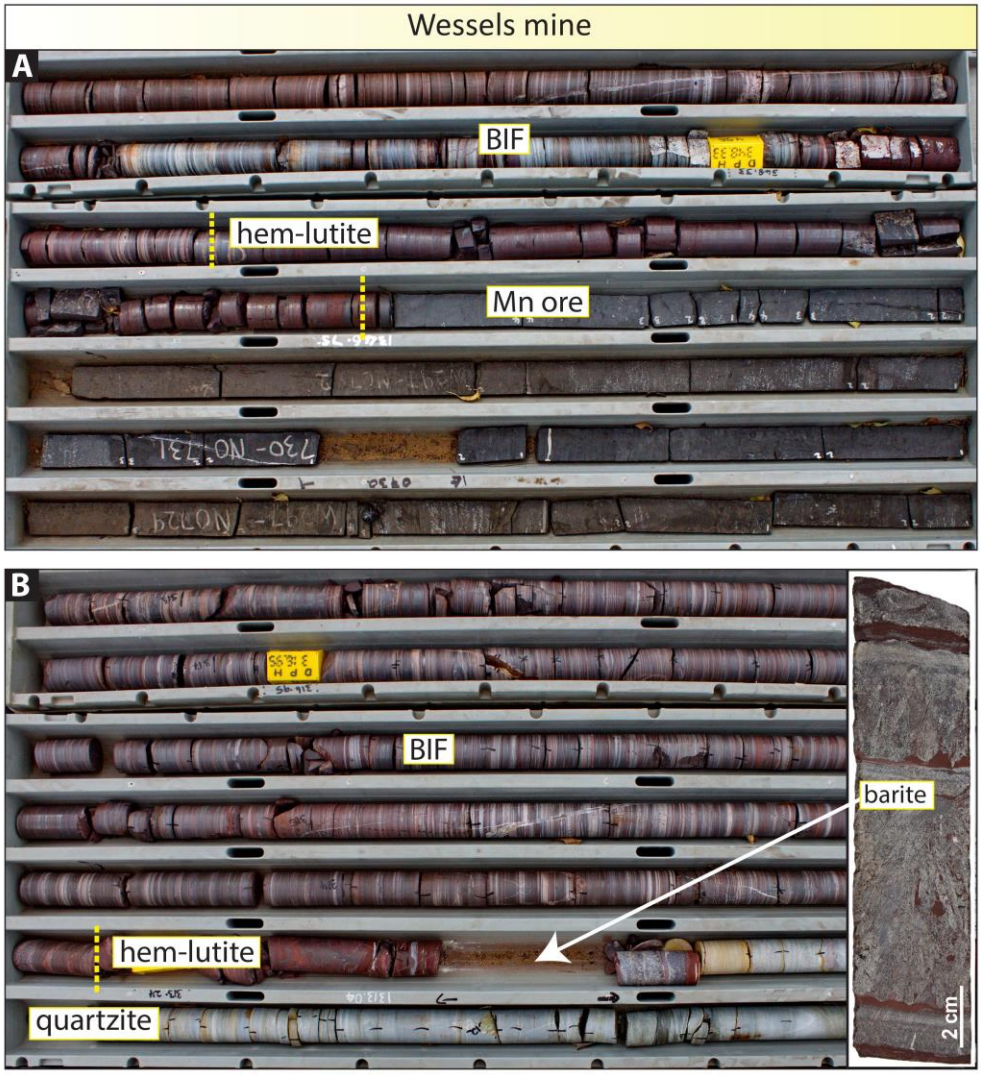

Figure 3. Drillcores W297 (A) and W290 (B) from Wessels mine sampled across anomalously high barium/strontium horizons in the Mn ore. Note the coarse-grained bladed barite from the unconformable contact of Hotazel with Olifantshoek (B).

With respect to the KMF, two drillcores from the Wessels mine (W290 and W297) and one from the N'chwaning III mine (SA8G, western domain) were sampled across their anomalously high-barium/strontium (weight percent-rich) horizons. The above drillcores exhibit the typical stratigraphy of the enriched Hotazel Formation i.e., succeeding hematite lutite-Mn ore(high-grade)-BIF cycles/units and sampled barite is hosted by Mn ore. Additionally, a coarse-grained barite sample from the unconformable contact between hematite lutite of the second unit and the overlying quartzite (Olifantshoek) was collected (Figure 2B). A significant number of aesthetic mineral specimens (n=17) from pockets of mineralization, comprising coarse-grained barite associations with garnet, hematite, carbonates, etc. derive exclusively from N'Chwaning (N'Chwaning I, north locality and N'Chwaning II and III) and were provided or obtained by local mining geologists and collectors.

Petrographic observations were made using both reflected and transmitted light microscopy, as well as scanning electron microscopy (SEM)-EDS techniques at the facilities of Glasgow and Durham universities, housing a Quanta 200F Environmental SEM with EDAX microanalysis and a Hitachi SU-70 FEG SEM respectively. More details available in Appendix III. Clean material being for the most part barite and occurring in vugs, veins and fracture-fillings was separated by micro-drilling from previously well-studied samples. All alteration minerals and specifically in the PMF, are extremely fine-grained and intergrown, so it was not always feasible to physically separate barite from co-existing phases. In a few cases, barite powder extracted from several vugs of the same sample was mixed into one powder, thus representing a sample average. Since silicate contamination in most samples was minimal and does not affect sulfur isotope measurements. Therefore, HCl acid rinse was employed to remove any readily soluble carbonates or exchangeable cations in potentially admixed silicates only for the samples that were further analysed for their $^{87}Sr/^{86}Sr$ isotopic composition, which were also that of highest purity.

Standard techniques (Appendix II) for sulfate isotopic analysis (Coleman and Moore; 1978) were used. Liberated SO_2 gases were analysed on a VG Isotech SIRA II mass spectrometer at SUERC, and standard corrections were applied to raw $\delta^{66}SO2$ values to obtain $\delta^{34}S$ values. Data are reported in $\delta^{34}S$ notation as per mil (‰) variations from the Vienna

Diablo Troilite (V-CDT) standard. Two barite standards, NBS127 and the internal BIS were used and reproducibility was around ±0.3‰ during the process. Sr isolation was done using ion exchange chromatography inside clean lab facilities and isotopes were measured on a thermal ionization mass spectrometer (TIMS) at SUERC using rhenium (Re) filaments (Appendix II). In situ $^{40}Ar/^{39}Ar$ analyses were conducted via laser ablation using a New Wave Research Laser UP-213 A1/FB and gas purifications and measurements were made with a Helix SFT (Thermo Scientific) multi-collector noble gas mass spectrometer at the NERC Argon Isotope Facility at SUERC. For more details and full $^{40}Ar/^{39}Ar$ results the reader is referred to Appendix I.

4. Results

4.1 Petrography

Barite samples were investigated in great detail with respect to their textural attributes, principal paragenetic associations and distinctive features of host lithologies. In the following sections, emphasis is placed upon the previously unexplored lithologies of the Postmasburg manganese field containing the target mineral (massive Fe-ore, conglomeratic Fe-ore) as well as on underexamined drillcore material from the Kalahari manganese field comprising Ba- and Sr-rich high-grade Mn ore. The occurrence of barite in the different

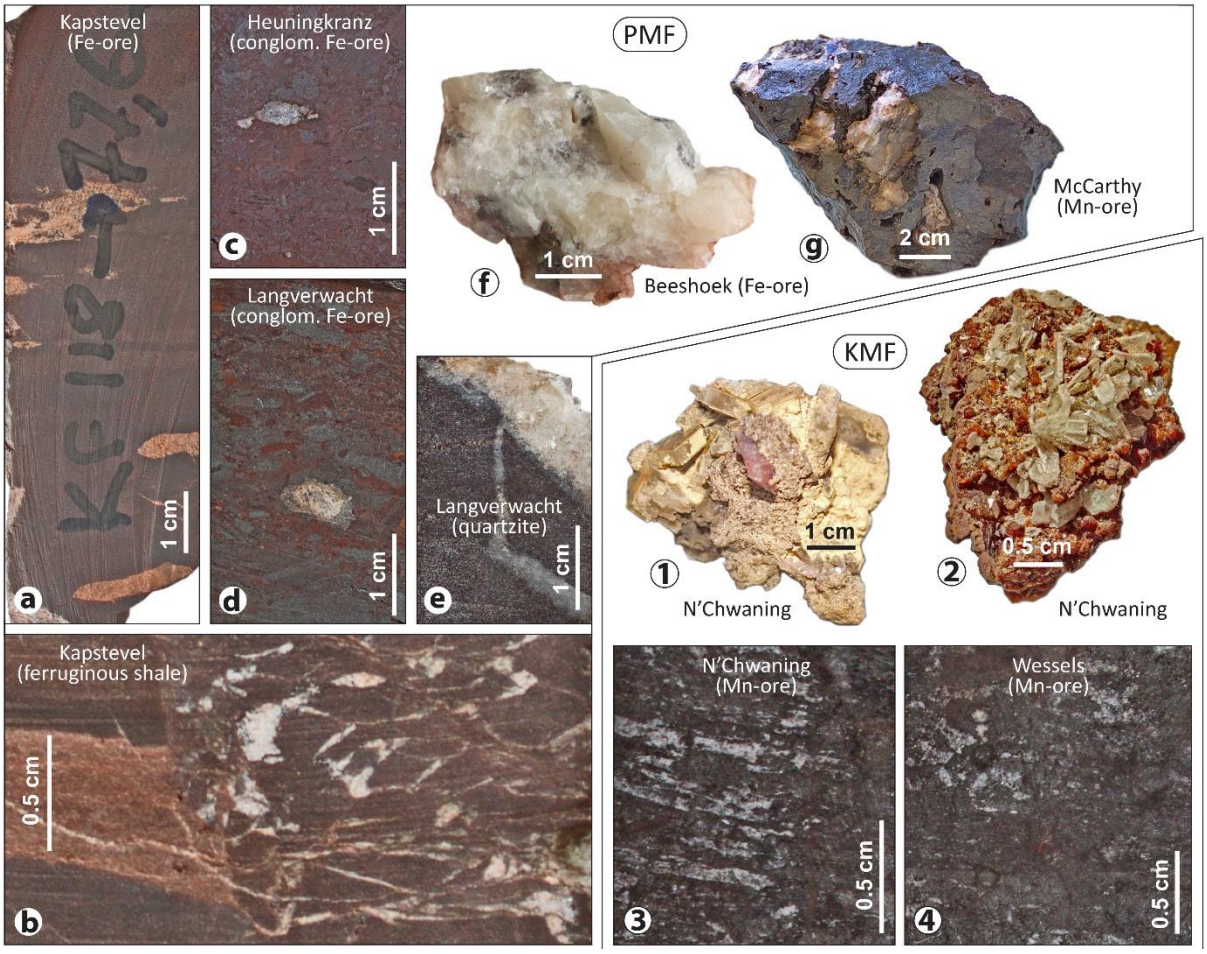

Figure 3. Distinct barite occurrences in the Postmasburg manganese field include: (a) occlusion of open-space (veins, vugs and lenses) in massive Fe-ore, (b) breccia cement and vein stockwork in ferruginous shaley material intercalated with Fe-ore, (c & d) lensoidal vugs in conglomeratic Fe-ore with evidence of hydrothermal reworking, (e) veins in quartzite (Olifantshoek Supergroup), (f) sparry crystals in Fe-ore and (g) tabular aggregates filling voids in Mn-ore (Wolhaarkop). Barite in the Kalahari manganese field has been generally regarded as a widespread and well crystallized phase and examples in this study comprise: (1 & 2) coarse platy crystals associated with rhodochrosite or andradite and (3 & 4) barite-rich associations developing interstitially to upgraded Mn-ore from drill core samples.

manganese ores types of the wider Postmasburg area is of equal importance and is being thoroughly described later on in this study together with the profusion of other alkali gangue species in these deposits. Selected features of the host lithologies merit a brief description because of the current lack of characterization in the literature.

Barite is undoubtedly the most abundant gangue in certain ore deposits (for e.g., Kapstevel, Kolomela mine) where it is macroscopically discernable as white to ochre-coloured open-space fillings (veins, pods, vugs) contrasting with the dark metallic surrounding matrix (Figure 3a). Its distribution in the previous locality extends to intercalated ''shaley'' material which shows textures of banding interruption and brecciation by a dense stockwork of minute barite veins (Figure 3b). Most notable are the small lensoidal barite-bearing vugs in reworked conglomeratic Fe-ore whereas in the case of overlying quartzites barite is mostly restricted to cross-cutting veins (Figure 3c-e). In rare instances, barite is well crystallized and occurs as large (up to 3 cm) crystals, sparry or intergrown with hematite and hosted by either Fe- or Mn-ore (Figure 3f, 3g). Studied samples from the Kalahari manganese field include both the typical pockets of tabular and euhedral platy barite aggregates which are usually intergrown with garnet, hematite or rhodochrosite and the comparatively more sparse and erratic occurrences as an accessory phase within the enriched Mn ore beds (Figure 3 / 1-4).

Massive Fe-ore (BIF- and shale-hosted)

Barite is very prolific within the studied drillcores from Kolomela mine (Figure 2), where it is seen concentrated along cracks, fractures, irregularly-shaped infills and veins that in many instances follow faint bedding planes but also run discordant to the weakly laminated ore texture which is subordinate in relation to the prevalent massive ore appearance. The above-described characteristics emphasize the epigenetic nature of the barite mineralization in this deposit. Barite here is part of a simple paragenetic association comprising mica of the muscovite-paragonite series, hematite and sporadically apatite. The micas cover almost the whole compositional range between the two end-members with the highest concentrations being 5.9 wt.% and 10.4 for Na_2O and K_2O respectively, although most of the analysed grains can be regarded as paragonite (Na_2O = 3.8 ± 1.3, n =9). Despite being predominantly platy crystalline, well-developed prismatic laths of paragonite is the norm in large barite-filled vugs

(Figure 4A). Where present, apatite mostly coats the outer rims of these vugs (Figure 4B). Sparse aggregates of kaolinite can be also found within minute veins (300-500 µm thickness) or in association with barite and specularite (coarse-grained hematite) infills which suggests that kaolinite is authigenic and has precipitated from the same alteration solutions that formed barite.

A series of textural observations regarding barite and paragonite distribution in the ore matrix illustrate the scale of barium metasomatism and the reactions that take place

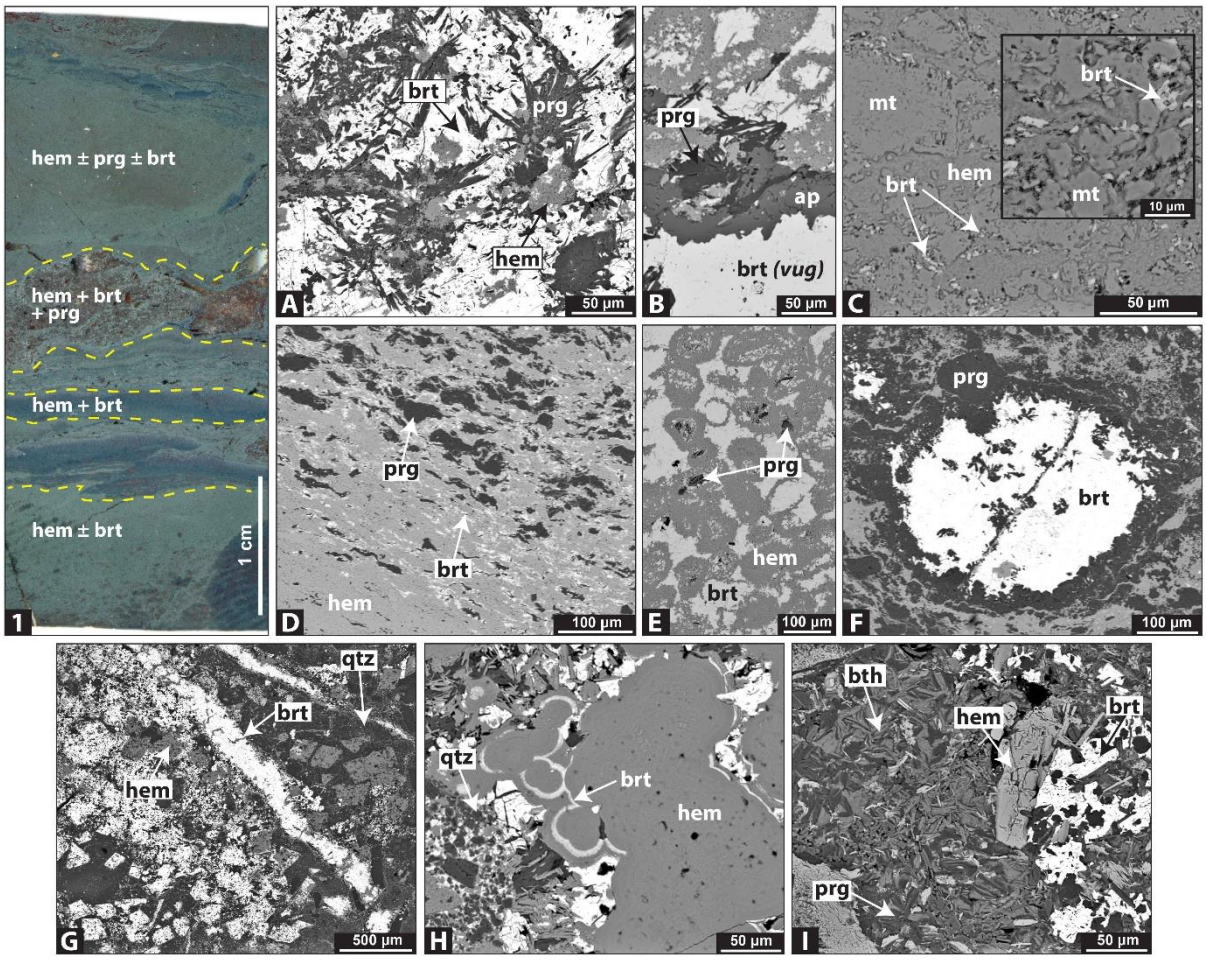

Figure 4. (1) Thin section scan of massive ore from Kapstevel. Barite and paragonite are not restricted to veins and vugs but occur as pore-filling cement in the ore matrix which displays various textures and emphasizes permeability during metasomatism. Back scattered electron (BSE) images. (A & B) Prismatic paragonite arranged in radiating arrays inside barite-vug with rims lined by apatite. (C) Microscopic barite disseminated in hematite-martite matrix. (D) Layering of metasomatic gangues in the ore matrix. (E) Relict metasomatized ooids reminiscent of the pristine Griquatown iron-formation. (F) Zoned barite-paragonite texture formed during alteration. (G) Carbonates of BIF-origin pseudomorphically replaced by hematite and barite. (H) Colloform hematite-barite textures in altered iron-formation. (I) Lath-like authigenic berthierine in ferruginous shale matrix associated with paragonite and barite. ap = apatite, brt = barite, bth = berthierine, hem = hematite, mt = martite, prg = paragonite, qtz =quartz

between the fluid(s) and host rock. As displayed in Figure 4.1, gangue mineralogy impregnates the iron-rich matrix, where it precipitates in various abundances, textures and habits interstitially to hematite. The former evidently supports that the ore matrix is permeable during the metasomatic processes, showing both primary and secondary fracture-related porosity. In particular, the ore matrix typically displays finely disseminated microscopic (2-10 µm) barite crystals that seem to occupy pore space in-between martite (former magnetite) grains and aggregates attesting to the BIF-origin of the Fe-ore (Figure 4C). Another common texture is that of preferred-orientation of both barite and paragonite on the micro-scale (Figure 4D), apparently being restricted to matrix with elevated mica concentrations.

Indications of early sedimentary-diagenetic textures having been preserved during metasomatic reactions are also evident throughout the ore zone. One such relict texture is that of hematite ooids (50-100 µm) that possibly have their origin in the clastic Griquatown iron-formation. In particular, the former are seen being overprinted by hematite or barite and their porous cores are commonly occupied by barite, paragonite or apatite (Figure 4E). Analogous textures being elliptical in shape but usually of larger size (up to 500 µm) exhibit cores of barite and rims of paragonite (Figure 4F). Their origin is obscure but they could represent reworked ooids or microconcretions formed in the weathering profile. Pseudomorphs after former carbonates are conspicuous in relict chert bands which are in turn hosted by altered BIF intercalated with the ore. These rhombohedral grains have been replaced by both hematite and barite (Figure 4G), the latter probably representing an event of later origin. Remarkable collomorphous textures comprising hematite and barite were also noted in the altered BIF (Figure 4H). These are associated with recrystallized platy hematite and a variety of micro-quartz indicating silica dissolution and transportation by the metasomatic fluids. Recrystallization of hematite is evident in the vicinity of infiltrating barite, where areas of significant porosity exhibit randomly oriented hematite plates of considerably greater size (100-500 µm) in comparison to the matrix (5-25 µm).

Berthierine $[(Fe^{2+},Fe^{3+},Al)_3(Si,Al)_2O_5(OH)_4]$ is seldom found as laths or blocky grains within the barite paragenesis but was seen more extensively in the studied ferruginous shale matrix, which also contains disseminated microscopic rutile, ilmenite, barite and apatite. The

high Fe content of this berthierine compares well with previously reported compositions that approached the idealized Fe-berthierine composition from the wider Kolomela region (Papadopoulos et al; 2022, in prep). Its coexistence with paragonite suggests an authigenic origin.

Conglomeratic Fe-ore

Descriptions for this clastic-type of iron ore are based on samples deriving from the western part of the Maremane dome (WMD) (Figure 1), showing however similar stratigraphic position to the lithology referred to as Doornfontein conglomerate in the literature, i.e., between underlying Fe- or Mn-mineralization and the cover of Olifantshoek clastic sediments. This clast-supported rock consists mainly of hematite-rich clasts which occasionally display prominent banding, possibly indicative of banded iron-formation (BIF) origin. These ferruginised BIF-clasts vary in length from less than one to several cm, are elongated, angular to sub-rounded and often fractured from later reworking. The presence of generally more rounded and considerably smaller hematite clasts (500 μm-0.25 cm) with no conspicuous banding, marks this iron-rich lithology as a conglomerate, however of very poorly sorted nature due to the abundance of angular clasts. It is worth noting that whatever the transportation distance for the different clasts, all of them show high Fe content despite of the textural differences and sizes of hematite and the presence or not of other minerals within the clasts.

Barite is more copious in the matrix where it is found in two distinct mineralogical associations: (a) barite + albite + Mn-carbonates + armbrusterite + braunite and (b) barite + muscovite ± apatite. Variations of the first paragenesis occur as cementing material (Figure 5.1), instead of mixtures of crystalline muscovite with microplaty hematite, which are the dominant species in the matrix. The alkali mineralogy is also seen being accommodated by a number of clasts (Figure 5.2), either in microfractures or layers generally being length parallel to the banding of BIF-clasts. Barite of the first assemblage is chiefly associated with broadly euhedral albite inside which forms microscopic (<10 μm) inclusions. The entire paragenesis is loosely zoned, with the Mn-silicate armbrusterite and Mn-carbonates generally forming in the outer zones of cementing infills and in contact with the iron-rich clasts and braunite

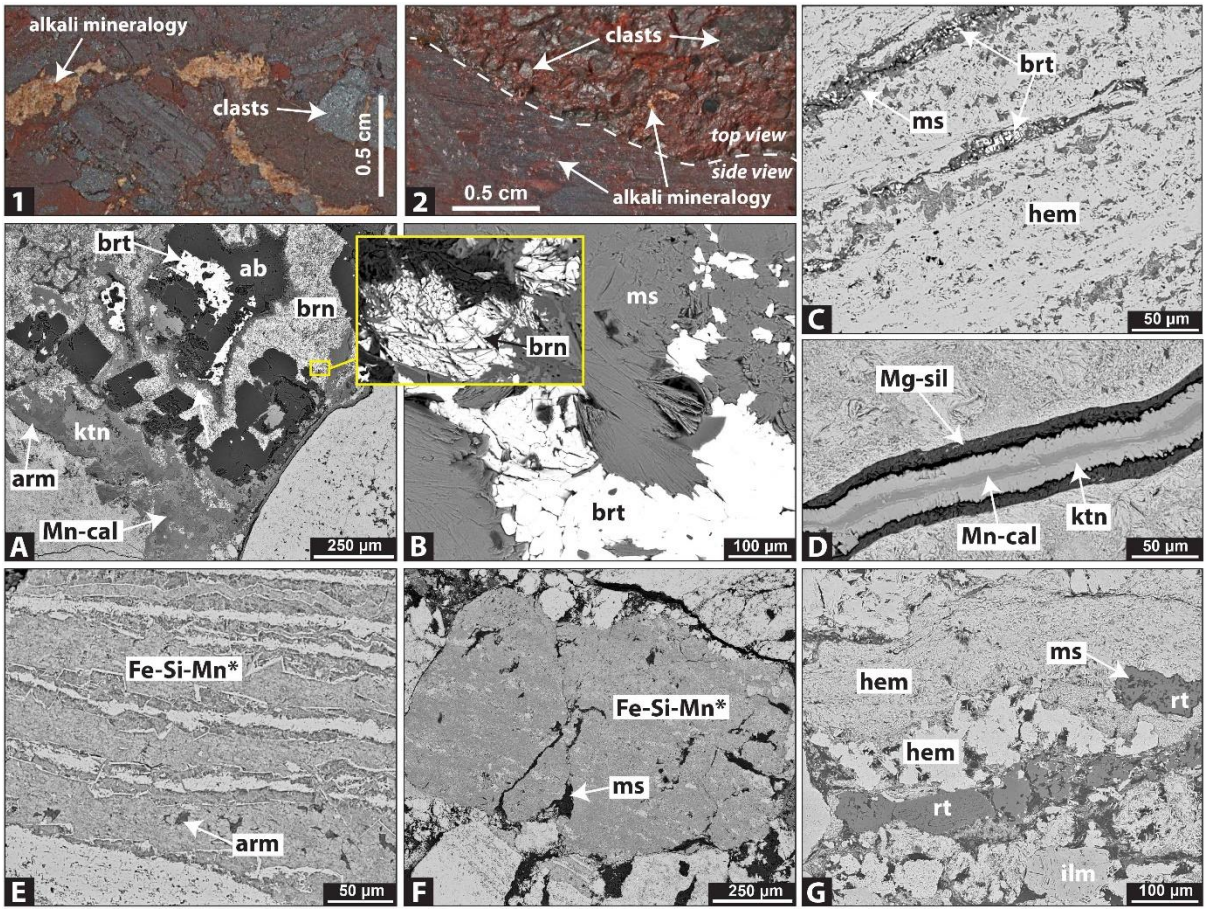

Figure 5. *(*1 & 2) Alkali mineralogy occurs conspicuously in the matrix and lesser within the clasts (sample photos). Back scattered electron (BSE) images. (A) Crude zonation of gangues (see also text) and barite being often enclosed by albite. (Inset) Common texture of braunite intergrown with carbonates. (B) Common barite-muscovite association occupying zoned lensoidal vugs. (C) Interstitial filling of barite and muscovite in clast. (D) Zoned, Mg- and Mn-bearing veinlets hosting carbonate phases. (E) Fe/Mn-rich clast comprising armbrusterite and an unidentified silicate. (F) Fragmentation by muscovite-filled cracks suggest earlier incorporation of the Fe/Mn clasts in the ore matrix. (G) Recrystallized microplaty hematite clasts in the vicinity of rutile-ilmenite aggregates. ab = albite, arm = armbrusterite, brn = braunite, brt = barite, hem = hematite, ilm = ilmenite ktn = kutnohorite, Mg-sil = unknown Mg-silicate, Mn-cal = manganoan calcite, ms = muscovite, rt =rutile. * unidentified silicate high in Fe and Mn.

crystallizing in the interiors along with albite (Figure 5A). The morphology of braunite is unusual in the sense that it is finely intergrown with Mn-carbonates and appears as clusters of very fine-grained crystals (Figure 5A, inset). Carbonate minerals display compositions from almost pure end-member rhodochrosite to intermediate kutnohorite and manganoan calcite. Compositional zoning patterns can be observed, with the less Mn-rich members growing around carbonates being richer in manganese.

Barite associated with coarse (100-200 µm) muscovite sheets is often seen filling cm-sized zoned lensoidal vugs that constantly comprise barite cores and muscovite rims (Figure 5B). The same paragenesis may be diffuse through iron-rich clasts, apparently occupying pore space between hematite plates (Figure 5C), although barite in this case is usually very fine-grained and negligible in comparison to its other occurrences in the Fe-ore. A network of veinlets traverses clasts and matrix and regularly show a Mg-rich lining corresponding to an unidentified mineral (possibly clinochlore) and a zoned centre comprising kutnohorite and manganoan calcite (Figure 5D). It is common for these veins to hug various clasts and produce a thin lining around them, thus generally suggesting later fluid infiltration.

One of the most noteworthy observations is that of several clasts containing Mn, specifically hosted by an unidentified phase having iron, manganese and silica, which usually coexists with armbrusterite [$K_5Na_6Mn^{3+}Mn_{14}^{2+}$ $[Si_9O_{22}]_4(OH)_{10}4H_2O$] (Figure 5E). The latter is a particular rare species that has been previously reported from Mn-ore in the wider Postmasburg area (Wolhaarkop breccia) (Moore et al; 2011). Crystal outlines forming laminae in the Mn-bearing clasts resemble skeletal textures and imply that replacement processes have been at play. These clasts were apparently incorporated in the matrix after having been metasomatized since the immediate surrounding Fe-ore matrix does not bear significant Mn and furthermore many such clasts appear fragmented by later muscovite-filled cracks (Figure 5F). The above observations for the presence of braunite, Mn-carbonates and silicates in the ore cement, clasts and veins denotes a degree of Mn transportation from underlying Mn-rich lithologies to the conglomeratic Fe-ore during alteration as well as localized open-space filling and/or replacement of the cementing material.

Accessory phases present in the matrix as well as in ferruginous clasts are apatite, zircon, rutile, ilmenite and a series of alumino-phosphate-sulfate (APS) minerals. Both rutile and ilmenite are prominent minerals within this ore-type and regularly compose a significant portion of the cementing matrix. Variable sizes and textural forms of hematite clasts in the vicinity of Ti oxides suggest recrystallization or replacements involving coarser-grained microplaty hematite (Figure 5G). Alumino-phosphate-sulfate (APS) minerals (svanbergite, florencite) are sporadically found in the matrix in the form of extensive mm-scale open-space

fillings running length parallel to or enfolding clasts and may be related to redistribution of P and LREEs after dissolution of former phosphates (chiefly apatite) in the underlying lithologies (e.g., Gaboreau et al; 2007). Crude compositional zonation between LREE- and Sr-rich members is common and euhedral crystals of minute size can be observed in fine-grained hematite matrix wrapping around clasts (Figure 6A, 6B). Clasts composed entirely of APS minerals most probably suggest formation prior to the surrounding muscovite-hematite cementing matrix or less likely very localized preferential replacement (Figure 6C).

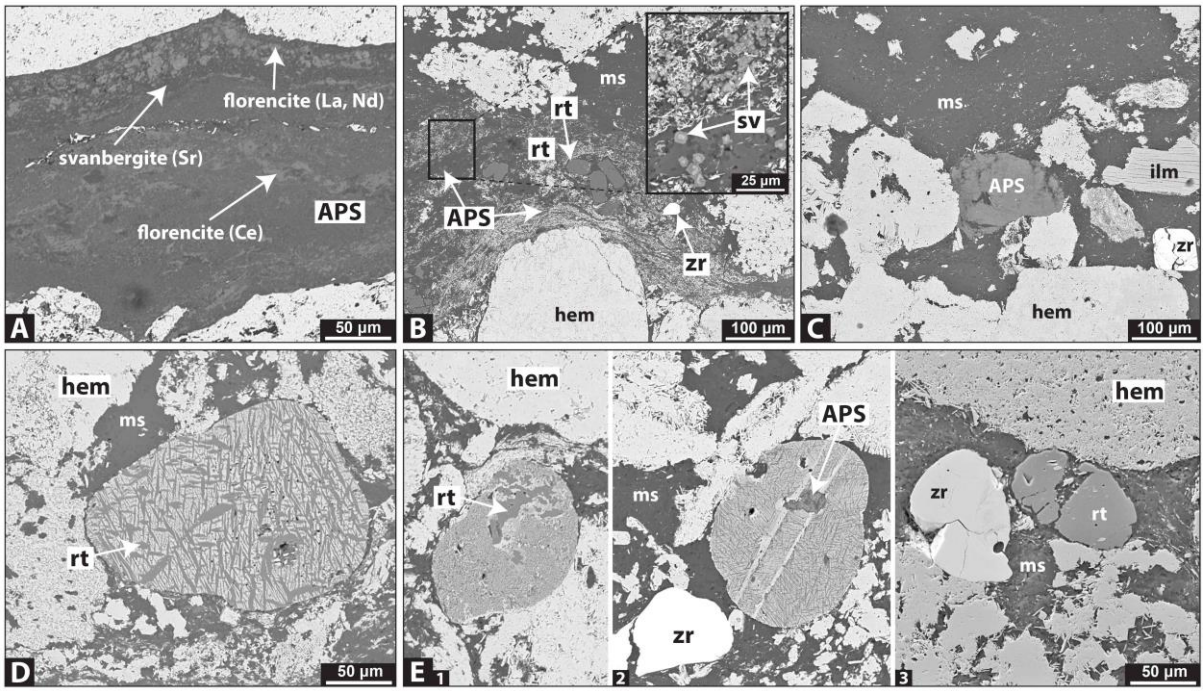

Figure 6. Back scattered electron (BSE) images. (A) APS matrix-infill parallel to clasts displaying compositional differences and crude zoning, with La/Nd- and generally REE-bearing members mostly lining the outer rims and svanbergite (Sr) occupying the centre. (B) Euhedral minute svanbergite with compositional zoning, thoroughly intergrown with fine-grained hematite engulfing ferruginous clasts. (Inset) Enlargement of the APS-rich matrix. C) APS-clast associated with ferruginized clasts, fractured ilmenite and zircon suggests formation prior to surrounding muscovite-rich matrix. (D) Lamellar, oriented intergrowths of hematite and rutile probably reflect exsolution of rutile from ilmenite. (E1-3) Exsolution of rutile from ilmenite, APS inclusions in Fe/Ti-rich clasts and rounded, fragmented zircon and rutile. APS = alumino-phosphate-sulfate minerals, hem = hematite, ilm = ilmenite, ms = muscovite, rt = rutile, sv = svanbergite, zr = zircon.

Clasts with lamellar, oriented intergrowths of hematite and rutile are presumably products of exsolution processes triggered by oxidation and remobilization of iron within the common oxygen sublattice (Figure 6D). Commonly found rutile inclusions in Fe/Ti-rich clasts support the scenario of replacement reactions through decomposition of Ti-rich minerals,

probably exsolution of rutile from ilmenite (Figure 6E1). Zircons (50-70 μm) are constantly rounded, zoned and at places intensely fragmented, much like certain co-existing Ti oxides grains (Figure 6E2-3), processes evidently occurring during their emplacement in the ore matrix and/or reworking by multiple fracturing-sealing cycles and fluid infiltration, as corroborated by various other textures. Overall, barite, although sparingly present in the studied samples, occurs mainly in the matrix of the clast-supported conglomeratic iron ore as vug-filling material and less commonly as suturing material within clasts. Invariably of textures though, it is attached profusely to alkali- (Na, K, Ca) and Mn-bearing associations.

High-grade Mn-ore (N'Chwaning & Wessels mines)

Barite from the Kalahari manganese field is as yet the most well-documented among all other occurrences in the wider region, although published descriptions from the high-grade manganese ore beds are brief and mainly comprise mentions of veinlets, vugs or traces amounts of barite filling secondary porosity (Beukes et al; 1995, Gutzmer and Beukes; 1996b). Moreover, not much detail is given in regard to its paragenesis.

Mn-ore hosted barite from drillcores showing anomalously high Ba and Sr is documented here to coexist primarily with Mn carbonates and oxides. Specifically, barite occurs chiefly as euhedral blocky to columnar crystal clusters filling secondary pore space in the recrystallized ore zone along with kutnohorite, rhodochrosite, calcite, strontianite, brucite and As-bearing apatite (Figure 7.1, 7A, 7B). These open-space occlusions are visible in hand specimen, range from 0.1 cm to more than 1 cm and exhibit broadly bedding-parallel development. Carbonate minerals and brucite in the vugs often display equant shapes and inclusions of ore mineralogy. The surrounding matrix comprises mixtures of braunite (II) with hausmannite, which are the chief constituents as well as disseminations of bixbyite and jacobsite as accessory phases. Hematite is also present, mostly is association with braunite and hausmannite, overall surrounding gangue phases.

Ore minerals form euhedral crystals adjacent or inside the vugs, indicative of the recrystallization processes induced by hydrothermal alteration. The composition of barite varies between that of pure end-member and Sr-barite, that can appear either as distinct or

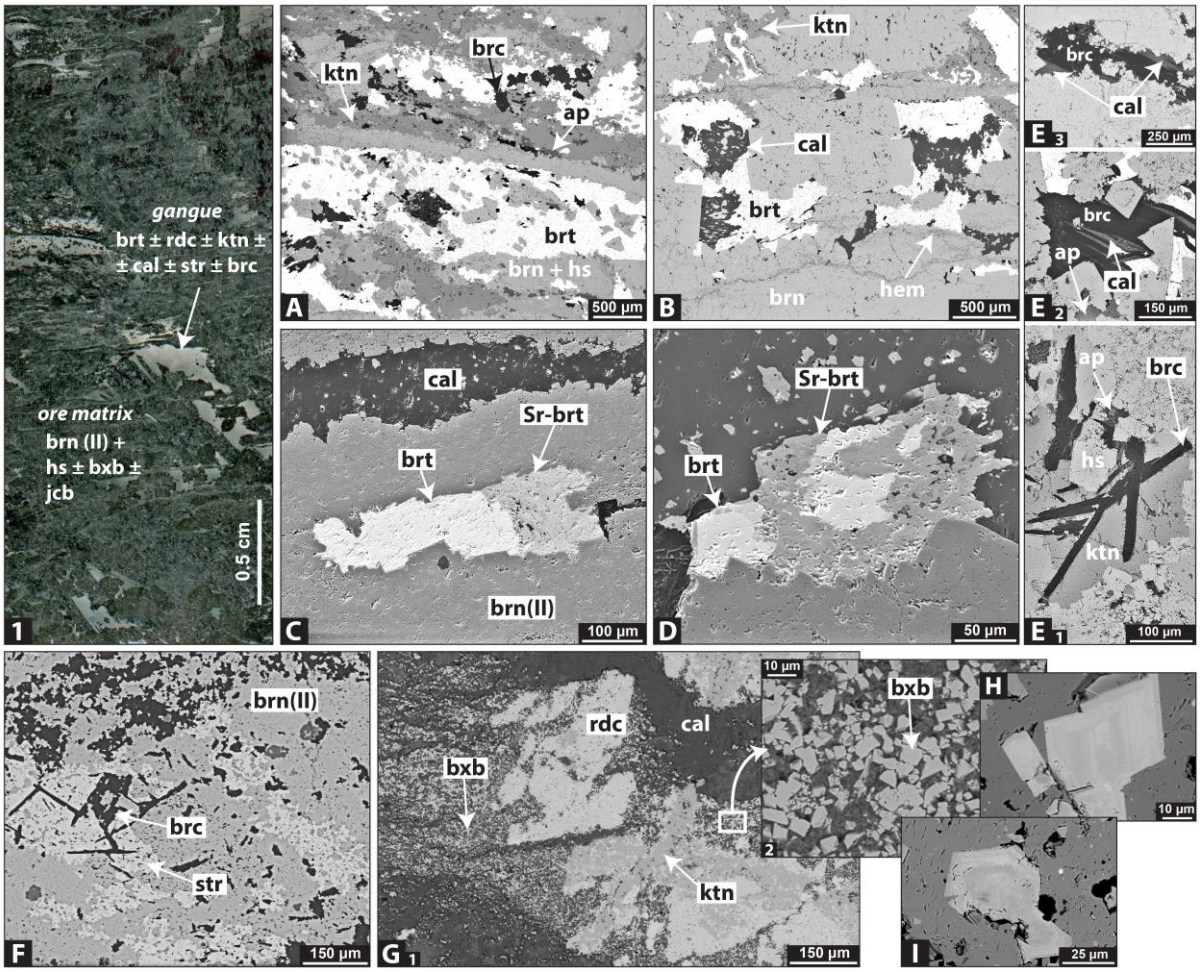

Figure 7. Back scattered electron (BSE) images apart from C and D which derive from secondary electron detection. (1) Thin section scan displaying cm-sized vugs consisting of hydrothermal gangues within the recrystallized Mn-oxide matrix. (A & B) Barite in coarse vugs coexisting chiefly with Mn carbonates and lesser with brucite and apatite. (C & D) Associations of barite and strontian barite highlighting changes during precipitations from the Ba/Sr-rich fluid. (E1-3) Elongated prismatic brucite is common. Exsolved calcite laminae emphasize the close association of the two minerals. (F) Widespread strontianite open-space occlusions in braunite matrix along with brucite. (G1-2) Microscopic bixbyite rhombs seemingly being formed by the breakup of Mn carbonates. (H & I) Euhedral and zoned Pb-bearing Mn oxide. ap = apatite, brc = brucite, brn (II) =braunite, brt = barite, bxb = bixbyite, cl = calcite, ktn = kutnohorite, hs = hausmannite, rdc = rhodochrosite, Sr-brt = strontian barite, str = strontianite.

intermixed phases inside vugs and are more easily distinguished by using secondary electron detection (Figure 7C, 7D). Brucite usually occurs as elongated prismatic crystals displaying lengths of up to 200 µm (Figure 7E1) or may fill open-space and manifest exsolved calcite laminae (Figure 7E$_2$, 7E$_3$), the latter affirming the contemporaneous presence of Mg^{2}+ and Ca^{2+} concentrations in the fluid, originally deriving from dissolution of pre-existing carbonates.

Extensive (0.5-1 mm) strontianite precipitates growing in open space between braunite can be also observed and may be the cause of wt. % Sr concentration in localized ore horizons. Brucite laths and needles were also found associated with the strontianite (Figure 7F). An interesting texture of minute bixbyite rhombs (5-15 µm) showing a close relationship with aggregates of Mn carbonates, seemingly being replaced by the former was regularly noted in the Ba/Sr-rich samples. Additionally, an unidentified Pb-bearing manganese oxide exhibiting rhombohedral or hexagonal outline was rarely seen associated with the barite-carbonate parageneses (Figure 7H, HI). Although the adsorption capacity on heavy metals such as Pb^{2+} is known for Mn oxide minerals (Feng et al; 2007), such species has not been previously reported from the KMF and further corroborates the existence of small amounts of Pb in the alteration solutions, evident in the well-documented kentrolite (Gutzmer and Beukes; 1996b).

Other selected barite occurrences (PMF and KMF)

Emphasis is given on selected barite occurrences from both fields to highlight its wide distribution and complex mineralogical parageneses. Ferruginous quartzite in the PMF, overlying a thick succession of Mn ore (Wolhaarkop breccia) at Heuningkranz locality, exhibits well-developed cm-sized rhodochrosite crystals that occupy coarse vugs, lined with evidently recrystallized specular hematite. Barite exists copiously in both the host rock and vugs, is associated with specularite, euhedral rhodochrosite, albite, and laths of muscovite and clinochlore, the latter also commonly seen as inclusions in barite (Figure 8A). In the same locality, barite is rather widespread also in Mn ore and in particular shows complex parageneses, coexisting with aegirine, albite, armbrusterite, serandite ($Na(Mn^{2+},Ca)_2Si_3O_8(OH)$), zoned rhombs of Mn carbonates and recrystallized braunite. These alkali-rich associations develop in vugs, interstitially to ore matrix or overgrow on silica-rich clasts that either represent chert or authigenic quartz, although barite likely being a late-stage phase is further seen deposited along the margins and/or replacing minerals such as serandite (Figure 8A, 8B).

Representative samples of the siliceous Mn ore-type (Wolhaarkop breccia) from the McCarthy mine, demonstrate that blocky or tabular barite crystals up to 6 cm in size are

present as void-fillings in the ore matrix and are macroscopically distributed very similar to the more abundant granular quartz lumps. On the basis of quartz crystal boundaries, remnant and fragmented grains it can be deduced that braunite is replacing the former. In turn, braunite is overgrown by later-formed hollandite (Figure 8D). Barite occurs as fracture-filling, commonly with a selvage of microplaty hematite, hosts inclusions of all formerly mentioned minerals and is often encompassed by equant quartz grains (Figure 8E).

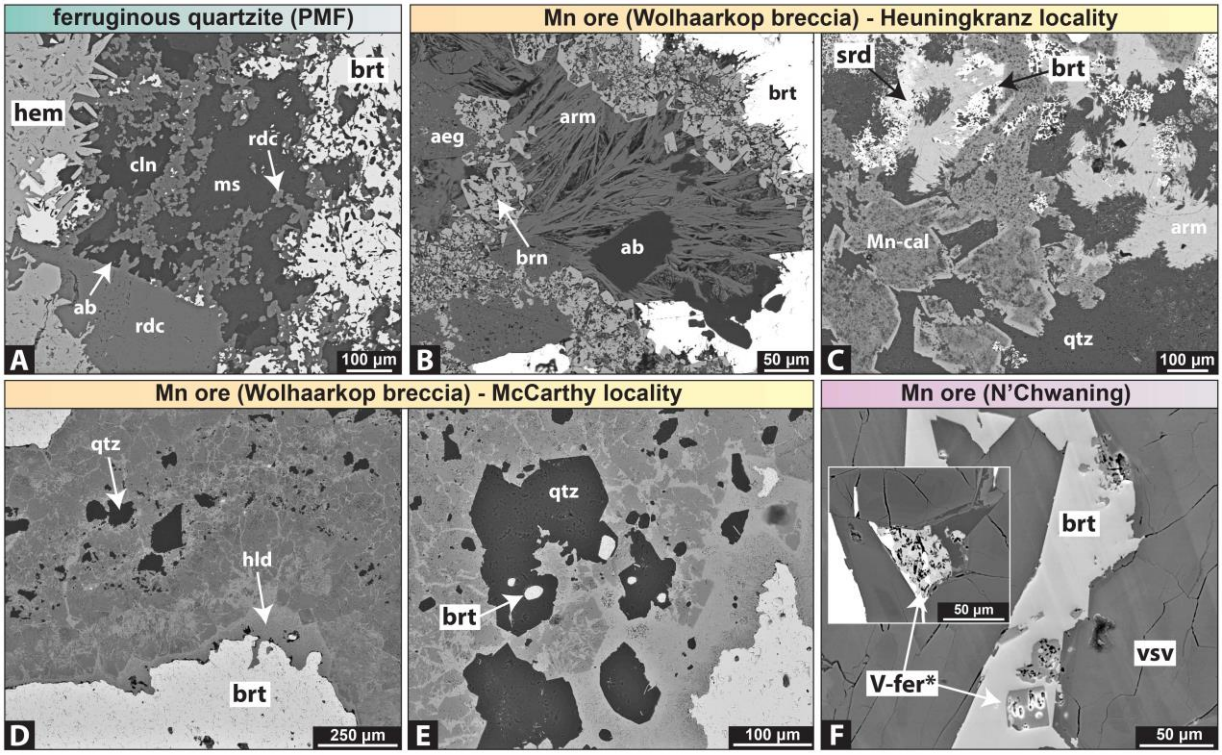

Figure 8. Back scattered electron (BSE) images. (A) Barite fillings in close affiliation and bearing inclusions of mica and rhodochrosite. (B) Barite associated with sodic-rich parageneses and recrystallized braunite. (C) Barite is a late-stage phase and seemingly overprints serandite and Mn carbonates. (D) Fracture-filling barite in contact with hollandite-braunite intergrowths and/or replacements as well as probably remnant quartz grains. (E) Barite inclusions in equant quartz. (F) Barite precipitates filling open space between equant vesuvianite commonly host a V- and Ca-rich arsenate, compositionally related to fermorite from the existing literature. ab = albite, aeg = aegirine, arm = armbrusterite, brn = braunite, brt = barite, cln = clinochlore, hem = hematite, hld = hollandite, Mn-cal = manganoan calcite, ms = muscovite, qtz = quartz, rdc = rhodochrosite, srd = serandite, V-fer* = unknown species, closely resembling fermorite and named here vanadium-bearing fermorite, vsv = vesuvianite.

Barite in the KMF is typically present in all sorts of calc-silicate and carbonate- or sulfate-bearing parageneses. Among the studied samples, an interesting occurrence is that of barite and its strontian counterpart precipitating along with calcite between well-developed

vesuvianite crystals. The latter for the most part display complex oscillatory concentric zoning, characterized by sharp changes in the abundance of Mn, Mg, Al, and lesser Si and Ca, a feature previously documented for this mineral in other localities (Gibson et al; 1995). Barite frequently hosts somewhat ragged minute (20-40 μm) crystals which comprise 49.3 wt. CaO, 19.0 wt. % P_2O_5, 30.7 wt. % As_2O_5 and 5.2 wt. % V_2O_5 (n=5). This composition is very similar to that reported from an arsenate species from the Sitapar manganese-ore deposit (Madhya Pradesh district, India) that generally shows small amounts of vanadium in its matrix (Herbert and Prior; 1911). In particular, this mineral is named fermorite [$Ca_5(AsO_4)_3OH$] and it occurs as pinkish to white veins in association with braunite, Mn oxides and bixbyite in its type locality. Taking into account the considerable vanadium accommodated by the barite-associated arsenate from the KMF, this mineral may be regarded as a vanadium-bearing fermorite and thus further research is suggested to be conducted in order to discern if this may be even identified as a new species.

4.2 In situ $^{40}Ar/^{39}Ar$ results

Paragonite - sample SD13 (PMF)

Paragonite in the dated sample is widespread in ore matrix but is predominantly contained in irregularly-shaped and somewhat contorted aluminosilicate-rich layers (Figure 9.1, 9.2). The layer chosen for dating comprises clusters of paragonite sheets, abundant interstitially precipitated barite that is also intergrown with hematite and apatite (Figure 9.4) and thinly scattered elongated rutile of apparently authigenic origin. This layer displays a relatively sharp contact with the ore matrix, along which a bedding-parallel fabric consisting of barite lenses enveloped by paragonite can be observed (Figure 9.2, 9C). Veinlets traversing ore matrix or terminating to the paragonite-rich layer were also picked out for dating. However, the former probably consist of mixed populations of paragonite that usually exhibit coarser and more conspicuous mica sheets, while lesser muscovite can be also present (Figure 9.3, 9.5). Rhombohedral textures with generally distinct outlines may occur within barite- or hematite-rich matrix and consist of paragonite (Figure 9.6), probably implying once again pseudomorphous replacement of former mineralogy by the alkali gangues.

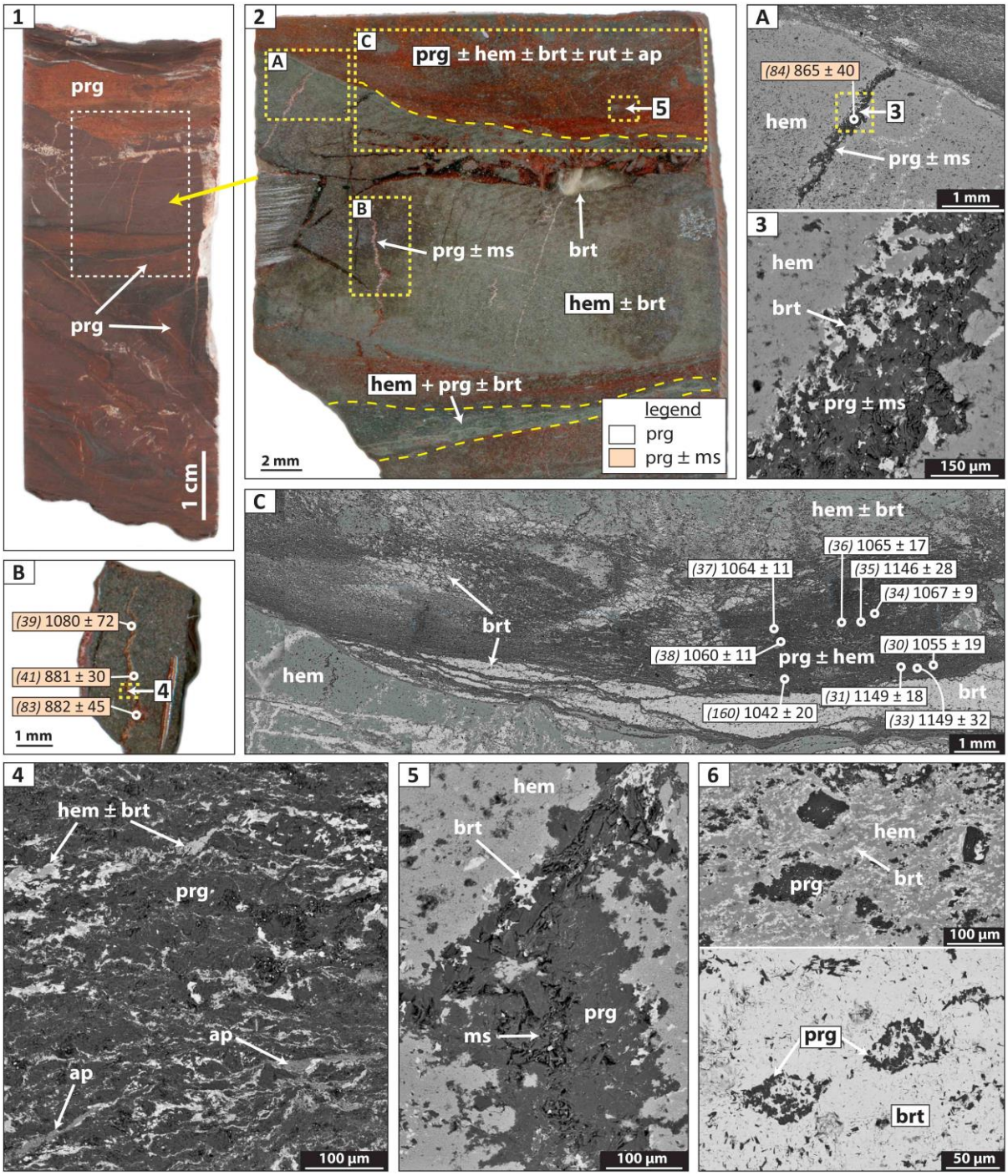

Figure 9. (1 & 2) Massive Fe-ore displaying contorted aluminosilicate-rich layers which for the most part consist of the targeted paragonite (sample photo and polished wafer scan). Dated areas are outlined in yellow. Back scattered electron (BSE) images. (3) Detail of possibly younger paragonite-muscovite veinlet comprising also barite. (4) Magnification of the dated paragonite-rich area showing the close association of barite, apatite and hematite surrounding clusters of paragonite. (5) Veinlet, similar detail as image 3. (6) Rhombs consisting of paragonite may indicate pseudomorphous replacement of former minerals, possibly carbonates. (A & B) Younger spot dates (877 ± 21 Ma, 2σ) with higher uncertainties in the veinlets may represent a waning alteration stage. (C) Laser spots on hydrothermal paragonite display a weighted mean of 1069 ± 8 Ma (2σ). Spot ages shown at 1σ confidence level. ap =apatite, brt = barite, hem = hematite, ms = muscovite, prg = paragonite, rt = rutile.

$^{40}Ar/^{39}Ar$ in situ analysis was performed on an ca. 2 x 3 mm area, using laser spot size of 85 µm and with focus on ablating for the most part mica material in-between other intermixed phases, i.e., barite and hematite (Figure 9C). Nine spots yielded dates ranging from 1041.8 ± 19.7 (1σ) Ma to 1148.9 ± 17.9 Ma (1σ) and have a weighted mean of 1069 ± 8 Ma (2σ, MSWD = 0.99, n=9). The data show normal distribution slightly skewed towards three older ages forming a bump (1146, 1148 and 1149 Ma) which are specifically ca. 75 Ma older than the calculated mean. No documented textural indication can account for the intra-sample difference in dates.

Four spot dates obtained from the veinlets in the ore matrix are much younger (Figure 9A, 9B), with three of them clustering around a mean of 876.8 ± 21.1 Ma (2σ, MSWD = 0.07) and the fourth outlier date being 1080 ± 72 Ma. All vein-hosted spots display larger uncertainties (from 30 to 72 Ma) in comparison to the layer-hosted spots, which is related to the lower $^{40}Ar^{*}$ concentration in the ablated gas. Smaller laser beam size (25-65 µm) and negligible potassium content in paragonite can explain the fact that a lot of the attempted spot analyses in these veins did not provide sufficient Ar gas despite the occasional presence of muscovite. Not much credence is given to these younger dates apart from that they maybe provide a tentative indication of waning alteration associated with younger muscovite generations.

Muscovite - sample BaQ2 (PMF)

Muscovite in the dated quartzite sample from the base of the Olifantshoek Supergroup (Figure 10.1) is representative of the distribution of muscovite in all similar studied samples. The mineral occurs as sheets of very small size (10- 25 µm), that can rarely grow up to 50 µm and are always seen in parageneses with barite, which may further comprise hematite. Veins consisting of blocky barite (50-100 µm) and similarly sized hematite or solely of coarse-grained hematite (specularite) traverse other areas of the sample. Quartz in contact with barite exhibits equant shapes and is coarser, thus probably recrystallized (Figure 10.2). It is common for disseminations of rutile to occur in muscovite fracture-fillings and the former to show dissolution textures supporting a remnant origin for the oxide (Figure 10.3, 10.4). Ilmenite is also seen fragmented and engulfed by submicroscopic barite veins.

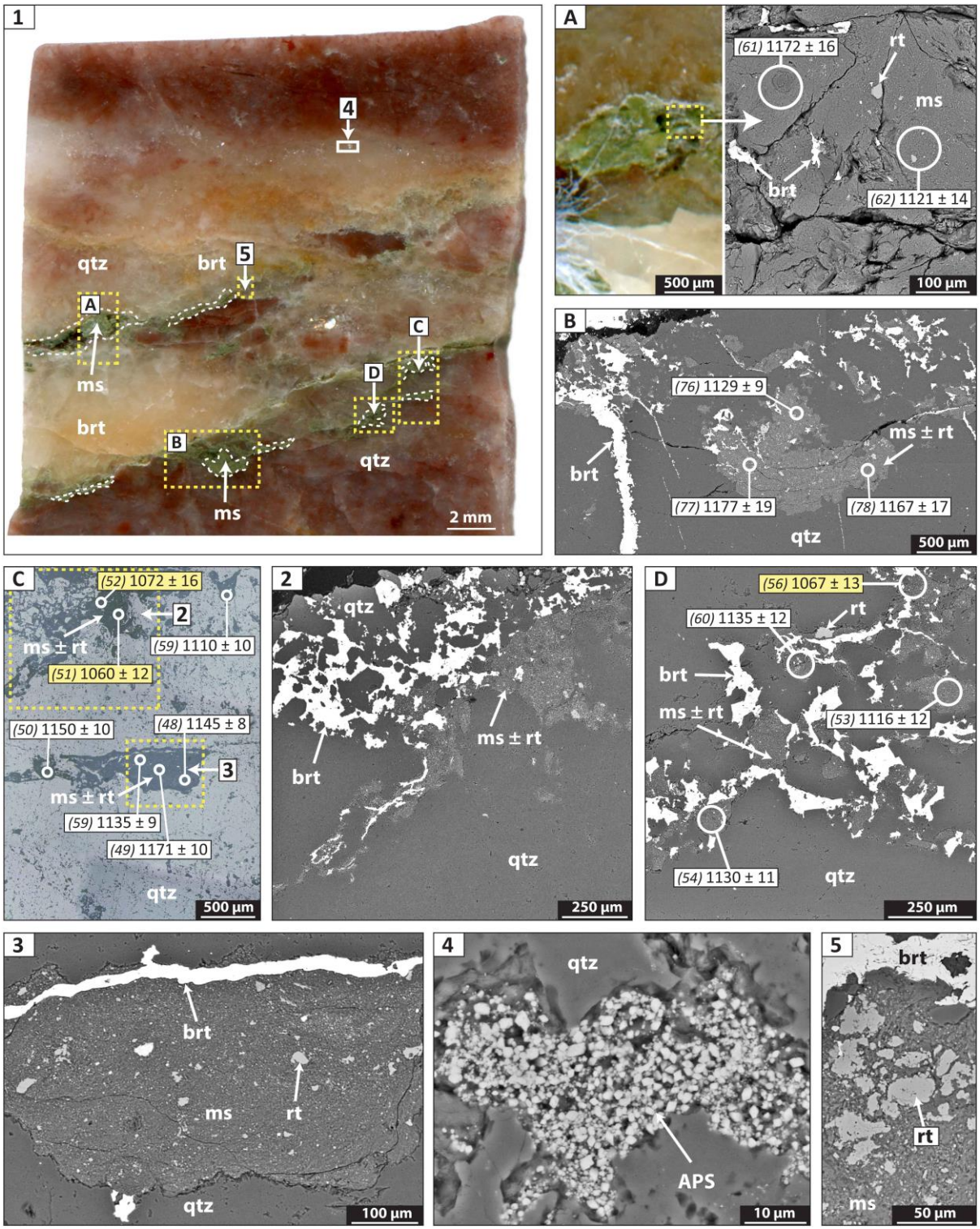

Figure 10. (1) Polished thin wafer prepared for in situ $^{40}Ar/^{39}Ar$ dating and outlined areas comprising spot analyses. Back scattered electron (BSE) images apart from image 5 which is SED and image C which is taken under reflected light opt. microscopy. (2) Recrystallized quartz in association with barite. (3 & 4) Disseminations of probably remnant rutile in muscovite (5) Submicroscopic euhedral to spherical APS minerals (florencite) precipitated in pore space. (A-D) Areas with obtained spot dates shown at 1σ confidence level and displaying a weighted mean of 1129 ± 4 Ma (2σ). In situ dates being about 65 myr younger than the weighted mean, are coloured in yellow. APS = alumino-phosphate-sulfate minerals, brt = barite, ms = muscovite, qtz = quartz, rt = rutile.

APS minerals are sometimes precipitated in considerable quantities within the quartzite pore space, or along small cracks and fractures and may therefore control its whole-rock REE composition. Their textural appearance is mostly of submicroscopic and euhedral or almost spherical grains clustering together (Figure 10.5). EDS analyses suggest primarily the presence of cerium (Ce), followed by lanthanum (La) and neodymium (Nd) and the absence of Sr, thus pointing to compositions closer to florencite. Apatite is very sparingly found in other quartzite samples, associated with barite or in the rock matrix and is therefore likely, that akin to the conglomeratic iron ore above, APS here are related to dissolution of former apatite.

Sixteen $^{40}Ar/^{39}Ar$ in situ spot analyses (85 µm laser spot size) yield dates ranging from 1059.6 ± 11.9 (1σ) Ma to 1177.2 ± 19.3 (1σ) Ma (Figure 10A-10D). Data have a weighted mean of 1129 ± 4 Ma (2σ, MSWD = 4.00, n=16) and display a somewhat bimodal distribution (two-peak shape, see also Figure 14 later on), with the highest and main peak at around the weighted mean and a second subordinate peak (spots 51, 52, 56) at around 1070 Ma (ca.65 myr younger). There is no available evidence for contaminating components and although muscovite is too small and intergrown with rutile, ablation of the targeted material is not expected to contaminate the Ar signal. There is also no evident geological reason for the younger spots (for example record of the cooling history or different mica generations). Nevertheless, younger spots immediately adjacent to the rest of the analyses are included in calculation of the weighted average age.

Muscovite- sample WBC (KMF)

Muscovite in this sample resides mostly within reddish mm-scale bands interbedded with clusters of coarse bladed to tabular barite that protrude into the silicate-rich bands (Figure 11.1). This intriguing specimen derives from the unconformable contact between the second hematite lutite unit and quartzite belonging to the Olifantshoek Supergroup at Wessels mine (Figure 2B). Mineralogically, the reddish bands consist of very fine-grained intergrowths of hematite, muscovite and barite that compose more iron-rich or potassium-rich domains depending on the concentrations of the admixtures. Coarser (50-150 µm) muscovite sheets are sparingly disseminated in this matrix. Ellipsoidal or irregularly shaped

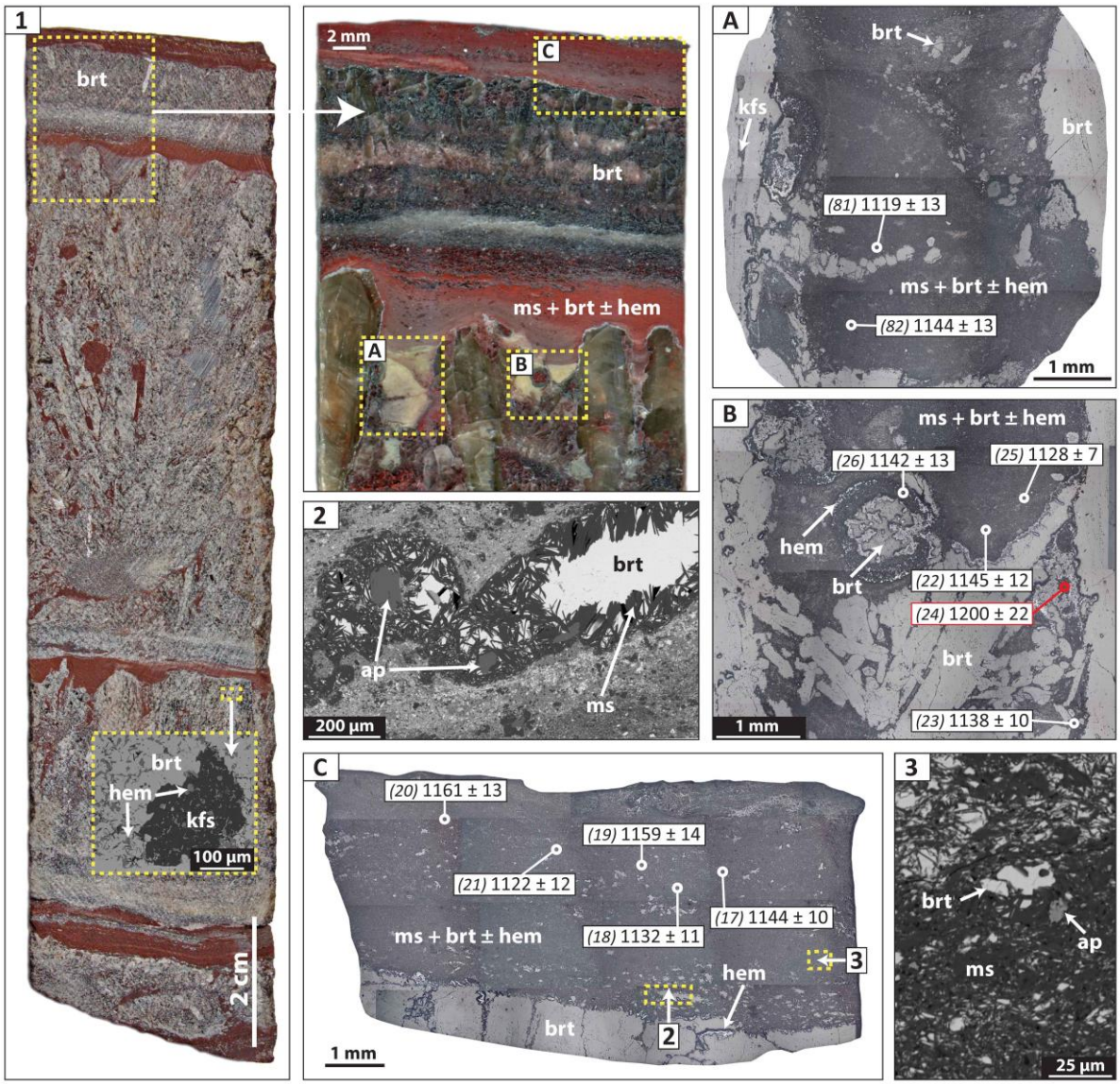

Figure 11. (1) Elongated and bladed barite with interrupting parallel bands that mainly consist of muscovite, hematite and barite. Areas comprising spot dates are outlined by yellow dotted line. (inset) Microplaty hematite associated with k-feldspar, both forming during reworking and brecciation of the coarse barite crystals (BSE). 2-3: back scattered electron (BSE) images. (2) Barite vugs in mica-bearing bands display a selvage of muscovite and ubiquitous apatite. (3) Matrix magnification showing a muscovite-rich area that also comprises hematite, barite and apatite. (A-C) Muscovite spot dates from different localities of the sample shown at 1σ confidence level and showing a weighted mean of 1137 ± 2 Ma (2σ). Rejected spot (24) is indicated in red.

barite-filled vugs populate a linear domain close to the bladed and almost perpendicular to the reddish bands, barite crystals. These vugs exhibit a selvage of muscovite (ca. 200 µm) running vertical to the edges of the barite-filled vugs and in addition may comprise euhedral (100-300 µm) apatite grains that are preferentially concentrated here (Figure 11.2). Microplaty to tabular hematite (up to 300 µm) can be also associated with the previous muscovite texture and is generally developed around barite grains or crystal fragments along

with K-feldspar (Figure 11.1), therefore suggesting later reworking and brecciation of the long, bladed barite.

Dates yielded by eleven UV laser ablation spot analyses range from 1119 ± 13.4 (1σ) Ma to 1200 ± 22 (1σ) Ma and show a weighted average of 1137 ± 2 Ma (2σ, MSWD = 2.72, n=11, 1 spot rejected). The age data display normal distribution and derive from both material within the reddish hematite- and barite-bearing bands (Figure 11C) and domains of higher muscovite purity, in the vicinity of bladed and reworked barite (Figure 11A, 11B). The age intrasample consistency is indicative of a single muscovite generation.

4.3 Sulfur isotopic composition of barite

The $\delta^{34}S$ values of the analysed barite (n= 93) vary between +16.7 and +29.5 ‰, (avg.= +24.9 ± 2.5 ‰, 1σ). However, most data (n=66) cluster around a relatively well-defined peak at +24.6 ‰, with only very few values (n=7) extending to lighter compositions and the remaining twenty samples exhibiting somewhat heavier isotopic values between +27 and +29.5 ‰ (Figure 12). The latter group is mainly governed by barite from massive Fe-ore (Kapstevel, Kolomela mine), which is on average 2.6 ‰ heavier in comparison to the rest of the studied barite from the PMF. A single analysis from Beeshoek Fe-ore (+27.2 ‰) and one iron-rich sample from Leeuwfontein (+27.0 ‰), both from the Kolomela region, apparently record this slightly heavier isotopic signal, although this requires further validation from more data. Barite departing from the former trend also exists in the Kolomela (+17.1 ‰), as well as in the Langverwacht (+16.7 ‰) and Heuningkranz (+17.3 ‰) localities. Nevertheless, barite is broadly compositionally similar between the various Postmasburg localities, regardless of host rock lithology and stratigraphic depth.

Barite from the Kalahari Manganese Field exhibits no significant difference in isotopic composition, which again is broadly irrespective of host rock and paragenetic association, except for nine samples. Slightly heavier $\delta^{34}S$ values (+27.5, +27.4, +27.1 and +28.2 ‰) correspond to blocky barite crystals associated with rhodochrosite or equivalent but finer-grained parageneses found in mm- to cm-scale vugs within Mn ore. Lighter values (+18.9, +19.9, +20.7 ‰) typically derive from assemblages comprising garnet, hematite and calcite.

Unpublished data from Gutzmer (1996) are also included in Figure 12 and overall fit well into the isotopic data suite from this study. A full list of short paragenetic and textural descriptions and analytical yields complements the summarized stable isotopic results for barite and can be found in Appendix II. The distinct compositional homogeneity shared by barite of both districts is suggestive of a single dominant reservoir as the main sulfur source. Otherwise stated, fluids acquiring sulfur during one or more hydrothermal pulses, must have circulated through and leached the same or very similar sulfur reservoirs. In addition to data uniformity, heavy $\delta^{34}S$ values is a possible indication of marine origin of sulfur and is discussed later within the broader geological framework of the deposits.

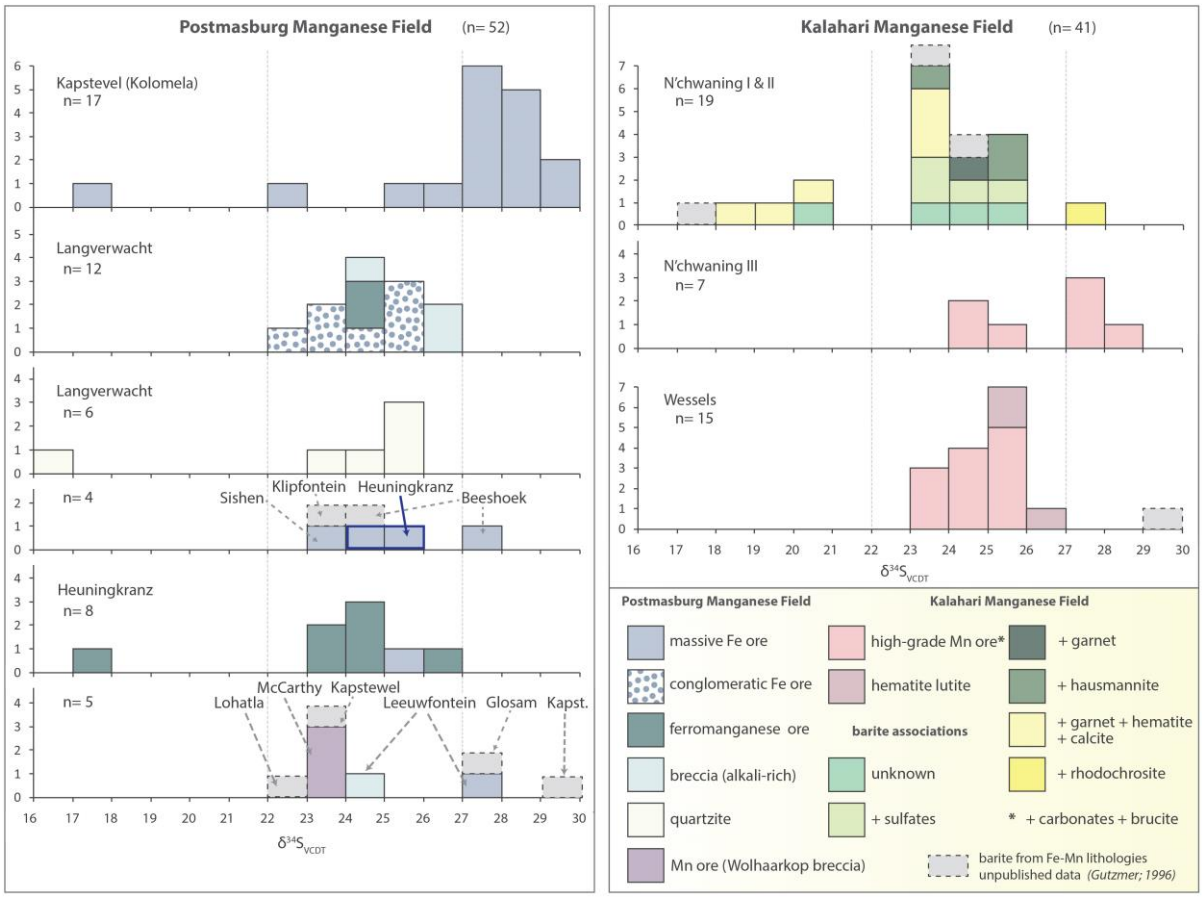

Figure 12. Sulfur isotope composition of 93 barite samples from different lithologies and parageneses of the PMF and KMF plotted in frequency histogram. Unpublished data (n=10, grey colour) from Gutzmer (1996) are also shown.

4.4 Sr isotopic composition of barite and country rocks

Sr isotopic analyses (n=43) were carried out on 32 barites from both districts, 5 carbonate minerals from the KMF and 6 whole-rock lithologies including Campbellrand and

Malmani dolomite, Mapedi shale and an ephesite(mica)-rich shale band from the ferromanganese ores of the Eastern belt (PMF, Eastern Belt = EMD). The whole tabulated data can be found in Appendix II. Sr data are displayed here in a $\delta^{34}S$ versus $^{87}Sr/^{86}Sr$ plot (Figure 13). Measured barite $^{87}Sr/^{86}Sr$ ratios exhibit a wide spread, from 0.70575 to 0.73818. However, if seven samples, most of which correspond to certain host rocks or localities, are excluded, then the remaining $^{87}Sr/^{86}Sr$ ratios of barite samples (n=25) fall between 0.71056 and 0.72278 (avg. = 0.71645 ± 0.00341, 1σ). This isotopic range is very representative of the range of $^{87}Sr/^{86}Sr$ values observed from a single locality, such as that of Kapstevel or

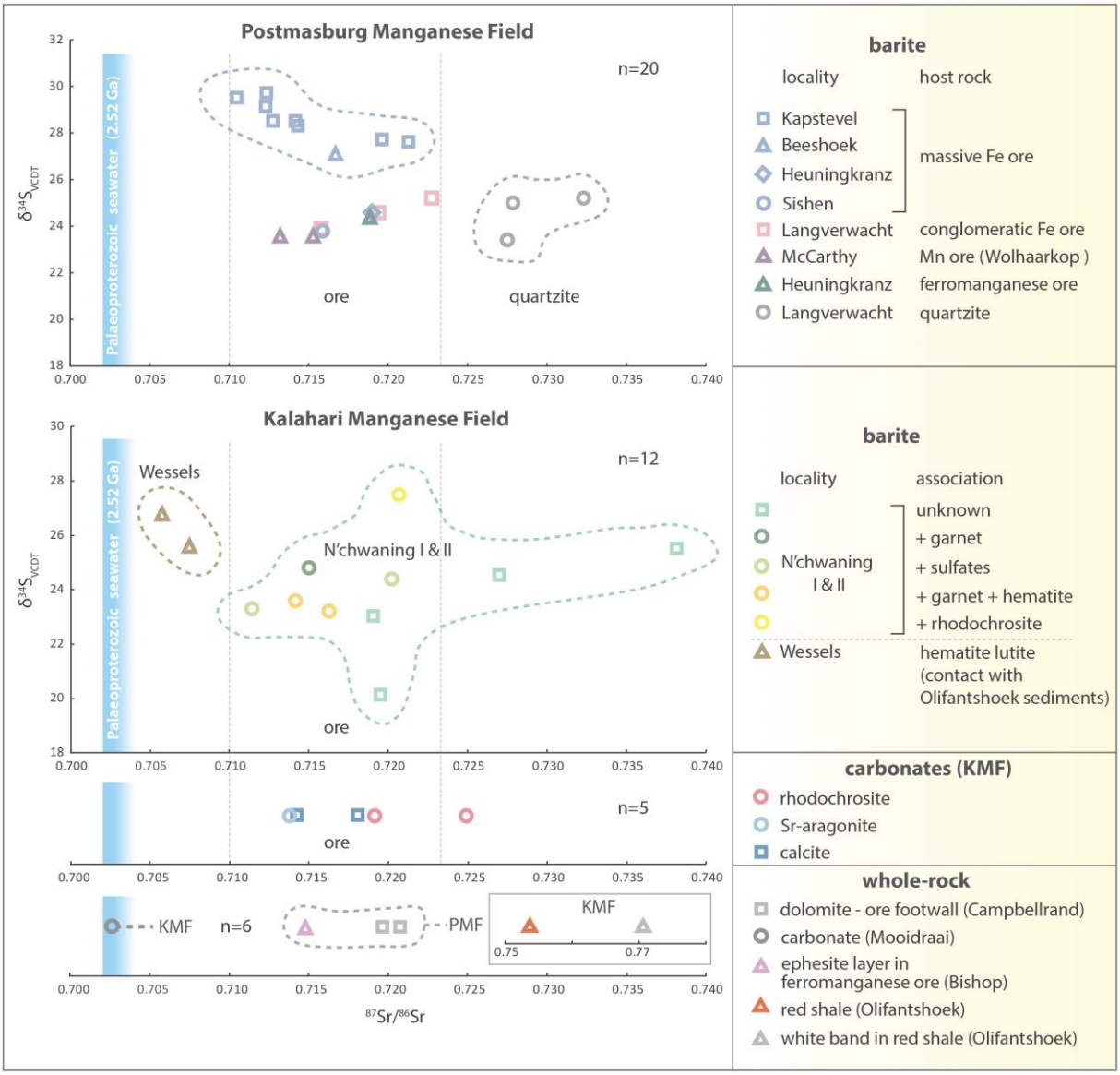

Figure 13. $\delta^{34}S$ versus $^{87}Sr/^{86}Sr$ plot encompassing all mineral-specific and whole-rock strontium fata from this study. Note that despite the appreciable spread, the majority of data fall between the two vertical dotted lines (0.71056 and 0.72278) and different localities display positive correlations that can be attributed to mixing of two separate fluids leading to barite precipitation (section 5.3.2. in detail).

Heuningkranz-Langverwacht. Positive correlations between sulfur and strontium isotopic compositions shown by different barite groups from distinct localities (Figure 13) are most likely indicative of fluid-mixing processes (see also discussion later on).

Quartzite-hosted barite (Langverwacht) coexisting with muscovite, yields distinctly more radiogenic values (between 0.72754 and 0.73231), that are only shared by barite crystals of unknown association in the KMF (0.72699, 0.73818), apparently co-developed with shigaite [$Mn_6Al_3(OH)_{18}[Na(H_2O)_6](SO_4)_2 6H_2O$] of burnt orange colour. On the contrary, strontium isotopic compositions of barite deriving from the Wessels drillcores is much less radiogenic (0.70575, 0.70743). Carbonates exhibit a fairly similar spread of $^{87}Sr/^{86}Sr$ ratios to that shown by the majority of barite (i.e., from 0.71419 to 0.72484). More precisely, calcite has the least radiogenic isotopic composition, whereas rhodochrosite exhibits the higher values. Dolomite from the ore footwall at Heuningkranz (0.71961, 0.72073) and ephesite-layers (mica/shaley layers) from the ferromanganese ore at Bishop (0.71468), display strontium isotopic compositions very close to barite average. Mapedi shales, uncorrected for their initial Rb, expectedly show extremely radiogenic values (0.75369, 0.77055) and specifically, the characteristic white bands are apparently more radiogenic than the red, hematite-rich bands. On the other hand, Mooidraai dolomite from the KMF shows very unradiogenic $^{87}Sr/^{86}Sr$ ratios, identical to that of contemporaneous seawater (0.70290).

5. Discussion

5.1 Evidence for regional-scale hydrothermal fluid metasomatism

An exhaustive survey of the previously under-examined barite mineralization in the Northern Cape reveals that this mineral can be considered as the hallmark of alkali metasomatism in the study area, in the sense that despite its limited abundance, at least in most cases, it is omnipresent in Fe- and Mn-rich lithologies and consistently associated with the gangue alkali-rich parageneses. $^{40}Ar/^{39}Ar$ results from this study act as indisputable evidence for a common link between the KMF and the PMF and specifically support the presence of related epigenetic processes from the northernmost tip of the KMF (Wessels, N'Chwaning mines) to the southernmost extremity of the PMF (Kolomela mine). As seen in

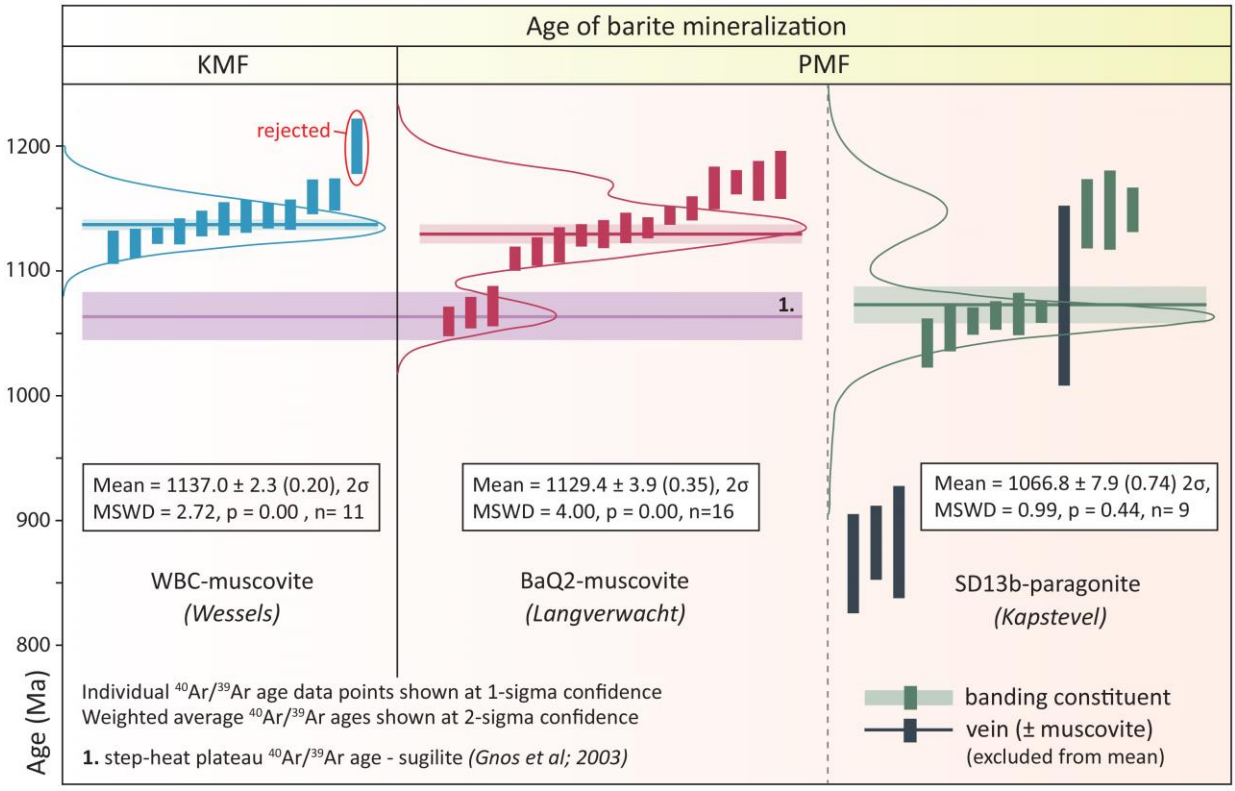

Figure 14. Plot illustrating distribution of in situ $^{40}Ar/^{39}Ar$ spot dates (1σ-confidence level) from micas associated with barite. Horizontal bars represent weighted mean ages (2σ-confidence level). Regional barite mineralization is broadly contemporaneous and in agreement with the Wessels sugilite age from the literature, overall corresponding to the Namaqua orogeny. Ages reported from Gnos et al (2003) have been recalibrated using the ^{40}K decay constant from Renne et al (2011).

Figure 14, the crystallization age of muscovite, cogenetically formed with barite, is practically the same (ca. 1130 Ma, 2σ) between localities extending over a total strike of ca. 150 km. This age coincidence, in conjunction with petrographic and isotopic data, corroborates the view of previous authors that hydrothermal fluid flow in the area is regional rather than reflecting localized unrelated events and moreover, that fluid migration most likely exploited major large-scale conduits such as the faults and thrust planes of the Blackridge thrust belt system or the unconformable lithological boundaries between the Transvaal and Olifantshoek Supergroups (Tsikos and Moore; 2005, Moore et al; 2011, Fairey et al; 2019).

All three mica/barite ages point to the Namaqua orogeny being the genetic factor of this heating event, which is generally bracketed between ca. 1.2 and 1.0 Ga. However, earlier ages of 1.35 Ga and going back as far as ca. 1.6 Ga have been also regarded as early rifting stages associated with this orogeny in South Africa (Cornell et al; 1986, Eglington; 2006,

Cornell et al; 2006). Interestingly, the paragonite age from Kolomela mine is very close to the single previously published Namaqua age (excluding indirect palaeomagnetic dating of hematite, ca. 1250 and 1100 Ma: Evans et al; 2001) deriving from step-heating $^{40}Ar/^{39}Ar$ sugilite dating in the KMF (Gnos et al; 2003). These overlapping, ''younger'' ages in comparison to rest of barite ages, specifically by about 70 Ma, may be an indication of a later hydrothermal pulse within the Namaqua orogeny, whereas the onset of hydrothermal fluid flow could be reflected by the older, ca. 1130 and 1137 Ma ages in both the KMF and PMF. It should be pointed out, that mica ages are regarded here as crystallization and not cooling ages, on the grounds that temperatures during hydrothermal overprint are not generally expected to have reached or exceeded the closure temperature for muscovite (>300^{o}C) (e.g., Hames and Bowring; 1994), at least according to available fluid inclusion data from Lüders et al (1999) and the overall geological setting and parageneses signifying a largely low-temperature regime. A long-lived hydrothermal system is compatible with both the extent of the similarly long-lasting tectonic forces related to the Namaqua orogeny and previous indications for more than one age peaks of mineralization in the KMF (Evans et al; 2001).

Intra-sample age variations are small in the KMF muscovite but samples from the PMF display small bumps in their age distribution profiles (Figure 14). No textural indication or other geological reasons can be easily identified to account for these intra-sample differences in dates. Quartz and especially hydrothermal varieties have been used in $^{40}Ar/^{39}Ar$ studies (for e.g., Harper and Schamel; 1977, Saito et al; 2018). This mineral is abundant in the host quartzite of sample BaQ2 and maybe also exists in the very-fine grained paragonite-rich layer from the Kapstevel iron ore, although not identified by SEM analysis. Contamination from ^{40}Ar, either present in the lattice of quartz or in fluid inclusions hosted by the former, may therefore be a possible explanation for the observed disturbances in the muscovite Ar-ages from the PMF. However, focusing on the main age peaks, for example in the paragonite age profile, spot age variations become rather insignificant. Considering the layered-distribution of this mineral in the iron ore and its association with interbedded and partially enriched shales, it can be hypothesized that formation of micas in this locality has been brought about by growth on precursory clays or silicate minerals during fluid introduction. Partial resetting and thermal loss of $^{40}Ar^{*}$ to yield the observed ages can be almost certainly excluded, since

it would have resulted in a much wider spread in data and consequently to inconsistent age profiles. Therefore, an authigenic hydrothermal origin for paragonite is a much-favored scenario and argon gas is suggested to have behaved similarly to an equilibrated closed system.

Nevertheless, age of barite mineralization appears to be coeval regionally and based on integrated rigorous petrographic examination of various Ba-rich and texturally distinct ore zones, geochronological and isotopic evidence, it can be reasonably predicted that the obtained ages are very likely to be replicated by other dating targets associated with barite in the Northern Cape and/or by different dating techniques. Importantly, the current ages are at variance with previous studies that have tentatively attributed barite mineralization to syn- or post-metamorphic events related to the 1.9-1.8 Ga Kheis orogeny. Our ages are also incongruous with the two Neoproterozoic $^{40}Ar/^{39}Ar$ ages reported from alkali assemblages in the PMF (Moore et al; 2011, Fairey et al; 2019), which still lack sufficient explanation.

5.2 Possible controls on ore genesis

Barite in the KMF is part of gangue assemblages affiliated with residual ore enrichment (carbonate leaching, recrystallization, authigenic mineral formation), the causing agent of which has been tectonically-expelled fluids (Beukes et al; 2016). It is therefore reasonable to interrogate the influence of fluids clearly belonging to the same regional system, on other preexisting Fe/Mn-rich entities and country lithologies in the area of effect. Even though this concept is not closely examined here, some aspects regarding the possible metallogenic role of the Namaqua-related alteration fluids are worth pointing out (more focus on this concept is given in chapters 5 and 6).

Barite in the studied lithologies has an epigenetic nature. It generally occurs as occlusion of open-space, including fractures, veins, vugs and lenses/pods of different size, ranging from couple of millimetres to several centimetres. Key paragenetic, compositional and textural characteristics are summarized in Figure 15. It is obvious from the current and other recent studies, that the PMF mimics the hydrothermal findings from the KMF to a great extend and that partial parallels between the mineralogical assemblages between the two

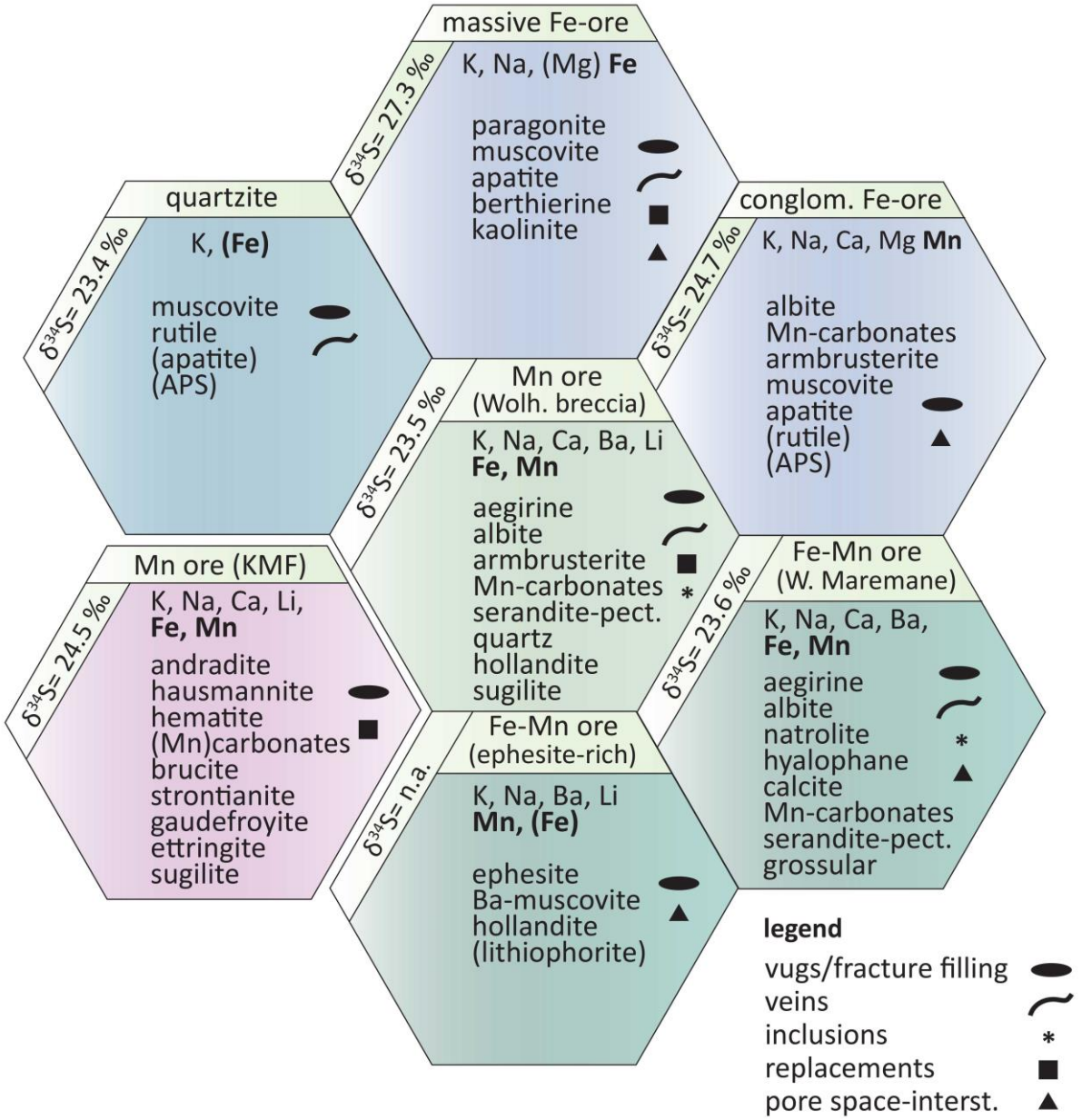

Figure 15. Schematic summary of the key paragenetic, compositional and textural characteristics of barite associations hosted by most of the different lithologies in the Northern Cape studied here. All hexagons represent PMF localities apart from the one noted as KMF (pink). Mentioned elements are hosted by gangues and Fe and Mn in bold notation highlight their presence in the former. The broadly similar sulfur isotopic composition, varying somewhat more prominently in the Kapstevel, is also displayed. Evidently, host rock exerts major control on barite parageneses, although not definitive for all studied barite occurrences (see also text).

ore fields exist. Evidently, host rock exerts major control on barite-bearing and overall alkali mineral parageneses, with different Mn ore-types displaying much higher mineralogical variability as regards barite associations than for example quartzite or various textural-types

of iron ore. Also apparent, is the presence of more compositionally diverse associations in Mn ore, involving Na, Ca and Ba, the latter also hosted in other phases (for e.g., banalsite, hyalophane, barytocalcite, witherite, hollandite, etc.) apart from barite. However, this observation is not replicated in the conglomeratic iron ore, where complex alkali-rich and Mn-bearing parageneses occur instead, or for example in the case of ferruginous quartzite, which hosts similar assemblages to the above. Moreover, Na may be present in barite associations, as for instance in the iron ore from Kapstevel and mineralogical diversity with respect to both barite parageneses and the overall host rock can be also low in certain types of ferromanganese ore, as evidenced by the ephesite-rich ores (Figure 15).

All of the above highlight that formation of the bulk of gangue mineralogy is controlled by the high content of alkalis in the fluid and the high Mn and Fe content of the country rocks, the latter also seen being hosted by hydrothermal phases (Figure 15: Fe and Mn noted in bold letters font) and therefore reflecting fluid-rock interactions and mobilization of ore metals. In certain instances, such as in the case of Mn-bearing assemblages in conglomeratic iron ore, small-scale migration of manganese from lithologies in proximity is evident. Replacement textures involving Mn-silicates or braunite and therefore supporting manganese mobilization, have been previously noted in the ores of the PMF (Gutzmer and Beukes; 1996a, Fairey et al; 2019). Overall, complex and highly variable parageneses in conjunction with textural characteristics and geochronological data from respective research in the wider area (chapters 3, 4, 5) support a multi-stage alteration history, comprising more than one fluid infiltration events and successive overprints. Pronounced replacement textures involving barite, possibly during waning-stage events, are also observed from both districts and equally for Fe and Mn ores.

Textural evidence for contemporaneity of ore and gangue mineral formation are difficult to be identified and such research would probably necessitate focus on ore mineral chemistry and generations, observation of large-scale outcrops and identification of major fluid-transportation discontinuities. In certain ore lithologies, such as the massive iron ore at Kolomela mine or the ferromanganese ore at Heuningkranz, infiltrating fluids permeate the ore matrix and are responsible for the precipitation of barite interstitially to hematite and

braunite. In such thoroughly intergrown assemblages, it is very likely that at least some ore mineral generations are related to the hydrothermal event(s). Barite, which possibly is a late-stage precipitation mineral, may fill both primary and secondary porosity that developed during the main alteration stage. The likelihood of hydraulic fracturing should also be considered, in view of the highly brecciated lithologies, especially in the WMD. Previous focus on hydrothermally altered BIF from the Heuningkranz locality revealed successive alteration fronts, hematitization, extensive silicification and fracturing-sealing cycles comprising gypsum-cemented breccias, that overall lend support to the above interpretation (Papadopoulos; 2016, Papadopoulos et al, in prep.).

In any case, concentration of barium and alkalis such as Na, K and Li in ores and country rocks in the form of barite, feldspars, micas, carbonates and other silicates is not in conformity with the ancient supergene models for the PMF, but instead illustrates a regional hydrothermal overprint in pre-existing lithologies. Associated processes require an enrichment of the alkali budget of the fluid(s), either from intra-stratal solution of minerals in the protores or most likely through external sources. These saline fluids can then effectively dissolve material and especially silica from prior Fe/Mn-bearing lithologies and carry ions into solutions over large distances. Even if supergene processes between 2.2 and 2.0 Ga have served as ground preparation for ore formation, one cannot discount the possibility of subsequent ore-enrichment, in view of the high geochemical mobility of the ore elements and the well-documented regional hydrothermal event(s). A consistent spatial association between the orebodies and the regional Transvaal-Olifantshoek unconformity exists and has been used as a strong indication for extensive laterization and karst formation in the models invoking supergene enrichment. In like manner, this spatial affiliation may be a key metallogenic factor, by signifying epigenetic hydrothermal enrichment processes, focusing on channels of higher permeability. Continuous alteration, metasomatism and residual enrichment of lithologies flanking the unconformity could have led to the development of the current Fe and Mn ore-grades, an idea also entertained by previous authors (Tsikos and Moore; 2005. Fairey et al; 2019). Considering all evidence that have emerged in the last decade from the PMF and the growing hydrothermal school of thought, ore enrichment processes in the region call for a revision.

5.3. Constraints on barite precipitation and fluid(s) provenance

5.3.1 Source of sulfur

$\delta^{34}S$ values for barite are remarkably constant (+24.9 ± 2.5 ‰, n=93) between the two ore fields of the Northern Cape, across a strike of ca. 150 km and despite the current evidence suggesting associated but distinct barite depositional ages (1137 ± 2 Ma for Wessels versus 1067 ± 8 Ma for Kolomela) within the time span of the Namaqua orogeny. This spatial and temporal homogeneity in sulfur isotopic composition is indicative of a single and uniform sulfate pool, which as mentioned earlier is considered to be marine-related. The limited S-isotope studies that have been previously undertaken on the wider Griqualand West basin as well as relevant S-isotope data from the Transvaal basin are summarized in Figure 16. The entire published dataset of sulfur isotope values from the Transvaal Supergroup shows a much wider range, with considerably more ^{34}S-depleted values, from approximately -31 to + 25 ‰ and can be found in Strauss and Beukes (1996) and references therein.

The possible sources of sulfate for barite mineralization in the study area include: (a) seawater sulfate released from direct dissolution of evaporites, (b) seawater sulfate modified prior to barite crystallization by mixing with sulfate-rich brines or meteoric fluids and (c) sulfate derived from the sedimentary succession and principally from oxidation of reduced sulfur preserved as sulfides in the sediments. Sedimentary-diagenetic pyrite obtained from shales interbedded with carbonates of the lower Campbellrand stratigraphy (Monteville & Reivilo Formations) display a range of sulfur isotope values between + 6.6 and +17.5 ‰ (avg. = +11.6 ± 3.7 ‰, n=9). Pyrite from the footwall clastic sediments to the Campbellrand succession (Schmidtsdrif) shows more homogenous and ^{34}S-depleted values, ranging between -0.1 and +3.5 ‰ (avg. = +1.1 ± 1.4 ‰, n=11). Similarly, a tight range of light isotopic values (-4 to 0 ‰, n=4) is shown by pyrite from the 2.7-2.5 Ga basement rocks (Bottomley et al; 1992). Abundant euhedral and framboidal pyrite is also present in the shales of the Olifantshoek Supergroup and specifically in the black shale unit (Cousins; 2016). Six analyses from the Mapedi shale obtained from drillcores NW of Hotazel, exhibit a wide range of $\delta^{34}S$ values, from +0.7 to values as high as +22.6 and 23.6 ‰, the latter two overlapping with the barite range from this study.

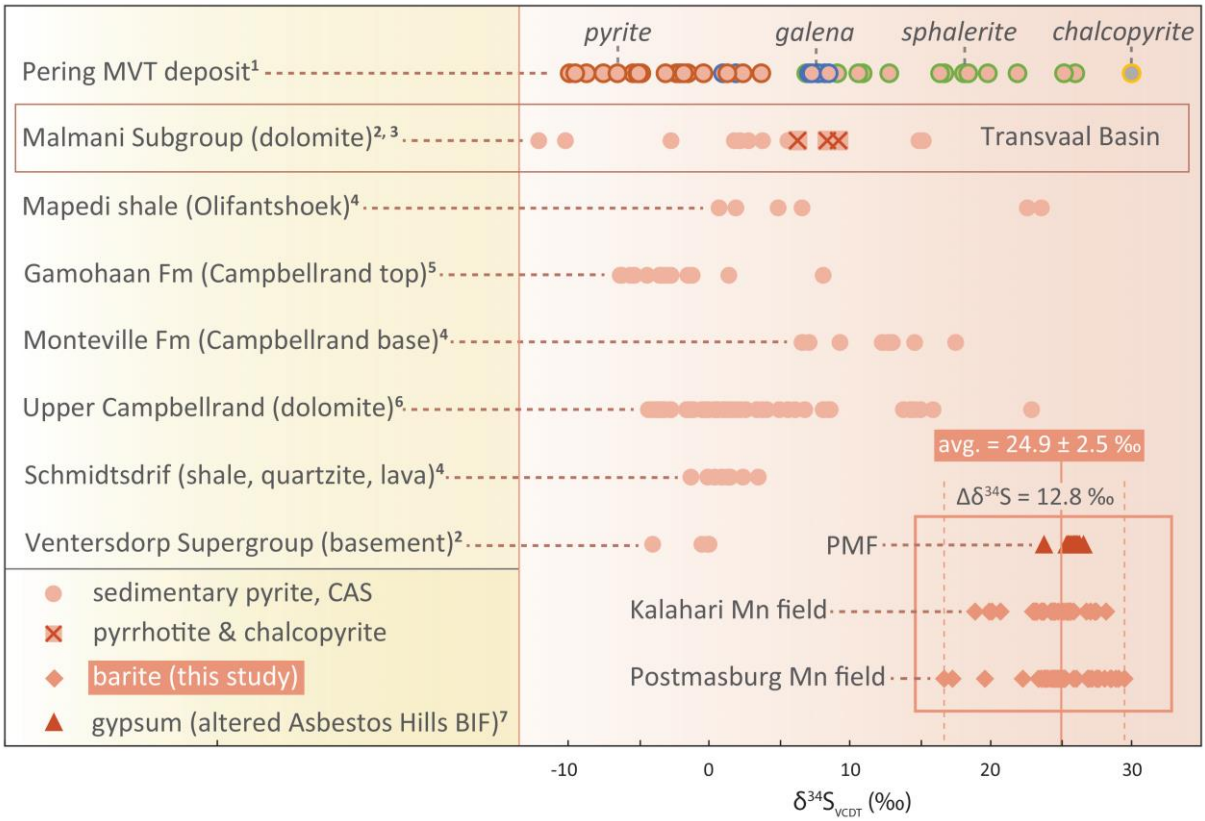

Figure 16. Sulfur isotopic distribution of various reservoirs in the Griqualand West basin in relation to that of studied barite from the Northern Cape. Data from the Malmani carbonates of the Transvaal basin are also included. Sources: (1) Huizenga et al; 2005 (2) Bottomley et al; 1992 (3) Buchanan and Rouse; 1981 (4) Strauss and Beukes; 1996 (5) Gandin et al; 2005 (6) Kamber and Whitehouse; 2006 (7) Papadopoulos et al; in prep.

All the above data, along with sulfides from the whole Transvaal dataset showing far lighter $\delta^{34}S$ values, have been interpreted by Strauss and Beukes (1996) to be a result of bacterial sulfate reduction (BSR), characterized by differences in sulfate supply and/or changes in the rate of reduction due to changing proportions of organic matter. This routine interpretation is seen in various closed, evolving diagenetic systems, where a trend towards heavier sulfur isotope ratios for sulfides is related to Rayleigh Distillation processes. In like manner, data from individual pyrite nodules from the Gamohaan Formation of the Campbellrand Subgroup, displaying a range of -6.2 to +8.1 ‰, have been also explained in terms of fractionation by sulfate reducing bacteria within the context of additional sedimentological and petrographic evidence for evaporite precipitation, associated with microbialitic sediments in the upper parts of the carbonate platform (Gandin et al; 2005). The in situ multiple S-isotope work of Kamber and Whitehouse (2007) on sedimentary pyrite from the 2.52 Ga Upper Campbellrand stratigraphy (Figure 16), further supports an origin by BSR

and revealed a very large extent of both mass-dependent (MDF) and mass-independent (MIF) isotopic fractionation for that time period.

The observed variations in $\delta^{34}S$ values of sedimentary-diagenetic sulfides of the study area are expected due to kinetic isotope effects as noted above, which can cause substantial isotope fractionation and generally produce lower sulfur isotopic values in sulfides than those of SO_4 in contemporaneous seawater. The range of $\delta^{34}S$ values of sedimentary sulfides is also highly dependent on whether the system is closed with respect to sulfide or sulfate (Ohmoto and Rye; 1979). Regardless of the aforementioned and the well documented BSR in pyrite, the key point, is that the homogeneous and heavy sulfur isotopic signal preserved in the Northern Cape barite cannot be explained by derivation from a local sulfide source, since sulfate produced by either abiotic or biotic low-temperature oxidation of sulfide minerals is accompanied by negligible fractionation (Seal et al; 2000). Therefore, in such scenario, the measured $\delta^{34}S$ values in barite should have been instead very close to those of the source sulfides.

On the other hand, barite isotopic values are a close match to those of the highly homogenous hydrothermal gypsum reported from altered banded iron-formation in the Western Maremane dome (Heuningkranz). Gypsum in this locality develops metre-scale veins and breccias, occupies vugs with carbonates and silicates and comprises different textural generations with remarkable sulfur isotopic homogeneity (+25.9 ± 0.3 ‰, n=12 ‰) (Papadopoulos et al; in prep). Origination of sulfate is suggested to be linked to dissolution of former evaporites in the Campbellrand Subgroup, evidence for which have been presented by Gandin et al (2005) and Gandin and Wright (2007) (section 5.3). Consequently, it stands to reason that gypsum and barite may belong to the same hydrothermal system and moreover share a common origin for sulfate.

The Malmani Subgroup, which is a correlative to the Campbellrand Subgroup in Griqualand West, has been also regarded by some researchers an evaporite-bearing sequence, in view of its sedimentological record which supports an equally shallow offshore marine depositional environment and comprises thinly and isopachous laminated

stromatolites, that typically mark transitions between carbonate platforms and overlying evaporites (Button; 1976, Pope et al; 2000). Although anhydrite is a rare component in the present-day carbonates, textural evidence indicate that sulfates were perhaps well-represented in the sequence in geologically earlier times (Buchanan et al; 1981).

$\delta^{34}S$ values for total sulfur in the Malmani dolomites exhibit a spread of 27 ‰, which has been proposed to record a temporal isotopic transition, corresponding to a change from a sulfate-poor ocean to one with a well-established sulfate reservoir and high BSR activity (Cameron; 1982). However, this pattern of values close to 0 ‰, becoming ^{34}S-depleted higher up in the carbonate succession, despite it being further noted by others researchers (Strauss and Beukes; 1996), is not persistent in all parts of the Transvaal Supergroup, since heavier values reappear in lower stratigraphic depths (Bottomley et al; 1992). ^{34}S-enriched pyrrhotite and chalcopyrite (up to +9.1 ‰) (Figure 16) found in calc-silicate hornfels, the latter derived from alteration of the Malmani dolomite during emplacement of the Bushveld Complex, have also been considered to reflect incorporation of a heavy anhydrite-derived sulfur signal, that in turn indicates the former presence of evaporites in the dolomite sequence (Buchanan et al; 1981). Based on a trace sulfate (supposedly anhydrite) study from the dolomite, the $\delta^{34}S$ value of contemporaneous (ca. 2.5-2.4 Ga) seawater sulfate has been estimated to be at ca. +15 ± 2 ‰ (Buchanan and Rouse, 1982).

The presence of the renowned 2.0 Ga Pering Pb-Zn Mississippi Valley-type (MVT) deposit (Wheatley et al; 1986a, Duane et al; 2004) in the wider study area warrants mention, given that sulfur-bearing brines have been involved in its formation and thus may point to an important sulfur reservoir for barite of this study. The origin of sulfur at Pering is tentatively linked to a highly saline brine leaching both metals and disseminated magmatic sulfur from the volcanics of the Ventersdorp Supergroup and the observed range of $\delta^{34}S$ sulfide values, from -9.9 to +30 ‰ (Figure 16), has been explained by Rayleigh fractionation during thermochemical reduction of sulfate (TSR) in a closed system (Huizenga et al; 2005). Dissolution of evaporites as a source of salinity and by inference sulfate has been excluded, despite fluid inclusion data from the same study indicating a halite-saturated and intriguingly

saline aqueous fluid for MVT deposits, that according to the authors has derived by evaporation of seawater.

Regardless of the exact source of sulfur and possible progressive TSR processes being responsible for the observed fractionation during sulfide precipitation at Pering, lack of evaporitic sulfur assimilation by the mineralizing brines along their flow path through the basin is puzzling and could perhaps indicate either laterally-restricted fluid conduits or narrowly-confined evaporite distribution. Generally, it is worth mentioning that it is very common for MVT deposits to inherit heavy seawater signatures and it is widely accepted that the ultimate sulfur source in these deposits is seawater sulfate contained by the sediments in various minerals and/or connate water, subsequently reduced by different processes (e.g., Field and Fifarek; 1985, Sangster; 1990, Leach et al; 2010).

Nonetheless, the uniformity of the sulfur isotopic fingerprint of barite within the regarded regional geological context of the Northern Cape, leaves little doubt for the origin of sulfate, which is almost certainly inherited from seawater or modified seawater. Sulfates such as gypsum and anhydrite are enriched in ^{34}S relative to the aqueous sulfate in solutions from which they precipitated by approximately 1.5 ‰ (Thode and Monster; 1961). Therefore, in the absence of post-depositional alteration (biological reduction, replacement), the $\delta^{34}S$ values of evaporites have been generally considered to be a close approximation of coeval seawater (see also section 5.3). In turn, the sulfur isotopic composition of barite mineralization should closely reflect that of the source, since any intermediate geochemical processes causing fractionation or mixing with other sulfur sources would in all likelihood produce a far more heterogenous isotopic signature.

Subtle variations in $\delta^{34}S$ values of barite may be interpreted as reflecting the original spread in isotopic values for evaporites of a given age, or more so, dissolution of distinct evaporitic lenses of slightly different age within the stratigraphic column. Local incorporation of other minor sulfur sources, further followed by fractionation processes may have punctuated the initial differences in certain instances. Greater scatter in sulfur isotopic ratios, caused by ^{34}S-depleted values from the localities of N'Chwaning (+18.9, +19.9, +20.1 and

+20.7 ‰), Heuningkranz (+17.3 ‰) and Kapstevel (+17.1 ‰), could be related for example to mixing with another sulfur-bearing fluid. Another factor affecting $\delta^{34}S$ barite ratios may have been dissolution and reprecipitation of barite, processes that despite the very low solubility of this mineral, have been suggested to occur from basin-scale hydrothermal districts and highly reducing systems in stratiform barite deposits (Johnson et al; 2004, Staude et al; 2011). The likelihood though of such processes being responsible for the ^{34}S-depleted values in the Northern Cape is considered to be very low. Essentially, the robust isotopic signal of such stratigraphically and lithologically diverse barite occurrences enables one to safely neglect to a first approximation the effects of potentially other sulfur sources than that of evaporites during investigation of the mineralization processes.

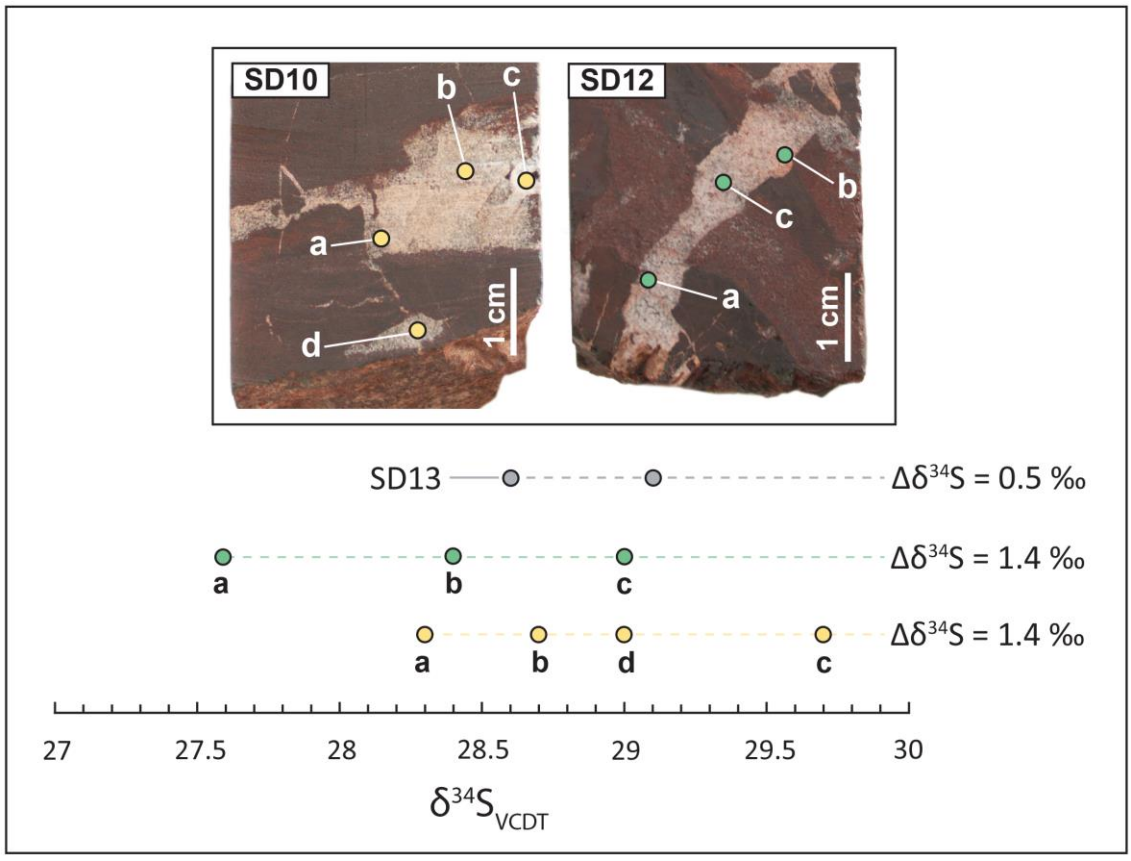

Figure 17. Measured extent of sulfur isotopic variation on the micro-scale, in fracture-filling barite from the Kapstevel locality (Kolomela). Although small, isotopic fractionation is regarded to be quantifiable (ca. 1 ‰) and in line with expected ^{34}S-enrichment during barite precipitation from the margin to the centre of fractures.

Rainwater-derived marine aerosols may also be a significant sulfate flux to the terrestrial environment over maritime regions, although these are dominant sulfur sources in

the strictly terrestrial settings such as gravel aquifers whereas the main contributor to groundwater has been shown to be bulk sulfur dissolved from the various lithological successions (Tostevin et al; 2016). There is extremely little likelihood that rainwater-derived sulfate would have equilibrated through time with the highly variable sedimentary sulfur of the Northern Cape lithologies in order to produce such a uniform isotopic signal as the one measured in barite and gypsum. Moreover, the apparent hydrothermal origin of barite, its co-occurrence with mica, garnet and feldspar, heating needed for mineralization as well as the age and nature of the regional alkali metasomatism exclude the possibility of coeval ancient rainwater (ca. 1.2 Ga) being a major source of sulfur for barite; however, not ruling out by all means the involvement in the overall mineralization processes, of meteoric water or solutions initiated as such.

An attempt to examine the behaviour of the sulfur isotopic composition of barite on the sub-sample scale is shown in Figure 17. During barite or in general sulfate formation, the light isotope (^{32}S) is removed preferentially over the heavy from aqueous solution, thus shifting isotopic composition of the sulfur-bearing fluid towards heavier values (e.g., Hanor; 2000). Sub-sampled domains from fracture-hosted barite seem to record an isotopic fractionation of up to 1.4 ‰, which is closer to 1 ‰ if 1σ uncertainties are also taken into account. Furthermore, although more speculative, material closer to the marginal parts of the occluded space displays lower $\delta^{34}S$ values than the central filling, therefore being in line with precipitation of barite from the edge to the centre of the fracture followed by small-scale fractionation of its sulfur isotopic ratios.

5.3.2 Strontium (Sr) isotope tracing

Introduction

$^{87}Sr/^{86}Sr$ isotopic systematics have been considerably applied on hydrothermally precipitated vein-type minerals with an aim to trace elemental sources, identify pathways of fluid flow and assess compositional modification of mineral-forming solutions due to mixing processes between fluids with distinct isotopic signatures. Barite has been particularly valuable in such tracer studies attempting to fingerprint preserved strontium reservoirs in the

mineralizing fluids and has helped generate important outcome regarding the ultimate origin and formation mechanisms of the mineral while also contributing to genetic models of ore deposits playing host to it (Lange et al; 1983, Kesler and Jones; 1988, Whitford et al; 1992, Galindo et al; 1994, Maynard et al; 1995, Valenza et al; 2000, Staude et al; 2011, Zou et al; 2022).

These provenance studies are premised on the assumption that the precipitated Sr-bearing mineral retains the Sr-isotopic composition of the fluid, which in turn is a measure of the contributions made by the various minerals dissolving at the source as well as along the fluid pathway prior to mineral precipitation. In broad terms, variations in Rb/Sr ratios of diverse lithologies result in distinctive $^{87}Sr/^{86}Sr$ fluid signatures that can be incorporated in epigenetic/hydrothermal barite. Hence, knowledge of the $^{87}Sr/^{86}Sr$ values of the presumed source lithologies or that present along potential flow paths is essential in drawing insights from the measured mineral data.

Following precipitation, barite is expected to maintain and accurately reflect the isotopic ratio of the fluid because of the lack of significant Sr-isotopic fractionation below 400^{o}C during sulfate crystallization (Matter et al; 1987) or other physicochemical reactions (Machel; 2004), its resistance to isotopic re-equilibration and wholesale aqueous dissolution (Hanor; 2000) and the fact that ^{87}Rb, the parent of ^{87}Sr, cannot be incorporated in its crystal lattice at concentrations higher than 100 ppb (Hofmann and Baumann; 1984), therefore obviating the need to apply corrections due to in situ radioactive decay of ^{87}Rb to ^{87}Sr. Lastly, the affinity of barite to incorporate high amounts of Sr in its crystal structure (7000 to 10000 ppm Sr; Monnin and Cividini; 2006) permits the use of very small samples and essentially renders the mineral insensitive to post-depositional contamination, which is best illustrated in examples such as that of primitive $^{87}Sr/^{86}Sr$ values preserved in Archean barite from the Pilbara Block of Western Australia (McCulloch; 1994).

Principal source and Sr/Ba reservoirs for Northern Cape barite - A first approach

The wide range of Sr isotopic ratios in the measured barite from the Northern Cape (0.7058 to 0.7382) comprises almost exclusively values that are variable and significantly

more radiogenic than that expected from a seawater origin, therefore favouring continental crust as the bulk source of Sr and by extension Ba. An ''enrichment'' in radiogenic Sr is expected in fluids percolating through sedimentary basins such as that precipitating barite in the Postmasburg and Kalahari manganese fields, which apparently have derived $^{87}Sr/^{86}Sr$ ratios in excess of seawater values from alteration of silicate minerals.

$^{87}Sr/^{86}Sr$ variation for the Phanerozoic Ocean is very well constrained using low-Mg calcitic fossils to range between 0.707 and 0.709, with the modern seawater value established to be 0.709183 (Hodell et al; 1990, Veizer et al; 1999). The earlier scene from the Palaeoproterozoic and Archean eons is more cryptic, with evidence suggesting a transition from an ocean dominated by hydrothermal input and Sr-isotopic values being marginally more radiogenic to coeval mantle, to a system with higher continental fluxes (Derry and Jacobsen; 1988, Kamber and Webb; 2001). Increasing continental runoffs eventually led to a substantial rise of the Sr-isotope composition during the Late Proterozoic and a maximum in the early Cambrian, with Sr-isotopic ratios becoming at that time similar to that of present-day seawater (0.708-0.709) (Dickin; 1995). Despite existing ambiguities and the poorly constrained timing of the $^{87}Sr/^{86}Sr$ excursion during the Palaeoproterozoic, all evidence suggests that Sr-isotopic ratios in the ocean would have been similar to or slightly lower from that of the Phanerozoic, broadly ranging from 0.7020 to 0.7055 (Faure; 1986, Veizer et al; 1989). Consequently, a marine Sr-isotopic signature can be safely excluded for the Mesoproterozoic barite mineralization in the Northern Cape, despite the strongly retained marine sulfate signal and the limited incorporation of seawater-like $^{87}Sr/^{86}Sr$ values in specific samples which is further discussed below.

Considering the age of barite, the preserved marine water signature and its epigenetic mode of occurrence in stratigraphically restricted horizons of Fe-Mn mineralization or lithologies in close association to the latter and the regional geological boundaries (Blackridge thrust belt and Transvaal-Olifantshoek unconformity), it can be reasonably surmised that Sr in the hydrothermal fluid and by inference Ba have been supplied from one or more of the following reservoirs: (a) the underlying Campbellrand carbonate platform and possibly other basement strata of the Schmidtsdrif Formation or the Ventersdorp Supergroup, (b) the Fe-

and Mn-ore host rocks, i.e., the Asbestos Hills and Hotazel iron-formations and (c) the clastic sedimentary succession of the Olifantshoek Supergroup which overlies the different ore lithologies.

Since barite in the PMF has apparently precipitated after a certain degree of fluid interaction with preexisting Fe- and Mn-rich sediments and deposits that are thought to have formed before the 1.2-1.0 Ga Namaqua-Natal orogeny, the Sr-isotopic ratios of the mineral may have been locally influenced also by these immediate host lithologies. The ratios of the latter are expected to be variable radiogenic, with $^{87}Sr/^{86}Sr$ values depending chiefly on the: (i) protore lithologies (carbonates and BIF) which generally lack detritus and have high Sr/Rb ratios, (ii) the accumulation of siliciclastic material with radiogenic Sr and high Rb content mainly from weathering and dissolution of the overlying Olifantshoek sediments during ore-formation and (iii) the Sr-isotopic composition of the ore-forming fluid(s) which almost certainly would have caused a shift towards more radiogenic values, since the Sr budget for at least some of these fluids would have derived from clastic lithologies as well, on the basis of the current supergene-focused ore genetic models.

As explained below, the current Sr-isotopic dataset for barite alone and the limited knowledge of the isotopic character of the surrounding lithologies hamper any attempt to confidently pinpoint the Sr/Ba reservoir(s) and ultimate source of the hydrothermal fluid(s) for all diverse barite occurrences on the regional-scale. However, combined S-Sr data and information from other studies still allow to cast light upon the formation mechanisms of barite, give clues on the effects of alteration on the host lithologies and point to the most likely bulk sources of Sr and Ba that are essentially responsible for the observed regional barite mineralization.

Barite in the Kalahari manganese field

The scarce $^{87}Sr/^{86}Sr$ data available from the study area are compiled in Figure18. Conducted research on a well-preserved succession of the Voëlwater Subgroup (Schneiderhan et al; 2006) offers the best available source of reference whole-rock Sr-isotopic signatures to help understand the Sr-isotopic composition of barite in the KMF. The overall

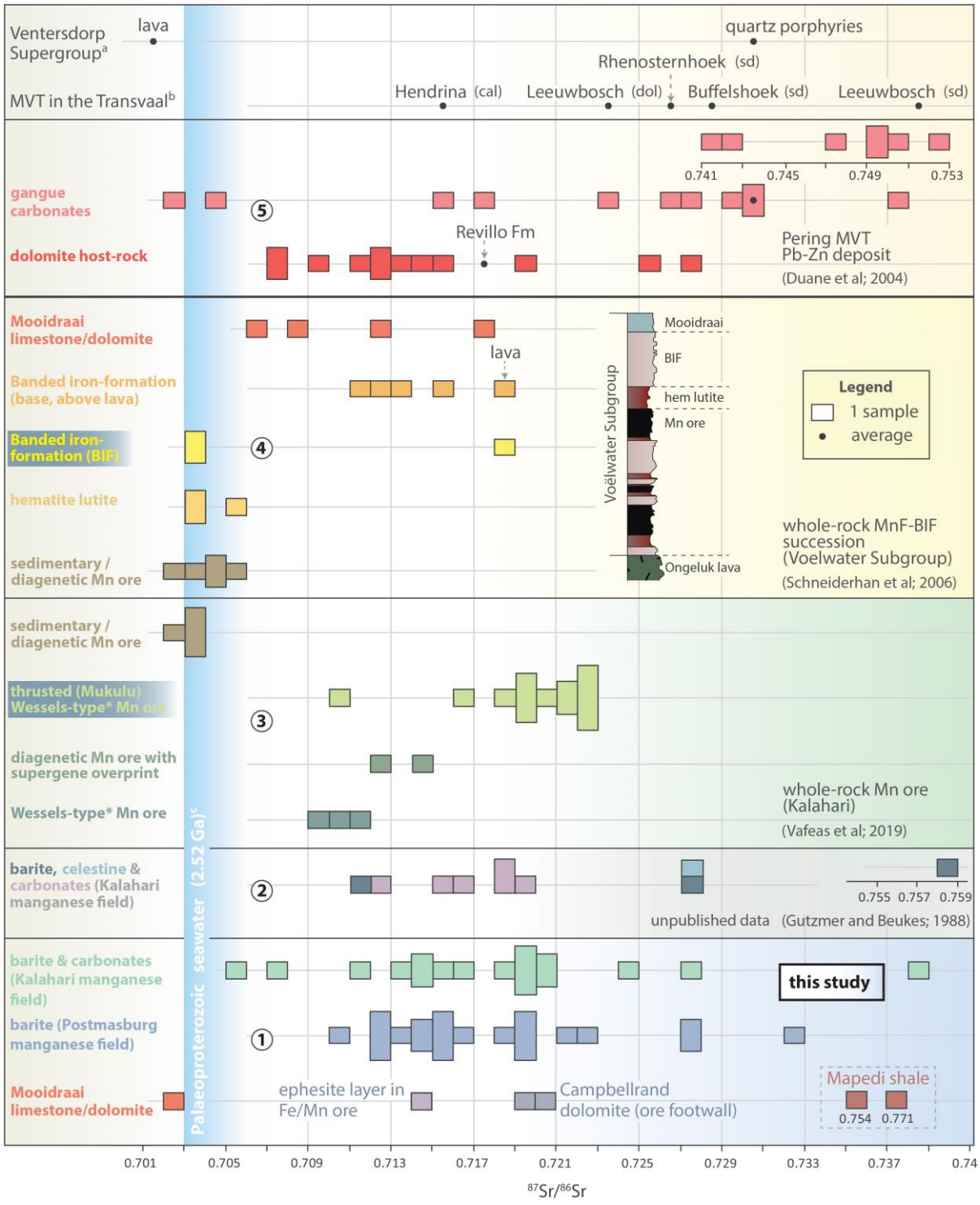

Figure 18. Comparative diagram of the strontium isotopic composition of barite and hydrothermal gangues (1,2) with that of different lithologies from the Northern Cape (1,3,4). $^{87}Sr/^{86}Sr$ ratios from Pb-Zn MVT deposits in the Transvaal and Griqualand West basins and from basement lithologies are also included (5). Values for the Mapedi shales have not been corrected for the time of barite mineralization (1.2-1.0 Ga) but after back calculations assuming different Rb and Sr concentrations, shale $^{87}Sr/^{86}Sr$ ratios (between 0.1-0.2 less radiogenic) are expected to partially overlap with the higher-end of barite values.

stratigraphy of the Voëlwater Subgroup (Figure 18.4) comprises chemical or biochemical metalliferous sediments (BIF, hematite lutite, stratiform Mn beds and limestone/dolomite) that have been considered by the previous authors as an opportunity to peer into the Sr-isotopic composition of their contemporaneous ca. 2.4 Ga seawater. The initial ratios are believed to have remained largely unaffected by virtue of the very small amounts of Rb that would have been initially incorporated in the sediment precursors, the largely absent clastic detritus and the only moderate diagenetic overprint that has affected the pristine lithologies since their deposition. Schneiderhan et al (2006) report a tight cluster of unradiogenic $^{87}Sr/^{86}Sr$ values which confirm the preservation of a seawater signature in these sediments but additionally present a range of markedly more radiogenic ratios from the same drill cores, all deriving from the southern part of the KMF. It is worth reminding that this area has not experienced the hydrothermal metasomatic event (Wessels event) forming barite and other alkali-rich gangues, during ore-upgrade of the northernmost part of the KMF.

In more detail, pristine carbonate-rich samples of bedded Mn ore, hematite lutite and BIF (n=10) of the Hotazel iron-formation are characterized by values between 0.7028 and 0.7057. These ratios agree with the above-presented estimates of contemporaneous seawater and moreover have been explained as to particularly represent Palaeoproterozoic seawater dominated in its Sr-isotope value by hydrothermal alteration of oceanic crust. The presence of synchronous low-temperature seafloor alteration was firstly reported by Cornell et al (1996) on the basis of observations on the continental flood basaltic andesites of the Ongeluk Formation which constitute the immediate basement to the Hotazel Formation. Interaction with a suspected 0.7025 seawater signature is believed to have caused a decrease of the initial $^{87}Sr/^{86}Sr$ Ongeluk-Hekpoort basalt values (0.7069-0.7071; Armstrong; 1997, Cornell et al; 1996) to contemporaneous mantle values. In any case, there is no doubt regarding the broad preservation of a 2.4 Ga seawater signal, despite Sr-isotopic values being slightly less or more radiogenic, the latter caused by a mild overprint by post-depositional fluids as suggested by Schneiderhan et al (2006).

However, Sr-isotope values from carbonate and oxide facies BIF at the base of Hotazel Formation and the directly overlying carbonates of the Mooidraai Formation (Figure 18.4) are

variable and much more radiogenic (0.7110 - 0.7223 and 0.7069 - 0.7179 respectively) than expected for Palaeoproterozoic seawater (0.7020 - 0.7055). This led the previous authors to invoke epigenetic fluid-rock interaction processes and post-depositional recrystallization in order to explain this signal. Interestingly, a single whole-rock analysis from Mooidraai carbonate in this study (sample M2), deriving from the central/northern KMF, shows a contrastingly different $^{87}Sr/^{86}Sr$ value of 0.7029 (Figure 18.1). This may suggest that Mooidraai Formation is not recrystallized or pervasively metasomatized as proposed by other researchers (Fairey et al; 2013), to a point where its pristine isotopic signatures have been regionally obliterated, a hypothesis which however requires further investigation. In addition, the low $^{87}Sr/^{86}Sr$ value from the Mooidraai sample further corroborates that the lithological succession studied by Schneiderhan et al (2006) has been influenced by epigenetic events, at least near the base and top of the Hotazel Formation, an observation which highlights the great need for in-depth petrographic analysis during whole-rock Sr-isotopic studies.

Nevertheless, as regards the Sr/Ba sources for barite in the KMF, it is evident that none of the reservoirs in the Voëlwater stratigraphy can supply sufficiently radiogenic Sr to the hydrothermal fluid(s) that precipitated barite (0.7114 - 0.7388, average = 0.7201 ± 0.0077, n= 10) and carbonates such as calcite (0.7142, 0.7180), Sr-rich aragonite (0.7136) and rhodochrosite (0.7190, 0.7248) in the N'Chwaning mine. Hydrothermal carbonates have also low Rb/Sr ratios (Whitford; 1992) but generally bear much lower Sr concentrations in their lattice in comparison to barite and thus are more susceptible to contamination and changes in their $^{87}Sr/^{86}Sr$ values during post-depositional alteration (Brand; 1991). However, the measured values for the N'Chwaning carbonates coincide with that of barite as well as with unpublished data for barite (0.71076 - 0.75862, n=3), celestine (0.72716) and carbonates (0.71239 - 0.71917, n=6) from (Gutzmer and Beukes; 1998, technical report), deriving primarily from the Wessels and lesser from the N'Chwaning and Black rock mines (Figure 18.2). This indicates that sulfate and carbonate gangue mineralogy have both acquired their Sr from a very radiogenic Sr reservoir.

The sediments of the Olifantshoek Supergroup (Gamagara/Mapedi shales and quartzites) appear to be the most plausible candidates to supply Ba and radiogenic Sr, given

that they form the immediate cover to the barite-hosting lithologies and the fact that orogenic-related hydrothermal activity in the broad vicinity of the Olifantshoek-Transvaal unconformity is believed to be pervasive in the wider region (Tsikos and Moore; 2005, Fairey et al; 2019) and confirmed to be coeval in the present study. Barium (Ba) is also expectedly more abundant in the shales than in the Hotazel Formation if a local source is principally regarded for this element. From the limited available data, red shales from the Gamagara/Mapedi Formation have an average barium concentration of 474 ± 249 ppm (n=13) (Yamaguchi and Ohmoto; 2006), in contrast to the much lower averages of the Hotazel iron-formation (37 ppm, from below detection to 147, n=12), Mooidraai carbonates (23 ± 9 ppm, n=6) (Tsikos and Moore; 1997, Schneiderhan et al; 2006) and that of Ongeluk lavas, with intermediate concentrations between the previous two (267 ± 178, n=104) (Cornell et al; 1996). Higher barium concentrations in the 'pristine' Mn ore beds ranging from 92 to 3800 ppm (average = 586 ± 961 ppm, n = 14) Schneiderhan et al (2006) almost certainly reflect alteration events, as it is implied by textural descriptions of replacement by barite and other minerals which have been attributed by the aforementioned researchers to localized late diagenetic or epigenetic fluid flow events.

A representative red and white banded shale from the Wessels mine analysed in this study displays extremely radiogenic Sr-isotopic ratios. Specifically, the red and hematite-rich shale portion has an $^{87}Sr/^{86}Sr$ value of 0.77055 and the white clay band one of 0.75369. These values are not corrected for an 1.2-1.0 Ga age, during which time fluid(s) are presumed to have passed through these rocks leaching Ba/Sr, but considering that Rb in the subsamples is likely in the range of hundreds of ppm (average red shale Rb: 187 ppm; Yamaguchi and Ohmoto; 2006), the $^{87}Sr/^{86}Sr$ ratios of the Mapedi shales are expected to have been much less radiogenic than the measured values. Precise back calculations are not presented here since Rb and Sr concentrations were not measured and apparently vary considerable in the formation (average Sr = 111.6 ± 70.3 ppm and Rb = 187.1 ± 57.5 ppm, n=13; Yamaguchi and Ohmoto; 2006), although it can be agreed that the anticipated ratios are approximately 0.1-0.2 less radiogenic and thus fall well within the range of the analysed barite and carbonates. In contrast to average shale comprising clays, feldspar and carbonate which account for more than 70% of the rock (Shaw and Weaver; 1965), the regarded red shale consists mainly of

quart silt, very fine-grained hematite and possibly scarce iron-rich clays. Discolouration of red shales to pale green-white is suggested to have occurred during diagenesis and leaching of Fe-bearing silicates whereas influence by hydrothermal activity is regarded as evident (Yamaguchi and Ohmoto; 2006, Land et al; 2017). It is thus unclear which mineral dissolution governed the isotopic composition of Sr in the fluid precipitating barite with radiogenic Sr as high as 0.7388 and 0.75862, giving also consideration to the fact that Sr exists primarily as a proxy for Ca in Ca-bearing species, which are not present in the Gamagara/Mapedi shales.

Vafeas et al (2019) suggested that the degree of metasomatic alteration overprinting the sedimentary/diagenetic Mn-ore beds in the KMF is reflected in their whole-rock $^{87}Sr/^{86}Sr$ isotope values (0.70325 ± 0.00033, n=4), which progressively increase from hydrothermally enriched (Wessels-type) ore (0.71045 ± 0.00079, n=3), to supergene ore lacking a previous hydrothermal overprint (0.71373 ± 0.00158, n=2) and finally to supergene-enriched ore (0.71789 ± 0.00506, n =13) associated with alteration (referred to as the 77 Ma Mukulu enrichment) of thrusted packages of Hotazel Formation below the Cenozoic Kalahari Formation (Figure 18.3). This interpretation though lacks rigorous mineralogical controls on the Sr source which as regards for example the Wessels-type ore, could well derive from a mix of barite, carbonates and other gangues.

In any case, $^{87}Sr/^{86}Sr$ values for the hydrothermally overprinted ore (Wessels-type) coincide with the lower end of the barite isotopic range but ratios for the latter can be markedly more radiogenic than all metasomatized and radiogenic Sr-enriched ores in Figure 18.3. Preservation of Sr from original carbonates can be perhaps responsible for a decrease in the whole-rock Sr-isotopic compositions of the variously altered Mn ores studied by Vafeas et al (2019). However, the KMF barite values evidently suggest that during the regional alkali metasomatism, Sr from comparatively more radiogenic reservoirs than that associated with the 'Mukulu' enrichment was acquired by the fluids. Further insights can be drawn from the difference in Sr-isotopic ratios (0.0042) between coexisting barite (sample NBRD1) and rhodochrosite (NBRD2), which is a clear indication for significant isotopic variations in the mineralizing fluid(s). These changes may be associated with complex mixing processes

between fluids from different lithological reservoirs or may perhaps represent succeeding stages of precipitation during a relatively protracted alteration.

A pair of samples from the Wessels mine, comprising barite hosted by hematite lutite, unconformable overlain by quartzites of the Olifantshoek Supergroup (sample WBC2) and barite vug-fillings in Mn ore (WB5), show very unradiogenic $^{87}Sr/^{86}Sr$ values (0.70575, 0.70743), in marked contrast to all other analysed and apparently coeval barite (Figure 18.1). As a consequence, these isotopic ratios cannot have derived from a siliciclastic source but may instead reflect the composition of the immediate host rock or that of an initial fluid originating from carbonate and/or evaporite dissolution. Mineralogical evidence [for e.g., hydrothermal strontianite, celestine or wesselsite ($SrCuSi_4O_{10}$)] suggest that Sr is a highly mobile element during the Wessels ore-upgrade and the original carbonate ore components can provide Sr in the range of hundreds of ppm (Tsikos and Moore; 1997, Schneiderhan et al; 2006). In all likelihood, variable radiogenic Sr of the hydrothermal fluid was locally diluted by Sr leached directly from the Hotazel Formation or alternatively, localized barite occurrences preserve the composition of a fluid characterized by lower Sr-isotope ratios. The latter could have derived for the most part from leaching of marine carbonates and/or evaporites from the Campbellrand platform. If the first scenario is favored, redistribution and prevalence of Sr from pristine carbonates without mixing and re-equilibration with excess radiogenic Sr introduced by the hydrothermal fluid is apparently very rare, as evidenced by the vast majority of highly radiogenic samples.

Barite in the Postmasburg manganese field and precipitations mechanisms

The considerable range of barite Sr-isotope ratios (0.71056 - 0.72137, average = 0.71474 ± 0.00380, n=8) from a single locality in the PMF showing pervasive barite mineralization (Kapstevel Fe-ore, Kolomela mine), illustrates that determination of the ultimate source of the specific fluid(s) responsible for precipitation of barite cannot be readily achieved using only its $^{87}Sr/^{86}Sr$ ratios. Petrographic evidence suggests that the protolith subjected to ore formation in the studied drillcores is primarily iron-formation but intercalations of altered and iron-enriched shales are also present.

Sr-isotopic compositional differences in barite may reflect the original fluid source deriving from a reservoir with inhomogeneous $^{87}Sr/^{86}Sr$ ratios or interactions with the rocks it has passed through, the latter characterized by different Sr-isotopic signatures. Intrasample variations ($\Delta^{87}Sr/^{86}Sr$ = 0.00201 ± 0.00050, sample SD10) suggest a certain degree of interaction between fluid and host rock in the precipitation site, although further data are needed to assess isotopic modifications and/or fractionations of the hydrothermal fluid. However, if the barite-forming fluid had been readily exchanging Sr isotopes with the surrounding sediments in the precipitation site, any attempt to characterize the ''primary'' composition of the fluid would be useless. The broad coincidence between the range of barite Sr-isotopic ratios from different localities can be taken as evidence for limited isotopic exchange with the immediate host rock and therefore the above scenario is not further regarded.

The much less radiogenic $^{87}Sr/^{86}Sr$ values (average = 0.71474 ± 0.00380) in comparison to that from the KMF barite being commonly > 0.72000 and as exceedingly high as 0.75862 and the fact that shales are readily available in the surrounding rock if not also have participated in metallogenesis, are probably signs that the isotopic composition of the precipitating fluid is governed by basement-derived Sr from the Campbellrand dolomites and partially mineralized iron-formation of the Asbestos Hills Subgroup or most probably from deep-seated volcanosedimentary rocks. Barite mineralization is again most likely subject to shale-derived Sr and essentially Ba, but an infiltrating fluid likely less enriched in ^{87}Sr, having largely equilibrated with lithologies underlying the Olifantshoek Supergroup is suggested to have been a substantial source of Sr as well.

$^{87}Sr/^{86}Sr$ ratios from the remaining barite (0.71324 - 0.7278, n=9) hosted by ferromanganese ore, chert-bearing Mn ore (Wolhaarkop), conglomeratic and massive Fe ore, all fall within the same range as that from Kapstevel Fe ore. Most interestingly, the investigated whole-rock Sr-isotopic composition of dolomite (0.71961, 0.72073) directly underlying ferromanganese ore (Heuningkranz) and of a gangue ephesite-rich (mica) ''shaley'' layer (0.71468) intercalated with ferromanganese ore (Bishop mine), also overlap with the above ratios (Figure 18.1). The extensive Campbellrand carbonate platform is one of the likely

fluid sources and Sr contributors, if also dissolution of associated ancient evaporites has been involved in the generation of fluids. Sr-isotope ratios from the upper stratigraphy of Campbellrand (Gamohaan and Kogelbeen Formations) have been recognized to reflect dissolved Sr in the waters from which the carbonates and stromatolites precipitated (Kamber and Webb; 2001). The same authors pointed out that the Campbellrand carbonate platform constitutes a blanket (several hundred to 1500 m thick) which would have isolated the upper part of the stratigraphy from potential hydrothermal Sr sources in the crystalline basement and furthermore that radiogenic Sr within the stratigraphy is inconsequential because shales are volumetrically minor in the succession and have much lower Sr content than those of carbonates.

Despite this indisputable retention of seawater $^{87}Sr/^{86}Sr$ values in the Campbellrand, parts of this extensive early Proterozoic carbonate succession could have been isotopically altered by ^{87}Sr-enriched fluids from different crustal sources during post-depositional processes of diagenesis, recrystallization and dolomitization. Dolomites typically display higher $^{87}Sr/^{86}Sr$ ratios than limestone or coeval seawater (e.g., Stein et al; 2002, Kimmig et al; 2021) and regardless of the significant amounts of limestone still comprising Campbellrand Subgroup, dolomite is also present and more than that is dominant in the stratigraphically equivalent Malmani carbonates of the Transvaal basin (Beukes; 1987, Sumner; 2006). On the grounds that samples analysed in this study apparently consist entirely of dolomite and moreover are host to micro-veins or domains containing dolomite with higher Mn-content (Synthesis, section 8.3), the high $^{87}Sr/^{86}Sr$ ratios (0.71961, 0.72073) evidently reflect post-depositional isotopic disturbance and in particular either the dolomite isotopic signature at ca. 1.2 Ga or most likely a composition resulting by Sr-uptake from the epigenetic alkali-rich fluids interacting with dolomite during the Namaqua orogeny. The value obtained from the ephesite-rich layer (0.71468) of another locality (Bishop) is suggested to reflect the Sr-isotopic composition of the dominant Na- and Li-rich mica, since sodium-strontium ion-exchange has been demonstrated to occur in synthetically produced brittle micas (Kodama et al; 2001). The similarity between the $^{87}Sr/^{86}Sr$ ratios of this gangue phase with coeval barite supports similar Sr sources as that presented above.

Evidence for the immediately surrounding host rock exerting control on the composition of hydrothermal fracture-filling gangues and probable Sr-exchange between fluid and host rock is evidently provided by the distinctly more radiogenic $^{87}Sr/^{86}Sr$ values of quartzite-hosted barite (0.72754 - 0.732308, n=3), overlying apparently syngenetic barite from both iron- and ferromanganese-ore (0.71580 - 0.72278, n=4) in the same locality. In view of all the above-presented data, such compositional differences can be explained by mixing of ascending deep basinal fluids with surficial meteoric or ambient shallow groundwater, the latter being responsible for an influx of elevated radiogenic Sr leached primarily from the siliciclastic Olifantshoek Supergroup as well as for the introduction of the bulk amounts of Ba needed for precipitation of barite.

Formation of barite is regularly explained through dynamic two-component mixing models, involving the interaction of a Ba- and/or Sr-rich fluid with one carrying dissolved sulfate (e.g., Hanor, 2000, Valenza et al; 2000), since the reaction between Ba, Sr and sulfate produces solids of very low solubility in natural waters, which essentially prohibit the synchronous existence of dissolved Ba and sulfate. Regarding barite in this study, the prominent seawater sulfate isotopic signature and the prevalent mixed continental Sr-isotopic signal, attest to an analogous precipitation mechanism for barite from mixing of two end-member fluids: (a) The first reasonably assumed to be saline and hot basinal fluids trapped within the deeper strata of the basin and forced to migrate upwards during the Namaqua orogeny. These brines carry isotopically heavy sulfate from dissolution of evaporites and variable radiogenic Sr after leaching dolomites, BIF and other basement strata and eventually combine with (b) a surficial cool water which greatly increases the $^{87}Sr/^{86}Sr$ of the fluid(s) by introducing elevated Sr-isotope ratios and dissolved Ba leached primarily from siliciclastic rocks. The positive correlation between $^{87}Sr/^{86}Sr$ and $\delta^{34}S$ values is typically interpreted as evidence of fluid mixing during barite precipitation (Kesler and Jones; 1980, Valenza et al; 2000, Gaškov et al; 2017). Similar moderate to strong covariation can be seen for barite of different localities and lithologies in the PMF and KMF (Figure 13), which further corroborates the scenario of two fluids mixing at varying ratios.

It is worth mentioning that Ba is a fundamental component of the alkali-rich metasomatizing fluids in the wider area and apart from barite, the element is present in parageneses comprising Ba-felspars (banalsite, hyalophane), -silicates, -carbonates, -oxides and -vanadates (Costin et al; 2015, Fairey et al; 2019, chapters 5 & 6). The solubility of barite is known to increase with increasing salinity and fluids undersaturated with respect to barite can result from mixing of barite-saturated solutions with differing NaCl concentration (Blount; 1977, Hanor; 2000). It is therefore likely that small amounts of barite seen in the alkali-rich parageneses have been precipitated exclusively from components carried by basinal brines, without the requirement of mixing with a Sr/Ba-rich meteoric-dominated fluid. Larger quantities of Ba and Sr could have been also transported in fluids sourced from other basinal strata with no involvement of evaporite dissolution. A lot of the aforementioned Ba-bearing assemblages may be sulfur-free, something explained either by previous removal of sulfur being present in the solution during prior barite precipitation or indeed by complete absence of sulfur in the initial basinal water segment.

In this regard, the siliciclastic Olifantshoek sediments and surficial waters may have been dominant but not necessarily the exclusive Ba reservoir, similarly to what has been suggested above for radiogenic Sr, a component that could have derived from diverse entities acting as fluid sources, ranging from indigenous dolomites, BIF and other basement lithologies to possibly distant granitoids of the Namaqua metamorphic belt, if the age, origin and geotectonic setting of mineralization is taken into account. Given the present dataset, leaching of various amounts of Sr from different sequences in the basin needs also to be addressed and such processes would have been dependent on composition and solubility of the wall-rock as well as temperature fluctuations and chemistry of the fluids. Regardless of the exact continental Sr source and the influence of different sedimentary rocks along the fluid(s) pathway, the inferred fluid-mixing formation mechanism for barite is common in several continental settings which share similarities with the epigenetic barite of the Northern Cape, such as for example that of Mississippi Valley-Type (MVT) Pb-Zn ore deposits (see also next section).

Data from the ancient Pering deposit in the Griqualand West basin, being ca. 100 km from the study area (Figure 1), have shown that carbonate wall-rock within and in proximity to the mine is rather radiogenic, ranging from 0.7104 (n=7) to 0.7208 (n=4) respectively (Duane et al; 2004). Moreover, $^{87}Sr/^{86}Sr$ values from the carbonate cements become progressively more radiogenic with each mineralization stage, reaching very high values (from 0.7295 to 0.7359 and 0.7477). This led to propose that fluids for the formation of the deposits have been derived either from the basement or more likely from the felsic volcanics of the underlying Ventersdorp Group during an active deformation stage at ca. 2.0 Ga. In the case of Northern Cape barite, involvement of deep-sourced, basement fluids as regards its strontium isotopic composition is very likely and together with the siliciclastic sediments of the Olifantshoek may explain the highly radiogenic members.

Northern Cape hydrothermal barite in comparison to other barite districts

Barite mineralization in the Northern Cape is mainly characterized by derivation of Sr predominantly from diverse continental sources (see previous sections & summary) and a fluid-mixing mode of formation involving brines carrying sulfate of evaporitic origin and surficial Ba/Sr-rich waters that have interacted with Rb-bearing siliciclastic sediments. These inferred elemental sources and genetic processes are further substantiated by the examination of other barite occurrences in the literature. Selected ranges of $^{87}Sr/^{86}Sr$ ratios for continental hydrothermal barite and surrounding lithologies are illustrated in Figures 19 and 20.

The wide range of Sr-isotopic compositions among the studied barite overlaps very well that observed elsewhere from basin-scale hydrothermal vein mineralization, which reflects different source lithologies and/or large time intervals of mineral-formation. In particular, hydrothermal vein-hosted barite in Western and Southwestern Germany, spatially distributed over distances of several hundred kilometers and hosted by crystalline basement (gneisses and granites) and supracrustal sedimentary rocks of diverse ages, display large scatters in their Sr-isotopic compositions, the latter broadly falling within the range documented for barite in this study, i.e., between 0.710 and 0.723 ($\Delta^{87}Sr/^{86}Sr = 0.013$) (Figure 19.1-3). The widespread mineralization in the above example covers events from Permian to

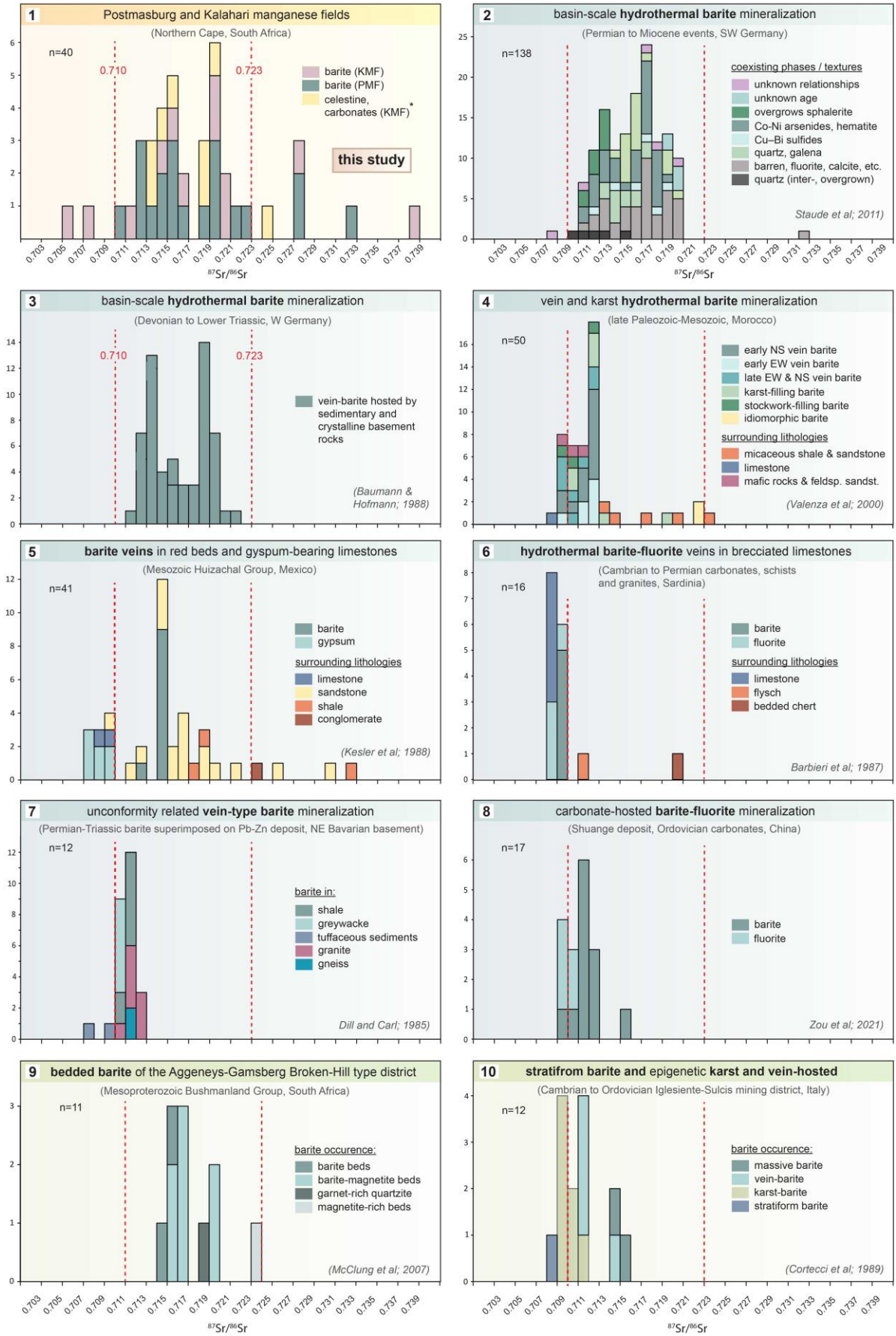

Figure 19. See next page.

Figure 19. Frequency histogram illustrating Sr isotopic composition of barite and hydrothermal gangues (celestine and carbonates) from this study (1) in comparison to other selected localities worldwide (2-10), including hydrothermal-type and stratiform barite. Red vertical dotted lines define the main spread of barite data from the Northern Cape. References and explanations in figure. * Celestine Sr data from the KMF not included in this study display similar values to barite.

Miocene but each distinct barite generation shows a more or less similar scatter in its Sr-isotopic composition. Sr has been acquired chiefly from other sources than the immediate host rock and regardless of the different sources of sulfur (leaching of basement sulfides or dissolution of evaporites), barite precipitation was induced by mixing of basement-derived fluids with sedimentary formation waters (Staude et al; 2011).

Taking into consideration that Sr and Ba of the Northern Cape barite appears to have derived from other sources in addition to clastic lithologies, parallels can be drawn between this and the vein and karst barite deposits in the Western Jebilet of Morocco (Valenza et al; 2000). These wide-scale hydrothermal deposits have been associated with rifting processes and the radiogenic Sr is interpreted to reflect a mix between ^{87}Sr-enriched Sr from Cambrian shale and sandstone and ^{87}Sr-depleted Sr derived from limestones and/or Triassic to Jurassic evaporites. It is noteworthy that early-vein and karst barite display a relatively narrow spread of $^{87}Sr/^{86}Sr$ ratios (0.70931-0.71946) which despite it exceeding significantly that of limestones (0.70839), it never extends to the very radiogenic values shown by idiomorphic barite (0.72257), which is within the range of clastic sediments and has certainly acquired Sr from them (Figure 19.4). A similar case involving less radiogenic Sr from dolomites, evaporites and BIF mixing with elevated radiogenic Sr from clastic sediments or previously mineralized lithologies can satisfactorily explain the measured isotopic composition of barite in this study.

Barite and gangue minerals in hydrothermal veins can exhibit relatively wide ranges in their Sr-isotopic signatures ($\Delta^{87}Sr/^{86}Sr$ = 0.04 - 0.09) (Barbieri et al; 1984, Carignan et al; 1997) but in a large number of case studies, $^{87}Sr/^{86}Sr$ ratios are more tightly clustered and reflect closed system reservoirs, strong control by the immediate host rock or highly evolved crustal sources. The unusually homogenous Sr-isotopic composition of barite (0.71322, ± 0.00074, 1σ) formed by remobilization of gypsum beds and hosted by red beds in the Galeana

barite district (Mexico), has been interpreted to reflect the isotopic composition of a small volume of clastic sediment, similar to that of a single oil field (Kesler et al; 1988). However, $^{87}Sr/^{86}Sr$ from the surrounding siliciclastic lithologies are very radiogenic and widely scattered (Figure 19.5), much like what is expected from the Olifantshoek sediments, regarded here to act as the main source of Ba and radiogenic Sr for the Northern Cape barite.

A similar situation in which barite $^{87}Sr/^{86}Sr$ ratios are strikingly homogeneous (0.70938 ± 0.00364, 1σ, n=16) and overlap with that of host rock carbonates can be seen in hydrothermal settings where the bulk of the Sr is provided by the carbonate wall rock with no significant contamination from surrounding silicates (Figure 19.6) (Barbieri et al; 1987). In this example, Sr in fluorite is believed to be governed by limestones whereas barite may have incorporated Sr from bedded cherts and flysch. Dill and Carl (1987) presented a model for circulating fluids close to the boundary between basement and foreland (overburden) lithologies, according to which unconformity-related barite mineralization obtains its Sr primarily by the various host-rock crustal segments straddling the unconformity, either that being gneiss, granite or shale (Figure 19.7). Although this study is based only on Sr isotopes and ignores the origin of sulfur, it provides good indications that lithologies close to the Transvaal-Olifantshoek unconformity which play host to the studied barite may have greatly influenced or locally prevailed on the Sr-isotopic composition of the fluid(s) by enriching it in radiogenic Sr.

Carbonate-hosted Ba-F (±Pb-Zn) deposits have generally Sr ratios more radiogenic than contemporaneous seawater, indicating diverse continental sources. These are imprinted on barite and/or fluorite either as mixed inhomogeneous isotopic signatures ($\Delta^{87}Sr/^{86}Sr$ up to ca. 0.09) or else as in the case of the Shuanghe Ba-F deposit shown in Figure 19.8, they may reflect a relatively closed system with a relatively homogeneous signature (0.71115 ± 0.00148, 1σ). In the latter deposit, this closed system is explained as being one of basinal brines trapped within the basement, which however have still been possibly mixed with meteoric waters containing highly radiogenic Sr before barite precipitation (Zou et al; 2021). Barite-fluorite (Pb-Zn) veins of the Sierra del Guadarrama in Spain show lower $^{87}Sr/^{86}Sr$ ratios (0.7154 - 0.7207) than in the host granitoids (0.7264 and 0.72944) (Figure 19.9), which in line

with evidence on a marine origin for sulfate, have been interpreted by the authors as indication of mixing between shallow saline brines from an evaporitic/marine environment with hot ascending fluids that have reacted to a variable extent with the host granitoids (Galindo et al; 1994). This example further illustrates that barite formed in a geodynamic setting as that of the Namaqua orogeny can often obtain mixed Sr-isotopic values, intermediate between that of its significantly more radiogenic host rock which likely provided the bulk of Sr and Ba and the lower isotopic ratios of the fluid carrying sulfate and percolating largely through sedimentary formations of marine origin.

Intriguingly, the broadly contemporaneous (mid-Mesoproterozoic) bedded barite of the Aggeneys-Gamsberg Broken Hill-type Pb-Zn-Cu district which lies ca. 500 km to the west of the Northern Cape barite mineralization displays highly radiogenic $^{87}Sr/^{86}Sr$ signatures (0.7164 ± 0.0028) (Figure 19.10), on top of the similarly elevated $\delta^{34}S$ values (27 ± 4.9 ‰) (further mentioned in section 5.2.3) (McClung et al; 2007). However, apart from the source for Sr and Ba which has been loosely attributed to evolved continental crust, the mode of barite formation between these two settings is markedly different, with the first involving seawater appreciably modified by BSR, sub-seafloor replacement and syn-sedimentary exhalative processes. Stratiform barite in intracratonic rift settings such as that of Aggeneys-Gamsberg district are expected to have distinctly more radiogenic Sr than coeval seawater (Maynard et al; 1995) whereas in other continental margin settings both sulfate and Sr can be in keeping with an essentially marine origin (Cortecci et al; 1989), while at the same time associated epigenetic karst and vein-barite may show elevated Sr signatures derived from sources other than carbonates, such as shales (Figure 20.1).

Gangue minerals (dolomite, barite, fluorite) and hydrothermal sulfides in Mississippi Valley-Type (MVT) Pb-Zn deposits have consistently more radiogenic Sr (initial $^{87}Sr/^{86}Sr$ typically up to 0.713) than host dolostones and unaltered carbonates, which gives evidence for the interaction of the ore fluids with lithologies along their migration path and transportation of the acquired signatures to the site of ore deposition (Leach et al; 2010 and references therein). Such radiogenic Sr-isotopes contrasting with the host carbonate are also characterizing certain Phanerozoic oilfield brines (e.g., Chaudhuri; 1978) and can be only

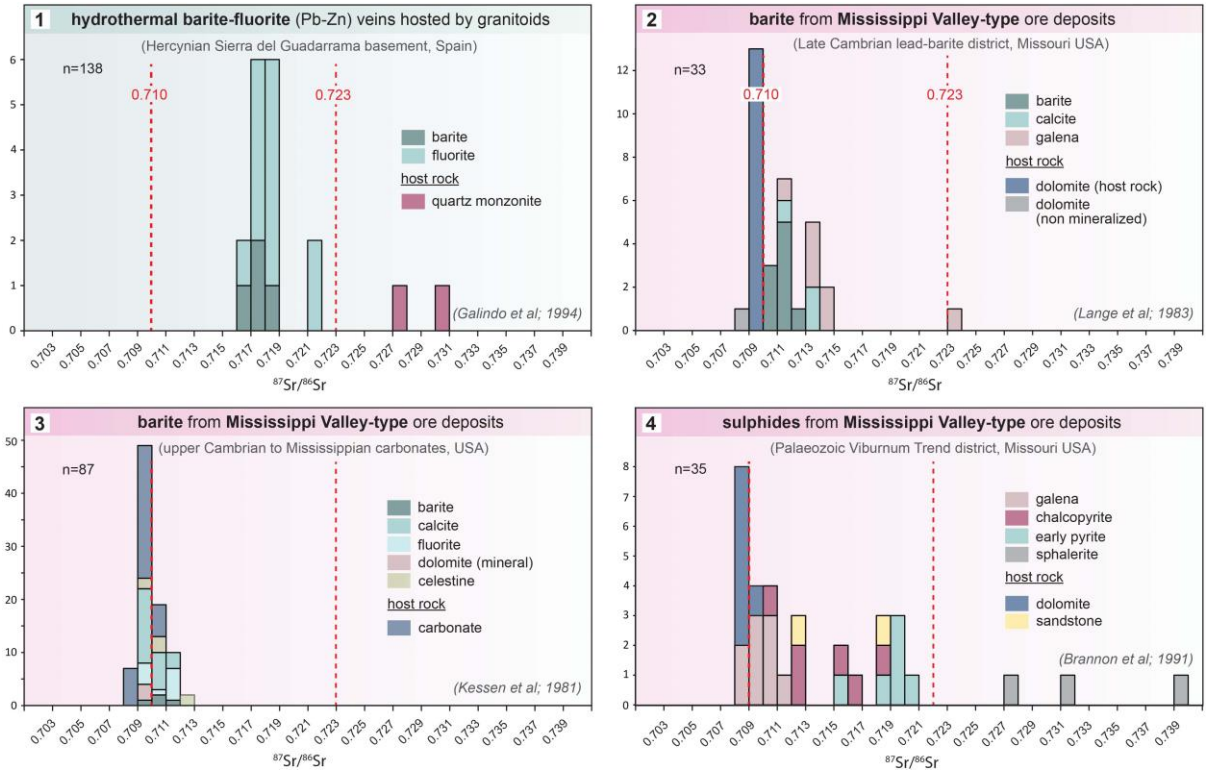

Figure 20. Frequency histogram of $^{87}Sr^{86}Sr$ ratios from barite-fluorite and MVT Pb-Zn deposits to compare with Northern Cape barite data (continuation of previous figure).

explained by invoking isotopic exchange with different sedimentary or metamorphic formations such as pelitic sediments, granites or gneisses.

Barite mineralization in this study bears significant resemblance with MVT deposits, in the sense that they are both products of large-scale fluid transport in the upper crust, driven within platforms by orogenic or large-scale tectonic events (further discussed in chapter 5, section 6.7.2). Furthermore, mineralization including precipitation of gangue barite, is usually associated with a two-fluid mixing model between metalliferous sedimentary brines and other fluids at the depositional site and most importantly, the deposited sulfides and sulfates inherit $\delta^{34}S$ values that derive mainly from evaporated seawater, i.e., typically saline residual brines from dissolution of evaporites stored in the basin sedimentary sequences. Fluid inclusions in gangue minerals from the KMF bear striking similarity to MVT deposits with respect to salinities and homogenization temperatures (Lüders et al 1999: 18 wt. % NaCl, T = 130-210^{o}C), which further underpins the involvement of basinal brines in the regional alkali metasomatism.

The appreciably higher initial $^{87}Sr/^{86}Sr$ ratios of the mineralizing fluids in comparison to that of the host rocks in most MVT districts, such as for example in the Pb-barite mineralization district (Viburnum mine) in Missouri (0.7104 - 07130 vs 0.7082 - 0.7089) (Figure 20.2), have been reasonably used to argue that there had been no isotopic equilibration with the dolomites and barite originated by mixing of two different fluids (Lange et al; 1983). The present set of Sr-isotope data in this study does not allow to adequately address this concept, although as expressed earlier two whole-rock signatures (0.71961, 0.72072) suggest that alteration fluids may have locally caused a homogenization of the isotopic character of the Campbellrand dolomite immediately below ore. In the example of Illinois-Ohio MVTs (Figure 20.3), minerals that usually equilibrate with the host rock (calcite, dolomite) are found in areas of sparce mineralization, whereas in contrast, most gangues emplaced in major mineralization districts show higher, silicate-derived $^{87}Sr/^{86}Sr$ ratios (Kessen et al; 1981).

In broad terms though, accurate characterization of the Sr-isotopic composition of mineralizing fluids can be particularly difficult, even for intensely researched MVT deposits such as the Viburnum Trend district above (Figure 20.4), let alone in the case of the complex alkali-metasomatic mineralization of the Northern Cape. A message to be drawn from the above example is that $^{87}Sr/^{86}Sr$ ratios can be difficult to interpret and in fact may represent a compositional range related to changes in fluid chemistry and fluid-rock interactions during the course of mineral precipitation. As stated by Brannon et al (1991), Sr isotopic results from this district do not conform well with to expected trends for MVT and in particular, Sr in some of the paragenetically early sulfides is very radiogenic (up to 0.74034), becomes less during the main ore deposition stage and again more radiogenic in later stages. It is interesting to note the overlapping $^{87}Sr/^{86}Sr$ ratios of gangues with country sandstones and the broadly comparable isotopic range between Northern Cape barite and this district.

Summary

Hydrothermal barite hosted predominantly by Fe- and Mn-rich lithologies of the Northern Cape displays variable and highly radiogenic $^{87}Sr/^{86}Sr$ values (0.71238 - 0.73818)

that indicate derivation from evolved continental crust, similar to most epigenetic systems comprising vein-type barite. Regarding barite in the KMF, Sr and Ba have been evidently supplied by reservoirs being much more radiogenic than the lithologies of the Voëlwater stratigraphy, apart from couple of much less radiogenic values (0.70743, 0.70575) that may reflect local dilution by Sr leached directly from the Hotazel Formation or alternatively a fluid characterized by lower Sr-isotope ratios, leaching carbonates and/or evaporite from the Campbellrand Subgroup. As concerns PMF, the range of radiogenic Sr-isotopic ratios in barite may reflect derivation either from a single reservoir with inhomogeneous $^{87}Sr/^{86}Sr$ ratios or most likely is indicative of interactions with diverse rocks carrying variable but significantly radiogenic Sr-isotopic signatures at all times. These are suggested to be deep-seated volcanosedimentary rocks (Ventersdorp) and lesser dolomite and previously mineralized BIF. High $^{87}Sr/^{86}Sr$ ratios (0.719610, 0.720727) in Campbellrand dolomite below Fe/Mn ore, also replicated in ephesite-rich layers (0.71468) hosted by Fe/Mn in another locality (Bishop), clearly reflect epigenetic isotopic disturbance either during dolomitization or most probably during the Namaqua orogeny. In stark contrast, results from the Mooidraai carbonates (0.7029) suggest that they are not pervasively metasomatized and that drillcores used in prior studies to extract information on the ancient ocean (Schneiderhan et al; 2006) have been influenced by epigenetic events. Strong evidence for shale-derived Sr/Ba is provided by the $^{87}Sr/^{86}Sr$ values of quartzite-hosted barite (0.72754 - 0.732308), being among the most radiogenic in the dataset and in agreement with the very radiogenic values of the Mapedi shales (i.e., 0.75369 and 0.77055, not corrected for age of barite formation).

Formation of barite was induced by mixing of: (i) deep, hot and saline basinal fluids with variable radiogenic Sr with (ii) surficial meteoric or ambient shallow groundwater introducing elevated $^{87}Sr/^{86}Sr$ ratios and dissolved Ba by leaching of siliciclastic rocks. Sr values of the first (i) were obtained by large-scale circulation in the sedimentary sequences and fluids remained trapped within the deeper strata of the basin before being forced to migrate upwards during the Namaqua orogeny. Siliciclastic sediments of the Olifantshoek Supergroup appear to have been among the major contributors of Ba, if not also of radiogenic Sr, but the Sr budget of the brines in particular, is strongly suggested to have been also controlled by diverse lithologies deeper than the Fe/Mn host rock entities, which acted as fluid sources and

ranged from indigenous dolomites, BIF and basement lithologies to possibly distant granitoids of the Namaqua metamorphic belt, if the age, origin and geotectonic setting of mineralization is taken into account. Although the exact source of the radiogenic Sr of the fluid cannot be ascertained and is almost certainly a result of diverse reservoirs, comparable Sr isotopic ranges exist in basin-scale hydrothermal vein mineralization, reflecting different silicate-bearing source lithologies and/or large time intervals of mineral-formation. Moreover, the inferred fluid-mixing formation mechanism and overall geological setting bears similarities with Mississippi Valley-Type (MVT) Pb-Zn ore deposits.

5.4 Neoarchean to Palaeoproterozoic evaporites in the Transvaal Supergroup and implications for seawater-sulfur reconstructions

5.4.1 Introduction

Despite of its hydrothermal nature, barite in the Postmasburg and Kalahari manganese fields may constitute an important archive of seawater sulfate, which albeit modified to some degree, perhaps still provide a great opportunity to peer into the palaeoenvironment of the early Palaeoproterozoic. To fully understand the potential implications of the sulfur isotopic fingerprint of the Northern Cape barite on the evolution of Proterozoic, a review on seawater sulfur isotopes is considered as vitally important and will be first presented. The isotopic composition of seawater sulfur has fluctuated widely through time and its secular evolution has been determined in great measure through the study of chemical sediments. In particular, reconstructions of the sulfur isotope age curve for the Phanerozoic show a variation from approximately +10 to + 30 ‰, which comprises as major features a pronounced maximum with $\delta^{34}S$ values around + 30 ‰ during Cambrian, a decrease to a Permian minimum at -10 ‰ and finally an increase towards the value for the modern ocean at +21 ‰ (Claypool et al; 1980, Strauss; 1997 and references therein). At the same time, the long oceanic residence time of sulfate (ca. 25 Ma) (Holland; 1984), implies that its isotopic composition should have been uniform throughout the oceans at any given time (Hanor; 2000).

In contrast to Phanerozoic, the sulfur isotopic record in Precambrian times is quite fragmentary by virtue of the paucity of relevant data from evaporites, which in turn is ascribed to the different oxidative atmospheric conditions, high bicarbonate saturation in seawater and low sulfate concentrations at that time (Grotzinger and Kasting; 1993, Bekker et al; 2006, Lyons and Gill; 2010). Absence of evaporites from the Precambrian geological record is also reasonably attributed to their poor preservation potential, owing to their particularly soluble constituents which can be readily dissolved from meteoric waters if not sealed (Claypool et al; 1980). Another fundamental issue regarding the Proterozoic Eon is the lack of reliable geochronological data, which commonly demands for the measured sedimentary sulfate to be poorly bracketed within time spans of hundreds of million years. In light of this lack of evaporite-derived sulfate data, the present seawater sulfur isotope curve for the Proterozoic has been supplemented by a substantial record of trace sulfate data termed as carbonate-associated sulfate (CAS) and disseminated total sulfur data, the latter chiefly represented by sedimentary pyrite and seen mostly in earlier literature. This trace sulfur in Precambrian sediments in conjunction with very sparse data from ancient evaporites and other isotopic geochemical evidence have helped to formulate our current understanding regarding the Precambrian sulfur cycle (e.g., Planavsky et al 2012; Strauss et al 2013).

CAS refers to sulfate incorporated into the carbonate lattice as a substitute of CO_3^- during carbonate precipitation (Staudt and Schoonen; 1995) and has been shown by many studies to be a trustworthy palaeproxy of the isotopic composition of seawater sulfate. Specifically, many studies comparing sulfur isotopic data from evaporites with time equivalent CAS showed that diagenetic processes do not compromise significantly the measurements of CAS (Kampschulte and Strauss; 2004, Gill et al; 2008, Guo et al; 2009), despite clear evidence in some cases indicating loss of CAS from the rocks and therefore changes of its initial concentration. However, the potential of incorporation of isotopically altered sulfate due to BSR or sulfide oxidation from the pore waters into ancient chemical sediments during diagenesis cannot be entirely excluded and it has been acknowledged for example with respect to Meso- and Neo-Archaean carbonates (Domagal-Goldman et al; 2008). Furthermore, a sample-specific approach during interpretation is always important

since analyses deviating considerably from the mean value of a dataset could be an indication of BSR processes, as in the case of the 2.1 Ga Tulomozero Formation (Reuschel et al; 2012).

It should be also mentioned that the measured range of $\delta^{34}S_{CAS}$ for carbonates of a given age, such as for example that of the early Palaeoproterozoic Espanola Formation in North America may display considerable ranges (from +15 to +29.1‰, avg. = 20 ± 4.4 ‰, n=8) (Planavsky et al; 2012). High $\delta^{34}S$ variability (as much as ca. 20 ‰) is routinely seen in the Palaeoproterozoic CAS record and most importantly is recorded by lithological sections representing only million-year time scales (Gill et al; 2005). In comparison, sulfur isotopic shifts of similar $\delta^{34}S$ magnitude in the Phanerozoic are spread over time spans of tens to hundreds of millions of years, which has led to suggest the presence of a smaller marine sulfate reservoir in the Proterozoic, mainly as a result of lower atmospheric oxygen levels (Gellatly and Lyons; 2005). Apart from geological reasons, analytical challenges related to insufficient removal of sulfates and sulfides before CAS determination and very low concentrations of CAS or total sulfur have also led to problematic results, with low yields obtained especially in the earlier studies (e.g., Buchanan e al; 1981), in which many results described as disseminated sulfur may in reality represent mixtures of sulfates and sulfides. Nevertheless, after taking into account the aforementioned potential drawbacks and limitations due to scarcity of evaporites, trace sulfur has been widely regarded as an extremely valuable palaeoceanographic proxy.

5.4.2 A revised sulfur isotopic age curve for the Proterozoic (this study)

In brief, according to the widely cited reviews of Claypool et al (1980) and Strauss (1993), the fragmentary existing record comprises $\delta^{34}S$ values between ca. **+10 and +18 ‰** for the **earlier Palaeoproterozoic**, slightly higher values (from **+15 to + 25 ‰**) for the **late Palaeoproterozoic** and more or less constant values fluctuating around **+20 ‰** for the remaining **Meso- and Neo-Proterozoic**, before the pronounced increase around +30 ‰ which marks the transition into the early Cambrian. Meanwhile, $\delta^{34}S$ values from whole-rock sulfate mainly governed by sulfides are distributed over a much wider range which also encompasses lighter values. Several publications addressing the $\delta^{34}S$ of Proterozoic marine sulfate have

appeared since then, thus warranting essential an updated assessment of the Proterozoic dataset.

In light of this, the available sulfur isotopic record for the Palaeo- and Meso-Proterozoic has been critically evaluated and compiled into a new comprehensive sulfur isotopic age curve, constructed for the current study (Figure 21). This figure is based on data from the earlier review studies mentioned above, later compilations comprising both evaporite-related sulfate and CAS (Bekker et al; 2006, Thomazo et al; 2009, Planavsky et al; 2012, Strauss et al; 2013) as well as more recent case studies addressing ancient seawater (Blätter et al; 2018, Tapio et al; 2021). Emphasis is given on marine bedded sulfate deposits and CAS from the extensively studied early Proterozoic (**indicated in dark blue**) since these are presumably the best proxies for seawater while sulfide and disseminated sulfur data are **indicated in light blue**. An assessment of the pristine nature of sulfates as well as documented textures are also denoted by the use of additional **black symbols**. Data from sulfates of disputable origin, i.e., featuring radiogenic $^{87}Sr/^{86}Sr$ ratios, magmatic sulfur or previously noted by other workers to show no global applicability (for e.g., the ca. 2.1 Ga barite deposits from the Indian Shield), are included in the curve but are instead marked with **grey colour**. Noteworthily, what becomes apparent from the succeeding critical appraisal of the available record is that much of the evidence regarding the global oceanic sulfur isotopic signature that is being reproduced in palaeoenvironmental studies, is at least to some extent based on questionable data and critical gaps exist as regards the evolution of seawater $\delta^{34}S$ during the history of the early earth.

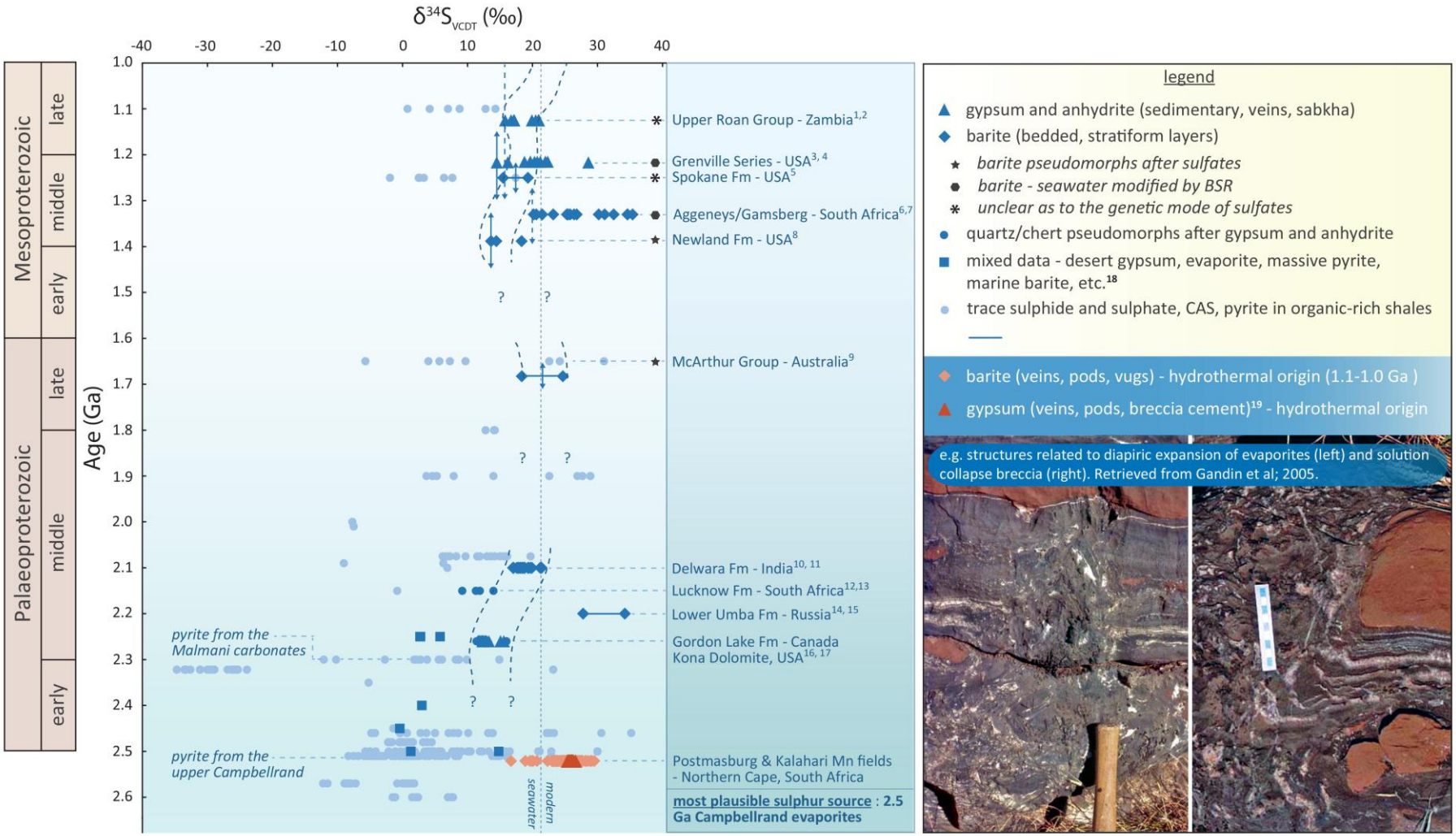

Figure 21. Updated seawater sulfur isotopic age curve for the Palaeo- and Meso-Proterozoic constructed for this study. Emphasis (dark blue) is given on sulfate and CAS data and their reliability is further discussed in the text. Age uncertainties are displayed with vertical arrows. The sulfur isotopic composition of the 1.0-1.2 Ga barite from this study is attributed to old (2.5 Ga) evaporites and its enrichment in ^{34}S is closely examined in sections 5.4.5 and 5.4.6. Source of data: (1) Dechow and Jensen; 1965 (2) Claypool et al; 1980 (3) Brown; 1973 (4) Whelan et al; 1990 (5) Rye et al; 1983 (6) McClung et al; 2007 (7) von Gehlen et al; 1983 (8) Strauss and Schieber; 1990 (9) Muir et al; 1985 (10) Hoefs and Bauman; 1991 (11) Deb et al; 1991 (12) Master et al; 1993 (13) Schröder et al; 2008 (14) Melezhik and Fetisova; 1989 (15) Grinenko et al; 1989 (16) Cameron; 1983 (17) Bekker et al; 2006 (18) Farquhar et al; 2000 (19) Papadopoulos et al (in prep).

5.4.3 The late Palaeoproterozoic and Mesoproterozoic

As illustrated in Figure 21, the sulfur isotopic age curve lacks almost entirely credible data for a period of approximately 700 Ma, between the mid-Palaeoproterozoic and mid-Mesoproterozoic (from ca. 2.0 to 1.4 Ga), with the only exception being that of McArthur basin, which has preserved excellent carbonate and chert pseudomorphs after anhydrite, gypsum and halite, originally believed to have been deposited in sabkha-like marginal marine to lacustrine environments (Walker et al; 1977, Muir et al; 1980). Sulfur isotopic data are available from barite pseudomorphs of the Eastern Creek Formation (Muir et al; 1985) and suggest a range between **+18.4 and +24.7 ‰** (avg. = +19.9 ‰, n=13) for the original ca. **1.7 Ga** seawater sulfur source. Unpublished $\delta^{34}S$ barite values collected from diagenetic nodules and fault zones in the McArthur Group display a wider and partly overlapping range between +19.9 and +31.5 ‰ (Walker et al; 1983), that almost certainly reflects both diagenetic and post-depositional processes. The bottom line though is that $\delta^{34}S$ values fluctuating closely around +20 ‰, i.e., not much different from that of barite in the Northern Cape, seemingly characterize the late Proterozoic seawater sulfur, as it is further discussed below.

The remaining **Mesoproterozoic** (ca. 1.4 to 1.0 Ga) comprises a somewhat more coherent record of isotopic data from sedimentary sulfate, much like the early-mid Palaeoproterozoic (ca. 2.3 to 2.1 Ga) (Figure 21). Barite pseudomorphs after gypsum found in the Newland Formation (1450 - 1325 Ma) display rather unradiogenic $^{87}Sr/^{86}Sr$ ratios and textures of differential compaction around barite crystals, suggesting formation while the sediment was still soft. Therefore, the three representative sulfur isotopic ratios obtained from these pseudomorphs **(+13.6, +14.4 and +18.3 ‰**) are believed to closely approach that of contemporaneous seawater in a lacustrine environment connected to the Proterozoic Ocean (Winston and Roberts; 1986, Strauss and Schieber; 1990). Comparable barite data (between +15.5 and +19.3‰) associated with Cu-Ag mineralization from the much younger Spokane Formation (1250 Ma) (Rye et al; 1983) are considered questionable since the genetic mode of the mineral is unclear.

Somewhat firmer evidence for the sulfur isotopic composition of seawater between ca. 1.3 and 1.1 Ga derive from anhydrites of marine evaporitic origin interbedded with the

Upper marble of the Grenville Series (North America). A range of $\delta^{34}S$ values between +14.5 and +28.6 ‰ (**avg. = +21.4 ± 3.6 ‰**, n=15) obtained from these sulfates has been considered as a close equivalent of seawater with an age between 1300 and 1150 Ma (Brown; 1973, Grant et al; 1986). However, subsequent detailed analysis of the anhydrite (n= 89) revealed a distinct isotopic evolution up section, with the oldest evaporitic lenses averaging at +8.2‰ and progressively younger ones exhibiting averages of +19.6, +27.2, +26.7 and +19.1 ‰ respectively (Whelan et al; 1990). This trend was found to be generally repeated in the $\delta^{34}S$ values of biogenic pyrite along with a coincident decrease in the $\delta^{13}C$ values of marble, thus leading to suggest anhydrite precipitation in a restricted basin with concurrent large-scale bacterial sulfur reduction. This proposed scenario of what has been termed in the literature as 'chemical event' is revisited in the last section. In essence, basinal processes occurring in the above example are responsible for a large spread of evaporitic $\delta^{34}S$ ratios, from +4.2 to +30.2 ‰ ($\Delta\delta^{34}S$ = 26 ‰), which calls for dense sampling and isotopic analysis of the whole stratigraphic extent of evaporitic units where available.

The previous isotopic ratios are in broad terms comparable to that yielded from the loosely coeval (bracketed between 1300 and 950 Ma) sedimentary anhydrite beds in the Upper Roan Group (Central Africa Copperbelt). Two separate datasets exhibit ranges from +13 to +21‰ (avg. = 16.6 ± 2.3 ‰, n=10) (Dechow and Jensen; 1965) and from +15.8 to +21 ‰ (avg. = +18.6 ± 2.1 ‰, n=8) (Claypool et al; 1980). Despite the homogeneity of these Copperbelt sulfates, descriptions of the isotopically measured material include nodules in ore shales, veins in Lamprophyre dikes or veins cutting schists, overall adding uncertainty as to their pristine origin. In summary, after revisiting the existing sparse data of anhydrite and barite pseudomorphs after sulfates it can be inferred that **late Palaeoproterozoic and Mesoproterozoic seawater** is characterized by sulfur isotopic values between **ca. +14 and +21 ‰**, while heavier values (for e.g., from the Grenville sulfates) are most probably associated with BSR. An example demonstrating the latter case and included in the reconstructed curve of Figure 21 is bedded barite associated with the Broken Hill-type massive sulfide deposits of the ca. 1.3 Ga Aggeneys-Gamsberg district in South Africa. Elevated $\delta^{34}S$ values from this locality (from +20.2 to +35.4 ‰, avg. = +27.6 ± 5.2, n=15) are interpreted to reflect pore waters rich in seawater sulfate from a restricted basin modified by BSR (McClung et al; 2007).

This isotopic modification has apparently caused an increase of about 10.6 ‰ on average from the +17 ± 3 presumed composition of Mesoproterozoic seawater according to Strauss (1993).

5.4.4 The early Palaeoproterozoic

Contrastingly to the above-mentioned report, a higher-resolution $\delta^{34}S$ record tracks the sulfur isotopic evolution of the Early Proterozoic era (ca. **2.3-2.0 Ga**), which has received much attention due to the renowned Lomagundi event (Karhu and Holland; 1996) and solid evidence for the former presence of evaporites including the remarkably well-preserved ca. 2.0 Ga evaporitic succession in the Onega Basin of Russia (Blättler et al; 2018). The well-constrained chronostratigraphic context, as well as congruity between different sulfur isotopic datasets from this period, give fair confidence in the reported $\delta^{34}S$ ratios. Following the rise of atmospheric oxygen and the initiation of the oxidative sulfur and iron cycles in the early Palaeoproterozoic, sulfate evaporites are believed to appear in abundance during the Lomagundi event (ca. 2.22-2.1 Ga), a period characterized by a profound positive $\delta^{13}C$ excursion, high atmospheric oxygen and presumably high burial rate of organic carbon (Bekker et al; 2006).

High CAS concentrations in time-equivalent lithologies have been used to argue for a large marine sulfate reservoir (Planavsky et al; 2012), which has been preserved in the sediments through processes acting within an evaporitic environment much like that of the Phanerozoic and modern times. The above is based on evidence suggesting the distinctive progressive precipitation of carbonates and sulfates during evaporation of seawater (Warren; 2006), with occurrences of halite that dominate the Archean evaporite deposits being insignificant between ca. 2.2 and 2.0 Ga (Reuschel et al; 2012). As noted by some of the previous researchers, rare sulfate pseudomorphs and halite abundance in the aftermath of Lomagundi may indicate a return to lower sulfate concentrations in the ocean, a hypothesis which however requires further investigation.

Kona Dolomite and the correlative marine sabkha sediments of the Gordon Lake Formation are inferred to monitor the onset of the Lomagundi carbon isotope excursion and

contain abundant indicators of vanished evaporites that may have reached an aerial extent of over 1400 km along the margin of the Superior Craton (Chandler; 1988). Nodular anhydrite in sediments deposited immediately inland from the shore and barite lenses from the **>2.22 Ga** Gordon Lake Formation show collectively a narrow range of $\delta^{34}S$ ratios from **+11.7 to +15.6 ‰** (avg. = +12.7 ± 1.2 ‰, n=15) (Cameron; 1983, Bekker et al; 2006) (Figure 21). The sabkha tidal-flat setting postulated for the lower part of the above formation is corroborated by a series of textural indicators such as replacement nodules of gypsum and silica after anhydrite, all described in great detail by Chandler (1988). Likewise, a shallow-marine lagoonal to open-tidal setting has been suggested for the stratigraphy of the Kona dolomite of the Marquette Range Supergroup, encompassing in its upper part stratiform stromatolites, halite hoppers, silicified evaporite beds, collapse breccias and chert pseudomorphs after gypsum and anhydrite (Taylor; 1972, Wohlabaugh; 1980). Earlier unpublished $\delta^{34}S$ values from chert pseudomorphs (between **+11.4 and +16.0**) (Hemzacek; 1987, Feng; 1986) have been replicated by Planavsky et al (2012) in CAS from the same formation ranging from +**11.2 to +13.9 ‰** (avg. = +12.7 ± 0.9 ‰ n=6), overall providing compelling evidence for a seawater $\delta^{34}S$ signal averaging at **ca. +14 ‰** in the beginning of Lomagundi.

Palaeoproterozoic carbonates from the 2.3-2.05 Ga time interval examined by the previous authors display relatively narrow ranges of $\delta^{34}S_{CAS}$ in each of the studied unit, but significant fluctuations ($\Delta\delta^{34}S$ = 41 ‰) exist within the approximately 300 Ma period. Furthermore, despite some overlaps, the correlation between CAS and evaporite-related data from this period is rather poor, possibly also due to the scarcity of the latter and the fact that certain such datasets are more ambiguous. In fact, barite beds of the ca. 2.1 Ga Delwara Formation in India, which yield $\delta^{34}S$ values from +17.1 to +21.2 ‰, are accompanied by way too radiogenic $^{87}Sr/^{86}Sr$ ratios to reflect coeval seawater (Deb et al; 1991). Similarly, evaporitic evidence associated with the 2.2 Ga ^{34}S-rich barite layers (between + 27.8 and +34.2 ‰) of the Lower Umba Formation (Russia) should be interpreted cautiously, since they are believed to have been deposited in a continental rift lake setting and show much lower $\delta^{13}C$ than that of contemporaneous Lomagundi carbonates (Melezhik and Fetisova; 1989, Melezhik et al; 1999).

On the other hand, reports of $\delta^{34}S$ values from the **2.2-2.1 Ga** Lucknow Formation of the Transvaal Supergroup are based on convincing evidence for pseudomorphed marine evaporites with relict Ca-sulfate. As a result, an obtained CAS range between **+9.2 and +14 ‰** has been regarded as the first direct evidence for seawater sulfate precipitation on a platform with open access to the ocean, without strong influence of continental run-off (Schröder et al; 2008). The said authors argued that other evaporites during the Lomagundi, such as that of the Gordon Lake Formation, may on the contrary reflect local environments as a consequence of their deposition in basins with restricted connection to the ocean. However, as it can be seen above, results from Lucknow are in fact congruent with broadly time-equivalent ones from the Lomagundi dataset. It is also worth mentioning that five out of seven CAS analyses from Lucknow obtained by Planavsky et al (2012) range between **+23.4 and +26 ‰** and although never discussed in that study, they seem to capture a much heavier $\delta^{34}S$ signal within the evaporite sequence. A slightly more ^{34}S-depleted and robust isotopic signal in comparison to Lucknow, derives from the analysis of pseudomorphs of sulfate crystals and nodules from the **ca. 2.1 Ga** Tulomozero Formation (Fennoscandian Shield, Western Russia), a thick succession associated with playa-like and coastal sabkha to intertidal marine settings that has preserved an abundance of evaporite relicts (Melezhik et al; 2005). A broad coincidence between $\delta^{34}S_{CAS}$ ranging from **+8.3 to +15.8 ‰** (avg. = +10.9 ± 2.7 ‰, n = 6), $\delta^{34}S_{ANHYDRITE}$ = **+9.6 ± 1 ‰** (n=77), $\delta^{34}S_{BARITE}$ = **+11 ± 3.1 ‰** (n=16) and sulfates of similar age, suggest a globally homogenous sulfate pool with respect to its sulfur isotopic composition and a sulfate concentration of >2.5 mM for the Early Proterozoic (Reuschel et al; 2012).

A follow-up and consequential example of research undertaken on a drill core intersecting Palaeoproterozoic (**ca. 2.0 Ga**) sediments in the Onega Basin (Fennoscandian Shield) that correspond to the Tulomozero Formation, clearly demonstrated the presence of preserved evaporite minerals (halite, anhydrite, gypsum, magnesite) within an ca. 800 m-thick evaporite succession, in that way extending the record of pristine evaporites by almost a billion years (Blätter et al; 2018). Reported sulfate $\delta^{34}S$ values lie between **+5 and +9.5 ‰** (+5.9 ± 0.7, n=42), i.e., results which are considerably lighter than all rest of the early Palaeoproterozoic data. Recently, an unmineralized anhydrite- and gypsum-rich unit

associated with the Palaeoproterozoic Rajapalot Au-Co system (Finland) has been interpreted as indication of evaporite strata and in particular has been correlated with the evaporite successions of the Onega basin on the basis of textural and sulfur isotopic similarities (Tapio et al; 2021). In detail, average $\delta^{34}S_{ANHYDRITE}$ = **8.9 ± 0.4 ‰** (n=19) and $\delta^{34}S_{GYPSUM}$ = **11.2 ± 0.7 ‰** (n=4) are in good agreement with data of similar age, although somewhat heavier than that from the pristine evaporites of the Onega basin. Lastly, sulfate data from the compilation of Thomazo et al (2009) that also included in Strauss et al (2013) are not followed by good geological documentation and are considered as possibly unreliable.

In summary, early Palaeoproterozoic has a more continuous record as regards its seawater sulfur isotopic composition, constrained by all merged data between **ca. +8.0 and +16.0 ‰**, with the exception of the ca. 2.0 Ga pristine evaporites of the Onega basin which are characterized by a lighter range of values averaging at **+6 ‰**. Altogether, the above currently suggest a persistently lighter seawater sulfur isotopic signature for that time period and a general lack of heavier values around or above +20 ‰ which apparently are more common during the late Palaeoproterozoic and Mesoproterozoic. All of the foregoing, provide a very useful basis for the interpretation of the $\delta^{34}S$ seawater values suggested by the Northern Cape barite. Further refinement of the sulfur isotope age curve for the Proterozoic depends on new discoveries and measurements of pristine sedimentary sulfate as well as on new radiometric ages that will further narrow down current age uncertainties related to periods of evaporite formation.

5.4.5 Evaporites in the Northern Cape and hydrothermal barite mineralization

Picking up again on deciphering the origin of sulfur in the Northern Cape sulfates (barite and gypsum) and determining if the measured $\delta^{34}S$ values have any bearing in reconstructions of the sulfur isotope age curve for the Proterozoic Eon, two things are regarded unambiguous right from the start. Firstly, in spite of the unequivocal hydrothermal origin of these minerals, their regional sulfur isotopic signature can be only explained by precipitation from a homogeneous seawater reservoir which has been apparently mobilized in response to a major orogenic event. Secondly, the determined age of barite mineralization places an upper limit for this seawater sulfur source at late Mesoproterozoic, something that

instantly adds value to this large and uniform dataset, even as it offering proof that an 'old' and large seawater sulfur reservoir has been preserved in the Neoarchean to Proterozoic sediments of the study area until the Namaqua-Natal orogeny. The major question then would be if this measured uniform sulfur pool could reflect evaporites as old as ca. 2.5 Ga, originally hosted by the Campbellrand carbonate sequence or if it is related to a younger (up to ca. 1.2 Ga) and unidentified evaporitic source in the study area.

As mentioned earlier, Palaeoproterozoic strata provide copious physical evidence for former evaporites through the presence of pseudomorphic mineral replacements and a series of preserved textures indicative of evaporitic dissolution. According to the most recent compilations (Pope and Grotzinger; 2003, Evans; 2006, 2007) this records extents as back as the 2.25 Ga saline giant (estimated as 4500 km^3) in Chocolay-Gordon Lake succession on Superior Craton, although traces of marine evaporites are known from several older formations, including ten from the Archean. In fact, thirteen localities present evidence for marine evaporites prior to the 2.52-2.56 Ga Campbellrand platform evaporites, with the oldest known record represented by silicified pseudomorphs after evaporite crystals occurring in the 3.43 Ga Strelley Pool Chert in Pilbara Craton (Allwood et al; 2007).

Among this long record commonly comprising pseudomorphic textures, the Neoarchaean Campbellrand-Malmani carbonate platform bears a substantial amount of petrographic, field and isotopic evidence suggestive of the former presence of widespread evaporites in the basin, which are presented in great detail in Gandin et al (2005) and Gandin and Wright (2007). Some of the complex fabrics seen within carbonates have been interpreted by other researchers (e.g., Sumner and Grotzinger; 2004) as being of microbial origin but the detailed sedimentological study by Gandin et al (2005) leaves little doubt as to their replacive origin related to calcitization of originally evaporitic sediments. Deposition in shallow evaporitic subaqueous to sabkha environment has been ascribed to the Kogelbeen and Gamohaan Formations, on grounds of depositional and early diagenetic petrographic features (e.g., microbial laminites, stromatolites, tepees, gypsum nucleation cones, calcite nodules after gypsum and selenite pseudomorphs, diapir-like structures, solution collapse breccias, etc.). Formation of the aforementioned features is suggested to have occurred

during early diagenesis and through the early stages of burial, although late diagenetic hydrothermal waters are most likely surmised to have been the causative agent for the development of collapse breccias.

This obviously complicates the scenario of sulfur being sourced from these evaporites and mobilized between 1.2 and 1.0 Ga to produce hydrothermal sulfates, since apparently evaporitic sulfates have been replaced from the early on, much similar to the majority of ancient evaporite deposits. However, presuming that the temporally and spatially extensive carbonate basin has been replete in evaporites, partial preservation until much later on during the geologic evolution of the basin cannot be entirely excluded. Considering also the remarkable preservation of the ca. 2.0 Ga evaporites in the Onega basin and the good retention of CAS even in much older sediments, the above hypothesis is not entirely unreasonable. Moreover, several lines of evidence for evaporites are not only found in the laterally equivalent Malmani beds of the Transvaal basin, but also in the Carawine Dolomite of the Hamersley Province in Australia, which has long been known to exhibit similar stratigraphic and structural patterns to the Transvaal (e.g., Trendall; 1968). In particular, Carawine platform appears to have been largely an evaporative shallow subtidal setting with high and fluctuating salinities, according to the distribution of readily recognized pisolite layers, tepee structures, stromatolites and pseudomorphs after gypsum (Simonson et al; 1993 and references therein). Furthermore, some authors have related formation of BIF-hosted iron ores in the Hamersley Province with hot upward-flowing basinal brines that interacted with evaporites (Angerer et al; 2014).

Removal of soluble material, including evaporites, from carbonate successions is common and eventually results in the formation of collapse breccias, but such processes can sometimes take place after dolomitization or even metamorphism and recrystallization of the strata (Eliassen and Talbot; 2005, Melezhik et al; 2005). Extracted sulfate from dissolution-collapse breccias associated with such late dissolution processes following metamorphism, has been suggested to contain relicts of the primary evaporite minerals on the basis of only slight isotopic differences between the two (Tucker; 2001, Reuschel et al; 2012). Structures attributed to upward-ascending evaporite diapirs as well as solution collapse breccias are

present in the Campbellrand carbonates, although the timing of formation has been suggested to coincide with late diagenesis (Figure 21). The exact mode and processes of evaporitic preservation may be elusive, but the $\delta^{34}S$ barite signal manifests that seawater sulfur was largely stored in the broad vicinity of the Fe and Mn ores, even though it may have been mobilized more than once since the initial evaporite precipitation, possibly through the formation of intermediate breccias.

The widely accepted models for metal accumulation in the Postmasburg manganese field invoke mainly development of palaeokarsts and open karst sedimentation under surficial weathering sometime between 2.22 and 1.8 Ga, although processes of groundwater dissolution, fracturing and subsidence of overlying BIF lithologies into underground cavities have also been regarded for some of the deposits (Gutzmer and Beukes; 1996a). In the occasion that 'freshwater' karst lakes were forming where evaporite-baring rocks lied near the surface, the $\delta^{34}S$ values of the former would reflect those of the original sulfates, although probably being enriched in ^{34}S similar to modern settings. In fact, considerable fractionation of the sulfur isotopes could have occurred by BSR, either in the shallow sediments or in the anoxic water column (Matrosov et al; 1975). The mode of subsequent sulfate preservation in the metalliferous sediments though cannot be ascertained, even more so the pathways and following processes that led to the 1.2-1.0 Ga sulfate mineralization.

On the other hand, it is regarded as much more plausible that inter-stratal dissolution processes were temporally associated with the regional deposition of barite and alkali minerals in the ores and therefore these processes have been invoked by a tectonic event that was responsible for large-scale fluid migration through the basin. During the course of this fluid flow, sulfate released from sites with preserved evaporites complexed with barium largely derived from clastic rocks to form barite and gypsum. Although the well-documented evaporites of the Gamohaan and Kogelbeen Formation are considered as the main sulfate source, one should also explore the possibility of other evaporite beds having been present in the wider stratigraphy.

Archean sediments overlying volcaniclastic rocks in the Pilbara Block have been shown to contain evaporites (pseudomorphs of nahcolite, bladed barite deposits) and higher up in the succession are mentioned to be interbedded with BIF (Lewy; 2012). However, no such evidence is known from the Asbestos Hills BIF overlying Campbellrand and this possibility is utterly hinges on the considered depositional setting of iron-formations, which is generally accepted to have been deep water basinal rather than a shallow platform (Konhauser et al; 2017). Some researchers though have stressed that water depth should have been shallow enough to form large carbonate platforms (Morris; 1993) or have argued that BIF successions do not reflect oceanic basins but restricted ones, with vertical and lateral lithofacies changes being controlled by fluctuations in water supply versus evaporation (Lewy; 2012). Evaporites in the Asbestos Hills BIF remains merely a hypothesis for the time but the origin of abundant riebeckite in this succession (in fact named after crocidolite) has been regarded as being metasomatic (Hodgson; 1965) and thus its genesis could further provide clues for the 'missing' evaporites. It is possible that the required Na- and Mg-rich solutions may have involved dissolution of local evaporites releasing highly saline fluids, as envisaged for the magnesio-riebeckite of the Limbo Formation in Bolivia (further discussed in chapter 5 and Synthesis, part 2). Finally, Mooidraai carbonates overlying the Hotazel Formation in the KMF host typical features of subtidal to lagoonal environment such as microbialaminites and laminated stromatolites as well as solution-collapse breccias that may be linked to former evaporites. However, clear indicators for evaporites such as pseudomorphs after sulfates or molds appear to be absent, something that has been attributed to neomorphic processes as well as lack of surface exposure of the carbonate formation which prohibits investigation (Kunzmann et al; 2014).

The close spatial relationship of preexisting evaporitic rocks and lithologies that both host and have essentially provided the Fe and Mn for the deposits of the study area, indicates the potentially critical role of evaporites as a fluid and ligand source. Apart from supplying the desired sulfur for regional barite precipitation, their important consequences with respect to metallogeny, either during genesis or hydrothermal overprinting of the Northern Cape deposits will be further examined later in this thesis (Chapter 5).

5.4.6 Reexamining the early ocean through the prism of epigenetic barite formation

Following the confident assignment of barite sulfate to evaporites of the Campbellrand Subgroup, the remaining question concerns our ability to extract reliable isotopic information from the composition of barite regarding the source evaporites. As one may expect, evaporites are enriched in ^{34}S, since sulfur isotopic fractionation from sulfate solution into gypsum and by extent sulfates is around 1.65 ‰ (Hanor; 2000). Furthermore, temporal evolution of the sulfur isotopic composition of the water column can be responsible for variability in $\delta^{34}S$ with respect to the position within an evaporitic sequence. Both the lowest and mean values have been considered as the closest approach to the value for the coeval ocean in the literature. Given the large dataset, the mean value of the Northern Cape barite (+24.9 ± 2.5 ‰, n=93) could be regarded as a better approximation of the seawater, which expectedly would be lighter by 1-2 ‰, i.e., around +23 ± 2.5 ‰. Even if the measured values reflect CAS or relict sulfate somehow preserved in solution breccias previously formed from evaporites, any additional isotopic fractionation would move the $\delta^{34}S$ ocean value at approximately +21 ± 2.5 ‰. Although reasonable, this estimation is at odds with the recorded range of the early Proterozoic (ca. from +8.0 to +16.0 ‰) and in particular is heavier between 5 and 13 ‰. Then again, a value close to +20‰ is apparently comparable with seawater values displayed for most of the late Palaeo- and Meso-Proterozoic.

Compositional constraints on ancient seawater demand that the deposition of the evaporite succession occurred in an open-marine environment, an interpretation that has been a matter of some dispute, especially for the scarce records of Proterozoic evaporites. For example, as mentioned earlier, evaporites of the Lomagundi event have been interpreted as precipitates in intracratonic rifts or back-arc basins connected to the open ocean but some authors have argued for a more restricted basin. It is common knowledge that separating truly marine evaporites from lacustrine deposits in Precambrian is a difficult exercise and requires carefully integrated studies. All preserved evidence from Campbellrand succession support a marine origin for evaporites. However, the fact that brines in particular subbasins can evolve in their own pathway and sulfate concentration can vary in basins of the same age

as well as throughout the evolution of the same basin (e.g., García-Veigas et al; 1995, Ayora et al; 2001), is certainly something to keep in mind even when considering large basins.

Having said that, the most important implication presented by Gandin and Wright (2007) is that evaporite precipitation in Neoarchean restricted basins may have been driven by microbes and especially cyanobacteria that were oxidizing seawater in an otherwise largely reducing ocean, while contemporaneously supporting bacterial sulfate reduction (BSR) in the anoxic conditions of the degrading organic matter, right beneath stromatolites and microbial mats. BSR has been clearly demonstrated in pyrite of the Gamohaan Formation also by Kamber and Whitehouse (2006), within a broader context of short sulfur supply and cycling of sulfur between reservoirs, eventually driven by the fluctuation in free-oxygen within the water column. In light of the foregoing, it is likely that the isotopic composition of the original sulfates may have been affected by these processes and as a consequence the Northern Cape hydrothermal sulfates derived from these evaporite precipitates are perhaps not indicative of the coeval seawater isotopic composition. In fact, the heavy $\delta^{34}S$ barite and gypsum values are likely to reflect a first-order trend of bacterial sulfate reduction, much like the younger evaporitic lenses in the Grenville Series (section 5.4.3), which are characterized by much heavier (between ca. +20 and +30 ‰) but rather uniform isotopic signatures within each bed.

Increased $\delta^{34}S$ values in evaporites have been proposed to derive by brines accumulated in restricted evaporitic basins and details regarding their isotope systematics have been explored by Holser (1977) in a model invoked to explain large worldwide increases in the $\delta^{34}S$ values of sulfate during the Phanerozoic. These increases have been termed as 'chemical events', may take millions of years before they are restored and are regarded as records of a abrupt addition of a large volume of ^{34}S-enriched brine from a basin to the ocean. The mechanism involves brines forming through evaporation of seawater at the basin surface and subsequently settling in the bottom of the basin where under anoxic conditions and BSR may become enriched in ^{34}S. Although the details may differ for the Campbellrand platform, this model highlights another avenue through which evaporites in barred basins can obtain distinct and heavier isotopic values from that of the contemporaneous ocean.

To summarize, barite of this study provides indirect but compelling evidence that validate all previous physical evidence for the presence of extensive evaporites in the Campbellrand carbonate platform. We further suggest that Northern Cape barite serves as a palaeo-environmental indicator for bacterial sulfate reduction occurring in a more restricted basin and therefore corroborates previous research on the study area supporting fluctuations in sulfur supply and the widespread presence of microbes. In that sense, sulfur isotopic data are not proxies of the global marine cycle, but broadly preserve a first-order evaporitic signal. Uniformity throughout the basin is testament to that, since significant overprints on the original signature by other sulfur sources are extremely unlikely to result in such a narrow range. Application of multiple sulfur isotopes (i.e., δ^{34}, $\Delta^{33}S$ and $\Delta^{33}S$) on barite can place additional constraints on biological reactions partitioning isotopes and thus further illuminate its origin (Johnston et al; 2008).

In the broader framework of the early Earth's history, the presence of MDF and BSR/sulfur disproportionation at that time is in concert with growing evidence (e.g., Siebert et al; 2005, Kamber and Whitehouse; 2006) that prior (ca. 2.5 Ga) to the increasing range of $\delta^{34}S_{pyrite}$ and the global atmospheric oxygenation (ca. 2.4-2.3 Ga), Neoarchaean was marked by a complex transition period with fluctuations in atmospheric oxygen levels and in oxidative sulfur cycle that have left their fingerprint in the sediments. The large and affiliated former evaporite deposits of the Campbellrand-Malmani platform and Hamersley basin may indicate substantial oxidant reservoirs of marine sulfate but local anoxic 'niches' were almost certainly also present and the global redox budget apparently re-organized itself through the course of hundreds of millions of years before the fundamental changes in oceanic sulfur concentrations during late Proterozoic.

6. Conclusions

Hydrothermal activity in the Northern Cape has been so far regarded as localized and negligible and so very few studies have addressed its origin and characteristics by focusing exclusively on the high-grade Mn ore of the Kalahari manganese field (KMF). This study builds upon recent research on the Postmasburg manganese field (PMF) and presents the first concrete evidence for a genetic association between hydrothermal alkali metasomatic

processes in the two ore fields. Not only stratigraphically and lithologically diverse barite displays similar paragenetic trends but also isotopic fingerprints and crystallization ages, all supporting a link with the regional tectonometamorphic event of the 1.2-1.0 Ga Namaqua-Natal orogeny. The principal outcomes of this research are summarized below.

(1) Barite mineralization associated with Fe/Mn lithologies in the Northern Cape is related to a single wide-scale regional hydrothermal event, genetically linked to the 1.2- 1.0 Ga Namaqua orogeny.

(2) In situ $^{40}Ar/^{39}Ar$ mica ages from three different localities, textural/paragenetic evidence and a remarkably homogenous sulfur isotopic signature (24.9 ± 2.5 ‰, 1σ) provide concrete evidence for a common epigenetic history of the Kalahari and Postmasburg Manganese fields.

(3) Regionally, barite occurs in association with alkali (Na-, K-, Ca-) minerals, the composition of which is controlled primarily but not exclusively by the nature of the host rock (i.e., Fe-, Mn-ore or other country lithology).

(4) Highly radiogenic $^{87}Sr/^{86}Sr$ ratios of barite (0.71238 - 0.73818) indicate derivation from different crustal sources, comprising primarily clastic sediments (Olifantshoek Supergroup) but also deeper chemical sedimentary sequences (carbonates, iron-formation), basement lithologies and possibly even distant granitoids of the Namaqua metamorphic belt.

(5) The extensive Campbellrand carbonate-evaporite sequence has apparently served as regional aquifer during the Namaqua orogeny, permitting deep basinal fluids to migrate along regional geological boundaries, react with Fe- and Mn-rich entities and mix with shallow cold fluids before precipitating barite, in a comparable way to that seen in Mississippi Valley-Type (MVT) Pb-Zn ore deposits.

(6) Despite its epigenetic nature (veins, vugs, occlusion of open space, replacements, intergranular porosity), barite has precipitated by large-scale, channelized hydrothermal

infiltration involving highly saline alkaline fluids, that may have acted as ore-enrichment factors. This calls for a revision of the current ore genetic models for the PMF.

(7) 1.2-1.0 Ga hydrothermal barite provides indirect but compelling evidence that validate all previous physical evidence for the presence of extensive 2.5 Ga evaporites in the Campbellrand-Malmani carbonate platform and it is further suggested to serve as a palaeo-environmental indicator for bacterial sulfate reduction occurring in a more restricted basin during evaporite formation, in line with previous studies.

PART TWO

Kalahari Manganese field (KMF)

Chapter 3

New textural, isotopic and in situ $^{40}Ar/^{39}Ar$ age constraints on the origin, nature and duration of Mn-ore hydrothermal enrichment in the Kalahari manganese field, South Africa

Abstract

The Kalahari Manganese field (KMF) owes its renowned mineralogical heritage to tectonic-related metasomatic processes that converted low-grade sedimentary manganese ore to high-grade oxide-rich ore during the ca. 1.2-1.0 Ga Namaqua orogeny (Wessels-event). Although the timeframe is unambiguous, details on the lifespan and stages of the event(s), as well as on the nature, origin of fluid(s) and interactions with the Hotazel rocks are largely missing. Here, we present in situ UV laser $^{40}Ar/^{39}Ar$ data from massive and banded sugilite that extend the oldest bound of the period of hydrothermal activity by at least 75 m.y. The hydrothermal system related to ore enrichment had been long-lived (from at least 1139 ± 5 Ma to 1063 ± 18 Ma) and most likely characterized by different thermal pulses/events and distinct episodes of sugilite formation, different populations of which can be forensically identified within the boundaries of a single sample by in situ $^{40}Ar/^{39}Ar$ laser probe and textural evidence. A first approach on O-H isotopic fingerprinting using diverse ore-gangue mineralogy reveals that $\delta^{18}O$ of the mineral-forming fluids range from ca. -3 to + 8 ‰ and δD values from -28.0 ‰ to -58.5 ‰, excluding a single amphibole (-118.8 ‰). The origin of these fluids and causative agent of hydrothermal upgrade in the KMF is attributed to sedimentary basinal brines, stored and largely equilibrate with the units of the Transvaal Supergroup prior to their infiltration in the ore. $\delta^{18}O_{fluid}$ may have been on average heavier (5.3 ± 1.4 ‰) during early calc-silicate precipitation than throughout main and later stages (0.2 ± 2.8 ‰), which points to dilution of isotopically heavier brines after interaction with a lighter host rock or mixing with contemporaneous meteoric water. The observed uniformity in the $\delta^{18}O$ values of gangue silicates is attributed to large water to rock mass ratio and fluid buffering during mineral precipitation, despite the overall extensive fluid-rock interactions. $\delta^{18}O$ measurements of

garnet-hematite or garnet-hausmannite pairs are found to be useful as potential monitors of temperatures of formation and suggest results (T = 120-210^{o} C) that are in agreement with previous reports. Among the dated sugilite specimens, previously undocumented Al-rich endmembers exist. Sugilite, which marks Wessels event, is suggested to form through metasomatic reactions contemporaneously with at least some of the present aegirine and its precipitation to be chiefly controlled by introduction of Li from an external source. Considering the regional geological context, a possible relationship between sugilite and ephesite in the Fe/Mn ores of the neighboring Postmasburg Manganese field with respect to Li sources, warrants further research.

1.Introduction

The giant Kalahari manganese Field (KMF) represents roughly 50 percent of the world's total known land-based manganese resources and occurs in three manganiferous units interbedded with banded iron-formation of the Palaeoproterozoic (ca. 2.2 Ga) Hotazel Formation (Laznicka; 1992, Tsikos and Moore; 1997). Metal enrichment of its northwestern portion has resulted in a Mn oxide-rich ore of very high economic grade (>44 wt. % Mn) and has been attributed to fault-controlled and laterally infiltrating hydrothermal fluid flow causing carbonate leaching, residual enrichment at the expense of carbonate-rich sedimentary protore, localized metal redistribution, and recrystallization and precipitation of a staggering diversity of over 200 declared mineral species found in vugs, veins and fault zones around manganese orebodies (Gutzmer and Beukes; 1995, 1997, Cairncross and Beukes; 2013).

This major hydrothermal metasomatic event, known as Wessels-event, is linked to distant collisional tectonics further to the west of the ore field, with supporting evidence comprising mainly gangue sugilite and norrishite $^{40}Ar/^{39}Ar$ ages and indirect palaeomagnetic dating of hematite, that all overlap with the time range of the ca. 1.2-1.0 Namaqua orogeny (Evans et al; 2001, Gnos et al; 2003). Although a wealth of information does exist regarding the geology of the enriched deposits and there is confidence in the general timeframe of the upgrade-event indicated by the radiometric ages, unanswered questions remain regarding

the lifespan and stages of mineralization, the origin and characteristics of alteration fluids and the processes of fluid-protore interaction.

The oxidizing and alkaline character of the involved fluid(s) during gangue precipitation is unequivocal but a lack of agreement exists concerning the temperature range (from <200 to > 400), nature of the involved hydrothermal fluid(s) and ultimate origin of their high salinity, the latter of which remains unknown and has been partly attributed to metasomatic interaction with the protore (Dixon; 1985, Miyano and Beukes; 1987, Lüders et al; 1999). Evidence for sodic metasomatism in the Hotazel iron-formation (Tsikos and Moore; 2005) and emerging data for an extensive alkali suite of minerals in the neighboring Postmasburg Manganese field, the latter also including sugilite of however younger age (620 ± 3 Ma), has led researchers to suggest that epigenetic fluid flow was extensive and possibly related to the Hotazel-Olifantshoek unconformity (Moore et al; 2011, Costin et al; 2015, Fairey et al; 2019). This hypothesis has been recently confirmed and a basinal evaporitic origin of the hydrothermal fluids expelled during Namaqua orogeny has been substantiated by regional stable isotopic research on metasomatic barite (chapter 2).

This study revisits sugilite from the Wessels mine where underground exploitation of high-grade manganese ore is being carried out at present in an aim to dissect age information extracted from rigorous in situ $^{40}Ar/^{39}Ar$ dating of different textural varieties and possibly refine the current age constraints on mineralization. We also make an inaugural step to investigate the stable isotopic composition (O, H) of mineralogically variable targets associated with hydrothermal ore-enrichment, seeking to further illuminate the isotopic characteristics, origin and evolution of the alteration fluids along the context of geochronological, mineralogical, textural and other available geological evidence. Our analysis highlights the great complexity of the system but also demonstrates that useful information can be still obtained by application of light stable isotopic techniques on ore and gangue minerals from the KMF. The emerging patterns largely coincide with previous findings implying low-temperature and largely basinal fluids being central to ore-upgrade. As a consequence, focus on textures, parageneses, age, isotopic fingerprints, elemental sources

and formation mechanisms of sugilite and other gangues of the KMF is suggested as a potentially promising means of further elucidating the enrichment processes.

2. Geological setting and previous work

The Palaeoproterozoic (ca 2.2 Ga) stratabound manganese deposits of the Kalahari Manganese Field (KMF) (Figure 1A) belong to the Hotazel Formation of the Transvaal Supergroup and are situated close to the western margin of the Kaapvaal Craton (Tsikos et al; 2003, Cairncross and Beukes; 2013). The late Archean to Palaeoproterozoic (2.65 to 2.0 Ga) units of the Transvaal Supergroup were deposited mainly in shallow-sea environments and comprise basal carbonate platforms (Campbellrand Subgroup), overlain by economically important BIF (Asbestos Hills Formation), succeeded by glacial diamictite (Makganyene) and volcanic sequences (Ongeluk Formation), lastly followed by the Hotazel Formation of the study area. Hotazel Fm grades upwards into dolomitic rocks of the Mooidraai Formation, which are unconformable overlain by the Palaeozoic Dwyka diamictite (Fairey et al; 2013). Both the Hotazel and Mooidraai Formations can be seen in the area being unconformably transected by the siliciclastic units (red/green shales, quartzites) of the Olifantshoek Supergroup (Figure 1B), which are developed immediately atop of a regional angular unconformity surface with a maximum age limit of ca. 2.3 Ga (Cornell et al; 1996, Land et al; 2017).

The KMF is for the most part covered by sands of the Kalahari Formation and the only natural outcrop is restricted to a small hill in the northwestern part of the area known as Black Rock (Beukes et al; 2016). To date, open cast and underground mining has focused on the southernmost and northernmost part of the field (Figure 1A). The Hotazel Formation overlies lavas of the Ongeluk Formation and is constituted of three laterally extensive manganese ore horizons (lower, middle, upper beds), interbedded with banded iron-formation (Tsikos and Moore; 1997) (Figure 1B). The protolith ore, referred to as braunite lutite in the literature, has been upgraded in the northwestern part of the KMF by a structurally-controlled and pervasive hydrothermal event which took place between ca. 1.3 and 1.0 Ga during the Namaqua orogeny (Beukes et al; 2016). Residual manganese enrichment during this event was accompanied by the formation of a wealth of peculiar gangue mineral assemblages

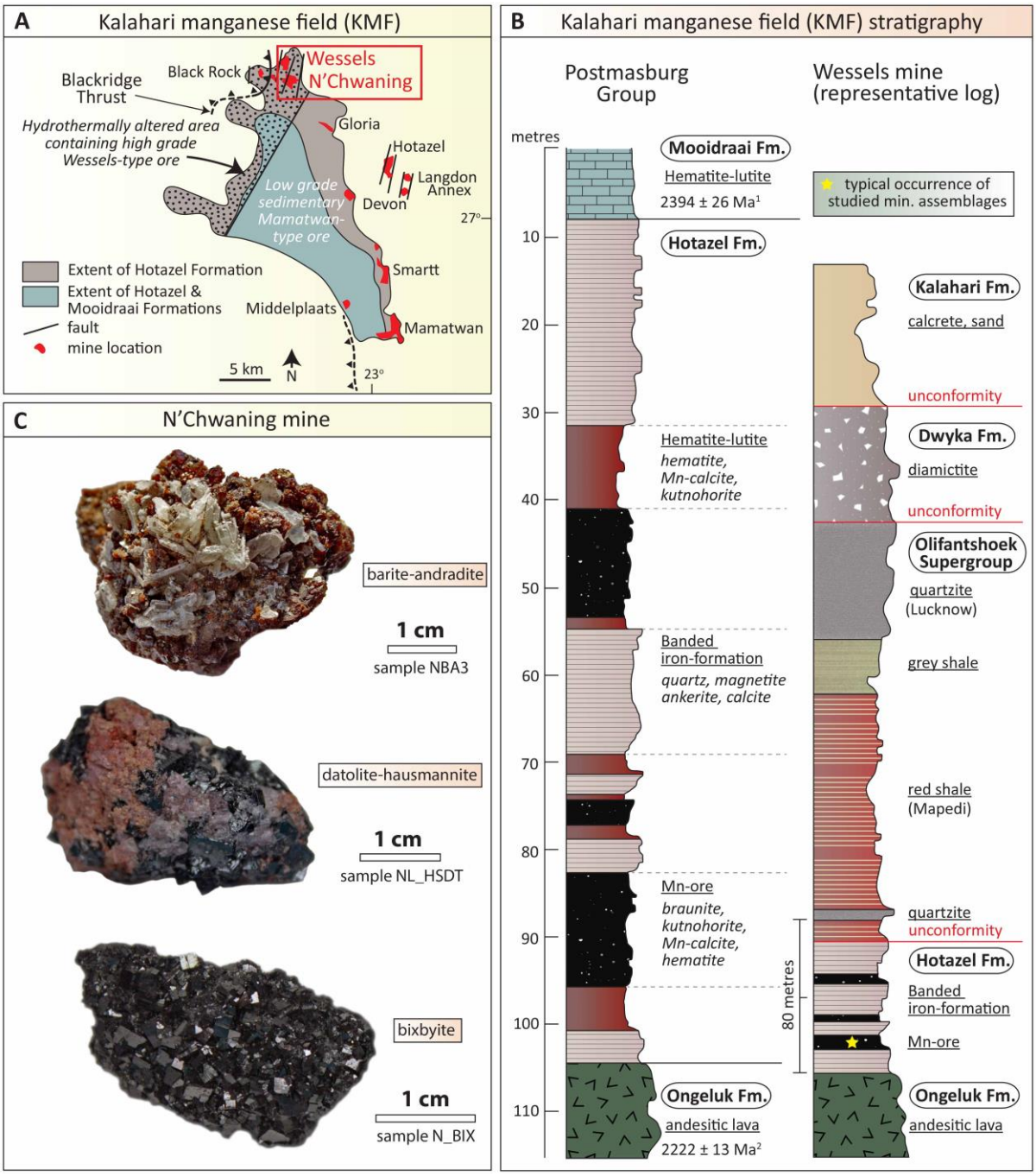

Figure 1. (A) Locality map of the Kalahari manganese field showing the two ore-types, current ore exploitation sites including Wessels and N'chwaning mines (this study) and approximate distribution of Blackridge thrust fault (after Tsikos and Moore; 2005). (B) Simplified stratigraphic column showing Hotazel Formation within the Postmasburg Group and representative drillcore at Wessels mine. Redrawn from Burger; 1994 and Tsikos and Moore; 1997. (C) An assortment of crystalline gangue and ore minerals analysed in this study for their isotopic composition.

(Cairncross and Beukes; 2013), the alkali-rich nature of which is reflective of the infiltrating fluids of unknown origin which had temperatures between 130° and 210° C (Lüders et al;

1999) or between 270° and 420°C (Miyano and Beukes 1987; Dixon; 1985, 1989), depending on the author.

The lower manganese ore bed is highly endowed with layers or seams of sugilite, a sodium-potassium, ferric-iron silicate of the milarite group firstly described from the Wessels mine from Dunn et al (1980). This mineral has been mined as a gemstone due to its purple violet-lilac colour, caused by the presence of Fe^{3+} and Mn^{3+} in its lattice (Shigley et al; 1987), that made it desirable to the collectors. $^{40}Ar/^{39}Ar$ age constraints on the former and the unusual associated oxymica norrishite (Gnos et al; 2003: 1048 ± 5.9 and ca. 1010 Ma), provide the best proof to date for the association of hydrothermal ore-upgrade with the timing of the Namaqua orogeny, although hematite palaeomagnetic dating (Evans et al; 2001: ca. 1250 and 1100 Ma) and other less precise ages also exist (Dixon; 1988, 1989). The western edge of the KMF is traversed by the prominent Blackridge thrust fault system, which has a N-S strike, resulted in significant stratigraphic duplication and developed in response to compression tectonics during the controversial Kheis orogeny (either 1.8-19 Ga or 1.3-1.2 Ga: Cornell et al; 1998, Van Niekerk; 2006).

3. Sample availability and analytical methods

26 samples comprising well-crystallized, aesthetic mineral associations (Figure 1C) chiefly from N'chwaning and lesser from Wessels mine were provided by mining employees and collectors during a field trip in the Northern Cape in 2018. A full list and information on mineralogical parageneses are attached to the stable isotopic results further below (Table 2). Additionally, three samples (aegirine iron-formation, aegirine-banded sugilite and barite) previously used in other relevant research were included here for isotopic studies. Unfortunately, details with regard to the exact stratigraphic location of the samples is not available but according to the individuals who collected and supplied the samples, they derive primarily from the lower Mn bed and were extracted after underground Mn exploitation had ceased. All three analysed sugilite samples derive from Wessels mine.

All petrographic examinations were conducted firstly under optical microscopy (SUERC) and subsequently using SEM/EDS techniques at the universities of Glasgow and

Durham, on a Quanta 200F Environmental SEM with EDAX microanalysis and a Hitachi SU-70 FEG SEM respectively. As regards stable isotopic work, the rather coarse-grained specimens allowed for pure chips to be handpicked on finely crushed material, whereas fine-grained targets were micro-drilled from polished wafers previously studied under SEM. Purity of samples was further evaluated by quantitatively determined oxygen yields (always > 80 % and mostly > 85 %) (Appendix II) which supports only negligible contamination by admixtures, if any at all in most cases.

Oxygen isotope analyses were facilitated via laser fluorination (SUERC), using ClF_3 as the fluorinating agent and applying the basic methodology of Sharp (1990). Oxides and garnet were pre-fluorinated overnight under vacuum. OH-bearing minerals were degassed overnight (250°C) and pre-fluorinated for one minute before infrared laser heating. Aegirine overnight pre-fluorination resulted in sample reaction and associated isotopic fractionation from 1.3 to 5.8 ‰, therefore one minute pre-fluorination was used instead. This is attributed either to sample impurities or most likely to the very fine-grained and acicular habit of this pyroxene in the samples used. Similarly, sugilite was pre-fluorinated for one minute, since a fifteen-minute treatment was found to produce fractionations of 0.9 ‰ on average. Converted CO_2 was analysed on a VG Isotech SIRA series II dual inlet mass spectrometer. Hydrogen from degassed samples (150°C) was extracted by in vacuo bulk heating using the method of Donnelly et al (2001) and measured on a VG Optima mass spectrometer at SUERC. All isotopic data are reported in standard delta notation, relative to Vienna Standard Mean Ocean Water (V-SMOW). Repeat analyses of international and lab standards gave a reproducibility of ± 0.3 ‰. and ± 2‰ for oxygen and hydrogen respectively.

In situ $^{40}Ar/^{39}Ar$ analyses were conducted via laser ablation on thin polished wafers using a New Wave Research Laser UP-213 A1/FB and gas purifications and measurements were made with a Helix SFT (Thermo Scientific) multi-collector noble gas mass spectrometer at the NERC Argon Isotope Facility at SUERC. Details on the method can be found in Appendix I and full $^{40}Ar/^{39}Ar$ results in tables therein.

4.Results

4.1 Sample characterization and in situ $^{40}Ar/^{39}Ar$ data

All four studied sugilite samples verify that massive and banded occurrences can be essentially polycrystalline and polymineralic material and therefore laser ablation for $^{40}Ar/^{39}Ar$ purposes should be preceded by rigorous petrographic analysis. Its massive form comprises aggregates of several smaller individual and compositionally variable crystals that can be fibrous or granular and coexist mostly with calc-silicate minerals. Banded sugilite also typically comprises very fine-grained sugilite that in most cases is intricately mixed with other species and similarly to the massive form, may display grains of varying composition.

Sample SW1, is a translucent massive purple-lilac sugilite (Figure 2.1) which macroscopically resembles the silica-rich and hence less pure gem material described by Shigley et al (1987) from Wessels mine, i.e., chalcedony mixed with and colored by purple manganoan sugilite. However, microscopic investigation reveals no free silica content, but instead a paragenesis comprising mainly sugilite, pectolite [$NaCa_2Si_3O_8(OH)$] and aegirine, the latter probably contributing to the silica-rich appearance of the sample. Optical microscopy and particularly backscatter imaging illustrates that an area of violet material can be essentially very inhomogeneous and consist of irregular masses of fine-grained (mostly between 5 and 25 μm) or fibrous sugilite surrounding aegirine, while being interspersed by patches of pectolite (Figure 2.2, Figure 3A). Quantitative EDS analyses for sugilite are standardless and normalized to hundred percent by the EDS software; however, comparisons with data from the literature (Table 1) render them as sufficiently robust for the needs of the current study. It is noted that significant amounts of calcium were detected in a number of analyses that were rejected from average composition calculations.

The latter element is constantly below detection limits in microprobe analyses of sugilite and has been reasonably regarded as contaminant calc-silicate (pectolite) in previous studies (Taggart et al; 1994), thus leading to subtraction and recalculations. Nevertheless, EDS data can be still used to make valid comparisons between compositionally different sugilite

and suggest that at least two different varieties exist (see also Table 1). Prominent changes in brightness under back-scattered electron imaging further corroborate the above.

Table 1. Average chemical composition of sugilite and osumilite analyses from Wessels mine.

Sample	Sugilite (S1)	Sugilite (S2)	osumilite	Wessels[a]	roedderite [a]	Bruce [b]
	n=24	n=6	n=17	n=23	n= 4	n= 5
SiO_2	71.24	76.45	62.77	69.97	67.25	72.46
Al_2O_3	3.02	11.45	-	0.88	0.93	7.31
Fe_2O_3	10.72	-	-	12.88	-	0.61
FeO	-	-	8.52	-	8.57	-
Mn_2O_3	3.54	1.61	-	2.37	-	3.51
MnO	-	-	4.10	-	3.38	-
CaO	-	-	-	0.07	1.08	bdl
MgO	-	-	13.66	-	7.41	-
Na_2O	5.62	5.40	6.18	6.25	6.57	6.04
K_2O	4.63	5.10	2.76	5.03	4.34	4.82
LiO_2	-	-	-	3.10	-	4.49
Total	100.00*	100.00*	100.00*	97.90	99.26	100.09

References: [a]Dixon; 1985, 1988, [b]Moore et al; 2011. When available lithium is calculated from 3 Li pre formula unit. See text for S1 and S2 sugilite. *Data normalized to 100% by EDS software.

Compositional variation is mostly observed in the aegirine- and pectolite-rich matrix of the sample, where sugilite produces distinct chemical zonation around what appears to be aegirine cores or relict fragments cemented and possibly replaced by Fe-rich sugilite (S1*-brighter), sequentially followed by more typical Mn-rich varieties (S1-darker) (Figure 2.2, Figure 3B). According to EDS analyses, Fe_2O_3 varies considerably, but no differentiation is made here between Fe-rich and Fe-poor varieties. However, BSE imaging in this sample indicates that sugilite is more enriched in iron constantly where in contact with aegirine and is mostly there that conspicuous compositional changes occur. In certain instances, aegirine masses can be characterized as relict, implying that sugilite crystallization, at least in some

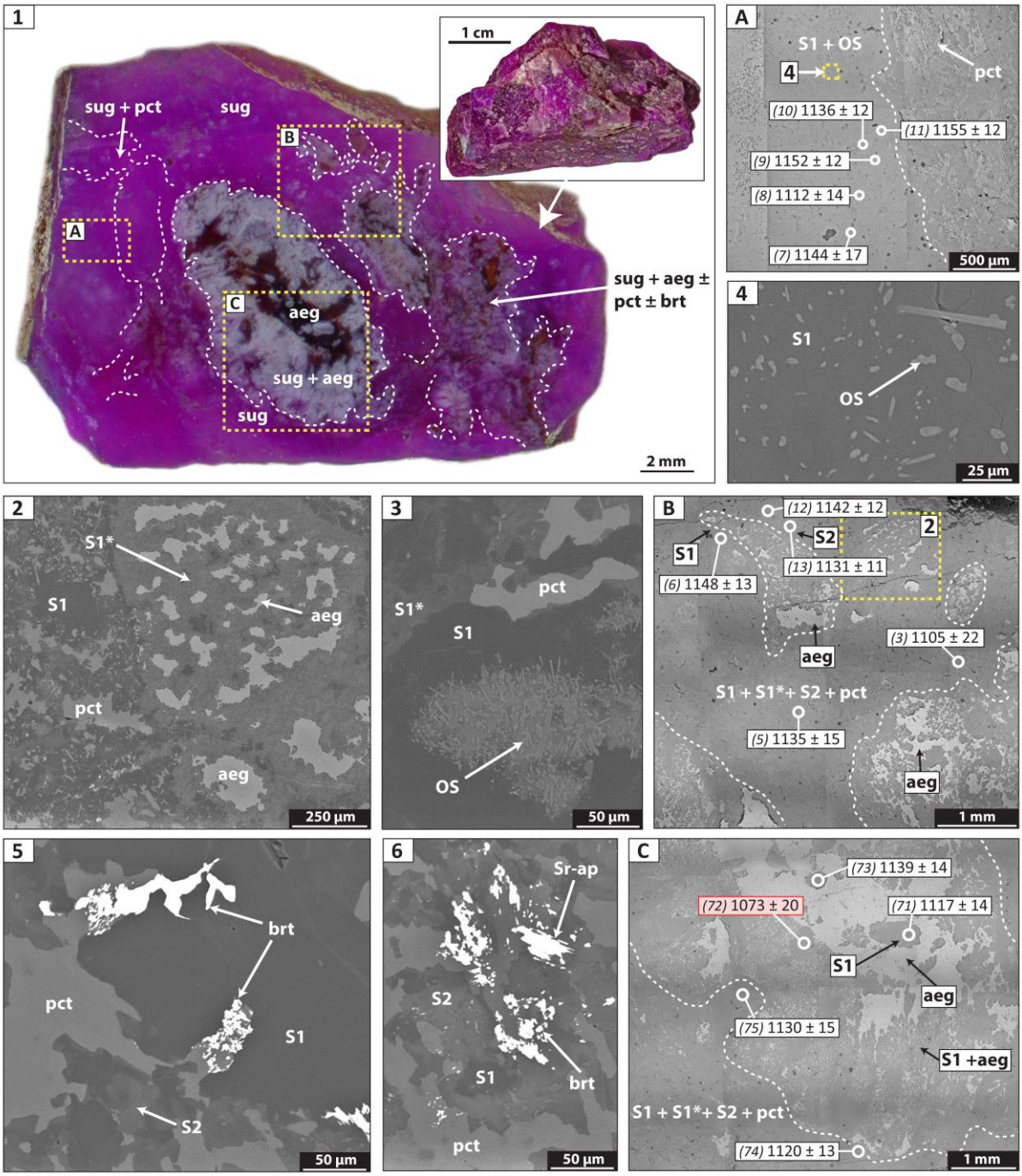

Figure 2. (1) Massive purple sugilite with aegirine-pectolite inclusions. Yellow dotted line outlines targeted dating sites. Back scattered electron (BSE) images. (2) Aegirine relict fragment replaced by Fe-rich sugilite (S1*) and surrounded by pectolite and another variety of sugilite with higher Al content (S1). (3) Fine-grained osumilite (roedderite) prismatic grains, rich in Mg. (4) Scattered osumilite is sugilite mass. (5 & 6) Barite and strontian apatite are commonly seen overprinting phases such as pectolite and sugilite. (A-C) Reflected light maps showing distribution of dates from sugilite assemblages with a weighted mean of 1133 ± 2 Ma (2σ, n=14). Rejected spot date is outlined in red. Laser spots are shown to approximate scale and dates at 1σ confidence level. aeg = aegirine, brt = barite, pct = pectolite, OS = osumilite (roedderite), S1 or sug = sugilite, S1* = Fe-rich sugilite, S2 = Al-rich sugilite, Sr-ap = strontian apatite.

occurrences, post-dates that of aegirine. Another Al-rich variety was rarely found in the matrix, intermixed with the dominant sugilite (S2 sugilite, Table 1).

Moreover, manganoan sugilite masses can be sometimes seen intergrown with fine-grained (5-50 µm) prismatic crystals (OS), usually matted together in dense aggregates (Figure 2.3, 2.4). This species has composition broadly comparable to that of sugilite, although constantly rich in magnesium (Table 1). This is another presumed milarite group mineral, most likely belonging to the osumilite subgroup similar to sugilite. Additional evidence for this derive from a single previous report of textually equivalent roedderite [$KNaMg_2(Mg_3Si_{12})O_{30}$] or another osumilite in sugilite-rich assemblages from the Wessels mine (Dixon; 1988). Minor barite and strontian apatite are also present in the purple sugilite mass and are clearly seen overprinting pectolite and sugilite, occluding open space between sugilite grains or pseudomorphically replacing individual crystals of the milarite-group mineral (OS) (Figure 2.5, 2.6).

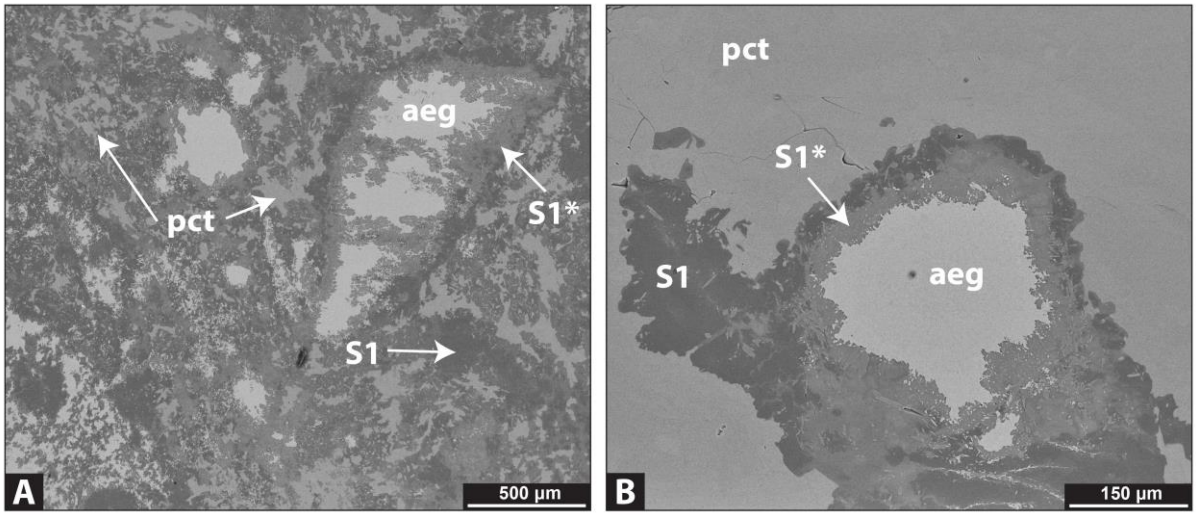

Figure 3. Back scattered electron (BSE) images. (A) An area of violet 'sugilite' material can be very inhomogeneous and consist of intricately mixed masses of fibrous sugilite and patches of pectolite, generally surrounding aegirine. (B) Zoned assemblage comprising an aegirine-core, surrounded by Fe-rich and then Al-rich sugilite, all enveloped in pectolite. aeg = aegirine, pct = pectolite, S1 = sugilite, S1* = Fe-rich sugilite.

Sample SP1, is purple massive crystalline sugilite overgrown on Fe/Mn host-rock and most likely developed in a vug or 'pocket' within the stratigraphically lower Mn ore bed (Figure 4.1, 4.2). In detail, the host rock is rich in hematite and hausmannite with lesser

braunite and andradite being present, which may imply that the sample was also in close proximity to a fault zone, where zones of ferruginized and silicified wall-rock usually develop and minerals such as hematite, aegirine and andradite are always present (Beukes et al; 1995, Gutzmer and Beukes; 1996b). In cross section, sugilite occurs as mm-scale spherical clumps, blebs or interconnected globules within a silica-rich matrix comprising mainly aegirine-augite and subordinate pectolite. The structures occupied by sugilite display a crude zonation, with broadly monomineralic aggregates filling the rims and core areas consisting of sugilite with densely disseminated fine-grained aegirine and minor pectolite (Figure 4A). Although it is unclear if carbonate ovoids, concretions or comparable textural features of the pristine carbonate material in the protore exert control in the textural development of these sugilite assemblages, the occurrence of equivalent but smaller micron-sized globular structures filled by aegirine and sugilite in the host rock further suggests a possible link between the two (Figure 4.1 inset). Considering the general metasomatic nature of alteration in the ore zone and the previously reported replacements of carbonate ovoids by sparitic calcite and hausmannite (Beukes et al; 1995), the above link is fairly substantiated.

Andradite occurs only in the wall rock, producing a mottled texture within a fine crystalline matrix of mainly hausmannite and hematite. Some of the dispersed large round 'mottles' may be further overprinted by microplaty hematite closely associated with braunite-II and traversed by microscopic barite veinlets (Figure 4.3). Locally, mottled texture consisting primarily of hematite implies pseudomorphous replacement of andradite. Calc-silicates of the serandite-pectolite solid solution mostly occupy the space along the contact between host rock and sugilite, where they seemingly pool within mm-scale domains, overall creating a broad zonation. Pectolite is further seen traversing through the sugilite-aegirine globules, most likely precipitating in later micro-cracks. Aegirine and aegirine-augite are generally very-fine grained but clusters of subequant and coarser (50-150 µm) crystals can be also observed in association with sugilite (Figure 4.4). In like manner to the previous sample, syn-crystallized barite and strontian apatite are regularly present and clearly overprint areas with well-defined boundaries that comprise mostly pectolite (Figure 4.5).

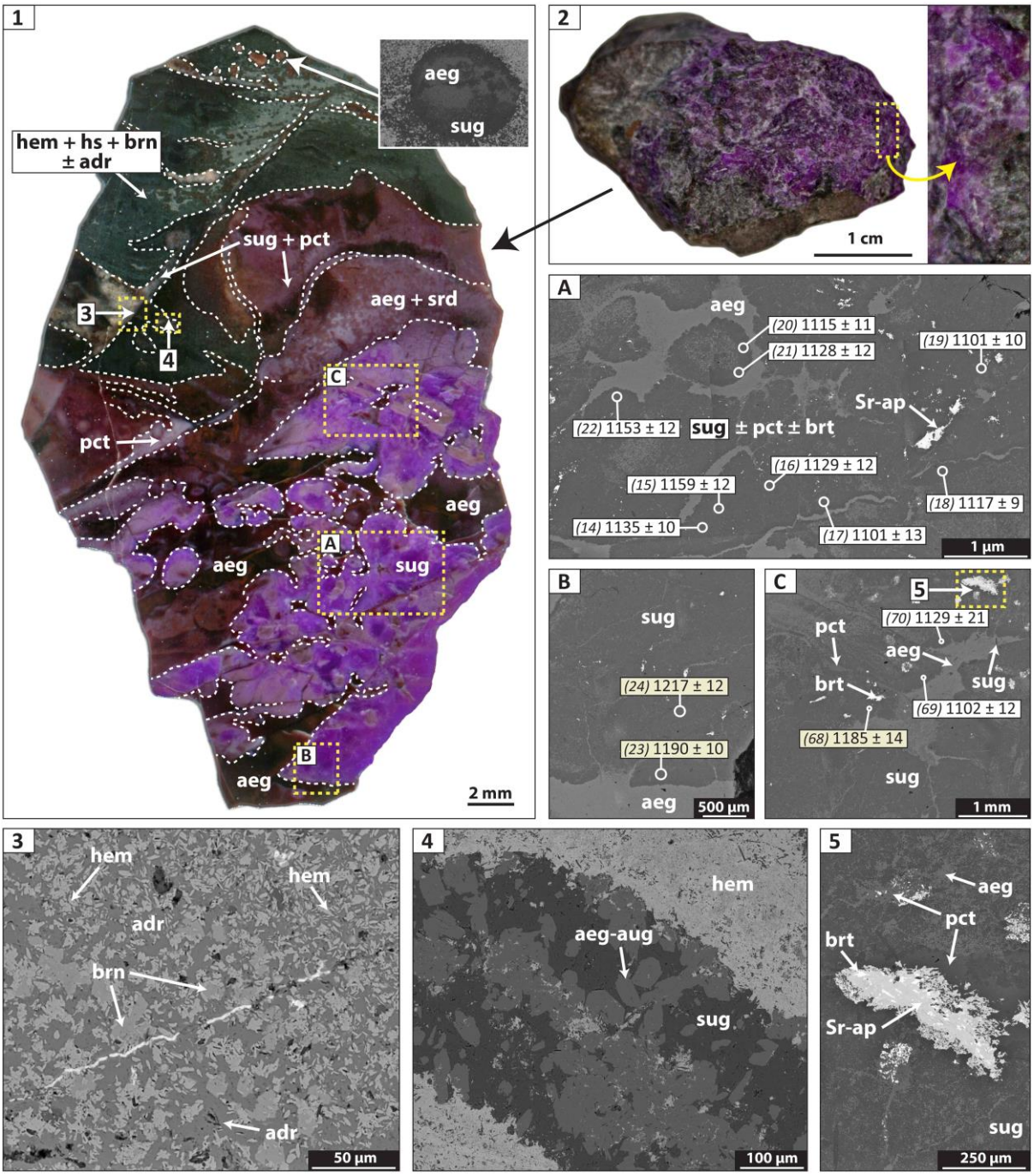

Figure 4. (1) Thin polished sample wafer prepared for dating. Targeted sites are outlined in yellow dotted line. Note the sugilite 'globules' and the pectolite-serandite zone in between them and the host rock. (inset) micron-sized ovoid filled by aegirine and sugilite. (2) Massive sugilite on Fe/Mn host rock. Back scattered electron (BSE) images. (3) Andradite-hematite-rich matrix traversed by barite veinlet (white). (4) Coarse-grained equant aegirine associated with sugilite. (5) Barite and strontian apatite overprint pectolite-rich domains. (A-C) BSE maps showing distribution of sugilite dates, displaying a weighted mean of 1139 ± 5 Ma (2σ, n=14). Dates shown at 1σ confidence level. adr = andradite, aeg-(aug) = aegirine-(augite), brn = braunite, brt = barite, hem = hematite, hs =hausmannite, pct = pectolite, Sr-ap = strontian apatite, srd = serandite, sug = sugilite.

Fourteen $^{40}Ar/^{39}Ar$ spot dates yielded a spread of ca. 116 Ma, i.e., difference between

youngest and oldest spot date (Figure 4A-4C). Specifically, dates range between 1001 ± 10 Ma (1σ) and 1217 ± 12 Ma (1σ) and display a weighted mean of 1138.6 ± 4.8 Ma (2σ, MSWD = 4.00, n= 14). Distribution of these data is slightly skewed towards older dates. However, there is no systematic correspondence between distinctly older dates (spots 23, 24, 68) and location in the sample and no apparent textural reason explains the observed differences, apart from maybe the presence of finely intermixed different sugilite generations.

Sample SB1 comprises dull-pinkish sugilite of the banded textural form (Figures 5.1, 6.1), that is interlayered with aegirine-rich bands and most certainty derives from the contact between the lower manganese bed and the underlying hematite lutite. Microlamination is conspicuous owing to aegirine laminae, while the usually thicker, mm-scale sugilite bands are seen again being composed of a dense network of globular structures or ovoids that is commonly interrupted by aegirine-rich domains. Scattered patches of aegirine (broadly 100-500 µm) are present in the pinkish sugilite bands, but otherwise, this layered-material is quite monomineralic in places, consisting chiefly of sugilite. High magnification of sugilite matrix reveals that it may consist of discrete (5-15 µm) and finely intergrown crystals of compositionally different sugilite (S1 and S1*), with variable iron content (Figure 5.3, 5.4). Small interstitial space between fine sugilite grains is regularly filled by serandite or pectolite (Figure 5.4, 5.5) and rarely tephroite (Mn_2SiO_4), the latter observed mostly as small disseminated masses in the cores of sugilite ovoids (Figure 5.6).

One of the prominent features in this sample is the occurrence of cross-cutting kentrolite ($Pb_2Mn^{3+}{}_2(Si_2O_7)O_2$) veinlets, which possibly suggests a later introduction of lead. The mineral distribution spreads also laterally, mostly along aegirine-bands and in proximity to the veinlets, where it displays an extremely fine-grained habit probably caused by small-scale interstitial filling between aegirine and sugilite grains (Figure 5.2, Figure 6A). Occasionally, slightly coarser sugilite (25-40 µm) co-exists with kentrolite in these veinlets and could perhaps represent a later recrystallized generation, although the occurrence of similar but kentrolite-free sugilite veinlets complicates the scene. Barite is finely disseminated throughout the sample and usually occurs in clusters of very fine-grained material (Figure 6.2, 6.4). Aegirine forms tightly intergrown, irregularly-shaped or somewhat globular masses that

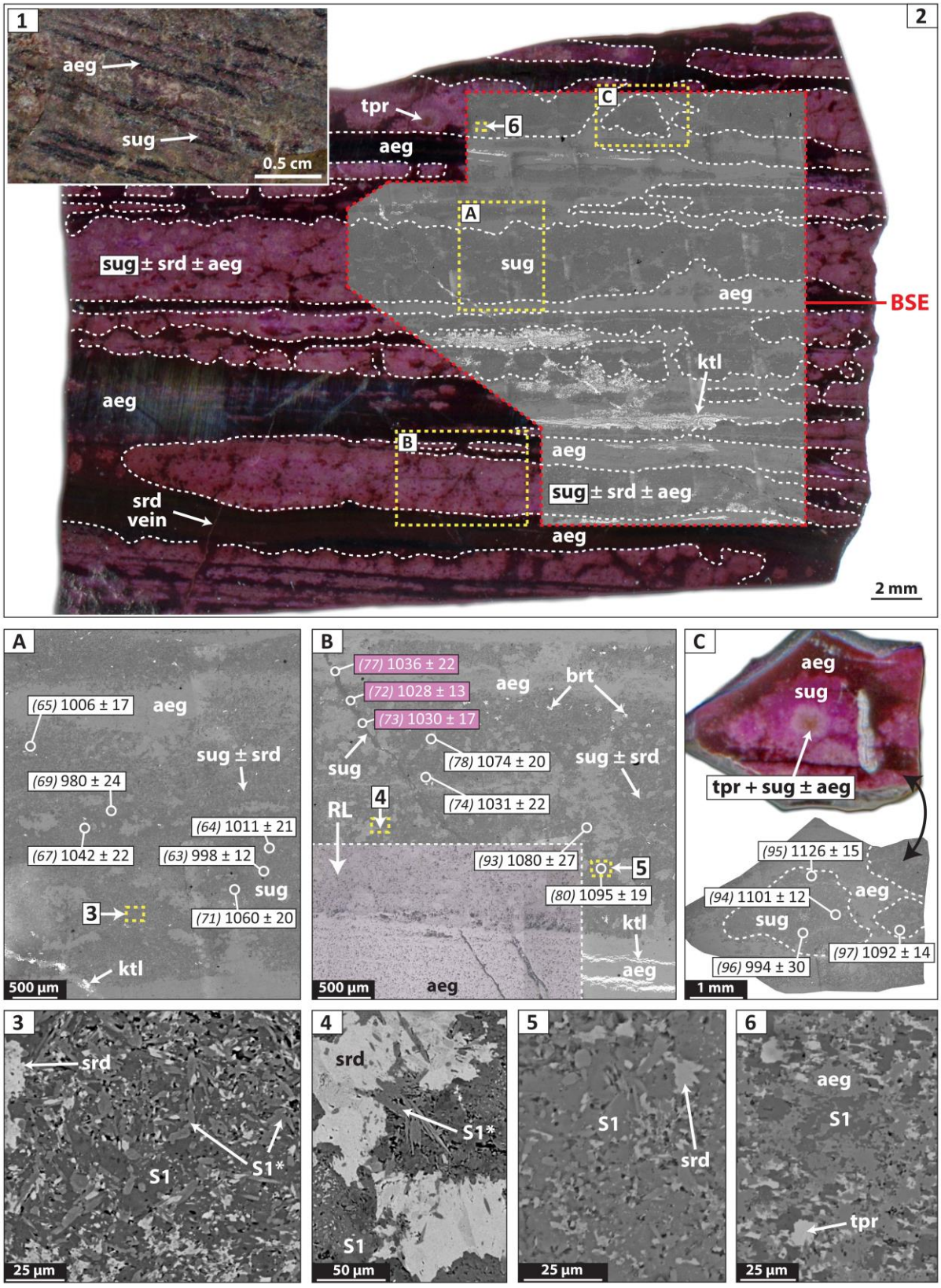

Figure 5. Sample detail (1) and polished wafer scan (2) of banded sugilite sample, displaying conspicuous aegirine- and sugilite-rich alternating layering and cross-cutting sugilite- and kentrolite-filled veinlets. (3-5) Back scattered electron (BSE) images. (3) Magnification of sugilite matrix reveals finely intergrown and compositionally variable crystals. (4 and 5) Serandite-pectolite commonly fill interstitial space in sugilite bands. (6) Tephroite is another phase rarely observed. Continues in next page.

Figure 5. (continued) (A-C) Composite BSE-reflected light maps showing distribution of spot dates. Three dates obtained from a sugilite micro-vein (spots 72, 73, 77) are coloured in pink (see Figure 8 later on). Dates shown at 1σ confidence level. aeg = aegirine, brt = barite, ktl = kentrolite, nrs = norrishite, S1 or sug = sugilite, S1* = Fe-rich sugilite, sug =sugilite, srd = serandite, tpr = tephroite.

host sugilite in their cores and are commonly surrounded by a thin discrete rim of serandite (Figure 6.3). The above textural form of aegirine apparently overprints the kentrolite-sugilite veinlets. In agreement with the previous sample (SP1), banded sugilite probably forms metasomatically on a former lithology that most likely is hematite lutite. The latter is described as purplish red rock, with prominent brown and pink carbonate laminae and small reddish carbonate ovoids in proximity to the ore (Schneiderhan et al; 2006).

Twenty-eight spot dates were obtained collectively from sample SB1. Sixteen $^{40}Ar/^{39}Ar$ spot dates were collected from banded and ovoid-filling sugilite, range from 980 ± 24 Ma (1σ) to 1126 ± 15 Ma (1σ) and display a normal distribution with a weighted mean of 1060 ± 11 Ma (2σ, MSWD = 1.13) (Figure 5A-C, 6A). The is no discernible textural control on the ages across the sample and the age scatter is apparently not high, but the ca. 145 Ma age difference between spots 69 and 95 is perhaps related to a geological reason involving mixed mineral populations as discussed later on (section 5.1). The remaining twelve $^{40}Ar/^{39}Ar$ analyses were determined from sugilite micro-veins (Figure 5B, 6A), occasionally associated with kentrolite, as well as from a distinct sugilite-aegirine band (Figure 6A) with conspicuous purple colouration (purple layered-sugilite). These data yield collectively a spread from 1028 ± 13 Ma (1σ) to 1125 ± 13 Ma (1σ), although intra-vein or intra-domain heterogeneities are much smaller. For example, four spot dates from the purple/magenta-sugilite band (Figure 6B) range from 1044 ± 9 (1σ) to 1075 ± 18 (1σ), i.e., difference of ca. 20 Ma. A later figure in the discussion (Figure 8), provides a comprehensive synopsis of the age data from this sample and attempts to further explain the observed small-scale age variations. The calculated weighted mean age of the sample (all twenty-eight spots) is 1064 ± 4 Ma (2σ, MSWD = 4.00, n= 28) and the data show a normal distribution.

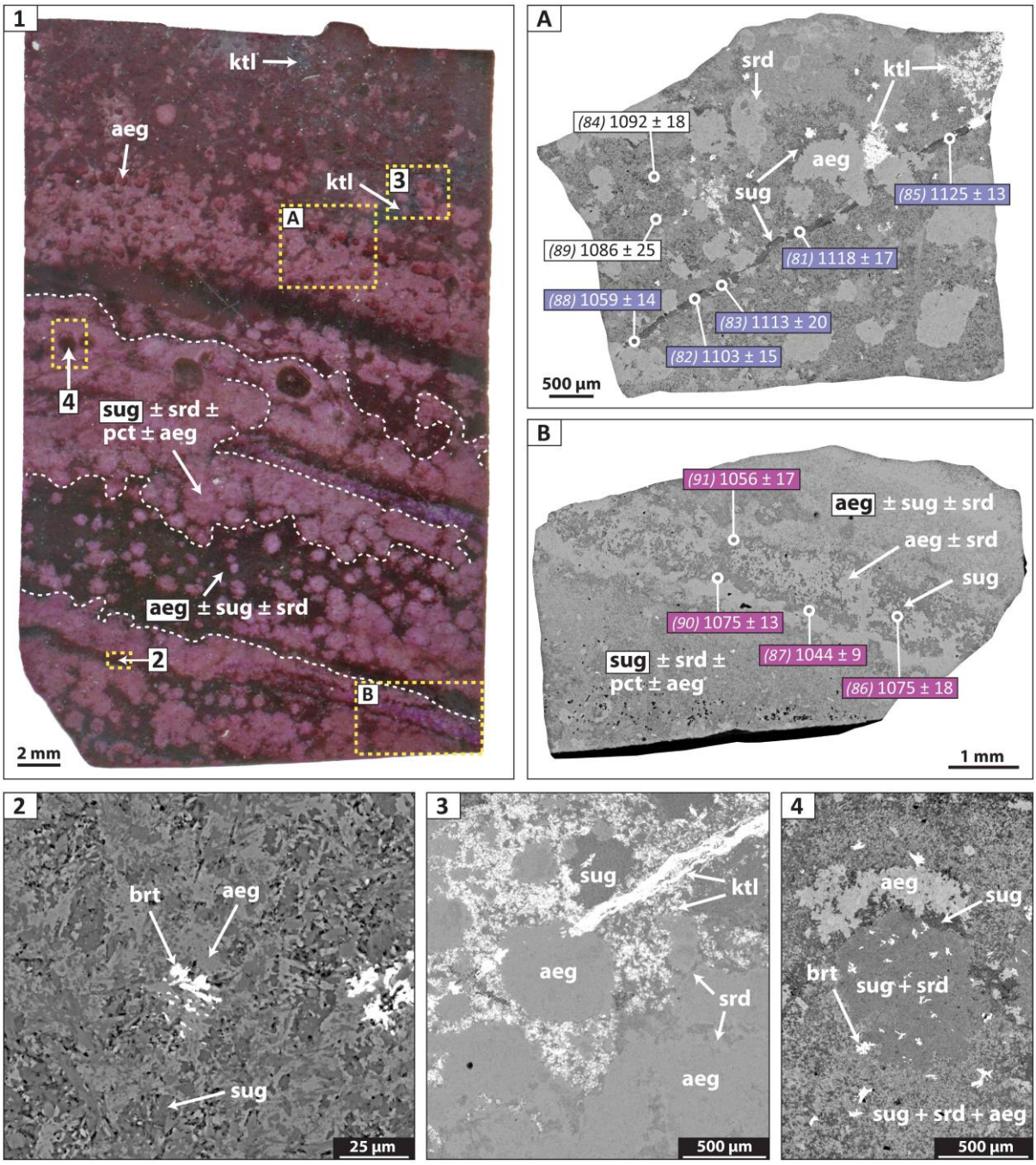

Figure 6. (1) Polished thin wafer of the banded sugilite sample exhibiting pronounced ovoids. Sites targeted for dating are outlined in yellow dotted line. Back scattered electron (BSE) images and maps. (2) Barite disseminations in sugilite-aegirine matrix. (3) Globular aegirine masses surrounded by a thin serandite-rich rim apparently overprint kentrolite veinlet. (4) Barite dispersed throughout a matrix of intricately mixed sugilite, aegirine and serandite, also displaying nodules/ovoids largely composed of sugilite. (A & B) SEM sample maps illustrating distribution of obtained spot dates (colour-coded) within a sugilite micro-vein (A) and a pronounced, almost bedding-parallel sugilite-aegirine purple band (B). Dates shown at 1σ confidence level. aeg = aegirine, brt = barite, ktl = kentrolite, pct = pectolite, sug =sugilite, srd = serandite.

4.2 Garnet-hematite associations

Two of the garnet-hematite-barite associations isotopically studied here, were prior investigated with the aid of scanning electron microscopy. The host rock around which andradite coatings form is very hematite-rich, but also displays ubiquitous cross-cutting andradite veinlets and bedding parallel development of andradite, seen constantly being finely intergrown with hematite (Figure 7.1). Composition of andradite may not vary much, but still crude compositional zonation was detected between crystals forming at the outer rim (essentially sample surface) and the inner margin, i.e., along the contact with the host rock. Specifically, according to thirteen EDS analyses, andradite appears to be marginally more manganese- and aluminum-rich (Al_2O_3 = 1.93 > 1.37 wt. %, MnO = 5.70 > 5.54 wt. %) away from the host rock and progressively acquires more iron-rich compositions (Fe_2O_3 = 31.7 > 29.1 wt. %) towards its contact with the host lithology. The pervasive layer-controlled occurrence of andradite in the iron matrix of the sample, along with the above compositional observations and textural evidence for hematite- and andradite-rich alternating laminae, imply that its precipitation is caused by metasomatic interactions, possibly with a preexisting silica-bearing mineral such as quartz or braunite.

The corona of garnet crystals developed around the iron- and silica-rich rock, further hosts hausmannite and apatite, both seemingly precipitating in the interstitial space between andradite (Figure 7A). Complex networks of veinlets traverse the sample and notably, garnet-barite veinlets overprint ones bearing solely hematite (Figure 7B). The size of both hematite and andradite in the matrix is broadly similar, ranging broadly from 10 to 30 μm. Certain sample domains though, display higher porosity and textures of microplaty to spherical hematite, tightly intergrown with apatite and andradite (Figure 7C1-3). These microscopic hematite spherules are generally smaller than 5 micron (can be even smaller than 1 μm) and their formation is probably related to metasomatic processes associated with formation of andradite.

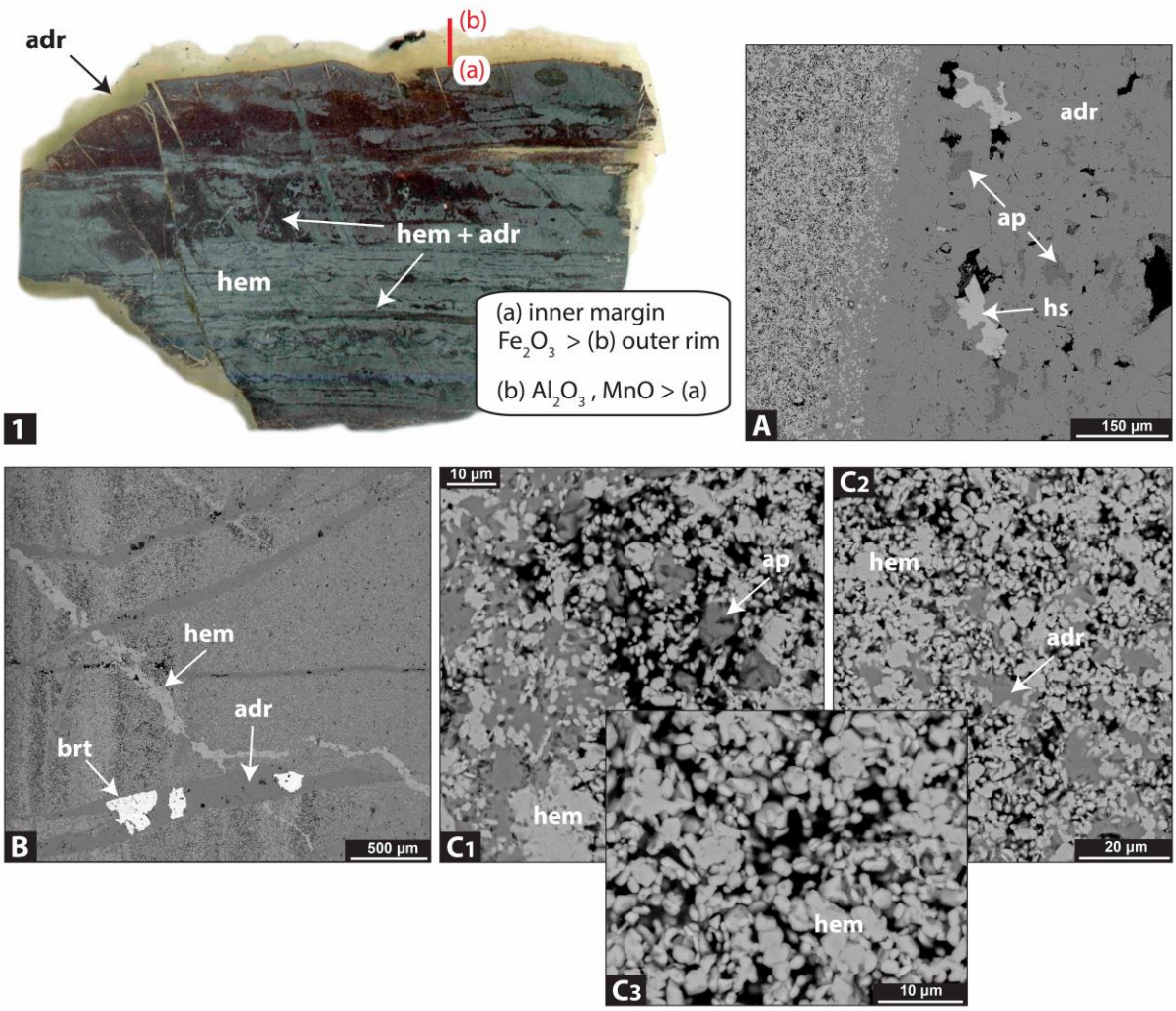

Figure 7. (1) Polished thin section scan showing an andradite corona around hematite-rich rock, which is also pervasively metasomatized by andradite. Back scattered electron (BSE) images. (A) Hausmannite and apatite occlude open space between garnet grains. (B) Garnet-barite veinlets support coprecipitation of the two phases and further overprint veinlets composed of hematite. (C1-3) Areas of higher porosity in the banding comprise microscopic hematite spherules intergrown with fine-grained apatite and andradite. adr = andradite, ap = apatite, brt = barite, hem =hematite, hs =hausmannite.

4.3 Stable isotope geochemistry

Thirty-three samples were analysed for their oxygen isotopic composition, among which four were also investigated for their hydrogen isotopic values. The results are displayed in Table 2 along with a short paragenetic description and $\delta^{18}O_{fluid}$ calculations for two separate temperatures, 130° and 210°C (see also discussion). All samples come from the two major mines in the KMF, primarily from N'Chwaning and lesser from Wessels mine and are representative of the early and main stages of hydrothermal ore-enrichment as presented in

more detail later on. $\delta^{18}O$ isotopic results for garnet (N'chwaning) range from +5.8 to +9.7 ‰ (avg. = +7.8 ± 1.4 ‰, n=8). A single aegirine form the same mine shows a value of +10.6 ‰ and the same mineral from Wessels displays a very homogenous oxygen isotopic composition (+11.1 ± 0.6 ‰, n=3). $\delta^{18}O$ values for Wessels sugilite are very close to that of aegirine and range from +10.6 to +13.2 ‰ (n=4).

The remaining silicate minerals analysed also share comparable heavy $\delta^{18}O$ ratios. Specifically, single isotopic analysis on Mg-arfvedsonite, muscovite and pectolite show values of +11.4, +11.5 and +10.6 ‰ respectively, whereas analysis of datolite returned a somewhat lighter oxygen isotopic value (+8.2 ‰). Measured $\delta^{18}O$ ratios of oxides are distinctly lighter than that of silicates. Hematite displays a range from -4.2 to +0.6 ‰ (avg. = -1.0 +1.9 ‰, n=8), bixbyite values are close to zero (+0.2, +0.4, +0.6 ‰) and likewise, hausmannite isotopic composition ranges between -4.5 and -0.4 ‰. δD isotopic values for muscovite and pectolite are -56.4 ‰ and -58.5 ‰ respectively, datolite is somewhat isotopically heavier (-28.0 ‰) and Mg-arfvedsonite exhibits a noticeably lighter δD value of -118.8 ‰.

Table 2 (next page). Stable O and H isotopic compositions of gangue and ore minerals and calculated $\delta^{18}O$ fluid values for temperatures of $130^{O}C$ (1) and $210^{O}C$ (2) (see also text for explanations).

sample ID	mineral	formula	description / paragenesis	$\delta^{18}O_{min}$	$\delta^{18}O_{fluid}$[1]	$\delta^{18}O_{fluid}$[2]
			N'Chwaning			
N1	aegirine	$NaFe^{3+}Si_2O_6$	aegirine from microbanded iron-formation	10.6	0.3	5.2
NBA1	andradite	$Ca_3Fe^{3+}_2(SiO_4)_4$	bladed barite on coarse-grained brownish-red andradite	9.7	5.7	8.9
NBA2-g	andradite	$Ca_3Fe^{3+}_2(SiO_4)_4$	orange andradite and barite on intergrown hematite crystals	5.8	1.8	5.0
NBA3-g	andradite	$Ca_3Fe^{3+}_2(SiO_4)_4$	wine-red garnet, hematite and barite coating Mn host-rock	7.5	3.5	6.7
NBA4	andradite	$Ca_3Fe^{3+}_2(SiO_4)_4$	red andradite, platy hematite, barite and calcite	6.3	2.3	5.5
N_HSA1-g	andradite	$Ca_3Fe^{3+}_2(SiO_4)_4$	tiny calcite and barite on andradite and hausmannite mass	9.2	5.2	8.4
N_HSA2-g	andradite	$Ca_3Fe^{3+}_2(SiO_4)_4$	hausmannite on reddish-orange andradite	7.9	3.9	7.1
NBSG	andradite	$Ca_3Fe^{3+}_2(SiO_4)_4$	prismatic gaudefroyite, barite, ettringite and garnet association	6.9	2.9	6.1
NBGH	andradite	$Ca_3Fe^{3+}_2(SiO_4)_4$	prismatic gaudefroyite, calcite and barite on red andradite	8.8	4.8	8.0
NBA2-h	hematite	Fe_2O_3	orange andradite with barite and hematite	0.5	2.9	4.3
NBA3-h	hematite	Fe_2O_3	wine-red garnet, hematite and barite coating Mn host-rock	-3.4	-1.0	0.4
NB1	hematite	Fe_2O_3	platy hematite attached on barite cluster	-0.5	1.9	3.3
NB2	hematite	Fe_2O_3	euhedral hematite, barite and calcite on altered host rock	-4.2	-1.8	-0.4
N_HEM	hematite	Fe_2O_3	calcite masses on intergrown hematite metallic crystals	0.2	2.6	4.0
NCL_1	hematite	Fe_2O_3	sharp celestine crystals and prismatic hematite association	0.6	3.0	4.4
NCL_2	hematite	Fe_2O_3	sharp celestine crystals sitting on hematite and red garnet	0.4	2.8	4.2
NL_ET1bx	bixbyite	$Mn^{3+}_2O_3$	calcite-ettringite association on bixbyite and garnet host-rock	-0.4	-	-
NL_ETA1bx	bixbyite	$Mn^{3+}_2O_3$	bixbyite-rich host rock coated by ettringite and calcite crystals	-0.6	-	-
N_BIX	bixbyite	$Mn^{3+}_2O_3$	cluster of cubic bixbyite crystals with minor ettringite and barite	0.0	-	-
NHSA1-hs	hausmannite	$Mn^{2+}Mn^{3+}_2O_4$	hausmannite intergrown with red andradite and later calcite	-0.4	7.5	8.2
NHSA2-hs	hausmannite	$Mn^{2+}Mn^{3+}_2O_4$	intergrown pyramidal hausmannite on massive orange andradite	-4.5	2.9	4.1
			Wessels			
SW2_h	hematite	Fe_2O_3	hematite from microbanded sugilite- & aegirine-bearing iron-formation	-1.8	0.5	3.8
SW2-a	aegirine	$NaFe^{3+}Si_2O_6$	aegirine from microbanded sugilite- & aegirine-bearing iron-formation	11.7	1.4	6.3
W11	aegirine	$NaFe^{3+}Si_2O_6$	aegirine from microbanded aegirine-bearing iron-formation	10.6	0.3	5.4
SB1-a	aegirine	$NaFe^{3+}Si_2O_6$	aegirine from banded alkali-rich hematite lutite	10.9	0.6	5.2
SW1	sugilite	$KNa_2(Fe^{3+},Mn^{3+},Al)_2Li_3Si_{12}O_{30}$	massive purple sugilite with minor aegirine and pectolite inclusions	13.2	-	-
SW2-s	sugilite	$KNa_2(Fe^{3+},Mn^{3+},Al)_2Li_3Si_{12}O_{30}$	sugilite from microbanded sugilite- & aegirine-bearing iron-formation	11.4	-	-
SB1-s	sugilite	$KNa_2(Fe^{3+},Mn^{3+},Al)_2Li_3Si_{12}O_{30}$	sugilite from banded alkali-rich hematite lutite	11.7	-	-
SP1	sugilite	$KNa_2(Fe^{3+},Mn^{3+},Al)_2Li_3Si_{12}O_{30}$	sugilite crystals on aegirine-rich braunite manganese ore	10.6	-	-
				δD	**$\delta^{18}O$**	
SW2-l	Mg-arfvedsonite	$(Na,K)Na_2)(Fe^{2+}_4Fe^{3+)}Si_8O_{22}(OH)_2$	Mg-arfvedsonite vein from sugilite- & aegirine-bearing iron-formation	-118.8	11.4	0.5	6.3
WBC	muscovite	$KAl_2(AlSi_3O_{10})(OH)_2$	barite and hematite muscovite associated with bladed	-56.4	11.5	2.9	7.4
			N'Chwaning			
PCT	pectolite	$NaCa_2Si_3O_8(OH)$	fine pectolite growths and elongated kutnohorite clusters on manganese ore	-58.5	8.2	-0.4	4.1
NL_HSDT	datolite	$CaB(SiO_4)(OH)$	fine prismatic datolite on intergrown hausmannite and andradite	-28.0	10.6	-2.8	2.8

5. Discussion

5.1 Timing and duration of metasomatic ore-upgrade processes

Sugilite [$KNa_2(Fe^{3+},Mn^{3+},Al)_2Li_3Si_{12}O_{30}$], is a six-membered double-ring cyclosilicate with a milarite-type structure that contains potassium (ca. 4-5 K_2O wt.%: Wessels sugilite) between two double-ring units (Dixon; 1985, Armbruster and Oberhänsli; 1988). Its high abundance in the enriched high-grade manganese ore at Wessels mine, provides a unique opportunity for dating the hydrothermal event that has influenced the northernmost part of the Kalahari Manganese field and that is difficult to constraint otherwise. Previously published $^{40}Ar/^{39}Ar$ ages from Gnos et al (2003) give proof that despite it being an unusual case, in the sense that it had never been used for Ar-Ar dating prior to that study, it is a highly suitable mineral to accurately date hydrothermal enrichment in the study area and relevant districts.

$^{40}Ar/^{39}Ar$ ages of three texturally distinct sugilite samples from the Wessels mine (Figure 8) reinforce the previous age constraints on hydrothermal alteration in the KMF and therefore firmly tie the so-called 'Wessels event' to the Mesoproterozoic Namaqua-Natal orogeny. Previous $^{40}Ar/^{39}Ar$ analyses by Gnos et al (2003) were performed on a single, inclusion-free gem-quality sugilite crystal that yielded a plateau age of 1048 ± 6 Ma, interpreted as crystallization age and expectedly corresponding to a single event. Similarly, a hand-picked black flaky norrishite crystal yielded a more discordant spectrum which led to the assignment of two separate ages to the mineral, an ca. 1010 Ma crystallization age and a subsequent and more tentative alteration age of ca. 850 Ma. Contrastingly, in situ $^{40}Ar/^{39}Ar$ ages in our study derive from massive and banded sugilite textures, which comprise polycrystalline and polymineralic material that apparently hosts denser age information. In order to directly compare previously reported ages with that from the current study, the former were recalculated using the latest decay constants by Renne et al (2011) to be 1063 ± 18 Ma (2σ) for sugilite and 1026 ± 29 Ma (2σ) for norrishite.

There is a good intrasample concordance between the in situ UV laser $^{40}Ar/^{39}Ar$ dates, with no extreme differences measured and despite documented variations in sugilite composition and texture. However, spot dates span a considerable range in all three samples,

with most prominent being that of sample SP1 (ca. 100 Ma, from 1217 ± 12 Ma to 1101 ± 10 Mα, 1σ) and SB1 (ca. 140 Ma, from 1126 ± 15 Ma to 980 ± 24 Mα, 1σ). The likelihood that intrasample age variability may be related anyhow to Ar gas measurements can be excluded, since ^{39}Ar concentrations are constantly high in the obtained data. Physical contamination from another K-bearing phase is also very unlikely and is plausible only in sample SB1 where serandite is present and some potassium can perhaps substitute for sodium in its structure. This has been taken into account during analysis and serandite-rich areas were avoided, at least on the two-dimensional space. Ionic porosity and subsequently closure temperature for sugilite has been calculated to be in the range of amphiboles or mica (Fortier and Giletti; 1989). In consideration of the presumably low temperatures achieved during metasomatism of the ore, it is reasonable to assume that the ^{40}Ar/^{39}Ar ages represent timing of crystallization rather than cooling ages. Thermal diffusion of Ar following precipitation should be negligible if any, although the very fine-grained size and fibrous sugilite textures may exert some control on closure temperature of the mineral.

Theoretically, the weakly bound crystallographic sites hosting potassium in sugilite can be easily affected by ion exchange and diffusion loss, which increases the chance of disturbances in the Ar system. Contamination by excess ^{40}Ar, incorporated into the sugilite lattice during the Wessels event cannot be entirely excluded and thus may be an age disturbing factor for certain spot dates, although such process would most likely have caused much more erratic age profiles. The very good consistency between weighted mean ages from two massive sugilite samples and the previously published flat step-heating age spectrum reveal no apparent signs for any of the above. Instead, as illustrated in Figure 8, there are indications for textural control on the obtained spot ages, at least in the banded sugilite sample. Microscopic sugilite veinlets or macroscopically distinct mm-scale bands of vivid magenta colouration comprise spot dates that are broadly grouped together. The older vein-related ages (micro-vein A) in comparison to the surrounding matrix may be explained by younger and probably mixed sugilite age domains in the matrix, that either precipitated or had been thermally reset in response to later fluid pulses represented by younger veinlets (micro-vein B).

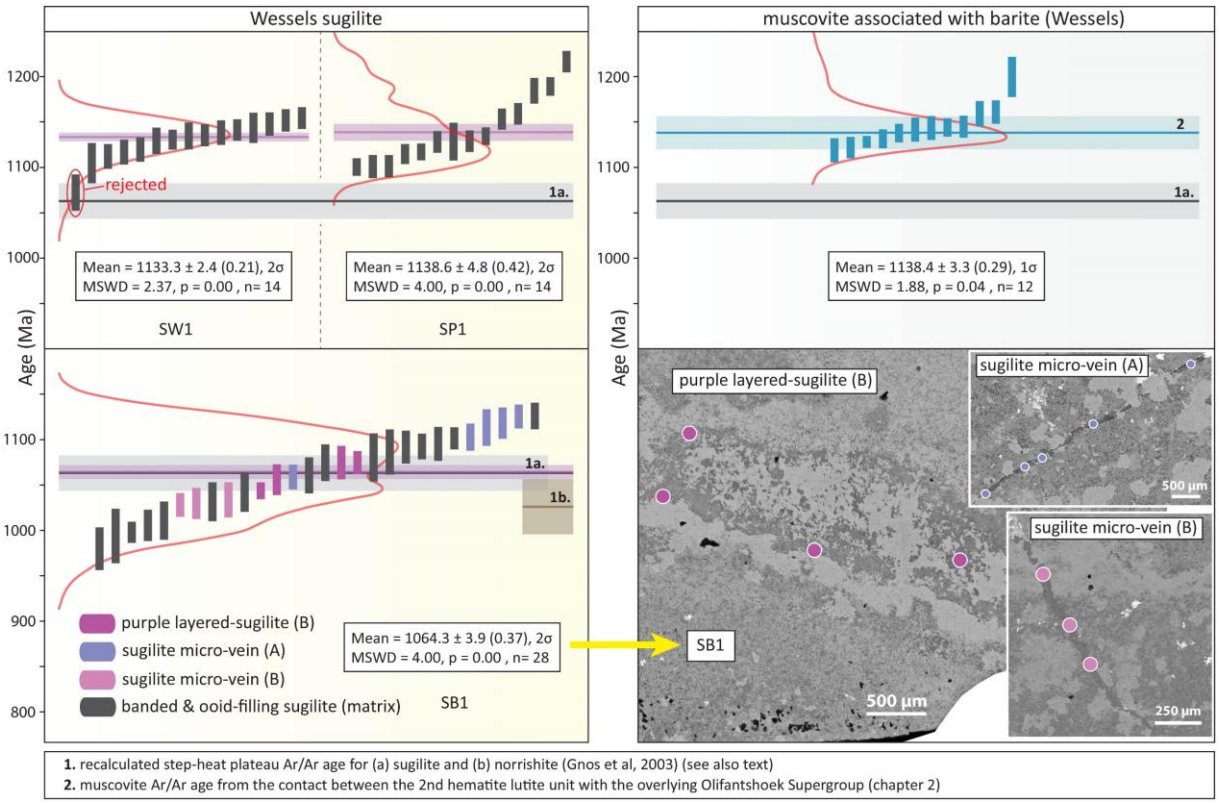

Figure 8. Plot showing distribution of $^{40}Ar/^{39}Ar$ spot dates (1σ-confidence level) from the three studied sugilite samples, with horizontal bars representing weighted mean ages (2σ-confidence level). Other relevant age data (1a, 1b, 2) from Wessels mine are also included. Selected in situ laser spot locations from sample SB1 (banded sugilite) are shown to emphasize the relatively distinct age domains in this sample. Collectively, hydrothermal activity spans from ca. 1139 to 1064 Ma (75 m.y.).

However speculative the above scenario is, textural observations from this sample clearly demonstrate that sugilite has crystallized during more than on stages and kentrolite formation was perhaps associated with sugilite precipitation or recrystallization. On this account and based on all yielded in situ spot dates, it becomes apparent that a large number of analyses (i.e., > 25), covering different domains of sugilite bands, may be required in order to both document the whole span of age information as well as report ''accurate'' weighted mean ages for specific samples. Interestingly, the yielded weighted average age for sample SB1 (1064 ± 4 Ma) overlaps with the sugilite crystal (1063 ± 18 Ma) dated from Gnos et al (2003), which not only adds further confidence in the notion that our in situ $^{40}Ar/^{39}Ar$ age is indeed geologically meaningful and reflect the ''real'' age, but also suggests **distinct episodes of sugilite formation**. Overall, we interpret at least some of the intrasample age variations as reflecting either Ar-isotopic contributions from mixed sugilite populations with slightly different crystallization ages or generations corresponding to distinct hydrothermal pulses that may have been separated by an interval of ca. 60-70 Ma.

At this point emerges that the present suite of radiometric ages can be used to give insights into the duration of hydrothermal circulation in the area. There is a perfect agreement between the massive sugilite ages from this study and the $^{40}Ar/^{39}Ar$ crystallization age of muscovite (Figure 8) seen associated with coarse bladed barite in drillcores from the same mine (chapter 2). This set of ages can serve as a maximum age constraint for the Wessels event of alteration and unequivocally extends the oldest bound of the period of hydrothermal activity to between 1139 ± 5 Ma and 1133 ± 3 Ma, i.e., by approximately 70 Ma. Age information presented by Dixon (1988, 1989) from six poorly constrained sugilite samples dated by the Rb-Sr (1351 ± 291 Ma) and Pb-Pb method (1270 ± 30 Ma), as well as a Pb-Pb galena age from N'Chwaning mine (1270 ± 20 Ma), similarly argue for an onset of the alteration period that is much earlier than the sugilite age from Gnos et al (2003). Although more age data are needed to pinpoint the early and main stages of this event, it can be safely stated that at least as far back as ca. 1140 Ma, an established hydrothermal system was present, precipitating barite and sugilite of metasomatic nature along with sodic and calc-silicate species.

Later stages of alteration are represented by the banded sugilite age coinciding with that from Gnos et al (2003), i.e., ca. 1064 Ma. Unpublished $^{40}Ar/^{39}Ar$ step-heating spectra from three sugilite samples nurture further confidence in the above data, suggesting an even later active system. Specifically, three plateau ages (1037 ± 7, 1012 ± 14 and 993 ± 5 Ma, ages not recalculated with the same decay constants for direct comparisons) suggest sugilite formation taking place between ca. 1040 Ma and 990 Ma (Gutzmer and Beukes; 1998, technical report). The entire spread of ages from published and unpublished results may be used to suggest that the regarded hydrothermal system was long-lived and congruent with the active Namaqua convergence in the west of the Kalahari Manganese field. Distribution of our age data suggests a duration of nearly 75 m.y. and this time span is extended to more than a 100 m.y. if some of the more robust reported ages are also included.

This extensive period is unlikely to represent a continuous and evolving hydrothermal event but instead, it is more plausible that multiple and/or distinct episodes have collectively attributed to the enrichment of the ore and precipitated different generations of

hydrothermal gangue minerals. Orogenic fluids may have been driven episodically in response to major events within the ca. 200 m.y. documented timespan of the main phase of the orogeny (1.2-1.0 Ga). Syn-tectonic granitoids in the eastern foreland of the active Namaqua orogen apparently provide evidence for more intense periods of igneous activity and emplacement in the crust during ca. 1190 ± 30 Ma and 1040 ± 30 Ma (Robb et al; 1999, Clifford et al; 2004, Eglington; 2006). Intriguingly, sugilite ages from this study broadly correspond with these distinct time periods and may therefore have been products of separate thermal pulses and associated orogenic fluid infiltration within a more prolonged period of convergence (at least 200 Ma or more) to the west of the Kaapvaal Craton.

5.2 Constraints on alteration fluids

5.2.1 Occurrence and parageneses of isotopically studied phases

Oxygen and hydrogen isotopic composition of minerals precipitated during the metasomatic enrichment at Wessels and N'Chwaning mines may provide an opportunity to obtain a better understanding of the origin and characteristics of alteration fluids and reconstruct fluid-rock interactions. Before any assessment of the isotopic results, it is instructive to outline our limited textural observations in conjunction with existing knowledge on the occurrence and paragenetic sequences of the analysed minerals, the latter deriving from published textural analysis and cross-cutting relationships (Kleyenstüber; 1984, Gutzmer and Beukes; 1996b, Gutzmer and Cairncross; 2002). In general terms and according to the existing literature, isotopically measured gangue silicates can be regarded as early phases, whereas oxides may be attributed to the main stage of hydrothermal alteration. However, minerals such as hematite and andradite have been linked to different precipitation episodes during all three (early, main, late) considered stages of alteration.

In particular, garnet (andradite, grossular, henritermierite, etc.) is mostly part of the sugilite calc-silicate association, which is thought to characterize the early stages of ore formation and occurs as metasomatic lenticular bodies, bedding parallel veins or cement in fault breccias. The association of andradite with sugilite and pectolite is therefore regarded to be common and is also seen in sample SP1, where additionally, later pseudomorphous

replacement of andradite by hematite seemingly takes place. However, as discussed earlier, sugilite associations at Wessels most likely form during an alteration period spanning over tens of millions of years, an observation that decreases confidence for the presence of clearly distinct early and main stages or an exclusively early occurrence of sugilite in the paragenetic sequence. It is more likely that sugilite and other associated minerals precipitated as early and/or main stage minerals, however, during more than one hydrothermal pulse. Mg-arfvedsonite (amphibole) is also part of the calc-silicate assemblages, although cross-cutting relationships indicate a later formation than that of coexisting sugilite and aegirine. The exact place of aegirine in the paragenetic sequence is also not known but it has been attributed along with most other silicates to an early stage, possibly after oxidation of the host rock and prior to the main ore modification (Tsikos et al; 2003, Tsikos and Moore; 2005). Much like sugilite though, banded aegirine occurrences coexisting with the former mineral in samples from this study may have formed during both main and later alteration stages, as geochronological data suggest.

Rose-coloured datolite from N'Chwaning mine occurring in ferruginised fault breccias has been studied for its fluid inclusions content and is attributed to the main alteration stage. Hence, it can be surmised that the analysed datolite-hausmannite-andradite gangue association represents the main alteration event. Other paragenetically affiliated phases described from datolite-bearing vugs are andradite, tephroite, jacobsite and xonotlite [$Ca_6Si_6O_{17}(OH)_2$] (Gutzmer and Cairncross, 1993). Finally, despite the lack of previous documentation, muscovite in massive hematite lutite is arguably related to the early stages of alteration on the basis of geochronological data (chapter 2).

More arduous can be the assignment of the analysed garnet to the documented paragenetic sequence, since more than one stages of andradite formation are reported to exist. Specifically, andradite has been documented to occur as: (a) early phase filling secondary porosity with hematite and braunite II, (b) younger generations coating hematite, braunite II and hausmannite and (c) late cross-cutting associations with sulfates, gaudefroyite and carbonates among other minor phases, although in this later case it is likely that andradite has not formed contemporaneously with coexisting minerals. Moreover, andradite is typically

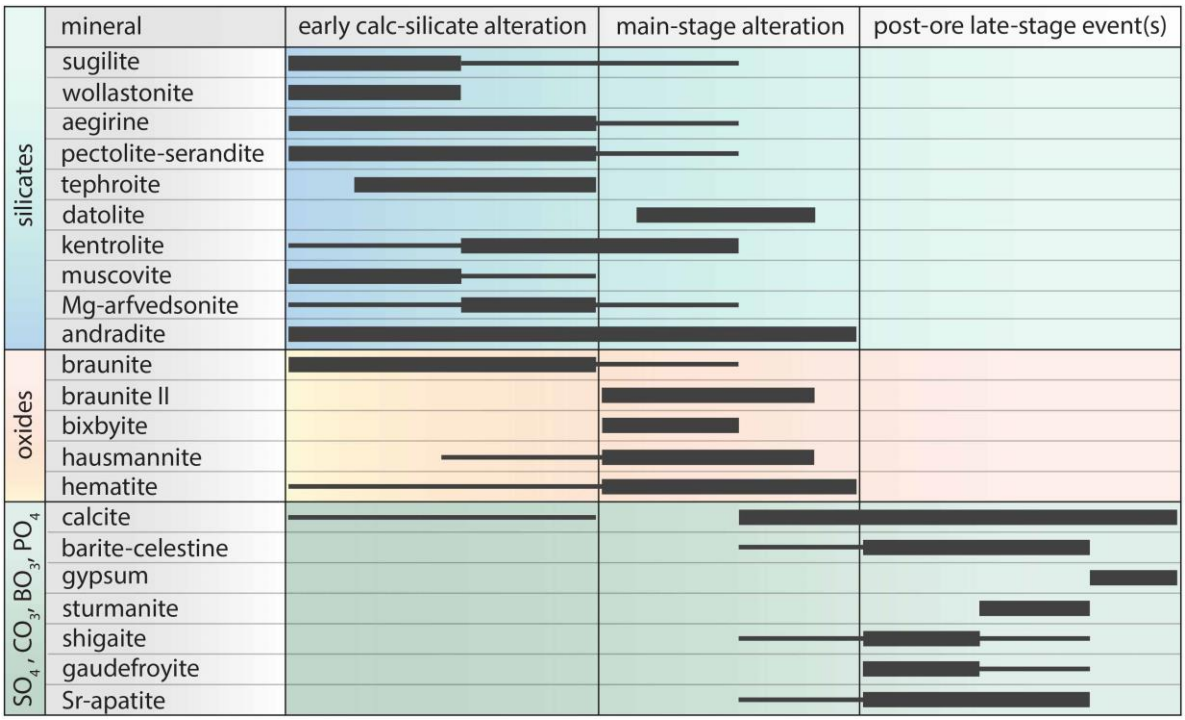

Figure 9. Simplified paragenetic sequence of the Wessels event of hydrothermal-metasomatic alteration with emphasis on minerals that are reported and analysed in this study. Color coding simply emphasizes the different mineral groups. Modified from Gutzmer and Beukes (1996b) and Lüders et al (1999).

intergrown with hausmannite in oxide-rich ore that characterizes the higher degree of main stage alteration. Hematite and hausmannite are the most common minerals forming during alteration processes and younger generations and veins comprising both these species have also been reported to postdate the main phase of ore-formation. Bixbyite along with hausmannite, braunite II and hematite are believed to typify main stage high-grade ore, which embodies an intermediate degree of alteration.

In view of all the foregoing, it can be inferred that the analysed andradite-hausmannite, in like manner to the specimens of hausmannite on andradite matrix from N'Chwaning displayed in Gutzmer and Cairncross (2002), are more closely associated with the main stage of hydrothermal fluid flow. Likewise, bixbyite and andradite-hematite assemblages described in Table 2, most likely also illustrate the main event, whereas coexisting minerals such as gaudefroyite, barite and calcite or hematite-calcite-sulfate associations are perhaps later products of the waning phase of hydrothermal alteration, which as the previous authors have suggested is responsible for most of the mineral diversity in the mine. Furthermore, microscopic investigation of sample NBA3 supports syn-

crystallization of andradite and at least some of the observed hematite, both developing seemingly on precursor hematite lutite. Spatially, garnet-hematite associations could be related with ferruginised or silicified wall-rock alteration in vicinity of fault zones (Gutzmer and Beukes, 1995) or they could be part of lenticular bodies or mineral 'pockets' occurring in proximity to the lower orebody. Figure 9 provides a synopsis of the paragenetic associations described above, in this way providing a basic framework for the following isotopic constraints on fluids-rock interaction, source and composition.

5.2.2 Oxygen isotopes

Oxygen isotope compositions of oxides and silicate minerals are shown in Figure 10, along with relevant isotopic data from the Hotazel iron-formation for comparison purposes (Tsikos; 1999, Tsikos et al; 2003). This diagram illustrates two significant features. Firstly, the range of isotopic values shown by all silicate minerals apart from garnet and pectolite is rather small, from +10.6 to +13.2 ‰ (average = +11.3 ± 0.8 ‰, n=11), with most values showing only marginal differences that essentially fall within the analytical error. The implications of this remark are discussed below but at first glance, this suggests a possible isotopic equilibrium of the regarded phases with the mineral-forming fluid and maybe a broadly cogenetic precipitation for some of them. Secondly, the plot depicts the clear dichotomy between the

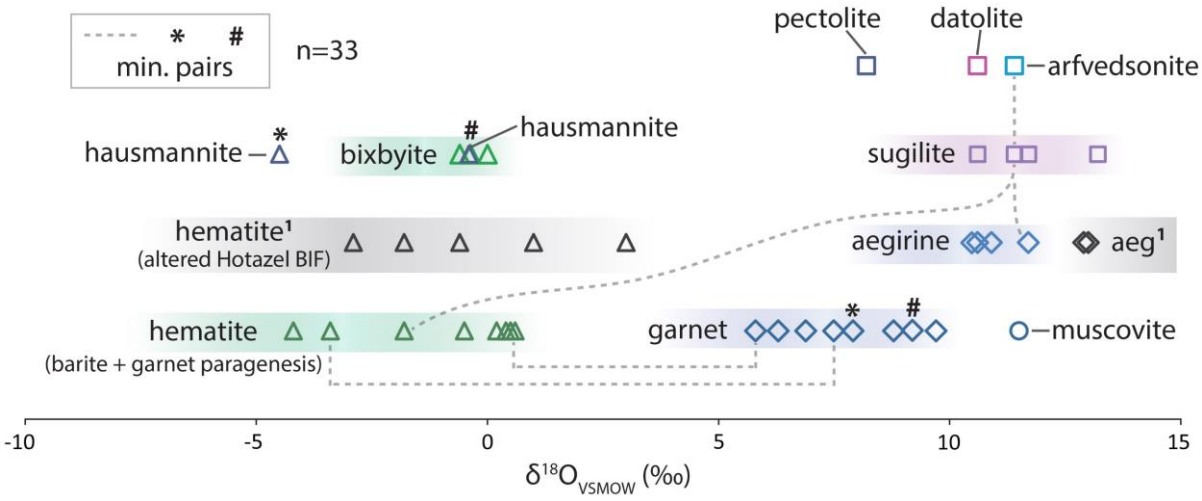

Figure 10. Diagram depicting ranges of $\delta^{18}O$ values for various silicate and oxide minerals related to the Wessels alteration event. Co-existing phases are connected with dashed line. Hematite and aegirine (acmite) isotopic compositions from the Hotazel iron-formation (1) are from Tsikos (1999).

heavy $\delta^{18}O$ values of silicates, which cluster around +11 ‰ (if garnet is excluded) and the much lower $\delta^{18}O$ values of iron and manganese oxides ranging broadly from ca. -4.5 to 0 ‰.

This large isotopic difference between oxides and silicates is observable in various mineral pairs or assemblages, comprising coexisting: (i) garnet and hematite, (ii) hausmannite and hematite or (iii) sugilite, aegirine and hematite. This variation likely reflects isotopic fractionation processes related and occurring between cogenetic phases forming in equilibrium with the alteration fluid or otherwise are sign of a more complex open-system in which disequilibrium exchange reactions take place between fluid(s) and gangue minerals precipitating during different stages. In order to approach the challenging task of fluid evolution during interaction with the host lithologies and further tackle the yet poorly constrained origin of the involved fluid(s), the oxygen isotopic composition of the latter need to be firstly approximated on the basis of measured $\delta^{18}O$ values.

This approach suffers from a number of limitations, the principal of which are the following: (a) Isotopic exchange has to take place between a mineral and a fluid being in isotopic equilibrium. (b) Lack of isotopic equilibrium is likely in the regarded low-temperature mineralisation system, where measured phases may have precipitated at temperatures well below 200^{o}C (further discussed below). (c) The fractionation behaviour between the mineral and the fluid needs to be previously determined by either natural, theoretical, experimental or semi-empirical data. (d) The temperature at which a mineral is formed is a prerequisite for determination of the oxygen isotope composition of the fluid from which it precipitated and ideally has to be measured by means of fluid inclusions or else be estimated using another geothermometer. (e) Lastly, in ancient (Mesoproterozoic) mineralization systems, diffusional resetting and re-equilibration of isotopes in certain minerals in response to late-stage or subsequent recrystallization events may have occurred.

Petrographical observations can provide at least a first appraisal regarding textural equilibrium, which can be subsequently reevaluated by analysis of the isotopic data. It should be noted that published temperature-dependent isotope fractionation curves are not available for some of the uncommon phases isotopically measured here such as sugilite,

hausmannite and bixbyite. Furthermore, where such exist, caution must be exercised and especially in case of extrapolation of the fractionation data outside the experimentally investigated temperature range. In addition to the above, the inferred δ isotopic values of fluids can be impacted by uncertainties in the temperature of deposition and fluid chemistry (in particular salinity) and so different scenarios are discussed below.

The diversity of mineralogical species in the KMF, even among the phases measured here for their oxygen isotopes, implies a multi-stage fluid-rock interaction history, spanning as earlier discussed over a tectonically-active period of 75 m.y. or more. In addition, identification of crustal fluid sources by means of investigation of their stable isotope composition has been accurately characterized as a very difficult task (Hoefs; 1987). Taking into consideration all aforementioned limitations, it is recognized that none of the minerals alone can be plainly used as a clear-cut indicator of temperatures of hydrothermal alteration or as tool of incontrovertible isotopic tracing of fluid characteristics. However, readings from different minerals interpreted along with other lines of geological evidence are shown in the next paragraphs to be capable of providing rough constraints on fluid composition and/or temperature at the very least, which ultimately, eminently illuminate fluid sources.

There is a lack of agreement regarding the temperature of the postulated hydrothermal-metamorphic fluids, that highlights problems imposed by the large spectrum of conditions under which the regarded phases can form and by the complexity and rather unusual character of available parageneses. Fluid inclusion data from ore (hematite and hausmannite) and gangue minerals (calcite and datolite) indicate high-salinity fluids and a temperature range from 210^{o}C (early alteration-stage) to about 130^{o}C (main and post-ore stage) (Lüders et al; 1999). However, predictions on the basis of thermodynamic stability of mineral such as hydrogarnets, glaucochroite ($CaMn^{2+}SiO_4$), tobermorite [$Ca_5Si_6O_{16}(OH)_24H_2O$] and xonotlite had previously led to estimations of temperatures well above 200^{o}C, in particular ranging between 270^{o} and 420^{o}C under conditions of 0.2-1 kbar (Miyano and Beukes 1987; Dixon; 1985, 1989). For all of the following $\delta^{18}O$ fluid calculations, only the quantitative information derived from fluid inclusions (130^{0}-210^{o}C) is used and the latter is evaluated against data obtained by different mineral pairs in this study.

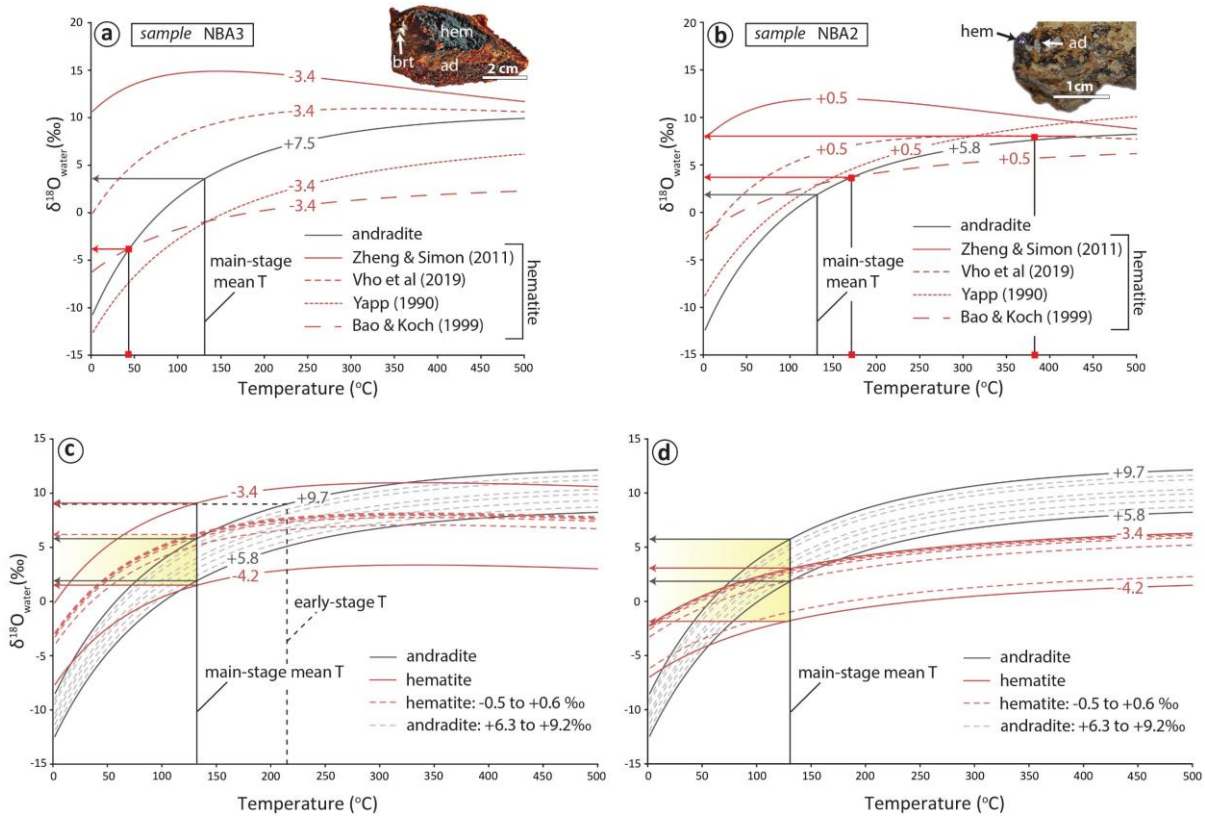

Figure 11. Mineral-water oxygen isotopic fractionation curves for garnet-hematite pairs from this study (a, b) (samples NBA2 and NBA3) as well as garnet and hematite from different parageneses (c, d), all deriving from N'Chwaning mine. Calculated fluid compositions shown (black arrows) are based on the previously determined temperature range (130-210°C) by Lüders et al (1999), in which the first and last value are thought to characterize the main/post and early alteration stages respectively. Red arrows and rectangles show calculated temperatures and fluid compositions (this study) for different scenarios of garnet-hematite in equilibrium.

As shown in Figure 11, fluid $\delta^{18}O$ compositions estimated from two andradite-hematite pairs vary significantly with respect to: (a) the selected fractionation function for hematite and (b) the assumed temperature of formation. Textural information deduced from microscopic investigation suggests that andradite and microplaty hematite of sample NBA3 are cogenetic. However, the fact that no intersection occurs between the garnet and hematite fractionation curves (Figure 11a) points to disequilibrium conditions or possibly precipitation of these two phases at different temperatures/stages. It is worth noting that depositional temperature ranges permitted by the equations of Yapp (1990) and Bao and Kock (1999) are 25-120°C and 30-140°C respectively, whereas the regressed and internally consistent fractionation functions by Vho et al (2019) can be applied for a temperature range of 0-900°C, as well as for mineral assemblages rather than solely individual couples. For these reasons, the latter equations were preferred over that of Zheng (1991, 1993a, 1993b) for all

calculations presented below unless otherwise noted. The minimum temperature (<50°C) obtained by apparent isotopic equilibrium of the andradite-hematite pair using the fractionation factor from Bao and Kock (1999) seems unrealistic and thus geologically meaningless.

If the mean temperature reported for the main alteration-stage is used instead (i.e., 130°C), $\delta^{18}O$ fluid composition calculated for andradite of sample NBA3 is +3.5 ‰, a value that differs considerably from the isotopic ratio obtained from coexisting hematite (-1.0 ‰). As stated above, this is perhaps an indication that the two minerals formed at different temperatures or that a fluid with composition close to about 0 ‰ has undergone a certain degree of isotopic exchange after interacting with the host rock and before mineral formation. Two possible scenarios can be: (a) an infiltrating fluid with heavy $\delta^{18}O$ signature shifts towards lighter $\delta^{18}O$ values after interaction with isotopically lighter host rock, the latter being hematite lutite or an already oxidized iron-formation characterized by negative oxide $\delta^{18}O$ values (Tsikos et al; 2003) or (b) $\delta^{18}O$ fluid values become heavier during precipitation of andradite after interaction with an isotopically heavier, probably silica-rich host rock. Fluid-rock interactions are further illuminated below with the aid of the remaining measured samples and perhaps indicate an isotopic exchange history involving incorporation of $\delta^{18}O$ host-rock values during garnet precipitation.

In contrast to the above-examined pair, andradite-hematite association of sample NBA2 displays isotopic equilibrium at a far more realistic temperature of about 175°C. Calculated $\delta^{18}O$ of the involved fluid is +3.8‰ (Figure 11b), which is also not too distant from the previous garnet (NBA3-g: +3.5 ‰). Much higher and likely unrealistic temperature readings are obtained when using the equation by Vho et al (2019), which further correspond to a heavy oxygen isotopic ratio for the alteration fluid (+7.9 ‰). Calculations can be extended to the remaining measured hematite-garnet $\delta^{18}O$ values, on the assumption that these minerals derive from the same mine and therefore could roughly characterize the same alteration stage, involving fluids of comparable physicochemical parameters. Bearing in mind all above presented limitations, a crudely estimated range of the $\delta^{18}O$ fluid composition being in equilibrium with andradite is from +1.8 to +5.7 ‰ (average = +3.4 ± 1.4‰, n=8) (Figure

11c). Similarly, estimations on the basis of hematite values suggest a slightly lower range, from -1.0 to +3.0‰ (average = +1.4 ± 1.9‰, n=8) (Bao and Kock (1999).

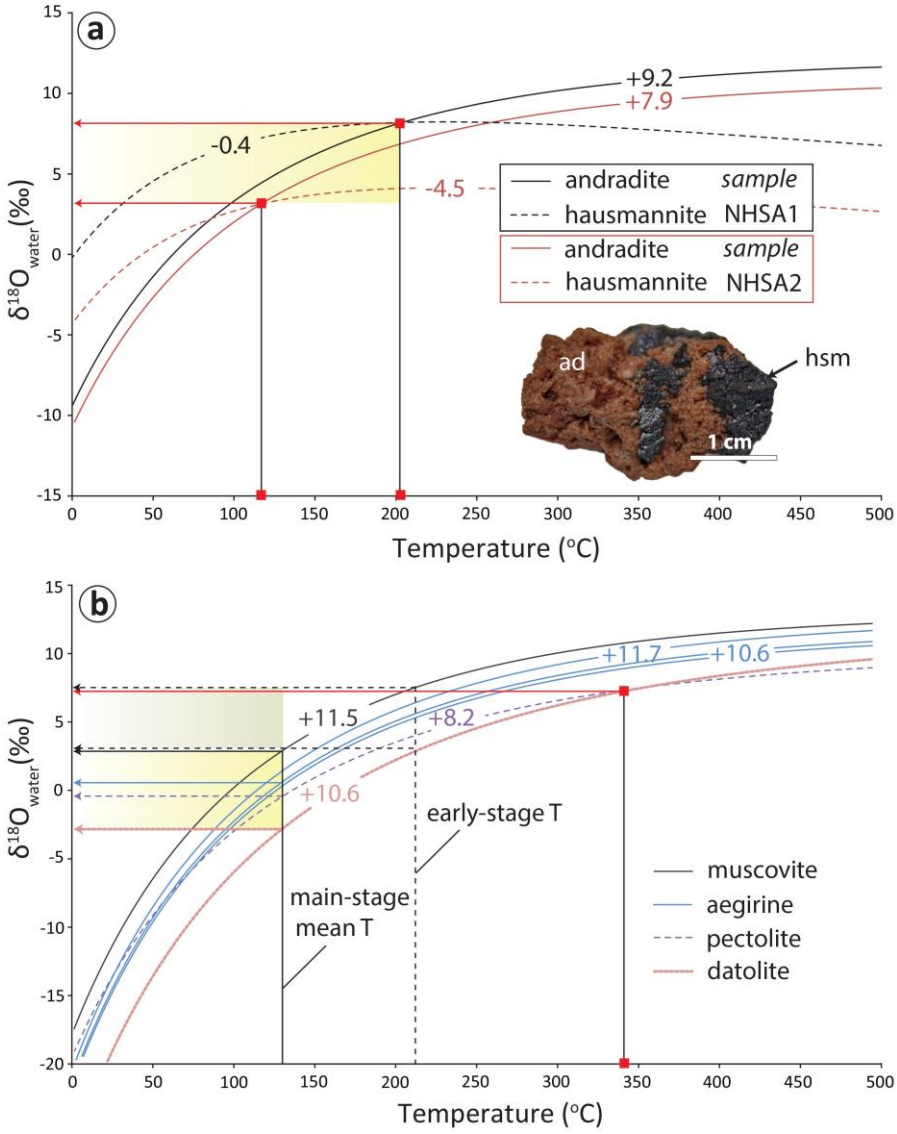

Figure 12. Mineral-water oxygen isotopic fractionation curves for garnet-hausmannite pairs (a) and silicate gangues (b) presumably crystallizing during the early (muscovite, aegirine, pectolite) and main stage (datolite) of alteration. Red arrow and rectangle show a postulated temperature and fluid composition (pectolite-datolite), the former (i.e., 350°C) being probably unrealistic since minerals 'in equilibrium' derive from different samples.

If fluid temperatures had been higher, approximating that suggested for the early stage (210°C), the above calculated $\delta^{18}O$ fluid ranges become between +5.0 and + 8.9 ‰ (average = +7.0 ± 1.4‰) and from -0.4 to +4.4 ‰ (average = +3.0 ± 1.9‰) for andradite and hematite respectively. Calculated isotopic fluid compositions from both minerals overlap in the range between +2 and +3 ‰, which is perhaps evidence for conditions close to isotopic

equilibrium and suggests that this range likely reflects the 'true' isotopic fluid composition. Estimations based on the equation by Vho et al (2019) point to slightly higher but generally overlapping values (+1.8 to +5.2 ‰) (Figure 11d). The measured isotopic composition of bixbyite (-0.4 to 0 ‰) may approach very closely that of the mineral-forming fluid, in like manner to the hematite-water pair (Bao and Koch; 1999), i.e., suggesting a value closer to the range predicted by hematite.

In summary, a formation temperature-range from 130 and 210°C and a fluid oxygen isotopic range from about +2 to +5.0 ‰ is generally reasonable for the majority of measured garnet and hematite, although lighter isotopic values may also characterize fluids responsible for the formation of oxides. Broadly comparable data are obtained from two hausmannite-andradite pairs (Figure 12a). Hausmannite can be regarded as a manganese spinel and hence the fractionation equation of jacobsite (iron spinel) is used here instead to gain rudimentary insights into $\delta^{18}O$ fluid values. Usage of these fractionation factors returns geologically reasonable temperatures, equivalent to the early and main stages from Lüders et al (1999). Specifically, temperatures of 120 and 200°C and equally heavy oxygen isotopic ratios for the fluid (+3.2 and +8.2 ‰) are obtained. In light of this, the above approximation made for hausmannite may potentially yield reliable guidelines for fluid compositions, owing possibly to analogous bonding characteristics with jacobsite. However, this hypothesis requires support from rigid experimental data.

The estimated temperature range (120-200°C) is consistent with low-temperature metasomatic garnets from the literature which are believed to have formed at about 170°C through interaction between hydrothermal solutions and marine sediments (Easton et al; 1977). Furthermore, older and isotopically light andradite (+1.0‰) from the stratigraphically underlying Ongeluk Formation in the study area suggests analogous formation mechanisms and temperatures between 160 and 185°C from quartz-garnet pairs (Gutzmer et al, 2001). It should be noted though, that the geothermometer by Zheng (1993a) suggests temperatures as low as 95°C for the previous case, thus emphasizing that such estimates in low-temperature geological settings must be treated with caution and always interpreted in conjunction with other evidence. Along the same lines, data solely from this study do not

eliminate the possibility of temperatures in excess of 200°C or above, either developing locally or during the earlier stages of alteration.

The rest of the measured silicates imply broadly similar fluid isotopic compositions. Aegirine, pectolite and amphibole (presumably early-stage phases) indicate $\delta^{18}O$ fluid values broadly between +4 and +6 ‰ (average = +4.6 ± 0.9‰) for a temperature of 210°C, whereas datolite (main stage) displays a distinctly lower fluid isotopic value of -2.8‰ (Figure 12b). Muscovite, apparently also an early phase based on its documented age, indicates a fluid value of +7.4 ‰ (Figure 12b). Micas have been shown to have very high oxygen diffusivity (Fortier and Giletti, 1991) and therefore possible isotopic exchange between muscovite and coexisting hematite or barite at low temperatures may increase the magnitude of error in the above calculations. A speculative temperature of ca. 340°C is suggested by the intercept between pectolite and datolite fractionation curves, which should not be considered since these two derive from different samples.

In contrast to the preceding data, a fluid isotopic value of -0.9 ‰ and a temperature of 105°C is deduced by an aegirine-hematite pair (sample SW2). Tsikos (1999) estimated a much higher temperature of 250°C from a similar mineral pair but argued that since hematite has suffered only minimal isotopic exchange during aegirine formation, isotopic equilibrium and hence temperature estimates have little validity and syn-crystallization of the above minerals is rather unlikely. On another note, it seems reasonable on the basis also of estimations by other researchers (Miyano and Beukes; 1987) that certain phases such as amphibole or muscovite in this setting may have formed at temperatures even higher than 200°C, a hypothesis which collectively with other silicates (aegirine or pectolite) would in turn indicate slightly heavier oxygen isotopic values for the associated fluid(s), probably ranging from +5.3 to +8.8 ‰ (for e.g., T=250°C). In any case, most of the above estimations (between ca. + 4 and + 7.5 ‰) largely overlap with the range predicted by the whole oxide-garnet suite (+2 to +5 ‰) and at the same time extend this array to lower values, near -3 ‰, for silicates such as datolite.

Reverting to Figure 10, our $\delta^{18}O$ data for aegirine are broadly consistent with that previously documented for two aegirine separates from Hotazel iron-formation (Tsikos; 1999), which gave values of approximately +13 ‰. Interestingly sugilite shows very similar $\delta^{18}O$ values between +10.6 and +13.2‰ (average = +11.7 ± 1.1 ‰, n=4) and so does datolite (+10.4‰) and amphibole (+11.6‰). Since sugilite is a silicate mineral, an ^{18}O-enrichment in relation to the fluid is expected and is plausible to be as high as about 10‰, but since fractionation is controlled by the proportion of different bonds (Si-O, Al-O, etc.) among other parameters (e.g., Taylor and Epstein; 1962, Garlick; 1966), this enrichment is not possible to be easily determined. However, the coincidence between ^{18}O-enrichment in all measured silicates is intriguing. Collectively, the small range in isotopic values exhibited by all studied silicates (+11 ± 1.2 ‰, n=12) corresponds to fluid isotopic ratios clustering around + 5 ‰ and in particular from ca. -3.0 to + 8.0 ‰. Therefore, O-isotope fractionation between fluid(s) and silicates can be quite significant (6-14‰), with the latter being constantly ^{18}O-enriched, but $\delta^{18}O$ variation among most precipitated phases is very small (1-3‰).

Leaving out the effects of temperature and fractionation between fluid and precipitating gangues examined above, the chief remaining variables affecting the isotopic evolution of alteration fluids are the composition of the host rock and the extent of fluid-rock interaction. Metasomatising fluids in the KMF recrystallize minerals, dissolve carbonates, leach silica from braunite and precipitate new oxide and silicate phases (Beukes et al; 1995). By virtue of a number of dissolution-precipitation processes, chemical exchange reactions and diffusion mechanisms, infiltrating fluids are expected to evolve isotopically as they react with the host rock, although rigorous isotopic constraints on such evolution are not available. On the other hand, it is plausible that especially in a scenario of high water/rock (w/r) ratio (Taylor; 1977), an appreciable amount of fluid could have passed through fractures in the rock without significant isotopic exchange or otherwise could have modified and dominated over the surrounding rock isotope ratio during metasomatic processes responsible for gangue precipitation, hence potentially imprinting its ‘signature’ on hydrothermal silicates.

Quartz $\delta^{18}O$ values from the altered Hotazel iron-formation suggest that the mineral essentially remained isotopically unexchanged during alteration processes oxidizing the rock

whereas hematite originating from oxidation of magnetite reveals a shift in the oxygen isotopic values by approximately 2-3‰, interpreted as the result of interaction with a low-$\delta^{18}O$ fluid, possibly of meteoric origin (Tsikos et al; 2003). It is unclear though, if oxidation processes recorded in iron-formation are synchronous or prior to the Namaqua ore-upgrade event. Rather more reliable clues on fluid evolution are available from hydrothermal carbonates paragenetically linked to the Wessels metasomatic event, which indicate precipitation from a CO_2-bearing hydrothermal fluid enriched in both ^{18}O and ^{13}C and having acquired its characteristics after decarbonation of the pristine Hotazel Formation (Gutzmer and Beukes; 1998, technical report). However, different trends in isotopic evolution of carbonates attributed to Rayleigh distillation processes and later carbonate-forming events emphasize the difficulties associated with tackling fluid sources solely by investigation of carbonate minerals.

On the other hand, it is believed that critical information on fluid isotopic composition and evolution can be deduced from hydrothermal minerals in this study. Uniformity in $\delta^{18}O$ values observed in gangue silicates can be mainly attributed to two reasons: (a) relative isotopic homogeneity in the pristine mineral-forming fluid (-3.0 to + +3.0 ‰) owing to large water to rock mass ratio (w/r ratio) and precipitation within a small temperature range (more or less between 130 and 210^oC) or (b) isotopic exchange and equilibration after extensive interaction of the fluid with the surrounding rocks, further accompanied perhaps by a lower w/r ratio. This second scenario is discarded on the basis of several grounds explained below.

Bulk rock $\delta^{18}O$ values of surrounding rock fluctuate by more than 15 ‰. If oxygen isotopic composition of the fluid has largely been controlled by interaction and/or equilibration with the compositionally inhomogeneous stratigraphic succession of the Hotazel Formation, the resulting fluid would be characterized by a large variation of isotopic values, likely reflected also in the measured samples. There is no doubt that extensive leaching and recrystallization has taken place during fluid(s) infiltration in the Hotazel Formation and that the presence of a dynamic system impacted not only by fluid source but

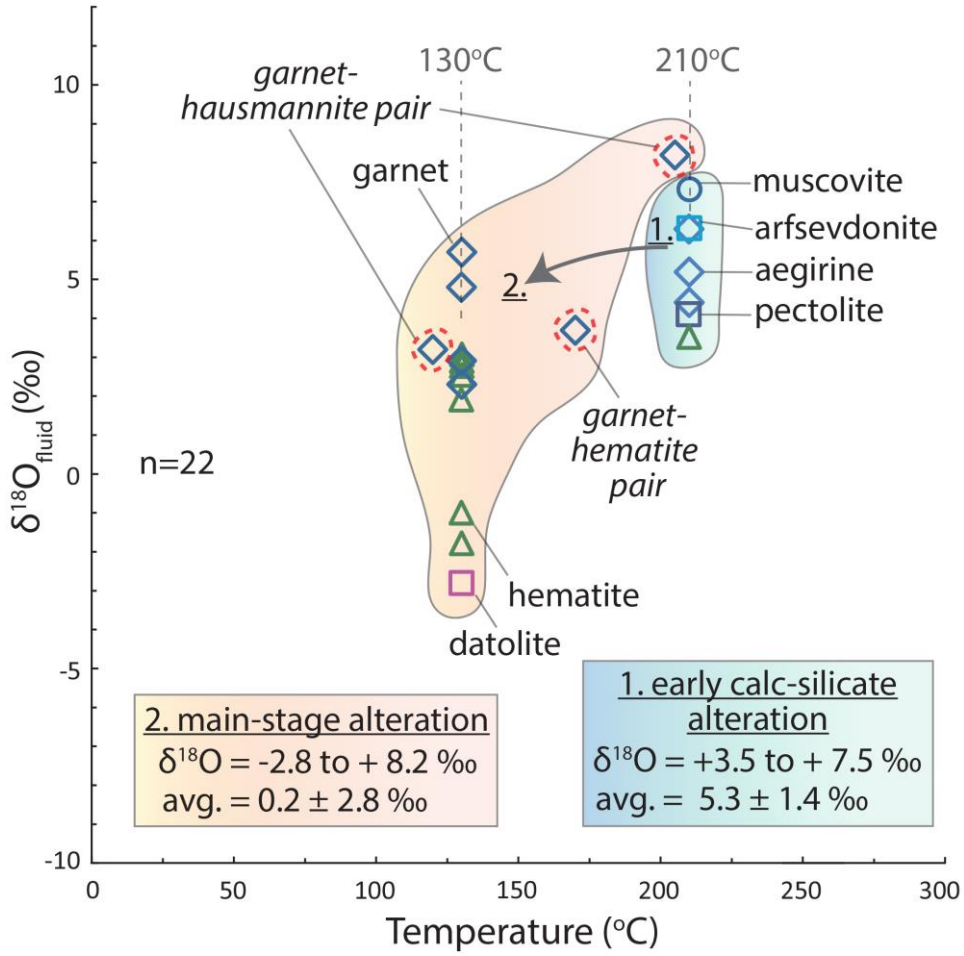

Figure 13. $\delta^{18}O_{fluid}$ versus temperature plot, illustrating estimated fluid compositions from this study for the postulated early and main stages of alteration. $\delta^{18}O$ fluid ratios predicted by gangue silicates broadly cluster around + 5 ‰ (between + 1.8 and 8.2 ‰) for both stages. The temperature range used (130-210°C) is from Lüders et al (1999) and mineral pairs in red circles represent suggested temperatures of formation calculated in this study (i.e., 120, 175 and 200°C).

also fluid-mixing and fluid-rock interactions is a rather realistic scenario. Specifically, fluids may have exchanged isotopes with dissolved carbonates or braunite, the latter possibly providing released silica for gangue formation and causing an ^{18}O-shift to higher $\delta^{18}O$ values. Furthermore, another reasonable hypothesis can be that restricted oxygen reservoirs in the host rock led to characteristic compositions of silicate gangue minerals. However, the coincidence in $\delta^{18}O$ values between different silicates, from different stratigraphic horizons and different mines is difficult to explain, unless oxygen isotopic compositions are chiefly externally buffered. Informed by ongoing research in the wider area of the Northern Cape that reveals comparable $\delta^{18}O$ values to that in the KMF regardless of variability in the surrounding rock (chapters 5 & 6), we strongly suggest that the isotopic signature of regional-

scale fluids is largely preserved, at least in the composition of some of the hydrothermal gangue minerals in these ores. To the extent that this presumption is true, important implications arise, since it is implied that certain such hydrothermal minerals can be efficiently used to identify the hydrothermal fluid source.

Using the available fractionation curves, we deduced that metasomatic processes may have taken place mostly within the temperature range between 120-200^{o}C, similarly to results by Lüders et al (1999) and almost certainly involved generally low-$\delta^{18}O$ fluids with oxygen isotopic ratios between ca. -3 to + 8 ‰ (avg. = +3.7 ± 2.8 ‰, n=21). If the measured minerals are paragenetically assigned to the crudely determined early, main and post-ore stages, then it turns out that early-stage $\delta^{18}O$ fluid values may have been on average heavier (5.3 ± 1.4 ‰) than that of the main stage (0.2 ± 2.8 ‰ ‰) (Figure 13), which is a reasonable assumption in a possible case where isotopically heavier brines are diluted after interaction and leaching of a lighter host rock or mixed with large amounts of contemporaneous meteoric water. The wider oxygen isotopic variation shown by garnet in contrast to the other silicates could be an indication of temporal variation in fluid composition due to wider isotopic exchange between fluids and the host rock or fluid mixing, especially if circulation occurs during later alteration stages.

The main conclusions steaming from this initial oxygen isotopic analysis in the KMF are: (a) The observed uniformity in the oxygen isotopic values of gangue silicates can be attributed to fluid buffering during mineral precipitation despite the documented fluid-rock interactions upgrading the ore. (b) $\delta^{18}O$ measurements of gangue mineral pairs such as garnet-hematite or even garnet-hausmannite can be cautiously used as monitors of formation temperatures and suggest results that agree with previous reports.

5.2.3 Hydrogen isotopes

Most rocks contain little or no molecular water and so the hydrogen isotope composition of hydrous minerals that form during alteration may be used to infer the hydrogen isotope composition of the fluid from which these minerals formed and hence illuminate its origin. Published laboratory and empirical calibrations relating the isotopic

compositions of minerals to that of ambient water are rather limited though and certainly not available for minerals such as pectolite and datolite. Therefore, the few δD values (n=4) in this study can only provide a rough hint of the associated fluid isotopic composition.

The experimentally determined kaolinite fractionation factors are preferable at low temperature settings (<300°C) instead of the muscovite calibration provided by Suzuoki and Epstein (1976) (see: Bowers and Taylor; 1985, chapter 5). Supposing a formation temperature of 200°C, δD of the fluid in equilibrium with muscovite is calculated to be -41.6 ‰, i.e., ca. 15 per mil heavier than the measured value -(56.4 ‰). δD_{min} values of datolite (-28.0 ‰) and pectolite (-58.5 ‰) are also heavy in contrast to the much lighter amphibole (-118.8 ‰). Metasediments typically have δD from -40 to -100 ‰ and metamorphic waters from -20 to -65 ‰ (Sheppard; 1986, Hurai et al; 2015). Hydrothermal waters display much broader compositional variety, which reflects fluid-rocks interaction and mixing processes occurring in different mineralization systems prior to mineral precipitation. Therefore, it would be very difficult to link the measured values to a particular fluid origin without the use of other geological information.

However, the generally heavy δD values in conjunction with the positive $\delta^{18}O$ fluid values (i.e., δD-$\delta^{18}O$ isotopic space) shown by most gangue and ore phases point towards fluids that share similar characteristics with metamorphic waters, modern basinal brines recovered from oil fields or ore-forming fluids involved in Mississippi-Valley type (Pb, Zn, Cu, Ba and F) deposits (e.g., Taylor; 1974, Ohmoto et al; 1986, Richardson et al; 1988, Kessler et al; 1997, Shanks; 2014). Specifically, data from fluid inclusions in MVT deposits cover a larger range than modern basinal brines and may show distinct values depending on the district, but for the most part, their O-H signatures are comparable to that from the KMF. Although more research is needed, it seems that this elementary δD analysis along with $\delta^{18}O$ values support the concept of basinal fluids being the dominant fluid source during ore enrichment processes. Preliminary hydrogen isotope data (-76.8 to -92.1 ‰, see also synthesis, section 8.1.3) from ongoing research further encourages this premise. In addition, the fact that trapped meteoric signatures with δD values < 100 ‰ have been documented from micas associated with extensional detachments in several metres depth (Bons et al; 2020), but are

apparently rare in the low-depth alkali metasomatic mineralogy of the KMF, is another indication that basinal fluids had been buffering the system and their signatures have been largely preserved.

The only exception is the D-depleted amphibole value (-118.8 ‰). Amphiboles from most igneous rocks have δD values in the range -80 to -60 ‰ (Taylor and Sheppard; 1986). Lighter δD amphibole values from such settings have been related to magmatic water loss during degassing or assimilation of hydrothermally altered rocks bearing clays and alunite and characterized by very light (up to -126 ‰) δD values (Chambefort et al; 2013). Similar δD signals in the KMF could have derived from dilution of hydrothermal fluids by contemporaneous meteoric water infiltrating in the same faults and discontinuities, an aspect also important in the evolution of MVT fluids.

5.2.4 Source of fluids

Fluids of different origin (meteoric, magmatic, hydrothermal, metamorphic, geothermal, etc.) carry chemical and isotopic ‘‘signatures’’ which often can be used to elucidate their source. It is known that the principal fluid component in shallow hydrothermal systems is typically meteoric water (Hurai et al; 2015), which however can be modified by cation- and isotope-exchange reactions with the surrounding rocks, acquire higher salinities and in the case of tectonically-active or magmatic settings, this water can penetrate deep into the crust and circulate through basement rocks (Cartwright and Buick; 1999, Gleeson et al 2003, Oliver et al; 2006). It is evident by now that all currently available data from the KMF strongly suggest that alteration fluids circulated through the ore field during the timing of relatively distant collisional tectonic episodes of the Namaqua orogeny. These fluids carry the signal of an evolved, heated meteoric water showing increased salinity, ^{18}O enrichment and to some extent, possibly preserved δD values.

The origin of the fluids can be attributed to solutions stored in the deeply buried sedimentary units of the Transvaal Supergroup, with which they largely equilibrated prior to their infiltration in the ore. The exact role of basement or more distant lithologies in their isotopic character remains unknown, but fluid features can be largely attributed to their

passage through different lithologies in the basin including the Campbellrand carbonate-evaporite reservoir from which they may have acquired the bulk of their salinity, as opposed to previous suggestions relating salinity chiefly to interaction with the carbonate-rich sedimentary protore (Lüders et al; 1999). If fluid flow had been focused on the Transvaal-Olifantshoek unconformity (e.g., Fairey et al; 2019) interaction with the silicate-rich lithologies of the latter could have further enriched the $\delta^{18}O$ values of these oxidizing alkaline fluids. All of the above fit the general pattern of sedimentary basinal brines being the main fluid source during the Wessels alteration event. It is pointed out that brines are generally defined as natural heated waters with salinity higher than that of seawater (35 g kg^{-1}) and are commonly prevalent in crystalline rocks, sedimentary basins and hydrothermal systems (e.g., Horita; 1989a, 1989b). Despite the very large ranges in $\delta^{18}O$ and δD values displayed by basinal brines, those of the highest temperature and salinities from various basins rich in carbonate rocks and evaporites exhibit very similar isotopic signatures ($\delta^{18}O$ = +7 ± 3‰ and δD = -10 ± 30 ‰: Ohmoto et al; 1986) which are also very close to the ones from the KMF.

5.3 Alkaline character of metasomatism and sugilite formation

5.3.1 Sugilite in manganese deposits and alkaline massifs

Sugilite is not only one of the most striking and attractive gangue alteration products at Wessels mine but can also contribute to the better understanding of alteration processes by providing critical information on: (a) timing and episodes of ore enrichment and (b) fluid sources and interactions with the host rock. Regarding the later, unanswered questions include: (i) the degree to which compositional characteristics of the Hotazel rocks and/or infiltrating fluid(s) dictate the formation of sugilite assemblages, (ii) illuminating chemical metasomatic reactions between low-grade minerals and hydrothermal solutions that resulted in precipitation of these assemblages as well as (iii) unravel the pre-alteration mineralogical composition of rocks hosting sugilite, or in other words upon which lithologies of the KMF does sugilite forms. All of these matters have not been adequately addressed so far and the only research with focus on chemistry and textures of the sugilite-bearing associations from an entirely geological and not a mineralogical or gemological point of view, has been that of Dixon (1985, 1988, 1989).

Sugilite can be regarded as a relatively rare mineral, hitherto noted only from nine localities worldwide (Cairncross; 2017), six of which represent manganese deposits that may consist of different Mn-ore minerals (for e.g., braunite, hausmannite, rhodonite, manganese carbonates) but invariably host a wealth of peculiar Mn^{3+}-bearing and other alkali-rich phases including serandite-pectolite, aegirine-namansilite (-$NaMn^{3+}Si_2O_6$), Mn-rich alkali amphiboles, norrishite [$KLiMn^{3+}{}_2(Si_4O_{10})O_2$], andradite, piemontite, armbrusterite [$K_5Na_6Mn^{3+}Mn_{14}{}^{2+}$ $[Si_9O_{22}]_4(OH)_{10}4H_2O$] and other unusual species (Dunn et al; 1980, Lucchetti et al; 1988, Kawachi et al; 1994, Cabella et al; 1990, Moore et al; 2011). None of the publications addressing sugilite-bearing assemblages approach directly and in detail, mechanisms of their formation within the related geological context. The only exemptions are the study by Kawachi et al (1994), which provides thorough sugilite compositional comparisons between diverse localities and that by Moore et al (2011), which emphasizes the sugilite-bearing alkali-rich parageneses in the Postmasburg Manganese field (PMF) and suggests an origin associated with epigenetic regional-scale hydrothermal activity.

As accurately noted by the previous authors, formation of manganese-bearing sugilite and its rarity are tied to the essential high alkali content of the host rock, including lithium (ca. 2.5-3 wt.%), that necessitate additional hydrothermal/metamorphic processes modifying pre-existing manganese-rich rocks and increasing their alkali content, at least on a local scale. The above rationale has been postulated, as noted above, for sugilite occurrences in karst-related manganese deposits at the Bruce mine (PMF), as well as the Cerchiara mine in the Liguria Province (Italy), where submarine exhalative manganese sediments have presumably experienced hydrothermal metasomatism of unknown origin, induced by diffuse interaction with alkali-rich fluids enriched in Na, K and Li and lesser Ba, Sr, Ca and Cu (e.g., Kolitsch et al; 2018). Regarding the two localities in Australia (Woody and Hoskins mine), the occurrence of sugilite in oxidized assemblages is linked to later metamorphism of submarine manganese-rich sediments (Ashley; 1986, Hawthorne et al; 1995) and although the origin of the high alkali content is not thoroughly discussed, it is evidently attributed to the host rock. More cryptic is the mention of massive sugilite from Madhya Pradesh, India (Clark et al; 1980), since its exact locality is unknown, but the host manganese orebodies are again confined

within a large Archean metamorphic core complex where extensive reworking has most certaintly taken place.

It is important to note that an exceptionally manganese-rich host rock is not a necessity for sugilite formation. In particular, either bright purple-pink-mauve manganese-bearing sugilite varieties, like the one from Wessels, can exist in lithologies such as marble in the case of the Mont Saint-Hilaire mineralogical district (Canada) (Horváth and Gault; 1990, Robinson et al; 1995), where alkaline intrusive sills have apparently provided the required alkalis, or brownish yellow Mn-free members such as the type material from the Iwagi islet (Japan), may apparently prevail in aegirine syenite (Murakami et al; 1976). In the latter case, sugilite accounts for up to 8 wt. % of the quartz-free and aegirine-poor part of the rock and becomes negligible or totally absent near quartz syenite, which possibly provides another compositional control for its occurrence at least in igneous environments. Sources of alkalis and particularly lithium can be undoubtedly attributed to the alkali-rich nature of the syenite, which is thought to have formed by metasomatic alteration of biotite granite, while the observed parageneses conform to the general pattern of occurrence seen in manganese deposits and comprise andradite, pectolite, aegirine and albite. A comparable alkaline massif hosting massive sugilite has been recently reported from Tajikistan (Cairncross et al; 2017).

5.3.2 Sugilite formation in the Kalahari Manganese field

Wessels mine hosts the most voluminous amounts of sugilite (between 12 and 15 tons) and the highest-quality gem crystals in comparisons to all previous localities (Shigley et al; 1987, Cairncross et al; 2017). Despite the generally erratic occurrence of alkali-rich gangue assemblages in high-grade ore, sugilite associations are unequivocally abundant in cracks, patches and pockets of mineralization in the lower manganese orebody, from where almost all gem-quality material has been extracted, and to a lesser extent in the hanging wall (iron-formation) and footwall (hematite lutite) to the manganese ore. Its occurrence as massive material filling space between brecciated blocks of manganese ore is reported to be much less common (Dixon; 1988) Figure 14 illustrates concisely Wessels sugilite occurrences and mineralogical, compositional and stable isotopic characteristics of the host lithologies that are valuable in our attempt to understand its origin and formation.

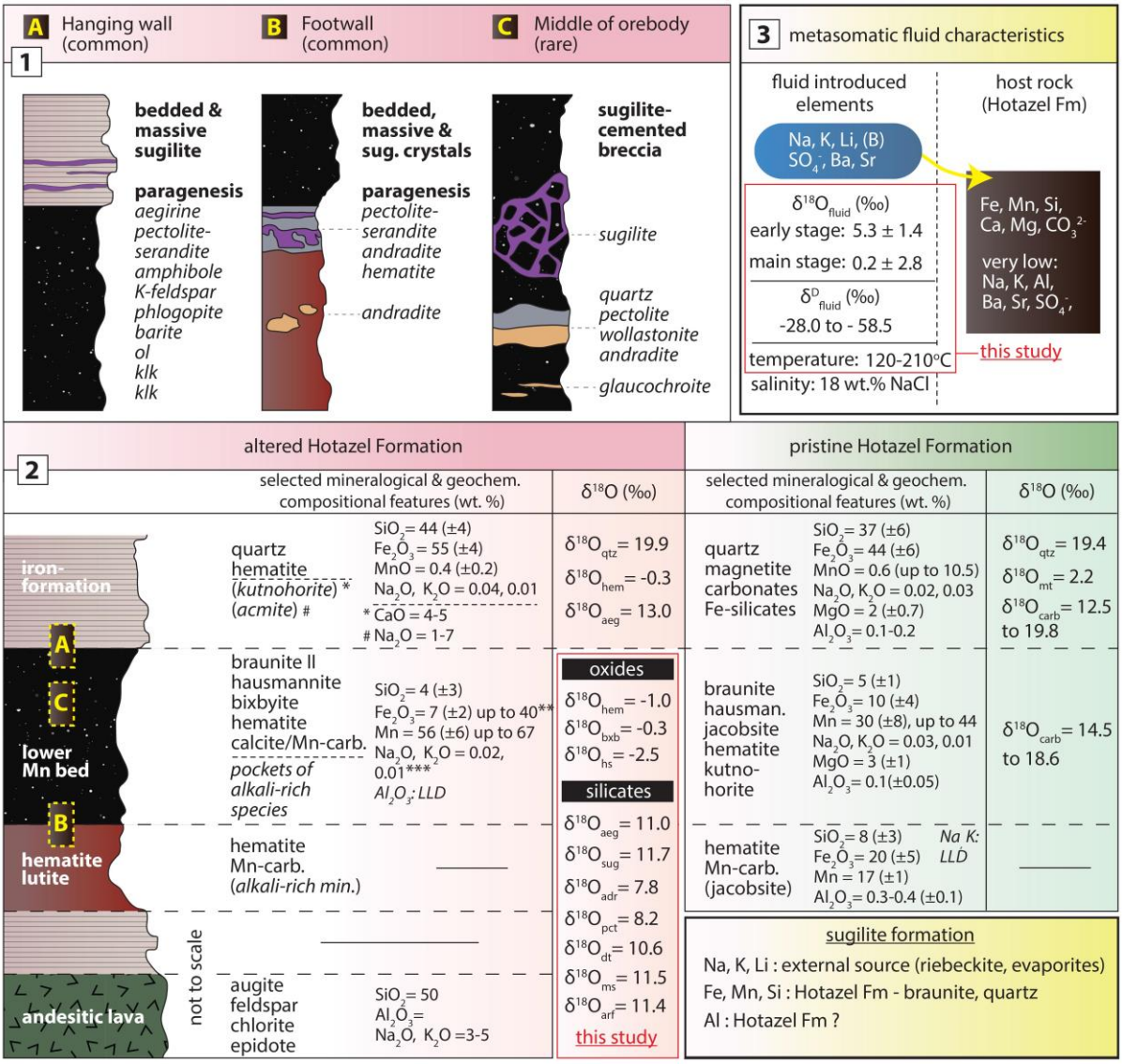

Figure 14. (1 & 2) Main modes of sugilite/calc-silicates distribution within the upgrade Mn ore of the Hotazel Fm. Inspired by Dixon; 1988. Chief mineralogical and geochemical characteristics of the stratigraphic succesion (different literature sources) are tabulated to illustrate changes during metasomatic alteration and emphasize the absence of critical elements (Na, K, Li and perhaps Al) for sugilite formation, which necessitate introduction from the basinal brines. Oxygen isotopes from the literature (Tsikos; 1999) and this study are also shown (reported versus SMOW). (3) Synthesis of major fluid characteristics from this study and Lüders et al (1999).

Layers or seams of sugilite spread laterally along conceivably compositional suitable layers and although they have a restricted lateral extent, grouped layers are documented to spread for more or less 15 consecutive metres and show thicknesses of ca. 15 centimetres (Dixon; 1985, 1988, Shigley et al; 1987). Despite the widely accepted first-order control of normal faults on fluid circulation, the above-described development of sugilite implies channelization of fluid flow parallel to the sedimentary layering and its concentrated abundances in the ore bed probably indicate locally higher permeability and/or compositional

control from the host rock. Control-zoned mineralogical sequences involving apart from sugilite, calc-silicates such as pectolite, andradite, wollastonite and vesuvianite led Dixon (1985, 1988) to draw comparisons with metasomatic calc-alkaline skarns. While features seen in the studied samples, such as preservation of the original sedimentary bedding and globular structures (ovoids, concretions) consisting primarily of sugilite, aegirine and pectolite, attest to the metasomatic nature of alteration, a closer compositional examination of sugilite and its host rocks may perhaps shed more light upon mechanisms governing its formation and the role of hydrothermal fluids.

The wide compositional range shown by sugilite occurrences worldwide, spreads along a zone of restricted Fe-Mn ratios and the prominent compositional characteristic is that of Al-rich Fe-poor end-members and vice versa (Figure 15a). EDS analyses from this study are reliable enough to warrant that sugilite from Wessels has apparently much wider compositions than what it has been previously reported. Unpublished microprobe data from Dixon (1988) overlap with that for Al-rich sugilite of this study, thus supporting our findings for the presence of Al-rich endmembers at Wessels. In addition, our limited dataset suggests that banded textures are generally more iron-rich whereas massive sugilite may host higher amounts of aluminium, although more research is needed to validate this assumption.

Contrasting host lithologies have been invoked by researchers to explain differences in sugilite and specifically Al-rich sugilite from the neighbouring PMF, has been affiliated to its karstic-related manganese-rich host sediments, which also show a close association with aluminous shales (Moore et al; 2011). Siliceous and ferruginous manganese ores in the wider PMF have been reported to host between 1.4 and 10.0 wt. % Al_2O_3 respectively (Gutzmer and Beukes (1996a), which is orders of magnitude higher than the negligible amounts seen in the Hotazel Formation. Although the concept of host rock control on composition may be true to some extent, an aluminum-rich analogue of sugilite (aluminosugilite) with composition similar to the one from Khumani has been reported from manganiferous metacherts of the Cerchiara mine, Italy (Nagashima et al; 2020). On top of that, Wessels sugilite can apparently be still very Al-rich and Fe-poor despite the very low Al_2O_3 abundances in the host lithologies (iron-formation: 0.1-0.2, Mn ore: 0.1, hematite lutite: 0.3-0.4 wt. % respectively) (Figure 14.2),

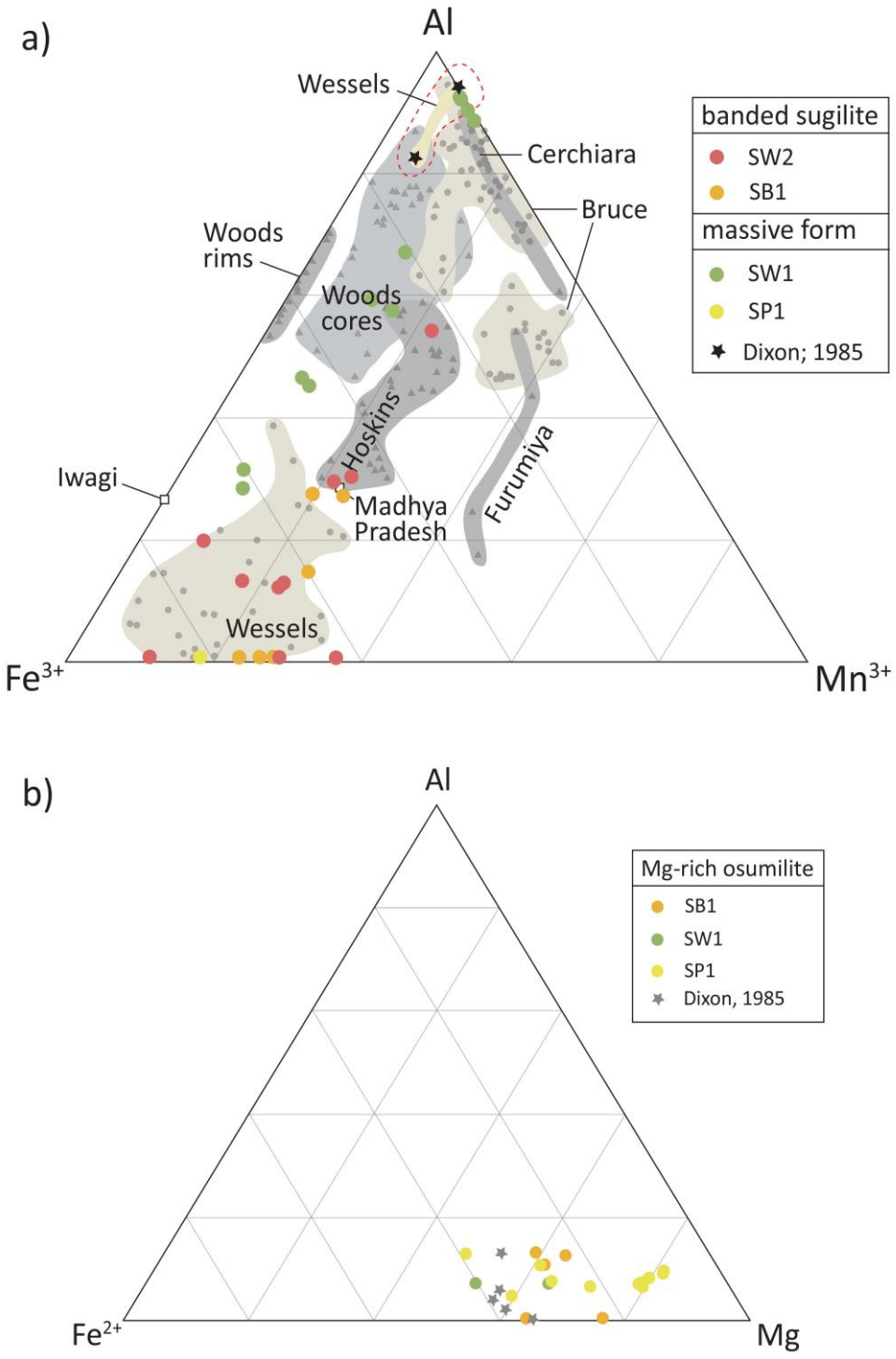

Figure 15. (a) Comparative ternary Al-Fe-Mn plot displaying variations in sugilite composition from different localites worldwide including previous data from the KMF, as well as from this study. Note the wider compositiona range from this study and Al-rich varities (massive sugilite) overlapping with unpublished data from Dixon; 1985. All other sugilite data are taken from Kawachi et al; 1994 and Moore et al; 2011. (b) Comparison between roeedreite (Mg-rich osumilite) from Dixon; 1985 and a fine-grained prismatic mineral seen associated with banded and massive sugilite in this study.

perhaps it being preferentially formed within the slightly more Al-rich hematite lutite unit. Introduction and mobilization of aluminium and its remaining constituents also needs to be considered and as explained further below is indeed evident for certain sugilite occurrences.

On the other hand, cations such as Mg^{2+} needed for the formation of the Mg-rich osumilite-group mineral, seen coexisting with Al-rich sugilite in this study and compositionally overlapping to some degree with that previously reported from Dixon (1988) (Figure 15B), may have been locally sourced by dissolution of the carbonate fraction of the manganese ore. Iron is readily available from hematite, that is more abundant in the hematite lutite unit and in iron-formation, whereas the major manganese reservoir needed for precipitation of the chiefly manganese-bearing Wessels sugilite can be satisfied by invoking breakup of braunite and Mn-carbonates from both the ore and hematite lutite unit. Iron-formation may have also provided lesser amounts of manganese (Figure 14.2), although it needs to be reminded that sugilite formation most likely occurred later than BIF oxidation, during which removal of their bulk alkali content and possibly some of the associated metals had already taken place. Silica, again may have been largely sourced from braunite but also from quartz in iron-formation, depending on the principal host rock each time. However, most critical for sugilite formation are without any doubt its alkali components.

According to Gutzmer and Beukes (1995), the major chemical changes caused by hydrothermal conversion of pristine low-grade to high-grade Wessels-type ore are oxidation of Mn^{2+} to Mn^{3+} and losses of CO_2, SiO_2 and CaO from the parent rock, that are accompanied by substantial volume decrease but no major redistribution of manganese. It has been also stated that the chemistry of gangue hydrothermal minerals formed during the Wessels alteration event exhibit a very close relationship to the composition of the precursor Mn ore, further emphasizing that it contains small amounts of Al, Na, K, Ba, Sr and SO_4^{2-} (Gutzmer and Beukes; 1996b). Such claim though fails to clarify the origin not only of sugilite itself, but also that of most of the observed alkali- and particularly Na-enriched assemblages, since saline fluids derived solely from Hotazel Formation may have been enriched in Ca and Mg but not in the other alkali components found widespread in the gangue phases. Especially, the large amounts of Na and Li hosted by various species are virtually absent in the pristine host

lithologies (Figure 14.2). Instead, formation of alteration minerals necessitates involvement of an external fluid source, which as corroborated by O-H isotopes is almost certainly in the form of hot, saline and alkaline brines. Latest research extended to the neighbouring PMF, has identified a regional-scale hydrothermal system with many shared characteristics between the two localities, involving fluids that have acquired their Ba, Sr and SO_4^{2-} load from evaporites, shales, carbonates and possibly other lithologies in the wider basin (chapter 2).

In an earlier study, the presence of aegirine-rich iron-formation at Wessels has been explained by Na-metasomatism, succeeding an earlier oxidation and leaching event at the expense of carbonate-bearing iron-formation and manganese ore (Tsikos and Moore; 2005). The postulated reaction between quartz and hematite from the precursor BIF and fluid-introduced Na is believed to have formed aegirine along a narrow zone immediately flanking the manganese ore, where fluid flow would have been promoted by the higher permeability of manganese units due to their higher initial carbonate content. Sugilite studied by Dixon (1985, 1988) is also reported to occur in vicinity of the upper gradational contact of the lower manganese unit with the overlying iron-formation. As seen in the studied samples, banded and massive sugilite occurs very rarely if ever as a separate phase and even the common variety referred to as 'gel sugilite' among collectors is always contaminated by calc-silicates and aegirine-augite, both seen finely intermixed with fine sugilite crystals.

A simultaneous metasomatic deposition of sugilite and aegirine appears to be a plausible scenario, although in one sample (SW1) indications of sugilite overprinting aegirine were noted. If sugilite is being formed, at least locally, at the expense of iron-formation and through equivalent processes to that described by Tsikos and Moore (2005) for aegirine, chemical reactions would additionally require the involvement of Mn, K, Al an Li. A certain degree of elemental redistribution, especially with respect to Mn, along with fluid introduction of alkalis from an external source is suggested here to be paramount during precipitation of gangue mineralogy. Although there is no doubt that sugilite is localized at Wessels mine and broadly flanks the lower manganese bed (Figure 14), recent discoveries of sugilite- and aegirine-bearing iron-formation overlying the uppermost manganese bed or sugilite found within quartzite (Tsikos pers. comm.), the latter occurrence perhaps related to

discoveries during the mid-2000s of sugary white quartz impregnated with granular sugilite (Cairncross; 2017), demonstrate that other structural and permeable pathways, such as the regional Transvaal-Olifantshoek unconformity, also play a role in channeling of sugilite-forming solutions and elements such as Li and Mn are transported across stratigraphic horizons.

No attempt will be made here to construct hypothetical chemical reactions for sugilite formation. In any case, textural evidence such as the bedded form or globular structures resembling diagenetic concretions suggest that sugilite has formed, at least partly as a result of replacement mechanisms at the expense of prior phases. Its intimate association with pectolite and calc-silicate phases or species such as amphiboles and garnets (Taggart et al; 1994, Cairncross; 2017), generally highlights the requirement of a silica-rich host rock. As summarized in Figure 14, both quartz from iron-formation and braunite could have been presumably involved in its formation by providing silica, whereas manganese almost certainly derives from the latter mineral. Although at the moment, the ultimate sources of alkalis remain elusive, the current and other recent studies (chapter 2), have unequivocally shown that these elements are introduced by basinal brines that have possibly exploited a range of lithologies in the sedimentary basin. It is reasonable to assume that both the documented presence of evaporites and the widespread riebeckite-crocidolite in the Asbestos Hills BIF provide elegant sources, particularly for lithium and sodium respectively. This hypothesis is in contrast to previous authors (Lüders et al; 1999) who attributed important part of the fluid salt load to interaction with the carbonate-rich sedimentary protore or simply inferred that the fluid had an alkaline character after equilibration with the host rock (Gutzmer and Beukes; 1996b). Further interrogation using Li isotopes on mineral-specific targets may further elucidate the origin and pathways of the brines.

As noted above, aluminum is also an element whose presence in sugilite and in particular in the Al-dominant endmembers is somewhat problematic, since it is almost absent in the pristine stratigraphy and therefore must have been either concentrated during alteration processes or partly introduced by the metasomatic fluids. Another important aspect accompanying sugilite formation is emphasized through the whole suite of available

stable oxygen isotopes from pristine and altered Hotazel Formation (Figure 14), which in conjunction with the extensive preceding isotopic analysis (section 5.2), support that fluid-rock interactions have not altered significantly the $\delta^{18}O$ ratios of the infiltrating fluid responsible for precipitation of sugilite and other metasomatic silicates. Overall, sugilite formation seems to be regulated by elemental availability, i.e., infiltrating fluid chemical composition and probably other characteristics (temperature, oxidation state of Fe-Mn) rather than by bulk composition of the host rock.

5.3.3 Lithium - A prime control for sugilite formation

Probably the most salient factor controlling sugilite formation is the availability of lithium. This claim is substantiated below by a number of aspects in regard to its occurrence. It is reminded that sugilite contains ca. 3 wt. % lithium in tetrahedral site. Other verified hosts of lithium at Wessels are norrishite (ca. 2 wt.%) and Li-bearing amphibole, namely kornite (ca. 0.8 wt.%) (Gnos et al; 2003). Li incorporation in manganese-bearing amphiboles is a feature recorded in manganese ores of the Madhya Pradesh district (India) and Hoskins mine (Australia) (Hawthorne et al; 1995). Other potential hosts of lithium or its abundance in the host rock remains elusive. It is certain though that the precursor Hotazel Formation would contain negligible amounts if any at all. Kawachi et al (1994) reported a single analysis of 1100 ppm Li from the host rock to sugilite (Hoskins mine), however without giving any details on its mineralogy. Data from an ongoing whole-rock Li survey in the wider Northern Cape area has shown that Li is detectable but only in small amounts within the high-grade and barium-rich ore at Wessels (80 ppm) and N'Chwaning (20 ppm) and almost absent from the Mapedi shales (<10 ppm) that directly overlie Hotazel Formation (data shown in chapter 6).

The restricted occurrence of Khumani sugilite in the PMF (Moore et al; 2011), seemingly demonstrates that despite the abundance in calc-silicates and comparable alkali assemblages to that of the KMF, sugilite can be contrastingly present only in negligible concentrations. The same information about sugilite is extracted from other localities in the PMF (Heuningkranz-Langverwacht) which despite the ubiquitous and rare alkali assemblages, apparently do not host sugilite (Fairey et al; 2011). As an example, ongoing research by the author in the manganiferous Wolhaarkop breccia from the former area has revealed the

presence of abundant armbrusterite [$K_5Na_7Mn_{15}[(Si_9O_{22})_4](OH)_{10}4H_2O$)], a mineral typically associated with sugilite in Khumani, but found here only in association with other sodic-rich phases (aegirine, albite, serandite, etc.). The extent of sugilite in the wider PMF is unknown but it can be expected that extensive mining and exploration drillcores in the area would have identified widespread occurrences of this vivid purple mineral. The above considerations imply that specifically in the northernmost part of the KMF, an exceptionally large amount of lithium was embodied in the metasomatic brines. This characteristic alteration signature has not been yet identified in the rest of the PMF with the only exemption being that of Khumani sugilite and the presence of the Li-bearing mica ephesite in ferromanganese deposits from several abandoned mines in the eastern PMF (Lohatla, Gloucester, Bishop). Ephesite contains between 1.5 and 1.7 wt.% Li, i.e., concentrations comparable to that of sugilite. Its origin and timing of formation though, is regarded to be very different, linked to syn- or post-metamorphic fluids related to the much older Kheis orogeny (1.8-1.7 Ga) (Gutzmer and Beukes; 1996a). However, considering the regional geological context of alkali metasomatism and lack of age constraints for ephesite formation, a possible relationship between sugilite in the KMF and ephesite in the neighboring PMF with respect to Li sources, warrants further research.

Furthermore, the source of Li has been suggested here to be associated to former evaporites in the basin, most likely lying within the Campbellrand Subgroup (Gandin and Wright; 2007 chapter 2). High to very high lithium concentrations in brines have led several authors to suggest that water-rock interactions and processes of lithium enrichment occur along their flow path (Millot et al; 2010b, Mertineit and Schramm; 2019, Dugamin et al; 2021). That is to said that Li enrichment solely from evaporitic minerals is not necessarily a process that can explain high Li values in fluids, since lithium incorporated in the former during evaporation from seawater produces enrichments by a factor of around 100 or else 24 mg l^{-1} (Fontes and Matray; 1993). Apart from hydrothermal waters, high concentrations of Li in brines may be associated with either nonmarine evaporites or extremely concentrated evaporites (Vine; 1976). Since the precise mechanisms of lithium enrichment in sedimentary formation waters remain unclear, more research using lithium isotope geochemistry in the Northern Cape Province may aid to elucidate these processes.

5.4 Conclusions

Textural, compositional, isotopic and geochronological analysis of sugilite-bearing assemblages and other gangue minerals from the enriched ore of the Kalahari Manganese field can provide paramount information towards the development of a more comprehensive picture of the timing, duration, origin, evolution and role of fluids during this major hydrothermal ore-upgrade event. On the basis of small but sufficient dataset the following conclusions can be drawn:

(1) In situ UV laser $^{40}Ar/^{39}Ar$ data of massive and banded sugilite can provide reliable estimates of the hydrothermal activity responsible for high-grade ore formation in the KMF.

(2) A combination of textural evidence and in situ $^{40}Ar/^{39}Ar$ spot date analyses suggest the presence of distinct episodes of sugilite formation, therefore indicating that depending on each sample, this method may require high-spatial resolution to both deduce an accurate weighted mean age and in addition more detailed age information.

(3) The hydrothermal system related to ore enrichment had been active during at least two distinct pulses, around 1139 ± 5 Ma and 1063 ± 18 Ma respectively and thus can be regarded as long-lived.

(4) O-H isotopic fingerprinting using diverse ore-gangue mineralogy indicates that $\delta^{18}O$ of the mineral-forming fluids probably ranged from ca. -3 to + 8 ‰ and δD values from -28.0 ‰ to -58.5 ‰. Early calc-silicate precipitation was possibly characterized by heavier $\delta^{18}O_{FLUID}$ values on average (5.3 ± 1.4 ‰) than main and later stages (0.2 ± 2.8 ‰), during which original fluids were altered and diluted after mixing with meteoric water and interactions with the host rock.

(5) According to the isotopic characteristics, timing of mineral formation and overall geological setting, infiltrating hydrothermal fluids can be safely characterized as sedimentary basinal brines, that have prior equilibrated with various strata of the Griqualand West basin and have been expelled and migrated with mechanisms analogous to that of Mississippi-Valley-type deposits.

(6) Uniformity in $\delta^{18}O$ values of gangue silicates is attributed to large water to rock mass ratio and fluid buffering during mineral precipitation, despite the overall extensive fluid-rock interactions.

(7) Broad readings on the temperatures of fluids can be potentially provided by $\delta^{18}O$ measurements of certain mineral pairs (garnet-hematite or garnet-hausmannite), as it is suggested by temperature coincidence with previously reported results (T = 120-210^{o} C).

(8) Sugilite of banded and massive form is closely associated with aegirine and metasomatic textures resembling the pristine rock and thus, it is suggested to form at the expense of prior phases (braunite, quartz, hematite) by replacement mechanisms involving introduction of Li, Na and K by basinal fluids, originally leached from riebeckite-rich BIF and evaporites among other lithologies. Specifically, lithium availability is suggested as the most salient factor controlling sugilite formation.

Chapter 4

In situ multiphase $^{40}Ar/^{39}Ar$ dating of sugilite and 5 coexisting minerals reveals fluid-induced ^{40}Ar loss owing to a newly emerging regional Neoproterozoic event that resets gangue associations of the hydrothermally upgraded Kalahari Manganese field, South Africa.

Abstract

The northmost part of the Kalahari manganese field has experienced hydrothermal ore upgrade by tectonically-driven alkali brines between 1.2 and 1.0 Ga. At present, timing of this hydrothermal alteration is based on robust but limited age data whereas younger available ages from the wider area suggest a possibly more complex thermal evolution since Proterozoic times. New in situ multiphase $^{40}Ar/^{39}Ar$ laser-probe data from an association of sugilite, potassic magnesio-arfvedsonite, K-feldspar, phlogopite, lipuite and norrishite from Wessels mine yield a range of apparent ages which spans from 1107 ± 14 to 284 ± 4 Ma. The oldest ages provide additional proof of the timing of local hydrothermal enrichment during Namaqua orogeny and set new constraints on the late precipitation of associated gangue minerals at 1037 ± 8 Ma. The 'younger' spot dates reveal a temporally distinct episode of reheating, depicted by an isotopic disturbance of the Ar-system mainly in sugilite, norrishite and K-feldspar and lesser in phlogopite. The documented ^{40}Ar-loss in these phases is attributed to fluid introduction responsible for precipitation of the coexisting lipuite at ca. 650 Ma, while the waning stages of this event and subsequent cooling below the Ar-closure temperature of K-feldspar and sugilite occurred at ca. 500 Ma. The Neoproterozoic (ca. 600 Ma) overprinting event in the KMF is consistent with ages obtained from comparable alkali-rich assemblages in the neighboring PMF some 120 kilometres to the south. Emerging evidence suggest a temporal relation of the thermal disturbance of the geochronological clocks in the wider area of the Northern Cape to the distal (~500 km) Pan-African orogeny. Our study emphasizes the need for further research to gain insights on this puzzling issue.

1. Introduction

The Ar-Ar method is a powerful tool for constraining thermal histories and timing of hydrothermal fluid circulation and mineralization in a variety of geological settings and ore deposits (e.g., Marchev and Singer; 2002, Yang et al, 2014, Mark et al 2017, Guo et al, 2019). In particular, the high resolution in situ UV laser method has great potential in revealing age information from multiphase K-bearing assemblages in which mineral separation is impossible and thus incremental heating of potentially polymineralic material can homogenise or obscure distinct and complex age clusters. Although K-bearing Mn oxides (hollandite-group) have been successfully used for $^{40}Ar/^{39}Ar$ dating of supergene manganese enrichment (Vasconcelos et al; 1994b, Bikerman et al; 1999, Spier et al; 2006), dating hydrothermally enriched or modified manganese ores by targeting associated K-bearing gangue minerals such as feldspars and micas or other less common gangue mineralogy found in such ores, remains very scarce to this day.

Kalahari Manganese field contains a number of common and rare K-bearing minerals which are evidently associated with the hydrothermal metasomatic alteration affecting its northernmost part by means of dissolving original carbonate material, redistributing metals and upgrading low-grade pristine (up to 38 wt. % Mn) to high-grade (>47 wt. % Mn) altered manganese ore (Beukes et al; 1995). Age information for this upgrade has been derived from $^{40}Ar/^{39}Ar$ dating on assemblages containing sugilite or norrishite (Gnos et al; 2003), characteristic of the hydrothermal calc-alkaline gangues and the wealth of well-crystallized uncommon minerals in the KMF. Very little published data exist on the paragenetic occurrences and origin of other potential gangue $^{40}Ar/^{39}Ar$ dating targets, much less attempts have been made to date these minerals in seeking to expand our knowledge on the timing and origin of the Wessels hydrothermal event or even the post-Wessels alteration history of these ores, with the exception of recently formed Mn oxides (Gutzmer et al; 2012).

In this study, we describe the paragenesis of K-feldspar in aegirine-bearing iron-formation and provide a detailed description of a bedded sugilite occurrence associated with a multiphase K-bearing assemblage which includes common (K-feldspar, phlogopite, magnesio-arfvedsonite) and rare (norrishite, lipuite) minerals. The variability of K-bearing

mineral content found in this specimen render it as an ideal testing ground for high spatial resolution dating in an aim to improve our interpretation of $^{40}Ar/^{39}Ar$ data from multiple coexisting dating targets of hydrothermal origin. Our obtained $^{40}Ar/^{39}Ar$ ages disclose a disturbance of the Ar-Ar clock and call into question the concept of a thermally and tectonically stable geological environment at Wessels mine since Mesoproterozoic times.

2. Geological background

Wessels mine is located at the northwestern part of the Kalahari manganese field (Figure 1A), an area encompassing the well-preserved Hotazel Formation and its world-renowned giant manganese ores hosting unique mineral specimens (Cairncross and Beukes; 2013). Hotazel Formation belongs to the Postmasburg Group which is the stratigraphically uppermost sequence of the Late Archean to Palaeoproterozoic Transvaal Supergroup in the Griqualand West basin (Figure 1B), the latter occurring at the western margin of the Kaapvaal Craton (Moore et al; 2011).

The basal part of the Postmasburg Group is represented by the glacial Makganyene Formation which was deposited on a regional unconformity (Polteau et al; 2006). This unit is followed by a succession of basaltic andesites and hyaloclastites of the Ongeluk Formation (Cornell et al; 1996) which in turn grades into a chemosedimentary succession of iron-formation interbedded with Mn ore (Hotazel Formation). In particular, Hotazel succession is characterized by a threefold cyclicity of microbanded iron-formation, hematite lutite (fine-grained carbonate-rich hematite rock) and manganese ore, all previous developing in discrete sedimentary layers (Figure 1C) (Beukes; 1983, Tsikos et al; 2003). Locally, Hotazel Fm grade upwards into carbonates of the Mooidraai Formation which is directly overlain by the unconformable Palaeozoic Dwyka diamictite. Hydrothermal metasomatic alteration which took place in a stockwork fashion along normal faults, joints and bedding planes, resulted in the formation of a high-grade ore in the northernmost part of the Kalahari manganese field, where the thicker and most economically viable lowermost manganese unit is currently being mined underground (Beukes and Gutzmer; 1995). This enrichment resulted in precipitation of alkali-rich gangue mineralogy including sugilite, amphibole, aegirine and barite present in

samples from this study and is regarded as a 1.2-1.0 Ga tectonometamorphic event related to the Namaqua-Natal orogeny (Gnos et al; 2003, chapter 3).

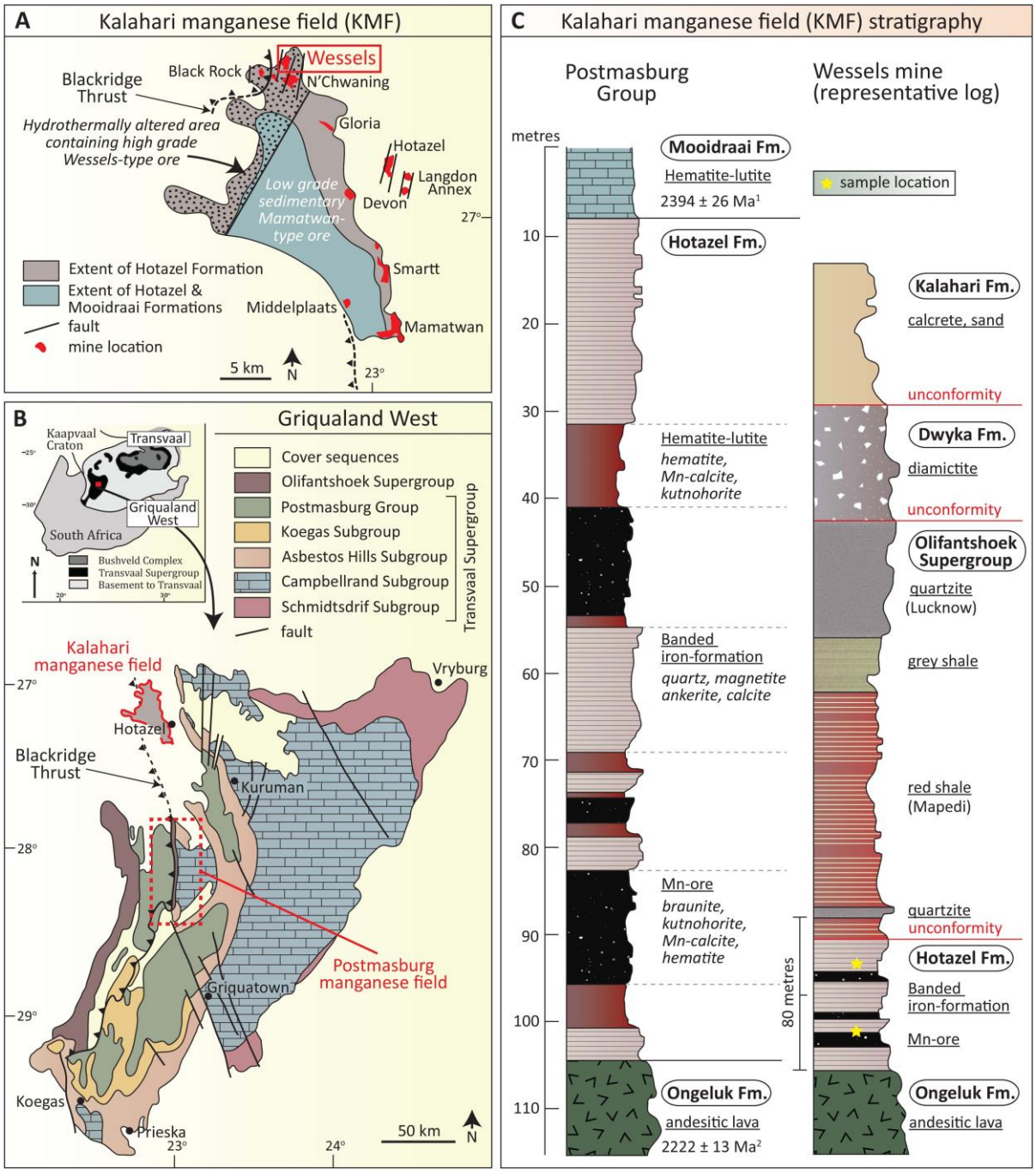

Figure 1. (A) Locality map of the KMF showing the distribution of low- and high-grade Mn ore, localities of manganese mines, major structural features and geographic extent of lithostratigraphic units overlying the Hotazel Formation. Modified after Tsikos and Moore; 2005. (B) Geological map, locality and stratigraphy of the Griqualand West basin. Note the regional Blackridge Thrust belt extending into the KMF. Modified after Schröder et al; 2011. (C) Simplified stratigraphic column of the Postmasburg Group (Makganyene Fm at the base not shown) and representative drillcore at Wessels mine. Redrawn from Burger; 1994 and Tsikos and Moore; 1997.

Over most part of the study area, red-grey shales and quartzites of the Olifantshoek Group unconformably overlie the Hotazel and Mooidraai Formations, composing the stratigraphy profile encountered in drillcores at Wessels mine (Figure 1C). This same unconformity has a regional character since the same Olifantshoek clastic sediments can be observed in the wider region to unconformably overlie the stratigraphically lower Asbestos Hill BIFs and carbonates of the Campbellrand Subgroup as well as associated Fe-Mn deposits contained in the neighboring Postmasburg Manganese field (Figure 1A). Moreover, this feature has been implicated as a potential conduit for regional hydrothermal fluid flow (Tsikos and Moore; 2005, Fairey et al; 2019). Another regional structure is the Blackridge Thrust which deforms and duplicates older strata of the Transvaal Supergroup and is believed to be related to the controversial 1.9-1.7 Ga Kheis orogeny (Stowe; 1986, Cornell et al; 1998, Eglington; 2006). This regional thrust spans more than 270 kilometres, from the hydrothermally upgraded part of the KMF, south into the PMF and down to Prieska.

3. Materials and methods

This study is chiefly focused on a bedded sugilite sample from Wessels mine acquired from an anonymous mineral collector and almost certainly characterizing the calc-alkaline seams mined from the lower manganese orebody. Another seven samples of altered iron-formation were supplied by the collection of Rhodes university, South Africa and are originally derived from stratigraphically equivalent horizons at Wessels mine as well as from iron-formation overlying the uppermost manganese unit at N'Chwaning mine. Thin sections were studied under both optical and scanning electron microscope at the university of Glasgow using a Quanta 200F Environmental SEM. In situ $^{40}Ar/^{39}Ar$ analyses were conducted at the NERC Argon Isotope Facility at SUERC. A New Wave Research Laser UP-213 A1/FB was used to ablate the sample and gas purifications and measurements were made with an attached Helix SFT (Thermo Scientific) multi-collector noble gas mass spectrometer. For details of the stable analytical techniques and $^{40}Ar/^{39}Ar$ dating the reader is referred to Appendix I. Ages reported from Gnos et al (2003) have been recalibrated using the ^{40}K decay constant from Renne et al (2011).

4. Results

4.1 Mineralogy of aegirine-bearing iron formation

Aegirine-bearing iron-formation comprises variable modal amounts of quartz, hematite and aegirine distributed predominantly in: (a) mm-thick and compositionally pure aegirine laminae alternating with hematite layers or (b) laminated aegirine-hematite-quartz assemblages or veinlets of subordinate occurrence within micro-banded quartz and hematite iron-formation (Figure 2A). Unless being coarse-grained (200-500 µm) and on the order of few millimetres, aegirine laminae are not macroscopically distinguishable from chert- and hematite-bearing laminae but under the microscope, fine-grained aegirine can be rather conspicuous being moderate to strongly pleochroic. EDS analyses pick up solely elements that suggest it being a pure Na-end member of the aegirine-augite series. Distribution and textures

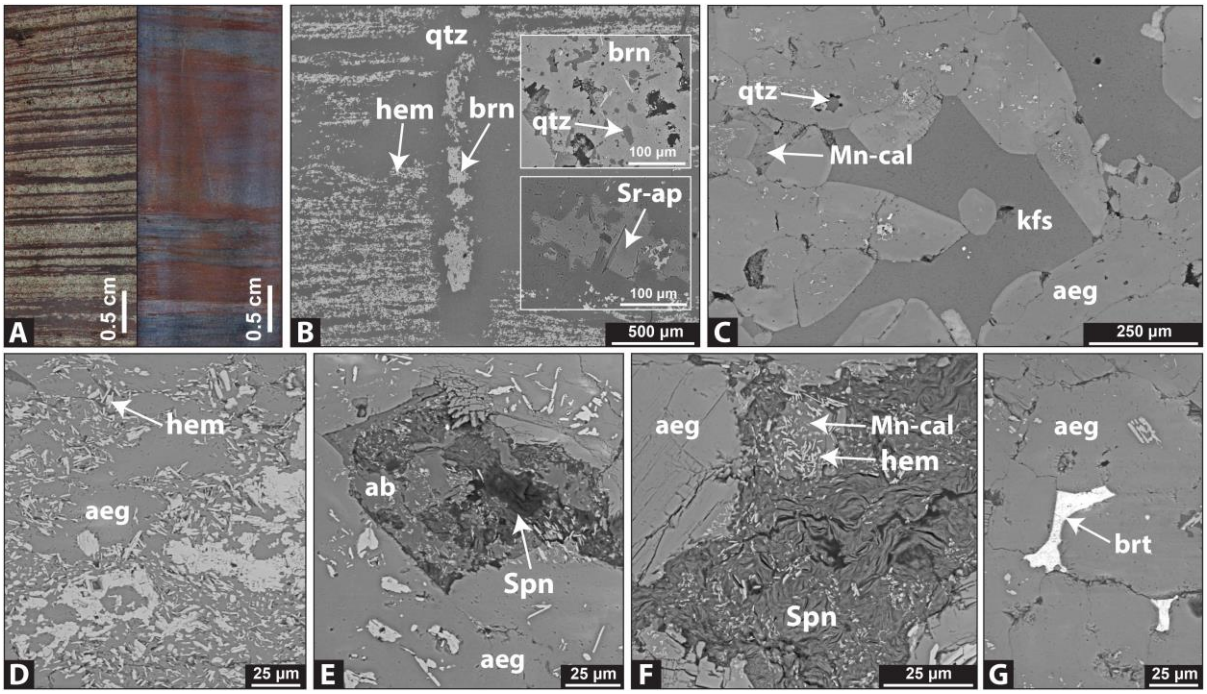

Figure 2. Backscattered electron (BSE) images. (A) Altered Hotazel iron-formation characterized by aegirine-hematite alternating bands (left) and hematite-quartz lamination with subordinate mm-thick aegirine laminae (right). (B) Braunite cross-cutting veinlet. (insets) Vug surrounded by recrystallized quartz and filled by braunite and aegirine (top) or strontium- and REE-bearing apatite (bottom). (C) Xenomorphic K-feldspar in-between coarse-grained aegirine hosting Mn carbonates, quartz and hematite. (D) Microplaty hematite surrounding aegirine. (E & F) Albite being replaced by saponite-talc, the latter documented here only from the N'chwaning mine. (G) Barite occludes open space in-between aegirine. ab = albite, aeg = aegirine, brn = braunite, brt = barite, hem = hematite, kfs = K-feldspar, Mn-cal= manganese-bearing calcite, qtz= quartz, Spn = saponite, Sr-ap= strontian apatite

of aegirine closely resemble the occurrences described by Tsikos and Moore (2005) from the Hotazel succession, hence focus is given here on additional features and accessory minerals. An infrequent but notable feature is that lamination can be disrupted by veinlets containing a mix of braunite, aegirine and barite which rarely expand also laterally along bedding and precipitate the previous minerals in vugs (up to 500 µm) surrounded by recrystallized quartz (Figure 2B). Apatite displays analogous distribution in vugs, is usually seen associated with braunite and commonly hosts strontium and REEs (mainly dysprosium). Microscopic chernovite-(Y) [$Y(AsO_4)$] was also positively identified as inclusions in aegirine. K-feldspar and albite are the principal accessories phases recognized in the aegirine-bearing laminae and typically possess xenomorphic textures suggesting crystallization after earlier formed aegirine (Figure 2C).

Minute microplaty-hematite and quartz inclusions in coarse-grained (100-200 µm) aegirine provides evidence for the development of aegirine at the expense of pre-existing quartz and hematite assemblages as previously suggested by Tsikos an Moore (2005). Notably, recrystallized hematite plates commonly encompass individual aegirine crystals (Figure 2D). A fine-grained fibrous mineral was scarcely observed overgrowing on gangues such as albite or precipitating in-between aegirine grains (Figure 2E, 2F). A stoichiometrically calculated formula of $Ca_{0.2}Na_{0.2}Mg_{2.9}Fe^{2+}_{0.1}Mn^{2+}_{0.1}Si_{3.5}Al_{0.5}O_{10}(OH)_2 4H_2O$ suggests that it belongs to the talc-saponite, both end-members of which have been previously reported from the KMF (Gutzmer and Beukes, 1996b) and are seen here as alteration product of possibly diopside, although magnesium may have been also sourced from former carbonates. Barite is paragenetically affiliated with the previously mentioned alkali-rich minerals and its characteristic texture is indicative of open-space filling (Figure 2G).

4.2 Description of multiphase K-bearing mineral assemblage and in situ $^{40}Ar/^{39}Ar$ data

Sample SW2 is a representative example of bedded sugilite from the Wessels mine (Figure 3.1). The first thing that struck one's attention is the deep purple sugilite microcrystals and the glassy dark blue alkali amphibole (K-magnesio-arfvedsonite, see below) on the sample surface (Figure 3.2), the latter further occupying evident cross-cutting veins of dark

blue colouration. Both of the aforementioned minerals display bedding-parallel development throughout the sample, with sugilite though being pervasive and amphibole restricted to less than a handful of µm- to mm-thick laminae. The conspicuous fine lamination of the sample is characterized by alternating fine-grained hematite, aegirine ($NaFe^{3+}Si_2O_6$) and sugilite [$KNa_2(Fe^{3+},Mn^{3+},Al)_2Li_3Si_{12}O_{30}$] thin (1-5 mm) parallel laminae (e.g. Figure 3.3). These fine layers practically define distinct compositional zones, particularly in relation to the alkali contents of the rock, with sodium generally confined in the aegirine and sugilite laminae and potassium, lithium, manganese and aluminum being strictly limited to the sugilite laminae.

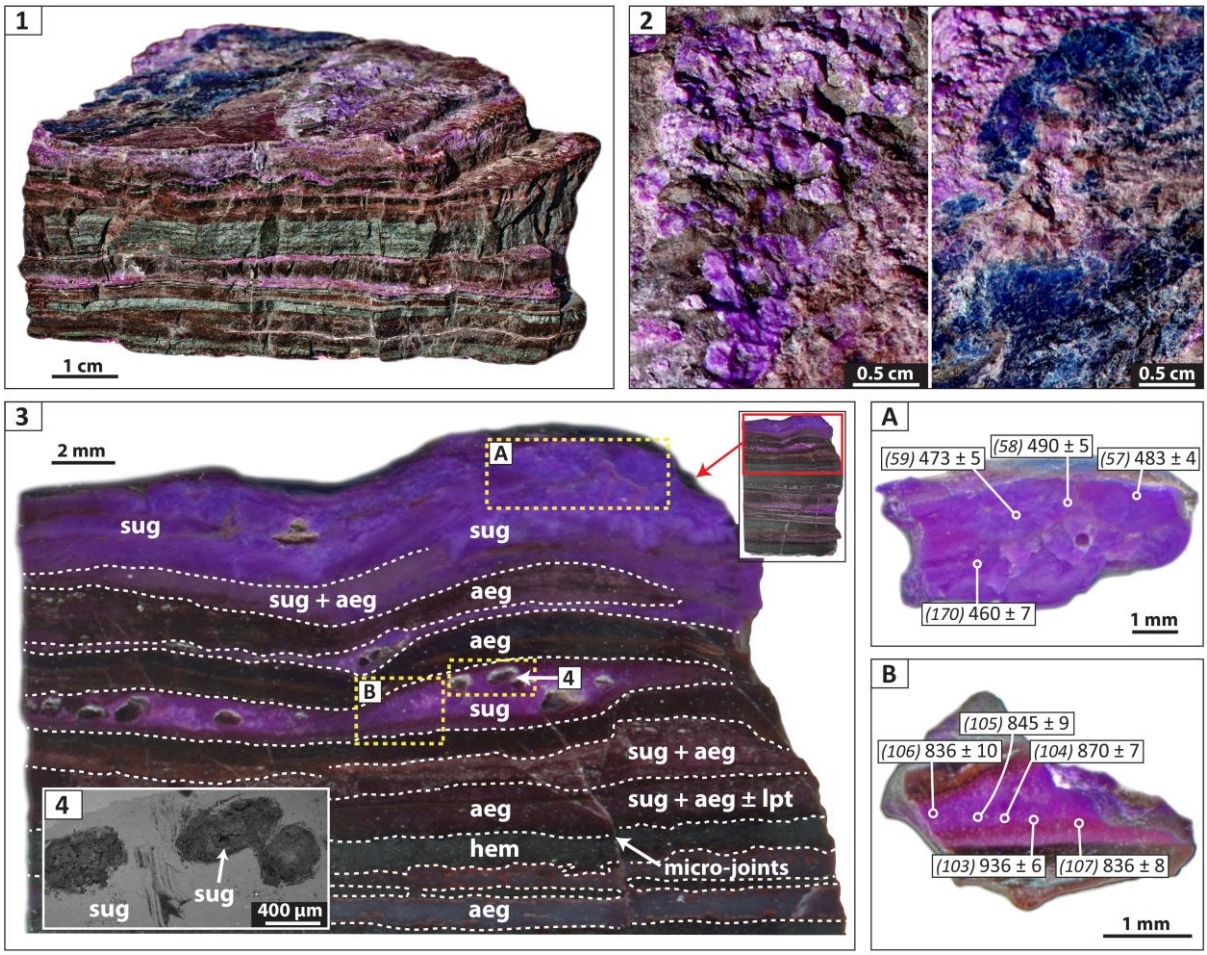

Figure 3. (1) Photo of sample SW2 showing bedded sugilite (purple) and magnesio-arfvedsonite (blue) in a metasomatized laminated rock comprising in addition mostly alternating hematite and aegirine mm-scale layers. (2) Detail of sample surface showing sugilite (left) and magnesio-arfvedsonite (right). (3) Polished sample wafer demonstrating compositional fine lamination. Laser spot locations are within yellow dotted line. (4) High porosity indicated by ellipsoidal voids filled by fibrous sugilite (BSE). (A) 'Young' (479 ± 28 Ma, 2σ) purple sugilite and (B) 'old' (876 ± 36 Ma, 2σ) reddish-purple sugilite layers, the latter better approximating Wessels hydrothermal metasomatism. Laser spots (85 µm) are circled, spot and mean ages (Ma) are reported at 1σ.aeg = aegirine, hem = hematite, lpt = lipuite, sug = sugilite

The sparse amphibole layers and veins likewise contain sodium and potassium and in addition are the principal host of calcium in this sample, in contrast to the typical calc-silicate (pectolite-serandite, $NaCa_2Si_3O_8(OH)$ - $Na(Mn^{2+},Ca)_2Si_3O_8(OH)$) assemblage seen in the same stratigraphic zones and found here only in trace amounts.

Four accessory minerals are further observed to be paragenetically associated with sugilite and aegirine, which are namely K-feldspar, phlogopite, norrishite ($KLiMn^{3+}{}_2(Si_4O_{10})O_2$) and lipuite ($KNa_8Mn^{3+}{}_5Mg_{0.5}[Si_{12}O_{30}(OH)_4](PO_4)O_2(OH)_24H_2O$). The former minerals form compositional laminae along the main bedding planes, although in a somewhat more irregular fashion in comparison to sugilite and aegirine and following sugilite, control the remaining potassium content of the sample. Microscopic phlogopite and norrishite veins can develop discordant to bedding and similar relationships are exhibited by braunite veinlets. Hematite laminae are also commonly disrupted by later precipitated aegirine, which also appears as recrystallized, granular and coarse-grained (up to 300 μm) in phlogopite and sugilite associations, possibly indicating a late-stage emplacement of all the latter minerals. Although for the most part individual laminae are monomineralic, aegirine laminae also show admixtures, principally of sugilite and lesser of hematite and phlogopite whereas K-feldspar domains always contain sugilite. A thin selvage of recrystallized hematite and aegirine is frequently observed outlining K-feldspar and phlogopite domains which mostly host fine-grained lamellar and prismatic textural varieties of phlogopite and K-feldspar respectively. Lipuite mainly forms in the vicinity of small joints and areas with higher porosity. A prevailing textural feature, observed in different compositional layers and primarily in sugilite, is the high porosity between the intricately mixed mineralogy. Distribution and size of hematite plates suggest pseudomorphic replacement of former magnetite. On the basis of hematite textures and the general occurrence of sugilite close to the contact of the lower manganese orebody with either the underlying hematite lutite or the overlying iron formation, it can be surmised that the studied sample derives from the aforementioned lithologies and probably represents an altered iron-formation.

Sugilite laminae in the uppermost part of the sample exhibit ellipsoidal voids (ca. 500 μm), a feature of secondary porosity, of which their interior is occupied by randomly

orientated aggregates of fibrous sugilite (Figure 3.4). Scarcely observed ovoidal structures composed of sugilite may be related to pristine carbonate ovoids or remnant dissolution textures in relation to metasomatic processes. Moreover, sugilite laminae on polished surfaces manifest two subtly different coloured varieties, one deep purple and one reddish-purple (e.g., Figure 3A, 3B), both however consisting of very fine-grained and texturally similar sugilite. A small number of EDS analyses (n=14) does not show significant compositional differences between the various sugilite layers in the sample. Among the trivalent cations Fe_2O_3 is dominant, ranging between 5.0 and 15.3 wt. % (average = 12.2 ± 3.1 wt. %), which in agreement with sugilite data from Wessels mine (Dixon, 1988; Gnos et al; 2003). Al_2O_3 ranging from 1.6 to 7.4 wt.% falls also within the existing range, although it being on the higher side, with two analyses standing out (10.6, 10.9 wt.%). The latter characterize an Al-dominant sugilite end-member which was only observed to occur in small quantities in the amphibole vein. The chemical composition of the dark blue alkali amphibole (Figure 4A) exhibiting strong pleochroism was measured by EDS on thirteen locations within the sample. The general chemical formula of the amphibole supergroup is $AB_2C_5T_8O_{22}W_2$, where sites are mainly

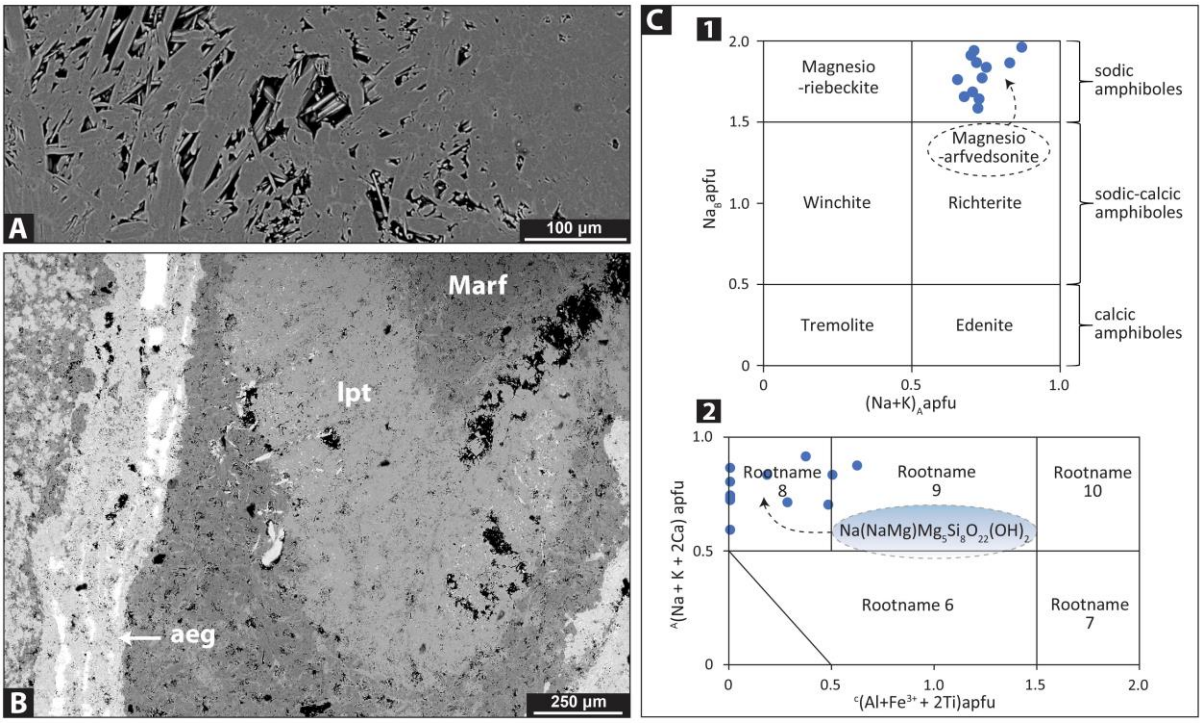

Figure 4. (A) BSE image of K-magnesio-arfvedsonite displaying fine-grained prismatic euhedral crystals. (B) Tiny lipuite crystals occupying porous space inside an older (section 4.2) and paragenetically non-affiliated K-magnesio-arfvedsonite vein. (C1) Amphibole classification graph by Leake et al; 1997 and Hawthorne et al; 2012 (C2) suggest that plotted EDS analyses clearly reflect a sodium amphibole, which however also hosts ca. 4 wt.% K_2O and smaller amounts of calcium, manganese and iron. aeg= aegirine, lpt = lipuite, Marf = (K) magnesio-arfvedsonite.

occupied as follows: A = Na, K, Ca, Li, B = Na, Ca, Li, C = Mg, $Fe^{,2+,3+}$, $Mn^{2+,3+}$, Al, Ti, T = Si, Al and W= OH^-, F, l, O^2 (Hawthorne et al; 2012). On the basis of the above cation distribution and regarding iron as wholly trivalent, the following two formulae were calculated for the studied amphibole using 23 oxygens, $K_{0.7}(Na_{1.7}Ca_{0.3})(Mg_{4.0}Mn^{2+}_{0.6})Si_{7.9}O_{22}(OH)_2$ and $K_{0.7}(Na_{1.9}Ca_{0.1})(Mg_{3.0}Mn^{2+}_{0.6}Fe^{3+}_{0.5})Si_{8.0}O_{22}(OH)_2$. The first formula represents an iron-free composition and the latter an amphibole with Fe_2O_3 ranging from 3.5 to 11.7 wt. % (average = 8.2 w.%). Elements not analysed for, such as Li^+, F^-, Cl^- and OH^- can have a significant effect on the calculated formula. In particular Li can be an important constituent in alkali amphiboles and either that or sodium substituting into the A site can explain the observed deficits in cations. Whatever the source and exact magnitude of error is, consistently high potassium values (3.9 ± 0.7 wt. %, n=13) in the A tetrahedral site observed here are important in richterite and arfvedsonite.

According to the classification plot by Leake et al (1997), amphibole in this study classifies as magnesio-arfvedsonite (Figure 4B), however if sodium substitutes for potassium into A site as it is most likely, Na_B apfu falls below 1.5 and data plot into the richterite field. On the basis of the new classification scheme by Hawthorne et al (2012) which utilizes Ca_B and Na in relation to the other cations in B site, this mineral categorizes as sodium (magnesium-iron-manganese) amphibole and not sodium-calcium amphibole in which group richterite belongs (Figure 4C). Both blue richterite and arfvedsonite showing vivid colours from dark red to blue or pale-green have been reported from Wessels mine (Dixon; 1988, Von Bezing et al; 1991) as well as the Li-bearing alkali amphibole kornite (Gnos et al; 2003). More recently, Gu et al (2019) mentioned richterite as part of a sugilite parageneses at N'Chwaning but did not provide mineral chemical data. It is beyond the scope of this study to resolve the above discrepancy and by all means, the considered mineral is an alkali amphibole for which the prefix 'potassic (K)' is used here to place emphasis on the significant concentration of this alkali, followed by the name 'magnesio-arfvedsonite'. The term magnesio-arfvedsonite is also used for short. Three analyses on lipuite from this study show a composition very similar to the single other worldwide occurrence described from N'Chwaning mine (Gu et al; 2019). On the basis of a total cation number of 27.5, its calculated chemical formula is

($K_{0.9}Na_{6.4}Mn^{3+}_{4.7}[Si_{11.6}O_{30}(OH)_4](P_{0.8}O_4)O_2(OH)_24H_2O$) and the K_2O content is on average 3.24 ± 0.04 (n=3).

In situ $^{39}Ar/^{40}Ar$/ data

A total of 117 $^{40}Ar/^{39}Ar$ spot dates were obtained from all six K-bearing phases, ensuring incorporation of different parageneses and compositional laminae across the sample. The full $^{40}Ar/^{39}Ar$ dating results are reported in Appendix I. Distribution of age data was surveyed using probability density plots (PDP) and kernel density estimations (KDE) and all following reports are based on the latter. Sample observation using UV laser microprobe allowed a relatively easy identification of areas of interest mainly due to the strongly contrasting compositional layering of the sample, yet still spots analyses may have incorporated neighboring minerals and hence detailed notes are reported below when there is such a suspicion. Collectively, the obtained spot dates range from 1107 ± 14 to 284 ± 4 Ma (1σ).

Eighteen spots on phlogopite grains from three different layers yielded $^{40}Ar/^{39}Ar$ dates from 805 ± 13 Ma (1σ) to 1088 ± 11 Ma (1σ), which are normally distributed, showing only a skewed flat negative tail leading down towards younger ages (n=5). The calculated weighted mean is 1006 ± 8 Ma (2σ, MSWD = 6.82, n=18). These dates derive for the greater part (n=13) from a single phlogopite layer contained in aegirine laminae and precipitated along the contact with a hematite lamina (Figure 5B, 5C). Spots of 85 microns in size were positioned on areas (100-400 µm) of lamellar phlogopite in between coarse-grained prismatic aegirine (Figure 5C) and therefore may be contaminated by the latter as well as by hematite inclusions. Excluding two younger dates (805 ± 13 and 837 ± 8 Ma, *spots 112 and 117*) which confidently reflect pure phlogopite, apparent ages in this lamina differ by up to 59 ± 2 Ma. *Spot 139* was purposely placed outside the phlogopite laminae and into a matrix of intergrown phlogopite and aegirine and although it probably represents an admixture, it was included in the phlogopite ages since the obtained date (1060 ± 12Ma) falls within the documented time span and is evidently controlled by phlogopite-hosted $^{40}Ar^*$. The paragenesis phlogopite-aegirine was frequently seen forming irregularly-shaped infills and lenses within aegirine laminae.

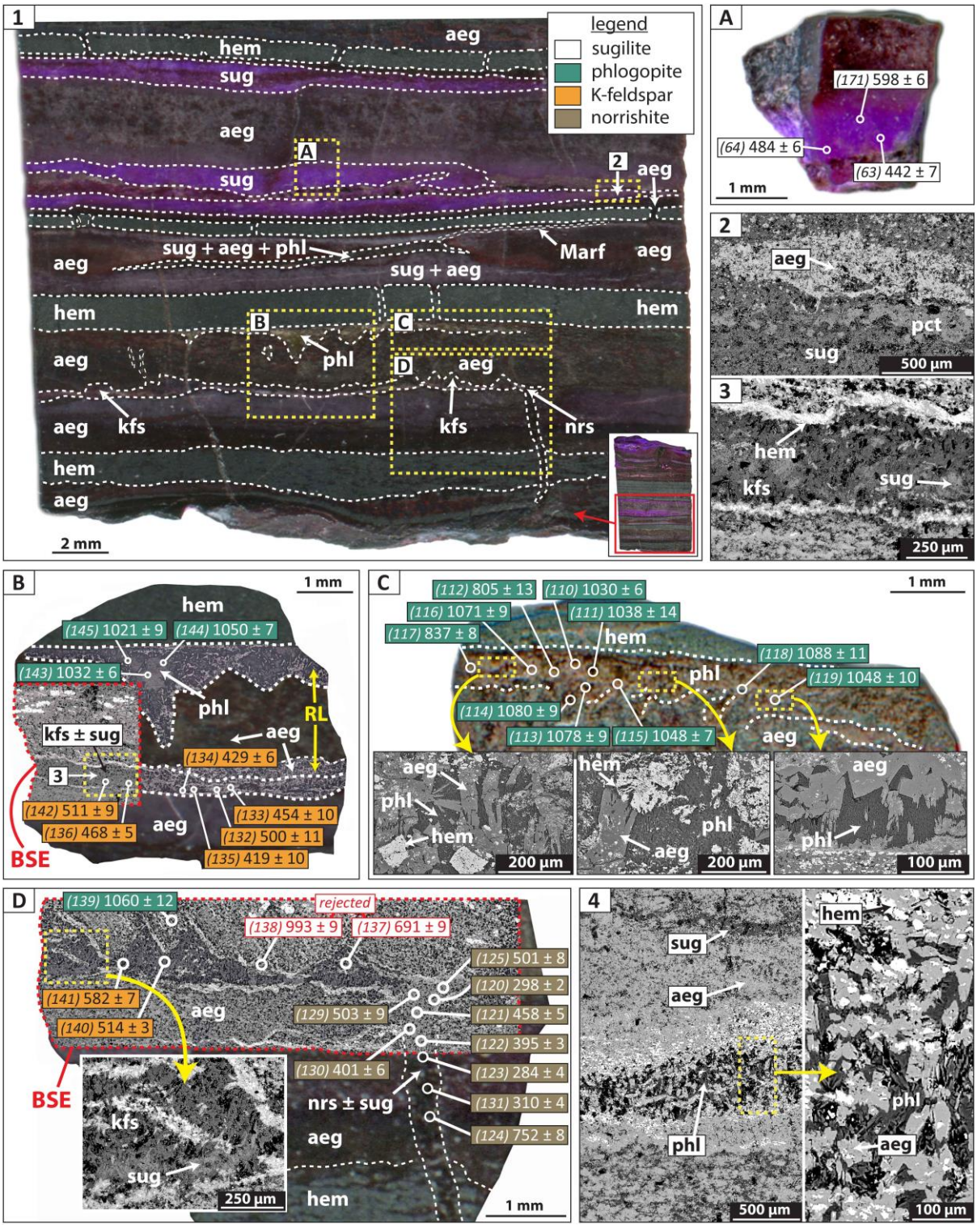

Figure 5. (1) Polished wafer scan showing the chiefly bedding-parallel development of accessory K-bearing minerals (phlogopite, K-feldspar, magnesio-arfvedsonite). Yellow dotted line outlines targeted dating sites. (2) Pectolite within sugilite laminae is only subordinate. (3) K-felspar is usually intergrown with fibrous sugilite and form laminae bounded by microplaty hematite and aegirine. (4) Phlogopite lens comprising coarse-grained granular aegirine overprinted by hematite implies localized recrystallization (BSE). (A) Sugilite laminae commonly show disparity in Ar-Ar ages. (B, C & D) Composite BSE-reflected light-scanned images. Remnant phlogopite (1007 ± 9 Ma, 2σ, n=13) in proximity to K-feldspar laminae comprising reset dates (479 ± 7 Ma, 2σ, n=8). Insets are BSE images. Note the coarse-grained aegirine around targeted phlogopite sites and the close association of K-feldspar with sugilite.

Figure 5. (continued) Norrishite veinlet shows very inhomogeneous age data. Laser spots are circled and spot ages (Ma) are shown at 1σ. aeg = aegirine, hem = hematite, kfs = K-feldspar, Marf = magnesio-arfvedsonite, nrs = norrishite, pct = pectolite, phl = phlogopite, sug = sugilite

Hematite forming inclusions or overprinting coarse-grained aegirine within these structures supports recrystallization associated with phlogopite precipitation (Figure 5.4). The remaining spot dates (*146, 147, 148, 150*) mostly reflect intergranular phlogopite closely associated with prismatic aegirine and platy hematite or sparse masses in sugilite laminae and differ with each other by up to 125 ± 40 Ma and with the estimated weighted mean by 19 ± 9 Ma (Figure 6.3, 6B, 6C).

Thirteen in situ $^{40}Ar/^{39}Ar$ dates were collected from mixed K-feldspar grains contained within two distinct thin laminae also hosting sugilite and negligible pectolite. The spot dates of these analyses range between 419 ± 10 Ma (1σ) and 582 ± 7 Ma (1σ), with a weighted mean date of 502 ± 5 Ma (2σ, MSWD = 4.0, n=13) and are drastically different from the obtained phlogopite dates in close proximity (ca. 2 mm) (Figure 5B, 5D). Age data display an asymmetric bimodal distribution with the most prominent age peak being at ca. 505 Ma, followed by second peak at ca. 560 Ma. Fine-grained fibrous sugilite being intimately intergrown with the dating target in certain areas and phlogopite occurring in the vicinity may explain the outlier spots *137* and *138* (691 ± 9 and 993 ± 9 Ma) (Figure 5.3, 5D) which were rejected from the K-feldspar age calculation. Laser spot size used for all previous gas acquisitions was 65 µm in order to minimize contamination from coexisting sugilite and spots were allocated on areas that exhibited >90 K-feldspar content on the surface (Figure 6A). Age variation within individual laminae is still 72 ± 1 and 163 ± 3 Ma respectively which could reflect partial contamination from other phases. Nevertheless, the rather good degree of consistency between K-feldspar $^{40}Ar/^{39}Ar$ dates from different layers adds confidence to the assumption of a single mineral population controlling the obtained ages and thereby the estimated weighted average age of K-feldspar.

Nine $^{40}Ar/^{39}Ar$ spot dates were analysed from norrishite filling a microscopic cross-cutting vein which is affiliated with one of the dated K-feldspar layers (Figure 5D). The spot analyses yielded highly variable $^{40}Ar/^{39}Ar$ dates ranging from 284 ± 4 Ma (1σ) to 752 ± 8 Ma

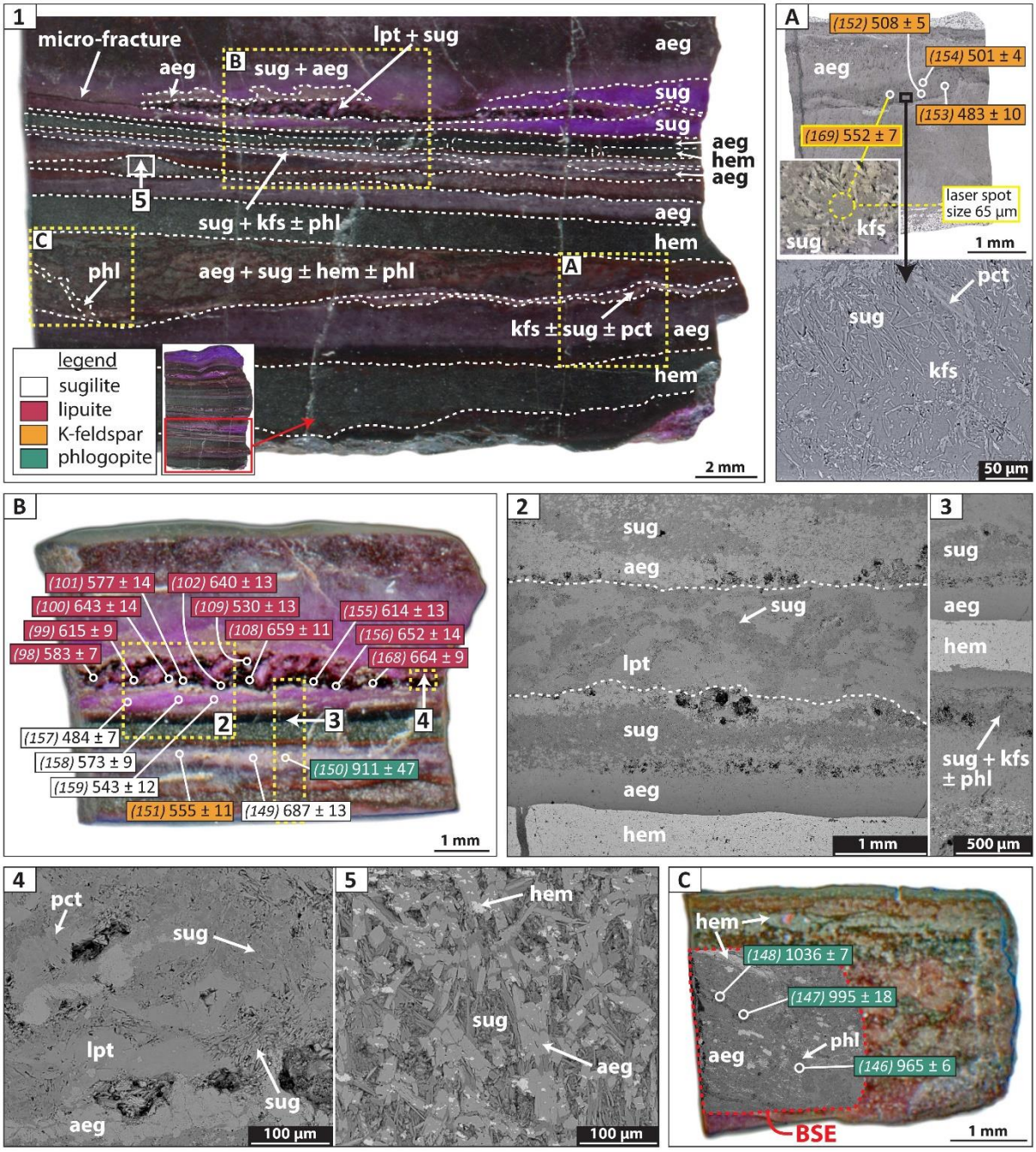

Figure 6. (1) Polished wafer scan with outlined targeted Ar-Ar areas in yellow. Note that lipuite (square B) develops in proximity to a minute micro-fracture. (2-5 are BSE images). (2) Lipuite-sugilite association contained in distinct laminae showing boundaries of high porosity. (3) Thin porous laminae in proximity to lipuite comprising young sugilite and K-feldspar Ar-Ar dates and remnant phlogopite. (4) Granular lipuite masses are intricately mixed with needles of sugilite and minor pectolite, but occasionally allow for ablation of lipuite within 65 or 85 micron-sized circles. (5) Granular recrystallized aegirine with late-stage precipitated sugilite. (A) Reflected light microscope (top) and digitally manipulated BSE image to accentuate the texture (bottom) displaying the presence of sugilite fibers within K-feldspar laminae, the later ablated inside 65-micron laser spots. (B) Detail of lipuite-containing target area showing a weighted mean of 616 ± 6 Ma (2σ, n=10) for this mineral. (C) Intergranular phlogopite in aegirine-hematite broadly layer retains original argon. Laser spots are circled and spot ages (Ma) are shown at 1σ. aeg = aegirine, hem = hematite, kfs = K-feldspar, lpt = lipuite, pct = pectolite, phl = phlogopite, sug = sugilite

(1σ) and displaying a non-normal distribution with three poorly determined peaks at ca. 300, 400 and 500 Ma. There is no apparent relationship between date and position of spot within the vein. Although EDS analyses clearly documented a wide presence of norrishite in the vein, which also has a distinct brighter appearance under backscattered electron imaging due to its higher manganese content in comparison to other gangues, some contamination from coexisting sugilite cannot be ruled out. In a like manner to the dominant feature seen in the rest of the sample, space occupied by intricately associated platy norrishite grains is very porous. The much higher ^{40}Ar and ^{39}Ar measured counts with respect to background levels render the above as robust measurements and thus are further considered in the discussion below.

Fifteen spots on lipuite granular masses from two different sample areas yielded dates ranging from 530 ± 13 Ma (1σ) to 673 ± 11 Ma (1σ) and a weighted mean of 613 ± 5 Ma (2σ, MSWD = 3.99, n=15). Age data are scattered but show a slightly asymmetric bimodal distribution with the most pronounced peak at ca. 584 Ma and a second one at ca. 650 Ma. There is no apparent relationship between date and geographic distribution within the sample, given that 10 spots are paragenetically associated with fibrous sugilite and confined within a thin lamina in the vicinity of a minute joint (Figure 6.2, 6.4, 6B), whereas the rest 5 spot dates derive from within a cross-cutting K-magnesio-arfvedsonite vein disrupting the uppermost part of the sample (Figure 7.1, 7B). In the latter case, lipuite co-occurs with K-magnesio-arfvedsonite but is not necessarily paragenetically affiliated with the latter, in view of it being precipitated in areas of higher porosity, overprinting veins boundaries and spilling into adjacent sugilite- and aegirine-rich areas (Figure 7.2, 7.5). Lipuite ablates in a distinct way, producing ellipsoidal pits on a somewhat softer material and this can be used as an additional criterion for assessing the mineralogical purity of the analysed spots (Figure 7.3, 7.4). A traverse across the lipuite infill in Figure 7B (*spot 84-88*) exhibits a shift from younger to older dates (586 ± 9 to 673 ± 11 Ma), of which the latter spot (*88)* corresponds to a rather spherical laser ablation pit, possibly implying incorporation of material from amphibole or sugilite occurring beyond a lipuite cover. It is thus noted that exclusion of these older dates (n=4) moves the lipuite weighed mean age towards ca. 600 ± 6 Ma.

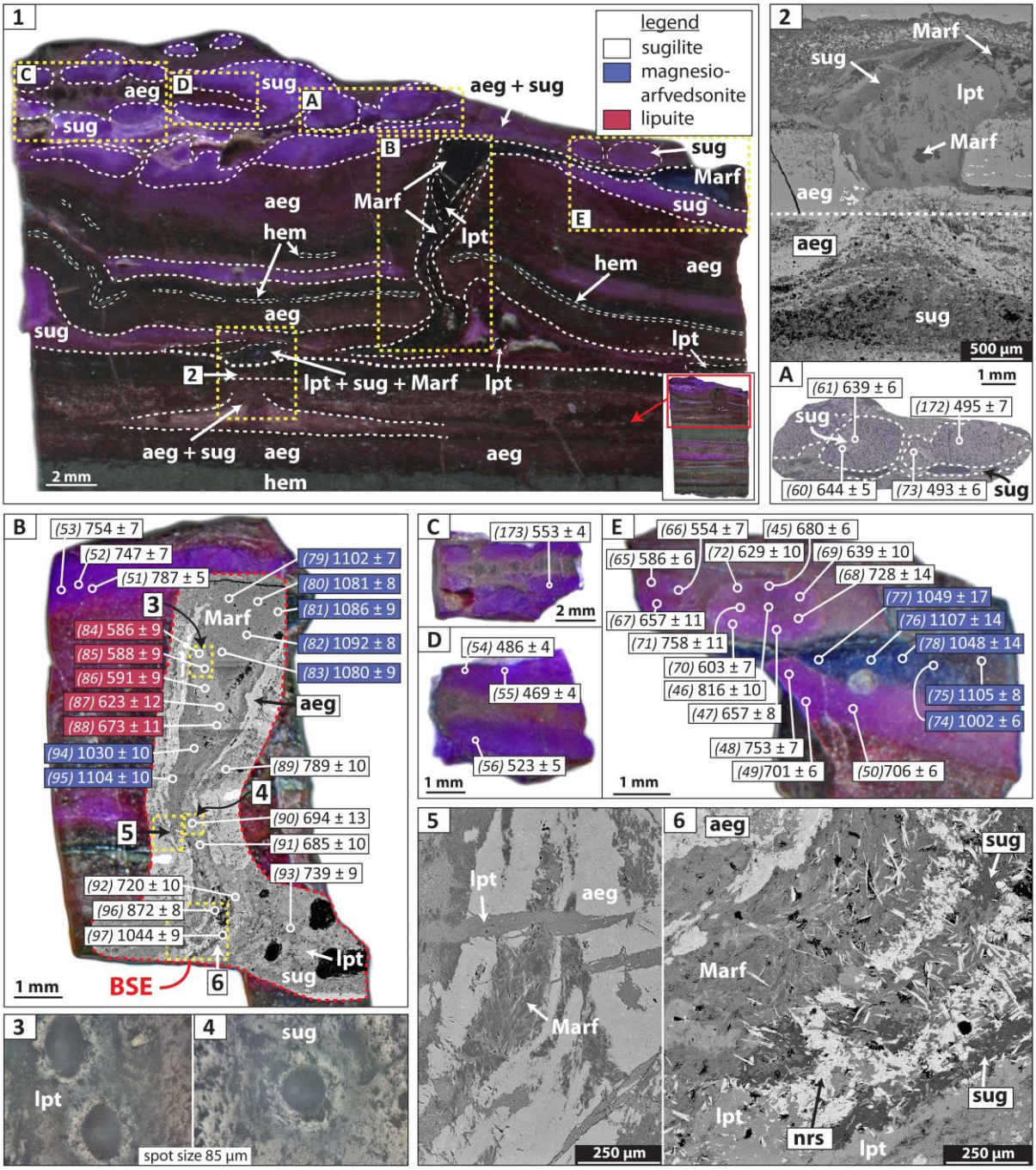

Figure 7. (1) Polished wafer of the topmost sample part disrupted by a minute cross-cutting amphibole vein. Dating sites outlined by yellow dotted line. (2) Lipuite crystallizes discordantly to aegirine-sugilite laminae and encompasses arfvedsonite. (3 & 4) Laser ablation pits on lipuite are ellipsoidal, an additional post-analysis criterion to distinguish them from nearby sugilite pits. (5) Lipuite overprinting vein boundaries supports a later origin. (6) Needlelike norrishite associated with a remnant (1044 ± 9 Ma) Al-dominant member of sugilite. (A, C & D) Reflected light and polished wafer images of the targeted sugilite ovoidal structures showing young (532 ± 35. Mα, 2σ, n=8) and rather variable dates. (B) Composite polished wafer-BSE image of the central amphibole vein and young (608 ± 8 Ma, 2σ, n=5) paragenetically non-affiliated lipuite. (E) Sugilite reset-dates are highly inhomogeneous but distinctly older (669 ± 22 Ma, 2σ, n=14) in the vicinity of arfvedsonite. Laser spots are circled and spot ages (Ma) are shown at 1σ. aeg = aegirine, hem = hematite, kfs = K-feldspar, lpt = lipuite, Marf = magnesio-arfvedsonite, nrs = norrishite, pct = pectolite, sug = sugilite

Twelve spot dates were collected from fine-grained (50-100 µm) tabular K-magnesio-arfvedsonite cross-cutting sugilite and aegirine layering and pooling in an adjacent domain along bedding (Figure 7.1, 7B, 7E). The population of spots dates ranges from 1002 ± 6 Ma (1σ) to 1107 ± 14 Ma (1σ) and shows a weighted mean of 1069 ± 6 Ma (2σ, MSWD = 3.97, n=12). Data distribution is slightly skewed left towards older ages showing a peak at ca. 1095 Ma. A weak relationship between location of analysis and date exists, with the latter being somewhat younger (on average ca. 56 Ma) closer to lipuite or sugilite.

Finally, forty-nine spots collected from sugilite aggregates display the widest range of apparent ages from 442 ± 7 Ma (1σ) to 1044 ± 9 Ma (1σ). Clear-cut relationships are observed between distribution of analyses and acquired dates. Data are skewed right towards younger ages with a conspicuous peak at ca. 482 shown in KDE plot and corresponding to a weighted mean age of 479 ± 17 Ma (2σ, MSWD = 0.054, n=11). The former dates are represented by purple sugilite of the topmost monomineralic layer (Figure 3A, 7.1, 7A, 7C, 7D) as well as by a thin (0.5-1mm mm) reddish-purple sugilite and K-feldspar laminae, with minor associated pectolite and phlogopite, forming in the vicinity of the lipuite occurrence (Figure 5.2, 5A. 6.2, 6B). A handful of older sugilite ages (e.g., 639 ± 6, 644 ± 5 Ma, *spots 60, 61*) also exist in the aforementioned occurrences and therefore a degree of overlap with the following age group. The majority of spot dates define a weighted mean of 655 ± 14 Ma (2σ, MSWD = 1.24, n=31) and a not-too-distant major peak at ca. 690 Ma (KDE plot), highlighting together with the relatively small MSWD, the rather moderate scatter of this second group of dates. The previous dates correspond to sugilite hosted by the dated amphibole vein and the sugilite layer and ovoidal structures occurring in the immediate vicinity of K-magnesio-arfvedsonite (Figure 7B, 7E). No clear relationship can be discerned between dates and location of analysis, despite the density of analysed spots within the ovoidal sugilite structures. It is noted though that the oldest age (816 ± 10 Ma, *spot 46*) derives from the centre of the two-dimensional section of one such structure. The remaining spot dates were acquired from a distinct reddish-purple sugilite laminae (n=5) and additionally from the Al-dominant sugilite end-member (*spots 96, 97*) associated with needlelike norrishite and found within the central K-magnesio-arfvedsonite vein (Figure 3B, 7.6, 7B). The weighted mean of these last spot dates is 892 ± 32 (2σ, MSWD = 0.64, n=7).

5. Discussion

5.1 $^{40}Ar/^{39}Ar$ data interpretation and implications for the alteration history of the KMF

$^{40}Ar/^{39}Ar$ age results obtained in this study exemplify the importance of detailed age information that complex targets can disclose when interrogated by the high-resolution ultraviolet laser ablation technique. Compositional and textural information for the relationship between K-bearing minerals within the same metasomatically overprinted sample, combined with high-spatial resolution in situ $^{40}Ar/^{39}A$ analyses, are seen throwing light upon how argon is behaving during the evolution of a thus far poorly constrained low-temperature hydrothermal system, since Proterozoic times. In this regard and as discussed below, the extracted age information reflects two distantly spaced in time geological events imprinted on altered iron-formation of the Hotazel Member. One associated with the main hydrothermal enrichment of the giant manganese ores of the KMF and a second more elusive alteration event of unknown extent and origin that has thermally disturbed and/or recrystallized pre-existing gangue mineralogy. This disturbance in the Ar system is evidently depicted in Figure 8 which includes individual spot dates and probability density distribution curves (PDPs and KDEs) for all six potassium-bearing phases.

At present, direct geochronological constraints on the structurally-controlled hydrothermal enrichment of the northernmost part of the Kalahari Manganese field are limited to data derived essentially from the minerals sugilite and norrishite which have yielded $^{40}Ar/^{39}Ar$ ages of 1048 ± 6 Ma and 1010 ± 7 Ma respectively (Gnos et al; 2003). Earlier obtained Pb-Pb (1270 ± 30 Ma) and Rb-Sr (1350 ± 269 Ma) ages on sugilite have been refined by recent studies which have set the time span of hydrothermal activity in the area between 1139 ± 3 Ma and 1064 ± 3 Ma, ages that in turn coincide with the main pulses of igneous emplacement during the Namaqua-Natal orogeny (chapter 3). New $^{40}Ar/^{39}Ar$ ages from K-magnesio-arfvedsonite (1069 ± 6 Ma) and phlogopite (1006 ± 8 Ma) in this study corroborate the previously established timing of hydrothermal activity in the KMF and evidently suggest formation of these minerals during the latest stages of alteration. This in agreement with the

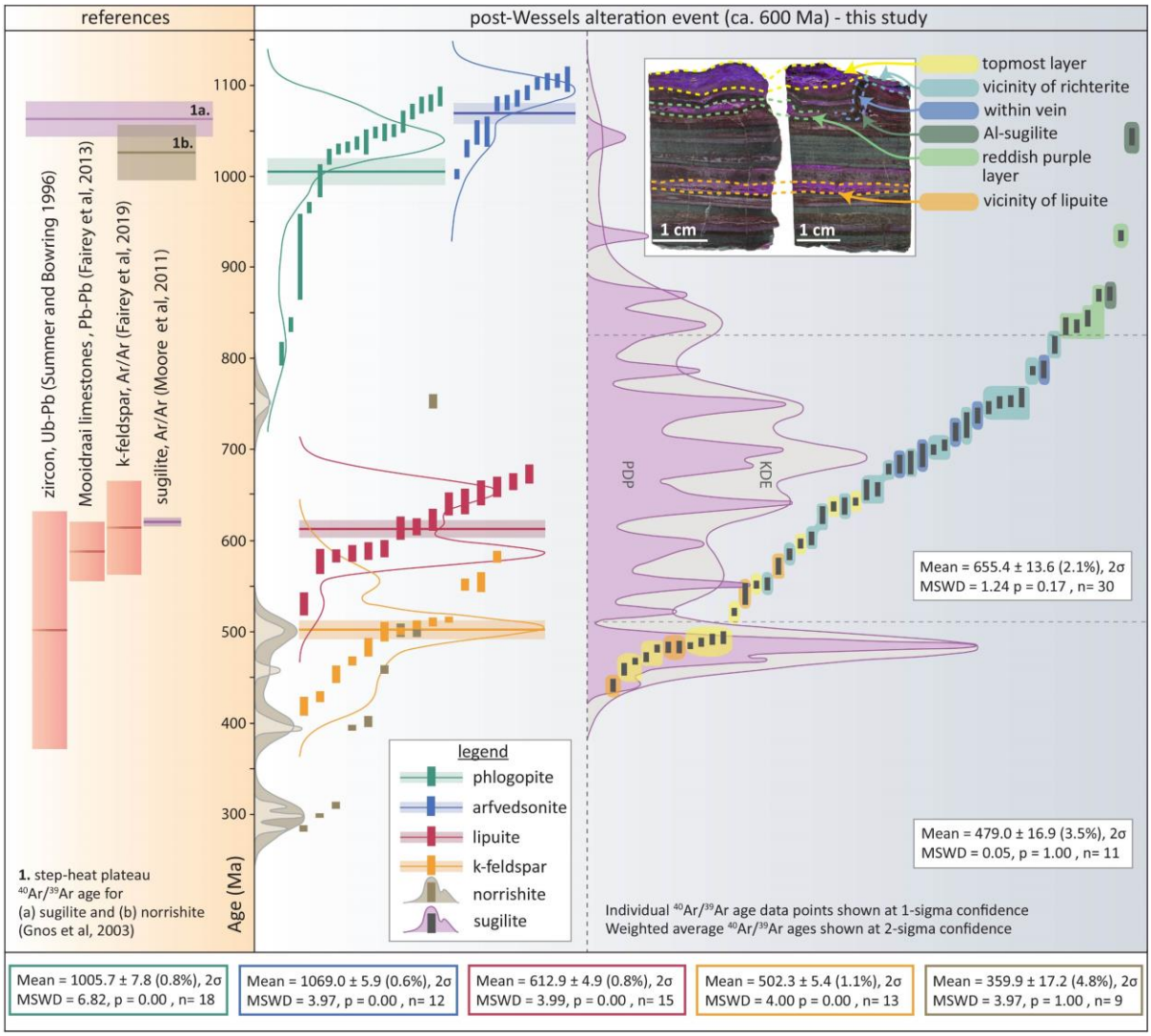

Figure 8. Age distribution profiles of in situ $^{40}Ar/^{39}Ar$ ages (1σ) for all 6 dating targets, weighted mean averages represented by horizontal bars (2σ) and kernel density estimation plots (KDEs). Colour-coded individual ages of sugilite are matched with their corresponding textural/compositional characteristic or location in the sample as that delineated in the upper right corner. References from available Namaqua and younger ages from the KMF and PMF are also included. Note the mildly disturbed age profiles of the older minerals, the conspicuous Ar-loss profile of sugilite related to the ca. 600 Ma lipuite emplacement age and the prominent peaks at ca. 500 Ma which coincide with the closure of the Ar-system.

observed textures of cross-cutting arfvedsonite veins dislocating sugilite-aegirine bedding and phlogopite being associated with recrystallized aegirine.

High-temperature common amphiboles in igneous and metamorphic settings such as hornblende or glauconite show excellent argon retention properties (McDougall and Harrison; 1999), but contrastingly, amphiboles like arfvedsonite or riebeckite in low-temperature metamorphic or hydrothermal settings have been shown to be less retentive of

radiogenic argon ($^{40}Ar^{*}$) (e.g., Tulloch and Dunlap; 2006). For example, the latter authors have argued that Ar-closure temperature for arfvedsonite in late-stage alteration related to granite emplacement is expected to be much lower than that of hornblende (ca. 500°C) for instance and more in the range of the $^{40}Ar/^{39}Ar$ white-mica system (350-445°C) (Hodges; 1991, Harrison et al, 2009). High MSWD (>1) and probability distribution plots indicate that the 'true' age of the targeted K-magnesio-arfvedsonite and phlogopite has been almost certainly influenced by heated fluids subsequently to their deposition (Figure 8). Hence, ages recalculated for MSWD ≤ 1 would more accurately represent crystallization ages. The recalculated ages are 1091 ± 7 Ma (n=10) and 1037 ± 8 Ma (n=16) for K-magnesio-arfvedsonite and phlogopite respectively, being thus 22 ± 1 and 31 Ma older. Although this may not seem as a substantial age difference, it notably demonstrates the thermal disturbance of the ca. 1.0 Ga aforementioned minerals. A combination of low A-site occupancy and chemical composition controlling ionic porosity of arfvedsonite, as well as its rather fine-grained size (50-100 μm) may be the causative agents for a considerable decrease in T_c of the mineral in comparison to that of other amphiboles (Dahl; 1996, Scharf et al; 2016). The latter scenario renders in turn more feasible the case of Ar-loss in response to fluid circulation subsequently to the main Wessels event, having though equivalently low-temperature (ca. 200-400°C) (Gutzmer and Beukes 1996b; Lüders, 1999), in accordance with the expected shallow-level brine-related alteration in the geological regime of the KMF. Other authors (Wartho; 1995a) have interpreted argon loss profiles in amphiboles in terms of mixtures of different mineral generations or contamination by potassium-rich less retentive phases. Amphibole spot ages in this study are thought to represent monomineralic aggregates but since lipuite is seen precipitating in the same vein minor contamination cannot be entirely excluded.

Nevertheless, apart from explaining the mildly disturbed phlogopite and K-magnesio-arfvedsonite age profiles, an interpretation invoking extensive loss of radiogenic argon ($^{40}Ar^{*}$) is also the most geologically reasonable explanation for the large age inhomogeneity and gradients of sugilite that exist at the mm- if not μm-scale. The measured ages ranging from 442 ± 7 Ma (1σ) to 1044 ± 9 Ma (1σ) can be interpreted as the result of reheating and possibly recrystallization related to fluid introduction which has caused loss of the previously

accumulated $^{40}Ar^{*}$ within sugilite lattice. We consider the emplacement of lipuite along joints and small-scale discontinuities in the sample to be central to understanding the sugilite age profile. According to Gu et al (2019) who first described this entirely new phyllosilicate mineral from the neighboring N'Chwaning mine, lipuite is characterized by SiO_4 tetrahedral sheets which are linked together by a series of cations such as Na^{+}, K^{+}, $Mn^{3+,}$ Mg^{2+} and P^{5+}. Apart from phosphorus, these elements could have been sourced by former calc-silicate sugilite-pectolite assemblages, aegirine and braunite. N'Chwaning lipuite is in addition documented from analogous parageneses, i.e., coexisting sugilite, pectolite and richterite among others and regularly hosts norrishite and namansilite ($NaMn^{3+}Si_2O_6$) inclusions. Its precipitation apparently postdates that of hematite, aegirine and braunite in view of commonly observed replacement textures.

As illustrated in Figure 8, lipuite has a weighted mean age of 613 ± 5 Ma (2σ) which falls in between two sugilite age components, an older and not too distant mean age of 655 ± 14 Ma representing the bulk of analysed spots and a younger well-established weighted mean age of 479 ± 27 Ma, which is further underpinned by contemporaneous K-feldspar (502 ± 5 Ma). However, if the tentative bimodal age distribution of lipuite is regarded, then the older age peak at ca. 650 Ma overlaps with the mean sugilite age of ca. 655 Ma. Considering lipuite as precipitate of a novel reheating event at ca. 613 Ma, sugilite age spread can be explained by variable resetting and thermal re-equilibration of an originally ca. 1.0 Ga sugilite, which has retained values close to its originally accumulated $^{40}Ar^{*}$ only in the Al-dominant analysed variety (1044 ± 9 Ma, *spot 97*). Other factors controlling the age variability of sugilite on the short temporal scale and closer to the ca. 655 Ma weighted mean could potentially be different episodes of precipitation, removal and redistribution of trapped argon during recrystallization, variability in thermal diffusion of argon during initial cooling or differential thermal reset in response to the cross-cutting amphibole vein formed at the waning stages of the ca. 1.0 Ga hydrothermal event. Furthermore, certain age spots could represent mixed ages not only from different sugilite populations but also different potassic-rich mineral grains. This is a limitation induced by the fine-grained and intricately associated mineralogy but also by the laser-probe method which only allows for two-dimensional observation of the ablation spot circles.

Nothing is known of lipuite suitability for $^{40}Ar/^{39}A$ dating, its diffusional behavior and Ar-closure temperature but in principle, it being a K-rich phyllosilicate means that it is presumably a suitable target. Age data from this study show a systematic age spread (MSWD=3.9, n=15) which according to probability plots reflect two closely arranged populations. Timing of the perceived alteration event causing thermal reset of older gangues would reasonably correspond more closely with the earliest crystallization age of lipuite, marked by a weighted mean age of 643 ± 7 Ma (2σ, MSWD=1.24, n=9). The latter age further overlaps with the reset age for the bulk of dated sugilite in the sample, which is 655 ± 14 Ma (2σ, MSWD = 1.24, n=31). The above promising results on lipuite confirm that it is suited for $^{40}Ar/^{39}A$ dating and despite its current rarity it begs for suchlike applications on other uncommon hydrous K-bearing silicate or phosphate accessories found in pegmatites, such as englishite or tiptopite (e.g., Peacor et al; 1987), that can potentially illuminate the alteration history of their settings. Variation in $^{40}Ar/^{39}A$ sugilite age with respect to the location of the laser ablation sites is related to: (1) the presence of distinct sugilite laminae and (2) the sugilite paragenesis and on occasion the vicinity of sugilite to younger (lipuite) or older (magnesio-arfvedsonite) phases (Figure 8). The single observation of K-feldspar weighted mean age (502 ± 5 Ma) essentially overlapping with the youngest and most conspicuous sugilite weighted mean age (479 ± 27 Ma), the latter being controlled not only by spots on coexisting sugilite-K-feldspar laminae but mainly by 'young' sugilite spot ages from the topmost monomineralic sugilite layer, provides solid evidence for a geologically meaningful episode beyond which no significant Ar-loss occurred.

In other words, the aforesaid younger episode at ca. 500 Ma has bearing on the emplacement of lipuite and thermal reset of gangues but is associated with either the age of cessation of hydrothermal activity or most probably the cooling history of thermally disturbed sugilite and K-feldspar. It has been demonstrated that especially low-temperature alkali-feldspar is sensitive to even mildly elevated temperatures and $^{40}Ar^{*}$-loss from this mineral is controlled directly by subgrain micro-textures (Alberéde et al; 1978, Harrison and McDougall; 1982, Parsons and Lee; 2005). The considerable age spread of dated K-feldspar (MSWD=4.0) possibly indicates diffusive loss of argon during cooling below the T_c. K-feldspar is documented in this study being paragenetically affiliated with albite and barite in aegirine-

bearing iron-formation, meaning that at least one feldspar generation was crystallized during Namaqua orogeny (1.2-1.0 Ga). As a result, the 'young' ca. 500 Ma K-feldspar represents either a later generation or most likely a product of thermal reset during the ca. 650 Ma fluid alteration event. Such interpretation appears to be compatible with older 'remnant' ages of 691 ± 9 and 993 ± 9 Ma (spots *137* and *138*) obtained from a lamina mapped by SEM as K-feldspar.

According to its age distribution profile, norrishite has indisputably suffered Ar-loss, displaying the younger recorded ages in the sample at ca. 300 Ma (n=3). Previously dated norrishite from Wessels has shown a slightly discordant age spectrum with younger age steps defining an ca. 850 Ma age, interpreted to reflect alteration by fine-grained clay minerals along its rims (Gnos et al; 2003). Recoil-implanted ^{39}Ar has been also invoked to explain younger age steps by the previous authors. Whatever the correct interpretation and geological meaning of the above alteration age, in this study norrishite has been shown to be either heavily altered or unsuitable for dating at least in its very fine-grained and porous textural form. However, if norrishite is as suggested prone to alteration and had lost $^{40}Ar^{*}$ both before the ca. 600 Ma hydrothermal event but also later on, a very scattered age profile, much like the one obtained, could have been produced.

5.2 Revision of sugilite $^{40}Ar/^{39}Ar$ geochronology and nature of the ca. 600 Ma event

Although several attempts on sugilite dating so far have shown that it is generally retentive of radiogenic ($^{40}Ar^{*}$) argon (Gnos et al; 2003; chapter 3) and consequently can provide age constraints on ancient low-temperature hydrothermal events (ca. 1 Ga), this study clearly demonstrates that argon loss may occur after its deposition. The thermal response of the mineral to fluid-related heating, at least as documented in this study from Wessels mine, is characterized by partial re-equilibration of the Ar-system with regard to the heating event. Despite some ambiguous interpretations, owing also to dating of possibly mixed mineral populations and phases, a signal recording various degrees of thermal reset is shared by almost all other K-bearing minerals associated with sugilite. This is of particular interest since the studied sample is supposed to have followed a simple cooling history, with

the Ar-clock behaving as a closed system after the hydrothermal metasomatism at ca. 1 Ga, by reason of it being accommodated by lithostratigraphic successions considered to be at large thermally undisturbed since the Proterozoic times. In the absence of any collisional tectonics and associated hydrothermal-metamorphic events along the edges of the Kaapvaal Craton, the only recorded radiometric ages in the KMF following Wessels event are linked to the onset of supergene chemical alteration along the Kalahari unconformity at 77 ± 7.5 Ma (Vafeas et al; 2018) and subsequent recent supergene cycles (27.8 to 5.2 Ma) which resulted in the local upgrade of pristine ore to high-grade todorokite-manganomelane manganese ore (Gutzmer et al; 2012).

Crystal structure refinements of sugilite reported by Armbruster and Oberhänsli (1988), have demonstrated that K resides in a large cavity (C site) situated between two double-ring silicate units, while Na and Li possess distorted coordination in their corresponding sites. The possibility of excess argon residing in the cyclosilicate structure of sugilite was discarded by Gnos et al. (2003) who presented $^{40}Ar/^{39}Ar$ step-heating spectrums displaying correspondence between the highest step age and the most gas-rich step. The same authors suggested low diffusive Ar-loss and a closure temperature in the range of amphiboles or micas (probably >400^{o}C) on the basis of low ionic porosity of sugilite, a measure that can be calculated as a proxy of the diffusion behavior of silicate minerals (Fortier and Giletti; 1989).

Another attempt of sugilite $^{40}Ar/^{39}Ar$ dating on material occurring in the Postmasburg manganese field (PMF), some 70 km to the south of the KMF and hosted by comparable alkali-rich assemblages within manganiferous sediments at Bruce iron-ore mine, yielded an age of 620 ± 3.3 Ma (Moore et al; 2011), thus showing great resemblance with the sugilite reset age in this study (655 ± 14 Ma). This 'young' sugilite age was tentatively interpreted by the previous researchers as representing isotopic resetting during a subsequent thermal event, on the grounds of it being a product of the same ca. 1.0 Ga hydrothermal event responsible for ore enrichment at Wessels mine. The coincidence of our $^{40}Ar/^{39}Ar$ age with that from Bruce mine provides strong evidence for such a secondary alteration event. Another important argument in favor of a thermal reset of the Bruce mine sugilite is a series of recently

acquired $^{40}Ar/^{39}Ar$ ages from diverse calc-silicate gangue assemblages belonging to the Postmasburg manganese field lithologies, invariably recording a strong Namaqua orogenic signal between ca. 1.2 and 1.0 Ga and therefore suggesting coeval Namaqua-related hydrothermal activity (chapters 2, 5 and 6). Additionally, a recent study identified an earlier Neoproterozoic event having affected the PMF manganese ores in proximity to the Blackridge Thrust and the Olifantshoek-Transvaal unconformity at around 628 Ma (Fairey et al; 2019). In particular, $^{40}Ar/^{39}Ar$ in situ ages on K-feldspar showed a range between 681 ± 3 and 517 ± 6 Ma, with two distinct means at 648 ± 20 and 557 ± 27 Ma. These mean ages closely resemble the ones obtained in this study (ca. 650 and 500 Ma), which are interpreted as corresponding to the initiation of thermal reset and cooling below the closure temperature of the studied minerals respectively or recording a late-stage pulse of the ca. 600 Ma. In yet another example, U-Pb dating of the Mooidraai Formation in the KMF yielded a discordia line with a lower intercept age of 588 ± 31 Ma, for which the most likely interpretation invoked a superimposed Neoproterozoic fluid alteration introducing uranium into preexisting stylolites developed throughout the limestone sequence (Corfu et al; 2009, Fairey et al; 2013). Furthermore, U-Pb zircon analyses from a tuff within the upper Campbellrand dolomite in the neighboring PMF provide additional, though less reliable evidence for a disturbance at Neoproterozoic times, supported by a lower intercept age of 502 ± 129 Ma which has been interpreted as evidence for Pb-loss (Sumner and Bowring; 1996). However small, this number of emerging Neoproterozoic ages (Figure 8) imply that a variety geochronologic clocks in the Northern Cape have been affected by secondary alteration which likely shares the same origin as the one rigorously documented in the present study.

The nature of this thermal event remains elusive for the time being. However, taking into consideration the very mild disturbance of the Ar-system recorded by arfvedsonite and phlogopite and the partial isotopic re-equilibration displayed by the sugilite age profile it can be deduced that the temperature was barely in excess of the closure temperature (T_c) of the abovementioned minerals. T_c of sugilite could have been instead somewhat lower than previously suggested (>400°C) owing to grain size or mineral chemistry but lack of complete thermal overprint of the sample generally suggests the presence of a low-temperature fluid. Moreover, the few remaining sugilite ages from the same mine have not recorded this

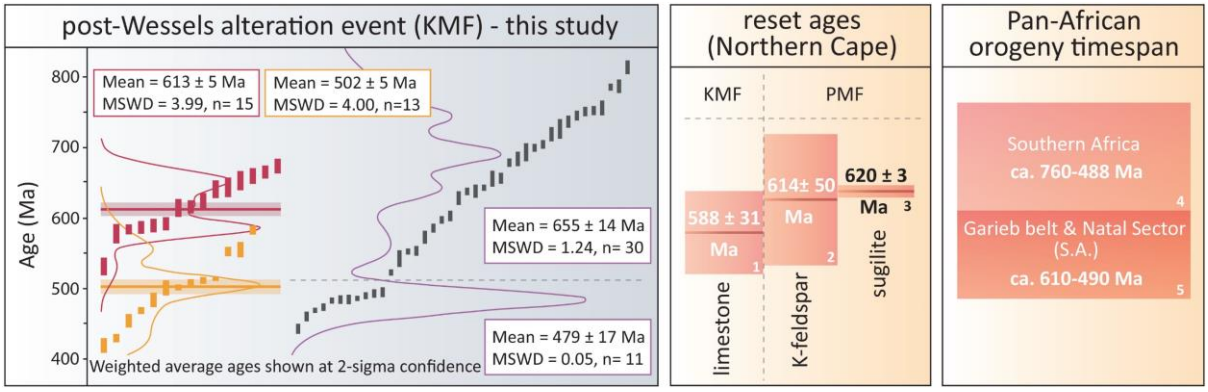

Figure 9. Comparison of $^{40}Ar/^{39}Ar$ age data related to the secondary alteration event at ca. 600 Ma against ages from literature, highlighting the overlap with the Pan-African orogeny. (1) (Fairey et al; 2013, Corfu et al; 2009 (2) Fairey et al; 2019 (3) Moore et al; 2011 (4) Kröner and Stern; 2004, Gray et al; 2006, Lehmann et al; 2016 (5) Jacobs and Thomas; 1996, Frimmel and Frank; 1998.

thermal reset. Hence, this event can be envisaged as localized transient reheating focusing possibly on prior fluid conduits such as normal faults, while heat could have been conducted away rapidly from gangue mineralogy or reduced due to contribution from 'cold' meteoric fluids lowering temperature during fluid-rock interaction. $\delta^{18}O$ values obtained by broadly monomineralic aegirine, sugilite and magnesio-arfvedsonite laminae, exhibit very good homogeneity, ranging from 10.6 to 11.7 (chapter 3). This indicates that there has been no significant isotopic exchange between the oxygen isotopes of the introduced fluid and the preexisting gangue mineralogy since the latter retain an $\delta^{18}O$ signature that has been previously interpreted to reflect the isotopic composition of regional saline and alkali-rich basinal brines (chapter 3). The only additional information provided by the presence of lipuite is the introduction and/or redistribution of phosphorus during this secondary alteration.

Despite the localized imprint of this event, the emerging ca. 600 Ma radioisotopic signal in the Northern Cape suggests that the causative agent of fluid generation and migration was probably a shared response to a **pervasive but stratigraphically restricted large-scale event**, much like the prior Wessels event. The age similarity between this Neoproterozoic event and Pan-African orogeny has been previously noted along with the vast distance (~500 km) between the study area and the documented Pan-African orogenic belt (Moore et al; 2011, Fairey et al; 2019). Figure 9 illustrates the timespan of recorded Pan-African ages (610-490 Ma) in the Gariep belt and Natal Sector of South Africa, which also

preserve mica cooling ages (1006-976 Ma) from the Namaqua orogeny (Renne et al; 1990, Frimmel and Frank; 1998). Interestingly, the younger sugilite and K-feldspar ages from this study strongly clustering at ca. 500 Ma, coincide with the final movements of the pan-African orogeny in the distal Damara belt encompassing the Kalahari Craton (Gray et al; 2006). The dynamic coupling between tectonic evolution of the crust and continental-scale groundwater fluid flow was firstly stressed out by Oliver (1986) and since then both field and basin modelling evidence have demonstrated transportation of fluids over distances of the scale of hundreds of kilometres within extensive sedimentary basins (Kharaka et al; 1985, Garven; 1995). Specifically, the Ar-Ar system was employed to document regional-scale fluid migration related to continent-continent convergence along distances of approximately 180 kilometres (Mark et al; 2007). Whereas at this point we remain uncertain as to the exact origin of the ca. 600 Ma event in the Northern Cape, we consider the possibility of fluid migration as a far-field response to the distal Pan-African orogeny to be a likely scenario, which however requires further study before it can be ascertained.

6. Summary and conclusions

In this paper, we revisited the alkali gangue mineralogy associated with the ore upgrade of the Kalahari manganese field and placed focus on the K-bearing minerals as a means to extract new $^{40}Ar/^{39}Ar$ age information on timing of hydrothermal activity. The high-spatial resolution dating approach permitted critical isotopic information to be obtained from six distinct mineral targets recording highly variable ages. On the basis of mineralogical, geochronological and cross-cutting relationships and in accordance to previous studies, the documented alteration processes at play have been the following:

(1) Sodic metasomatism related to hydrothermal upgrade of the manganese ore at Wessels mine produced aegirine- and sugilite-bearing iron-formation and in like manner altered hematite lutite. K-feldspar, albite, phlogopite and barite among other gangues precipitated as part of this event.

(2) Magnesio-arfvedsonite veins formed during the late stages of alteration.

(3) An episode of reheating caused partial to complete thermal resetting of sugilite and K-feldspar and resulted in minor Ar-loss from phlogopite. Coevally formed lipuite provides the best estimate of this fluid-assisted reheating which occurred at around 643 ± 7 Ma.

(4) Cessation of hydrothermal activity and/or cooling below the Ar-closure temperature of K-feldspar and sugilite took place at ca. 500 Ma.

Our study asserts that caution should be exercised when interpreting sugilite and coexisting alkali-rich mineral dates as crystallization ages during any future endeavors to further resolve the timing, origin and duration of hydrothermal activity in the Northern Cape. In light of comparable radioisotopic ages from the wider area we strongly encourage such research in order to investigate the emerging link between hydrothermal activity and the Pan-African orogeny which although still puzzling, seems to slowly gain substantiating evidence.

PART THREE

Postmasburg Manganese field (PMF)

Chapter 5

Petrographic, $^{40}Ar/^{39}Ar$ geochronological and stable isotopic evidence for hydrothermal metasomatism of the Postmasburg manganese field during the Namaqua orogeny. Constraints on Fe-Mn mineralization along the western margin of the Kaapvaal Craton, South Africa.

Abstract

The lately discovered western arm (WMD) of the Postmasburg manganese field (PMF) comprises Fe- and Mn-orebodies that essentially lie within the regional Blackridge thrust belt, but otherwise are texturally and stratigraphically equivalent to the presumed 2.0-1.8 Ga karstic-controlled supergene ore accumulations occurring eastwards in the Maremane dome. The profusion of alkali-bearing minerals seen in these ores has been recently documented as the result of regional tectono-thermal events paired unequivocally with the 1.2-1.0 Ga Namaqua orogeny and probably to lesser extent with a later Neoproterozoic thermal event.

The present work reinforces the concept of a genetic link between the metasomatic upgrade of the Kalahari manganese field (KMF) and epigenetic processes recorded in the PMF, by providing in situ $^{40}Ar/^{39}Ar$ dates for hydrothermal Ba-feldspar, phlogopite and other silicates that cover the full time-span of the orogeny, ranging from ca. 1188 to 920 Ma. Specifically, mica evidently record early alteration whereas hyalophane-calcite veins likely record late-stage events of this complex, protracted and multi-stage mineralization system. Our detailed petrographic study in the PMF (WMD) reveals a wealth of diverse minerals (n=42), many comparable to its northern counterpart (KMF) and some firstly reported here, such as apophyllite, macedonite, pyrobelonite and tamaite. The mineralogical record of this locality is further expanded to include unidentified Ba- and Mn-rich silicates, hyalophane, grossular, Mn-carbonates, diaspore, hollandite-coronadite and a series of mica (muscovite, Ba-muscovite, paragonite, celadonite, phlogopite). A series of complex zoned mineral

assemblages in vugs, cross-cutting veins, various replacements, extensive and texturally diverse breccias comprising hematite, aegirine, muscovite, feldspar, hematite and braunite, attest to the repeated reworking of these lithologies. The alkali-rich mineral assemblages developed through a series of reactions with the host rock that caused at least some documented redistribution of the ore metals, more pronounced in late hematite precipitation and replacements by braunite. The associations of banded micas with hematite-rich ore domains and layer-controlled development of other gangue assemblages, emphasizes control from previous layering and possibly points to a shale-like precursor, such as the Olifantshoek shale units, being overprinted.

All recent findings have implications for the evolution of the western margin of the Kaapvaal Craton, which has been pervasively infiltrated by fluids over a horizontal extent of at least 150 km. Similarities between $\delta^{18}O$ (ca. +2.0 to +7.0 ‰, T=215^{o}C) and δD fluid (-65 to -45 ‰) isotopic compositions with that obtained from the hydrothermally upgraded KMF and fluids in Mississippi Valley-type Pb-Zn deposits, suggest that regional-scale infiltration of paleo-fluids involved a broadly uniform source of basinal brines, stored, heated and equilibrated with the successions of the Transvaal Supergroup, before tectonic expulsion and fluid-buffered circulation through the ores produced the pervasive alkali-enrichments. The conspicuous Namaqua overprint in proximity to the Blackridge thrust fault system (Namaqua front), and pre-Namaqua age signals from micas and ore-matrix silicates (1575 ± 12 Ma, age peaks at ca. 1668 and 1491 Ma), that do not conform to the range of Kheis orogeny but broadly overlap with igneous activity associated with the early stages of the Namaqua orogeny in the outer terranes (ca. 1600 Ma), call for a reappraisal of this controversial orogeny and in particular Kheis Province, (eastern Namaqua front), which should be seen as another tectonic zone within the extensive Namaqua Province. Our results contribute to a model that genetically links fluid flow events across the Northern Cape through regional features and structures and focuses on the geodynamic environment of the Fe and Mn ores, as well as on the potential influence of hydrothermal processes in ore genesis, for which little consideration has been paid so far.

1. Introduction

The manganese orebodies of the Postmasburg manganese field (PMF) are widely regarded as pertaining to the supergene genetic type, overall representing residual karst-related accumulations modified by diagenetic/low metamorphic and later supergene processes (Gutzmer and Beukes; 1996a, 1997b). Previous research on these deposits has largely focused on bulk-rock composition and ore mineralogy, despite the presence of many and exotic gangue species that have comparable nature to that of the neighboring Kalahari Manganese field (KMF) and have been broadly attributed to syn- or post-metamorphic events synchronous to the ca. 1.9-1.7 Ga Kheis orogeny.

However, more recent studies that placed main focus on the signatures of alkali gangues (Moore et al; 2011, Costin et al; 2015, Fairey et al; 2019), which are common constituents in new ore discoveries somewhat 10-20 km to the west (wider Kolomela) of the type-locality ores but also within previously unexplored material in the vicinity of the giant iron ore mines in the area (Sishen-Khumani), have provided evidence that hydrothermal assemblages locally superimposed on precursor manganese and ferromanganese ores are much richer and complex than previously recognized and therefore resuscitated interest in the history of hydrothermal activity in the area. Specifically, both common Ba-, Na-bearing and calc-silicate phases such as aegirine, albite, natrolite, banalsite, pectolite-serandite and rare alkali-bearing species such as sugilite, norrishite, noélbensonite or armbrusterite show affinity to Namaqua-related (1.2-1.0 Ga) hydrothermal gangues from the KMF, although two separate $^{40}Ar/^{39}Ar$ ages contrastingly suggest the presence of a distinct Neoproterozoic (ca. 620 Ma) event. A following study on regional barite mineralization established a link between the hydrothermal system in both districts, by providing stable and radioisotopic results supporting common fluid sources expelled during the Namaqua orogeny (chapter 2).

As shown by recent exploration and localized exploitation, PMF ores still bear economic value despite the existence of the neighboring giant KMF and most importantly research on these deposits can potentially furnish good exploration tools and enhance our knowledge on fluid circulation in ancient sedimentary basins. Informed by the former studies, we revisit localities in the wider Kolomela region with an aim to further assess the origin,

characteristics and evolution of the hydrothermal fluid event(s) that have influenced the PMF ores and attempt to provide new age constraints on the formation of alkali-rich assemblages. We further seek to shed light upon the relationship of alkalis and ore genesis, expanding on previous work pointing to a regional-scale hydrothermal ore-upgrade mechanism for preexisting Fe-Mn lithologies (Fairey et al; 2019. Chapter 2).

Isotopic approaches on this mineralization are almost non-existent to date and are apparently impaired by the very fine-grained nature of hydrothermal assemblages and intimate mineralogical intergrowths encountered in these ores. In this study, we attempt to partially overcome this obstacle by thorough petrographic investigation using SEM/EDS techniques prior to material extraction for O-H isotopic analyses and the use of laser ablation in situ $^{40}Ar/^{39}Ar$ where potentially applicable. Our results demonstrate that isotope fingerprinting and geochronology in these ores can provide invaluable information, which in particular corroborates gangue mineral formation in response to the widespread Namaqua-related hydrothermal activity in the Northern Cape. We discuss our results in the wider geotectonic framework, as well as in the context of other alkali-rich Fe/Mn districts worldwide and emphasize that current postulated models should be revisited to encompass the recently documented extensive epigenetic processes. The proximity of the ores to the Namaqua orogenic front is particularly stressed. Although the exact role of hydrothermal activity on the formation of these deposits is still under question, a postulated model invoking regional-scale basinal brine infiltrations and bearing resemblances to Mississippi Valley-type Pb-Zn deposits is presented here as an alternative ore-enrichment mechanism in the wider area. Many inconclusive results regarding the pre-Namaqua origin of the deposits prompt the need for further investigation.

2. Geological background

The ferromanganese ore deposits of this study are hosted by the Postmasburg Manganese field (PMF) of the Northern Cape Province of South Africa, which further contains some of the largest BIF-hosted iron deposits in the world and is restricted to a geographical area known as the Maremane Dome (Figure 1B) (Beukes et al; 2003). The latter is an anticlinal structure formed between 2.35 and 2.25 Ga compression and defined by a thick (over 2 km) succession of folded dolostones of the Campbellrand Subgroup and overlying iron-formations of the Asbestos Hills Subgroup (Ghaap Group) of the Neoarchaean-Palaeoproterozoic Transvaal Supergroup (Beukes; 1987, Altermann and Hälbich; 1991). In the wider regional setting, the former strata are conformably overlain by lithologies of the Transvaal Supergroup (Ghaap and Postmasburg Groups) comprising siliciclastic rocks and BIF of the Koegas Subgroup, overlain by glacial sediments of the Makganyene Formation, followed by the Ongeluk Formation andesitic lavas and finally by the economically significant sediments of the Voëlwater Subgroup (Figure 1A) (Tsikos and Moore; 1997). The latter hosts the famous Kalahari Manganese field (KMF) located ca. 130 km from the study area and constituted of a succession of iron-formation (Hotazel Formation) and interbedded Mn ores overlain by the Mooidraai Formation carbonates.

Supergroup	Group	Subgroup	Formation	Predominant lithology	Approximate thickness (m)
Transvaal	Postmasburg	Voëlwater	Mooidraai	Carbonate with minor chert	300
			Hotazel	BIF with Mn ore	250
			Ongeluk	Andesitic lava	900
			Makganyene	Diamictite	50-100
	Ghaap	Koegas		BIF, shales and wackes	240-600
		Asbestos Hills	Griquatown	Clastic textured BIF	200-300
			Kuruman	Microbanded BIF	150-750
		Campbellrand	Gamohaan	Carbonate, shale and chert	1500-1700
			Kogelbeen		
			Klippan		
			Papkuil		
			Klipfonteinheuwel		
			Fairfield		
			Reivilo		
			Monteville		
		Schmidtstdrif		Shale, quartzite, carbonate	10-250

Figure 1A. Simplified stratigraphy of the Transvaal Supergroup in the Griqualand West basin. Modified after Beukes and Smit; 1987.

Manganese ore bodies of the PMF had been the most important commercial resource of manganese before the discovery of the giant KMF (Gutzmer and Beukes; 1996a). According to the prevailing model by the previous authors, these deposits were formed on a paleo-erosion surface during a period of intense weathering that occurred in response to marine regression and uplift and of the Kaapvaal Craton. Strata of the Transvaal Supergroup that were exposed to an oxidizing atmosphere were eroded and a regional unconformity between the Ghaap Group and the lowermost Postmasburg Group is believed to have been developed (Beukes; 1987, Grobbelaar et al; 1995). This regional feature is thought to control all primary

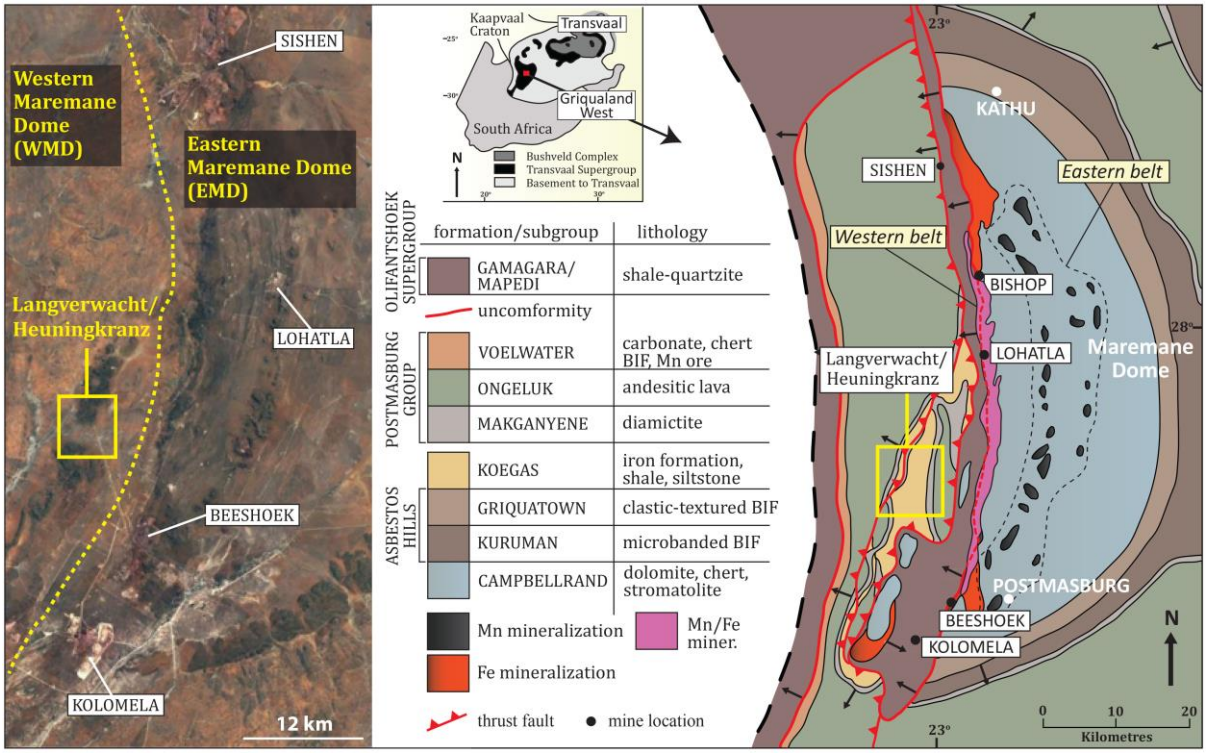

Figure 1B. Detailed geological map of the study area and associated lithostratigraphy. The two manganese ore types used in the literature (Eastern- and Western-Belt type ores) are shown but not further discussed in this study (see also text for more details). Instead, the simple geographic subdivision between Eastern and Western Maremane dome deposits (EMD and WMD - see also google earth image at the left) is used to allow for comparisons between older studies that first described these ores from the main Maremane dome area and more recent studies that focused on new discoveries of mineralized lithologies towards the west of the dome. The study area is indicated with a yellow square. Modified after Moore et al; 2011.

ore formation in the PMF, including BIF-hosted iron ores and dolomite-hosted manganese orebodies. Ore formation was followed by subsequent deposition of the clastic sediments of the Olifantshoek Supergroup. An important iron-rich lithology forming part of the commercial iron ore in the region is a type of clastic/detrital deposit, characterized by hematite-rich

matrix and enriched iron-formation pebbles, known as the Doornfontein Conglomerate (Van Schalkwyk and Beukes; 1986).

Previous studies that dealt with the petrography and mineral chemistry of the manganese ores in the PMF (Plehwe-Leisen and Klemm; 1995, Gutzmer and Beukes; 1996a, 1997b) have suggested that two ore types are present, namely Eastern Belt or siliceous-type and Western Belt ore ferruginous-type deposits (Figure 1B). The siliceous ores were formed from manganese sourced from leaching of chert-rich manganiferous (1-3 wt. % MnO) dolomites of the Fairfield Formation and are hosted by a residual karst breccia with remnant chert fragments, known as the Wolhaarkop breccia. Subsequent slumping of BIF into the developing cave system is suggested to have facilitated iron-ore enrichment and locally formed inverted stratigraphy. The ferruginous ores formed by similar supergene, karst residual enrichment processes from dissolution of carbonates of the chert-free and manganiferous (2-3 wt. % MnO) Reivilo Formation and are confined in the central part of the Maremane dome. Ferruginous ores are more closely associated and intercalated with the basal shales of the Olifantshoek Supergroup, are well-layered and host Al- and Li-rich silicates and oxides (de Villiers; 1943b, 1960, Gutzmer and Beukes; 1996a, 1997b).

Both ore types consist mainly of braunite and/or hematite and of lesser bixbyite and partridgeite (iron-poor Mn_2O_3). These minerals are thought to have formed during subsequent recrystallization and burial diagenesis/metamorphism during the 1.8-1.7 Ga Kheis orogeny (Gutzmer and Beukes; 1996a). Supergene enrichment is also reported to have overprinted these ores. As seem in Figure 1B, manganese ore bodies of the PMF extent almost without interruption along a strike of nearly 60 km and occur as irregular stratabound beds, lenses and pods of variable size that generally straddle the angular erosional unconformity.

Aegirine, albite, barite and Ba-muscovite have been mentioned from these ores but were tentatively attributed to processes of burial diagenesis/metamorphism during the 1.8-1.7 Ga Kheis orogeny or to later hydrothermal fluid flow (de Villiers; 1945, Gutzmer and Beukes; 1996a, 1997b). Rich and complex alkali assemblages, including aegirine, albite, rare Ba-Na-Mn-As-V species and associated with the Eastern Belt ores as well as with newly

explored localities (WMD, Figure 1B), have been regarded to be much younger (ca. 620 Ma) (Moore et al; 2011, Fairey et al; 2019). This study deals only with ferruginous Mn ores from the Langverwacht-Heuningkranz locality (Figure 1B), where the younger age constraints derive from. The subdivision between siliceous and ferruginous ores is not followed hereon, since this classification fails to accommodate the different characteristics of these ores, presented in both older and recent studies (Fairey et al; 2019). Instead, a purely geographic subdivision is employed to refer to ores from the Eastern (sensu stricto) Maremane dome (EMD) and the Western Maremane dome (WMD, this study). Furthermore, the term ferromanganese ore is used in the place of ferruginous Mn ore.

3. Drillcore stratigraphy and sampling

For the purpose of this study, focus was placed on six drill cores from the Heuningkranz and Langverwacht localities which occur in the wider Kolomela area (WMD) (Figure 1B, 2). Specifically, fifty-three samples were retrieved from revisited drillcores kept at the collection of Rhodes University (South Africa) and previously studied by Fairey (2013, 2019) and Bursey (2018). Detailed logs can be found in the previous studies. However, for the purpose of consistency and to allow for comparisons and major features to be pointed out, these logs have been redrawn here and are contextualized in Figure 2.

The broad stratigraphy at Heuningkranz comprises: (i) Siliceous manganese ore (Wolhaarkop breccia) at the base, grading into or abruptly followed after brecciated rock by (ii) ferromanganese ore that is unconformably overlain by the basal red shales of the Olifantshoek Supergroup. On top of the latter the andesitic Ongeluk lavas occur. The alkali-rich manganese ore zones display wide textural variability (e.g., drillcore SLT015), involving changes in thickness and composition of both ore matrix and intercalated banding/layering as well as appearances of macroscopically vuggy ores or ones essentially speckled by tiny and spherical vugs (termed as microbreccia). Ore zone in the former drillcore is more iron-rich at the base and gradually becomes more manganese-rich upwards (Fairey et al; 2019), something that is in contrast to the expected reverse compositional changes across stratigraphy presented by Gutzmer and Beukes (1996a). A type of conglomeratic Fe ore is intersected by the drillcores right above the ferromanganese ores and directly below the red

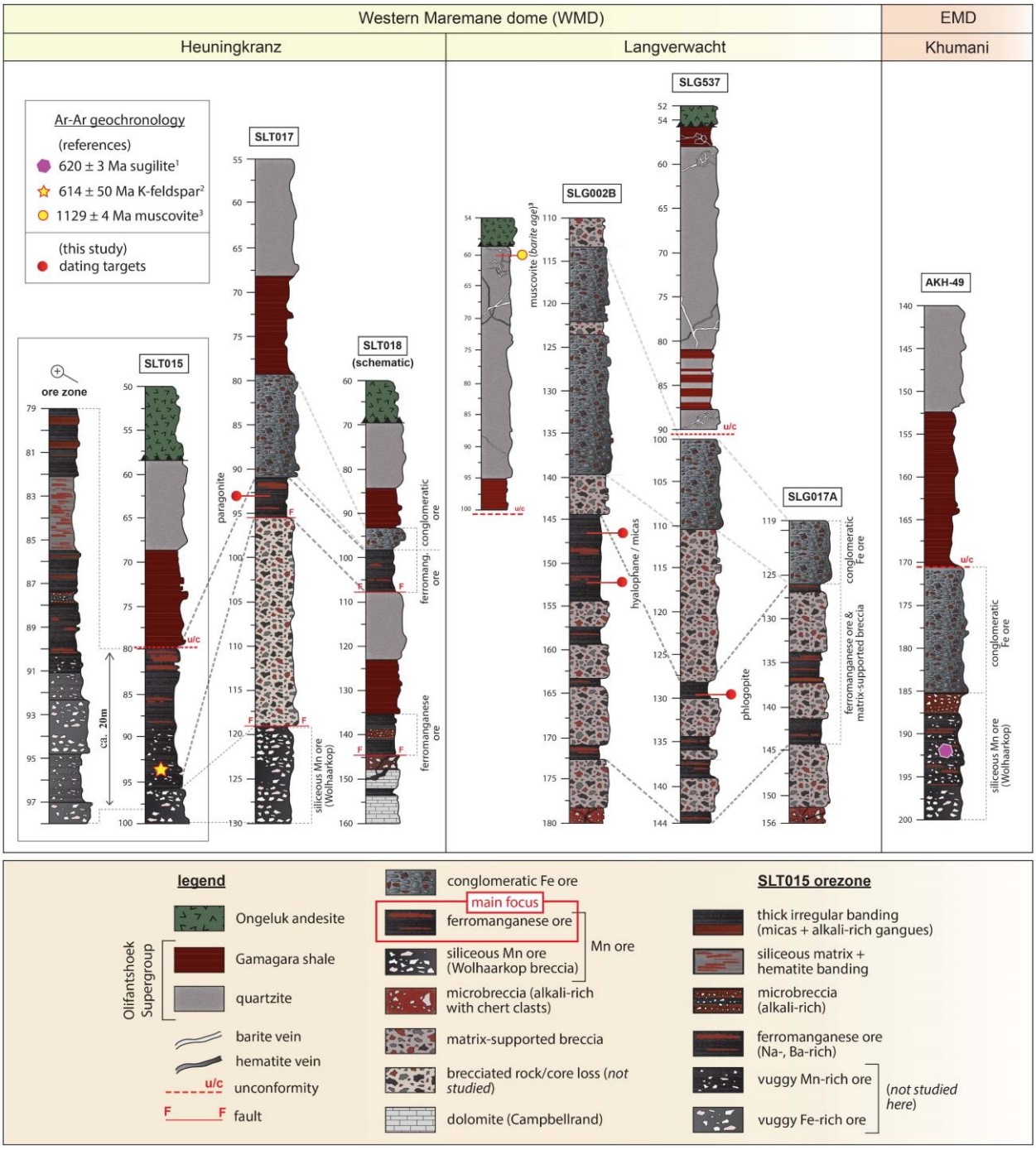

Figure 2. Stratigraphic logs of drillcores containing ferromanganese (Fe-Mn) ore in the WMD and manganese (siliceous) ore in the EMD. Dashed lines follow the extent of Fe-Mn and conglomeratic Fe-ore ore across different drillcores, where sampling was focused. Note the siliceous Mn-ore (Wolhaarkop breccia) underlying core SLT015, the complex breccias associated with the ore zones and the close proximity of the latter with the unconformity. Previous Ar-Ar data and dating targets from this study are included. References: (1) Moore et al; 2011 (2) Fairey et al; 2019 (3) chapter 2.

shale unit. This stratigraphy is reminiscent to the one encountered in the EMD (AKH-49, Khumani, Bruce mine) and therefore the Fe ore in the WMD drillcores can be regarded as a stratigraphic equivalent of the Doornfontein Conglomerate, despite potential mineralogical,

textural and compositional differences between the two. Faulting and strata duplications may be also present (SLT018), as well as extensive brecciation and core loss (SLT017). On the basis of observations on these drillcores, the textural variety of which has been simplified here for illustration purposes, it can be deduced that the morphology and distribution of these ores in the WMD is very erratic and complex, comprising bodies of varying thickness and different types of intercalated breccias and intermediately enriched rock.

Drillcores in the neighboring Langverwacht locality display broadly similar stratigraphy. The major differences are: (i) the absence of any siliceous Mn ore type, (ii) repetition of ferromanganese ore zones particularly enriched in alkalis (Ba/Na) and interrupted by thick matrix-supported breccia units, showing also significant alkali enrichments. The former is regarded to be the most prominent feature in the studied SLG drillcores, which can host both continuous (i.e., 10 metre thick) and irregular orebodies showing generally abrupt transitions with the intercalated breccias. (iii) very well-developed and thick Fe ore that once again macroscopically exhibits signs of brecciation and alkali enrichment and (iv) conspicuous hematite and barite veins and fillings in the quartzites overlying the ores. Depths from the surface, in which deposits occur, collectively range from ca. 80 to 200 metres.

Sampling in this study was focused solely on the ferromanganese ore from the WMD cores and certain types of the associated breccias. Sample depths of minerals that were identified and dated later on in this study are shown in Figure 2, together with previously obtained geochronological results. A handful of additional samples from the AKH-49 drillcore (EMD) and Kapstevel locality (Kolomela Fe ore mine) were also included for stable isotopic analyses.

4. Methods

Identification of ore and gangue minerals was based on a combination of optical and scanning electron microscopy, the latter carried out on a Quanta 200F Environmental SEM with EDAX microanalysis and a Hitachi SU-70 FEG SEM, housed in the universities of Glasgow and Durham respectively. After careful examination under the SEM, four samples were

selected for in situ $^{40}Ar/^{39}Ar$ dating. Lack of material of sufficient purity greatly impeded stable (O-H) isotopic analysis which was limited to a small number (twenty-two) of selected targets. All samples subjected to isotopic analysis were earlier petrographically well-characterized using polished thin sections that were studied under SEM microscope in order to achieve the best possible clean mechanical separation by micro-drilling. No acid treatments were employed in order to avoid potential fractionation effects that have been shown to occur in silicates even using short times of exposure under for example HCl. Purity of samples was also evaluated subsequently to analysis by quantitatively determined oxygen yields (mostly > 90 %) (Appendix II), generally supporting low contamination, given also how intricately mixed these fine-grained minerals are.

Oxygen isotope analyses were facilitated via laser fluorination (SUERC), using ClF_3 as the fluorinating agent and applying the basic methodology of Sharp (1990). All minerals were pre-fluorinated under vacuum for one minute before infrared laser heating, to avoid sample reactions of these fine-grained and not well-constrained minerals, apart from hyalophane (15 min) and oxides (overnight). OH-bearing and hydrous minerals were degassed overnight (250^{o}C) for oxygen analyses. Converted CO_2 was analysed on a VG Isotech SIRA series II dual inlet mass spectrometer. Hydrogen from degassed samples (150^{o}C) was extracted by in vacuo bulk heating using the method of Donnelly et al (2001) and measured on a VG Optima mass spectrometer at SUERC. All isotopic data are reported in standard delta notation, relative to Vienna Standard Mean Ocean Water (V-SMOW). Repeat analyses of international and lab standards gave a reproducibility of ± 0.3 ‰. and ± 2‰ for oxygen and hydrogen respectively.

In situ $^{40}Ar/^{39}Ar$ analyses were conducted via laser ablation on thin polished wafers using a New Wave Research Laser UP-213 A1/FB and gas purifications and measurements were made with a Helix SFT (Thermo Scientific) multi-collector noble gas mass spectrometer at the NERC Argon Isotope Facility at SUERC. Details on the method can be found in Appendix I and full $^{40}Ar/^{39}Ar$ results can be found in tables therein.

5. Results

5.1 Mineralogy and textural attributes

5.1.1 Ferromanganese ore

The ore minerals dominating this unit are braunite and hematite which chiefly compose a fine- (< 50 µm) to very fine-grained (< 10 µm) massive groundmass interrupted by (Figure 3a-d): (a) mm- to cm-sized vugs filled with various silicate, carbonate and sulfate species (b) generally coarser grains, infills or clasts which regularly show varying degrees of replacement by the aforementioned minerals and (c) cm-thick brownish-red coloured bands which on the microscale can be thinly laminated and consist of intricate intergrowths of both ore and gangue phases. The latter fabric is arguably the most notable textural feature in all studied drillcores and gives a laminated appearance to the ferromanganese ore encountered

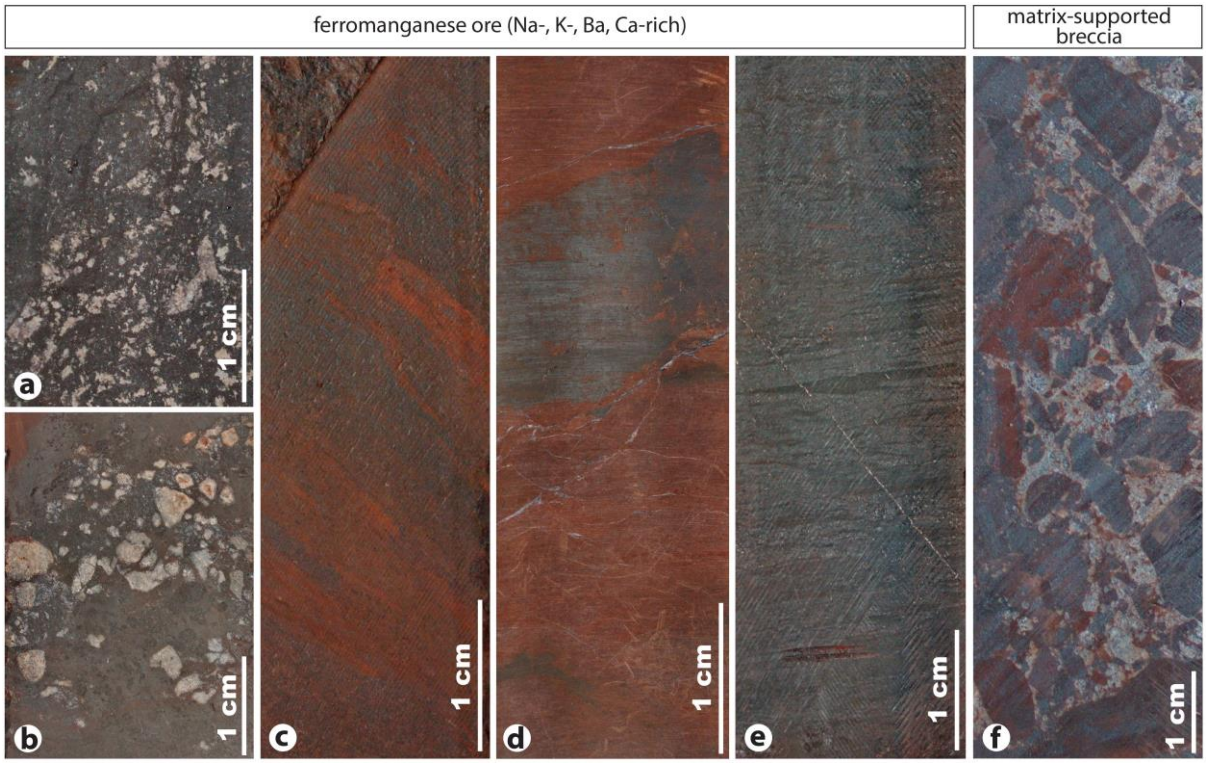

Figure 3. Representative samples of the ferromanganese ore zone. (a) Vuggy ore with abundance of alkali-rich alteration mineralogy. (b) Ore comprising coarser and more angular infills, many of which represent metasomatized chert fragments. (c) Reddish brown irregular banding in ferromanganese ore consisting of K-, Na- and Ba-bearing phases (e.g., hyalophane, natrolite, etc.). (d) Banding resembling the prior image, though consisting predominantly of mica (muscovite-paragonite series). (e) Typical occurrence of black ferromanganese ore displaying alternating laminae of braunite and hematite. (f) Matrix-supported breccia with ferruginous angular clasts and matrix comprising chiefly hematite, aegirine and hyalophane.

in the zones of alkali-enrichment. Likewise, ore occurrences with no conspicuous gangue mineralogy may exhibit distinct planar microbanding, caused predominantly by dark braunite and dull grey hematite streaks, which resemble textural characteristics of a finely laminated sediment (Figure 3e). In only few cases among the studied samples, braunite- or hematite-rich intervals appear to lack banding and can thus be fairly characterized as massive ore, but these do not generally exceed a length of a few centrimetres. The different textural and mineralogical attributes of the ore zone lithofacies are presented at length by Fairey et al (2019), therein included a rather comprehensive description of gangue mineralogy. Hence, the following section focuses on novel and nonreported data, providing an in-depth analysis of the **gangue mineral associations** firstly found in the groundmass of the ore zone and then of the phases being accommodated in pronounced vugs and veins.

Matrix-hosted gangue mineralogy

Laminated ferromanganese ore hosts intercalated cm-sized bands of irregular shape and brownish red colour which can pinch out in the sample scale and are composed either of: (i) ubiquitous mica such as muscovite, paragonite and barian muscovite, typically intergrown with texturally variable ore minerals of which hematite is the dominant, as well as other accessory phases or (ii) alkali-rich phases, in particular celsian-hyalophane ($BaAl_2Si_2O_8$ - $(K,Ba)[Al(Si,Al)Si_2O_8]$), natrolite ($Na_2Al_2Si_3O_{10}2H_2O$) and banalsite ($BaNa_2Al_4Si_4O_{16}$), forming alternating layers for the most part within braunite-rich ore intervals. Evidently, mica are not homogeneously distributed throughout the ore but they are principally concentrated in bands with ample coexisting hematite. The same is not true for alkali-rich gangues which can be found in varying abundances throughout the entire ore.

Phyllosilicate-rich bands is one of the few visible features by transmitted light-microscopy in the otherwise opaque matrix, despite them still being stained by hematite. The broad textural appearance of these bands is shale-like and they consist of extremely fine-grained mica and hematite fibers wrapping around widespread coarser mica grains (25-50 μm) and more sparsely scattered hematite and braunite aggregates (Figure 4A). Microscopic micas also occupy interstitial space in very fine-grained (<10 μm) hematite- and braunite-ore groundmass adjacent to the mica-rich bands (Figure 4B1, C). Hematite and mica are aligned

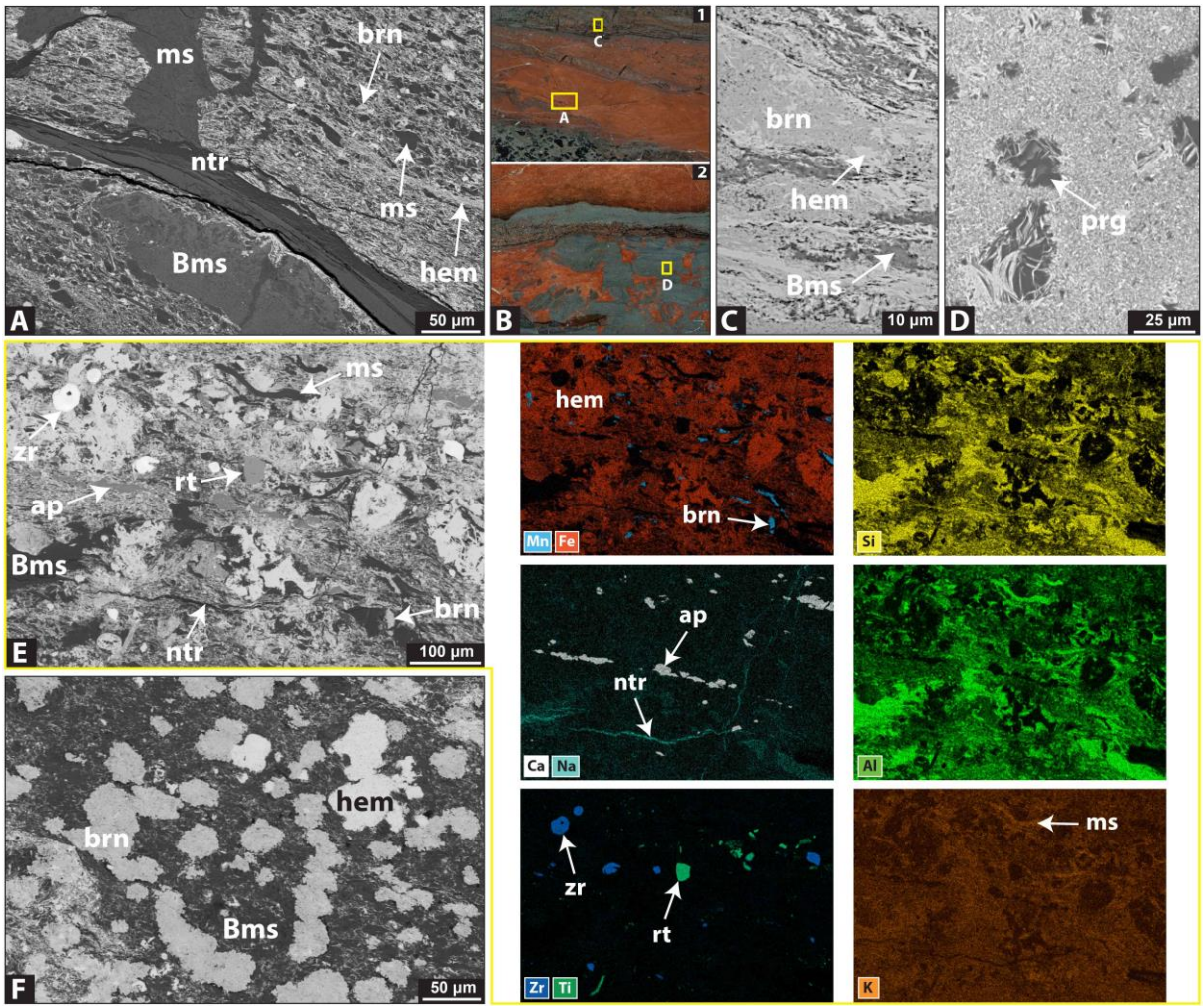

Figure 4. Back scattered electron (BSE) images. (A) Muscovite- and hematite-rich band interrupting ferromanganese ore and exhibiting textures which support secondary formation of mica and alkali minerals Grain allignement is also conspicuous. (B1 & C) Detail of ore groundmass (B1=thin section scan) displaying development of barian muscovite within braunite-hematite matrix. (B2 & D) Hematite-rich ore matrix (B2=thin section scan) evidently disrupted by secondary paragonite which also infiltrates inbetween hematite plates. (E) (left) Ore matrix with conspicuous elongated muscovite, streaks of apatite, natrolite microveins and clasts being replaced by barian muscovite, hematite and lesser braunite. (right) EDS compositional maps showing distribution of major elements and thereby of ore and gangue mineralogical phases. (F) Hematite replaces braunite aggregates. ap = apatite, Bms = barian muscovite, brn = braunite, hem = hematite, ms = muscovite, ntr = natrolite, prg = paragonite, rt = rutilte, zr = zircon.

on wavy banding planes that are reminiscent of soft-sediment deformation textures and possibly attest to a diagenetic/metamorphic origin for this bedded fabric or otherwise a metasomatic replacement origin of a former layered sediment. Mica-rich bands comprising principally paragonite and lesser muscovite also exist and further contain minerals exclusively concentrated here, i.e., ubiquitous apatite and rutile ($TiO_{2\ matrix}$ = 2.1 ± 1.0 wt.%, n=8), ilmenite and zircon. Apatite occurs as individual coarse crystals or aggregates up to 100 µm in size and rutile as somewhat smaller grains, often forming masses parallel oriented to the

phyllosilicate-rich matrix. EDS spectra confirm the presence of F, S, Al, and Si in apatite, most likely hinting to the presence of submicroscopic APS minerals. Zircon is either rounded or shows irregular margins and is commonly fractured. Despite the aforementioned phases being indicative of a possible clastic/sedimentary origin for the phyllosilicate bands, overall, the ore manifests a complex and highly metasomatic nature which is emphatically highlighted by a series of textures involving ore minerals, mica and other silicates, a selection of which is presented below.

Hematite-rich matrix is seen being disrupted and offset by monomineralic areas consisting of muscovite or paragonite sheets which corroborates the secondary origin of the latter (Figure 4B2, D). Paragonite has been previously confirmed by bulk-rock XRD analysis of clay-rich matrix (Fairey et al; 2019) but its textural characteristics and parageneses have not been stressed. Micro-fractures are commonly seen being filled by paragonite and other mica along with natrolite, banalsite, barite and braunite. In places, coarse (up to 200 μm) elongated muscovite is observed developing banding-related preferred orientation and folding while at the same time its barian counterpart apparently replaces micro-clasts along with specular hematite and lesser braunite (Figure 4E and 4F, EDS maps).

Paragonite also fills near-isometric botryoidal or angular structures (50-100 μm) of unknown origin, sometimes made up of hematite and paragonite concentric interlayers which resemble colloform textures (Figure 5A). Surrounding matrix consists of densely-packed platy hematite or can be porous and display iron-rich ooids which are interstitially occupied by anhedral masses of paragonite and apatite (Figure 5B). This textural characteristic greatly resembles the pervasive paragonite metasomatism of hematite ooids seen in drill cores from the Kolomela mine hosting alkali-enriched iron ore (chapter 2). Concentrically-zoned structures comparable to that described above are also seen associated with massive braunite, which hosts either muscovite or natrolite infills that may further display a thin hematite selvedge (Figure 5C).

Natrolite commonly rims braunite clasts, which possibly implies preferential development of sodium-bearing silicates around areas thought to represent former quartz

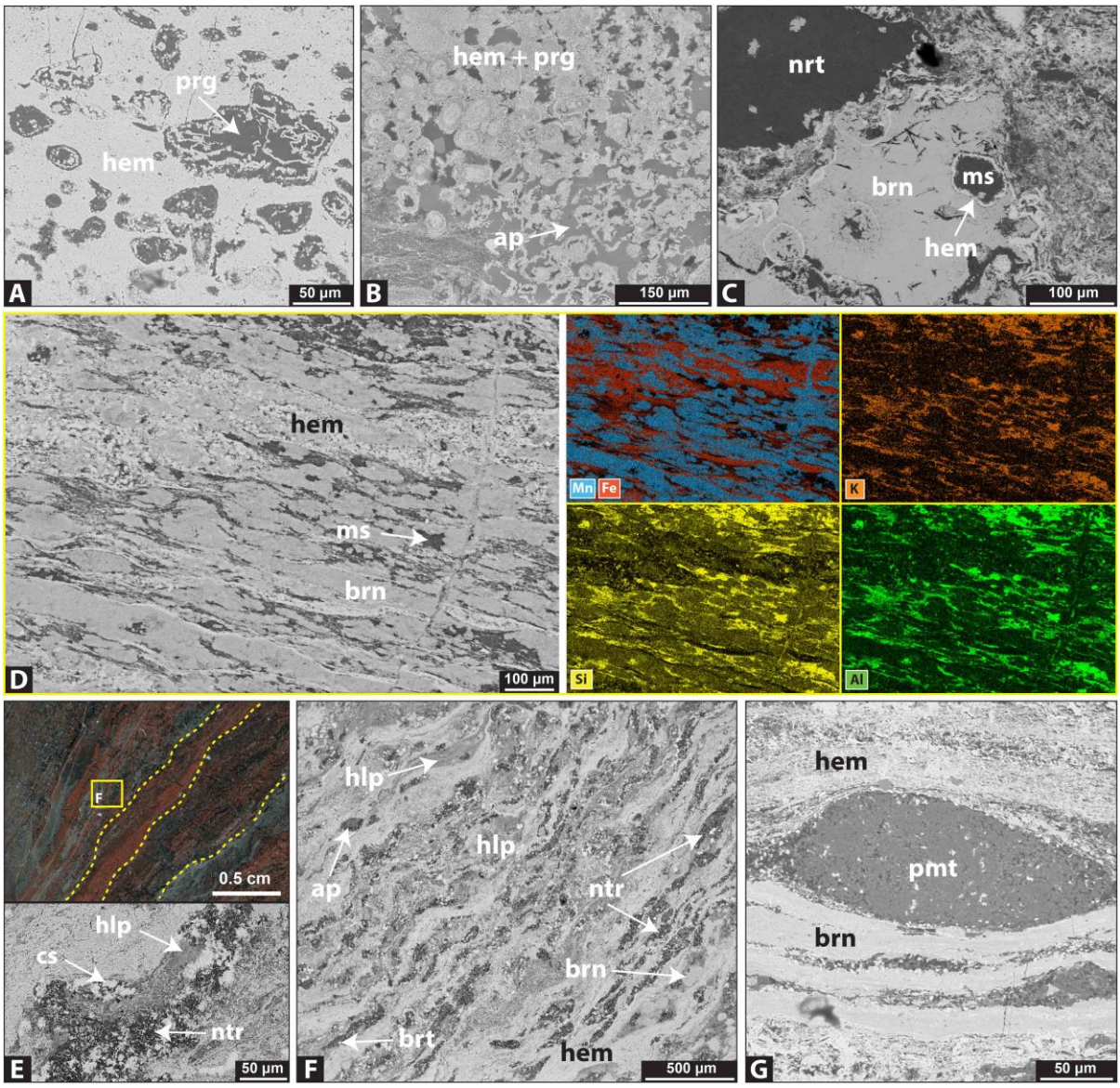

Figure 5. Back scattered electron (BSE) images. (A) Paragonite and hematite concentic layering probably develops upon former sedimentary/diagenetic structures. (B) Iron-rich ooids interstially filled by paragonite and apatite in ferromanganese ore are similar to metasomatic textures described from the iron ore at Kolomela. (C) Concentrically-zoned structures consisting of muscovite, natrolite and hematite, encased in braunite. (D) (left) Muscovite and hematite wrapping around flattened braunite concretions. (right) EDS elemental map highliting muscovite distribution. (E) Mica-free gangue-bearing laminae (thin-section scan) comprise feldspars and silicates such as natrolire (down). (F) Detail of the previous sample stressing the finely alternating laminae consisting of ore minerals (bright areas) and gangue phases (dark areas). The brightest specks are barite. (G) Piemontite of possibly replacive origin in ore matrix. ap =apatite, brn = braunite, brt = barite, cls = celsian, hem = hematite, hlp = hyalophane, ms = muscovite, ntr = natrolite, pmt = piemontite, prg = paragonite.

clasts. In many instances, the latter are apparently products of former replacement by braunite, akin to similar textures reported from ores in the wider area (Gutzmer and Beukes; 1996b, Fairey et al; 2019). Furthermore, muscovite and barian muscovite are observed in braunite-rich laminae, comprising discrete braunite concretions or thin (100 µm) continuous

aggregates that are flattened parallel to bedding and sometimes seen encased by microplaty hematite (Figure 5D).

Barian muscovite contains up to 4.11 wt.% BaO (average = 2.81 ± 1.2 wt.%, n=12) and hosts appreciable FeO and MnO (average = 2.68 and 1.40 wt. % respectively, n=12). In contrast, mica classified using EDS analyses as phlogopite or possibly as Mg-rich celadonite (further mentioned in the section) are scarcer and were not observed as principal banding constituents. Braunite is dominantly aluminum-free but when associated with mica-rich matrix its Al_2O_3 concentrations range between 2.1 and 4.9 wt.% (average = 3.2 ± 0.9), therefore pointing to a possible affiliation between formation of the two. Hematite can also host appreciable amounts of manganese (2.5 ± 1.3 wt. % Mn_2O_3, n=9).

As regards the **mica-free brownish red bands** which consist instead of **alkali-rich gangues**, these are for the most part intricately interlayered with fine-grained braunite-hematite assemblages and may display pronounced undulation on the micro-scale (Figure 5E, F). Mineralogy of these gangue-bearing laminae is highly variable but mostly comprises natrolite, banalsite, hyalophane, celsian and subordinate barite and apatite. Fine aggregates of reddish-brown Mn-ich epidote identified as piemontite [$Ca_2(Al,Mn^{3+},Fe^{3+})_3(SiO_4)(Si_2O_7)O(OH)$] are seen in rare occasions associated with banalsite, particularly in braunite-rich laminae. Piemontite also fills elliptical concretions or clasts oriented parallel to bedding plane, most likely denoting yet another replacement texture (Figure 5G). Its chemistry is consistent with that described by Fairey et al (2019) from the same locality, showing low Fe_2O_3 and high Al_2O_3 and Mn_2O_3 content (13.8 and 24.3 wt.% respectively, n=3).

Aluminum-rich parageneses were found in a ferromanganese ore zone some 10 metres thick (Figure 2, drillcore SLT-018), interbedded between shales and quartzites within an irregular stratigraphy with apparent faulting and duplications. On closer inspection, these assemblages appear to consist primarily of Ba-bearing muscovite, **diaspore** and a highly aluminous Mn-bearing silicate, all of which are not exclusive to phyllosilicate-rich layers but also occur in increased concentration within braunite-rich groundmass with lesser hematite.

The silicates are generally dispersed in the matrix as irregularly shaped crystal aggregates in close association with diaspore (Figure 6A). The latter broadly shows similar distribution to the rest, which implies a genetic link between them. Diaspore occurring as cryptocrystalline groundmass occupies quite extensive areas (up to 2 mm) and its fine blade-like crystals are visible only when disseminated in braunite matrix. This is the first documented occurrence of diaspore in the WMD ores; however, this mineral is apparently widespread in shales lenses associated with the EMD ferromanganese ores, i.e., Lohatla mine, Bishop, etc. (Gutzmer and Beukes; 1996a, 1996b). EDS analyses of the Mn-bearing silicate reveal very high MnO content (average = 39.7 ± 3.6 wt. %, n=4) and an Al to Si ratio of about 1.5. The following calculated formula $Si_{1.7}Al_{2.5}Mn_{2.7}Mg_{0.4}$ reported on 12 oxygen basis shows chemical resemblance to spessartine [$Mn^{2+}{}_3Al_2(SiO_4)_3$] but since Al-Si substitutions are required to achieve a matching chemical formula which will still show a silica deficit, our mineral cannot be confidently identified as such. In other respects, its habit is mostly anhedral and tends to form along with barian muscovite at the rims of diaspore infills.

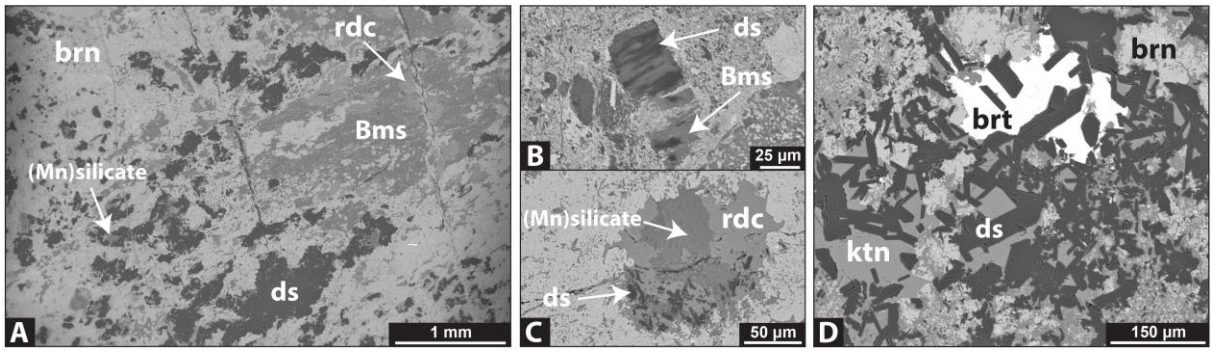

Figure 6. Back scattered electron (BSE) images. (A) Copious Ba-muscovite and diaspore aggregates in braunite-rich matrix. Mn-carbonates and an unidentified silicate with very high Mn content also develop locally. (B) Synchronous replacement of grain by gangue phases. (C) Small patch with coexisting rhodochrosite and diaspore needles. (D) Coarse prismatic diaspore associated with barite and kutnohorite in recrystallized braunite matrix. Bms = barian muscovite, brn = braunite, brt = barite, ds = diaspore, ktn = kutnohorite, rdc = rhodochrosite.

In one striking example, Ba-muscovite and diaspore seemingly replace a euhedral grain or clast in a manner akin to exsolution lamellae, thus further suggesting syn-crystallization of the regarded phases (Figure 6B). Braunite hosts substantial Al_2O_3 (up to 5.25 wt. %) similarly to the one associated with mica-rich bands. Patches (Figure 6C) and coarse (0.5 - 1 cm) vugs and veins of Mn-carbonates (kutnohorite, rhodochrosite) and barite also characterize this ore zone and are linked with manganese mobilization seen in the form of

braunite micro-veins. It is noteworthy that prismatic to tabular diaspore crystals up to 300 µm in size are found associated with barite-carbonate associations and braunite surrounding the latter is generally coarser, euhedral and recrystallized (Figure 6D). Observed replacements of clasts set in a ferruginous groundmass by the entirety of the former minerals further complicates the scene.

Vug- and vein-filling alteration mineralogy

Vugs of various sizes (mm- to cm-wide) are omnipresent in the ore zone and generally show patchy distribution. However, certain sequences are crowed with abundant irregularly shaped and light-coloured vugs, infills or angular clasts which contrast with the black matrix, thus giving the ore a speckled appearance. In proximity to coarse-grained vugs, the entire ore groundmass displays a mosaic texture on the microscopic scale, which is composed of fine crystalline braunite and microvugs (50 - 100 µm) of variable composition. These minute vugs generally mimic the composition of their coarse-grained counterparts but may further show wider mineralogical diversity including mica being almost certainly of secondary origin. Mineralogy of the smaller vugs is very difficult to discern by optical microscopy because of the highly opaque surrounding ore matrix.

On the basis of SEM-EDS analysis, in the vicinity of large vugs with cores consisting of coarse-grained calcite and usually twinned albite rims (Figure 7.A1), microvugs may comprise more than ten species including albite, K-feldspar, celsian, hyalophane, aegirine, muscovite, serandite, pectolite, calcite, barytocalcite, barite, witherite and fluorapatite to name a few. Such an example is given in Figure 7.A2. Results from an automated phase distribution analysis of these areas using inbuilt EDS software that makes use of brightness differences, show approximate concentrations of 73.3 wt. % braunite, 17.4 wt. % albite, 3.9 wt. % fluorapatite, 2.4 wt. % barytocalcite and 3.0 wt.% of remaining Na-bearing species and mica, such as aegirine, pectolite-serandite and muscovite-celadonite (Figure 7B). A network of microscopic veins consisting predominantly of albite and aegirine also traverses the vuggy ore.

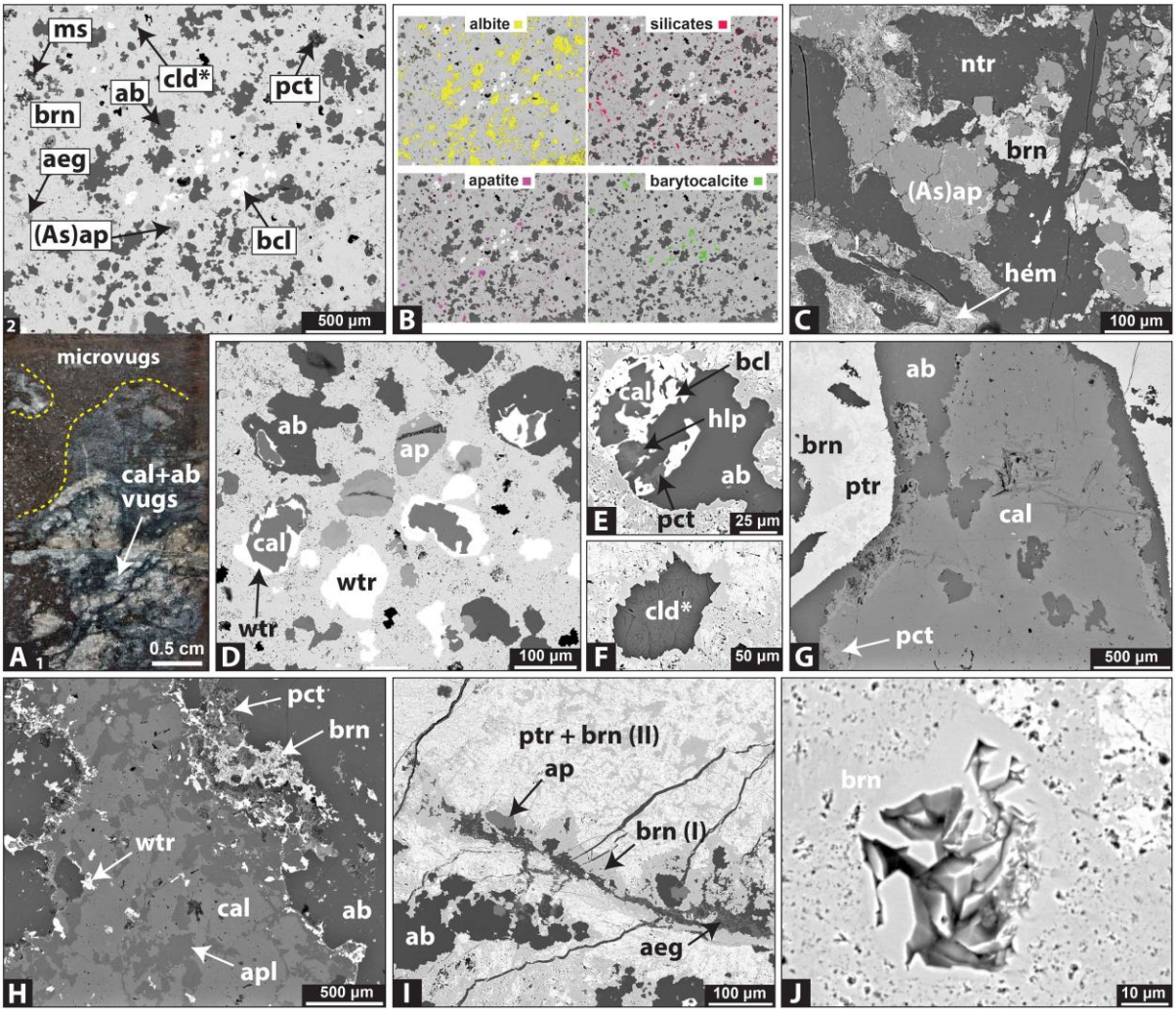

Figure 7. Back scattered electron (BSE) images. (A1) Vuggy ferromangense ore displaying matrix crowed with coarser infills and microvugs in their proximity (photo). (A2) Typical mosaic texture composed of braunite and minute vugs which consist of silicates, carbonates, apatite and barite. (B) EDS mineralogical distribution map of image A. Coloured silicates (red) include aegirine, muscovite and pectolite. (C) Apatite aggregates associated with natrolite and recrystallized ore minerals. (D) Witherite forms later and/or replaces calcite. (E) Polymineralic microvug hosting feldspars, silicates and carbonates. (F) Microvug filled by unknown Mg-rich mica, possibly celadonite. (G) Zoned vug with calcite core and pectolite-albite rim. (H) Apophyllite aggregates precipitating with calcite and witherite, possibly during later stages of hydrothermal activity. (I) Ore texture highlighting the difference in brightness between braunite (I) around gangues (dark) and braunite (II) + partidgeite surrounding matrix (bright). (J) Massive braunite matrix may consist of tightly-packed euhedral crystals, as highly magnified porous areas suggest. ab = albite, aeg = aegirine, ap = apatite, apl = (hydroxy)apophyllite, (As)ap = arsenic-apatite, bcl = barytocalcite, brn = braunite: for (I) vs (II) see text, cal = calcite, cld* = celadonite (not stoicheiometrically validated), hlp = hyalphane, ntr = natrolite, pct = pectolite, ptr = partridgeite, wtr = witherite.

It is interesting to note that apatite being closely associated with albite vugs, apart from fluorine (2.76 ± 0.5 wt. %, n = 6), can also host a significant amount of As_2O_3, ranging between 2.2 and 11.7 wt. % (average = 5.43 ± 3.6 wt. %, n = 6). AsO_4^{3-} and VO_4^{3-} can substitute for PO_4^{3-} in apatite, as it has been shown from various natural and synthesized samples

(Kutoglu; 1974, Sha and Chappell; 1999) and this clearly indicates the presence of arsenic in the mineralizing fluid forming these vugs. The presence of the rare **As-rich tokyoite** [$Ba_2Mn^{3+}(VO_4)_2(OH)$] found as inclusions in banalsite veins underpins the aforementioned and further validates synchronous transportation of As and V together with Ba and Na in the solution. This species was discovered for the first time by Costin et al (2015) in the same ores in parageneses along with noélbensonite [$BaMn^{3+}{}_2(Si_2O_7)(OH)_2H_2O$], K-feldspar, witherite, and serandite, where the latter is partly replacing it. As-rich apatite is also observed as euhedral grains within phlogopite-filled vugs or as crystalline aggregates in close relationship with braunite idioblasts, microplaty hematite and natrolite, all hosting finely dispersed barite and serandite-pectolite inclusions (Figure 7C). Vugs occupied exclusively by coarse euhedral apatite (up to 100 μm) are found at times traversed by later albite-filled microfractures.

Microvugs are broadly monomineralic but in some cases Na-, K- and Ca-bearing species (albite, serandite-pectolite, hyalophane) coexist with apparently later crystallized Ba- and Ca-bearing associations (barytocalcite, witherite), which may also grow on earlier-formed calcite, barite or other phases (Figure 7D, E). Witherite, for example, clearly forms along calcite crystal boundaries, lines microscopic calcite-filled vugs or is seen pseudomorphically replacing serandite and pectolite grains. Most EDS analyses on vug-filling mica readily demonstrate a muscovite or phlogopite composition whereas a certain few show the presence of a high-Mg and very low Al-bearing member of the series with the estimated chemical formula: $K_{0.67}(Al_{0.1}Mg_{2.4})Si_{4.3}O_{10}(OH)$ (Figure 7F). This can be described as an Fe-free, Mg-rich (23.7 ± 0.2 MgO wt.%, n=3) analogue of celadonite, although further analysis would be needed to accurately characterize it.

Many of the coarser vugs exhibit a distinct phase zonation, where Mn- and alkali-bearing silicates such as albite, serandite-pectolite or natrolite develop around cores of authigenic quartz, K-feldspar or calcite (Figure 7G). Another species reported here for the first time in these ores is the Ca-bearing hydrate **(hydroxy)apophyllite** [$(KCa_4(Si_8O_{20})(OH,F)8H_2O$]. Its existence is confirmed stoichiometrically by the estimated formula $K_{0.83}Ca_{3.65}(Si_{8.5}O_{20})(OH,F)8H_2O$, the low totals (ca. 85%) and the observed euhedral tabular habit. Where present, apophyllite coexists with calcite, witherite and pectolite (Figure 7H),

forms aggregates of fine crystals (50-100 µm), occludes open space in coarse-grained calcite-filled vugs or fills microscopic veinlets. The close association between apophyllite and calc-silicates and in particular carbonates leads to suggest formation during the later stages of the hydrothermal activity. The mineral is also known from the main hydrothermal alteration event of the Kalahari manganese field, where it is member of the association pectolite, datolite, prehnite, and inesite (Cairncross et al; 2000). However, the current research has revealed evidence from the same district for origination as primary or recrystallization product during fluid flow at recent times (Synthesis, Part 2).

Altogether, vugs and infills are seen being dispersed either in: (a) **braunite groundmass** [**braunite (I)**, also noted as braunite (brn) in figures] or (b) a matrix of different mineralogical composition and higher manganese content, consisting of **partridgeite** and lesser but compositionally different braunite [**braunite (II)**]. Vugs and veins can be locally enveloped by braunite which appears darker than the surrounding ore matrix under BSE imaging (Figure 7I) and displays composition typical to braunite (I), i.e., average SiO_2 = 12.7 ± 1.1 wt. % and CaO = 2.0 ± 0.6 wt. %, n =8). Contrastingly, analyses of the brighter Mn-rich crystalline matrix surrounding vugs show an essentially Si-depleted braunite [**braunite (II)**] (SiO_2 ≈ 1 ± 0.4 %, n=3) and a similarly Si-poor mineral (2.4 ± 1.1 wt. %, n=4), however with a much higher Mn^{3+} content (96.6 ± 2.8 wt. % Mn_2O_3, n=4). The latter most certainly represents partridgeite, an informal name introduced after studies of the EMD ferromanganese ores to distinguish iron-poor anisotropic a-Mn_2O_3 from iron-rich isotropic bixbyite [$(Mn,Fe)_2O_3$] that was present in these ores (De Villiers; 1943a, Gutzmer and Beukes; 1996b). Partridgeite has also been mentioned from the WMD ores being in close association with braunite (Fairey et al; 2019). This difference in silica content between braunite (I) coating silicate-bearing vugs and partridgeite + braunite (II) in the surrounding matrix, possibly points to mechanisms of alkaline solutions depleting preexisting braunite while synchronously scavenging silica for their formation.

The habit of braunite which can potentially provide clues on its mode of origin is not readily detectable. The mineral occurs predominantly as massive, i.e., uniformly indistinguishable very fine crystals whereas locally, a granular texture of homogenous grain

size can be observed. Porous vugs filled by braunite (Figure 7J) allow one to conceptualize a possible assemblage of very fine (5-10 µm) interlocking, euhedral dipyramidal crystals as largely being the constituents of the visibly massive braunite matrix. Subhedral idioblasts or granular braunite aggregates are however seen associated with alteration mineralogy and most certainly reflect either diagenetic recrystallization or a later hydrothermal origin.

As mentioned earlier, fine-grained hematite occurs intercalated with braunite in microlaminae successions, but it may also compose zones of several centimetres where it is by far the dominant phase. Aegirine proliferates in this hematite-rich matrix and potentially signifies preferential precipitation in preexisting iron-rich ore intervals or else may be closely related to iron remobilization during hydrothermal alteration. Aegirine or aegirine-augite can be quite ubiquitous and displays: (a) extremely fine-grained varieties that are intricately associated with hematite and together compose scattered micro-concretions with accretionary textures (Figure 8A1) and (b) granular aggregates of coarser grains (20 - 100 µm) which are arranged in structures resembling former clasts and are overprinted by the predominant hematite-aegirine matrix (Figure 8.A2, B). Both hematite and aegirine here can be manganese-bearing (up to 3.8 wt. % and 11.9 MnO wt. % respectively), which supports manganese transportation by alkaline solutions. In addition, braunite in these samples is contained in cm-wide irregularly shaped patches, as disseminations or rims around assemblages of albite and aegirine (Figure 8C). These alteration patches or vugs exhibit a thin (300 - 500 µm) aegirine-rich reaction rim with the hematite-aegirine ore groundmass (Figure 8D). Other species regularly seen associated with the iron-rich ore matrix are mica (muscovite, phlogopite) and hyalophane.

A series of textures suggests mobilization of iron followed formation of braunite or even hydrothermal vugs. For example, large braunite concretions are seen occasionally being wrapped around and cut off by Mn-bearing hematite within a matrix that also displays laterally discontinuous Al- and Si-bearing hematite laminae (Figure 8E). In another sample, alkali-bearing zoned vugs that are entirely enveloped in manganese matrix are seen being fragmented by a mass of infiltrating hematite (Figure 8F), which macroscopically develops relatively sharp contacts to the main ore matrix. Samples with well-developed hematite and

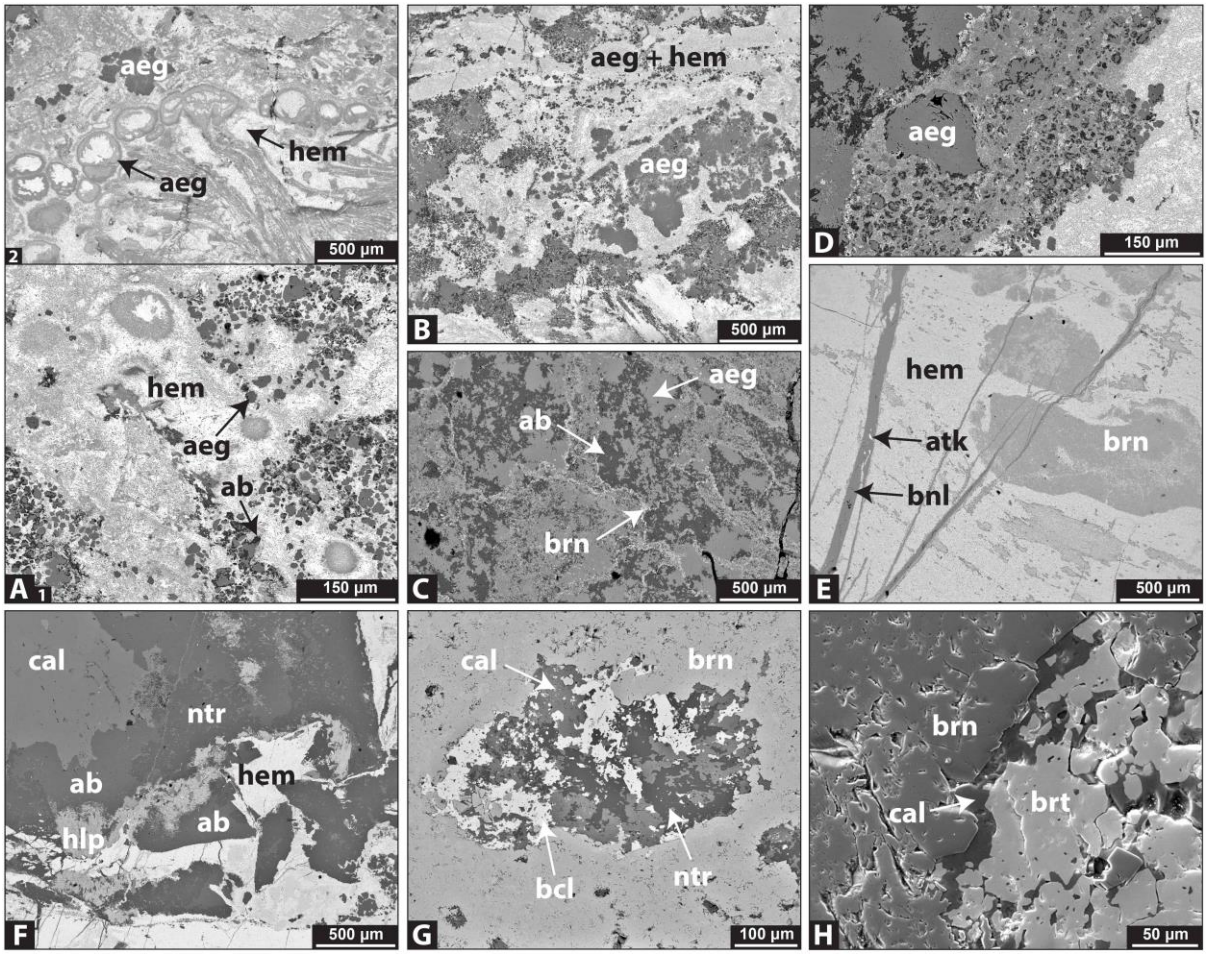

Figure 8. Back scattered electron (BSE) images. (A1 & A2) Fine-grained aegirine and hematite filling micro-concretions in iron-rich matrix. (B) Aggregates comprising coarse aegirine are overprinted by the surrounding matrix. (C) Braunite in iron-rich ore intervals is limited to alkali-bearing patches, supporting co-genetic formation. (D) Thin aegirine reaction rim between matrix and vug. (E) Coarse braunite concretions overprinted by hematite and later cross-cut by banalsite veins bearing As-tokyoite. (F) Later-formed hematite evidently infiltrates and fractures former vug filled by alkali-rich phases. (G) Calcite forms thin corona and/or grows on barite occupying vug. (H) Abundant microvugs in proximity to barite occurrences host calcite and barium carbonates which may have originated by replacement of barite. ab = albite, aeg= aegirine, atk = As-tokyoite, bcl = barytocalcite, bnl = banalsite, brn = braunite, brt = barite, cal = calcite, hem = hematite, hlp = hyalophane, ntr = natrolite.

braunite alternating lamination may locally exhibit textures that are discordant to banding and apparently consist of hematite of later origin.

Barite-filled vugs appear to be scarcer in comparison to other metasomatic textures and commonly show characteristic zonation, with calcite or manganoan calcite located at the rims and coarse tabular barite (up to 300 µm) or irregular aggregates occupying the interior (Figure 8G). The presence of equant coarse braunite (50-250 µm), having formed by

recrystallization as inclusions in barite, is common in vugs that are several millimetres large and further contain other silicates such as hyalophane. The former braunite may also host prismatic hausmannite. Widespread in proximity to barite mineralization are vugs hosting barium carbonates and calcite which are likely to have precipitated as replacements products of barite (Figure 8H). Replacement of sulfates such as anhydrite by calcium carbonate occurs during many geological processes at very low temperatures but carbonates such as witherite and strontianite have also been also described to originate from replacement of barite (Chang et al; 1996, Hanor; 2000).

Strontianite is the least abundant among the documented carbonates and is seen filling microvugs or as inclusions in calcite. Highly dispersed patches with Ba-bearing associations in ore matrix were also noted to host a **Mn-rich silicate** with lamellar grains, rather consistent chemistry and low but invariable barium content. Oxide weight percentages for a total of 100 wt.% are: SiO_2 = 48.4, Al_2O_3 = 7.0, MnO = 39.0, MgO = 1.1, CaO = 1.0 and BaO = 4.0 (n=6). The percentages of the major components show some **resemblance with that of armbrusterite** $[K_5Na_6Mn^{3+}Mn^{2+}{}_{14}[Si_9O_{22}]_4(OH)_{10}4H_2O]$ which has been reported from the PMF ores (Moore et al; 2011) but lack of essential alkalis (Na, K) and higher manganese content indicate that this Ba/Mn silicate is probably a different, not previously reported species.

5.1.2 Microbreccia and matrix-supported breccia

Altered rock termed as ***microbreccia*** exhibits cm-wide intervals in drillcores (Figure 2; *SLT015, SLT018,* Figure 9A) and is emphasized here for its particular texture, comprising densely disseminated micron- to mm-sized clasts in reddish and principally hematite-rich matrix. Under microscopic examination, the observed complex mosaic consists of angular or subrounded quartz clasts (50-500 µm), which are regularly replaced and veined by K-, Ba- and Ca-bearing gangue phases. Sodium is seemingly absent from the parageneses. In further detail, matrix appears as a very fine-grained mixture, presumably of hematite and muscovite whereas larger patches of Mn-bearing hematite (between 0.6 and 4.1 wt. %, average = 2.3 ± 0.8 wt.% Mn_2O_3, n =14), braunite, apatite and Mn-carbonates (kutnohorite, rhodochrosite) fill interstitial space between quartz clasts (Figure 9B, 9C). EDS analyses of the matrix show

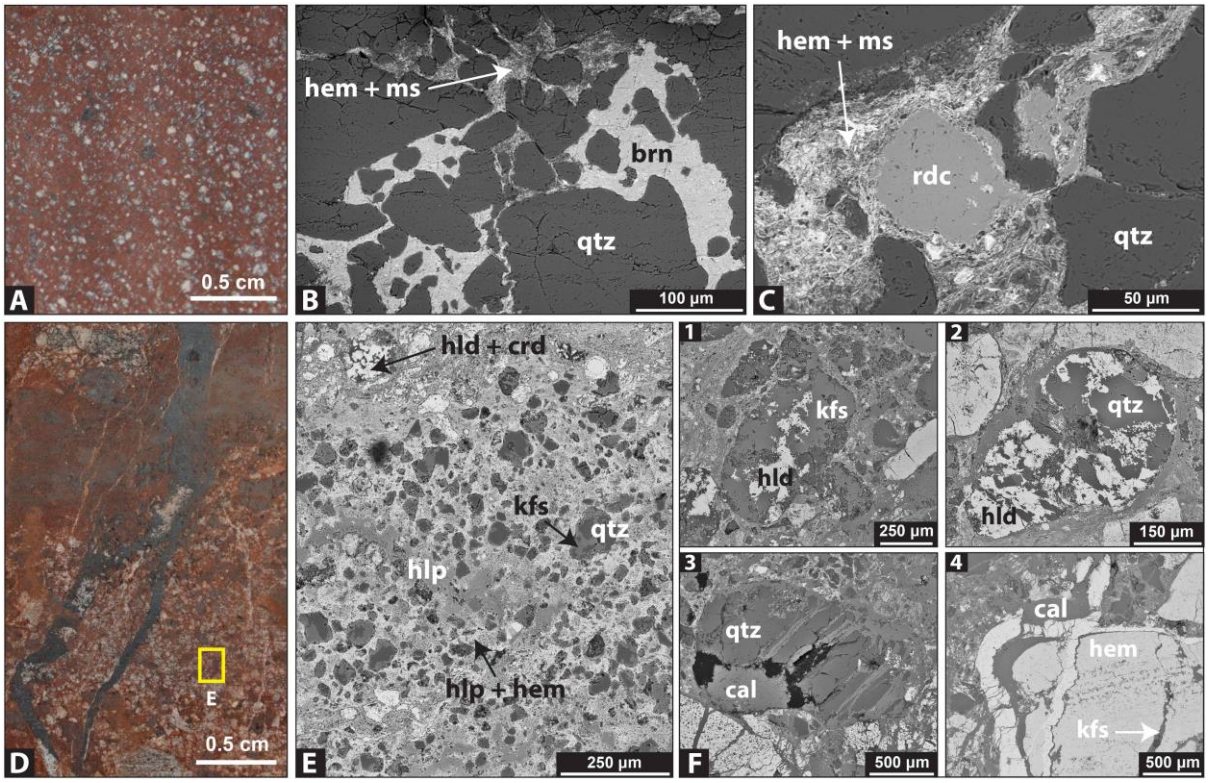

Figure 9. Back scattered electron (BSE) images. (A) Microbreccia consisting of microscopic clasts of quartz and alkali-bearing phases set in a hematite-rich matrix (photo). (B & C) Matrix between quartz clasts comprises fine-grained hematite and muscovite and coarser Mn-carbonates and braunite. (D) Hollandite vein metasomatizing the surrounding microbreccia matrix. (E) Matrix mineralogy next to hollandite-bearing vein supports wall-rock interaction, since it comprises hollandite, coronadite and hyalophane. (F) Quartz clasts enveloped, fractured and replaced by K-feldspar (1), hollandite (1, 2) and calcite (3, 4). brn = braunite, cal = calcite, crd = coronadite, hem = hematite, hld = hollandite, hlp = hyalophane, kfs = K-feldspar, ms = muscovite, rdc = rhodochrosite, qtz = quartz.

the following oxide weight percentages: SiO_2 = 31.7, Al_2O_3 = 22.1, Fe_2O_3 = 36.1, Mn_2O_3 = 0.9, Na_2O = 0.5, K_2O = 4.7, overall validating the presence of fine-grained hematite, braunite and muscovite constituents. Coarse-grained muscovite and rhodochrosite observed as rims on quartz clasts suggests partial replacement of the latter. Microscopic barite inclusions occur in rhodochrosite and coarse (100 µm) subrounded zircon crystals are found sporadically in the matrix. In addition to hematite, calcite is also documented to host appreciable manganese (ca. 3 wt. % MnO).

In the vicinity of hollandite [$Ba(Mn^{4+}{}_6Mn^{3+}{}_2)O_{16}$] veins (Figure 9D), infiltration of Ba, Mn, and Pb in the matrix of the microbreccia unit is recorded by the presence of hollandite, coronadite and hyalophane which are seen intermixed with hematite, K-feldspar, phlogopite,

and calcite. Most of the aforementioned species participate in pronounced replacements of quartz clasts (Figure 9E). For example, incomplete dissolution of the original quartz clasts provides an opportunity for the following replacement textures to be discerned (Figure 9F): (1) clasts with hollandite cores and K-feldspar rims (2) hollandite clasts enveloped by calcite (3) clasts traversed and replaced by calcite or (4) ferruginous laminated clasts overgrown and fractured by K-feldspar, hollandite and calcite. Ferruginization of certain clasts apparently originates by microplaty or specular hematite replacement and most likely do not represent remnants of formerly iron-enriched units.

The above-described metasomatic textures and reactions suggest that hollandite, despite it being widely known from mineral assemblages produced by supergene weathering, is related here to late hydrothermal veins, much in agreement to what has been documented from metamorphosed manganese deposits and hydrothermal settings (Hiroyuki; 1986, Yasuyuki; 1996). Coronadite, the Pb end-member of this Mn oxide group, as well as pure hollandite end-member displaying ca. 19 wt.% BaO, occur as disseminations and fine aggregates in microplaty hematite matrix. However, most EDS analyses demonstrate substitution between BaO and PbO, with PbO values ranging between ca. 2 and 14 wt. % (n=6).

Inside veins, hollandite forms blocky euhedral crystals that show strong anisotropy and are interrupted by tabular or xenomorphic barite, a texture corroborating most likely late transportation of sulfur and manganese through these breccias. Barite may exhibit coronadite rims whereas minute calcite veins, apparently formed later than hollandite, are seen precipitating along the edges of barite (Figure 10A). This may indicate replacement of the latter in similar fashion as earlier noted from the ferromanganese ore. Furthermore, arsenic is present in the Ba-bearing fluid as it is implied by a peculiar **As-rich hematite** concentric layering that usually develops around calcite cores (Figure 10B, C). This unusual hematite occurrence hosts 6.6 wt. % As_2O_5 and also contains 2.4 and 2.9 wt.% of SiO_2 and Al_2O_3 respectively. Several studies have shown that iron oxides accept arsenic (As) into their structure and its sorption on hematite is the highest among other oxides, as well as strongly pH-dependent (Singh et al; 1996, Di Iorio et al; 2018). Assuming that arsenic in the hematite

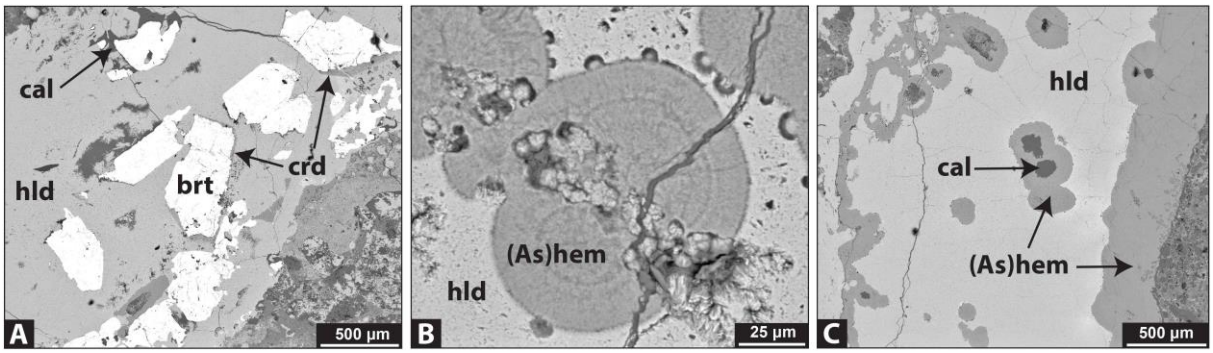

Figure 4. Back scattered electron (BSE) images. (A) Tabular and xenomorphic barite in hollandite vein, possibly displaying replacement by later calcite infiltration. (B & C) Peculiar spheroidal textures with concentric layering consist of As-rich hematite and may show cores of calcite. (As) hem = Arsenic-rich hematite, brt = barite, cal = calcite, crd = coronadite, hld = hollandite.

is arsenate [As(V)], this could indicate a highly alkaline environment, in which As(V) sorption is increased.

Finally, ***matrix-supported breccia*** is a term used here for a highly variable unit of brecciated rock, occurring particularly in the SLG cores (Langverwacht) as thick (up to ca. 20 metres) intervals in-between ferromanganese ore. This unit is characterized by an abundance of angular clasts, ferruginous laminated clasts and compositionally diverse vugs accommodated either by siliceous or otherwise iron- and sodic-rich groundmass. Quartz is present in the matrix but sodic-rich phases such as aegirine seem to be widely distributed and in many instances can be the dominant cementing phase. Figure 11 portrays a characteristic example of a coarse natrolite-filled vug (upper part), its reaction rim (middle) and aegirine-rich matrix hosting ferruginous clasts (bottom part). Natrolite consists of compact masses of translucent and largely inclusion-free crystals, although sparse disseminations of barite and hyalophane were also noted filling microfractures.

Moving inward from vug to matrix, intermediate zones consist of laths of aegirine which in most cases displays a length between 100 and 300 µm and coexists with equant apatite that also crystallizes as coarse grains (up to 100 µm) (Figure 11A). The latter hosts inclusions of barite and natrolite (Figure 11B, 11C), confirming synchronous precipitation during formation of the breccia. Calcite with inclusions of barite and K-feldspar infills coated by hyalophane, demonstrate that the two feldspars can coexist in these hydrothermal

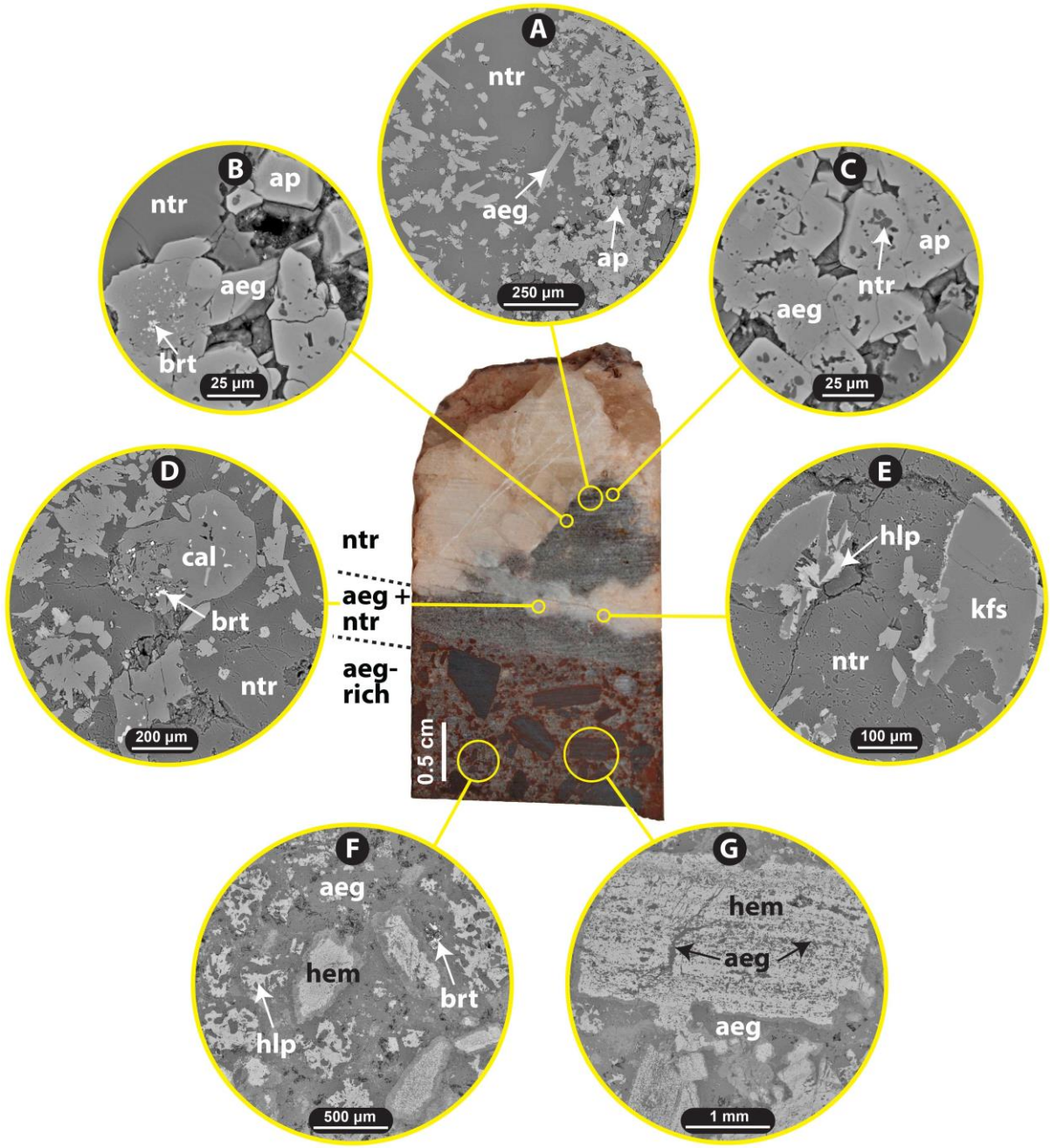

Figure 11. Large natrolite vug within matrix-supported breccia (centre). Back scattered electron (BSE) images (A-G). (A, B & C) Coarse-grained aegirine and apatite with natrolite-apatite inclusions form a 'reaction rim' between the large natrolite-vug and the Fe- and Na-rich groundmass of the breccia. (D) Calcite with barite inclusions. (E) Coexisting K-feldspar and hyalophane. (F) Breccia matrix is very rich in aegirine and hematite. (G) BIF-clasts possibly derived from reworking of conglomeratic Fe-ore exhibit aegirine replacement textures. aeg = aegirine, ap = apatite, brt = barite, cal = calcite, hem = hematite, hlp = hyalophane, kfs = K-feldspar, ntr = natrolite.

assemblages and indicate changes in the environment during mineral growth with synchronous presence of barium and potassium in the fluid (Figure 11D, 11E).

Successively, the sodium-rich matrix consists chiefly of coarse-grained aegirine with prismatic crystals (up to 500 μm) intruding or being encased by patches of hyalophane, natrolite and lesser barite (Figure 11F). A Mg-bearing silicate is also seen being intergrown with natrolite in the breccia cement and EDS analyses (n=3) suggest that it is stevensite [$(Ca_{0.2})Mg_{2.1}(Si_4O_{10})(OH)_2$], a later alteration product that has formed after natrolite and/or pectolite, in line with other analogous occurrences in literature (Elton et al, 1997). Angular hematite clasts are copious in the matrix and the ones displaying prominent banding can possibly represent BIF-clasts. Their source is enigmatic though since BIF are not present in these drillcores and derivation from the overlying conglomeratic iron ore would require major reworking of the succession involving dissolution, fracturing and collapse processes. These clasts may exhibit a thin (100-200 μm) corona of aegirine around them and furthermore are fractured and interstitially replaced by aegirine (Figure 11G), textures that draw some similarities with the altered aegirine-rich Hotazel iron-formation from the KMF (chapter 4, Tsikos and Moore; 2005).

5.1.3 Summary

In summary, the alkaline character of the ore zone is portrayed by the following mineral associations, the vast majority of which are paragenetically interpreted as hydrothermal: (a) **micas** (muscovite, paragonite, Ba-muscovite, phlogopite and some magnesium end-members). These are to a large extent associated with hematite and may partly represent earlier diagenetic/metamorphic processes, but clear examples of hydrothermal mica (for e.g., muscovite, phlogopite) also exist. (b) **Na-, Ba-, Ca- and CO_3-bearing associations** which are the dominant vug-filling components and mainly comprise albite, aegirine-augite, natrolite, serandite-pectolite, banalsite, piemontite, barite, calcite, barytocalcite and witherite. (c) **K-, Ba-, Ca- and CO_3-bearing associations**, which differ from the previous in the sense that sodium is minor or totally absent and sulfur and/or CO_3^{2-} more abundant. These chiefly comprise K-feldspar, hyalophane-celsian, barite, calcite, manganoan calcite and rhodochrosite, while apophyllite and grossular (see section 5.2.3) are also documented to occur in lesser quantities.

Further findings include: (1) **Arsenic-bearing species** being apatite, hematite and As-tokyoite and (2) Very localized **Al-rich associations**, defined by diaspore and an unidentified

Al-rich manganese silicate. The relationship between ore-minerals [braunite, braunite (II), hematite, partridgeite] and alkali assemblages is unclear. The former appear to be diagenetic/low grade metamorphic but there is also evidence supporting recrystallized and hydrothermal varieties [hematite, braunite, braunite (II)], as well as minor but exclusively hydrothermal Mn-oxide species (hollandite-coronadite).

5.2 Ar-Ar sample description and results

To establish the age of alkali metasomatism within the ore zone we obtained mineral-specific in situ $^{40}Ar/^{39}Ar$ ages of four samples comprising the following phases: (a) phlogopite (b) hyalophane and (c) paragonite. In addition, age data were obtained from the ore matrix and specifically from areas hosting two very fine-grained but chemically distinct K-bearing aluminosilicates, which again allows for these data to be broadly regarded as mineral-specific, even though some degree of uncertainty exists. A detailed petrographic description of each sample precedes the presentation of Ar-Ar results.

5.2.1 Vuggy ferromanganese ore: sample 537-7

This sample represents a typical occurrence of vuggy ferromanganese ore with pronounced alternating hematite-braunite microlamination. In detail, matrix bears a profuse display of microscopic vugs filled by diverse gangue mineralogy. The right side of the polished wafer (Figure 12.1) contains ample voids with cores filled by barite and calcite or manganese carbonates growing in their outermost parts. Macroscopically, these vugs can be seen as extensive open-space filling (Figure 12.2) and may also host silicates such as aegirine, natrolite and hyalophane. Once more, textural evidence suggests that barium carbonates and calcite occupying barite-free vugs have probably formed later than or have overgrown on barite (Figure 12.3). Authigenic apatite is also common in the matrix and as open-space occlusion. Siderite is widespread as large interstitial aggregates in hematite-rich matrix, which seemingly promotes its formation. On the other hand, **hydrothermal phlogopite microvugs** are preferentially contained in braunite-rich matrix and are surrounded by microvugs comprising silicates (serandite, aegirine-augite, natrolite), carbonates (calcite, kutnohorite, strontianite, barytocalcite) and an unidentified Ba/Mn silicate also encountered in analogous parageneses from other drillcores (Figure 12.4, 12.5). Barite can also be constituent of these assemblages (Figure 12.6).

All laser ablated phlogopite-filled vugs were previously confirmed as such by EDS analyses which further showed no compositional variations. Subsequently, these were marked on the composite reflected-light map which bears considerable visual similarity with

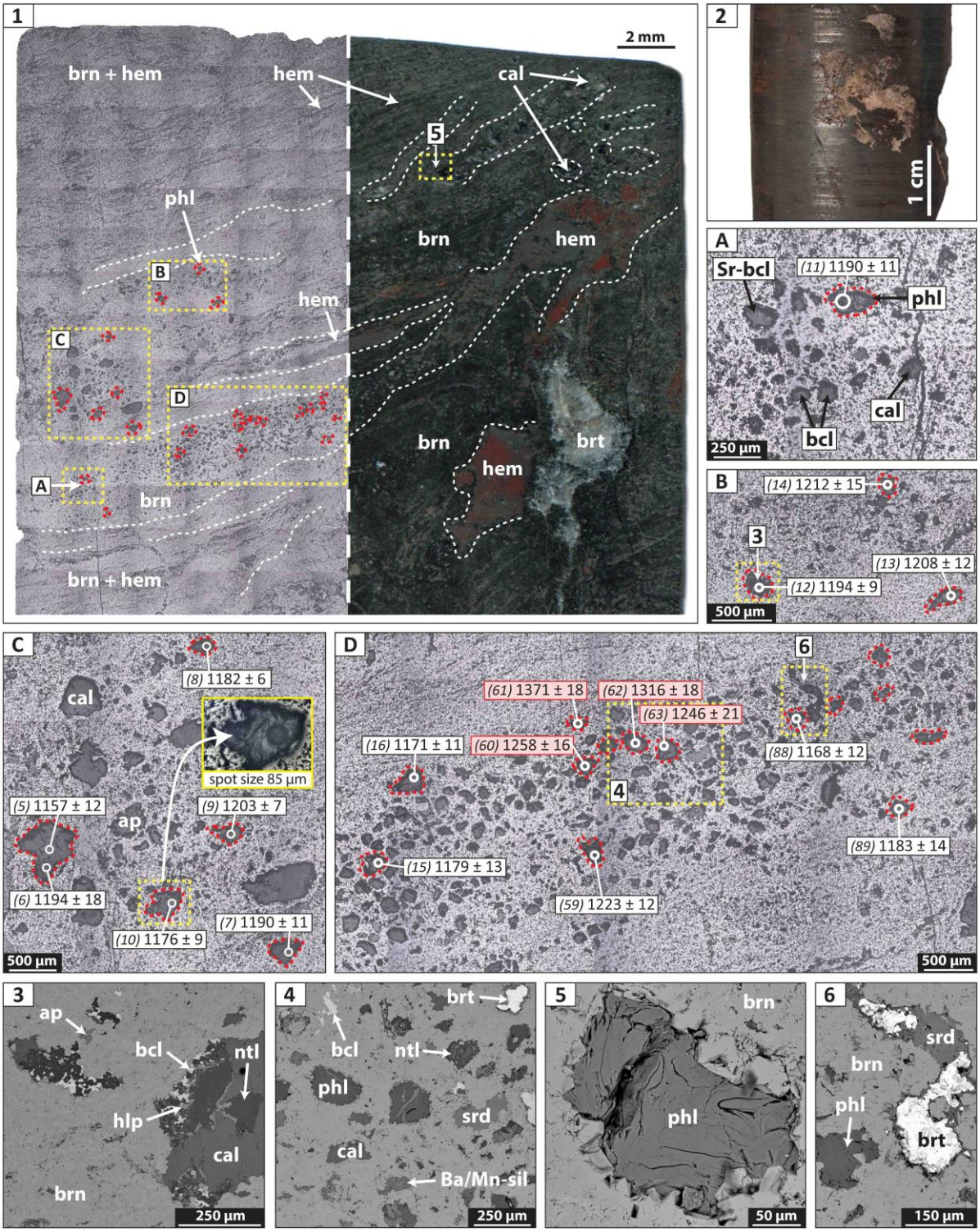

Figure 12. (1) Reflected light (RL) microscopy photograph mosaic (left) and polished-block scan (right) showing selected locations for $^{40}Ar/^{39}Ar$ dating. (2) Vug-filling cement from the same sample comprising mostly barite and lesser carbonates and silicates. Back scattered electron (BSE) images (3-6). (3) Ba-carbonates most likely form later or at the expense of barite-filled vugs. (4-6) Representative textures of the dated sample area, where phlogopite of hydrothermal origin is surrounded by the same Na-, K-, Ca and Ba-bearing assemblages seen throughout the ore zone. (A-D) Enlargement of the framed areas (RL), showing also ablation pit under UV light (C, inset). 'Older' spot dates clustered together are coloured in red (D). ap =apatite, Ba/Mn-sil = unknown Ba-Mn-rich silicate, bcl = barytocalcite, brn = braunite, brt = barite, cal = calcite, hem = hematite, hlp = hyalophane, ntl = natrolite, phl = phlogopite, Sr-bcl = strontian barytocalcite, srd = serandite.

imaging provided by the ultraviolet (UV)-laser $^{40}Ar/^{39}Ar$ system and therefore can function as a great tool to guide analysis. A laser spot size of 85 µm was effectively used in all of the targeted microvugs, which in general range between 100 and 300 µm in size. Nineteen spot dates obtained range between 1156.9 ± 12.1 Ma (1σ) (spot 5) and 1370.6 ± 18 Ma (1σ) (spot 61), with a weighted average of 1196.6 ± 4 Ma (2σ, MSWD = 3.99, n=19). Difference between minimum and maximum date is considerable (214 ± 6 Ma) but for the majority of data no apparent correlation between date and location in sample or surrounding vug-mineralogy (Figure 12A-D) can be easily discerned. Instead, the large spread of data is controlled essentially by few older dates which derive from vugs that are clustered together (spots 60, 61, 62, 63) (Figure 12D). Rejection of these data reduces significantly the spread (ca. 67 Ma difference), with remaining dates showing a calculated mean of 1188.1 ± 4.4 Ma (2σ, MSWD = 0.88, n=15). Possible implications of these 'older' apparent ages are further explored in the discussion.

5.2.2 Calcite-hyalophane vein: sample L2B-10

This sample is characterized by a thick calcite-rich vein that seemingly cross-cuts massive ferromanganese ore (Figure 13.1, 13.2). The latter is pervasively microlaminated at the microscale, specifically displaying mildly undulating hematite and braunite laminae. The vein additionally hosts a pale yellowish-brown mineral with composition ranging between hyalophane and celsian, that occurs as clusters of mostly xenomorphic crystals filling interstitial space between calcite grains. Equant to subequant syngenetic barite is found as inclusions in both feldspar and calcite as well as in the surrounding ore matrix. Apart from the vein-hosted gangues, potassium can also be detected in bulk analyses of the matrix with higher porosity (K_2O = 1.45 wt. %), which further show increased aluminum values (Al_2O_3 = 5.21 wt. %); thus, indicating the presence of other silicates in the ore groundmass.

Another accessory phase firstly reported from these ores is **tamaite** [$(Ca,K,Ba,Na)_{3\text{-}4}Mn_{24}(Si,Al)_{40}(O,OH)_{112}21H_2O$], the Ca-analogue of ganophyllite. It is found as micaceous platy crystals forming on the edges of hyalophane with the surrounding calcite, as well as in the interiors of 'secondary' hydrothermal braunite crystals. (Figure 13.3, 13.4). EDS analyses give SiO_2 = 43.3, Al_2O_3 = 7.4, MnO = 34.5, CaO = 1.2, K_2O = 0.7 and BaO = 8.6 wt. %, suggesting a

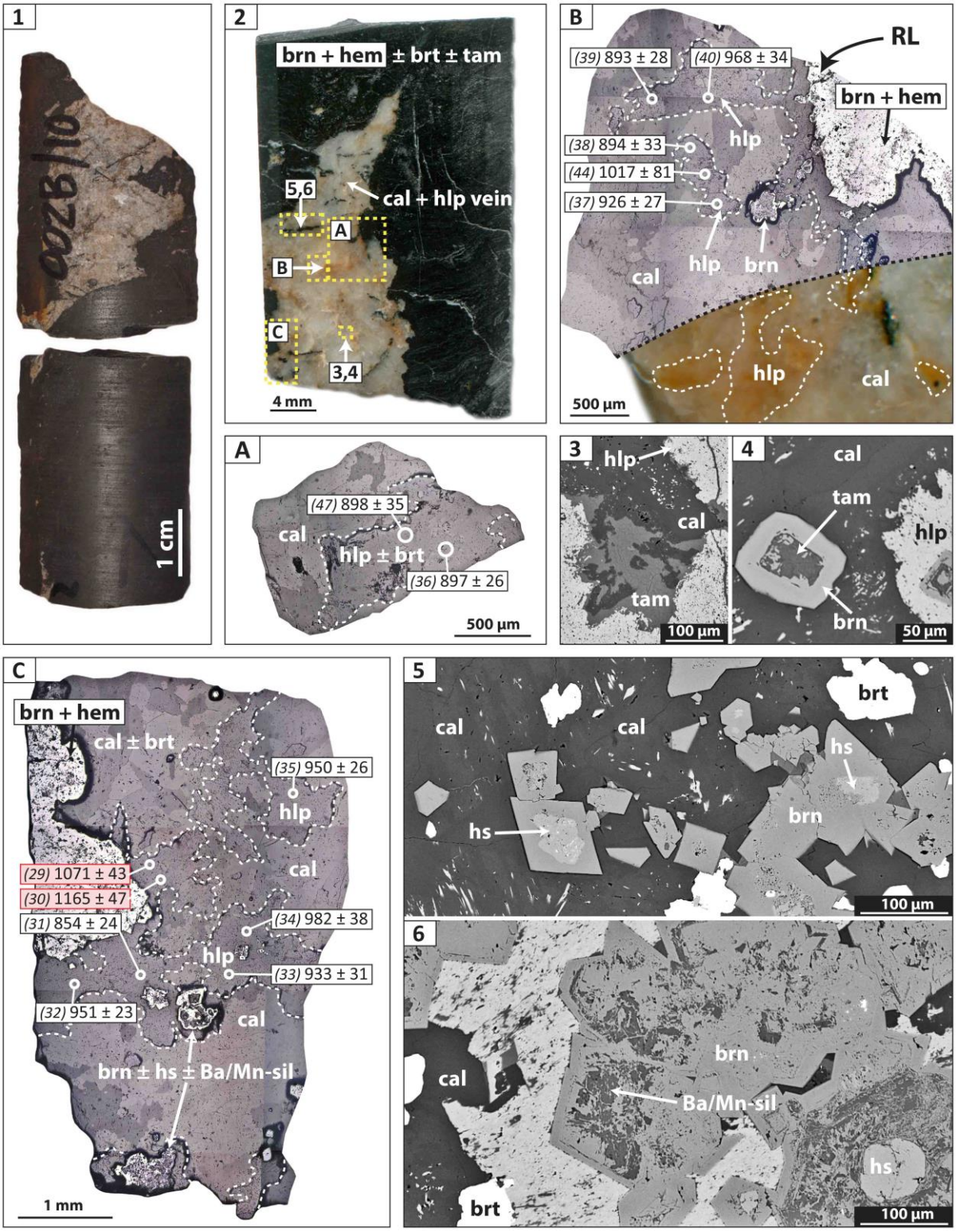

Figure 13. (1 & 2) Braunite-hematite microlaminated ore cross-cut by calcite-rich vein containing minor hyalophane and Mn-minerals. Back scattered electron (BSE) images (3-6). (3 & 4) The rare manganese phyllosilicate tamaite forms as part of the late Ba/Ca-alteration hydrothermal assemblage and fills the interiors of newly-formed braunite. (5 & 6) Equant braunite grains enclosing hausmannite or a Ba/Mn silicate indicate manganese transportation along with the alkali-rich fluids on the microscale. (A-C) Reflected light maps of the dated areas. The two oldest dates rejected from the final weighted average are coloured in red (C). Ba/Mn-sil = unknown Ba-Mn-rich silicate, brn = braunite, brt= barite, cal = calcite, hem = hematite, hlp = hyalophane, hs = hausmannite, tam = tamaite.

composition very similar to that documented from its very limited worldwide occurrences. Both in the Val Graveglia mining district in Italy and the Shiromanu manganese mine in Japan, tamaite is considered as to have formed during late-stage hydrothermal activity or low-grade metamorphism and coexists with many rare species also known from the PMF such as tokyoite and gamagarite (Matsubara et al; 2000, Hughes et al; 2003). Lastly, a characteristic texture in the specimen is that of clusters of rhomb-shaped recrystallized braunite (50-100 μm) seen entrained in the calcium-rich vein, which implies some degree of manganese transportation with the metasomatic fluids. Braunite cores are often occupied either by hausmannite, as it is confirmed by its distinct anisotropism exhibited under the optical microscope, or by the Ba/Mn silicate seen elsewhere in the ore zone (Figure 13.5, 13.6).

Fourteen analyses of celsian-hyalophane yielded a range from 854 ± 24 Ma (1σ) (spot 31) to 1165 ± 46 Ma (1σ) (spot 30) and have a weighted mean of 933 ± 8 Ma (2σ, MSWD = 4.5). Dates are randomly distributed within the vein, with the three older (spots 29, 30, 44) showing also the higher uncertainties (from 43 to 82 Ma). The significant age spread (310 ± 22 Ma) is once more governed by the aforementioned older dates. Owing to the widely variable and generally low potassium content of the targeted feldspar, areas between 110 and 155 μm were ablated and yet a small number of analyses did not yield sufficient argon gas. A noted drawback resulting from the large laser size is that ablated material released during gas extraction tends to clutter the surroundings of ablated pits and blurs laser optics for an extensive area around them, in that way prohibiting in most cases a dense pattern of analyses. Given that no feldspar grain boundaries were visible during laser ablation, spot analyses are also not grain-specific, which is noted here since it may bias apparent ages to some degree. The likely meaning of the total age range is explored further below within the general geological context but the obtained age broadly agrees with that of phlogopite.

5.2.3 Celsian-hyalophane vein and silicate-rich ore matrix: sample L2B-8

One of the most notable features of this sample are the extensive celsian-hyalophane veins/open space-fillings and the zone between these and the braunite-rich ore matrix. The ore displays a more ‘’shaley’’ appearance alluding to higher phyllosilicate and hematite content (Figure 14.1, 14.2). Potassium content in the feldspar vein is highly variable and

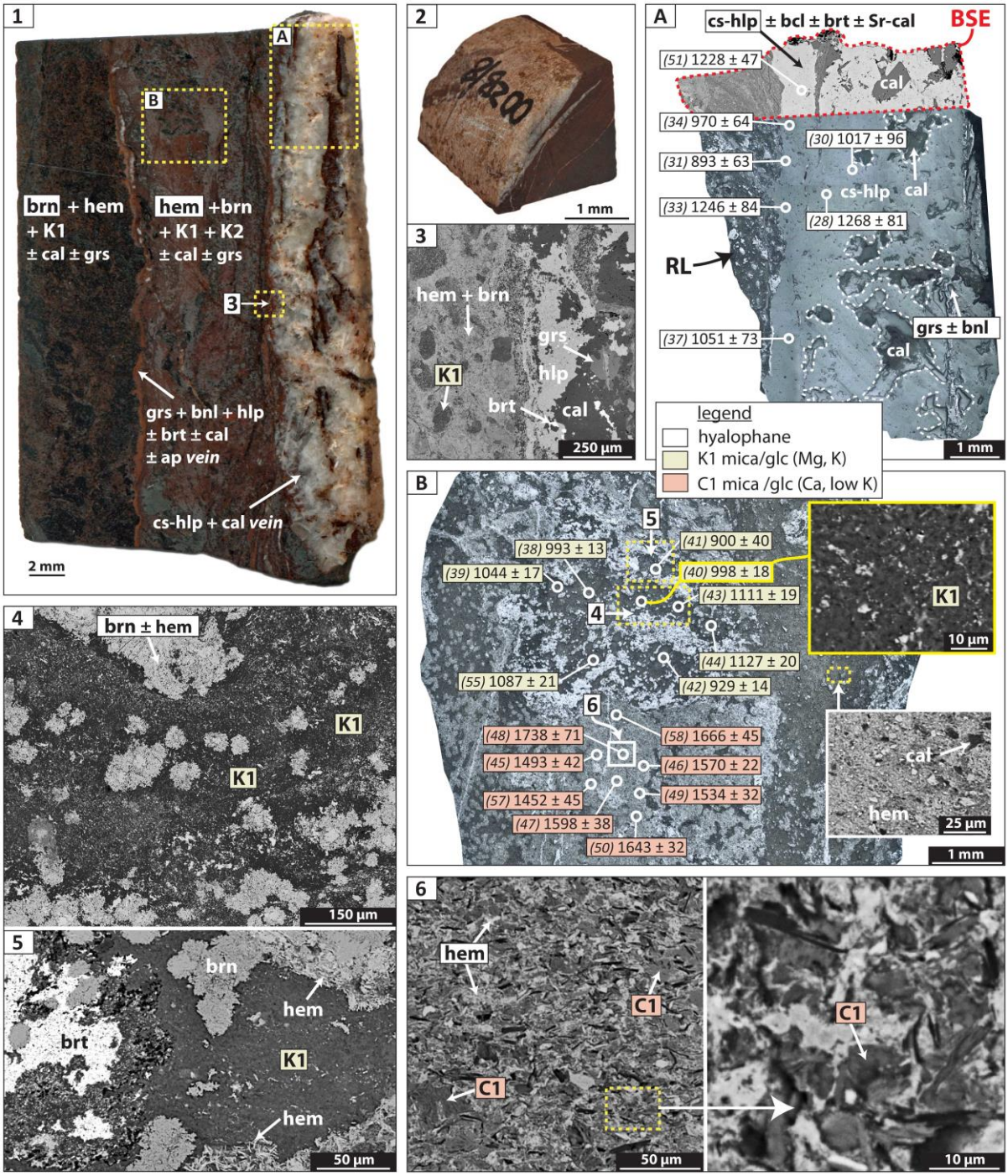

Figure 14. (1 & 2) Celsian-hyalophane open-space occlusion (white) adjacent to transitional hematite- and phyllosilicate-rich zone between the former and the Fe-Mn matrix. Back scattered electron (BSE) images (3-6). (3) Calcite with barite inclusions, Mn-carbonates, grossular and other gangues develop interstitially to celsian crystals. (4-6) Two distinct mica identified as members of the glauconite-celadonite series occur as intricately mixed sheets with braunite and hematite in ore matrix. K1 and C1 abbreviations represent these two silicates, exhibiting higher potassium and calcium respectively. (A) Reflected light (RL)/BSE composite map showing distribution of $^{40}Ar/^{39}Ar$ hyalophane dates in the alteration vein. (B) Distribution of $^{40}Ar/^{39}Ar$ mica dates from two bulk areas of the matrix which apparently comprise two chemically and geochronologically distinct generations (RL). Fine details in insets (BSE). ap =apatite, bcl = barytocalcite, bnl = banalsite, brn = braunite, brt = barite, cal = calcite, cs = celsian, grs = grossular, hem =hematite, hlp = hyalophane, Sr-cal = strontian calcite.

mostly below detection limit for EDS sensitivity, however the element was successfully picked up (K_2O = 1.34 ± 0.49, n=4), particularly in vicinity to the matrix. The major remaining phases found in the predominantly celsian open-space filling are calcite, barite and garnet (Figure 14.3) with composition very close to grossular endmember as outlined later on. Calcite hosts traces of Mn- and Ba-carbonates such as barytocalcite, strontian calcite and kutnohorite as well as silicates representative of the alkali metasomatism such as pectolite-serandite and banalsite. Barite and calcite cross-cutting veinlets seen commonly in the sample confirm that these evidently later generations fill open space subsequently to formation of granular and well-crystallized feldspar aggregates.

Two distinct **potassium-bearing aluminosilicates** displaying different brightness under SEM occur in the ore groundmass. Texturally, they appear as sheets or needles but are so fine-grained and intimately intermixed with the ore minerals as to be difficult to analyse with high level of confidence (Figure 14.4-14.6). Nevertheless, a number of EDS analyses performed on visually homogenous material shows rather uniform results, suggesting that the two aluminosilicates bear variable but broadly similar iron and manganese concentrations (FeO = 8.3 ± 4.1 wt.%, MnO = 5.7 ± 3.5 wt.%, n=12) but differ in their alkali content. Specifically, one exhibits higher potassium and magnesium values (K_2O = 8.3 ± 1.6 wt.%, MgO = 9.3 ± 3.8 wt.%, n=6) and the other is depleted in potassium (from below detection to 0.7

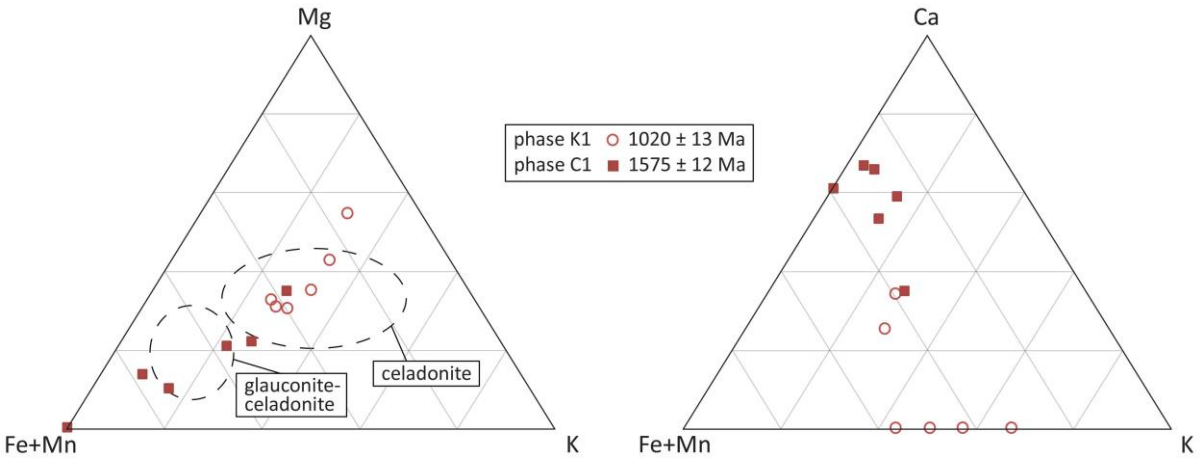

Figure 15. Ternary classification diagrams for phyllosilicate minerals based on their (Fe-Mn)-K-Mg and (Fe-Mn)-K-Ca ratios. Drawn after related diagrams for dioctahedral silicates involving glauconite and celadonite (Maciag et al; 2019, Yamashita et al; 2019). Plotted data are EDS analyses of silicate-rich material deriving essentially from the Ar-Ar dating sites. Mineral identification is inconclusive and therefore the dating targets are mentioned hereon as K1 and C1.

wt.%, n=6) but hosts much higher calcium content (CaO = 3.4 ± 1.2 wt.%) (Table 1). The following stoichiometric formulas are obtained on the basis of 11 oxygens for the two phases respectively: (a) $K_{0.7}(Ca_{0.2}Mg_{0.9}Fe_{0.4}Mn_{0.4})(Al_{1.6}Si_{2.7})O_{10}(OH)_2$ and (b) $K_{0.3}(Ca_{1.7}Mg_{0.3}Fe_{0.6}Mn_{0.3})Al_{1.3}Si_{2.7}O_{10}(OH)_2$.

Table 1. EDS analyses of the K-bearing aluminosilicates dated by $^{40}Ar/^{39}Ar$ in comparison to EMPA analyses of dioctahedral micas with broadly comparable stoichiometry. * Buckley et al; 1978

mineral	K1	C1	glauconite*	celadonite*
	n=6	n=6	n=12	n=14
SiO_2	40.74	37.13	50.38	52.55
Al_2O_3	20.69	16.88	7.49	3.90
FeO	6.54	10.04	20.34	15.87
MnO	6.50	4.93	-	-
CaO	2.89	22.12	0.57	0.27
MgO	9.33	2.49	3.65	6.34
K_2O	8.32	2.79	7.97	9.07
Total	95.00*	95.00*	92.64	89.92

Both analysed phases do not show great compositional resemblance to any of the common sheet silicates, apart maybe from the dioctahedral mica/smectites **glauconite and celadonite** (Buckley et al; 1978, Odin and Fullagar; 1988). The classification plot of Figure 15 (left) and the fact that the aforementioned minerals show an intrinsic K-deficiency (López-Quirós et al; 2020) that can explain the calculated low potassium levels, are further clues for a possible affiliation of these two matrix-hosted species with the above regarded Fe-rich phyllosilicates. However, as also seen in Table 1, this interpretation is ambiguous, since significant Al-Si and Fe-Mn substitutions are required to match the chemistry of these clays, which in addition do not host significant calcium as the studied phases. Furthermore, the geological occurrence of celadonite and glauconite is generally rather different than the envisaged terrigenous karstic environment of the PMF ores, with the first forming mainly in

deep-seas strata from alteration of basalts (Velde; 2014) and the latter occurring in carbonates and sandstones, but overall, in open-marine environments with limited terrigenous input (Hesse and Schacht; 2011). Another possible affiliation that could be investigated is with the magnesium-iron-manganese, calcium amphibole subgroups or even Al-rich members (for e.g., Al-rich pargasite: Bunch and Okrusch; 1973), but such determination is challenging and with the current analyses of this fine-grained material this has not been pursued further. XRD oriented mounts and other differentiation techniques for mica/clay minerals (e.g., Köster et al; 1999) could potentially lead to more conclusive results. On this account, these micas are labeled here as K1 and C1 to highlight the higher potassium and calcium content respectively. However, it should be noted that high levels of calcium were also detected within the matrix of the K1 domains (Figure 14.4) and its presence could be also related to other calc-silicate or carbonate gangues formed during metasomatism.

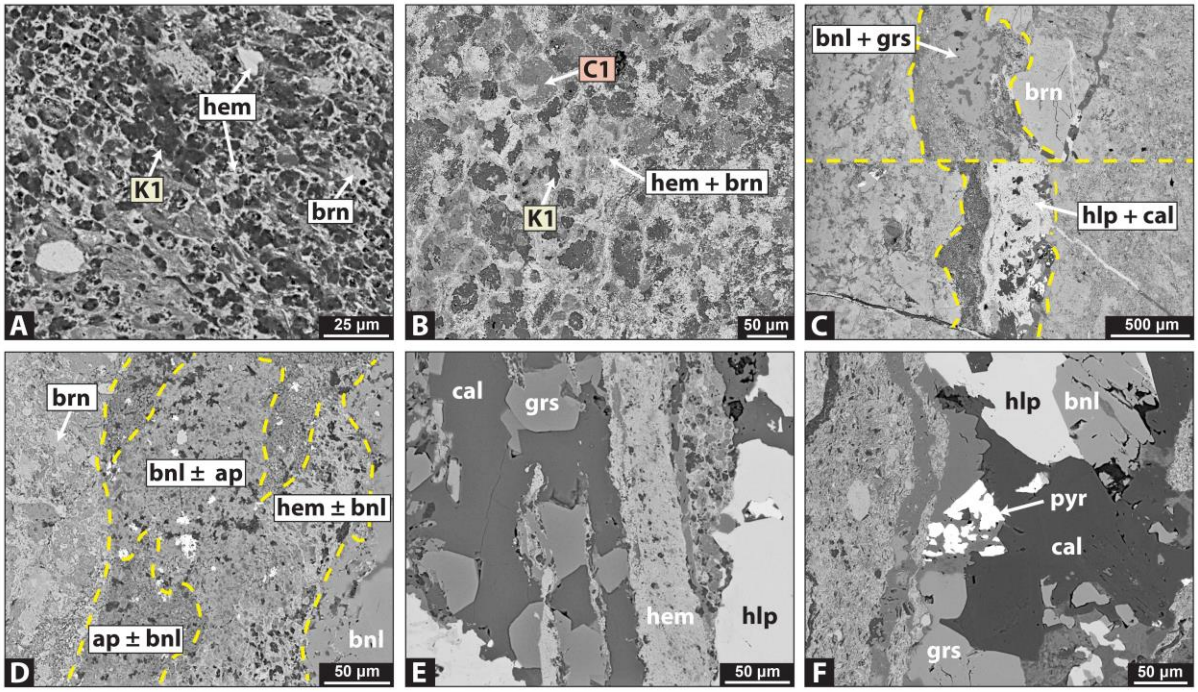

Figure 16. Back scattered electron (BSE) images. (A and B) Well-rounded textures or ovoids of unknown origin consist partly of secondary mica (glauconite-celadonite) and are set in a mineralogically complex matrix with hematite, braunite and various other gangues. (C) The same veinlet can be occupied by hyalophane or banalsite and grossular assemblages. (D) Apatite is intricately mixed with hematite and banalsite in hydrothermal veinlets. (E) Subhedral grossular evidently reworked by hematite. (F) A very rare lead manganese vanadate (pyrobelonite) is firstly reported here in association with the alkali assemblages. ap =apatite, bnl = banalsite, brn = braunite, cal = calcite, grs = grossular, hem = hematite, hlp = hyalophane, K1-K2 = glauconite-celadonite (see also text) pyr = pyrobelonite.

Although matrix is largely composed of a mineralogically indistinguishable fine-grained material, certain textures such as that of well-rounded microscopic ovoids can be noticed and seem to consist for the most part of the afore-described K1 and C1 mica (Figure 16A, 16B). It is unclear if these micro-textures indicate preservation of original sedimentary/diagenetic characteristics but at least the surrounding iron- and manganese-rich matrix displays complex morphologies and abundant hydrothermal gangues that point to later reworking. Intergranular space is occupied by fine-grained versions of the vein-forming minerals. Hyalophane veinlets (μm-scale) are seen grading into ones containing banalsite and interstitial **grossular**, an observation that highlights the close relationship of sodium, potassium, barium and calcium during stages of the metasomatic event (Figure 16C). At the same time, their outermost part consists of very fine-grained banalsite, apatite and hematite intermixed associations (Figure 16D). Using the existing garnet formulations (i.e., Gross = 100 x [Ca/Ca + Mg + Fe)], EDS analyses of garnet (n=4) show 62.1 % mole of grossular and 37.9 mole % of andradite for garnets reported for the first time in these ores. Its origin is certainly linked to the other alkali minerals and apparent reworking by hematite can be also observed on the micro-scale (Figure 16E). Another relatively rare mineral reported so far only from metamorphosed Fe-Mn deposits with complex skarns and secondary alteration events (Welin; 1968, Criddle and Symes, 1977) is the **lead manganese vanadate pyrobelonite** [$PbMn^{2+}(VO_4)(OH)$], which is seen in this specimen mostly as anhedral or prismatic microscopic (20-50 μm) grains being hosted by hyalophane veinlets (Figure 16F). For instance, one of the more recently documented occurrences in the Precambrian Iron Monarch deposit (South Australia) has been attributed to later alteration iron-mobilizing fluids (Pring et al; 2005).

Seven in situ $^{40}Ar/^{39}Ar$ ages from the <u>hyalophane</u> vein display a very large range between 893 ± 63 Ma (1σ) and 1268 ± 84 Ma (1σ) and a weighted mean of 1102 ± 29 Ma (2σ, MSWD = 4.0 (Figure 14A). The poorer precision in comparison to hyalophane of sample L2B-8 is reflected in both the higher date deviation (375 ± 49 Ma) and larger uncertainties (up to 96 Ma). Furthermore, similarly to sample L2B-8, large variations of potassium led to increased laser size and many terminated analyses due to little gas. Eight analyses (85 μm spot size) of <u>K1-rich matrix (celadonite)</u> yielded a range from 900 ± 40 Ma (1σ) to 1127 Ma (1σ), with a

weighted mean of 1020 ± 13 Ma (2σ, MSWD = 4.0) (Figure 14B). Despite the evidently multi-grained analyses and significant spread of data (227 ± 27 Ma), age results from this mica greatly resemble that of hyalophane, thus implying cogenetic formation or isotopic re-equilibration during metasomatic alteration, scenarios that are further discussed later on. Finally, eight spot analyses (85 µm spot size) of C1-rich matrix (glauconite) document a great age variability ranging from 1452 ± 45 Ma (1σ) to 1738 ± 71 Ma (1σ) (Figure 14B). Although it is uncertain from petrographic evidence if these ages characterize mixed mica populations or crystals of the same generation, this small data set displays a weighted mean of 1575 ± 12 Ma (2σ, MSWD = 4.0), which is distinctly different and at first glance unrelated to the formation of hyalophane and other alkali minerals.

5.2.4 Paragonite - banalsite assemblage in silicate-band disrupting ore: sample PM17-16

The distinctive characteristic of this sample is a wide irregularly-shaped band of brownish red material with creamish-yellow lenses disrupting the laminated ore structure and exhibiting fairly sharp contacts with it (Figure 17.1, 17.2). Ore groundmass displays pervasive metasomatism characterized by lenticular lamination (up to 1 mm) or equivalent structures (200-500 µm) which largely consist of banalsite and braunite. These minerals form at the rims of the lenses, which in turn are surrounded by an intricately mixed mass of hematite and braunite (Figure 17.3, 17.4). Minute veins comprising anhedral pyrobelonite and equant banalsite are observed transecting both the ore and the silicate-band.

A mica with the chemical formula $(Na_{0.5}K_{0.3})Mg_{0.2}Al_{1.4}(Al_2Si_{2.5})O_{10}(OH)_2$, apparently being paragonite, dominates the matrix of the µm to mm-scale irregular lenses that occur in the silicate-band and which are bounded by aggregates of banalsite. Discrete banalsite grains with euhedral or rounded crystals edges are common. Titanium and vanadium residing in analysed hematite and the sharp contacts of the silicate-band with the ore may indicate an allochthonous origin for this band, involving incorporation of shale material during some stage of ore brecciation. However, hydrothermal overprint is pervasive in the specimen and metasomatic processes can possibly also account for the observed sharp edges. A fine-grained mineral very hardly distinguished from paragonite under optical microscope, but

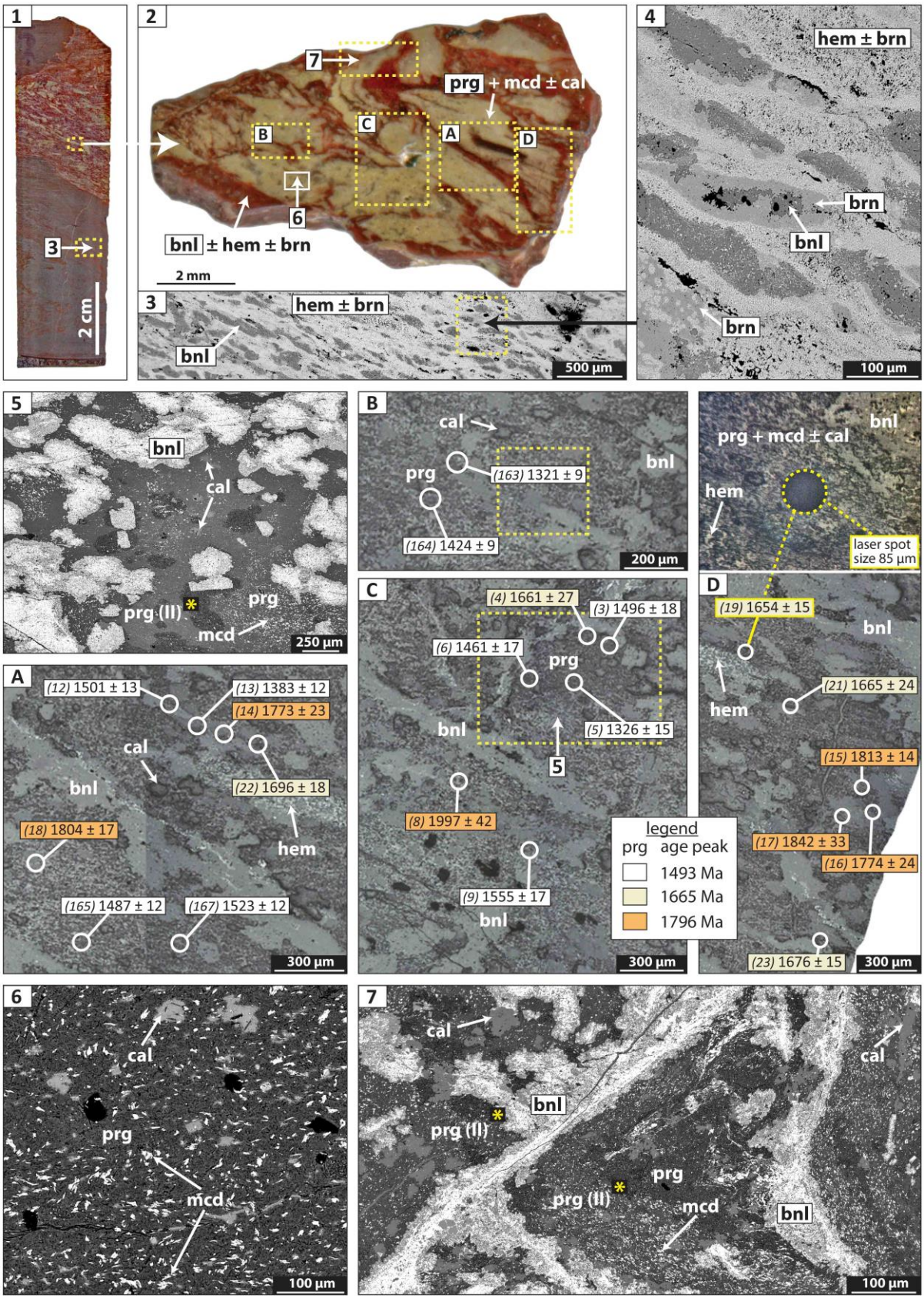

Figure 17. (1) Alkali-rich silicate band (brownish red) disrupting ferromanganese ore. (2) Closeup area of the paragonite- and banalsite-rich band from which all $^{40}Ar/^{39}Ar$ dates were obtained. (3-7) are back scattered electron (BSE) images. (3 & 4) Details of the hematite-rich ore matrix showing lenticular structures comprising banalsite and braunite. (5) Rounded and euhedral banalsite in a very fine-grained (continues in next page)

Figure 17. (continued) paragonite-rich matrix also containing calcite, macedonite and a poorly documented mica). (6 & 7) Very fine-grained macedonite ($PbTiO_3$) needles occur within paragonite matrix and are evidently related to the also Pb-bearing pyrobelonite seen in veinlets running through the sample. (A-D) Magnification of the yellow-framed areas (RL) displaying distribution of $^{40}Ar/^{39}Ar$ dates. The very wide range of generally 'old' dates shows no apparent relationship with respect to location in the sample but certain age peaks can be identified (see legend, text and section 6.2). bnl = banalsite, brn = braunite, cal = calcite, hem = hematite, mcd = macedonite, prg = paragonite, prg(II)* = silicate poorly defined as Mn-bearing paragonite.

appearing brighter under SEM due to it additionally containing manganese (MnO = 5.7 ± 1.1 wt.%, n=2), occurs interstitially to paragonite and potentially represents a different paragonite or mica species (Figure 17.5). It must be noted that the very fine-grained and intricately mixed minerals of the matrix hampered acquisition of conclusive SEM results.

Paragonite matrix also contains calcite disseminations and copious amounts of small (5-20 μm) needles of the very rare **lead titanate macedonite** ($PbTiO_3$) (Figure 17.6, 17.7). Its formation is undoubtedly related to the pyrobelonite veins and corroborates lead introduction by fluids but the fact that is limited to the silicate-band may be suggestive of the former concentration of titanium, probably in detrital preexisting phases such as rutile. This mineral was firstly discovered in quartz-syenite pegmatite veins cutting schists and amphibolite (Radusinović and Markov; 1971) and shortly after in skarn banded chert within metamorphosed Fe-Mn deposits (Burke and Kieft; 1971). Rutile, Mn-bearing mica and silicates (tephroite, kentrolite), aegirine, feldspars and calcite are mentioned as the main associations from the above localities.

Twenty-one analyses of paragonite yielded a very wide range of dates between 1320.5 ± 8.7 Ma (1σ) to 1997 ± 42.2 (1σ) (Figure 17A-D). This broad distribution of data comprises multiple peaks with the most pronounced being at ca. 1796, 1665 and 1493 Ma and subordinate younger peaks seen until 1320 Ma, the latter though defined only by two dates. (see also section 6.2 later on). The different spot dates are coloured according to the peak they are associated with. No systematic manner of age distribution can be observed. In fact, patches of older dates are apparently intermixed with younger ones and the difference between dates can be as high as ca. 390 Ma for ablation spots being only couple of microns apart (for e.g., spots 13 and 14, Figure 17C).

Since paragonite in this specimen is very fine-grained, ablation of intergrowths of different populations and/or interstitial K-bearing phases that were likely missed during petrographic examination may be related to the great scatter seen in the dataset. However, given the general geological context, disturbance of the Ar-Ar systematics is a more likely scenario. The thermal history of this sample, which most likely involves age reset during one or more events and its underlying geological significance are investigated in detail in the discussion.

5.3 Oxygen and hydrogen isotopes

As presented in great detail above, the bulk of hydrothermal phases are too fine-grained and intimately intergrown with each other, as well as with ore minerals, to permit reasonable mineral separation for stable isotopic analysis. Consequently, only few carefully selected targets from relatively coarse-grained zones were analysed. It is reminded that separation was achieved by micro-drilling areas that were previously examined under SEM and no other purification procedures were done prior to oxygen analysis. Therefore, a small degree of contamination is expected, but as both the obtained yields and $\delta^{18}O$ values suggest, data largely correspond to the regarded analysed species. Possible contaminants for each sample are reported in Table 2.

Regarding Langverwacht and Heuningkranz localities, single oxygen isotopic analyses of aegirine, natrolite and banalsite display values of +9.1, +13.5 and 11.6 ‰ respectively. $\delta^{18}O$ ratios of hyalophane are also very similar (+11.4 and +11.6 ‰). Micas exhibit a slightly wider range, from +8.1 to +12.9 ‰, however showing an average close to the previous silicates (+10.7 ± 1.9 ‰, n=5). Oxygen isotopes of armbrusterite are in the same range (+8.8 and +12.9‰), whereas berthierine from different stratigraphic depths displays scattered and much lower values of +11.1, + 7.5 and +5.7 ‰. A rather similar and limited range of oxygen isotope values is shown by silicates at Bruce mine. Specifically, sugilite has $\delta^{18}O$ ratios of +13.3 and +13.4 ‰ and armbrusterite +14.9 ‰. In contrast, hematite (specularite) displays negative values (-0.8 and -7.5 ‰). δD values of micas range from -60.7 to 78.7 ‰ and a single analysis of natrolite (65.1 ‰) falls within the former range. On the other hand, δD composition from a single armbrusterite sample (-126.8 ‰) is much different from that of micas.

Table 2. Stable O and H isotopic compositions of mostly silicate gangue minerals and calculated $\delta^{18}O$- and δD-fluid values for a temperature of 215°C (see also text).

sample ID	mineral	formula	description / lithology	Possible contaminants	$\delta^{18}O_{min}$	δD_{min}	$\delta^{18}O_{fluid}$*	δD_{fluid}*
Langverwacht (silicates in ferromanganese ore, breccias and quartzite)								
L2B-15	aegirine	$NaFe^{3+}Si_2O_6$	cement in matrix-supported breccia	hem, hlp, ntr	9.1	-	3.5	-
L2B-8	celsian-hyalophane	$(K,Ba)Al_2Si_2O_8$	vein producing wall-rock alteration in Fe-Mn ore	cal, brt, bcl	11.6	-	4.3	-
L2B-10	celsian-hyalophane	$(K,Ba)Al_2Si_2O_8$	calcite-hyalophane vein cross-cutting Fe-Mn ore	cal, brt, tam, hs	11.4	-	4.1	-
L2B-15-N	natrolite	$Na_2Al_2Si_3O_{10}2H_2O$	coarse vug in matrix-supported breccia	-	13.5	-65.1	3.5	-
L17A-10	paragonite-muscovite	$(K,Na)Al_2(AlSi_3O_{10})(OH)_2$	irregular banding in ferromanganese ore	hem, ap, brn	10.1	-71.6	4.3	-55.9
BaQ2	muscovite	$KAl_2(AlSi_3O_{10})(OH)_2$	vein in quartzite overlying conglomeratic Fe-ore	rt, ap, brt	-	-78.7	-	-63.0
Heuningkranz (silicates and oxides in ferromanganese ore, Wolhaarkop breccia and massive iron ore)								
PM17-16-bnl	banalsite	$BaNa_2Al_4Si_4O_{16}$	banalsite-paragonite large infill-vein in ferromanganese ore	prg, cal, mcd	11.6	-	4.0	-
PM15-2	paragonite-muscovite	$(K,Na)Al_2(AlSi_3O_{10})(OH)_2$	thick irregular mica-laminae in ferromanganese ore	hem, ap, rt	12.9	-68.8	7.1	-53.1
PM11-C	paragonite-muscovite	$(K,Na)Al_2(AlSi_3O_{10})(OH)_2$	thick continuous mica-laminae with sparse vugs	hem, rt	12.0	-60.7	6.2	-45.0
PM17-15	paragonite-muscovite	$(K,Na)Al_2(AlSi_3O_{10})(OH)_2$	irregular mica-lens in gradational contact to Fe-Mn ore	hem, hlp, rt	8.1	-75.6	2.3	-59.9
PM17-16	paragonite-muscovite	$(K,Na)Al_2(AlSi_3O_{10})(OH)_2$	banalsite-paragonite large infill-vein in ferromanganese ore	bnl, cal, mcd	10.3	-63.5	4.5	-47.8
WOLA2-ar	armbrusterite	$K_5Na_6Mn_{15}[(Si_9O_{22})_4](OH)_{10}4H_2O$	coarse armbrusterite vugs in Fe-manganiferous sediment (Wol.)	aeg, ab, cal, qtz	12.9	-	-	-
WOLC-ar	armbrusterite	$K_5Na_6Mn_{15}[(Si_9O_{22})_4](OH)_{10}4H_2O$	coarse vug with armbrusterite core and calcite-quartz rim (Wol.)	cal, qtz	8.8	-	-	-
HLT2	berthierine	$(Fe^{2+},Fe^{3+},Al)_3(Si,Al)_2O_5(OH)_4$	irregular berthierine-quartz infills in massive Fe-ore	qtz, hem, py	11.1	-	7.1	-
VLT10	berthierine	$(Fe^{2+},Fe^{3+},Al)_3(Si,Al)_2O_5(OH)_4$	berthierine vein with minor quartz and hematite in Fe-ore	qtz, hem	7.5	-	3.5	-
MAP1	berthierine	$(Fe^{2+},Fe^{3+},Al)_3(Si,Al)_2O_5(OH)_4$	ferruginous quartzite with berthierine-pyrite vugs and veins	py, hem	5.7	-	1.7	-
WOC-A1	hematite	Fe_2O_3	specularite lining rhodochrosite vugs in proximity to Fe-ore	rdc	-7.5	-	-3.5	-
Bruce mine/Khumani (silicates and oxides in Wolhaarkop breccia and iron ore)								
AKH49-C	sugilite	$KNa_2(Fe^{3+},Mn^{3+},Al)_2Li_3Si_{12}O_{30}$	coarse sugilite vug with minor albite and serandite (Wol.)	nrs, srd, ab	13.3	-	-	-
AKH49-D	sugilite	$KNa_2(Fe^{3+},Mn^{3+},Al)_2Li_3Si_{12}O_{30}$	minute sugilite vug in manganiferous sediment (Wol.)	nrs, srd	13.4	-	-	-
AKH49-G	armbrusterite	$K_5Na_6Mn_{15}[(Si_9O_{22})_4](OH)_{10}4H_2O$	coarse zoned-vug with armbrusterite rim (Wol.)	sug, srd, nrs	14.9	-126.8	-	-
BWS-hem	hematite	Fe_2O_3	crystalline coating on calcite and feldspar mass	py	-0.8	-	3.1	-
Kapstevel (silicates in massive iron ore)								
SD13	paragonite	$NaAl_2(AlSi_3O_{10})(OH)_2$	irregularly shaped paragonite-barite infill in Fe-ore	hem, brt, ap	-	-65.2	-	-49.5

6. Discussion

6.1 A shared alteration history of the Postmasburg and Kalahari manganese fields

The ore deposits of the PMF show evidence of profuse epigenetic fluid flow, rigorously documented here and in accordance with other recent studies, through the presence of complex gangue assemblages and metasomatic effects involving chiefly alkalis and alkali earths such as Na, K, Ba, Ca and Sr. A comparable epigenetic event induced by tectonically-expelled hydrothermal fluids has caused upgrade of the northwestern part of the KMF during the Namaqua orogeny (western sector of the Namaqua-Natal orogenic belt), between ca. 1.14 and 1.01 Ga (Gutzmer and Beukes; 1995, Gnos et al; 2003, chapters 3 & 4). In contrast, timing of the now amply recognized hydrothermal component of the PMF ores is until now very poorly constrained, mainly due to lack of suitable material for dating and the intricately mixed fine-grained mineralogy. The possible role of this hydrothermal activity as an ore upgrade mechanism during the long-term geological history of these ores is equally critical and has not yet been thoroughly considered.

The distinctly younger $^{40}Ar/^{39}Ar$ ages reported from two separate localities in the PMF ores (620 ± 3 Ma, 614 ± 50 Ma) have perplexed researchers who highlighted the otherwise comparable metasomatic effects with respect to Mn- and Fe-mineralization and the similarities in the paragenetic mineral record in both ore fields, over a distance of ca. 140 km (Moore et al; 2011; Fairey et al; 2019). Nonetheless, recent geochronological evidence by means of mica $^{40}Ar/^{39}Ar$ dating, as proxy for contemporaneous barite mineralization firmly associated with the aforementioned metasomatism, provided an unequivocal link between timing of major fluid migration in the two districts during the Namaqua orogeny (chapter 2).

Our attempt at establishing new age constraints on the regional-scale hydrothermal metasomatism using laser microprobe in situ $^{40}Ar/^{39}Ar$ geochronology reveals that detailed petrographic characterization and mapping of the fine-grained, K-bearing gangue mineralogy enable the acquisition of geologically meaningful ages. Specifically, the total range of $^{40}Ar/^{39}Ar$ ages (ca. 920-1188 Ma) deriving from gangues in ferromanganese ore of the

Western Maremane dome (WMD), i.e., occurrences extending towards the west of the type locality ores of the PMF, display close correspondence with the widespread barite mineralization in the area (ca. 1137-1067 Ma) as well as with the hydrothermal upgrade of the KMF (ca. 1140-1037 Ma) (Figure 18, see also references). Therefore, our geochronological data demonstrate that extensive fluid infiltration clearly relate to the Namaqua orogeny has caused crystallization and/or radiogenic isotope age homogenization of the alteration mineralogy encountered in the ores of both the PMF and KMF, in that way constituting a key part of their epigenetic history.

The origin of the type locality ferromanganese deposits of the Eastern Maremane dome (EDM), also referred to as Western belt in the literature, has been explained by invoking residual karst-forming processes followed by diagenesis and very low-grade metamorphism, events, tentatively bracketed between 2.22 and ca. 1.8 Ga (Armstrong; 1987, Gutzmer and Beukes; 1996a, Cornell et al; 1998). Pre-Namaqua *sensu lato* $^{40}Ar/^{39}Ar$ ages (Namaqua: 1.0-1.2 Ga, see also section 6.3) documented here from the PMF ores, provide the first solid evidence for an earlier origin of at least some phyllosilicate components found today associated with the ores. A closer interrogation of the age data draws attention to important aspects associated with the $^{40}Ar/^{39}Ar$ dating technique and in addition focuses more narrowly on coupling the measured ages with the broader geological and geotectonic setting of the area.

6.2 Interpretation and synthesis of age data

6.2.1 Namaqua ^{40}Ar-^{39}Ar ages

In situ UV laser age spots from all samples can be divided into two groups: (1) one which is characterized by dates apparently related to Namaqua orogeny (weighted means ranging from 920 ± 9 Ma, 2σ to 1188 ± 4.4 Ma, 2σ) and (2) a second group of considerably older and less robust dates (individual spot dates ranging from 1452 ± 45 Ma, 1σ to 1997 ± 42 Ma, 1σ), which however can potentially reveal insight into the geological history of the ores before the Namaqua overprint. Figure 18 shows distribution of spot $^{40}Ar/^{39}Ar$ dates for all samples at 1σ confidence, with horizontal bars indicating the associated weighted mean for

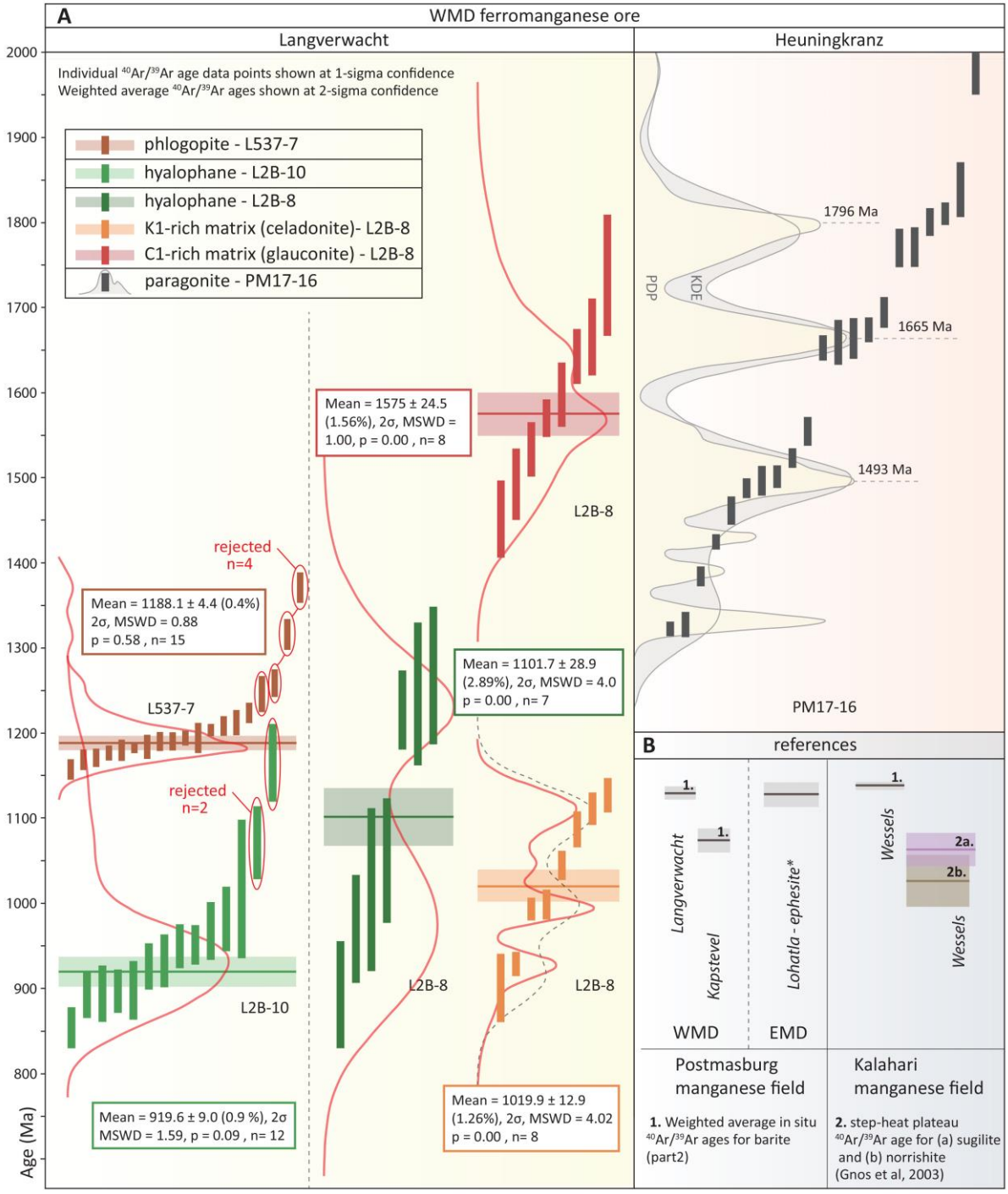

Figure 18. A) Age distribution plot of in situ $^{40}Ar/^{39}Ar$ ages (1σ) (vertical bars) from this study, colour-coded for each different target. Horizontal bars represent weighted mean ages (2σ) and red lines probability density plots (PDPs). Outliers rejected by weighted average calculations are circled in red. Plots originally constructed with IsoplotR and modified by the author. K1- and C1-rich matrix may represent celadonite and glauconite ages respectively but these phases have not been positively identified (see also text). Note the broad age coincidence between vein-filling hyalophane (L2B-8) and celadonite in adjacent matrix (L2B-8) as well as that between glauconite (L2B-8) and the older prominent age peaks of paragonite (PM17-16). Reference $^{40}Ar/^{39}Ar$ data (other studies) from the PMF and KMF alkali-rich metasomatic assemblages are also shown. *Ephesite age is from chapter 6.

each sample at 2σ confidence. Probability density plots represented by red lines and other related age data are also included. High MSWD values shown by some samples (i.e., considerably greater than one, e.g., Schaen et al; 2020) are not caused by analytical uncertainties but instead reflect a real scatter in the measured ages related with geological reasons which are dealt with below.

Phlogopite records the older and most robust Namaqua-related age in our dataset, derived from normally distributed values having a weighted average of 1188 ± 4.4 Ma (2σ, MSWD = 0.88, n=15, 4 of 19 spots rejected). Phlogopite belongs to the biotite group of trioctahedral mica which have been commonly used for $^{40}Ar/^{39}Ar$ dating in igneous and metamorphic settings (McDougall and Harrison; 1999 and references therein). Textural evidence from SEM analysis document its occurrence in the PMF ores mainly as microvug-filling mineral associated with a plethora of cogenetic hydrothermal gangue phases. Therefore, the origin of phlogopite is beyond doubt hydrothermal, akin to mica (phlogopite and biotite) veins found in other metasomatic settings in volcanic districts or Pb-Zn deposits (Belkin et al; 1988, Kotov and Skenderov; 1988).

In contrast to slowly cooled metamorphic rocks, phlogopite age in a low temperature hydrothermal regime with relatively short cooling history will approximate that of fluid infiltration and mineral deposition. Phlogopite in these ores most likely formed below the closure temperature (T_c) of the mineral, which is ca. 400°C (Hodges; 2003) and since diffusion in its lattice is slow, the weighted mean age of 1188 ± 4.4 Ma is interpreted here to be the crystallization age of phlogopite, associated with the early stages of Namaqua-related hydrothermal activity. This age broadly coincides with the previously reported ages for barite mineralization in the same locality (1129 ± 4 Ma, 2σ) and the KMF (1137 ± 2 Ma, 2σ), both of which are also considered to capture the early/main stage of hydrothermal modification of the ores (chapter 2). Formation age of the Li-mica ephesite (1121 ± 14 Ma) (Figure 18, references) occurring in the EMD ferromanganese ores is apparently also affiliated with the previous ages, as it will be addressed later in the thesis (chapter 6).

Although the spread of ages recorded by different phlogopite grains is relatively small (ca. 66 ± 12 Ma, n=15), four data points rejected by calculation of the weighted average, show elevated ages of up to ca. 183 Ma in comparison to the calculated sample age. These 'older' phlogopite-filled vugs are clustered together in the sample and are interpreted to reflect incorporation of extraneous ^{40}Ar. The term 'extraneous' has been used to describe the uptake of either excess and/or inherited radiogenic argon ($^{40}Ar^{*}$) by the analysed sample (Kelley; 2002). As described in Sherlock et al (2008), K fixed in a mineral lattice will constantly decay to $^{40}Ar^{*}$ and eventually become excess argon ($^{40}Ar_{E}$) when decoupled from the parent potassic mineral during the thermal and tectonic evolution of a sedimentary basin. $^{40}Ar_{E}$ can remain in the grain-boundary network until fluid migration causes removal of the radiogenic isotope. Fluids that become saturated in $^{40}Ar_{E}$ and circulate into a system can partly incorporate their exogenous signature by entering into mineral structures. Moreover, it is known that argon will be efficiently accumulated in the preferred 'sinks', which in this case are no other than mica, due to the higher solubility of argon in the latter as compared to other minerals (Foland; 1979, Dahl; 1996).

Taking the above-said into account, unevenly distributed excess argon trapped by phlogopite during its formation can perhaps explain the older phlogopite ages recorded in a single domain of the sample and is favored over an interpretation invoking inherited argon, i.e., control of radiogenic isotopic ratios from a recrystallized preexisting K-bearing phase, which would have possibly been responsible for a much wider scatter in the obtained phlogopite dates. Whatever the source of extraneous ^{40}Ar, all of the above highlight the need for an extensive age-scan of the sample during in situ analysis in order to identify the 'real' age.

$^{40}Ar/^{39}Ar$ data of **hyalophane** hosted by two separate calcite veins collectively range from 854 ± 24 Ma (1σ) to 1268 + 81 Ma (1σ). One of the two samples conforms to a normal distribution and has a weighted mean age of 920 ± 9 Ma (2σ, MSWD = 1.59, n=12, 2 of 14 spots rejected) and the other yields significantly scattered $^{40}Ar/^{39}Ar$ dates which give a much less precise weighted average of 1102 ± 29 Ma (2σ, MSWD = 4, n=7). If a bimodal distribution is regarded for the latter small dataset (Figure 18), then a younger age of 971 ± 40 Ma (2σ, MSWD = 0.76, n=4) and older one at 1239 + 41 Ma (2σ, MSWD = 0.08, n=3) occur. Argon

retention properties of hyalophane have not been studied thoroughly. However, it can be expected to behave in a manner similar to K-feldspar since it is an intermediate in the celsian-orthoclase series (McSwiggen et al; 1994).

At least one example from literature demonstrates the suitably of this material for $^{40}Ar/^{39}Ar$ geochronology by providing a well-defined plateau interpreted as cooling age, that was measured on hydrothermal hyalophane-quartz Alpine veins within an originally Variscan metamorphic core complex (Pamić et al; 2004). In yet another example, an $^{40}Ar/^{39}Ar$ stepwise-heating hyalophane plateau age has been interpreted to reflect late-stage hydrothermal activity following emplacement of pegmatites (Brandt et al; 2006). Acquired $^{40}Ar/^{39}Ar$ spot dates from hyalophane in this study are significantly younger as compared to that of phlogopite and the remaining ages from PMF. Contrastingly to the microlaminae-related hyalophane in ore matrix, its paragenetic occurrence in the dated samples possibly links it with calcite and barite of late-stage origin. Replacement textures and solubility mechanisms of chloride complexes have also led Fairey et al (2019) to attribute calcite and barium carbonate phases such as witherite and barytocalcite to a late event in the paragenetic sequence.

In this context, $^{40}Ar/^{39}Ar$ age distribution profiles of hyalophane may be also explained by loss of $^{40}Ar^{*}$ during reheating, related to the introduction of calcite-barite veins at the waning stages of hydrothermal alteration. Hence, the older dates from the two samples (1165 ± 46 Ma and 1268 ± 81 Ma, 1σ) may give a better estimate of the 'real' age which is closer to that of phlogopite. Partial or total recrystallization of K-feldspar, which can be used as a proxy for the thermal behaviour of hyalophane, can take place at temperatures of 20-200°C (Mortimer et al; 2012). The variety of hyalophane textures, from euhedral to xenomorphic, may imply that at least partial recrystallization has taken place. Lack of homogenization of the $^{40}Ar/^{39}Ar$ hyalophane age during a possible late-stage thermal event can be explained by different argon retentivities of feldspar grains or dating of a mixture of different grain populations, a complication further enhanced in this mineral by the requirement for large-size ablation pits (110-155 μm) due to low and variable potassium contents.

Diffusive loss of ^{40}Ar may have also occurred after mineral formation and during cooling (Flude et al; 2016), or due to kinetics related to neutron irradiation (Foland; 1992). However, fluid-induced reset and/or recrystallization is something commonly observed in natural K-feldspars (McLaren et al; 2007) and is considered here as a more likely scenario. Regardless of the mechanisms that may have impacted on the distribution of argon in hyalophane, its documented age is in the same ballpark as those of other minerals that overlap with Namaqua orogeny and furthermore, apparently reflects a late-stage thermal event. It is noteworthy that despite the potential pitfalls attached to $^{40}Ar/^{39}Ar$ dating of mixtures of low-potassium targets, such as celsian-hyalophane grains which in addition are hypothetically prone to $^{40}Ar^{*}$ loss, hyalophane in this study greatly preserves its original ca. 1.1-1.0 Ga cooling age.

Supporting evidence for a 1102 ± 29 Ma hyalophane age of sample L2B-8 derives from the immediate host-rock to the calcite-feldspar vein which as described earlier, is conducive to a thermal disturbance of the surrounding rock, in view of it forming a hydrothermal overprint 'domain' that extends markedly to the Fe-rich ore matrix and comprises a variety of alkali-rich gangues. The obtained mineral-specific age from this domain, reflects mostly argon contribution from the poorly defined sheet silicate referred here as K1 (possibly celadonite, other smectite/mica or clay) which gives a weighed mean of 1020 ± 13 Ma (2σ, MSWD = 4, n=8); thus, creating very clear contrast with another component of the aluminosilicate-rich matrix (mineral C1-glauconite/phyllosilicate or other Fe-rich smectite/mica) being only microns apart, which gives a weighted average date of 1575 ± 12 Ma (2σ, MSWD = 4, n=8). We interpret the first age (K1), which furthermore does not display a normal distribution, btu instead one comprising several peaks, as thermal reset and/or recrystallization of a preexisting silicate ore-component, in response to fluid introduction and coeval formation of the calcite-hyalophane veins. It is important to note that reported diffusional loss of argon and low apparent ages due to small crystal size and ^{39}Ar recoil effects occurring during irradiation of glauconite (Foland; 1984, Hess and Lippolt; 1986), are strong indications that $^{40}Ar/^{39}Ar$ glauconite results should always be interpreted with caution. Until the identity of the dated Fe-rich phyllosilicates is confirmed, interpretations should be limited

to the agreement of their ages with the regional alkali metasomatism, a coincidence that adds further constrains on the hydrothermal activity seen in these ores.

6.2.2 Pre-Namaqua ^{40}Ar-^{39}Ar ages

Interpreting the pre-Namaqua dates is less straightforward. The 1575 ± 12 Ma date presented above showcases the high $^{40}Ar/^{39}Ar$ age heterogeneity of different sample domains being only microns apart, which can be revealed with the aid of the laser microprobe technique. SEM analyses indicate that the former date is most probably representative of a multi-grained assemblage consisting of a single potassic phase (C1) intermixed with ore and other gangues minerals. The dating target seems to retain evidence of an earlier crystallization age. Assuming that these ores represent chemical deposits (Gutzmer and Beukes; 1996a), the 1575 ± 12 Ma age may relate to the timing of mineral formation and therefore could be more closely associated with the diagenetic/metamorphic evolution of the ores, which in turn would be much younger than what previously postulated by the aforementioned authors, i.e., ca. 1.8-1.9 Ga. However, certain things should be further considered.

The karstic ore genetic model entails a mixture of authigenic and detrital phyllosilicates being present in the ore matrix which would have collectively been reset during subsequent diagenetic and metamorphic processes if temperatures exceeded the isotopic closure temperatures of the primary phases. Lower greenschist metamorphic conditions (ca. 300-400^{o}C) have been reported from the Eastern Maremane dome (EMD) deposits (Plehwe-Leisen, 1985; Gutzmer and Beukes 1996b) but similar data are lacking from the WMD, which nevertheless comprise textures and mineralogy indicative of hydrothermal/metamorphic metasomatic processes. Therefore, mica ages are generally expected to reflect crystallization or even cooling ages after the heating event, unless clastic material from the overlying Olifantshoek sediments has been incorporated in the matrix during subsequent brecciation and has not been isotopically reset during rock consolidation. Furthermore, failure to identify excess ^{40}Ar incorporation can lead one to regard dates that are otherwise geologically meaningless. The large age range of phase K1 (1452 ± 45 Ma, 1σ to 1738 ± 71 Ma, 1σ) and the tentative bimodal distribution of the dates implies that argon contribution from different

reservoirs or excess ^{40}Ar cannot be ruled out. In the absence of textural indications affiliating the fine-grained potassium mineralogy of the matrix with a well-defined geological event or indicating that K1 is texturally older, these ages should be regarded with caution.

The paragonite-banalsite assemblage of sample PM17-16 also displays very scattered and 'old' pre-Namaqua ages which fail to provide an accurate estimate of paragonite formation. Despite the large intrasample age variability, some thermochronological information can be still acquired. $^{40}Ar/^{39}Ar$ spot ages (n=21) range from 1320 ± 9 Ma (1σ) to 1997 ± 42 Ma (1σ). The probability density plot (PDP) generated for this dataset displays a series of peaks the most prominent of which are at ca. 1794, 1668 and 1491 Ma with subordinate younger peaks until 1320 Ma (Figure 18). A kernel density estimation (KDE) of the same dataset illustrates nicely that by using the right kernel bandwidth, data smoothing can provide a clearer visualization of complex age distribution profiles obtained by high precision in situ $^{40}Ar/^{39}Ar$ data. KDE is a function that similarly to PDPs stacks a Gaussian bell curve on top of each measurement but standard deviation is determined by the local probability density. Hence, it has been proposed as a more robust alternative to the PDP with regard to detrital zircon populations (Vermeesch; 2015) but it has also found use in presentation of $^{40}Ar/^{39}Ar$ data (Schaen et al; 2020). Textural observations of closely related paragonite, banalsite and the rare lead-titanium perovskite known as macedonite suggest either a metamorphic origin or that of a hydrothermally overprinted phyllosilicate-rich ore matrix.

The dating profile of paragonite implies that either: (1) A series of thermal events has caused partial loss of its previously accumulated ^{40}Ar, therefore resetting the $^{40}Ar/^{39}Ar$ clock subsequently to its formation. In such case, the older spot age (1997 ± 42 Ma, 1σ) may best represent original crystallization and the bell-shaped dominant age peaks could reflect distinct thermal events, i.e., geological episodes. (2) The Namaqua metasomatic event has overprinted pre-existing paragonite but argon has not diffused efficiently out of the mineral and/or has been partially incorporated into newly crystallizing phases analogous to recycling argon processes which have been shown to occur during metamorphic reactions (e.g., McDonald et al; 2018). In this respect, variable argon retention by different domains in the

sample, due to the likelihood of mica not having been fully reset during low temperature hydrothermal activity, may lead to erroneous conclusions. In other words, the presence of a significant age gradient in the sample may be related to preservation of a partial record of the original formation age produced by a single thermal event at ca 1.2 Ga. (3) Excess argon trapped in paragonite during crystallization, fluid or other scattered microscopic inclusions hosted by missing mineralogical phases produces unrealistically elevated ages or (4) Physical contamination from another K-bearing phase of older age results in a 'whole-rock' age dataset. The latter scenario cannot be excluded since a fine-grained and Mn-rich material occurring interstitially to paragonite was noted during petrographic investigation, although it could not be further identified.

Regardless of which interpretation is most correct, this dating target highlights the caveats associated with $^{40}Ar/^{39}Ar$ geochronology of old and complex ore deposits which may have witnessed an intricate history involving multiple low-temperature events that may have disturbed $^{40}Ar/^{39}Ar$ systematics. No meaning is attached to a particular date from the paragonite age profile due to insufficient geochronological and textural information. Nevertheless, it can be said that a scenario of multiple resetting events tied to actual geological events is not regarded as an elegant explanation. On the other hand, emphasis should be placed on the fact that two of the dominant peaks at ca. 1668 Ma and 1491 Ma overlap with the age range of ore matrix documented by silicate K1 (from 1452 ± 45 Ma, 1σ to 1738 ± 71 Ma, 1σ, weighted mean: 1575 ± 12 Ma, 2σ), which in turn lies within the timeframe of other ''older'' geological events further to the west of the study area and not so much within the range of the deformational/metamorphic Kheis event, as that described at least by some researchers (more on section 6.3).

Overall, general lack of a detailed chronological framework of the study area allows only for the observation that at least some mica and K-bearing aluminosilicates found in the PMF ores preserve older diagenetic/metamorphic or generally thermal signatures that have not been eliminated during fluid introduction related to Namaqua orogeny. It should be noted though, that despite the existing ambiguity in age interpretations, our data provide the first age measurements from the PMF ores confirming an origin prior to the regional-scale

Namaqua overprint in the Northern Cape. It is then incumbent to place these ages in the broader geotectonic framework by reporting the current extent of the Namaqua tectonostratigraphic belt as well as the existing controversies regarding timing and duration of the precedent 'Kheis' orogenic events, aspects that remain poorly understood and for which there has been considerable debate up to this day.

6.3 Geotectonic framework of regional-scale fluid flow - (A short review)

The literature of the past 40 years or so may be found confusing with respect to subdivision and nomenclature of the lithostratigraphic units, relative age of formations, unconformities, tectonic boundaries and metamorphic history whilst revisions are sporadically being made. Comprehensive reviews of the complex regional geology have been compiled by a series of authors (e.g., Hilliard, 1999; Cornell et al, 2006) and a presentation of the aforementioned is beyond our scope. However, since new age information from this study may advance our understanding of the geotectonic evolution of the wider area, a synopsis emphasizing key points regarding the so-called Kheis Province and the pervasive Namaqua-Natal tectono-metamorphism are being examined at some length below. This short review is included here to maintain continuity between the geochronological interpretations and the following implications for ore genesis at the end of the chapter.

The Namaqua-Natal Province is an arcuate tectono-stratigraphic belt, i.e., has a geochronologically well-defined structural and metamorphic fabric (Stockwell et al; 1970), that runs alongside the western and southern margins of the Kaapvaal Craton (Figure 19). Northwestern extensions of this belt are believed to tie up with the Kibaran orogens of Central-East Africa and eventually with the worldwide Grenville orogeny (Cornell et al; 2006). Namaqua Province (western sector of the belt) consists of a number of tectono-stratigraphic terranes bounded by shear zones (Figure 19, 20). This relatively poorly constrained nappe complex of older (ca. 2000 Ma) or syn-metamorphic supracrustal metapelites, amphibolites, juvenile arc-related rocks (ca. 1600-1200 Ma) and later intrusive granitoids (ca. 1000 Ma) was assembled during a series of rifting, drifting and collisional Wilson cycles of the prolonged Namaqua orogeny (ca. 1600-1000 Ma, Namaqua *sensu lato*) and tectonically overlies the Kaapvaal Craton causing crustal thickening of the latter (Hartnady et al, 1985; Cornell et al,

1998, 2006). A convergent phase initiating at late Mesoproterozoic culminated in the main orogenic events which extended over 200 myr (ca. 1.2-1.0 Ga) and mark the widespread Namaqua fabric in the area (Namaqua *sensu stricto*). A narrow domain between the Kaapvaal Craton and the Namaqua Province has been termed as Kheis Province by some researchers and designated as a separate transitional zone with gradational structural and radiometric imprints (Tankard et al; 1982 and references therein). However, the exact boundaries of this zone and interpretation of the reported radioisotopic ages have been matters of considerable debate.

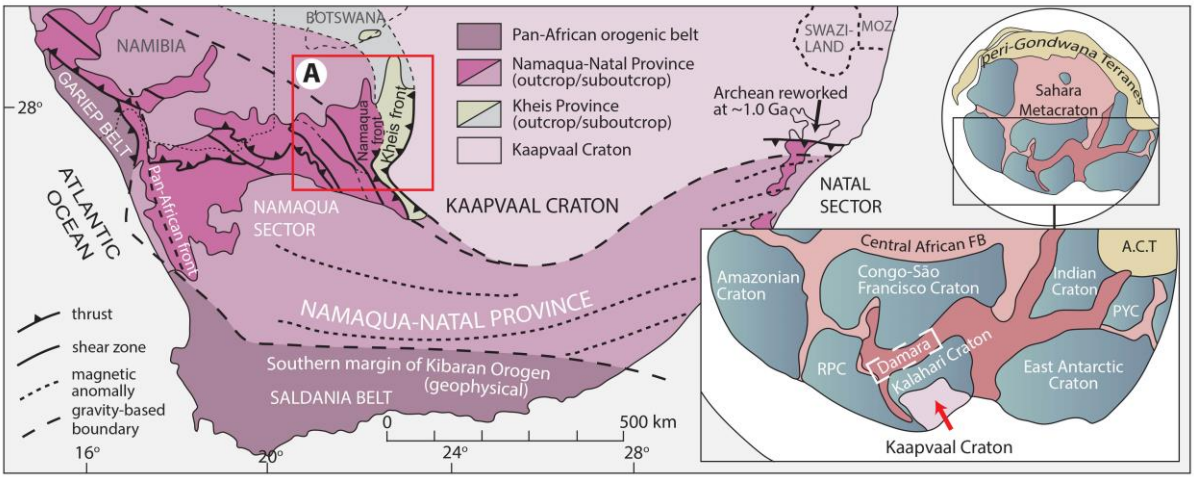

Figure 19. Development of the Namaqua-Natal belt in southern Africa after Cornell et al; 2006. (inset) The figure is derivative from Avigad et al; 2017.

As shown in Figure 20A the Kheis domain has a maximum width of ca. 80 km and supposedly shows evidence of a dominant tectono-metamorphic fabric formed between 1928 ± 4 and 1750 ± 60 Ma, a range deduced by a maximum Pb-Pb magmatic zircon age from a porphyry sample and a minimum Rb-Sr whole rock age on a later dolerite intruding lavas of the Hartley Formation of the Olifantshoek Supergroup, presumably metamorphosed during Kheis orogeny (Stowe; 1986, Cornell et al; 1998). Geotectonically, greenschist-facies metamorphism and north striking foliation of the Olifantshoek Supergroup is thus believed to represent an orogenic collisional event (Kheis orogeny) which gave rise to a regional fold and thrust belt of east vergence known as the Blackridge Fault (Stowe; 1986, Altermann and Hälbich; 1991). A 1713 Ma Rb-Sr model muscovite age and a 1780 Ma $^{40}Ar/^{39}Ar$ mica with no reported uncertainties or decay constants are the only coeval dates that have been reported from the immediately adjacent Kaaien Terrane (Nicolaysen and Burger; 1965, Burger and

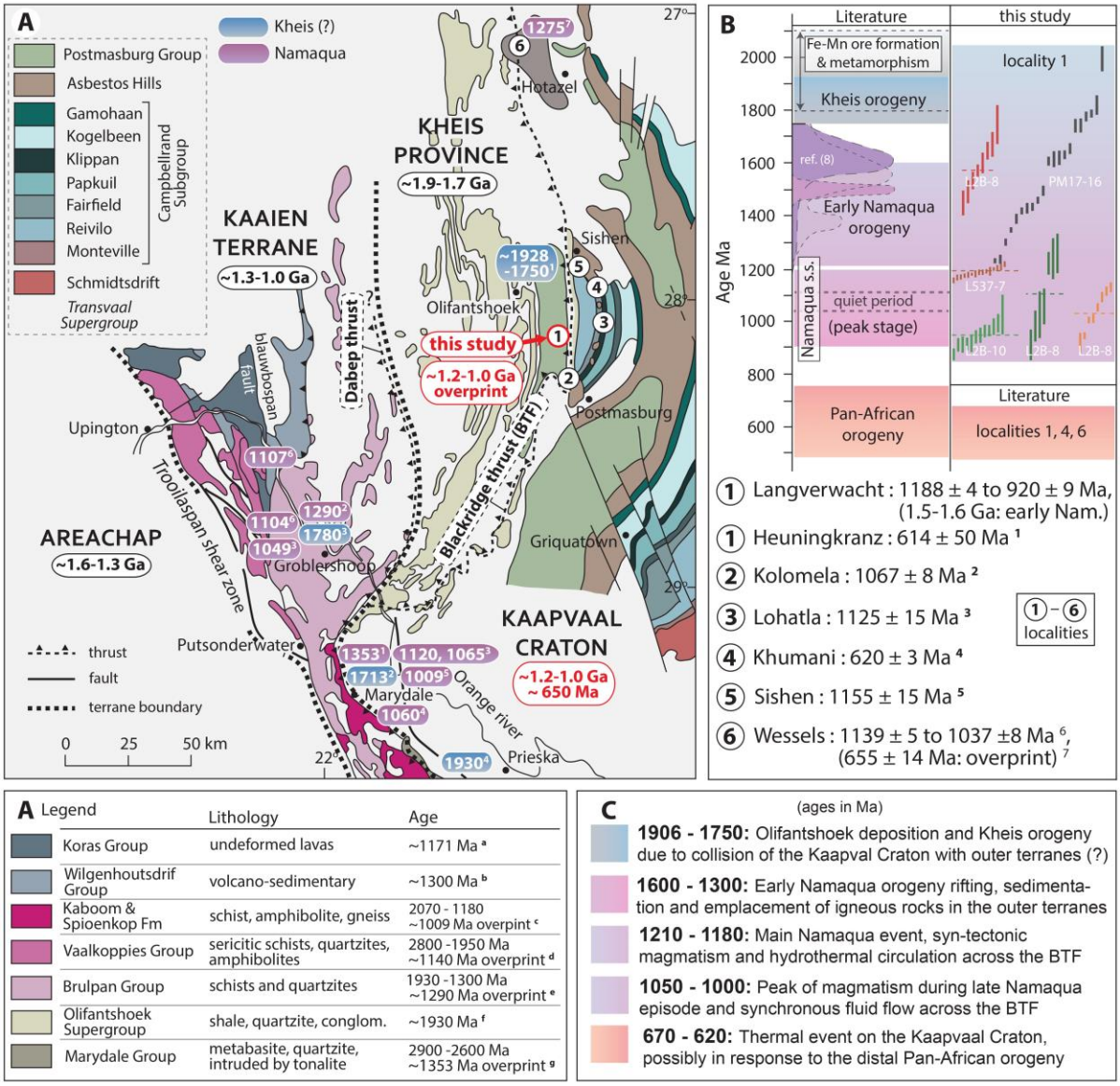

Figure 20. (A) Reconstruction of tectonic domains of the Namaqua sector based on Cornell et al; 2006, van Niekerk; 2016, van Niekerk and Beukes; 2019 and Cairncross and Beukes; 2013 (Kaapvaal Craton). Note the widespread Namaqua ages and lack of 'Kheis'-related ages on Kaaien Terrane, Kheis Province and Kaapvaal Craton. References: Kheis:(1) Stowe; 1986, Cornell et al; 1998 (2) Nicolaysen and Burger; 1965 (3) Burger and Coertze; 1974 (4) Barton and Burger; 1983. Namaqua: (1) Humphreys and Cornell; 1989 (2) Moen et al., unpublished data (3) Cornell et al; 2006 (4) Thomas et al; 1996 (5) Humphreys and Cornell; 1989 (6) Clifford et al; 1995 (7) Cornell et al; 2006. References from legend: (a) Gutzmer et al; 2000 (b) Barton and Burger; 1983 (c) Moen; 1999 (d) Barton and Burger; 1983, Moen et al., unpublished data (e) Cornell et al; 2006 (f) Cornell et al; 1998 (g) Cornell et al; 2006, Humphreys and Cornell; 1989 **(B)** Ages from this study plotted against both the well-constrained (Namaqua, Pan-African) and ambiguous (Kheis orogeny, ore formation) geological events (1) this study, Fairey et al; 2019, (2) chapter 2 (3) chapter 6 (4) Moore et al; 2011 (5) Rasmussen (pers. comm.) (6) Gnos et al; 2003, chapters 4 & 5. **C)** Sequence of major events taking place in the Namaqua sector based on all ages presented in this study.

Coertze; 1973). The Blackridge thrust Fault, evidence for syn-Olifantshoek Supergroup deformation and deep-seated metamorphism in garnet-hornblende-bearing schists (Humphreys et al; 1991) are indications of an orogenic event, which however remains poorly constrained with respect to geographic extent and absolute timing of events. Despite the scant information, it has been suggested that the ca. 1.8 Ga deformed Kheis Province is bounded by Blackridge thrust in the east and Dabep thrust in the west which in other words represent the Kheis and Namaqua orogenic fronts respectively (Figure 20A). Recently however, researchers have disputed the existence of the Dabep thrust due to absence of stratigraphic and geophysical evidence and further suggested a western extension of the Kheis Province to include the Kaaien terrane and a new western boundary for Kheis Province, that of the Kalahari Line (Corner and Durrheim; 2018, van Niekerk and Beukes; 2019).

$^{40}Ar/^{39}Ar$ ages from this study, deriving from an area west of the Kheis front, do not show evidence for an ca. 1.8 Ga Kheis orogeny but instead demonstrate a clear thermal reset during the Namaqua orogeny (from 920 ± 9 to 1188 ± 4 Ma) whilst older ages (1575 ± 12 Ma and from 1452 ± 45 to 1997 ± 42 Ma, peaks at 1860, 1668 and 1491 Ma) show more resemblance to rifting phases recorded in the rocks of the more distant external terranes of the Namaqua Province (Figure 20B), which took place at the beginning of the Namaqua or at the end of Kheis orogeny (Cornell et al; 1998). In particular, some overlap exists between pre-Namaqua dates from this study and zircon dates (ca. 1650) reported as reflecting intrusive and volcanic activity in the Bushmanland terrane (Aggeneys) as well as with Sm-Nd crustal residence model dates (ca. 1500-1750 Ma), regarded as emplacement ages in the Areachap, Bushmanland (Garies district) and Kakamas terranes (Figure 20A) (De Paolo et al; 1991, Eglington; 2006 and references therein). Another much older rifting-related Sm-Nd model age of 1930 Ma has been reported from a carbonatite near Prieska by Cornell et al (1986) and additionally, a younger age (1353 ± 33 Ma) of intrusive tonalite near Marydale has been ascribed to the early stages of Namaqua orogeny (Humphreys and Cornell; 1989). Furthermore, rifting and development of an ocean basin in the Areachap Terrane shown at the left in Figure 20A is suggested to have started as early as 1600 Ma (Cornell et al; 2006). Therefore, either continental collision and structural deformation related to the controversial

Kheis orogeny or extensional tectonics originating on the Craton during evolution of the outer terranes could have contributed to heating of fluids and expulsion along the Craton margin.

It is reminded that Pre-Namaqua ages in our study should be regarded with certain caution; however, it is instructive to note resemblances of the most probable mica ages with ages from the literature. In addition, events related to rifting, sedimentation or emplacement of igneous rocks during the early phases of Namaqua have not been adequately documented and not been given the same attention as the events of the main orogeny. Regardless of whether this age similarity between distant rifting-related magmatism and thermal disturbance (metamorphic or hydrothermal overprint) of the ferromanganese ores is coincidental or not, our data support the view of many researchers that there is a dearth of reliable ages for an ca. 1.8 Kheis orogeny whereas at the same time, the eastern foreland of the Namaqua Province (Kheis Province and Kaaien Terrane), as broadly depicted in Figure 20A, shows a good record of Namaqua ages deriving mainly from the K-Ar and Rb-Sr systems (e.g. Cornell; 1975, Nicolaysen and Burger; 1965, Barton and Burger; 1983) and more recently from the $^{40}Ar/^{39}Ar$ method (van Niekerk; 2006).

Lack of consensus on the nature and timing of the Kheis has led Moen (1999) to regard it as a sub-province of the Namaqua Province and later Eglinton (2006), in a detailed geochronologic review, to argue that there is no evidence for a major Palaeoproterozoic major orogeny but instead the 'Kheisian' fabric represents an early phase of the Mesoproterozoic evolution of the Namaqua Belt, associated with periods of igneous activity beginning as early as ca. 1.4 Ga within the Kheis Province (see also Moen; 1999 and Eglington and Armstrong; 2003). Confusion caused by the term 'Kheis' in literature is evident in many cases. Evans et al (2001) provides a paleomagnetic dating of hematite in ferruginized fault zones within the hydrothermally upgraded KMF between 1.28 and 1.18 Ga and Beukes et al (2016) refers to this as a 'Kheis' age, associated with tectonic expulsion of hydrothermal fluids during the initial stages of the Wessels upgrade event. Other researchers who presented Pb-Pb and Rb-Sr model ages ranging between 2.9 and 1.5 Ga for the Pering and Bushy Park Pb-Zn deposits hosted by the Campbellrand Subgroup, attributed mineralization and large-scale fluid migration to the development of a 2.0-1.9 Ga Kheis belt (Duane et al; 1991, 2004). Adding

to the confusion, poor age documentations have led authors to associate the above mineralization either to a 1.3-1.0 Ga Kheis event or to a 2050 Ma Bushveld thermal event (Huizenga et al; 2005, Cornell et al; 1998). In the absence of compelling evidence for the key features of a 'Kheis' orogeny and by virtue of current radioisotopic ages, we recommend that the eastern foreland of the Namaqua Province, i.e., Kheis Province, should be seen as another tectonic zone within the extensive Namaqua Province and therefore, the revised definition of the Kheis Terrane proposed by van Niekerk and Beukes (2019) is presently more suitable.

Moreover, attention should be drawn to the well-documented Namaqua signature on the edge of the Kaapvaal Craton (Figure 20A). Apart from the earlier Namaqua age determinations in the Kalahari Manganese field (KMF) (Gnos et al; 2003), recent mica ages from the Kolomela iron ore and ferromanganese ore of the Eastern Maremane dome (Lohatla mine) clearly attest to the eastward transgression of Namaqua-related tectono-thermal activity across the Blackridge Fault system and onto the Kaapvaal Craton (chapters 2 and 7). A U-Pb xenotime age of 1155 ± 15 Ma from a tourmaline vein cross-cutting high-grade iron ore at Sishen (Rasmussen, pers. comm.), further buttress this widespread thermal disturbance. These ages overlap with the syn-tectonic Namaqua granitoids (1.2-1.0 Ga) and moreover vaguely show a bimodal distribution (ca. 1188-1137 Ma and 1065-920 Ma). This is in agreement with the available emplacement dates during the ca. 1.2-1.0 Ga period, which has been previously characterized as distinctly bimodal, with more intense periods of igneous activity occurring at 1190 ± 30 Ma and 1040 ± 30 Ma (Robb et al; 1999, Clifford et al; 2004, Eglington; 2006). This feature of the Namaqua belt, largely restricted to the western domains of the orogen, has been reproduced by Evans et al (2001) in the paleomagnetic age data of the KMF hydrothermal upgrade. An ca. 100 Ma quiet period with no major representative events may therefore be echoed throughout the edge of the Kaapvaal Craton as emerging radiometric data suggest.

Noteworthily, ages obtained from alkali gangue mineralogy hosted by Mn- and Fe-deposits markedly shows that these minerals behaved as isotopically closed systems, remaining largely undisturbed by late fluid circulation and modern weathering. This is intriguing in the context of sparse evidence implying a subsequent Neoproterozoic thermal

event between ca. 670-620 Ma which has seemingly caused localized resetting of K-feldspar and sugilite $^{40}Ar/^{39}Ar$ clocks in both Kalahari and Postmasburg manganese fields (Moore et al; 2011; Fairey et al; 2019, chapter 4). Wide preservation of radiogenic argon ($^{40}Ar^{*}$), shown even by hyalophane from the vicinity of the ca. 600 Ma K-feldspar documented by Fairey et al (2019) in the Heuningkranz locality, imply that if the envisaged far-field response of these ores to the Pan-African orogeny stands to reason, then it should be characterized by low-temperature and erratically distributed fluid flow, unable to produce a pervasive radiometric imprint or that this signal has been hitherto largely missed. Likewise, extrusion ages of ca. 0.85-0.75 Ga by both sediments and volcanics in the external Namaqua terrains have been largely preserved despite being flanked by the Gariep Pan-African belt (ca. 570-507 Ma) (Frimmel and Frank; 1998, Kröner and Stern; 2005) which further brings into question the geological meaning of the ca. 600 Ma ages of the Kaapvaal Craton. The Natal sector of the Namaqua belt presents younger pan-African reworking between 530 and 490 Ma (Jacobs and Thomas; 1996). Inset of Figure 19 displays the location of the Kaapvaal Craton in respect to the distal Damara belt which records rift-related magmatism and granitoid plutons at ca. 760 and 650-488 Ma, i.e., Pan-African ages much closer to the ones from Kaapvaal. There is no doubt that much more geochronological studies are required to unravel if this signal represents a distal response to the Pan-African orogeny or an unidentified local event.

To summarize, the preceding investigation results in three main observations. (1) A large number of Namaqua radiometric ages flanks the Blackridge Fault system, thus reinforcing the concept of regional fluid-flow on both the Namaqua front and the Kaapvaal Craton. This strong overprint of radiometric ages may potentially conceal the earlier tectonic and mineralization history of the area. (2) Ferromanganese ores in proximity to the Blackridge thrust fault system (Namaqua front) display a conspicuous Namaqua overprint, but also carry older ages which may be used as clinching evidence to suggest that they are either in some way related to igneous activity associated with the early stages of the Namaqua orogeny (ca. 1600 Ma) or at least accentuate that the age of the speculated metamorphism affecting these ores during the poorly constrained Kheis orogeny should be reappraised. (3) Hitherto, the dominant age signature from the dated epigenetic events across the Blackridge Fault system

and on the Kaapvaal Craton is that of the Namaqua, despite emerging evidence for a possible distal Pan-African imprint on this area.

6.4 Genetic interpretation and paragenetic sequence of alteration mineralogy

Textural, stable isotopic and geochronological evidence from the current and other recent studies clearly demonstrate the epigenetic mode of formation for the complex K-, Na-, Ba- and Ca-bearing mineralogical assemblages occurring pervasively throughout the PMF ores. Previous work in the area has stressed that alkali-rich and other As- and V-bearing minerals in the metalliferous metasediments were produced by in situ alteration of the parent rock, which governs the composition and diversity of alteration assemblages (Moore et al; 2011, Costin et al; 2015). A first approach on the formation mechanisms of the most prevalent species and their paragenetic sequence has also been outlined, emphasizing evidence for sequential incorporation of alkalis in the alteration phases (Fairey et al; 2019). Genetic interpretations, the origin and characteristics of the metasomatic event(s) can be further illuminated by scrutinizing the distribution, parageneses and composition of distinct mineral species in these ores, many of the former reported here for the first time.

Phyllosilicate minerals have not been previously mentioned from these ores, with the only exemption being that of the Li-rich mica ephesite, which seems though to be restricted to the EMD ores, its presence closely related to the much higher aluminum bulk-rock concentrations and presumably higher Li availability. Phyllosilicates are not always present but their dense and primarily layered distribution in thin (i.e., cm-sized) intervals, macroscopically resembles the reddish brown ephesite layers seen in the EMD ores, despite compositional differences between the two. As outlined during petrographic analysis, an association was observed between Fe-rich (hematite) ore matrix and concentration of mica, with the two being intergrown and aligned parallel to bedding planes. Spot EDS analyses of ore matrix adjacent to interbedded mica laminae (referred here as *mica laminae ore* matrix) display a similar range of manganese abundance but expectedly higher concentrations of SiO_2 and particularly Al_2O_3 as opposed to ferruginous ore matrix elsewhere in the ore zone where mica are minor or apparently absent (Figure 21a). The textural observation that micas appear to be bound primarily to hematite-matrix is further confirmed by the strong positive

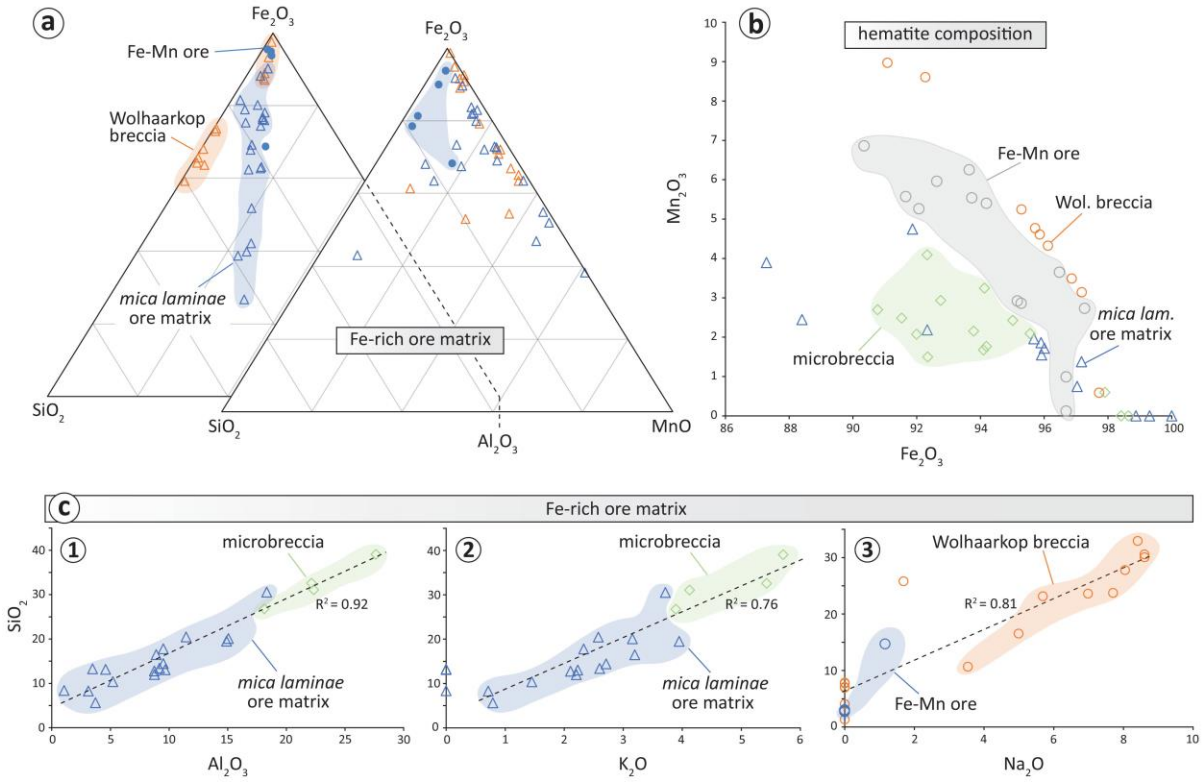

Figure 21. (a) Ore matrix spot EDS analyses obtained from areas adjacent to interbedded mica laminae (*mica laminae* ore matrix) exhibit generally higher Si and Al concentrations that reflect vey fine-grained silicates intermixed with and bound chiefly to hematite-rich matrix in ferromanganese ore (Heuningkranz-Langverwacht). (b) Mn substitutions in hematite are higher in the Fe-Mn ore matrix and Wolhaarkop breccia where manganese-bearing alkali minerals are present, as well as in microbreccia matrix hosting Mn-carbonates. Combined with textural analysis this implies Mn in the fluid and at least some hematite formation along with or after alkali mineral precipitation. (c) Positive correlation between SiO_2-Al_2O_3 and SiO_2-K_2O in ore matrix with intermixed mica (1-2) and between SiO_2-Na_2O (3) in the manganese-rich Wolhaarkop breccia, the latter caused by the high abundance of Na-bearing silicates. Data from the Wolhaarkop breccia are from ongoing research by the author.

correlation between SiO_2-Al_2O_3 and SiO_2-K_2O (R^2 = 0.92 and 0.76 respectively) in such matrix but also in Fe-rich matrix supporting chert and alkali-rich microbreccia (Figure 21c-1, c-2). In the latter case, muscovite in the cement has certainly formed during post-depositional reworking of the host lithologies and may therefore have a mixed authigenic-detrital origin. Nevertheless, the association of hematite and hydrothermal mica may point to a precursor rich in clays and iron oxides, such as the Olifantshoek shale units. Analyses from ongoing research on the Wolhaarkop breccia manganese-rich matrix (Heuningkranz locality) apparently do not show contrastingly higher manganese content, but however exhibit a

strong positive correlation between SiO_2 and Na_2O instead (Figure 21a, 21c-3), caused by the abundance of aegirine, albite and natrolite filling vugs and overprinting clasts in these rocks.

Compositionally, micas associated with the WMD ferromanganese (Fe-Mn) ore and in particular with hematite-rich intervals are distributed along the tie between Na and K end-members (muscovite-paragonite series) and from our limited data appear to have much wider compositional variations than previously reported by Fairey et al (2019) or mica from other Fe-Mn lithologies in the area (Figure 22a) that are very close to the end-members. Specifically, paragonite seems to be more common in ferromanganese ore, whereas muscovite is likely the dominant mica in different breccias and overlying (conglomeratic Fe-ore) or surrounding lithologies (quartzite) where sodium is generally more limited in the alkali parageneses. However, this division is apparently rough since paragonite is also documented from the barite-rich Kolomela (Kapstevel) iron ore. Barian muscovite occurs exclusively in the ferromanganese ore and shows an equivalent distribution to that of muscovite, although with clear signs of discordant development to the layered mica-hematite laminae that support its possible later formation by barium-rich fluids. Barian muscovite in the EMD ores displays both similar and more Ba-rich compositions to the one from the current study. A series of petrographic textures associating mica with replacement of ovoids or concentric-zoned structures, secondary fillings and vugs combined with geochronological data, demonstrate that their formation is linked to the Namaqua alkali-metasomatic event. However, the origin of layered and principally hematite-associated mica, as well as the occurrence of other Fe- and Mn-bearing unidentified phyllosilicates in the ore matrix is more elusive.

If one accepts the prevailing model for original ore accumulation within a surficial fresh-water depositional setting, then terrigenous detrital material including clays or smectites is reasonably expected to have concentrated in the protore prior to diagenesis or any later thermal event. In this regard, mica seen embedded in the ore zone as shale-like mm- to cm-thick laminae and coexisting with rutile, apatite and zircon may have formed by such phyllosilicate precursors within bands that may as well have partly preserved soft-sediment deformation or diagenetic textures on top of early-compositional signatures (i.e., Al, Ti, Zr). For example, micas have been reported to form syn-genetically in dolomites by the influx of

early diagenetic hydrothermal fluids and interbedded clastic material (Park et al; 2020). Preservation of pre-Namaqua age signals (ca. 1.6-1.5 Ga) in paragonite and other silicates (possibly glauconite-celadonite) support authigenic formation either by recrystallization or hydrothermal metasomatic processes well before the widespread 1.2-1.0 Ga hydrothermal event.

In another scenario, the crude layering of these ores, seen also in mica-free intervals with rhythmic interlayering of hematite and braunite, could have been formed by dissolution of earlier soluble phases, especially if evaporitic material had been present in the carbonate precursor (ca. 2.5 Ga Gamohaan Formation) (chapter 2). Different clastic lithologies overlying the orebodies, such as the Marthaspoort quartzite or the Gamagara/Mapedi shales, are seen ferruginised in different mines across the PMF and research on shales has further documented a probable metasomatic overprint and hydrothermal enrichment in K and HFSEs (Land et al; 2017). In this context, mica bands and layering of the ferromanganese ore could have originated, at least to a certain extent, through processes metasomatizing shale material.

Layer dependent alkali-rich and mica-free parageneses are also common in the ore zone and can be macroscopically mistaken for phyllosilicates, but instead comprise minerals such as banalsite, natrolite and hyalophane-celsian interlayered with ore minerals. These alkali-silicates may have also formed in reaction between hydrothermal fluids and pre-existing phyllosilicates marking layered sedimentary textures. However, distribution of alkali-rich minerals in discontinuities of all sorts, as for example that of prominent late calcite-hyalophane veins, emphasizes that there is no need for phyllosilicate precursors and that Si and Al are constituents of the circulating alteration fluids. Analyses of feldspars from different PMF ore lithologies show end-member compositions, with the exception mainly of ferromanganese ore, where intermediate compositions (banalsite, hyalophane) are commonly seen in veins, vugs and matrix (Figure 22b). Piemontite is another Mn-silicate that is seen replacing possible diagenetic textures in pre-existing sediments (i.e., ovoidal structures) and similarly to other manganese districts or manganiferous schists may have formed by reaction of oxides with clays or aluminous sheet silicates during low grade

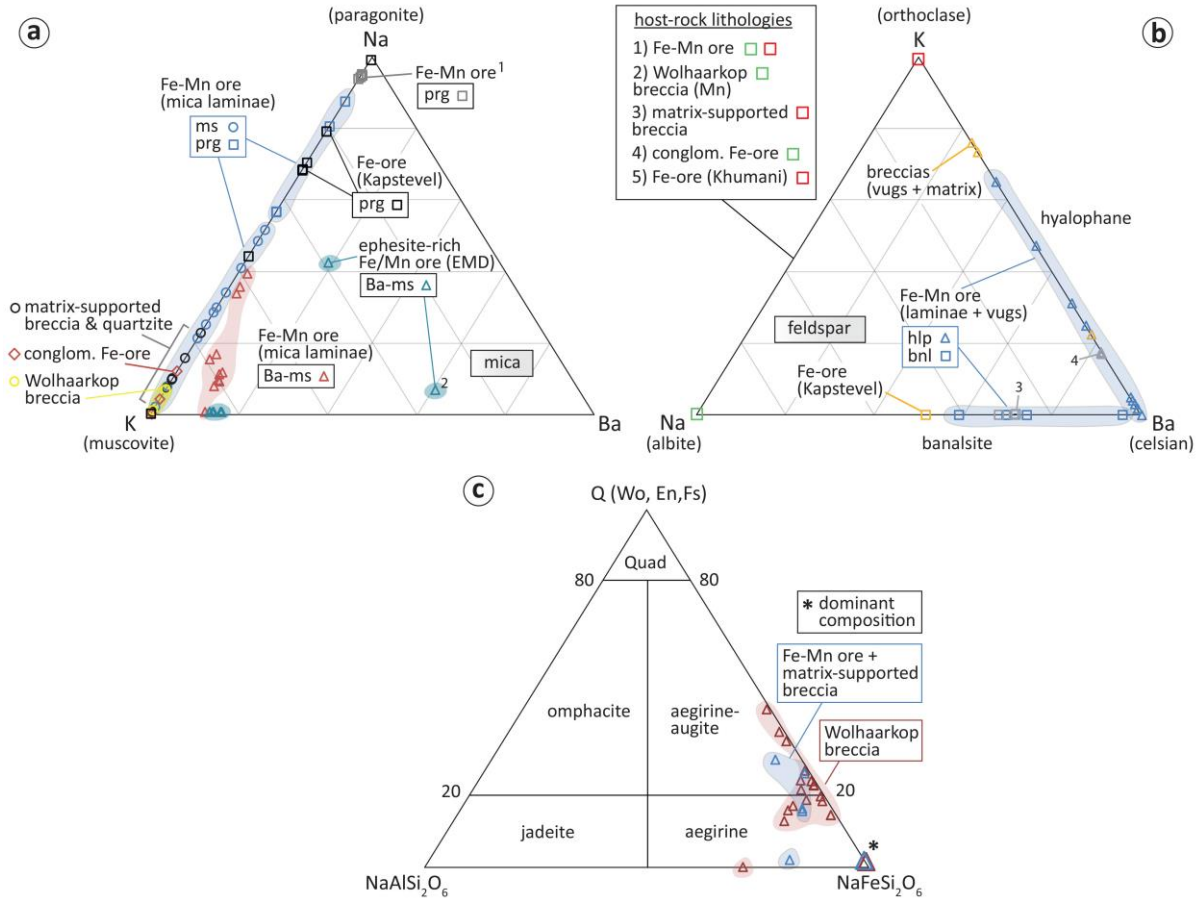

Figure 22. Compositional ternary diagrams for (a) mica (b) feldspar and (c) pyroxene from different ore lithologies. (a) There is a suggestion for muscovite being the dominant species in Fe-ore, breccia and quartzite where sodium in not so abundant in the alkali assemblages as in the Fe-Mn ore, although paragonite is also present in the Kapstevel Fe ore. Ba-muscovite is found in both WMD and EMD. (b) Feldspars shows end-member compositions, with the exception mainly of ferromanganese ore, where intermediate compositions (banalsite, hyalophane) are commonly seen in veins, vugs and matrix. (c) Pure end-member aegirine appears to be dominant but aegirine-augite also occurs, especially in the Wolhaarkop breccia where it is seen with Mn-carbonates and other silicates (ongoing research). References: 1: Ar-Ar dated paragonite (chapter 2) 2: Gutzmer and Beukes (1997b) 3: Fairey (2013) 4: Bursey (2018).

metamorphism (Coombs et al; 1985, Brusnitsyn; 2010), although it may be also a hydrothermal phase (Deer; 1982) and therefore related to the Namaqua alkali metasomatic event.

Micro-analyses of hematite presented by Fairey et al (2019) from the whole stratigraphic extent of the ore zone at Heuningkranz (SLT-015), revealed significant Mn_2O_3 substitutions (ca. 4 wt.% on average) for Fe_2O_3 in the hematite structure. Analyses

from this study confirm that Mn_2O_3 can reach up to ca. 6 wt.% in hematite and furthermore suggest that its manganese content is higher where manganese-bearing aegirine, serandite and other species are present in the vicinity (Fe-Mn ore matrix, Wolhaarkop breccia, etc.) (Figure 21b). On the other hand, manganese appears to be lower in Fe-rich mica laminae containing minor braunite and somewhat higher in breccia matrix where apart from braunite and muscovite, Mn-carbonates are also present. All the above may suggest that at least some hematite in the ore is formed during or as clearly suggested by cross-cutting textures, after certain alkali minerals and that availability of mobilized manganese in the fluid controls its composition. Another textural pattern worthy of mention is that aegirine seems to proliferate in hematite-rich ore matrix and accommodated vugs or in the iron-rich cement of breccias, something indicating that it either scavenges Fe from the immediate host rock or else may be closely related to Fe-remobilization during hydrothermal alteration. Its dominant composition is that of pure end-member but also extends to that of aegirine-augite, especially in the Wolhaarkop breccia, in which ongoing research has revealed abundant co-existing Mn-carbonates (Figure 22c).

It is clear from the mineralogy and textures discussed so far that the different species could not have formed concurrently. The same is suggested by the $^{40}Ar/^{39}Ar$ data which broadly suggest two distinct pulses related to formation of earlier micas and late-stage feldspar respectively. At the same time, suggestion of a paragenetic sequence seems futile at present considering the complexities of the system. Despite that, following the paragenetic scheme of Fairey et al (2019), a broad chorological division of the recorded mineralogy is presented, with the main aim of highlighting mobilization of ore metals taking place through formation of both ore and gangue minerals (Figure 23). It is interesting to note that from a single locality (Heuningkranz-Langverwacht), a minimum of **forty-two species** can be reported from **the PMF ores**. Taking into consideration the different solubilities of Na, K and Ba chloride complexes in aqueous fluids, as suggested by the previous researchers, as well as integrating all previous and current textural analysis and geochronological evidence, a tentative paragenetic sequence can be constructed. Furthermore, formation mechanisms and occurrences of the documented phases in other examples from literature can be

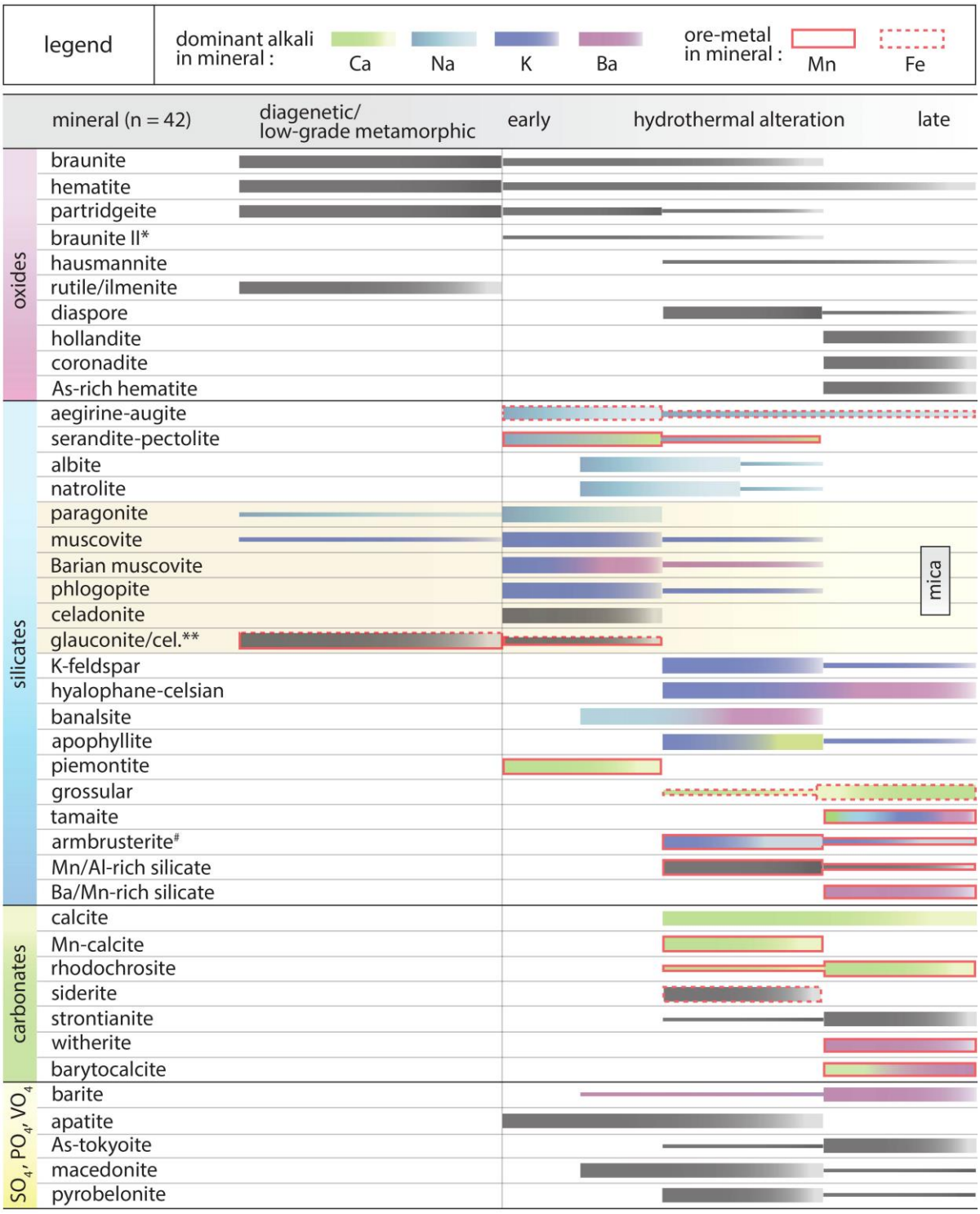

Figure 23. Paragenetic chart of the ore and gangue mineral constituents in the studied drillcores (WMD) based on previous work from Fairey et al (2019) and findings in this study (see text) Alkalis (colour-coded) and ore metals (red outlines) hosted by gangue minerals are noted to emphasize elemental transportation during the hydrothermal event. Notes: *: Braunite II is based on very limited analyses but textural indications support the presence of a compositionally distinct, Si-depleted braunite. **: These silicates need further research before they can be confirmed. #: Armbrusterite was not found in the studied drillcores but is abundant in the same locality (Heuningkranz, ongoing research) and has been also reported from Khumani (EMD).

integrated into the above attempt to further shed light upon alteration history. That being said, the following are deduced:

(1) mica and other phyllosilicates have a confirmed early hydrothermal and possibly diagenetic/metamorphic origin, the latter however requiring further investigation.

(2) In general terms, Na-bearing silicates most likely formed prior to K- and Ba-rich phases. Texturally, this is observed in coarser vugs comprising zoned parageneses (for e.g., serandite or albite lining a vug and K-feldspar or calcite filling its core), but it is also common for Na, K- and Ba-bearing phases to coexist (e.g., hyalophane with banalsite) in intricate relationships with no clear evidence of sequential deposition.

(3) Calcium-bearing silicates are more difficult to be assigned to the paragenetic sequence but according also to other Mn deposits, piemontite is perhaps an early hydrothermal if not earlier diagenetic/metamorphic phase, whereas both the composition and association of grossular with banalsite, hyalophane and calcite supports a hydrothermal origin for the garnet. Fe-rich varieties of garnet are widespread in the KMF and in general, garnet is very common in metamorphosed manganese deposits and rocks when admixtures of clay material are present (e.g., Dasgupta et al; 1987, Bühn et al; 1995). In contrast, its rarity in the PMF does not seemingly reflect an aluminosilicate-poor Fe-Mn host rock, but is probably related to the physicochemical conditions of alteration fluids, limiting garnet formation.

(4) Calcite, iron- and manganese-carbonates are scarcer than silicates and probably form across the main and late alteration stages in veins, vugs and breccia-cement material, but Ba-bearing carbonates in particular, are considered to be a later phase that also replaces barite, in accordance to similar evidence from the literature (Hanor; 2000). Another possible explanation for the presence of Ba-carbonates in barite-free parageneses is that surplus Ba and Sr in the fluids remain mobile after sulfur is consumed by barite precipitation.

(5) Barite is generally a late precipitate but it is seen across a range of parageneses as an accessory phase and previous age reports (chapter 2) support formation already from the early alteration stages, if the whole extent of the Namaqua alteration event is considered.

(6) Tamaite and apophyllite are rare species, firstly reported from these ores and combined, host the full suite of alkalis (Ca, Na, K, Ba). These phases possibly form during the

main and late alteration stages. Tamaite has been reported to coexist in Mn ores with tokyoite and gamagarite, phases also known from the PMF (e.g., Matsubara et al; 2000, Costin et al; 2015) and apophyllite is well-documented in the KMF (Gutzmer and Beukes; 1996b).

(7) An unidentified Mn-rich silicate with significant barium (ca. 4 wt.%) resembling armbrusterite is associated with the typical main to late-stage alkali-rich parageneses in vugs. In contrast, another Mn- and Al-rich phase is restricted to a single Al-rich paragenesis with diaspore, which can be tentatively attributed again to the main or later alteration stage, since Mn-carbonates and barite appear to have been formed synchronously with diaspore.

(8) Crystallization of the rare Pb-, V- and As-bearing phases macedonite, pyrobelonite, As-tokyoite and As-hematite indicate that circulating fluids concentrated these elements which are not particularly widespread in the rock mass, and precipitated them in distinct species. Such processes in other manganese districts have been attributed to late circulating hydrothermal fluids under decreasing temperature following metamorphism (Basso et al; 1992, Marchesini et al; 2001). Arsenic is also regularly present in hydrothermal apatite associated with alkali minerals, probably as As(V) like most studied natural apatites, even though it may have formed form solutions mainly containing As(III) (Liu et al; 2017). Furthermore, the above may indicate the absence of reduced sulfur or sulfur depletion in the fluid, the presence of which would have otherwise formed arseno-sulfides, similar to many magmatic-hydrothermal systems (e.g., Williams-Jones and Heinrich; 2005).

(9) Hollandite and coronadite can be regarded as late-stage hydrothermal phases, as deduced by their involvement in Mn-and As-bearing veins (As-hematite) associated with localized alteration of the ore matrix and replacement of former clasts.

(10) The origin of braunite and hematite is tied to the primary ore genesis and is therefore postulated to be burial diagenetic to low-grade metamorphic (prior to the 1.2 Ga Namaqua event). However, according to a series of textures indicating replacements by braunite and late hematite formation, at least some of these oxides are of hydrothermal origin. The same is true for minor hausmannite in veins, partridgeite and braunite (II) in vuggy ore-matrix. On top of textural evidence, the presence of certain gangues themselves, as seen in Figure 23, reflects that both Fe and Mn are scavenged by the host rock (i.e., mobilized) or introduced by fluid(s) and participate in assemblages where decreased manganese oxidation state (Mn^{2+}) prevails. However, redox changes with respect to manganese (Mn^{3+}, Mn^{4+}) also

occur and Mn^{3+}-enriched minerals (for e.g., piemontite) are apparently more closely associated with braunite, the index mineral of f_{O2}.

6.5 Origin and characteristics of palaeo-fluids

The combined oxygen and hydrogen isotope approach has been applied widely to trace the nature and extent of mineral-water exchange reactions and gain important insights into the fluid sources in a variety of mineralization systems (Sheppard; 1986, Shanks; 2014 and references therein). Hydrothermal minerals in the PMF ores may carry the ''fingerprint'' or ''signature'' of the paleo-fluids from which they have precipitated. However, drawing inferences from the measured $\delta^{18}O$ composition of minerals with regard to fluid source is not always straightforward and has certain limitations since the relationship between the δ values of minerals and fluids depend on the initial isotopic composition of the involved phases and extent of fluid-rock interactions, the temperature (i.e., the size of the mineral-H_2O fractionation factors) and conditions (equilibrium/disequilibrium) of isotopic exchange, as well as on the possibility of fluid mixing prior to mineral deposition and other geochemical parameters.

Therefore, key factors influencing the $\delta^{18}O$ values are taken into account in the following analysis, which further considers the available O^{18}/O^{16} isotope ratio-database from a previous study in the KMF (chapter 3) before any conclusions on fluid isotopic characteristics are reached. On the other hand, the D/H ratio of measured minerals can be a more definitive parameter in determining the fluid source in systems such as the regarded one, where mineralization fluid(s) is presumably the dominant hydrogen reservoir for the measured δD values of gangue minerals and significant modifications by exchange reactions are not anticipated. Despite that, a number of discrepancies exist concerning the reconstruction of the isotope composition of water that has equilibrated with minerals such as mica and these are also being considered below.

Available $\delta^{18}O$ data for hydrothermal gangue silicates from the PMF and specifically from ferromanganese ore at Heuningkranz locality and the Wolhaarkop breccia at Khumani mine are shown in Figure 25. The previously documented oxygen isotope range for gangue

silicates from the KMF is also included for comparison. It is instantly noticeable from this figure that a significant overlap exists between the PMF and KMF alkali-rich mineralogy, especially if hydrous phases bearing OH^- or H_2O (berthierine and armbrusterite) and possibly having more complex syn- and post-precipitation histories are excluded. $\delta^{18}O$ values of sugilite and aegirine from the KMF range from +10.6 to +13.2 ‰ (average = +11.6 ± 1 ‰, n=8).

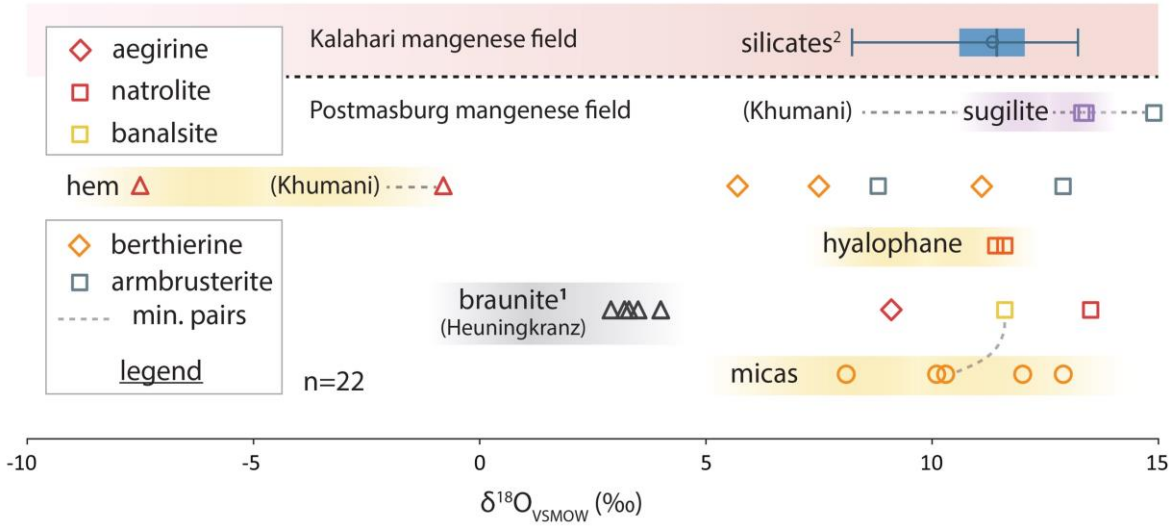

Figure 25. Oxygen isotope compositions of silicate gangues and hematite from the PMF. All samples are from Heuningkranz except from the noted sugilite, armbrusterite and hematite which derive from Khumani. Also included is the overlapping documented range and weighted mean of gangue silicates associated with the hydrothermal enrichment of the KMF (1: chapter 3) as well as $\delta^{18}O$ values for braunite from the study area (2: Fairey; 2013).

Sugilite from the PMF (Khumani) varies by only 1.6 ‰ on average from that of the KMF (2 samples: +13.3, +13.4‰), while a single $\delta^{18}O$ measurement from aegirine (+ 9.1‰) correspondingly varies by 2.5 ‰ from aegirine of the KMF. Considering also that aegirine of sample L2B-15 (this study) is almost certainly contaminated to some degree by isotopically lighter hematite, its true isotopic difference from the KMF aegirine should be even smaller. Interestingly, in accordance with what has been already demonstrated from the KMF (chapter 4), Khumani sugilite (PMF), which exhibits an $^{40}Ar/^{39}Ar$ reset age of 620 ± 3 Ma, appears to retain its initial oxygen isotopic composition.

Moreover, both feldspars (banalsite and hyalophane), despite being generally sensitive to secondary hydrothermal alteration which can modify their pristine isotopic composition, show a uniformity in $\delta^{18}O$ values (+11.6 ‰) and are compositionally identical to the silicate gangues from the KMF (average = +11.6 ± 1 ‰). Natrolite ($Na_2Al_2Si_3O_{10}2H_2O$), a

characteristic mineral of alkali metasomatism in the studied samples, typically associated with albite, calcite, pectolite and barite among others, also yields a comparable $\delta^{18}O$ value of +13.5 ‰, which presumably corresponds to the silica-oxygen tetrahedra and not the attached water molecule that should have been largely lost after sample degassing (complete dehydration at ca. 320°C: van Reeuwijk; 1974). Considering sampling drawbacks outlined earlier and the various possible contaminants that are expected to reduce sample purity, this consistency in $\delta^{18}O$ values is rather surprising.

On the contrary, $\delta^{18}O$ berthierine values as low as +5.7 ‰, from parageneses with pyrite and hematite in stratigraphically higher ferruginous quartzite, may be related to mixing with isotopically lighter meteoric water, although at least one berthierine sample (+11.1 ‰) from iron ore further replicates the average isotopic composition of silicates. Fluid mixing mechanisms involving meteoric water may interpret low $\delta^{18}O$ values (-7.5 ‰) of coarse hematite (specularite) associated with rhodochrosite from the same locality. Noteworthily, the above value along with a specularite oxygen isotopic composition of -0.8 ‰ from a feldspar-calcite paragenesis conflicts with a previous view suggesting heavier $\delta^{18}O$ values as an elemental attribute of specularite veining in the area (Papadopoulos et al; in prep) and implies more complex precipitation mechanisms or possibly more than one mineral-forming events.

Oxygen isotope composition of mica fluctuate within slightly wider intervals in comparison to the other alkali minerals, specifically from +8.1 to +12.0 ‰ (average = +10.7 ± 1.9, n=5). Textural and geochronological evidence indicate that mica in these ores can be both products of hydrothermal metasomatism or recrystallization during the Namaqua orogeny (e.g., muscovite, paragonite, phlogopite) and remnants of an older, probably diagenetic or metamorphic pre-Namaqua origin. It is known that recrystallization and late-stage hydrothermal activity can influence oxygen isotope retentivity of mica in metasediments (e.g., Bulle et al; 2020). This may account for the wider $\delta^{18}O$ range of micas in comparison to the compositionally uniform silicates. However, the same micas display a rather tight cluster of δD values, from -60.7 to -78.7 ‰ (average = -69.2 ± 6.6 ‰, n =7). The aforementioned O-H stable isotope data are combined and plotted on a standard δD_{water} versus $\delta^{18}O_{water}$ diagram

and the resulting scenario regarding the origin of fluids involved in the genesis of these minerals is discussed later on.

The δD and $\delta^{18}O$ values of the hydrothermal fluid can be determined indirectly on the basis of measured isotopic values in alteration minerals and the temperature of fluid being in equilibrium during mineral deposition. In view of the limitations mentioned above and the fact that large disequilibrium effects can be observed in low temperature mineralization systems, these calculations may be largely crude estimates, but nevertheless have the potential to shed light onto the alteration fluid characteristics and are valuable in the absence of fluid inclusion studies from these rocks. WMD ores in specific, lack any temperature constraints and information regarding EMD ores does not derive from direct fluid inclusion measurements. In fact, the unique assemblage of bixbyite, diaspore, ephesite, amesite, acmite (aegirine) and gamagarite seen in the type-locality EMD ores has been regarded as a feature of high-temperature conditions (De Villiers; 1983). Temperature estimates have been based on an experimental bixbyite thermometer, partly backed up by natural occurrences, which associates the amount of iron accommodated by the mineral structure with temperature.

A combination of the above, mineral thermal stabilities and other geological observations has resulted in the current view that bixbyite in the ferromanganese ore formed in a temperature range between 315 and 375°C (highest temperatures were around 470°C) whereas elsewhere in the ore field, where braunite is dominant, temperatures had been as low as 170°C or even lower, although the latter have not been quantified (De Villiers; 1983, Neil et al; 1994). Moreover, illite crystallinity and comparable parageneses of coexisting diaspore and pyrophyllite from the aluminous Gamagara shales overlying the deposits, also suggest temperatures between 300-400°C (Plehwe-Leisen; 1985, Gutzmer and Beukes; 1996b). Minerals typifying alkali metasomatism in the WMD ores such as felspars, aegirine, natrolite and other alkali-rich gangues are more likely to have formed within the lower suggested temperature range, probably between 150-250°C, akin to their counterparts in the KMF. This hypothesis can be further explored using the measured δ values of the minerals.

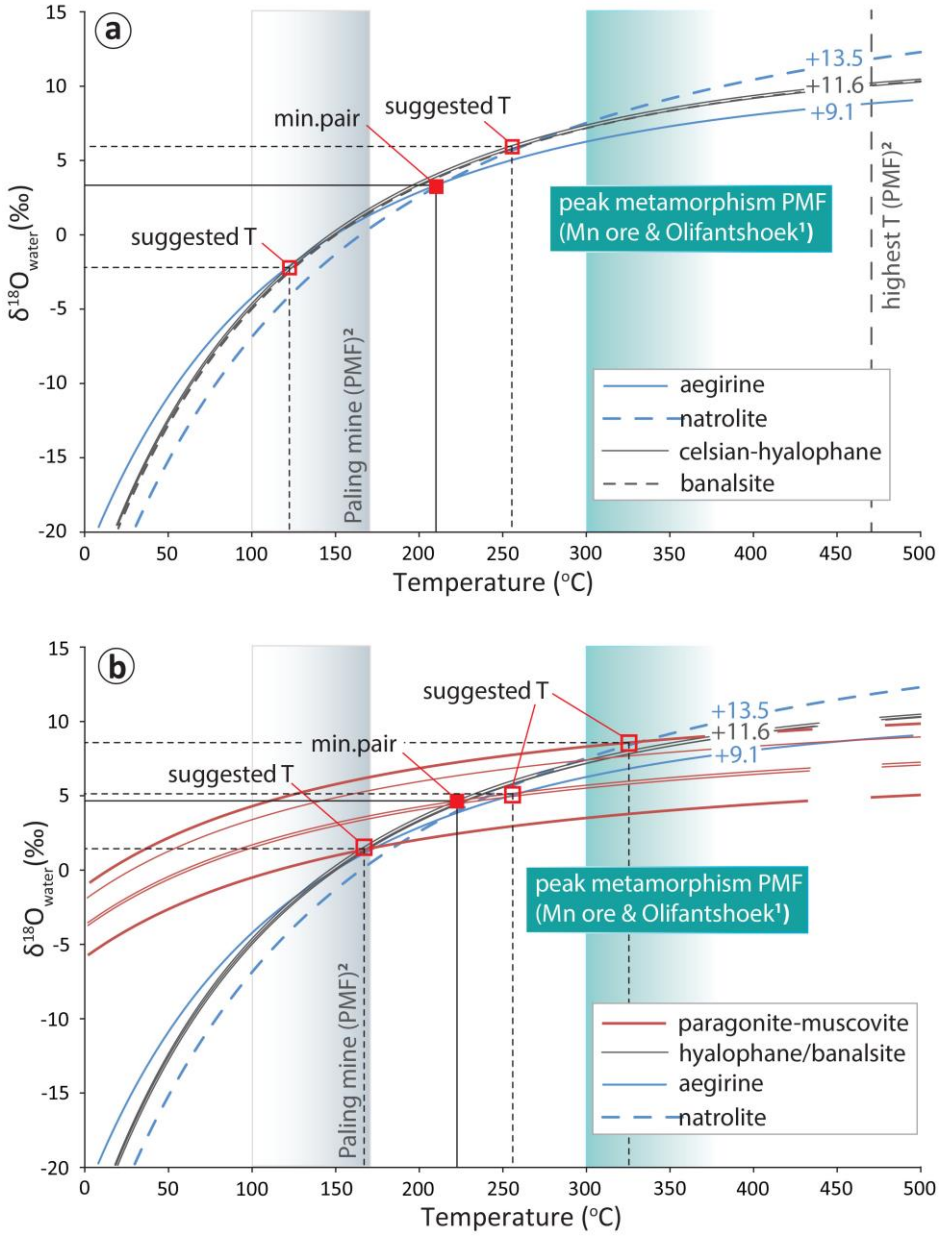

Figure 26. Minera-water oxygen isotopic fractionation curves showing data from the alkali-rich mineralogy (a) and mica (b) in the PMF ores (WMD). Fluid compositions (+3.5 to +7.1‰) are calculated using the suggested temperature from the natrolite-aegirine pair (215°C). Suggested temperatures (open square symbols) from the whole mineral suite range from 135 to 335°C, but cogenetic formation of phases used in these calculations is rather unlikely. Temperatures for the equivalent ore occurrences in the Eastern Maremane dome (170°C, 300-375°C and 470°C) are also shown (see text for details).

Since cationic substitution has generally minimal effects in silicates with the same structure (< 1 ‰ differences in δ), the experimental isotopic fractionation factors of k-feldspar can be used for hyalophane and banalsite. Likewise, the isotope fractionation factor of zeolite can serve as a reasonable approximation for natrolite. As seen in Figure 26a, a natrolite-

aegirine mineral pair from the same breccia (sample L2B-15), indicating crystallization of both phases over a narrow timespan, suggests a formation temperature of 215°C from a fluid with oxygen isotopic composition of +3.5 ‰. The apparent equilibrium temperature inferred from the banalsite-paragonite pair is not far off the previous one (230°C), although timing of formation of the considered mica is most likely prior to that of banalsite, which obviously casts doubt on the previous estimation. If the above estimate (215°C) is crudely regarded as a mean temperature for hydrothermal metasomatism in this locality and is in turn used in fractionation factors for the rest of the measured minerals, then alkali phases suggest $\delta^{18}O_{fluid}$ values ranging from +3.5 to +4.3 ‰ (average = +4.0 ± 0.4‰, n=6) and similarly mica imply a plausible wider but overlapping range from +2.3 to +7.1 (average = +4.9 ± 1.9‰, n=5) (Table 2). $\delta^{18}O$ values determined for braunite separates from these ores range from +2.9 to +4.0 ‰ (Fairey; 2013, Figure 25). Interestingly, this range of $\delta^{18}O$ values overlaps with the oxygen fluid composition calculated for the gangue phases.

Fractionation behaviour of braunite is not known. Hoefs et al (1987) have assumed that manganese oxides and hematite behave in similar ways as regards their oxygen isotope fractionation behaviour on the basis of similarities in measured values. However, braunite is essentially a silicate mineral and thus a probable enrichment in ^{18}O with respect to the mineralizing fluid is expected. A range of $\delta^{18}O$ values for braunite (+1.3 to +6.1 ‰) has been also reported from Bühn et al (1995) for the high temperature (T> 600° C) Otjosondu manganese formations. These authors suggested that braunite has the lowest capacity for ^{18}O enrichment among all other silicates (garnet, quartz, feldspar) in the studied paragenesis. Although further research is needed, the measured $\delta^{18}O$ values for braunite from Heuningkranz locality is likely to reflect more closely the fluid isotopic composition. In any case, the calculated fluid isotopic range compares well with the one documented for the early calc-silicate alteration in the KMF (+3.5 to +7.5‰), interpreted to represent sedimentary basinal brines with a prominent evaporitic component that have been stored in and largely equilibrated with the deeply buried sedimentary units of the Transvaal Supergroup prior to their infiltration in the deposits (chapter 3).

In the unlikely scenario of cogenetic formation of the studied phases under equilibrium conditions, the inferred isotopic temperature range, as also depicted in Figure 26, ranges from ca. 135° to 335°C (135°C: aegirine-celsian-banalsite assemblage and 335°C: mica-natrolite). In general, there are no mineral parageneses or other apparent geological evidence to support alteration temperatures much higher than 215°C, let alone as high as 335°C, although it is reminded that the above calculations are followed by a significant and indeterminable degree of uncertainty. In any case, a lower temperature range to that above is also compatible with the documented temperatures for hydrothermal enrichment in the KMF and in general with vein-hosted mineralization precipitated from sedimentary basinal fluids of different salinities (e.g., Gleeson et al 2003). Perhaps mica could have had a more complex isotopic history involving higher temperature gradients during prior low-grade metamorphism but our current data cannot elucidate that. In general terms, temperatures suggested for alkali mineral precipitation in the WMD are apparently at odds with the much higher temperature conditions postulated for the ephesite- and diaspore-rich assemblages in the EMD (Figure 26).

Knowledge of both δD and $\delta^{18}O$ of clay minerals has been suggested to permit direct insights into the temperature of formation (Delgado and Reyes; 1996). The application of ''single-mineral' geothermometer cannot be extended though to mica of this study since the equation relating the isotopic fractionation of oxygen with hydrogen is based on the empirical meteoric water-line (MWL) from Craig (1961) and thus in not suitable for compositions not satisfying this linear correlation. Nevertheless, there are two hydrogen-isotope fractionation calibrations for muscovite-water that may be possibly used to shed light on the δD value of the fluid. The first suggests a relatively linear decrease of $1000\ln a_{mineral\text{-}water}$ with decreasing temperature but derives from experiments in the temperature range between 450-800°C (Suzuoki and Epstein; 1976) and therefore requires extrapolation to lower temperatures. The second equation is essentially an empirical graphical calibration based on the behaviour of kaolinite and other hydrous silicates but is further backed up by a natural database that strongly suggests usage of this fractionation (i.e., between muscovite-sericite and water) at temperatures of about 300 ± 100°C (Bowers and Taylor; 1985, Ojala et al; 1995).

It should be noted that differences between the two calibrations can be as large as 40‰ at temperatures of about 300°C. As depicted in Figure 27a, the results of Bowers and Taylor (1985) suggest very small differences between the fractionation curves of muscovite and kaolinite. In a different experimental approach attempting to calculate the isotopic exchange between molecular hydrogen and hydrous minerals, Vennemann and O'Neil (1996) also concluded that muscovite-H_2O fractionations are essentially the same as those of kaolinite-H_2O at temperatures of 200-275°C. Therefore, well-established and experimentally determined kaolinite fractionation factors are preferable at low temperature settings instead of the muscovite calibration of Suzuoki and Epstein (1976), which may be instead suitable for higher temperatures.

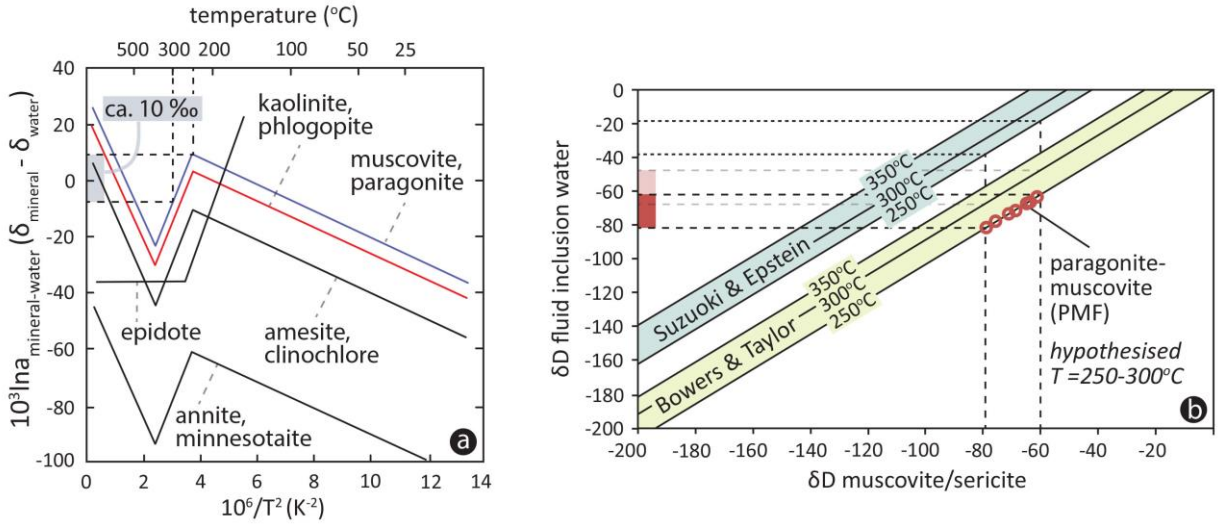

Figure 27. (a) Approximated equilibrium hydrogen isotope fractionation curves from Bowers and Taylor (1985) suggesting similar fractionation behaviour for common mica and clays. (b) Fractionation lines of Suzuoki and Epstein (1976) and Bowers and Taylor (1985) for muscovite at 300 ± 50°C. Also plotted are δD values of paragonite-muscovite from the PMF for a temperature range of 250-300°C which suggests δD of fluid between ca.-80 and -50‰.

With respect to the PMF ores, calculated δD fluid values using the latest kaolinite fractionation from Méheut et al (2010) and a temperature of 250°C agree very well with the small fractionations (between 0 and 10 ‰) at low temperatures predicted by Bowers and Taylor (1985) (Figure 27b). Specifically, this fractionation curve indicates fluids being on average 15.2 ± 1 ‰ heavier than that of associated mica, a relatively small difference if precision of analysis (± 3‰) is also considered. Constant δD_{fluid} values (from -45.0 to -63.0 ‰,

average = -54.1 ± 6.9‰, n=6) are a strong sign that H-isotope composition of the fluid dominates total hydrogen in the system. Intriguingly, natrolite (δD = -65.1) falls very close to this range, which likely suggests a common paragenetic origin. The estimated δD fluid range is in line with that of metamorphic fluids (ca. -20 to -65) but also overlaps with the very broad range exhibited by sedimentary basin brines (-150 to +20) or any type of evolved meteoric water (Ohmoto; 1986, Hurai et al; 2015).

$\delta^{18}O$-δD plots are commonly used to display modern day brines in relation to their likely source water and likewise have illuminated the origin of hydrothermal fluids associated with a variety of deposits (e.g. Shanks; 2014). In Figure 28a, both mineral (open symbols: mica, natrolite, armbrusterite, n=7) and fluid (filled symbols) δD isotopic values from the PMF are seen plotting near or partly inside the metamorphic- and magmatic-water respective boxes. This overlap is to be expected as hydrothermal waters typically occupy this isotopic compositional space in $\delta^{18}O$-δD plots and show variable D- and O^{18}-shifts as a result of modification by isotope exchange reactions with the different lithologies or other fluids. The characteristic ^{18}O-shift to the right of the meteoric water line (MWL) occurs principally due to isotopic exchange with ^{18}O-rich minerals in such systems and in the case of the hydrothermal PMF minerals is suggested to reflect the composition of sedimentary brines equilibrated with different lithologies contained in the Transvaal basin.

The very limited dataset does not allow for any observation of possible linear trends that would indicate fluid mixing. Additionally, a handful of previously determined data from the KMF (muscovite, datolite, pectolite, Mg-arfvedsonite) show in comparison a broader δD isotopic range, which likely highlights secondary variations after exchange reactions. Although as mentioned above, H-isotope composition of the fluid is believed to buffer the system, the case of Mg-arfvedsonite (KMF) and armbrusterite (PMF) showing such D-depleted values, is probably an indication that these minerals have formed in equilibrium or assimilated hydrogen either from a meteoric water source or an isotopically very light host rock, the latter being rather improbable. This hypothesis needs more supporting evidence since loss of water from amphibole during post-depositional alteration may also impact its δD value and the same may be true for water in the structure of armbrusterite. Furthermore, amphibole

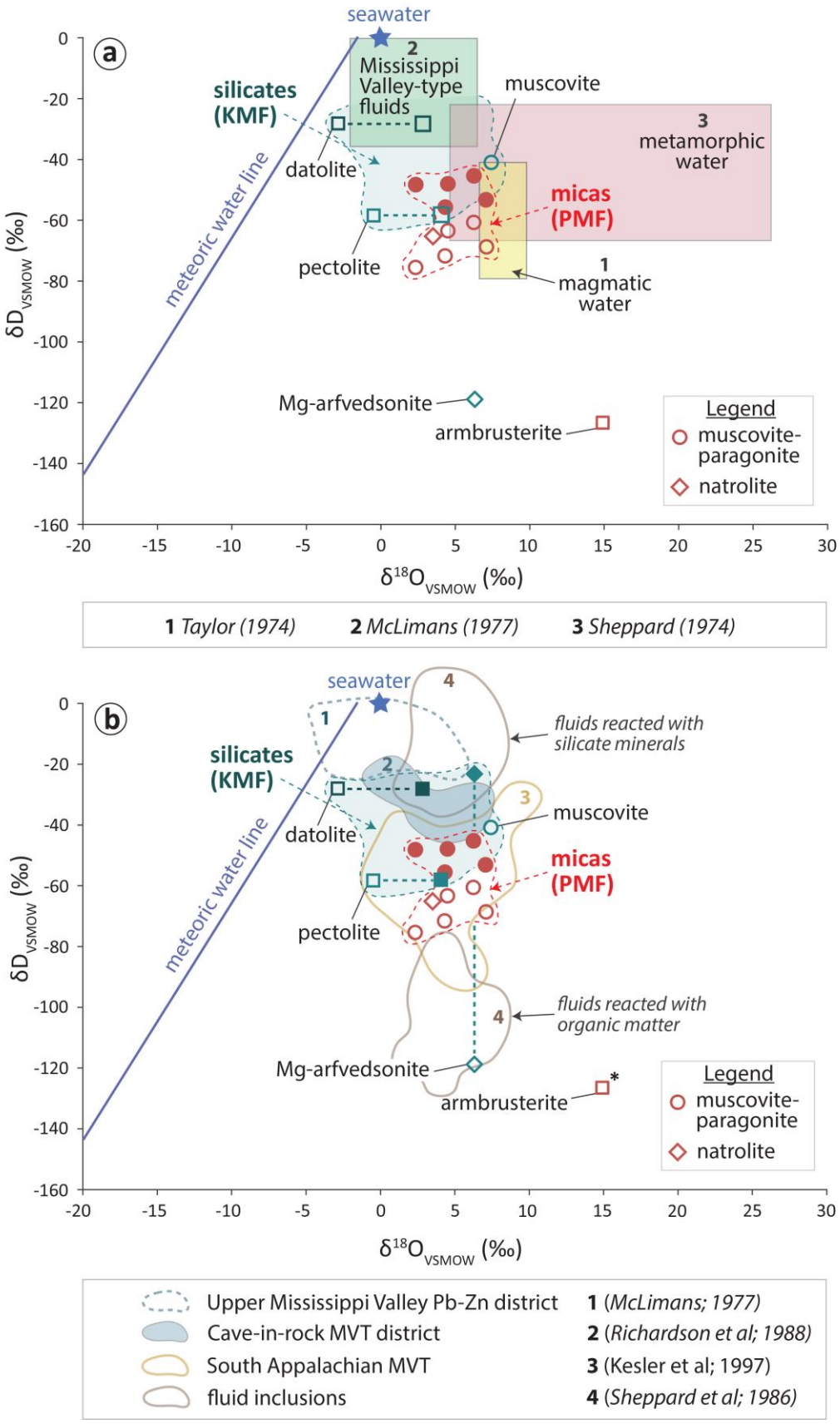

Figure 28. Oxygen and hydrogen isotope compositions of PMF and KMF hydrothermal gangues plotted against common water types (a) and compositions of MVT brines (b).

supposedly retains its molecular water after degassing (pre-treatment for H isotope analysis) at 150^{o}C, but the same may not be true for armbrusterite at the same temperature; therefore, significant fractionation may have occurred. At the same time, syn or post-depositional meteoric/groundwater circulation and fluid mixing phenomena with the infiltrating brines is a very plausible scenario.

Attention should be drawn to the isotopic similarity of the paleo-fluids circulating in the PMF ores and the contemporaneous solutions causing ore-enrichment in the KMF, with fluids in Mississippi Valley-type Pb-Zn deposits. This is delineated in Figure 28a & b. It is widely accepted that the chemical and isotopic characteristics of the mineralizing brines responsible for MVT deposits are very similar to those of sedimentary basin brines. O-H isotope systematics have been paramount in providing links between the two and as seen in Figure 28, mineral data from most MVT deposits plot close to the meteoric water line and just below seawater δD - $\delta^{18}O$ values. This highlights the origin of salinity in the ore-forming basinal brines, which is attributed to indirect evaporation of seawater and subsequent reflux into basement aquifers or to direct dissolution of evaporites (Hanor; 1994, Shanks; 2014). The latter scenario has been reasonably postulated for brines in this study. The fact that plotted micas show more affiliation with the fields defined from MVT deposits, rather than with metamorphic water, is supportive of their hydrothermal origin from a low-T sedimentary fluid.

δD - $\delta^{18}O$ values of fluid inclusions from ore and gangue minerals in MVT deposits exhibit a large vertical spread in this compositional space, much higher than modern basinal brines (Shanks; 2014) and some authors have stressed (e.g. Kesler et al; 1997, Sheppard et al; 1986) that this array of values is related to reactions with organic matter causing a shift to strongly negative δD values, water-rock interactions producing higher $\delta^{18}O$ values and dilution by meteoric water causing shifts to lower $\delta^{18}O$ values. The limited dataset from the Northern Cape does not suggest any of the above, although it can be surmised that if the precipitating fluid, at least for the measured phases, had acquired its isotopic composition after extensive interaction with the various wall rock lithologies, the observed isotopic homogeneity between KMF and PMF would have been very unlikely. Much like what has been

suggested for the KMF (chapter 3), fluid buffering is preferably invoked to explain both the documented interactions between fluids and host rock lithologies and isotopic uniformity. It is likely though that isotopic compositions of other gangues or ore minerals would differ, being more closely controlled by host rock compositions or later overprinting events such as the Neoproterozoic hydrothermal disturbance recorded in the wider area (Fairey et al; 2019, chapter 4).

To summarize, we reiterate that a single and broadly uniform source is of paramount importance to explain striking isotopic similarities between gangues from the two districts in this preliminary dataset, which gives sufficient reason to believe that fluid characteristics can be correctly predicted by measurement of gangue minerals. The involved aqueous solutions may have originated as trapped meteoric and/or formation waters, but were then heated, chemically evolved through time and equilibrated with different lithologies of the Transvaal Supergroup before circulating through the regarded ores. More precise and systematic research is needed to illuminate the more complex processes being at play, especially with respect to deposition of hydrous phases and possibly identify promising pairs for isotope geothermometry, in lithologies that otherwise provide very little opportunities for constraining their formation and alteration characteristics.

6.6 Effects of hydrothermal influence on ferromanganese ores and sources of alkalis

6.6.1 Inconsistencies with the current models

The nature of the relationship between the origin of the ores and alkali mineralization remains cryptic. Following indications presented by Moore et al (2011) for widespread alkali-metasomatic processes affecting the Fe- and Mn-rich rocks of the Transvaal Supergroup, Fairey et al (2019) considered the possibility of hydrothermal overprinting having served as an enrichment factor during the late Neoproterozoic, mainly through Mn remobilization on a local scale and further leaching of carbonate lithologies. This scenario was driven by inconsistencies in the existing models and the excellent potential of alkaline fluids to leach

and transport elements, something that was texturally evidenced by later replacement of hydrothermal gangues by braunite.

The overall geological setting, distribution and mineralogy of the ores may be compatible with the prevailing consensus that concentrations of Mn and Fe have been contributed for the most part from dissolution of Mn- and Fe-rich host carbonate lithologies (Gutzmer and Beukes; 1996a, 1997b). Under closer examination though, the mode and timing of carbonate dissolution, i.e., iron and manganese concentration with surficial weathering and lateritic mechanisms as ferro-manganiferous wad or fresh-water karst sedimentation during an extensive period of erosion between ca. 2.0 and 2.0 Ga., are confined to a very narrow timeframe of the complex structural and alteration history of the area. As a consequence, models do not account for major orogenic events developing regional thrust systems (Blackridge thrust) and duplications of the stratigraphic units (Cornell et al; 1998) or causing later reactivation of normal faults (Namaqua orogeny) (Altermann and Hälbich; 1991, Basson et al; 2018), but most importantly miss out the now well-documented large-scale fluid flow events that have affected the PMF ores during the Meso- and Neo-Proterozoic. Moreover, mineralization is spatially restricted to specific Formations of the Campbellrand stratigraphy (Fairfield, Reivilo and Papkuil Fm) that collectively have a thickness of ca. 170 metres, whereas ca. 800 metres of overlying carbonate sediments are not being considered to have played any role in ore formation. Surrounding lithologies that may have readily provided iron to the PMF ferromanganese ores at any stage such as the Asbestos Hills BIF, or even manganese (Griquatown IF avg. = 0.8 wt. %, up to 5.9 wt. %, n > 100: Oonk unpublished data, see Papadopoulos; 2016), are also not considered in the available models.

Inconsistencies extent to the stratigraphic and geographic occurrence of the ores, as well as to the postulated origin of the limited number of alkali-rich minerals reported in these early studies, the latter being incompatible with the proposed ore formation mechanisms (Gutzmer and Beukes (1996b) state that banded ferromanganese ores and chert bearing-manganese ores (Wolhaarkop breccia) form at completely different depositional settings (surficial vs subsurface palaeokarsts) and consequently are distributed in distinct belts. However, the stratigraphy of the WMD ores records the transition between both ‘’ore types’’

and additionally, ferromanganese ore does not display an occurrence corresponding merely to residual freshwater sedimentation processes in an open karst. In the studied drillcores from the WMD, massive to laminated ore develops interbedded with metre-thick sections of brecciated rock, ultimately overlain by ore-grade hematite mineralization of very poorly sorted conglomeratic nature.

Additionally, the speculated age of burial metamorphism (1.9-1.8 Ga) invoked by the same authors to explain the presence of albite, aegirine, Ba-muscovite, ephesite and barite in the EMD ores, along with the formation of the present ore-mineral assemblage comprising bixbyite, partridgeite and braunite, strongly contrasts with the Namaqua age (1.2-1.0 Ga) of regional metasomatism that is inarguably responsible for the formation of the majority, if not all of the aforementioned gangue species (chapters 2 & 6). In light of several inconsistencies, contradictions and lack of incorporation of recent and new data in the prevailing models, ore genetic mechanisms necessitate reevaluation. For example, a plausible scenario is that these metalliferous sediments have went through a series of Mn and Fe concentration processes from residual/sedimentary to regional metamorphic/hydrothermal, owing to circulation of succeeding events of fluid circulation. Further inspiration for the conditions, origin of alteration and effects of epigenetic events on the deposits may be perhaps drawn from geologically comparable Mn- and Fe-ore districts in the literature that show comparable signatures of alkali enrichment.

6.6.2 Analogous Mn-districts with alkali mineral suites

Districts with metamorphosed Mn- and Fe-rich lithologies and deposits worldwide are regularly cited for their wide variety of peculiar mineral assemblages, which in many cases have formed from hydrothermal processes under alkali-rich and oxidizing conditions, induced by tectonic deformation or thermal events of different origin (e.g., Ashley; 1986, Lucchetti et al; 1988). Therefore, it comes as no surprise that the PMF ores display this mineralogical wealth, although it must be noted that certain species seen here are of considerable rarity (for e.g., tamaite, macedonite, As-tokyoite, armbrusterite), with hitherto only a handful of other mentions in the literature. Perhaps the closest analogues to the Northern Cape ore province can be considered to be the following mineralogical districts: (a) Långban district in

Sweden (b) Liguria Province in Italy (Cerchiara, Val Graveglia) (c) Hoskins and Woods mine in Australia and (d) the Shiromaru and Hijikuzu mines in Japan (Matsubara and Nagashima; 1975, Ashley; 1986, Kato et al; 1987, Åberg and Charalampides; 1988, Lucchetti et al; 1988, Cabella et al; 1990, Kawachi et al; 1996, Holtstam; 1999, Jonsson and Hålenius; 2010). Other examples showing partial parallels with the Northern Cape deposits in the sense that they show a similar but narrower suite of alkali-rich gangues hosted in braunite/hematite-rich lithologies are the high-T-low-P Otjosondu Mn ore-bearing unit (Namibia), the metamorphosed Fe- and Mn-lithologies of the Iberian Massif (Spain) or the Mn deposits of the South Urals among many others (Bühn et al; 1995, Velilla and Jiménez-Millán; 2003, Brusnitsyn; 2010).

Shared characteristics between the above localities (a-d) are: (i) Braunite and hematite make up the bulk of the ore bodies, thus indicating highly oxidizing conditions, whereas in some cases hausmannite or rhodonite also add to the ore-grade. (ii) Preservation of banded textures and lamination to various degrees that may represent primary features. (iii) Generally low-grade metamorphism/hydrothermal events (prehnite-pumpellyite to upper greenschist facies conditions) have affected the broadly stratiform manganese ores, which are hosted by volcanosedimentary sequences and the large majority of them are thought to have originated in a submarine volcanic exhalative environment, a geological environment that is however markedly different to the presumed terrestrial environment of the PMF ores. (iv) Alteration features including Fe-Mn dominated banded skarns, veins and fissure-hosted mineral assemblages and metasomatic veinlets are present in all regarded localities and have been emanated either from an igneous intrusion or from tectono-metamorphic events triggering mobilization of fluids. (v) The enormous variety of generated gangue assemblages (for e.g., over 270 known species from Långban) includes alkali and/or Mn-bearing pyroxenes, amphiboles, garnets, epidote-group minerals, micas, carbonates, oxides, secondary hydrous phases, arsenates and oxychlorides enriched in Na, K, Li, Ca, Ba, Sr, but also elements such as As, V and Pb; therefore, closely resembling gangue mineralogy in the Northern Cape ore fields. As correctly stated by Ashley (1986), Mn-bearing silicate, oxide and carbonate assemblages are characteristic of metamorphosed stratiform Mn deposits but alkali-rich silicates in manganese ores such as that found in Hoskins mine (and

the study area) are not so common. Comparable assemblages comprising banalsite, natrolite, hyalophane serandite, grossular but also particularly unusual phases such as apophyllite, tokyoite, pyrobelonite, tamaite, gamagarite and macedonite between the study area and the regarded manganese districts is indeed intriguing and may point to similar genetic processes.

The present gangue mineralization in most of the above districts is considered as consequence of a multistage geological evolution encompassing successive stages of leaching, remobilization and reprecipitation of primary elements from the ores. However, there are no age constrains on the origin of this mineralization which in the case of Liguria Province, Hoskins mine and partly Långban district, it has been implied or suggested that no distinct hiatus exists between formation of ''primary'' ore minerals (braunite and hematite) and alkali assemblages, both being linked to progressive stages of poorly constrained regional metamorphic events. Following crystallization of braunite (Långban district), a series of complex assemblages linked to fissures and networks of veins are believed to successively form with decreasing P-T metamorphic conditions or on some occasions during post-metamorphic brittle deformation up to 0.9 Ga later (Jonsson and Broman; 2002). In this respect, the alkali-rich mineralogical suite of the PMF and KMF can be regarded at present as profoundly well-constrained among that of all other districts, at least in terms of timing of the principal hydrothermal event responsible for their precipitation, that is linked beyond doubt to the well-described tectonometamorphic event of the Namaqua orogeny (1.2-1.0 Ga).

6.6.3 Aspects on the relationship of alkali-rich gangues and ore minerals - Inferences for hydrothermal ore enrichment

Beyond gangues, probably the most important aspect of ore formation regards the origin of ore minerals themselves. According to the current consensus, the present Fe and Mn ore minerals in the PMF have been formed from concentrated Mn^{4+} oxide-hydroxide precursors (2.2-2.0 Ga), possibly reacting with quartz-derived silica during diagenesis and later recrystallized in the course of burial metamorphism coinciding with the controversial Kheis orogeny (1.9-1.8 Ga). The large lacuna (ca. 600-700 Ma) between ore-mineralogy formation and that of the main body of alkali-rich assemblages is a unique feature among all the aforementioned metamorphosed Mn-Fe districts and in consideration of the latest

geochronological data, which also tentatively suggest intermediate events at ca. 1.6-1.5 Ga, this scenario needs to be reexamined.

Contrary to ferromanganese crusts and nodules which are characterized by highly distinctive mineralogy, braunite is not diagnostic of any particular geological setting, given the fact that it is the most frequent Mn^{3+}-bearing mineral forming in manganese-rich lithologies and deposits from hydrothermal and sedimentary-diagenetic to metamorphic environments (Velilla and Jiménez-Millán; 2003). Minor quantities of Fe^{3+} and Al can replace Mn^{3+} in braunite, whereas Mn^{2+} sites regularly contain small amounts of Ca or Mg (Bhattacharya et al; 1984, Enami and Banno; 2001). It has been suggested that compositional differences in braunite and other dominant Fe/Mn minerals of metamorphosed ores are strongly controlled by initial differences in bulk composition and fO_2 among the protoliths (Bühn et al; 1995). For example, minor element composition of Ca-poor and Ti-rich shale-hosted braunite from the EMD Postmasburg ores has been linked to its host rock (Gutzmer and Beukes; 1997b). Although braunite was not systematically analysed for its composition in this study, some observations can still be made, also based on ongoing research in the Wolhaarkop breccia from the same locality, i.e., Heuningkranz.

Recalculations to balance stoichiometry showed that available analyses, particularly that from the Wolhaarkop breccia, deviate from ideal composition showing silica excess. High (>10-11 wt.%) SiO_2 concentrations are probably an analytical issue of the current data suite and may be related to software data normalization. Therefore, deviations in Si should be no more considered apart from their function as a means of broadly distinguishing between the dominant braunite (braunite I) and the scant Si-depleted braunite (braunite II) or partridgeite. Despite this, data regarding other cations compare well with that from the literature and are suggested to allow at least broad qualitative comparisons between localities and textural units (Figure 24). Thinly disseminated braunite occurring in laminae where mostly mica and hematite are present (*mica laminae ore* matrix) or braunite in iron-rich microbreccia matrix, has higher Al content, similarly to that measured in Si-depleted braunite from the highly aluminous ferromanganese ores of the EMD (Gutzmer and Beukes; 1997b) (Figure 24a). Aluminum content of braunite may reflect compositional features of the protore, i.e.,

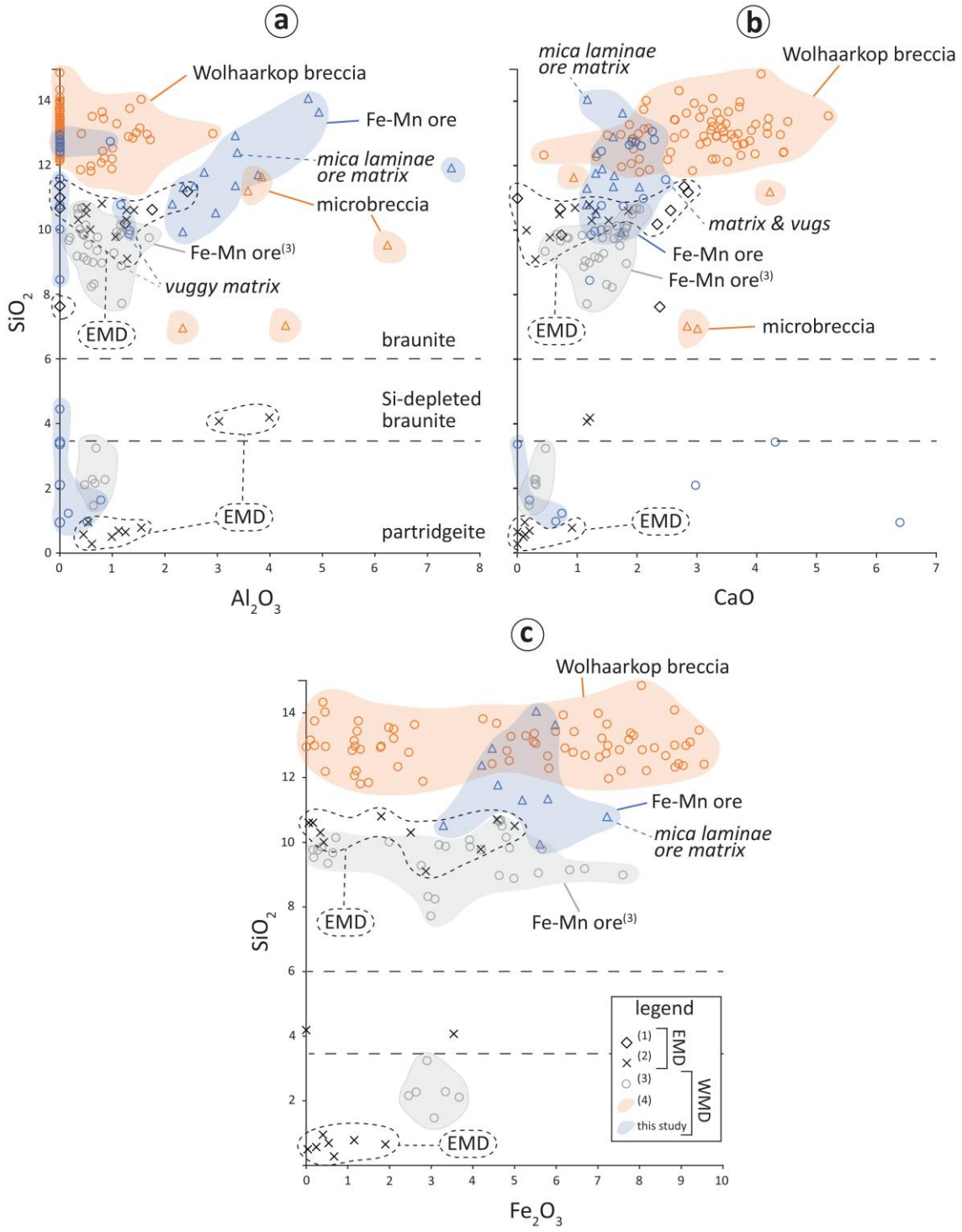

Figure 24. Compositional comparison between braunite from variable lithologies in the ore zone and different geographic districts (WMD versus EMD). Variations in silica of braunite are not greatly considered (EDS analyses, see also text). (a) Higher Al concentrations in braunite from ferromanganese ore, Al-silicate rich microbreccia matrix and mica-rich hematite matrix (*mica laminae ore matrix*) is suggested to reflect compositional characteristics of the protore or indicate a later hydrothermal origin by metasomatism inducing mobilization of Al. (b) Higher Ca in braunite from the Wolhaarkop breccia may be associated with the presence of abundant secondary carbonates (ongoing research) and indicate a replacive hydrothermal origin for the former as many textures suggest. (c) Iron substitution is significant in all studied braunite, although may be higher in the WMD ores. References: (1) Gutzmer and Beukes (1997b) (2) Fairey (2013) (3) ongoing research on the Wolhaarkop breccia (Heuningkranz, this study).

authigenic or detrital sheet silicates within an Fe-rich precursor rock that reacted with Mn-oxides to form braunite. Incorporation of Al in the structure of braunite may have occurred during syngenetic crystallization with primary silicates or throughout later recrystallization and precipitation of secondary hydrothermal mica, during metasomatism that also induced mobilization of Al.

Braunite in the Wolhaarkop breccia seems to have noticeably higher Ca (Figure 24b), which may be linked to the presence of abundant secondary carbonates, recently identified in this lithology (see also synthesis, Part 2, section 8.4.1). Many braunite textures seen in this metalliferous breccia support a replacive origin for this mineral, as well as a genetic relationship with alkali gangue species. In line with other mineralogical evidence, the presence of calcium in metamorphic braunite and its absence from sedimentary braunite in the Mary Valley manganese belt has led Ostwald (1982) to suggest that the former has been derived from reaction with carbonates present in the metamorphic assemblage. Incorporation of Fe^{3+} in braunite is highly variable and as seen in Figure 24c, iron reaches slightly higher concentrations in the WMD ores, possibly due to facilitated substitution of Fe^{3+} for Mn^{3+} associated with a lower Mn^{3+} / Mn^{2+} ratio in the bulk composition (for e.g., Velilla and Jiménez-Millán; 2003), a hypothesis which merits further investigation along with all the above indications deriving from this first crude compositional survey. The extent, chemistry and distribution of silica-depleted braunite (II) identified in the PMF also needs further attention since it may be associated with alteration of preexisting braunite from alkaline solutions during formation of gangue silicate mineralogy, in this manner representing a distinct alteration species, like the calcium-bearing braunite produced from alteration of primary braunite during the Wessels-type metasomatic event in the KMF (Kleyenstuber; 1984 Beukes et al; 1995). Differences in the minor element composition of braunite-partridgeite pairs is currently not fully understood but their systematic study seems to be an encouraging tool that can potentially further illuminate the protoliths and genetic environment of the PMF ores.

Despite all remaining questions regarding the genetic mode of formation and pristine environment of the protores, the key matter remains, i.e., if hydrothermal metasomatism

during Namaqua orogeny and/or the Neoproterozoic has acted as an ore-upgrade mechanism of preexisting lithologies; therefore, rendering these orebodies, to at least some degree, as of hydrothermal replacive origin. Skarn alteration units in the above presented ore districts, such as that of Långban, are generally thought to have formed by reactions of local nature causing recrystallization and remobilization of ore elements during different times after the primary ore-forming period/event (Åberg and Charalampides; 1988). Early theories in the previous example, tying ore genesis to metasomatic hydrothermal events related to granite intrusions, have been abandoned for the broadly accepted idea of an exhalative-sedimentary origin. Nevertheless, regional metamorphism loosely related to intrusive rocks has been responsible for a strong metasomatic overprint in felsic country lithologies, characterized by formation of Mn-silicates and oxides (Jonsson and Hålenius; 2010).

Redeposited veined manganese mineralization during later tectonic deformation is also reported from other localities (e.g., Brusnitsyn; 2010). A dynamic and multi-event alteration history in some of these Mn-districts (Cerchiara mine) can be also inferred by suggestions for the distinct formation of rare As-, V- and Mn^{3+}-bearing species by late circulating and strongly oxidizing fluids that scavenged these elements from different lithologies and utilized preferential pathways, such as fractures and brecciated rock sections (Lepore et al; 2015, Kolitsch et al; 2018). Regarding the broader petrogenetic environment of the previous district (Val Graveglia), formation of Mn-silicates and Mn-carbonates at the expense of braunite and quartz has been attributed to the main metamorphic event, that has also recrystallized precursor sedimentary oxides and hydroxides to form braunite ore (Marescotti and Frezzotti; 2000). Unfortunately, mentions of ore-grades or the concept of hydrothermal ore enrichment/upgrade during the tectono-thermal evolution of the above presented examples is not directly addressed. Generally, redistribution of critical elements subsequently to the initial metal accumulation, i.e., submarine exhalative processes, is vaguely regarded as minimal and localized, in most cases not producing strong changes with respect to overall composition.

In the case of South Africa though, KMF allows a thorough evaluation of the ore-enrichment processes during hydrothermal metasomatism, through observation of pristine,

non-metasomatized material and assessment of a massive dataset of geochemical and mineralogical information, which exhaustively record the different ore grades and substantiate the prodigious elemental transportation and redistribution. Similar observations and information are not available from the deposits of the PMF, where a range of epigenetic processes hide the potential distinctiveness of the pristine rock(s), at least in the available material and under core-scale observation. Although akin to the KMF, removal of carbonate material and probably silica, i.e., residual enrichment, had been essential in the production of the current ore grades in the PMF, it is still under question if compositional changes of the pristine carbonate lithology occurred exclusively during early, karst-related weathering, depositional and diagenetic processes or if changes took place also during later epigenetic events involving hydrothermal brines. In the latter scenario, geochemical modifications should not be restricted to carbonate rocks and sediments accumulated in karsts but may have also influenced lithologies surrounding the present ores, such as BIF, shales and quartzites. Indeed, metasomatic alteration involving ferruginization and alkali-mineral formation is recorded in both the Asbestos Hills iron-formation and the clastic sediments of the Olifantshoek Supergroup (Gutzmer and Beukes; 1996a, Land et al; 2017, Papadopoulos et al; in prep). Furthermore, the source of iron and manganese concentrated in the current ores may be also traced in other lithologies and in particular the Griquatown iron formation which hosts ca. 1 wt. % MnO (Papadopoulos; 2016), or previously mineralized lithologies, supplying remobilized iron and manganese during the Namaqua orogeny or the Neoproterozoic. Textural evidence supporting remobilization of critical ore metals, at least on the hand specimen scale, have been briefly presented in this and other recent studies (Fairey et al; 2019) and involve transportation of metals with alkalis, replacements by braunite, hematite veining and the presence of hematite and braunite in breccia cements.

Even supposing that all PMF ferromanganese deposits are genetically linked to karstification of carbonates, the origin of fluid(s) in many paleo-karst systems can be either meteoric, hydrothermal or a combination of the two and moreover, hydrothermal processes may be inextricably linked with karst formation or may have utilized a pre-existing karstic groundwater conduit system (Garvin; 1995, Bottrell et al; 2001, Bella et al; 2016). In that sense, formation of secondary carbonates for example, may have followed a hydrothermal

phase in the PMF deposits and subsequent dissolution during later metasomatic events may have been responsible for ore-upgrade, comparatively to processes recorded in the KMF. Although immediately unrelated to the above scenario, secondary carbonates are at least documented to precipitate during the Namaqua overprint in the ferromanganese ores (this study) and apparently in much greater volume in the underlying Wolhaarkop breccia (later section, 8.4.1), a lithology that should be implemented in any attempt to reconstruct the epigenetic history of these ores.

Contrastingly to the other Fe/Mn districts from the literature, where either igneous intrusions or tectono-metamorphic events trigger mobilization of metasomatizing fluids and production of banded skarns, lack of a distinct heat source characterizes the epigenetic history of the PMF ores. For example, alkali minerals including sugilite in Liguria Province, Italy (Cabella et al; 1990), can be regarded as the alteration effects of contact metamorphism following upon intrusion of granites, whereas in the KMF, sugilite is a hydrothermal precipitate from tectonically-expelled fluids related to a regional and relatively distal orogeny. Notably, igneous intrusions in the immediate surroundings of the hydrothermally enriched part of the KMF (Wessels & N'Chwaning mines), namely locally bostonite dykes, are also altered by the Namaqua hydrothermal event and are not considered to have played any role in fluid generation (Beukes et al; 1995). Evidence for contact metamorphism is also absent in the PMF, although some unusually high temperatures of ore formation have been suggested in the past regarding the central portion of the EMD deposits (T = 470^{o}C: De Villiers; 1983) and moreover, an Al_2SiO_5 polymorph was noted within a grossular-barite-feldspar paragenesis from the wider Kolomela area (chapter 6), which requires further investigation.

However, it has been shown that immediate heat source from a magmatic orebody is not prerequisite for Fe/Mn mineralization. Maybe the most relevant geological setting to that of the Northern Cape, which has not addressed thus far in the prior examples from the literature, is the Fe/Mn mineralisation of the Manganese Group of the eastern Pilbara in Australia. The long-lasted view for the formation of these ores has been challenged by Blake et al (2011), who propose a revised interpretation for ore genesis in this area. According to that, regional-scale hydrothermal alteration resulted in (a) manganese veining and

replacement of dolomite close to a regional unconformity, not always preceded and accompanied by carbonate dissolution (Carawine dolomite), and with barite also present in the margins of the orebodies (b) regional hematite mineralization, (c) several generations of hydrothermal breccias and (d) superimposed hydrothermal silicification. Most importantly, the former study suggested that Precambrian hydrothermal events in non-magmatic and non-orogenic settings can be widespread (apparently 700-900 km) and responsible for extensive mineralization, as well as that ancient structures within or at the edges of cratons can repeatedly act as fluid conduits and promote the formation of a remarkably complicated geological history. Manganese endowment of the Oakover Basin (eastern Pilbara) has been also mentioned to be related to fault-hosted high-grade hydrothermal deposits, occurring beneath and adjacent to sedimentary deposits, while the source of manganese is not attributed to dolomite (Carawine) (Jones; 2017). In yet another much different example, comprising an active tectonic setting and intense rifting processes, regional-scale Mn mineralization develops along an unconformity (Dill et al;2013), stressing further that such structures can act essentially as metal traps.

6.7 Epigenetic mineralization along the margin of the Kaapvaal Craton

6.7.1. A new model for Fe- and Mn-enrichment

Postmasburg and Kalahari manganese fields may be geographically ca. 140 km apart and differ with respect to their geology and mechanisms of initial metal accumulations, but at the same time share a common part of their epigenetic history that involves orogenic-related fluid circulation causing comparable metasomatic effects regionally. Our new results demonstrate that focused research on these regional alteration signals by combined petrographic, geochronological and stable isotopic analysis can be efficiently used to unravel both the common geological evolution and distinct alteration features between the two ore fields. A more coherent picture into the role of hydrothermal activity and metallogenesis in the Northern Cape can be obtained by consideration of the full suite of radiogenic and stable isotopic data hitherto produced, from the Fe-Mn deposits extending along the western margin of the Kaapvaal Craton.

Figure 29 is essentially a schematic block diagram that assembles all available geochronological data, outlines the suggested mode of alkali-mineral formation and regional fluid flow on the basis of ideas presented by previous authors (for e.g., Tsikos and Moore; 2005, Fairey et al; 2019) and provides possible sources for the dominant and critical elements in the circulating hydrothermal fluid(s). This diagram emphasizes that any attempt to accurately depict in the same figure the stratigraphic edifice below the KMF and PMF deposits, as well as the major regional structures, presents certain difficulties that derive from (1) lack of reliable knowledge of the stratigraphy in depth below the deposits due to limited drillcore data and almost complete absence of outcrops (2) existence of duplications of the stratigraphy that have resulted from intense thrusting during compressional tectonism and (3) very large differences in the postulated thicknesses of the Transvaal strata below the PMF and KMF that can be up to 2 km, owing to removal of the stratigraphy in the former ore field during an extensive period of erosion. Specifically, uplift, erosion and gentle folding of the Transvaal Supergroup strata is suggested to have occurred during the Kalahari orogeny (ca. 2.35-2.25 Ga) (Altermann and Hälbich, 1991), which was responsible for the formation of the anticline structure known as Maremane dome and subsequently the development of a regional unconformity (Figure 29), in the vicinity of which iron and manganese mineralization is very prolific. While it is beyond the scope of this study to address stratigraphic questions such as discrepancies and complexities regarding the highly contrasting thicknesses of units below the ores or regional development of thrusts, it is mentioned that the postulated extensive weathering of the Transvaal rocks before deposition of the Olifantshoek Supergroup, is expected to have produced vast amounts of detritus, which require a designated depositional site.

In any case, where focus should be placed is that even though the Northern Cape deposits are hosted by supracrustal successions in a cratonic environment that has only been affected by thin-skinned deformation tectonics and very mild metamorphism (ca. 2 kbar, 100-170^{o}C: Beukes et al; 1990), the available set of radiometric ages from the deposits, manifests that extensive fluid transport and heat due to orogenic processes has left a substantial record of its passage in the area. Specifically, hydrothermal fluid migration synchronous with the Namaqua orogeny has locally upgraded the sedimentary Mn ore beds of the Hotazel

Formation in the KMF (between 1139 ± Ma and 1037 ± 8 Ma) and more cryptically has been imprinted on a range of texturally diverse Fe- and Mn ores in the PMF (ages between 1188 ± Ma and 920 ± 9 Ma), including the occurrences from the current study (Heuningkranz-Langverwacht). The latter may show variances with respect to their exact genetic mechanisms but according to current models are collectively related to extensive regional weathering and associated surficial reworking (laterization, residual sedimentation, karst formation, etc.) of the Transvaal strata.

Subsequent regional fluid flow during a Neoproterozoic event that overlaps with Pan-African orogeny is also documented in the deposits (Wessels, Khumani, Heuningkranz: from 667 ± 14 Ma to 614 ± 50 Ma) and further indicates that hydrothermal events related to far-field tectonics are entrenched in the alteration history of these ores, and more specifically in the ample record of alkali phases. Older hydrothermal activity, as distal manifestation of tectonic events at the active plate boundaries to the west of the craton cannot entirely be ruled out and in fact repeated age signals from the ores themselves (1.6-1.5 Ga) may reflect exactly such thermal events. Despite expected differences with respect to brine characteristics and movement through the basin during different times, certain distinguishing features are suggested to have been common between orogenic-related alteration solutions and in particular the ones associated with the pervasive Namaqua orogeny.

Fluid temperatures are considered to have been low and largely fluctuating, subject to fluid evolution, fluid-rock interaction and mixing but generally, they would have been within a range between 130 and 250^{o}C. Heat would have been acquired from their burial at significant depth and the required engine to drive the observed large-scale fluid circulation would have been no other than tectonic compressional activity, in some cases perhaps remarkably distant from the study area. Oxygen and hydrogen brine isotopic compositions are also expected to have varied, especially after exchange with the host lithologies and contemporaneous meteoric water. However, the presumed high fluid/rock ratios allow one to peer into solutions precipitating alkali phases and suggest $\delta^{18}O$ ranges between +3.5 and + 7.5 ‰ and δD between -65 and -28 ‰. In light of all available data, it is suggested that fluids may be largely visualized as deep buried and heated brines from the Campbellrand sequence

and underlying lithologies, but possibly also sourced from the metapelites and granitoids of the Namaqua metamorphic belt further to the west, rising through the permeable carbonate sequence at shallow levels, while acquiring a significant part of their salinity by leaching evaporites and former evaporitic breccias that had been well-developed in the basin (chapter 2).

Extensive evaporites, interbedded with carbonates but possibly also with banded iron-formation are proposed to have acted as sources of S, Li and salinity but also as pathways of fluid flow due to their high solubility. Unidentified ancient non-marine evaporites may have also been major contributors to the lithium budget of the fluid. On the micro-scale, fluids followed closely spaced cracks, fissures and intergranular porosity but also laterally extending pre-existing features as implied by the observed metasomatic textures. Since secondary permeability has a large effect on fluid migration, the presence of regional lithological boundaries in the form of thrust decollement zones and low angle dipping faults that have been traced for distances of about 180 km in the Northern Cape (e.g., Altermann and Hälbich, 1990) or the regional Olifantshoek-Transvaal unconformity may have acted as a mechanism that repeatedly focused and forced laterally fluid migration. In particular, the latter can be seen as a sort of reactive fluid migration, in the sense that lithologies straddling these regional structures such as carbonates, BIF, shales and Fe- and Mn-protores have been reworked by processes replacing them, leaching additional material including silica, mobilizing iron and manganese and precipitating ore and gangue mineral phases, i.e., essentially causing mineralization along the migration paths of fluids. Ascending of pressurized fluids from deeper parts of the crust into the basin may have been induced by fluid overpressure (e.g., Kimmig et al; 2021), in turn resulting from increased fluid volume (essentially fluid heating) or decreased pore volume (compaction), processes that could have both occurred during the Namaqua orogeny.

As regards elemental sources, banded iron-formation for example and particularly the riebeckite-rich units, may have provided much of the alkali content and CO_2 for secondary carbonate formation besides critical ore metals. Hydrothermal fluids would have almost certainly acquired Ca^{2+}, Mg^{2+}, Mn and Fe during tectonic fluid expulsion, if not through prior

or syn-decarbonation reactions in the underlying dolomites and these elements would have been carried upward. Siliciclastic rocks supplied most of the Sr and Ba that is now isotopically preserved in regional barite occurrences. The nature of the fluids induced highly prolific conditions for elemental redistribution and mineralization mainly though chloride complexation and a series of long-lived processes discussed to some extent above, which overall culminated in ore enrichment. Vertical fluid circulation has been locally facilitated by systems of normal faults such as that seen in the KMF, that may have been reactivated and acted as conduits for downward infiltration of meteoric water, the latter also seen isotopically imprinted on gangue mineralogy. The above model may be exploratory, unrefined and lacking more focused research on specific localities and mechanisms of ore genesis but nevertheless emphasizes the pronounced hydrothermal modification of the Northern Cape lithologies which is more widespread than originally recognized, in contrast to the current consensus that focuses entirely on supergene processes.

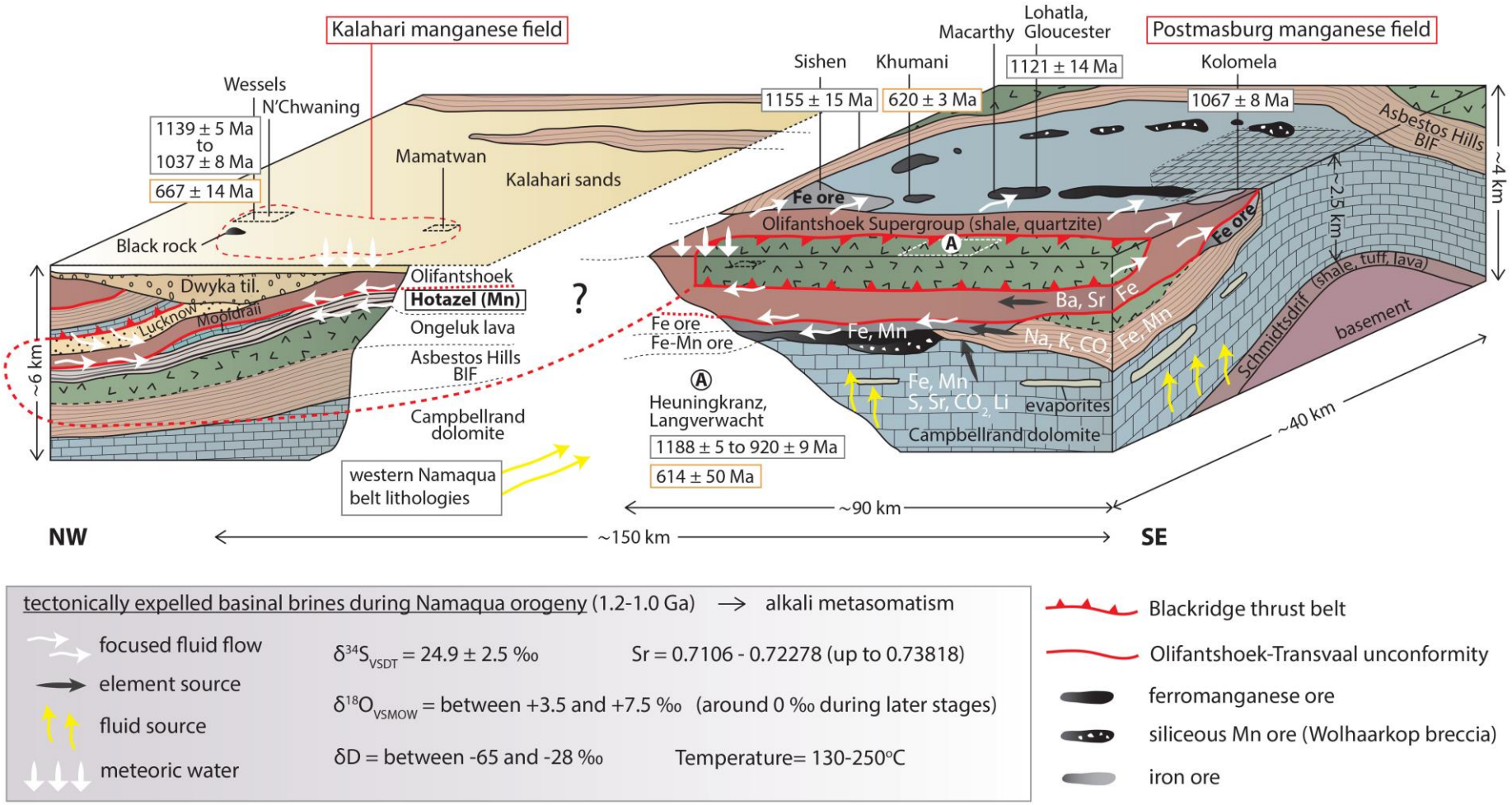

Figure 29. Conceptual representation of regional hydrothermal alteration along the western margin of the Kaapvaal craton, as a mode of Fe- and Mn-ore genesis or upgrade (see text for details). Basinal brines are tectonically expelled during the main stage (1.2-1.0 Ga) of the Namaqua orogeny, but possible also in the course of earlier (1.6-1.5 Ga) and later (ca. 600 Ma) events and generate highly prolific conditions for mineralization. Wavy white arrows represent fluid flow focused mostly along the regional structural and lithological boundaries. Note the stratigraphic thickness discrepancies below the ore units and uncertainties related to development of regional structures. References: S and Sr isotopes: chapter 2, O-H isotopes: chapters 3, 5 and 6. Ages: Heuningkranz-Langverwacht (A): this study, Fairey et al; 2019 & chapter 2, Wessels: Gnos et al; 2003, chapters 3 & 4, Khumani: Moore et al; 2011, Lohatla: chapter 6, Kolomela: chapter 2, Sishen: Rasmussen B.: pers. comm.

6.7.2. MVT-style mineralization in the Northern Cape

Comparable scenarios for sources and mechanisms of fluid migration have been invoked by researchers to explain the formation of the epigenetic low-temperature carbonate-hosted Mississippi Valley-type (MVT) Pb-Zn ore deposits (Leach et al; 2010 and references therein). Most importantly, as noted earlier, such mechanisms are mentioned from the regional-scale episodic hydrothermal alteration of the Precambrian Manganese Group in the Pilbara Craton (Australia) (Blake et al; 2011), deposits that are preserved in a lithostratigraphic setting showing many similarities to the study area. Akin to MVT districts, ore-upgrade in the KMF and widespread mineralization in the PMF have no direct genetic association with igneous activity, but the geotectonic setting, i.e., a large-scale tectonic event, facilitates the excretion of deep buried and heated fluids in the upper stratigraphic levels of the basin, where mixing with contemporaneous meteoric water may perhaps also occur. Despite differences in fluid chemistry, redox state and isotopic composition between different MVT localities and existing controversies on ore genesis (e.g., Gustafson and Williams; 1981, Wilkinson et al; 2009a, Leach et al; 2010), it is widely accepted that fluids derive mainly from evaporated seawater or dissolution of evaporites in the basin and display significant similarities with oilfield brines (Wilkinson; 2014), features that are also seen in the Northern Cape.

On the other hand, specific rock formations such as in the study area such as banded iron-formation and the siliciclastic rocks of the Olifantshoek Supergroup are expected to exert control over fluid chemistry and evolution as discussed above and therefore generate certain conditions unique to this setting. The envisaged replacement of shales by Fe- and Mn- bearing solutions, scavenging of elements such as Ba from siliciclastics or alkali elements and Fe from BIF and facilitated dissolution of silica in pre-existing lithologies due to increased fluid salinity are some features paired with the geology of the study area. In terms of traps and processes reducing oxidized metalliferous brines and ore genesis mechanisms in MVT ores, the two mineralization systems diverge significantly since alkali metasomatic parageneses in the study area imply largely alkaline oxidizing conditions.

Processes of thermal interaction within the cover rocks of the Kaapvaal Craton, similar to the ones described above are manifested by a large number of economic MVT Pb-Zn-F deposits (e.g., Pering, Bush Park: Griqualand West) that occur in the Malmani (Transvaal basin) and Campbellrand (Griqualand West basin) carbonate sequences as well as within mafic rocks of the Ventersdorp Supergroup (Duane et al; 1991, Martini et al; 1995, Altermann; 1997, Huizenga; 2005). However, age of mineralization is distinctly different from the Namaqua hydrothermal event, with ores of the Transvaal basin believed to have formed and metamorphically overprinted between 2.4 and 2.0 Ga and deposits in the Northern Cape somewhat later (2.1-1.9 Ga) during the controversial Kheis orogeny. It has been considered that early fluids were expelled from the craton margin by basin collapse already toward the end of deposition of the Ghaap Group (carbonates, BIF, siliciclastic) and major fluid expulsion accompanied the initiation of thrusting along the eastern Kheis margin (Duane et al; 2004).

Despite the age discrepancy between MVT mineralization and regional hydrothermal metasomatism in Fe and Mn deposits, the diversity of Pb isotopic compositions from the South African MVT deposits, suggesting model ages that range from 1.5 to 2.9 Ga (Duane et al; 1991), imply that metalliferous brines were sourced from different lithologies. As stated by Altermann (1997), model ages on galena may correspond to tectonic events between ca. 2.5 and 2.0 Ga as well as to the 1.7 and 1.2 Ga K/Ar ages obtained by neogenic micas (Altermann et al; 1992). Specifically, the previous authors emphasize remobilization of metal-carrying fluids connected to the Namaqua event and link fault-bounded Pb-Zn mineralization at the Bushy Park deposit (ca. 60 km SSE of the study area) to this orogeny, whereas on the other hand, propose that much earlier mineralization at Pering may be linked to active dewatering and transport of metals during BIF deposition (ca 2.4 Ga). Other major structures somewhat 80 km to the south of the study area such as the Griqualand Fault zone (GFZ) have been regarded as major targets for Pb-Zn exploration, with the deposits expected to occur northeast of GFZ (Altermann (1997).

Where attention should be drawn, with respect also to the now well-documented Namaqua (and/or early Namaqua: 1.5-1.6 Ga) and Neoproterozoic hydrothermal overprint events in the Northern Cape is that the passive western margin of the Kaapvaal Craton and

its relatively undeformed supracrustal successions have been apparently affected by multiple and craton-wide epigenetic fluid events during different times and this may have had important implications for Fe- and Mn-ore genesis. In that sense, Northern Cape should not be regarded as a geologically inert province where only weathering processes govern mineralizing systems but instead as a district evolving with the synergy between both tectonometamorphic-hydrothermal and supergene processes. It is also important to stress that its distance from active tectonic zones and lack of identified large igneous bodies do not pose a barrier for brine circulation. In fact, regional flushing of fluids, usually in response to continental collision, has been shown to be responsible for regional disturbance of isotopic systems and hydrothermal activity hundreds of kilometres from an orogen (Oliver; 1986, Kharaka et al; 1985, Duane et al; 1991, Garven; 1995, Wilson et al; 1999). As an example, Cu-Pb-Zn mineralization in the Congo Craton has been related to fluids penetrating 1.3 km of sediments and along at least 60 km of strike length (Duane and Saggerson; 1995), although in several other cases transportation of hundreds of kilometres is implied (Leach et al; 2010).

To summarize, attributing collectively the PMF ores to an existing ore deposit classification scheme may be futile because reconstruction of their evolution in time and space presents significant challenges due to a series of overprinting alteration events that may have synergistically enriched the precursor lithologies. Central to these may have been hydrothermal processes and MVT deposits can provide a useful analogue for understanding the basic concepts of fluid genesis related to orogenic fronts and spreading at great distances within sedimentary basins. Epigenetic sediment-hosted copper deposits associated with carbonates, shales and conglomerates, evaporite deposits (sabkhas), passive margins or intracontinental rifts and oxidizing metalliferous and sulfur-bearing brines (e.g., Cox et al; 2003) may be another relevant analogue for the metallogenic environment of the Northern Cape to be considered in future research.

7. Concluding remarks

Various and distinct Fe-Mn ore lithologies flanking the regional Transvaal-Olifantshoek unconformity along the western margin of the Kaapvaal Craton record the effects of an intense large-scale alkali ‘’flooding’’, imprinted in gangue mineralogy. Extensive hydrothermal

alteration associated with the Namaqua-Natal orogeny is not restricted to the intensively faulted and altered northern part of the KMF but is expressed throughout the WMD ores of the PMF. Similar mineralogical, stable isotopic and geochronological results from both ore districts of the Northern Cape build confidence in their shared spatial and temporal epigenetic alteration history, which involved comparable fluid sources and mechanisms of transportation.

The following key findings stem from this study:

(1) PMF and particularly its recently discovered western arm (WMD ores) displays far higher mineralogical diversity than previously recognized, with forty-two species reported from a single locality, comprising hyalophane-celsian, grossular, Mn-carbonates, diaspore, apophyllite, hollandite, coronadite, As-tokyoite, As-bearing apatite and hematite, unidentified Ba- and Mn-rich silicates and traces of rare species such as macedonite, pyrobelonite and tamaite.

(2) Most Na-, K-, Ba- and CO_3-bearing hydrothermal mineral associations are unequivocally paired with epigenetic processes during the Namaqua orogeny. Moreover, alteration processes have repeatedly reworked the host lithologies, as evidenced by complex zoned parageneses, cross-cutting veins, replacement textures and diverse breccias.

(3) The origin of layered mica/phyllosilicates (muscovite, paragonite, Ba-muscovite, phlogopite) associated mostly with hematite-rich ore portions requires further investigation, to elucidate the detrital derivation, involved diagenetic/metamorphic processes and/or textural control from previous shale-like precursors (i.e., Olifantshoek shale units).

(4) In situ $^{40}Ar/^{39}Ar$ geochronology can provide useful information on the timing of geological events in ancient and complex Fe/Mn mineralization systems, where suitable dating material is very limited, fine-grained and intricately mixed for reasonable mineral separation.

(5) $^{40}Ar/^{39}Ar$ dates for hydrothermal Ba-feldspar, phlogopite and ore-matrix silicates range from ca. 1188 to 920 Ma, recording both early and late-stage events of the conspicuous Namaqua overprint, that may potentially conceal the earlier tectonic and mineralization history of these lithologies.

(6) A handful of micas and ore-matrix silicates yield equivocal Pre-Namaqua $^{40}Ar/^{39}Ar$ age signals (1575 ± 12 Ma, age peaks at ca. 1668 and 1491 Ma) that better conform to early Namaqua-induced igneous activity in the outer terranes (ca. 1600 Ma), rather than to the poorly constrained and controversial 1.8 Ga Kheis orogeny, which is thrown further into doubt and requires reappraisal.

(7) By virtue of the now-well documented Namaqua radioisotopic ages on the edge of the Kaapvaal Craton, Kheis Province, i.e., eastern Namaqua front, should be better regarded as another tectonic zone within the extensive Namaqua Province.

(8) O-H isotopes values from gangue minerals suggest fluid buffering and calculated $\delta^{18}O$ and δD of the mineral-forming fluids are comparable to that from Mississippi Valley-type (MVT) Pb-Zn deposits. Moreover, certain mineralogical pairs (e.g., aegirine-natrolite) suggest realistic temperatures (ca. 200^{o}C) for the involved basinal brines.

(9) The PMF deposits have been developed in a geodynamic environment that may have involved a series of Mn- and Fe-concentration processes, from sedimentary to metamorphic/hydrothermal and locally supergene-related.

(10) Our data strongly suggest a revision of the ore genetic models for both Fe and Mn deposits in the PMF, which will place more focus on the now well-documented regional hydrothermal events and geotectonic history, as well as reexamine the role of regional structures as potential fluid conduits related to regional-scale mineralization.

Finally, it is stressed that much work remains to be done concerning the elucidation of the very complex epigenetic alteration history of the PMF deposits and in situ $^{40}Ar/^{39}Ar$ dating in

tandem with detailed petrographic examination and other isotopic systems may prove to be critical in future refinements of the currently suggested models.

Chapter 6

The ephesite-rich ferromanganese ores of Postmasburg Manganese Field. Insights into their origin and metasomatic processes through petrography, O-H isotopes, whole-rock Li geochemistry and geochronology documenting the easternmost arm of the Namaqua orogeny on the Kaapvaal Craton of South Africa.

Abstract

Postmasburg Manganese field (PMF) is from a mineralogical standpoint the poorer counterpart of the neighboring Kalahari Manganese field (KMF). In contrast to the timing (ca. 1.2-1.0 Ga) and broadly hydrothermal origin of the mineralogical suite of the latter, processes of gangue formation in the PMF are attributed to burial diagenesis/metamorphism (1.9-1.8 Ga) following accumulation of Fe- and Mn-rich sediments in ancient karsts/lakes during an extensive period of lateritic weathering (2.2-2.0 Ga). Revisiting key localities of ephesite-bearing (Na-, Al-, Li-rich) ferromanganese ores we present $^{40}Ar/^{39}Ar$ data supporting ephesite formation by metasomatic processes during the Namaqua orogeny (1.2-1.0 Ga), probably from an aluminosilicate precursor in the protore, i.e., ca. 700 Ma later than previously suggested. Petrographic investigation corroborates a replacive origin of ephesite and further records rare and newly reported phases such as gamagarite, barian goyazite and pyrophanite. Whole-rock Li data from Fe-Mn lithologies in the wider area indicate a predominant mica (ephesite, muscovite-paragonite) control on elevated Li concentrations (ca. 0.1-0.3, up to 1 wt. %) which in conjunction with their high abundance in certain localities (ca. 10 %, up to 60%) and specifically in the ephesite-lithiophorite-rich ores suggest an evaluation of the economic lithium potential. Sources of high required abundances of alkalis (Na, Li, Ba) are attributed to external sources and in turn, their transportation to mineralization sites ascribed to hydrothermal brines with $\delta^{18}O$ values between + 6.7 and + 7.4 ‰ and δD between -29.0 and -62.6 ‰, as opposed to the current view of alkalis being expelled from the ores themselves. These results add credence to previous hypothesis of orogenically-driven large-

scale fluid migration locally metasomatizing and reconfiguring Fe/Mn-rich and country rocks and reveal the association between the easternmost recorded arm of the Namaqua orogeny and the type locality PMF deposits. Based on inconsistencies with lateritic/bauxite models, we suggest that the unique Si/A ratio (<1) of the ores, not seen in equivalent ores in the PMF (wider Kolomela region), may not be an entirely pristine geochemical signal but instead also related to aluminum mobilization and formation of associated aluminous shales. Furthermore, Mn oxides such as hollandite and lithiophorite, similarly to diaspore, can be also products of hydrothermal processes prior to the recent supergene reworking of the ores. Closer scrutiny regarding ore genesis is needed and further research with advanced isotopic techniques such as lithium isotopes is justified.

1. Introduction

The ferromanganese ores of the Postmasburg Manganese field (PMF) at Bishop, Lohatla, Gloucester mines and their environs are marked by the presence of a distinctive and rare assemblage of gangue phases which includes diaspore, ephesite, lithiophorite, amesite, Ba-muscovite and gamagarite, minerals that denote a highly aluminum- and alkali- (Na, Li, Ba) rich setting. Current genetic models invoke supergene and karst-related accumulation processes to explain these geochemical signals and relate ore mineralogical composition, including formation of ephesite, to syn-metamorphic fluid expulsion following burial and compaction of sediments sometime between 1.9 and 1.8 Ga (Gutzmer and Beukes; 1996a, 1997b).

However, the available model has been based on petrographic, geochemical data and the presumed geological framework of the depositional environment. At the same time, geochronological or other isotopic data are absent from the area. The origin of the high aluminum environment is also not directly addressed and descriptions of the gangue paragenetic assemblages, chemistry and their textures are limited in comparison with that of ore-minerals. In addition, alkali signatures (Na, Li) of ubiquitous phases in these ores, such as ephesite, have also been documented from genetically related hydrothermal gangues in the wider region, encompassing the Kalahari Manganese field (KMF) and a series of Fe-Mn lithologies in the PMF (chapters 2, 3 & 5). The potential of ephesite-rich ores being associated

with the above metasomatic system has not been yet explored. Available descriptions of fracture- and vein-filling ephesite or thick discontinuous shale laminae rich in ephesite and diaspore (Gutzmer and Beukes; 1996a) are indications that this hypothesis is further worth exploring.

In this study, we place emphasis on the sources and formation mechanisms of gangue mineralogy attempting to further advance our understanding, not only of these unique ore occurrences but also of processes leading to alkali- and Li-enrichment in generally low-temperature regimes. Ephesite is an unusual Na- and Li-bearing (ca. 3.7 wt. % LiO_2 in the PMF) brittle mica, reported from very few localities worldwide. Micas are great tools in reconstructions of the origin and characteristics of hydrothermal fluids (e.g., Fulignati; 2020); therefore, a similar approach involving detailed petrographic observations, stable isotopic analysis (O-H) of ephesite and associated gangue and ore phases and ephesite $^{40}Ar/^{39}Ar$ dating is expected to unravel certain aspects of the origin and evolution of these ores. Since mineral lithium determination is challenging, we attempt a reconnaissance whole-rock Li-B study of few selected targets in the wider Northern Cape to gain insight into mineralogical control and concentrations. We further discuss the origin of the ores and the sources of the unusual Al-Li enrichments in the context of karst bauxites, Li-brines and processes of mobilization of these elements. Our comprehensive analysis shows major discrepancies with the present interpretation of the geological evolution of the PMF and proposes a reevaluation of the ore genetic models with focus on the tectonically-driven regional hydrothermal activity in the Northern Cape.

2. Geological background

The reader is referred to chapter 5 for a more thorough presentation of the local geology and current ore genetic models. Some additional notes regarding the occurrence of ferromanganese ores in the Eastern Maremane dome (EMD) (mentioned in the literature as ferruginous ores of the Western belt) are provided here. Ferromanganese ores occur as irregular bodies in the central part of the Gamagara ridge (noted in purple colour) (Figure 1A, 1B), where the base of the Olifantshoek Supergroup (Gamagara Formation) unconformably overlies Mn-rich dolomites of the Reivilo Formation (Campbellrand Supergroup) along a

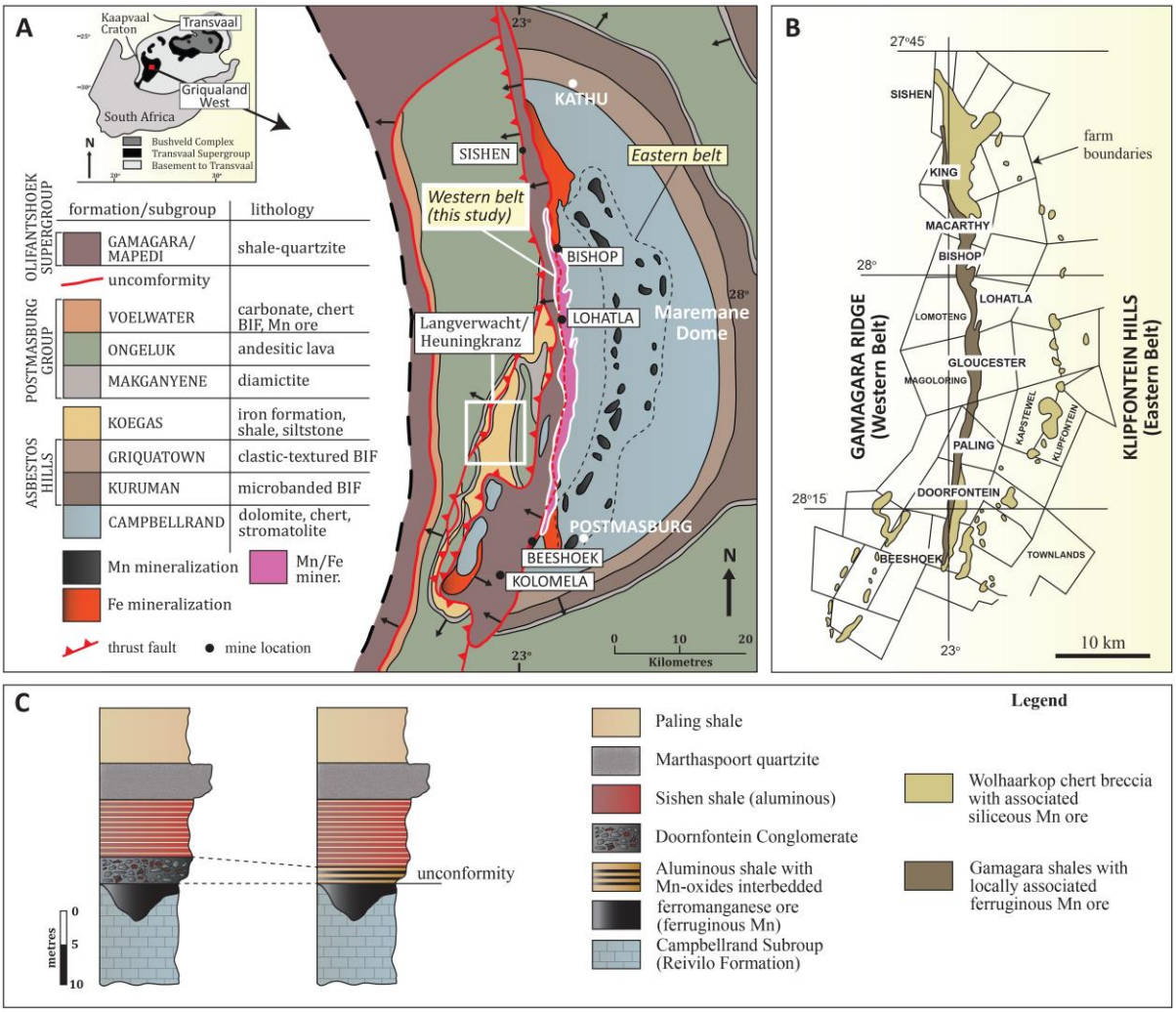

Figure 1. (A) Regional geological map of the Maremane dome in the Northern Cape and associated lithostratigraphy. The ephesite-bearing ferromanganese ores of this study occur in the central part of the dome along a regional unconformity and right below clastic sediments (Gamagara/Mapedi). Major manganese deposits mined in the past are found in the central and northern part of the study area (Lohatla, Bishop, Glosam). Modified after Moore et al; 2011. (B) Location of the ferruginous and siliceous deposits along the Gamagara ridge and the Klipfontein Hills respectively. Names of major farms are included. Modified after Gutzmer and Beukes (1987). (C) Schematic sections showing the typical occurrence of the ferromanganese orebodies, confined in karst depressions and overlain by the Doornfontein conglomerate (left) or grading up into aluminous shale of the Sishen Shale Member (right).

regional and presumably erosional unconformity, further associated with hematite iron mineralization in the wider area (Van Schalkwyk and Beukes; 1986, Gutzmer and Beukes; 1996a). In other words, their spatial distribution is controlled by the underlying manganese-rich dolomite beds, which are responsible for the occurrence of the large Glosam, Lohatla and Bishop deposits (Figure 1A), all mined in the past. Furthermore, ferromanganese ores are intimately associated with highly aluminous shales of the Gamagara Formation and hematite

pebble gritstones/conglomerates (known as Doornfontein conglomerate), both resting directly on or being interbedded with the ores (Figure 1C) (Gutzmer; 1996, Gutzmer and Beukes; 1996a). The transition of the deposits into the overlying siliciclastic sediments has been described as conformable (Gutzmer; 1996). The base of the orebodies is associated with intensively karstified dolomite and they are spatially confined within closed spaced pinnacles and deep solution cavities that are locally exposed due to mining operations (see also Figure 2D). Mineralogically, the associated aluminous shales are composed of pyrophyllite, diaspore, kaolinite, hematite, as well as minor illite, anatase and rutile, products of low-grade metamorphism and/or hydrothermal enrichment (Schalkwyk ;2005, Cousins; 2016).

Two varieties of ferromanganese ore have been traditionally distinguished on the basis of macroscopic appearance and mineralogical features: (a) fine crystalline bedded ores, interbedded with shale and conglomerates, characterized by soft sediment deformation structures and consisting of intimately associated braunite, hematite, partridgeite, ephesite and diaspore and (b) Coarse crystalline ores occurring as irregular pods, displaying textures such as veining, vugs and brecciation and comprising abundant bixbyite, diaspore and ephesite (Gutzmer and Beukes; 1996a, 1997b). The deposits are believed to have formed as residual palaeokarsts sediments during a period of intense weathering that preceded the deposition of the overlying siliciclastic sediments and subsequently, have been subjected to diagenesis and low-grade metamorphism (see also chapter 1 & chapter 5: section 1 for more details). The latter events formed the now observed mineralogy, including ephesite, before renewed karstification in recent times formed extensive canga deposits comprising supergene alteration phases such as romanechite, cryptomelane and lithiophorite Gutzmer and Beukes; 1996a). Other minor gangue phases such as barite, albite, acmite, apatite and Ba-muscovite have been only reported from the small and irregularly distributed siliceous manganese lenses, pods and sheet-like bodies (Figure 1A, 1B), associated with the Wolhaarkop breccia (De Villiers; 1960).

3. Sampling, materials and methods

Accessible areas with good exposures of manganese ore are particularly limited in the Postmasburg region. A visited outcrop of representative dense ferromanganese orebody was sampled at McCarthy locality (Figure 1) and additional material from a previous fieldtrip at the environs of Bishop and Kolomela mine, was also supplied by the collection of Rhodes University, South Africa. On the outcrop scale, ore appears as massive textured, is intensely fractured and shows resistance to fracturing by hammer (Figure 2A). It has a submetallic appearance, apparently due to its high hematite content, which is more striking in freshly broken surfaces showing metallic luster (Figure 2B). Interbeds with subtle black tint reflect higher manganese content. Furthermore, a crude bedding is hinted by reddish brown clayey layers, which most likely represent ephesite-rich beds (Figure 2C); however, it is important to stress that sample processing revealed that these ores are consistently finely laminated on polished surfaces, showcasing complex layered micro-textures. Despite of the widespread evident weathering, examples of fresher material do exist and sampling was focused on the latter.

The orebodies appear several metres thick and even if absolute estimates were not possible on the basis of macroscopic observations, it has been previously reported that ore thickness is highly variable and in the central part of the Gamagara ridge, it reaches a maximum of 17 metres (Gutzmer; 1996). The same applies to its shape which has been described in the past as highly irregular. Dolomite pinnacles and solution cavities are exposed in the area as a result of earlier mining operations (e.g., Glosam mine) and likewise, surficial dolomitic depressions were seen on the landscape of the McCarthy environs, hosting mostly accumulations of black angular fragments of ferromanganese ore and/or manganese bedrock (Figure 2D). These karstic structures possibly constitute the chief preservation mechanism of these ores from erosion since the Palaeoproterozoic Era. Certain outcrops display intense reddish colouration and cm-sized pisolites (Figure 2E) and are probably related to the Doornfontein Member of the Olifantshoek Supergroup, referred to in the literature as a hematite pebble conglomerate overlying the orebodies. Inversions and duplications of the stratigraphy are common locally and can lead to repetition of geological features such as the

Figure 2. (A & B) Ferromanganese ore in outcrop scale, fractured and rust-coloured due to high iron content, the latter evident in freshly broken surfaces showing metallic lustre. (C) Interbed of reddish-brown clayey material, almost certainly comprising abundant ephesite. (D) Surficial karstic depression filled with relict fragments of ferromanganese ore, most likely after local mining. (E) Iron-rich rock with spherical pisolites, possibly representing the Doornfontein hematite conglomerate. (F) Recent small-scale mining operations on the Postmasburg landscape.

erosional unconformity between the Transvaal and Olifantshoek Supergroup and apparently the orebodies themselves (local geologists, pers. comm.) Recently rejuvenated surficial mining of the easily accessible ore material can be seen on the Postmasburg landscape in the vicinity of the study area (Figure 2F).

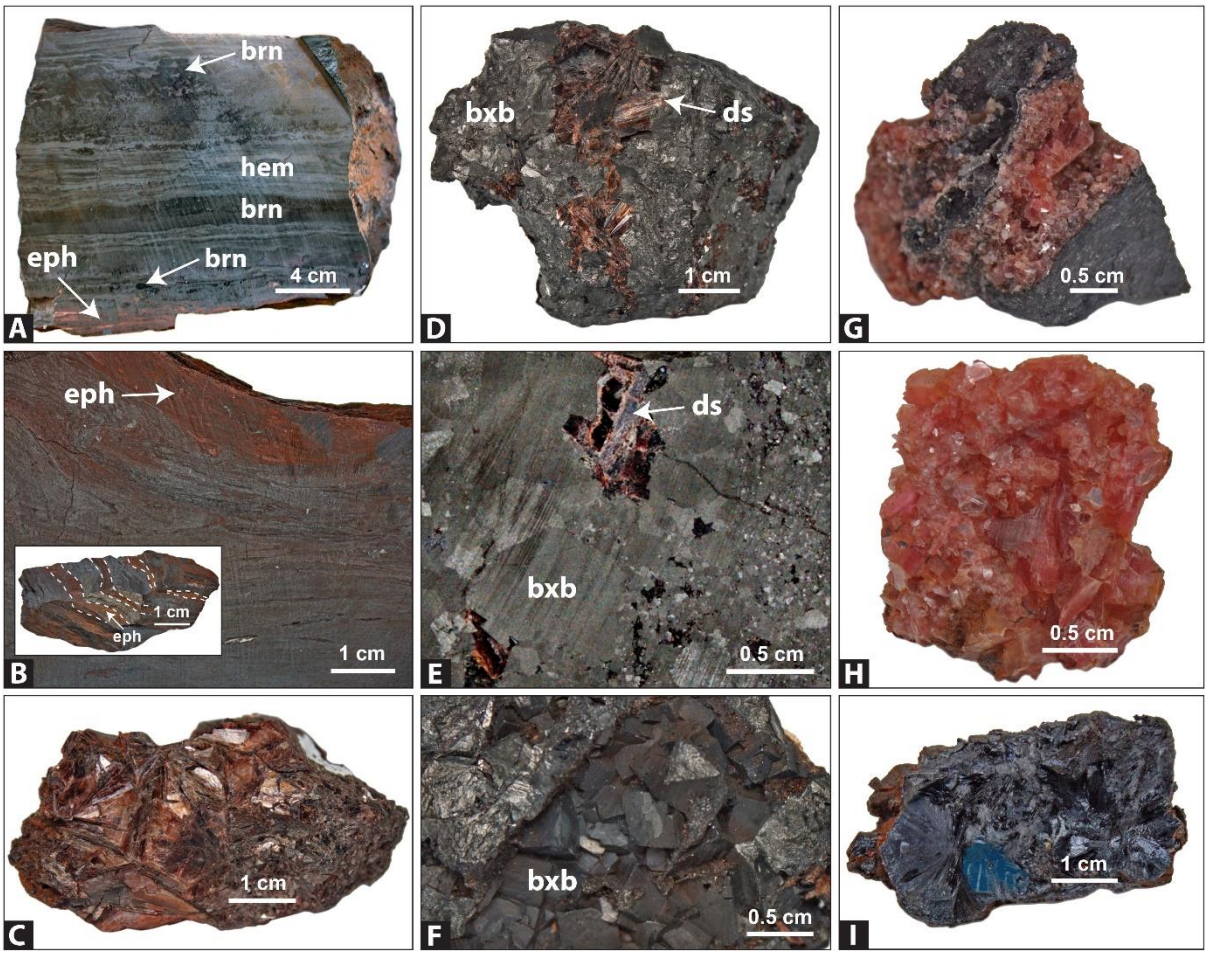

Figure 3. (A) Polished surface of ferromanganese ore exhibiting alternating hematite-, braunite- and ephesite-rich laminae as well as microconcretions (see text). (B) Ore from McCarthy displaying ephesite-rich interlayers. (C) Densely intergrown diaspore laths, with individual crystals exceeding one centimetre in length. (D to F) Coarse-grained manganese ore composed of well-developed bixbyite crystals and interstitially forming diaspore. Note the highly variable grain size of the granular ore texture. (G & H) Dark pink-red prismatic and platy ephesite clusters forming pockets inside manganese host rock. (I) Large crude crystals of bluish-black lithiophorite. brn = braunite, bxb = bixbyite, ds = diaspore, eph = ephesite, hem = hematite.

Petrographic investigations were focused on 6 representative samples from Bishop mine taken from the collections of Rhodes University, South Africa and another 4 samples collected on the field from the McCarthy farm (Figure 3A, 3B). Additionally, 6 mineralogical specimens kindly furnished by mineral collectors or acquired by traders were included in our database specifically for isotopic and geochronological analysis. The latter include: i) a solid mass of reddish brown highly lustrous laths of diaspore (Figure 3C) ii) coarse-grained manganese ore comprising dense clusters of sharp cubic bixbyite intergrown with coarse diaspore laths (Figure 3D-F) iii) an aggregate of thick dark pink-red prismatic crystals from Glosam mine (EPH1) (Figure 3G) and a mass of smaller hexagonal micaceous plates forming a pocket inside a manganese-rich host rock from Lohatla mine (EPH2) (Figure 3H) and iv)

coarsely crystalline black lithiophorite forming radial aggregates with a glistening appearance (Figure 3I).

The textures and mineralogy of samples were studied through examination of polished thin sections under reflected light and scanning electron microscopy at the universities of Glasgow and Durham using a Quanta 200F Environmental SEM with EDAX microanalysis and a Hitachi SU-70 FEG SEM respectively. Regarding whole-rock analyses, samples were crushed in a tungsten carbide swing mill at SUERC and analysed for major and trace elements (including lithium and boron) at ALS ltd. In particular, major elements were determined by a combination of whole-rock ICP-AES and ICP-MS analysis and trace elements (plus REEs) were detected by Li borate fusion prior to acid dissolution and ICP-MS analysis (package codes: ME-ICP06, ME-MS81 and ME-MS81D). Boron and lithium determinations were conducted using Na_2O_2 fusion and ICP-AES, which is the highest precision method for Li and B resource determination in known deposits and offers detection ranges of 0.001 to 10% and 0.02 to 50% for Li and B respectively (package code: ME-ICP82b).

Samples used for oxygen and hydrogen isotopic determinations are fairly monomineralic, with only minor impurities and material was easily extracted using a micro-drill. Ephesite samples were prepared for $^{40}Ar/^{39}Ar$ dating by crushing large and translucent micaceous crystals to grain sizes of couple of microns. These ephesite aliquots are expected to be monomineralic with only minor inclusions and purities exceeding 95 % as confirmed by optical and scanning-electron microscopy. Oxygen isotope analyses were conducted via laser fluorination at SUERC, using ClF3 as the fluorinating agent and applying the basic methodology of Sharp (1990). All minerals were pre-fluorinated under vacuum for one minute before infrared laser heating, apart from bixbyite which was left overnight. OH-bearing and hydrous minerals were degassed overnight (250°C) for oxygen analyses. Converted CO_2 was analysed on a VG Isotech SIRA series II dual inlet mass spectrometer. Hydrogen from degassed samples (150°C) was extracted by in vacuo bulk heating using the method of Donnelly et al (2001) and measured on a VG Optima mass spectrometer at SUERC. All isotopic data are reported in standard delta notation, relative to Vienna Standard Mean Ocean Water (V-

SMOW). Repeat analyses of international and lab standards gave a reproducibility of ± 0.3 ‰. and ± 2‰ for oxygen and hydrogen respectively.

$^{40}Ar/^{39}Ar$ data were obtained using an ARGUS V noble gas multi-collector mass spectrometer at SUERC. Gas extraction was conducted by laser step-heating using a 55 W CO_2 laser and heating steps were controlled by incrementally increasing laser power. Different numbers and sizes of steps of the laser heating schedule were used with an aim to establish the best preferences for dating this mica (Appendix I). Isotope extraction, purification, extraction line operation, and mass spectrometry were fully automated.

4. Results

4.1 Mineralogical and textural investigation

4.1.1 Ferromanganese ore

Ferromanganese ore displays well-developed bedding which is composed of alternating mm-sized laminae, each predominantly consisting in turn either of braunite, hematite or ephesite. These laminae exhibit an array of contorted and undulating textures, described by previous researchers as an indication of soft-sediment deformation processes (Gutzmer and Beukes; 1996a), but at the same time laminae are parted by irregular and discontinuous hematite- and ephesite-rich layers which resemble metasomatic alteration textures (Figure 4A1, 4A2). Ore and gangue mineralogy displays a homogeneous very fine grain size (<25 µm), only sporadically becoming coarser (50-100 µm) in regard to braunite and ephesite euhedral crystals. Ephesite is a rare sodium-lithium member of the highly aluminous margarite group, with the formula $Na(LiAl_2)Al_2Si_2O_{10}(OH)_2$. Laminae composed predominantly of this mica are macroscopically discernible as thin reddish brownish streaks, which under high magnification comprise densely stacked flakes (<20 µm) of partly parallel-oriented ephesite, submicroscopic hematite and occasionally diaspore (Figure 4B). Replacement of ephesite by sheaflike lithiophorite and development of kaolinite and hollandite $[Ba(Mn^{4+}Mn^{2+})_8O_{16}]$ are seldom seen straddling the edges of ephesite laminae, thus indicating preferential supergene reworking along small-scale erosional surfaces, fractures and joints (Figure 4C). In the studied samples, ephesite is not a minor constituent, neither is restricted to certain parageneses or laminae, but instead is rather pervasive in all sorts of finely laminated beds and sedimentary/diagenetic structures defining these ores.

A common and pronounced textural feature of many laminae is the occurrence of broadly spherical or ovoidal structures composed of either braunite, hematite or ephesite. These structures possibly relate to previously reported microconcretions from the same ores, show various degrees of replacement by manganese oxides of the hollandite supergroup and produce a mottling appearance on certain laminae, noticeable in hand specimen only with respect to coarser and aggregated braunite microconcretions. Specifically, concretions ca. 50-100 µm in diameter consisting of ephesite and occasionally surrounding hematite cores, are

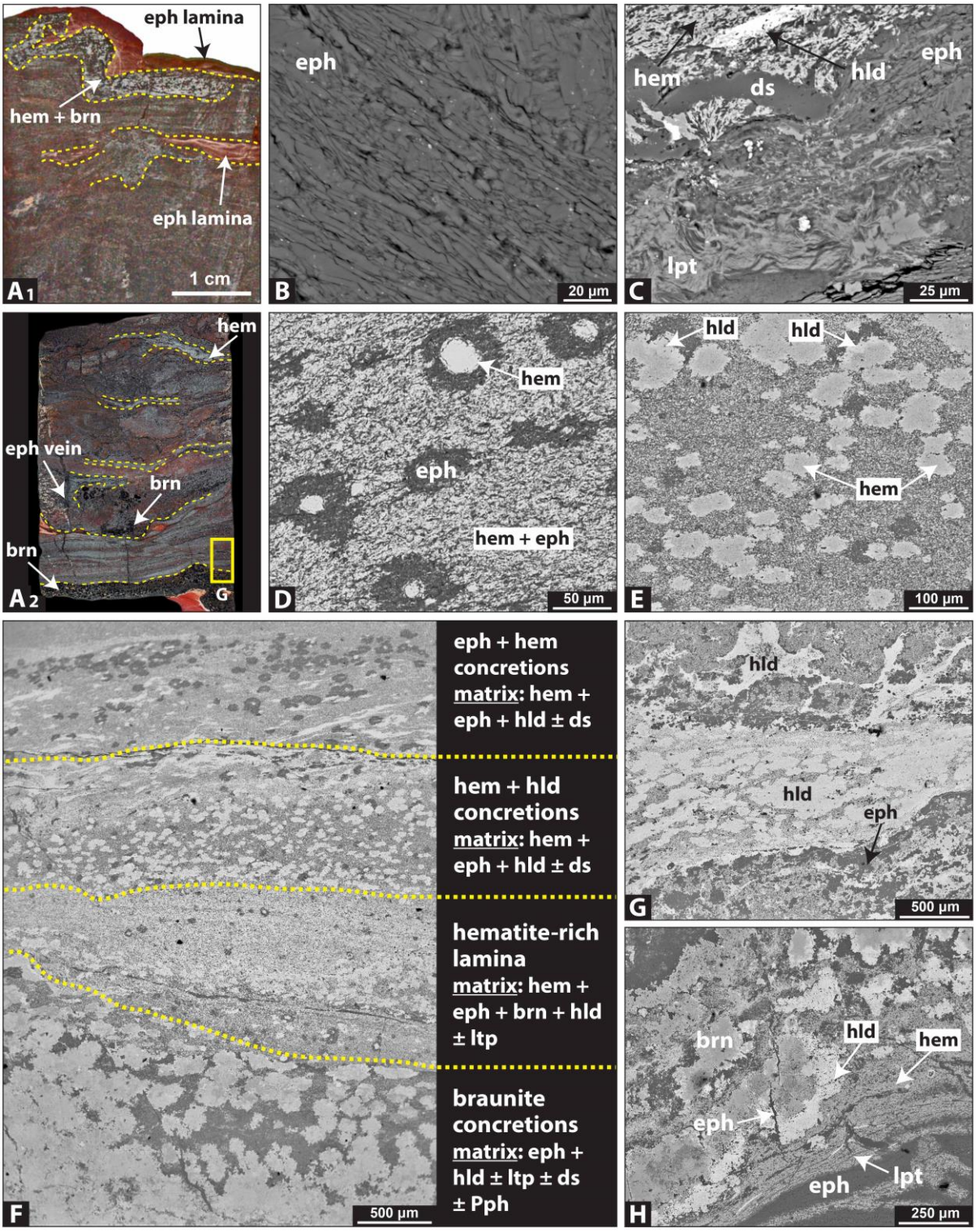

Figure 4. Backscattered (BSE) images. (A1) Contorted and irregularly developed laminae consisting of ephesite and ore mineralogy (photo). Note the braunite microconcretions (dark spots) within the top hematite-rich layer. (A2) Thin section scan depicting the complex layered and replacive textures involving abundant ephesite. (B) Densely stacked ephesite plates with broad parallel orientation. (C) Sheaflike lithiophorite developing at the edges of ephesite laminae. (D) Ephesite microconcretions with platy hematite cores. (E) Concretions with hematite cores and hollandite rims, probably related to metasomatic replacement of braunite. (F) Alternating microlaminae emphasizing the pervasive presence of ephesite (dark grey) and various replacive textures. (G) Ferrihollandite filling space interstitially to ore laminae. (H) Braunite aggregates partially overprinted by hollandite. brn = braunite, ds = diaspore, eph = ephesite, hem = hematite, hld = hollandite, lpt = lithiophorite, Pph = pyrophanite.

randomly distributed in a groundmass showing lamellar intergrowth of fine-grained hematite and ephesite (Figure 4D, 4F). EDS analyses of the fine-grained to cryptocrystalline groundmass (n=3), show high Fe_2O_3 concentrations (65.7 wt. %) and variable MnO (5.4-19.1 wt.%), Na_2O (1.9-5.9 wt.%) and Al_2O_3 (8.3-24.1 wt.%) content, which in turn reflect the presence of manganese oxides, ephesite, lithiophorite and diaspore. In similar fashion, distinct hematite-rich laminae are populated by concretions displaying mostly hematite interiors rimmed by hollandite (Figure 4E, 4F). Fe_2O_3 content of hollandite rims is high (up to 33.5 wt.%) and could be the result of finely intergrown hematite. However, coarser, and consistently iron-rich hollandite assemblages of seemingly replacive origin exist in the same sample and fill interstitial space along with hematite; thus, suggesting a formation that postdates that of ephesite laminae (Figure 4G). Notably, microscopic equant grains (15-25 µm) of this hollandite variety are seen forming thin coronas around lithiophorite. Collectively, Fe_2O_3 and MnO_2 concentrations of this hollandite range greatly between 15.4 and 66.1 wt. % (average = 42.9 wt.%, n=8) and between 30.2 and 68.5 wt.% (average = 46.9 wt.%, n=8) respectively. Positively correlated Fe_2O_3 - MnO_2 (r^2=0.94) and MnO_2 - BaO (r^2=0.65) concentrations imply that at least some hollandite occurrences can be accounted as ferrihollandite ($BaMn^{4+}{}_6Fe^{3+}{}_2O_{16}$), a relatively new end-member previously noted in hydrothermal manganese ores from India and Italy (Biagioni et al; 2014). Manganese oxides such as hollandite, coronadite and cryptomelane were documented from all studied samples but are generally confined to textures such as open space fillings and localized replacements without being widespread in the ore matrix. The BaO content of these oxides ranges widely from below detection to 25.3 wt. %, with an average of 12.5 wt. % (n=28). In contrast, variability in potassium is smaller, with K_2O values ranging between below detection and 2.2 (average = 0.7 wt. %, n=28). Coronadite, which occurs mostly as microscopic aggregates associated with hematite, forms a solid solution with hollandite and cryptomelane. Observed maximum contents of PbO were 29.9 wt. % (average = 12.7 wt.%).

Ephesite concretions are evidently of replacive origin but similar hollandite-hematite structures may also be related to metasomatic replacement of comparable concretions comprising braunite and partridgeite (iron-bearing a-Mn_2O_3), which have been regarded as being of early diagenetic origin by previous authors. Interestingly, previous mentions of

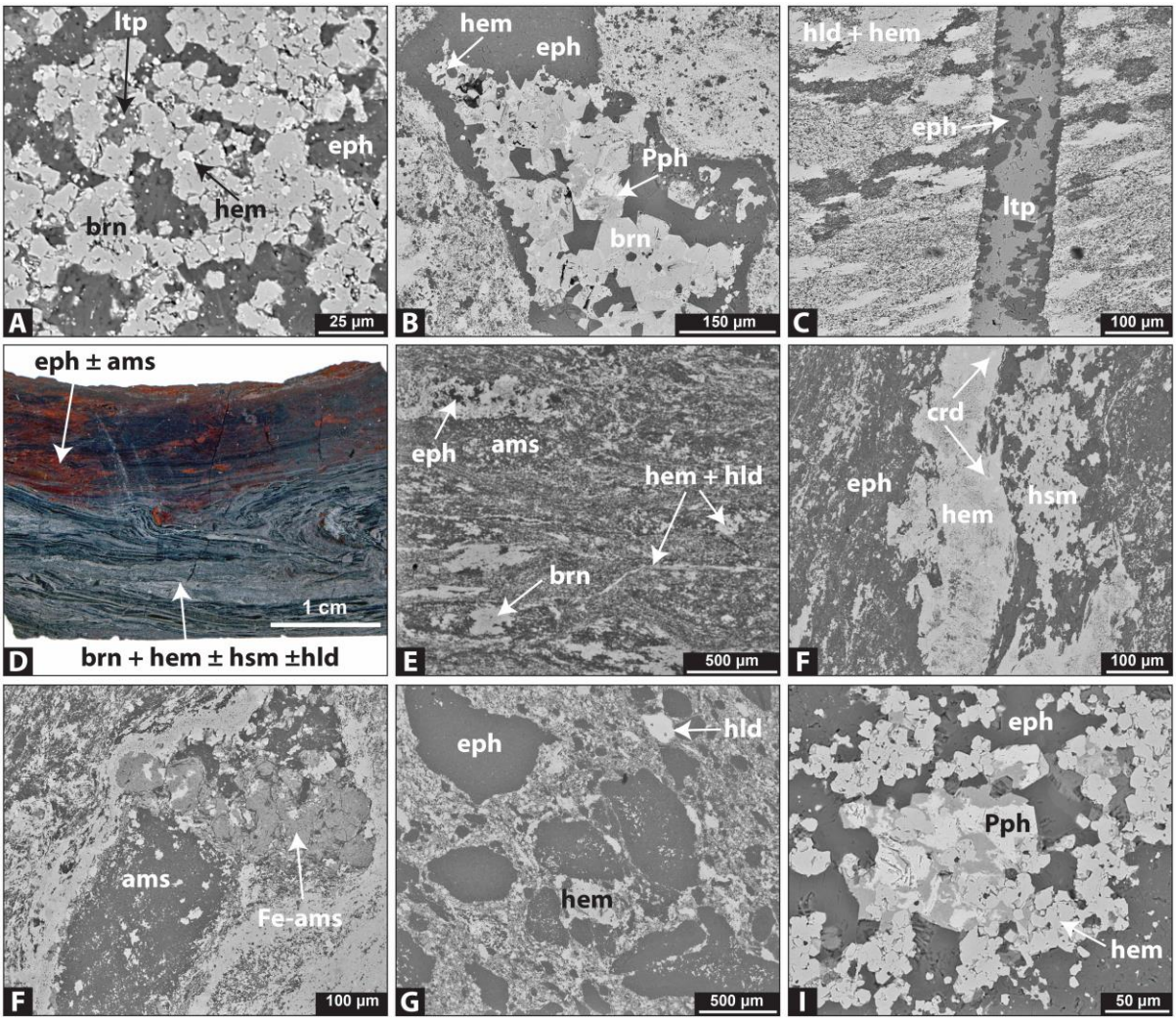

Figure 5. Back scattered electron (BSE) images (A) Granular braunite and platy hematite implying local recrystallization. (B) Mosaic-textured braunite and pyrophanite within coarse-grained ephesite infills. (C) Cross-cutting veinlet consisting of euhedral ephesite and lithiophorite. (D) Thin section scan. Contorted ore laminae and ephesite-amesite replacement zones. (E) Dispersed aggregates and laminae of ore minerals within a very fine-grained to cryptocrystalline matrix of ephesite, amesite and other ore phases. (F) Clusters of hausmannite and hematite laminae associated with coronadite. (G) Iron-rich amesite variety in close association with hematite matrix. (H) Angular ephesite clasts in a reworked matrix of hematite, ephesite and hollandite. (I) Pyrophanite syn-crystallizing with oxide of higher ilmenite content. ams = amesite, brn = braunite, eph = ephesite, Fe-ams = iron-rich amesite, hem = hematite, hld = hollandite, hsm = hausmannite, lpt = lithiophorite, Pph = pyrophanite.

concretions in ‘shaley’ laminae, contrarily report ore minerals (braunite, hematite) forming rims around cores of gangues (ephesite, diaspore) (Gutzmer and Beukes; 1996a). Nevertheless, coarse braunite aggregates (150-500 µm) confined in discrete laminae display marked partial replacement characterized by hollandite growing at the expense of primary braunite (Figure 4H). Figure 4F demonstrates how prevalent ephesite is, in a series of alternating ore laminae showing different concentrations and grain size of both ore and gangue phases. Localized recrystallization is suggested by matrix being in place enriched in

granular interlocking braunite and in addition, by hematite and ephesite infills that are discordant to bedding and host coarser mosaic-textured braunite (50-150 µm) (Figure 5A, 5B).

Although ephesite chiefly demonstrates a fine-grained micaceous habit in these ores, like that seen in ephesite laminae (Figure 4B), coarser (50-100 µm) and densely intergrown grains are also observed in the braunite-rich laminae. Supergene alteration is present in the studied samples but has seemingly advanced in an irregular fashion, affecting only certain areas or grains by forming manganese oxides. However, samples do exist where the origin of apparently supergene mineralogical phases such as lithiophorite is less obvious. Lithiophorite veins concordant to bedding, networks of veinlets comprising ephesite and lithiophorite equant crystals (Figure 5C) and finally the presence of lithiophorite inclusions within recrystallized braunite in the vicinity of microfractures, point to a close relationship between the origin of ephesite and crystallization of at least some lithiophorite.

Finely laminated braunite-hematite beds at McCarthy locality show complex, contorted and discontinuous laminae, most likely products of compaction during diagenesis as well as of metasomatic reactions forming ephesite and manganese oxide replacement-zones that are superimposed on the primary bedding (Figure 5D). Within these zones, ore mineralogy forms irregular layers, anhedral masses or individual grains dispersed in ephesite matrix (Figure 5E, 5F) and includes: (1) microcrystalline braunite aggregates (2) sparse fine-grained (25 µm) hausmannite clusters (3) layers of massive hollandite with coronadite inclusions, usually in close association with hematite laminae, the latter also hosting manganese (up to 4.6 wt.%), titanium and vanadium. Ephesite forms interstitial to the ore minerals and infrequently is intergrown with the highly aluminous phyllosilicate amesite [$Mg_2Al_2SiO_5(OH_4)$]. Lithiophorite occurs only in traces amounts in the ore matrix. Diaspore and an unidentified silicate with similarly high aluminum content was also noted in contact with amesite. Two analyses show very low compositional variability in this mineral, with FeO being 33.4 wt. % and MgO 14.6 wt.%; therefore, implying the presence of an iron-rich amesite (Figure 5G), with Fe^{2+} substituting for Mg^{2+} in its structure. However, obtained EDS data give a different structural formula from that emerging by complete iron substitution in the ideal composition, unless Fe^{2+} further substitutes for Al^{2+}. A single report from the literature

considers iron-rich amesite (ca. 22 wt.% FeO) as a replacement product of biotite during metasomatic alteration of granite (Taner and Laurent; 1984). Parageneses in this study suggest that formation of amesite is likely related to iron-rich solutions also forming hematite in the matrix.

Certain samples differ in being more clastic, with bedding restricted to contorted layering around clasts. In greater detail, these clasts consist primarily of ephesite, being coarser to that seen in the surrounding ephesite-rich ore groundmass (Figure 5H). This texture implies that at least some reworking of the ephesite-rich ore laminae must have occurred after the initial formation of ephesite. Ephesite clasts are usually rimmed by microplaty hematite and generally coarser hexagonal grains of **pyrophanite** ($Mn^{2+}TiO_3$), a mineral firstly reported here from these ores. Pyrophanite has been found in sodium-bearing associations within metamorphosed braunite-rich rocks and generally in manganese deposits (Bennet 1987b; Velilla and Giménez-Millán; 2003). Here, in accordance with the literature, pyrophanite is seen associated with recrystallized braunite. Moreover, it displays dark grey colour in reflected light but also exhibits patches or brighter grains due to ilmenite substitutions (Figure 5I). Barite is largely absent in the studied samples, being restricted to small-scale fillings within ephesite laminae or seen sparingly disseminated through them. It is reminded that previous documentation of intimately associated barite and diaspore at Paling and Glosam localities has been taken as indication of localized post-metamorphic hydrothermal fluid flow (Gutzmer and Beukes; 1996a).

To summarize the above petrographic observations, ephesite is a distinct alteration phase which is prevalent within primary banding, but also in zones that cut the original layering, as well as in later-stage veins. On that account: (1) its formation succeeded, to at least some extent, that of the chief ore minerals and (2) it is probable that apart from the relict sedimentary features, a lot of the diverse textural characteristics of these ores resulted from hydrothermal or metamorphic metasomatic processes.

4.1.2. Ephesite crystal pockets and thick 'shaley' monomineralic bands

The uncommon dark pink-red prismatic ephesite aggregates from Glosam and Lohatla mines and their relationship to the host rock were also studied in the SEM. Ephesite and diaspore aggregates of similar appearance have been reported to line cavities in the ferromanganese ores of the PMF (Cairncross and Dixon; 1995) and constitute attractive specimens for the collectors. Individual ephesite crystals in the sample EPH2 from Lohatla show a length between 0.2 mm and nearly one centimetre and although are for the most part compositionally pure, certain mm-scale grains closer to the host rock are crowded with inclusions of prismatic diaspore (100-400 μm) and amesite (200-300 μm), while space between crystals is filled by xenomorphic hematite and bixbyite (Figure 6A-D). An unusual textural type of bixbyite comprising aggregates of spherical micronodules can be observed developing between ephesite crystals (Figure 6C) and could reflect surficial deposition of Mn oxides around nucleation centers of organic origin (Zhang et al; 2015). Rarely, lithiophorite occupies minute fractures within crystals and encloses anhedral hollandite. Microscopic (5-10 μm) **gamagarite** [$Ba_2(Fe^{3+},Mn^{3+})(VO_4)_2(OH)$] inclusions were noted within diaspore prisms (Figure 6B). Dark brown to red coarse prismatic crystals of this rare vanadate species were firstly reported by De Villiers (1943b) as coarse-crystals in bixbyite-rich ores from Glosam mine and since then, it has been only found in the hydrothermally metasomatized braunite and hematite ores of the Val Graveglia manganese district in Italy (Marchesini and Pagano; 2001, Cairncross; 2019). Gamagarite inclusions along with the euhedral shapes of most mineral inclusions in ephesite, support the coexistence of chemical reactants (Na, Li, Al, Ba, V, Fe, Mg etc.) in the fluids that formed these minerals.

Host rock consists primarily of fine-grained braunite and hematite, intricately intergrown with coarser aggregates of ephesite. In general, the latter crystallizes interstitially to and disrupts the ore matrix (Figure 6E). Locally, patches of coarser euhedral braunite and diaspore are observed. The intermediate zone between ephesite crystals and ore matrix is characterized by well-developed prismatic ephesite of decreasing size (200-25 μm) towards the host rock and complex intergrowths of bixbyite, hollandite, diaspore, braunite and hematite, most likely reflecting a domain of late-stage precipitation or localized reworking involving meteoric fluids. The presence of microscopic veins with prismatic ephesite,

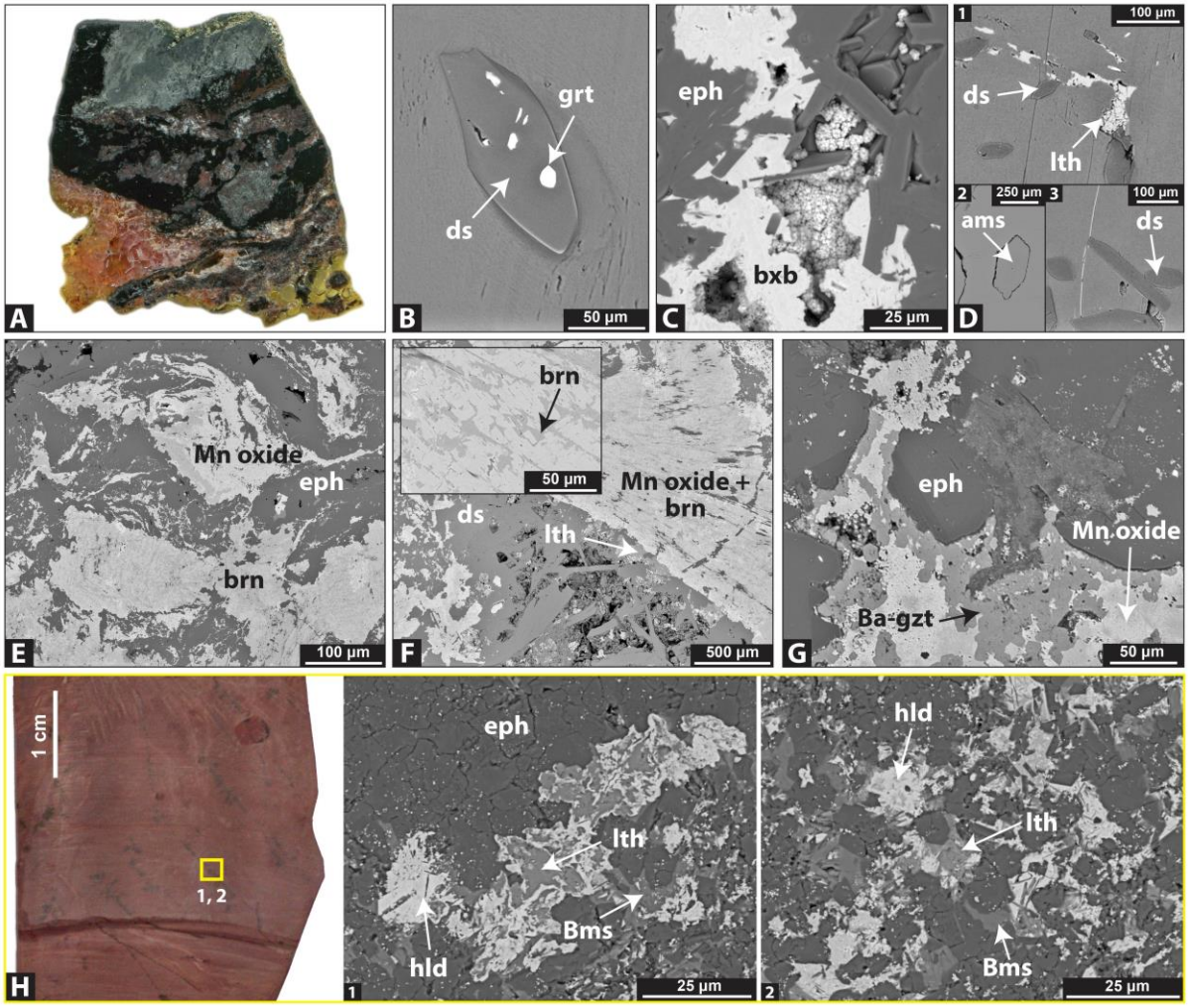

Figure 6. (A) Ephesite pocket separated from the braunite-rich host rock by an intermediate zone rich in Mn oxides (photo). Back scattered electron (BSE) images. (B) Barium manganese vanadate (gamagarite) inclusions in diaspore. (C) Bixbyite micronodules filling open space between ephesite. (D1-3) Lithiophorite occupies fractures within ephesite crystals which also host equant diaspore and amesite inclusions. (E) Ephesite forming interstitially to ore matrix, the latter consisting of braunite and Mn oxides such as hollandite, hausmannite or manganite. (F) Radial intergrowth of braunite and either hausmannite or manganite. (G) Barian goyazite (alunite) rhombs preferentially deposited in contact with ephesite. (H) 'Shaley' interval from Bishop intercalated with ferromanganese ore and consisting almost entirely of ephesite (photo). (1-2) Hollandite and lithiophorite fracture-fillings, seen sparsely within this bed. Ba-muscovite is not in paragenetic relationship with the previous. ams = amesite, Ba-gzt = barian goyazite, Bms = barian muscovite, brn= braunite, bxb = bixbyite, ds = diaspore, eph = ephesite, grt = gamagarite, hld = hollandite, lth = lithiophorite.

transecting fine-grained hollandite or cryptomelane matrix with up to 25.3 wt. % BaO and 2 wt. % K_2O (n=5), implies ephesite recrystallization during this later reworking. Contrastingly, ephesite veins previously reported to be common in the upper parts of the orebodies while extending to the overlying ferruginous and aluminous Gamagara shales have been suggested to reflect the main ephesite-forming event (Gutzmer and Beukes; 1996a); therefore,

determination of the exact timing and/or episodes of ephesite vein-formation can be only speculative with current evidence.

An unidentified grey-white manganese oxide with brownish tint under reflected light can be also observed forming radial intergrowths with braunite and is presumably either hausmannite or manganite, although more analytical methods are further needed to confirm this (Figure 6F). Another mineral apparently related to late-stage alteration is **barian goyazite** [$(Sr,Ba)Al_3(PO_4)_2(OH)_5H_2O$]. This uncommon phosphate belongs to the alunite supergroup and was positively identified by EDS analysis. Aggregates or distinct subhedral rhombs (5-25 μm) are seen almost exclusively in contact with diaspore or ephesite surrounded by manganese oxide-rich host rock (Figure 6G). In some cases, goyazite evidently replaces diaspore, indicating that it is an alteration mineral and the necessary aluminum is apparently provided by ephesite or diaspore. This barian variety of goyazite, showing 24.3 wt. % BaO (n=3) and almost no strontium (up to 1.1 wt. %) is particularly rare, considering that only one further occurrence exists in the literature, from a pegmatite province in Brazil (White; 1981). Small amounts of calcium (ca. 1 wt. %) and F (1.5 wt.%) were also picked up by EDS.

Ephesite laminae intercalated with ferromanganese ore-matrix are further observed composing discrete narrow (cm-thick) intervals (Figure 5H), which consist chiefly of ephesite and rare disseminations of accessory fine-grained minerals. According to this observation, it can be surmised that comparable 'shaley' intercalated beds seen in the field (Figure 2C), are similarly composed chiefly of ephesite. This is further supported by earlier mentions of 'shale' laminae within the ore, being rich in diaspore and ephesite as well as by textural descriptions associating manganese enrichment with replacement of oolitic shale (Gutzmer and Beukes; 1996a, De Villiers; 1944).

Thick ephesite bands from Bishop are translucent under transmitted light, exhibit pinkish to brownish colour and granular texture with inhomogeneous grain size (5-25 μm). Barian muscovite, barite and submicroscopic spherical hematite may form in the interstitial space between ephesite. Sheaflike aggregates of Ba-Al muscovite have been previously reported as a rare constituent of the braunite-rich ore at Gloucester mine, however with no

other textural information given. Its composition was calculated by microprobe analysis as being $(Ba_{0.6}K_{0.3}Na_{0.6}Mn^{2+}_{0.1}Fe^{2+}_{0.03}Al_{1.9})Si_{2.4}Al_{1.6}O_{10}(OH)_2$ (Gutzmer and Beukes, 1997b), which displays considerable replacement of silicon atoms by aluminum. Muscovite in this study is generally very fine-grained (<25 µm) and has analogous composition, corresponding to $(Ba_{0.13}K_{0.72}Al_2)Si_{2.7}Al_{1.6}O_{10}(OH)_2$. Aside from the lower barium content, the determined composition similarly shows aluminum substitution for silica, thus emphasizing the aluminum-rich setting during crystallization, in parallel to other gangues. Hollandite occurs only as a fracture-filling mineral in association with lithiophorite and occasionally microscopic euhedral grains of Ba-muscovite and ephesite (Figure $5H_{1-2}$).

4.1.3 Bixbyite-rich ore

Petrographic study of the coarse-grained bixbyite-rich ore confirms the existence of bixbyite $(Mn^{3+},Fe^{3+})_2O_3$ as the dominant ore phase, with abundant diaspore being also present. Cogenetic and coarse-grained hematite and braunite have been previously reported as ubiquitous phases in this ore-type but were found here only as minute inclusions within bixbyite. Cubic idioblasts of bixbyite with rectangular outline exhibit highly variable size from 300 µm to several millimetres (Figure 7A) and are commonly characterized by lamellar twinning under reflected light. Diaspore is intimately intergrown with bixbyite and forms laths of well-developed crystals (Figure 7B) or is observed as anhedral infill between the former. Coarse-grained (100-400 µm) idioblastic acicular crystals of diaspore may also contain submicroscopic inclusions of bixbyite or hollandite. An unidentified alkali-rich (Ca, Mg, Na) aluminosilicate was also observed developing interstitially to bixbyite grains.

Bixbyite-rich matrix is locally characterized by different colour shades, with darker and mostly anhedral patches and infills of up to 250 µm in size being also manganese- and iron-rich, but slightly different in composition. Two ore mineral phases can be resolved by means of scanning electron microscopy and EDS analyses. The predominant euhedral bixbyite [bxb(I)] aggregates described above (avg. Fe_2O_3 = 17.6 and Mn_2O_3 = 79.6 wt. %, n=7) and a second generation [bxb(II)] with slightly lower Fe and Mn content (avg. Fe_2O_3 = 15.1 and Mn_2O_3 = 77.8 wt.%, n=25), which however additionally bears alkalis (avg. $Na_2O + K_2O$ = 3.8 wt.

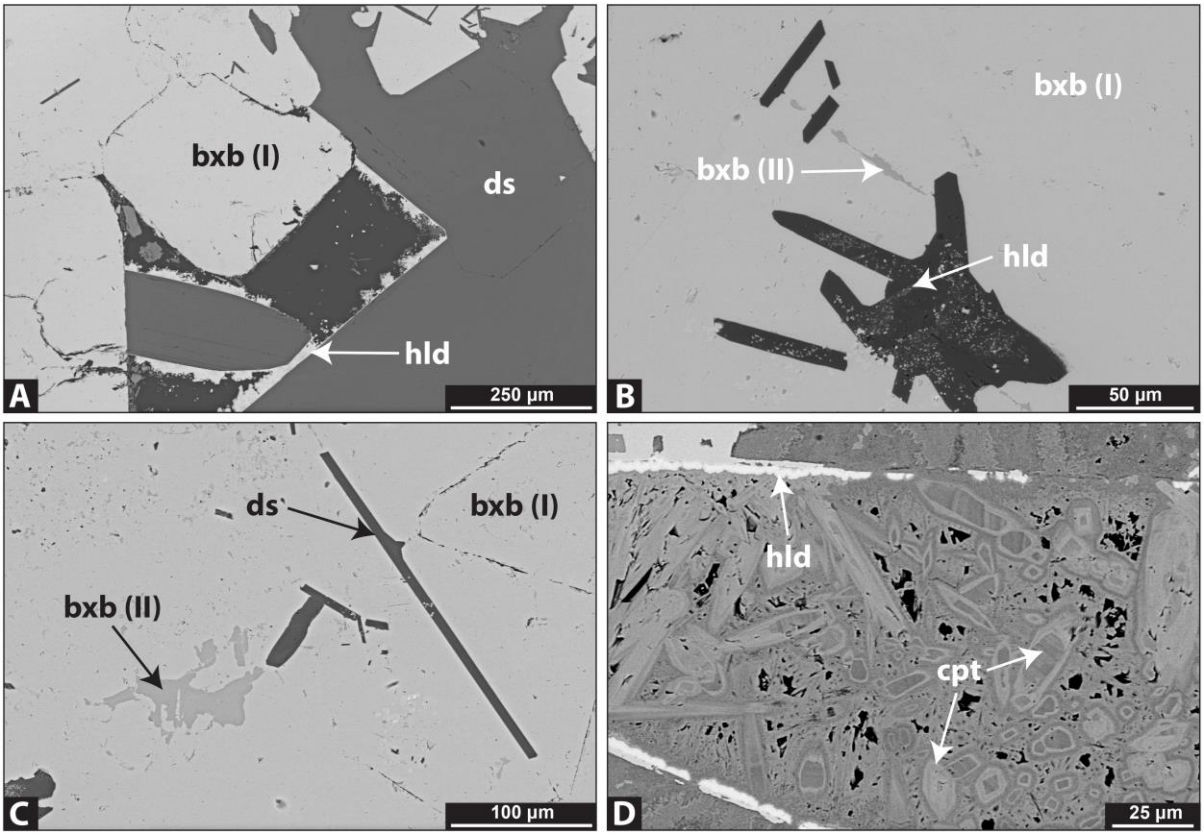

Figure 7. Back scattered electron (BSE) images. (A) Cubic euhedral bixbyite syn-crystallizing with diaspore. (B) Diaspore laths in bixbyite-ore matrix, the former exhibiting hollandite inclusions. (C) An iron-bearing manganese oxide (variety of bixbyite) that also hosts alkalis (Na, K), fills interstitial space in ore matrix and engulfs bixbyite, possibly replacing it. (D) Cryptomelane of late supergene origin displaying evident core-rim compositional variations. bxb (I) = bixbyite, bxb (II) = alteration product of bixbyite (see also text), cpt = cryptomelane, ds = diaspore, hld = hollandite.

%, n=25) (see also section 6.6 later on). The latter phase is seen mostly developing in-between bixbyite and is commonly but not always associated with Mn oxides of the hollandite Supergroup [hollandite (Ba), cryptomelane (K) and coronadite (Pb)]. In cases where it coexists with oxides, growth bands are usually visible, whereas in ore matrix this phase [bxb(II)] is apparently involved in replacements occurring along small fracture surfaces and grain boundaries (Figure 7C). An Fe-poor and anisotropic variety of bixbyite with the informal name **partridgeite** has been previously reported from the EMD ores but in contrast to the regarded Mn oxide [bxb(II)] in the current study, partridgeite from the literature has constantly very low iron content (Fe_2O_3 between 0 and 4.6 wt. %, mostly below 1) (Gutzmer and Beukes, 1997b) and hosts no alkalis. Based on the latter and on textural grounds, the Mn-rich oxide of the studied sample is presumed to represent an alteration product of the prevailing

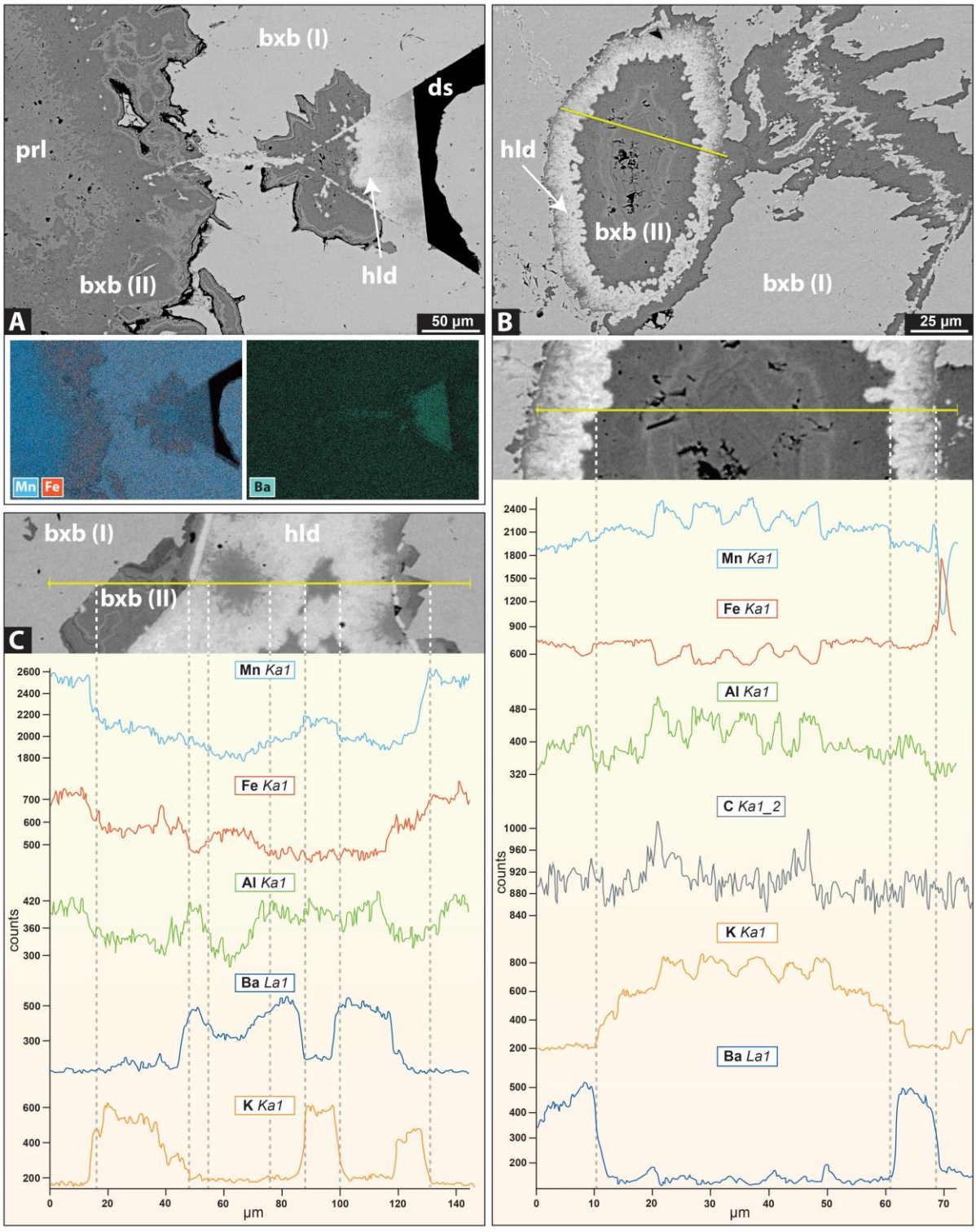

Figure 8. Back scattered electron (BSE) images, EDS elemental maps and line scan analyses. (A) Late pyrolusite associated with altered bixbyite (II) and hollandite filling microscopic late fractures. (B) Bixbyite (II) showing a thin corona of hollandite and very fine zoned texture, characterized by domains richer in either Mn, Al and K or Fe. Note the pronounced antithetic correlation between Fe and Mn, and Ba and K displayed in the line scans. (C) Similar bixbyite (II) - hollandite association with compositional variations. bxb (I) = bixbyite, bxb (II) = alteration product of bixbyite (see also text), ds = diaspore, hld = hollandite, prl = pyrolusite.

bixbyite, although this cannot be fully ascertained before integration of different identification methods.

On the other hand, much certainty exists with respect to late supergene fine-grained and poorly crystalline Mn oxides that define different generations and have precipitated to form parallel banded or concentric structures. For example, cryptomelane (K) usually occurs as aggregates of randomly orientated authigenic crystals or overgrowths with core-rim compositional variations (Figure 7D). As noted above, colloform-like structures or growth banding textures may also involve altered bixbyite [bxb(II)]. SEM line scan analysis and elemental maps help reveal the heterogeneous distribution of elements such as Mn, Fe, K and Ba and therefore delineate distinct oxide populations. For example, bixbyite (II) appears flanked by late pyrolusite at the edges of infills where hollandite (Ba) seemingly fills late microscopic fractures (Figure 8A). In another case, a central zone of bixbyite (II) is engulfed by a thin corona of radiating hollandite (Ba) crystals growing inwards to the core, whereas cryptomelane (K) develops further outwards in the vicinity (Figure 8B). The interior of this zoned-texture presents very fine distinct zones characterized by either higher Mn, K and Al or higher Fe content. Besides Mn and Fe, an antithetic correlation between K and Ba can be clearly observed in EDS line scans, in different textures involving the aforementioned oxides (Figure 8C).

4.1.4. An Fe-Al-rich sample from the Kolomela mine

A sample from Kolomela mine (somewhat 40 km from the study area s.s.) is petrographically examined here because of its generally high aluminum content, intriguing mineralogy and textures that may yield additional information on the alteration and ore genetic processes of the EMD ferromanganese ores. It is noted though that this sample (LF126) overlies iron ore in the stratigraphic profile and is not directly associated with ferromanganese ore. Notably, bulk rock Si/Al ratio is close to 1 (Appendix IV).

The main textural attribute is that of an iron- and aluminum-rich matrix displaying an abundance of mostly spheroidal textures (0.1 to 0.5 cm) which can be interpreted as resulting from colloidal solutions (Figure 9.1). Mm-sized white veinlets generally transect both the

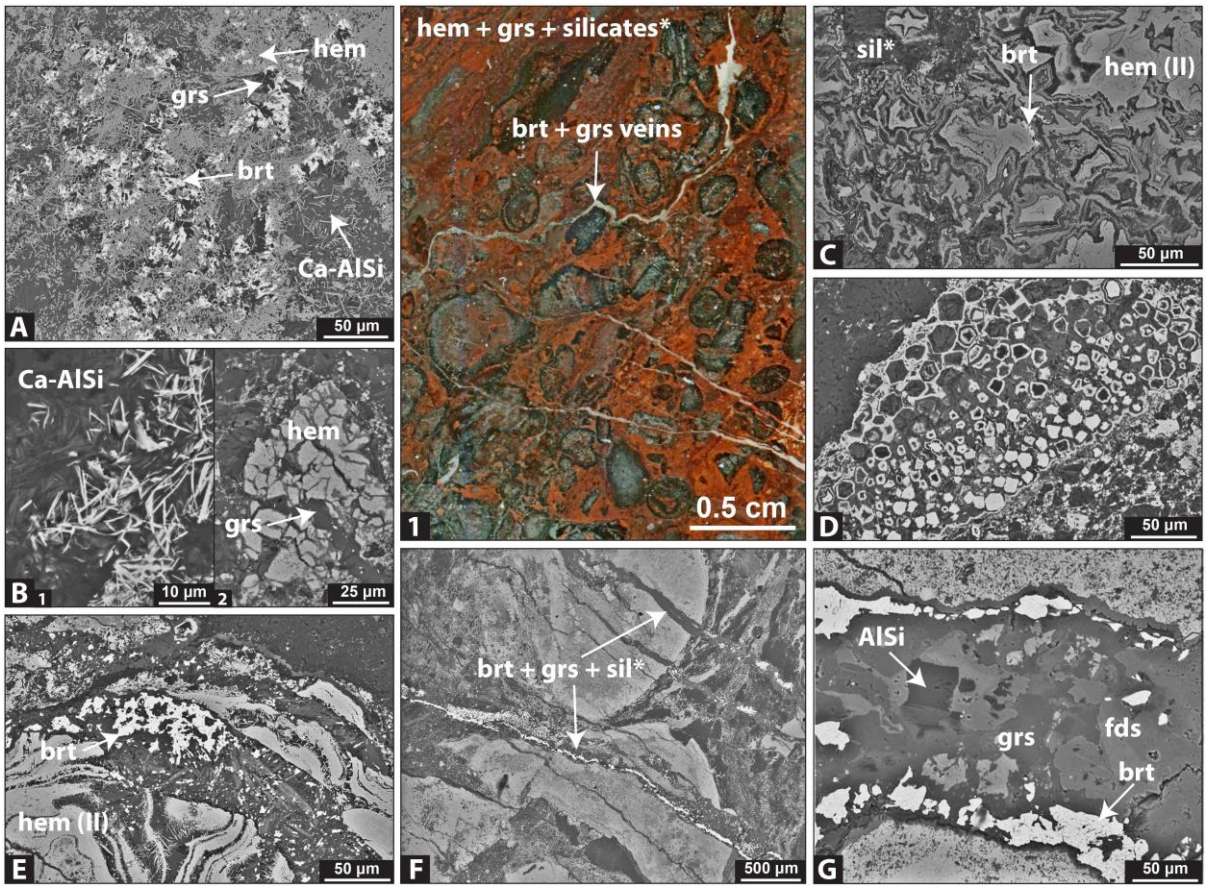

Figure 9. (1) Thin section scan showing the principal texture of the sample from Kolomela, i.e., iron-rich spheroids in a hematite- and silicate-rich matrix, transected by veinlets hosting barite and grossular among other phases. Back scattered electron (BSE) images. (A) Closely associated hematite, barite and grossular in a matrix also comprising fine-grained silicates with compositions partly overlapping with that of margarite (high Al) and paragonite. (B_1) Detail of the phyllosilicate- and hematite-rich matrix. (B2) Hematite clast fractured and filled by paragenetically later grossular. (C) Colloform textures involving Mn-bearing hematite and barite. (D) Concentric-zoned hematite and silicates. (E & F) Grossular + barite veinlets crosscutting earlier spheroidal textures. (G) Detail of late veinlet hosting banalsite, feldspars, garnet, barite and possibly andalusite (dark, see also text). AlSi = aluminosilicate with Al/Si = 2/1, possibly andalusite, brt = barite, Ca-AlSi = mixed fine-grained silicates, compositionally varying between margarite and paragonite-muscovite, fds = feldspar, grs = grossular, hem = hematite, hem (II) = hematite an/or hematite-rich groundmass bearing Mn, Si and Ti, sil* = mixed unidentified silicates hosting Na, Na, K, Fe, Ca and Mg.

groundmass and rounded textures and chiefly comprise barite and grossular. In addition to the latter two, microplaty hematite and unidentified aluminosilicates with varying compositions are the most common documented phases in the matrix, while the intimacy of their intergrowth supports a cogenetic relationship (Figure 9A). It is reminded that garnet has not been previously reported from the EMD but only from the WMD ores and the KMF (chapters 3, 5). Barite, As-bearing apatite, chalcopyrite and chalcocite are sparsely scattered

in the matrix. EDS analyses on fine-grained aluminosilicate-material of different shading broadly correlate with compositions overlapping with either that of margarite or paragonite-muscovite and apart from Na and Ca, varying amounts of K, Mg, Fe and Mn are apparently also hosted in their structure (Figure 9B$_1$). Certain textures such as microscopic (less than 100 µm) hematite clasts fractured and filled with grossular suggest a later origin for the latter (Figure 9B$_2$).

The spheroidal textures are seemingly composed of the same minerals seen in the matrix, which in contrast are characterized here by colloform habits. Their interiors commonly contain manganese hosted by hematite or cryptocrystalline hematite-rich groundmass [hem(II)] that further accommodates Ti and Si and appears darker than compositionally pure hematite. The rims of the rounded structures may display radiating textures, adjoined by colloform and/or rhythmic banding textures involving hematite, silicates and barite (Figure 9C). Microscopic hexagonal to rounded textures showing concentric-zoned hematite and silicates or overprints by hematite are seldom found in the matrix and may point to colloidal solutions (Figure 9D). Several veinlets cross-cutting the spheroidal structures provide evidence for an episode of late fluid infiltration and formation of the majority of blocky barite together with a number of different silicates and grossular (Figure 9E, 9F). A detail of such veinlet reveals precipitation of barite at the rims and several hydrothermal feldspars (banalsite and albite-anorthite solid solution members) occupying the core (Figure 9G). Interestingly, an aluminosilicate with an aluminum to silica ratio 2/1, coincident with the high aluminum values detected in other silicates in the sample (i.e., margarite, the Ca-analogue of ephesite) is also documented from the same paragenesis. Whether or not this phase represents an Al_2SiO_5 polymorph and in particular the low-T andalusite awaits confirmation.

4.2 Lithium and boron geochemistry

A total of 30 samples from the Maremane dome and the KMF were analysed for their whole-rock Li and B content. This first cursory scan comprises different lithologies, where these two elements are either presumed to be hosted by rare Li- and B-bearing minerals (e.g., sugilite, norrishite, ephesite, datolite, gaudefroyite) or their concentration is unknown due insufficient knowledge of possible mineralogical control on the elements. The results are

made available in Table 1 and additional major and trace elements for these samples can be found in the Appendix-IV.

Expectedly, the ephesite-bearing ore at Bishop displays the highest Li values (from 1060 to 4890 ppm) and correspondingly a homogeneous sample of a 10cm-thick bed, particularly rich in ephesite, shows a lithium concentration of 11090 ppm (1.11 wt. %). Interestingly, lithium seems to be virtually absent (<10 ppm) in the bixbyite-rich ore pockets and drops to extremely low concentrations in the manganiferous chert breccia (Wolhaarkop) at McCarthy (from <10 to 20 ppm). Nonetheless, Wolhaarkop seems to host some lithium, both at localities where sugilite has been documented, such as Khumani (200 ppm Li) or not, like Kolomela (700 ppm Li). High lithium concentration (1670 ppm) is also documented from an iron-rich sample with apparent pisoliths from the Kolomela iron ore mine. Boron is detected only in the ephesite-rich ore and in the sugilite-bearing Wolhaarkop breccia at Khumani but for most samples it is barely above detection limit (200 ppm), reaching values up to 400 ppm.

In similar fashion to the EMD ores, ferromanganese ore from the WMD exhibits considerable lithium concentrations although highly variable. Values range more uniformly, from 10 to 310 ppm (avg. = 136 ppm, n=7) at Langverwacht and show significant variations at Heuningkranz, ranging from 10 to 1990 ppm (avg. = 710, n=7), which generally indicates that these ores consistently contain Li-bearing phases, being most likely micas as discussed later on. Manganiferous chert breccia and iron-rich vuggy quartzite from Heuningkranz do not contain significant lithium. Two samples from Ba-rich zones within high-grade Mn ore of the KMF show moderate lithium concentrations (20 and 80 ppm). Subsequent thorough SEM study did not reveal the presence of anticipated Li-bearing phases such as sugilite, norrishite or amphiboles. Intriguingly, lithium content of the Gamagara/Mapedi shales overlying Mn ore at the same locality is below detection limit, despite the abundance of these rocks in white clays. Boron, is again detectable mostly in ferromanganese ore, ranging from 200 to 400 ppm whereas in two samples with evident alkali-rich veins, abundances shoot up to 1000 and 1500 ppm respectively. Finally, boron was below detection in the Mn ore of KMF but was found in the Mapedi shale in low quantities (300 ppm). It is pointed out that lithium concentrations in

Table 1. Whole-rock lithium and boron concentrations from selected samples across the Northern Cape.

sample ID	lithology	texture	locality	Li (ppm)	Li (wt. %)	B (ppm)
Eastern Maremane Dome (EMD)						
BSH89s	ferromanganese ore	stratified	Bishop	11090	1.11	200
BSH89	ferromanganese ore	stratified	Bishop	4890	0.49	300
BSH152	ferromanganese ore	stratified	Bishop	3980	0.40	200
MWA	ferromanganese ore	stratified	MacArthy	1060	0.11	200
GN-BX2	bixbyite-rich ore	coarse-grained	Lohatla	<10	<0.001	200
WOL1	manganifer. chert breccia	coarse clasts	MacArthy	<10	<0.001	<200
WOL3	manganifer. chert breccia	coarse clasts	MacArthy	20	0.002	n.a
AKH-G	manganifer. chert breccia	clasts / vugs	Khumani	200	0.02	300
WK135	manganifer. chert breccia	clasts / vugs	Kolomela	700	0.07	<200
LF126	ferruginous breccia	vugs / pisoliths	Leeuwfontein	1670	0.17	40
Western Maremane Dome (WMD)						
WOLA2	manganifer. chert breccia	clasts / vugs	Heuningkranz	20	0.002	200
WOLC	manganifer. chert breccia	clasts / vugs	Heuningkranz	10	0.001	<200
WOLA1	ferruginous quartzite	coarse vugs	Heuningkranz	<10	<0.001	<200
L2B-10	ferromanganese ore	stratified / veins	Langverwacht	10	0.001	1500
L2B-13	ferromanganese ore	stratified	Langverwacht	100	0.01	300
L17A-8	ferromanganese ore	stratified	Langverwacht	150	0.02	n.a.
L17A-10	ferromanganese ore	stratified	Langverwacht	310	0.03	400
L537-7	ferromanganese ore	stratified / veins	Langverwacht	10	0.001	1000
L537-12	ferromanganese ore	stratified	Langverwacht	120	0.01	n.a.
L537-9	alkali-rich breccia	clasts / vugs	Langverwacht	250	0.03	<200
PM15-2	ferromanganese ore	stratified	Heuningkranz	1010	0.10	200
PM15-3	ferromanganese ore	stratified	Heuningkranz	20	0.002	400
PM15-H	ferromanganese ore	stratified / vugs	Heuningkranz	10	0.001	400
PM15-I	ferromanganese ore	stratified / vugs	Heuningkranz	10	0.001	300
PM17-15	ferromanganese ore	stratified	Heuningkranz	1990	0.20	400
PM17-16	ferromanganese ore	stratified	Heuningkranz	1910	0.19	400
PM18-I	ferromanganese ore	stratified	Heuningkranz	20	0.002	400
Kalahari Manganese field (KMF)						
SA8G-6	high-grade Mn ore	coarse-grained	Wessels	20	0.002	<200
DK1	high-grade Mn ore	coarse-grained	N'chwaning	80	0.01	<200
MD1	shale	red / white laminae	Wessels	<10	<0.001	300

ferromanganese ore are not negligible and in certain samples are in fact analogous to those in clay deposits of economic significance or even pegmatites. This is further examined later on.

4.3 Oxygen and hydrogen isotopes

Mineral-specific oxygen and hydrogen isotopes are reported in Table 2. It is noted that minor impurities are expected in ephesite samples from Bishop mine (BSH70, BSH89, BSH89-s), whereas sample MWA from McCarthy represents a mix of primarily ephesite and lithiophorite, with minor contamination from other manganese oxides and/or hematite. $\delta^{18}O$ values for ephesite are very uniform, ranging from +11.4 to +12.1 (+11.8 ± 0.3 ‰, n=5), regardless of the locality. The same is replicated in the δD measured isotopic composition for this mineral, which is also rather homogenous (-52.3 ± 6 ‰, n=5). The ephesite-lithiophorite mixture (MWA) and pure lithiophorite separates yield much lower $\delta^{18}O$ values of +5.4 and +5.1 ‰ respectively. δD for lithiophorite also deviates from the measured ephesite values, displaying a significant decrease (-106.1 ‰), from which it can be inferred that a fluid with distinct hydrogen isotopic composition was responsible for its precipitation. The measured $\delta^{18}O$ values of diaspore from Glosam mine (+12.2 ‰) overlap with that of ephesite, whereas

Table 2. Stable O and H isotopic compositions of gangue and ore minerals from the ephesite-rich ferromanganese ores. Also tabulated are $\delta^{18}O$- and δD-fluid values for a temperature of 200°C (see section 6.6).

	mineral	locality	description / lithology	$\delta^{18}O$	δD	$\delta^{18}O_{fluid}$*	δD_{fluid}*
EPH1	ephesite	Glosam	pink prismatic crystals	12.1	-43.8	7.4	-29.0
EPH2	ephesite	Lohatla	pocket in Mn-rich host rock	11.4	-56.5	6.7	-41.7
BSH70	ephesite	Bishop	banded ferromanganese ore	12.1	-48.2	7.4	-33.4
BSH89	ephesite	Bishop	banded ferromanganese ore	11.7	-56.2	7.0	-41.4
BSH89-s	ephesite	Bishop	cm-thick ephesite laminae	11.5	-56.8	6.8	-42.0
MWA	ephesite (+ oxides) *	McCarthy	banded ferromanganese ore	5.4	-60.0	-	-
LIPH	lithiophorite	Lohatla	coarse crystalline	5.1	-106.1	-	-
NL_DS	diaspore	Glosam	clusters of bladed crystals	12.2	-108.5	17.8	-62.6
GN_BX2a	diaspore	Lohatla	bixbyite-rich ore	9.2	-99.7	14.8	-53.8
GN_BX2b	diaspore	Lohatla	bixbyite-rich ore	8.8	-93.7	14.5	-47.8
GN_BXa	bixbyite	Lohatla	bixbyite-rich ore	1.5	-	-	-
GN_BXb	bixbyite	Lohatla	bixbyite-rich ore	1.1	-	-	-

diaspore from Lohatla associated with bixbyite-rich ore has considerably lower oxygen isotopic composition (+9.2 and +8.8 ‰). Much like lithiophorite, diaspore exhibits low δD values, from -108.8 to - 93.7 ‰. Finally, bixbyite yielded uniform $\delta^{18}O$ values (+1.1 and +1.5 ‰), although distinctly lower than all other measured phases. The relationship of these ^{18}O-

depleted values with the isotopic composition of the mineralisation fluids and the rest of the gangues are discussed in a later section (6.6).

4.4. Step-heating $^{40}Ar/^{39}Ar$ results

Hand-picked ephesite separates derive from two distinct crushed samples (EPH1 and EPH2). A total of six multi-grain aliquots, i.e., essentially comprising more than one ephesite crystal, were analysed and selected data are summarized in Table 3 (see also Appendix I). The three aliquots from sample EPH1 yielded discordant step-heating spectra with somewhat saddle-like shapes and some older low-T steps. Integrated ages from two different aliquots are 1470 ± 50 Ma (2σ) and 1604 ± 46 Ma (2σ). Likewise, EPH2 yielded discordant step-heating spectra with pronounced old low-T steps. However, two out of the three aliquots give a plateau age of 1125 ± 25 Ma (2σ, MSWD = 1,42), consistent with an isochron age 1127 ± 21 Ma (2σ, MSWD = 1,7). These results are discussed in section 6.2.

Table 3. Selected $^{40}Ar/^{39}Ar$ data of ephesite (sample EPH2).

Step	Laser %	$^{40}Ar/^{39}Ar$	$^{40}Ar^*/^{39}Ar$	$\%^{40}Ar^*$	Age (Ma)	±	^{40}Ar	^{39}Ar	^{38}Ar	^{37}Ar	^{36}Ar
1	1.5	340.4783	166.8433	32.97697	1851.73	524.4903	0.0550499	0.0001612	0.0000981	0.000028	0.0001438
2	2	402.2315	264.56	50.89981	2427.994	262.2875	0.1019569	0.0002528	0.0000209	0.0000303	0.0001895
3	2.5	80.66845	61.70289	44.02697	916.397	306.8974	0.0283539	0.0003505	0.000083	0.0000788	0.0001101
4	3	131.3838	92.13143	67.28302	1240.126	67.88163	0.1400651	0.0010631	0.0001136	0.0000228	0.00017
5	3.5	88.26403	79.71617	88.74516	1114.955	9.515129	0.6325327	0.0071461	0.0002052	0.0000657	0.000286
6	4	79.40805	80.05078	99.45493	1118.445	12.96753	0.6848777	0.0086004	0.0001123	0.0000611	0.0000567
7	5	81.44991	82.98496	99.01295	1148.761	18.95435	0.488695	0.005983	0.0001021	0.0000891	0.0000806
8	6	50.2683	64.12912	82.60137	944.4462	281.6068	0.0203113	0.0004029	0.0000882	0.000075	0.0000662

6. Discussion

6.1 Lithium (Li) abundance and its hosts in the PMF

The manganese ores of Postmasburg and the neighboring Kalahari Manganese Field host common and rare gangues highly-enriched in Li, the most striking of which are sugilite and ephesite. Considering the geological framework, textural observations and the well-documented ore-upgrade mechanisms in the KMF, it is sensible to link the origin of Li with the passage of basinal brines through the lithologies of the basin. Therefore, addressing questions regarding Li concentrations, distribution and mineralogical control on this element in different ore types and country rocks is critical in order to better constrain the origin and evolution of hydrothermal fluid flow imprinted on the various Fe and Mn-rich lithologies of the Northern Cape.

The above matters are interrogated in this study by a reconnaissance survey on whole-rock Li concentrations of different lithologies, which confirms that it can be found in quite considerable quantities in the WMD ferromanganese ores (averages range between 136 and 710 ppm) and even more so in the ephesite-bearing ores of the EMD (average = 3310 ppm) and ephesite-rich intercalated beds (up to 1.11 wt.%). Conversely, the manganiferous Wolhaarkop breccia is seemingly Li-poor in comparison but can occasionally also host appreciable amounts (up to 700 ppm), something that implies wide variations for the concentration of this element, obviously linked to the mineralogical content. Geochemical plots between Li and analysed major and trace elements reveal weak to non-existent linear correlations at first glance, presumably due to high sample variability.

Nonetheless, if semi-log plots are used for data visualization (Li on the logarithmic scale), discernible trends appear, which however cannot be further quantified. Nevertheless, the most evident correlation is between Al_2O_3 and Li for ferromanganese ores of the two geographic districts, i.e., WMD and EMD (Figure 10a), where contrasting trendlines for the two localities suggest control by different minerals. A similar pattern is seen in the Na_2O versus Li diagram (Figure 10b), although correlation is moderately weaker for the WMD ores. Furthermore, there is a suggestive positive correlation between Li and potassium, seemingly

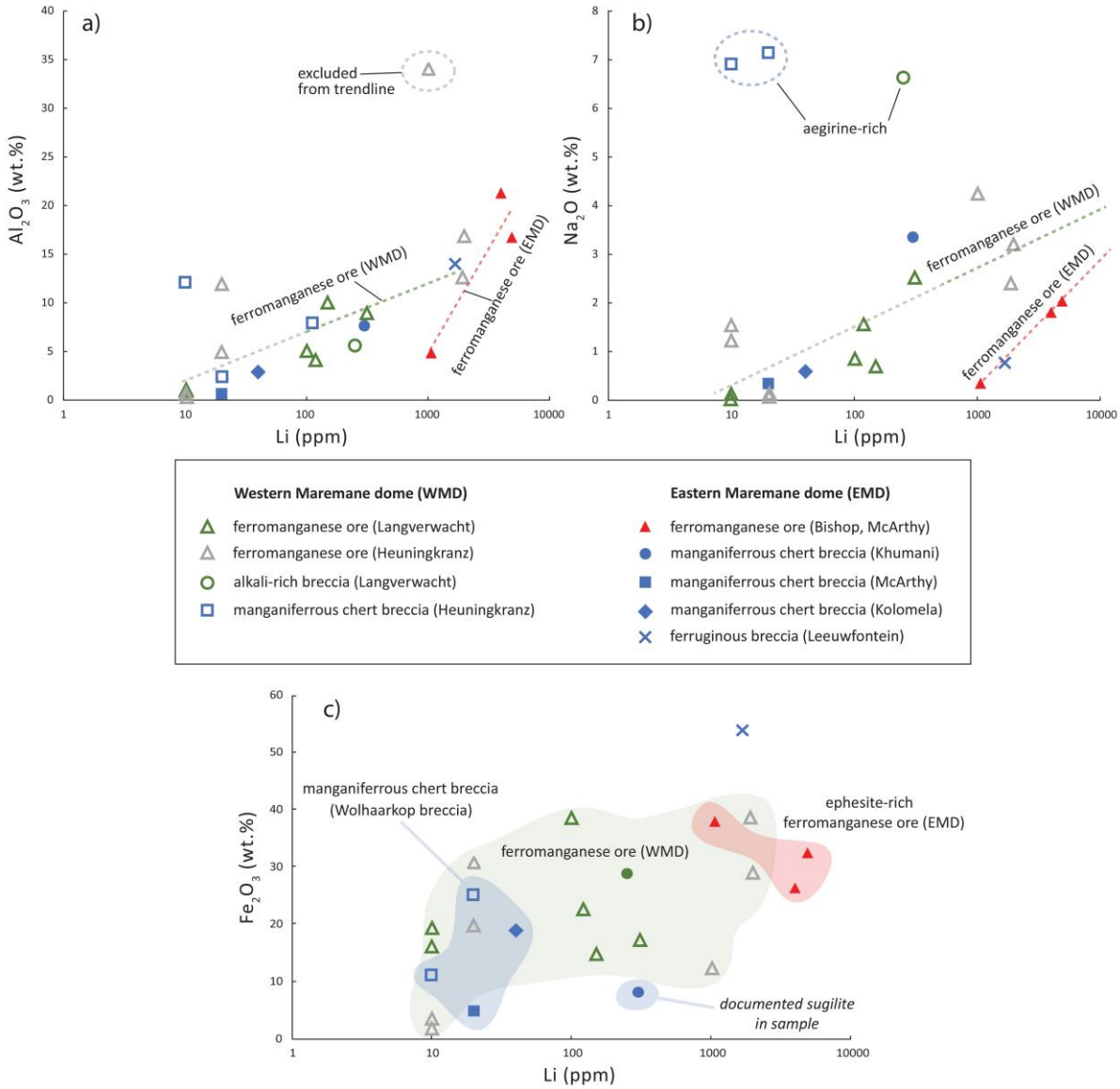

Figure 10. (a & b) Al_2O_3 and Na_2O versus Li semi-log plots showing moderate positive correlations, induced mainly by the presence of mica and/or other silicates in the ore. c) Fe_2O_3 versus Li plot displays higher Li concentrations in the more ''ferruginous'' manganese ore types, most likely due to higher content of micas in these ores. Wolhaarkop breccia is mentioned as manganiferous chert breccia here.

controlled only by few samples in the WMD ores. An outlier that has been purposely left out of the trendline calculation in Figure 10a, probably reflects the presence of other minerals apart from micas controlling aluminum concentration, such as banalsite ($BaNa_2Al_4Si_4O_{16}$) which is ubiquitous in this sample. Moreover, high Na_2O values (ca. 7 wt. %) exhibited by outliers in Figure 20b are the result of aegirine abundance and not of Na-bearing micas such as paragonite, therefore mineralogical control on low Li concentrations in these samples is obscured.

The different plots agree with petrographic observations and the well-established view that Li in sedimentary environments is concentrated in the clay-mica fraction of shales, the former being important carriers of many minor and trace elements including Li, F, Rb, Cs, Nb, Ta, etc. (Deer et al; 2003, Teng et al; 2004). The above results lead us to suggest that the elevated Li concentrations are chiefly controlled by micas and specifically ephesite in the EMD ores and other mica and/or silicates in the ferromanganese ores of WMD where no Li-bearing species have been reported so far. Of course, it cannot be ruled out that other phases or unidentified silicates partly control the measured Li concentrations. Excluding the possible presence of more unique species such as sugilite and norrishite seen in the KMF, amphiboles commonly host appreciable amounts of Li (Hawthorne et al; 1994). Rare Li-bearing members of this group (for e.g., leakeite, kornite) have been reported from the KMF (Gnos et al; 2003) and other manganese districts with high alkali content such as Hoskins mine, Australia (Hawthorne et al; 1995). Another mineral containing abundant Li is lithiophorite, which has been previously reported to be abundant in the EMD ores but at least in the studied samples has been only identified as an accessory oxide phase.

The most plausible scenario though, it that Li is primarily associated with silicate minerals, something corroborated by many studies in shales showing that structurally bound Li in silicates accounts for 75-91 wt. % of total Li (Phan et al; 2016). Fe_2O_3 plotted against Li illustrates nicely that Li concentration is generally higher in the manganese ore-types with higher hematite content which probably reflects and supports a higher abundance of clays in these ores (Figure 10c). Presuming that Li is chiefly hosted by micas in the WMD ferromanganese ores, the question arises then of how Li-rich are these micas, which are shown to be members of the muscovite-paragonite solution (Fairey et al; 2019, see also chapter 5), and furthermore what is their modal abundance or in other words if they can account for the measured whole-rock lithium values reaching up to ~0.2 wt.%.

To explore this concept further, we attempt to calculate the proportion and lithium content of muscovite-paragonite in these ores based on measured bulk rock Li concentrations. Despite the required assumptions and resulting limitations, this procedure can still provide crude estimates that can prove invaluable in origin identification of these

minerals. The varying amounts of Li (from min to max) that can be accommodated by a Li-bearing mineral with a muscovite structure have to be determined in the first place and pose our first major assumption. The second limitation is that in samples displaying high Li and sodium and low potassium, i.e., where paragonite is seemingly the primary host of Li, its proportion is difficult to accurately estimate. As expected, this is due to the presence of other Na-bearing phases in the samples, such as aegirine and is further indicated by the fact that calculations based on sodium concentration result in silica and aluminum deficits of ca. 1 wt. % and between 5 and 10 wt. % respectively. Consequently, any estimate of mica percentage can be solely based on aluminum.

The greatest amount of Li that can substitute for Al after necessary layer-charge rearrangements, i.e., Al decrease, increase in Si and octahedral occupancy in order to produce a rational theoretical formula for muscovite has been shown to be around 1.85 wt.% LiO_2, which is equivalent to 0.5 octahedral positions in the formula (Foster; 1960). From the relatively few published studies on Li-bearing muscovite that were considered, it seems that this mineral is hardly ever so Li-rich. Brigatti et al (2001) provide EMPA analyses of Li-containing muscovite from granitic pegmatites that range between 0.03 and 0.37 atoms p.f.u. Li (0.11 to 1.32 wt. % LiO_2) and further present possible substitution mechanisms for Li which indicate deviation of muscovite structure from its ideal dioctahedral character. Ferroan muscovite and phlogopite from another large pegmatite province show similar ranges between 0.01 and 0.38 Li atoms p.f.u. (Rosing-Schow et al; 2018). In yet another case, micas hydrothermally enriched in Li and hosted by granite exhibit much lower Li content in their formula (0.04 - 0.1 atoms p.f.u.) whereas coexisting biotite contains consistently more Li (up to 0.3). In view of the above, two muscovite formulas were chosen for our calculations, one with 0.03 octahedral Li representing a more ‘common’ occurrence and one with 0.37 portraying an ‘extremely Li-rich’ muscovite, that could be virtually found only in pegmatites. One out of the three samples with the highest Li concentration (1010, 1910 and 1990 ppm) in the WMD ferromanganese ore was discarded since aluminum in this sample is clearly shared by more than one phases. After assigning all potassium and corresponding Li to muscovite, paragonite was then calculated in accordance to the remaining aluminum.

The considered scenarios are the following: i) Assuming a chemistry for the gangue micas similar to that of low lithium-micas in pegmatites hosting 0.03 wt.% (300 ppm) Li, then the studied samples contain approximately between 3 and 6 wt. % muscovite and between 18 and 28 wt. % paragonite, all together accommodating total Li ranging between 93 and 124 ppm. There is ca. 1800 ppm of remaining Li as output from the above calculation though, which renders scenario one improbable. ii) In case that our micas are very rich in Li (0.37 wt. % or 3700 ppm Li) as in pegmatite districts, then muscovite and paragonite ranges are ca. 3-5 and 23-35 wt. % respectively and can host 2011 and 1510 ppm of Li, values not far from the measured ones. iii) Even greater Li values, like the theoretical estimates of Foster (0.5 wt. %) for the initial muscovite-paragonite results in Li deficits and/or very high mica percentage in the samples and can thus be regarded unrealistic. iv) The modal abundance of ephesite in the EMD ferromanganese is more reliably estimated to be ca. 38 wt. % at Bishop (sample BSH89) and ca. 7 wt. % at McCarthy (sample MWA) based on both Li or Na concentrations. A surplus of 276 ppm Li seen in the latter sample reflects the presence of lithiophorite, something further confirmed by petrographic analysis.

From all above considerations and accepting the inevitable sampling bias, it can be surmised that the proportion of micas in the WMD ferromanganese ore can range greatly from 26 to 40 wt. % whereas Li accommodated by their structure is on the high end of possible values, i.e., 0.37 wt. %. Consequently, these micas are informally defined as Li-rich muscovite-paragonite which is a solid indication that hydrothermal alteration instead of depositional/diagenetic processes are more likely to have been the genetic mechanism of formation for these minerals. Lithium content in any sedimentary rock is controlled by its detrital sources, processes of weathering and transportation/sedimentation which are known to increase total Li content (Rudnick et al; 2004), but also by post-depositional alteration processes (Teng et al; 2007). Increased Li concentrations in shales for example have been explained by circulation of Li-enriched pore fluids derived by alteration of volcanics (Phan et al; 2016). Micas containing Li and showing replacement textures within altered zones of granitic rocks are also regarded products of secondary origin (Konings et al; 1988). Hydrothermal replacement and Li-introduction in micas is also seen in zinnwaldite and lepidolite, chief Li-bearing components of pegmatites, that can also form as metasomatic

products of biotite (Cerný and Burt; 1984). It is thus inferred that Li uptake in the micas of WMD ores occurred via metasomatic replacement of prior clays similarly to ephesite (see also section 6.2), something that is further corroborated by isotopic characteristics of micas (chapter 5) and a series of other evidence from the same deposits.

In regard to the ephesite-rich ferromanganese ore in the EMD, the above presented calculations can be extended to the available whole-rock geochemical data from the mines of Paling, Gloucester, Lohatla and Bishop (Gutzmer and Beukes; 1996a) in order to get a rough estimate of ephesite and consequently Li concentrations. Much like our study, the previous authors did not present any other significant source of sodium in these ores other than ephesite, whereas mentions of aegirine and albite are restricted to the localities of Sishen and Mokaning (De Villiers; 1945a). Negligible control on sodium in these ores can be maybe derive from oxides resulting from recent supergene overprint. Nevertheless, if whole-rock sodium is assigned exclusively to ephesite and scenario (ii) is regarded (see above), then it can be surmised that the ores contain on average ca .9 % ephesite and up to 59 % in certain samples, which translates to a crude suggestion for about 1100 ppm of Li (up to 7100 ppm). Lithiophorite, has been also reported to be abundant in these ores, although scarce in the studied samples. Nevertheless, these results in conjunction with petrographic observations imply that ephesite is not a minor constituent but instead particularly widespread in the aforementioned localities to the degree that its economic lithium potential should be regarded. The fact that these deposits are readily available through surface mining and that Li-rich clay minerals such hectorite [$Na_{0.3}(Mg,Li)_3Si_4O_{10}(OH)_2$)] are currently considered as possible important sources of lithium in the future (e.g., Evans; 2014), attest to a reexamination of the PMF deposits with respect to their Li content and Li sources in the wider metallogenic province.

A plot that can be particularly helpful in visualizing Li-bearing micas and has been used in genetic studies of pegmatites is that by Tischendorf et al (2001a) shown in Figure 11. This classification diagram requires measured Li values, for example from mineral separates by ICP-ES or in situ laser-ablation analyses. Since only EDS analyses are available here, Li is not considered for all plotted dioctahedral micas apart from ephesite, for which Li is calculated

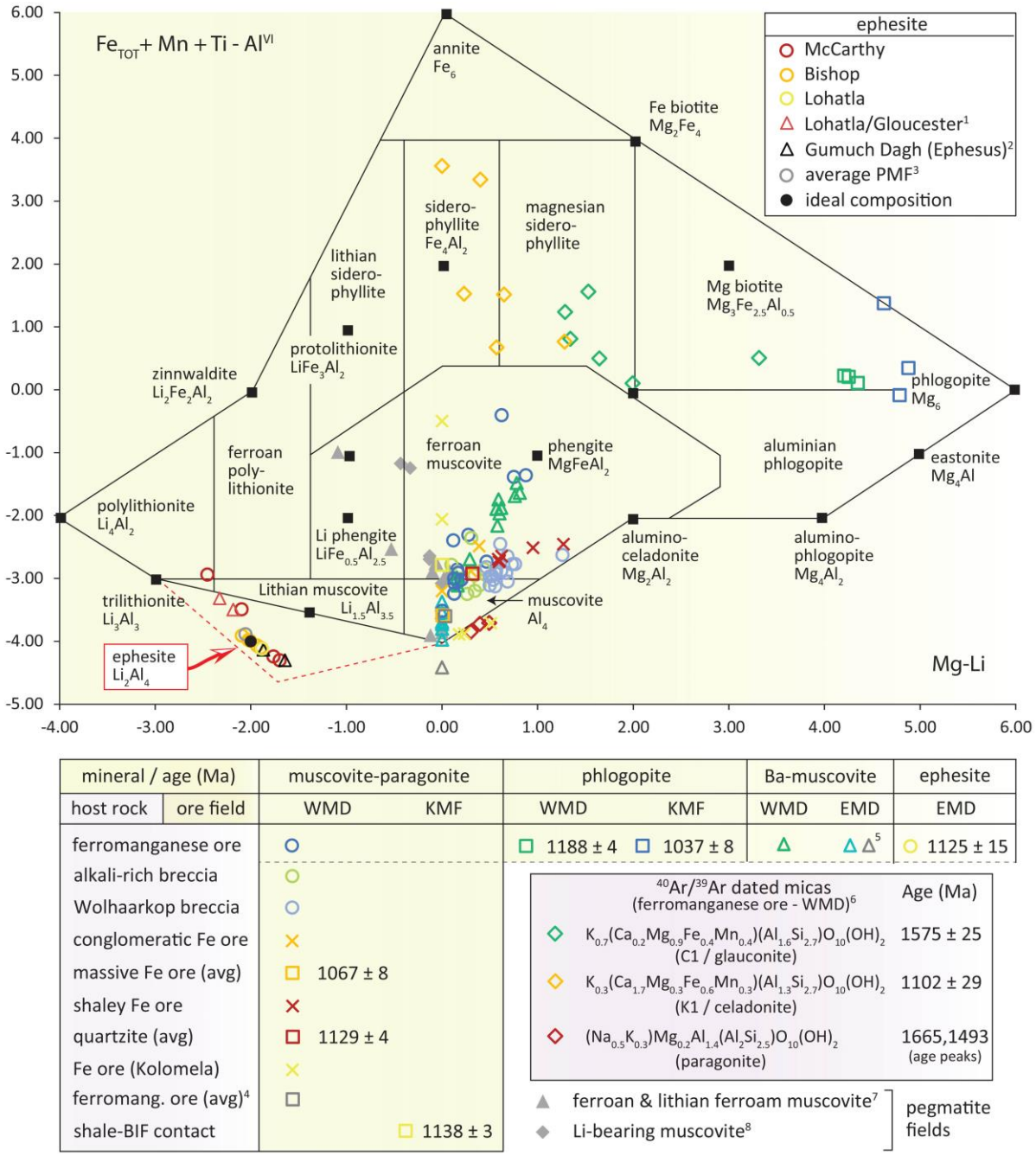

mineral / age (Ma)		muscovite-paragonite		phlogopite		Ba-muscovite		ephesite
host rock	ore field	WMD	KMF	WMD	KMF	WMD	EMD	EMD
ferromanganese ore		○		□ 1188 ± 4	□ 1037 ± 8	△	△△[5]	○ 1125 ± 15
alkali-rich breccia		○						
Wolhaarkop breccia		○						
conglomeratic Fe ore		×						
massive Fe ore (avg)		□ 1067 ± 8						
shaley Fe ore		×						
quartzite (avg)		□ 1129 ± 4						
Fe ore (Kolomela)		×						
ferromang. ore (avg)[4]		□						
shale-BIF contact			□ 1138 ± 3					

^{40}Ar/^{39}Ar dated micas (ferromanganese ore - WMD)[6]	Age (Ma)
$K_{0.7}(Ca_{0.2}Mg_{0.9}Fe_{0.4}Mn_{0.4})(Al_{1.6}Si_{2.7})O_{10}(OH)_2$ (C1 / glauconite)	1575 ± 25
$K_{0.3}(Ca_{1.7}Mg_{0.3}Fe_{0.6}Mn_{0.3})(Al_{1.3}Si_{2.7})O_{10}(OH)_2$ (K1 / celadonite)	1102 ± 29
$(Na_{0.5}K_{0.3})Mg_{0.2}Al_{1.4}(Al_2Si_{2.5})O_{10}(OH)_2$ (paragonite)	1665,1493 (age peaks)

▲ ferroan & lithian ferroam muscovite[7]
◆ Li-bearing muscovite[8]
pegmatite fields

Figure 11. Classification diagram of mica after Tischendorf et al (2001) along with Ar-Ar geochronological data from mica and silicates contained in the KMF and PMF. Dioctahedral micas are plotted with Li assumed to be zero but since they are shown to host significant amount of Li (see text), data points in the muscovite field would ideally move to the left and partly overlap with Li-bearing muscovite from pegmatite districts. Li content of ephesite is calculated from its formula using measured EDS data and a new field is created (dotted line) to include its composition. References: 1: Gutzmer and Beukes; 1997b, 2: Schaller et al; 1967, 3: Rosing-Schow et al; 2018, 4: Konings et al; 1988. Mineral EDS analyses and ^{40}Ar/^{39}Ar ages are from chapters 2, 4 and 5.

from its mineral formula using EDS data. The following empirical equation [Li_2O= (0.289 x SiO_2) - 9.658] recommended by Tischendorf et al (2001a) is used to calculate LiO_2 in trioctahedral

micas. Despite limitations, this plot along with available $^{40}Ar/^{39}$ ages from micas in the PMF and KMF (chapters 2, 4 and 5) still allow visual comparisons between minerals from different localities and lithofacies.

As indicated in Figure 11, muscovite-paragonite data expected to host significant Li, would move towards the left of the diagram if Li is indeed measured and considered in these phases. Nevertheless, most mica plot in the muscovite and ferroan muscovite fields and partly overlap with Li-bearing muscovite from pegmatites. Ferrous compositions seem to be associated with the ferromanganese and iron ores. Unidentified silicates/micas K1 and C1 (showing resemblance to celadonite/glauconite, see also chapter 5, section 5.2.2) plotted in the siderophyllite and Mg-biotite fields may not be accurate but nevertheless highlight the comparatively higher content of iron and magnesium in these phases. Ephesite from this study (see next section) gives an $^{40}Ar/^{39}Ar$ age (1125 ± 12 Ma) that is very close to that of hydrothermal muscovite (1130 ± 4 Ma), as well as to the age of the unidentified silicate K1 (1102 ± 30 Ma) hosted by ferromanganese ore in the WMD, the latter hosted by a sample that has also preserved older relict mica/silicate $^{40}Ar/^{39}Ar$ ages. The remarkable age similarity between ephesite (1125 ± 12 Ma) and hydrothermal muscovite associated with barite from the KMF (1138 ± 3 Ma) should be also pointed out and emphasizes possible derivation from fluids of related origin. The unusual chemistry of ephesite (further discussed in section 6.3) is accentuated in this plot, it showing the lowest Li to Al ratio among all Li-bearing micas and furthermore being very Li-rich. A new field is drawn here (dotted line) to include its composition from different localities. Overall, it is suggested that a much larger data set, one with preferably more homogeneous samples, is required to obtain better relationships between whole-rock lithium and mineralogy and gain deeper and meaningful insights. Nonetheless, this first attempt presented here shows much promise.

6.2 Interpretation of $^{40}Ar/^{39}Ar$ data and origin of ephesite

A major difficulty in dating ephesite, $Na(LiAl_2)Al_2Si_2O_{10}(OH)_2$, arises from its very low and variable potassium content, it being unusually rich instead in Na and Li. Potassium substitutions in the structure of ephesite are minor and were note picked up by EDS analyses during petrographic investigation but concentrations of up to 0.3 wt. % K_2O have been

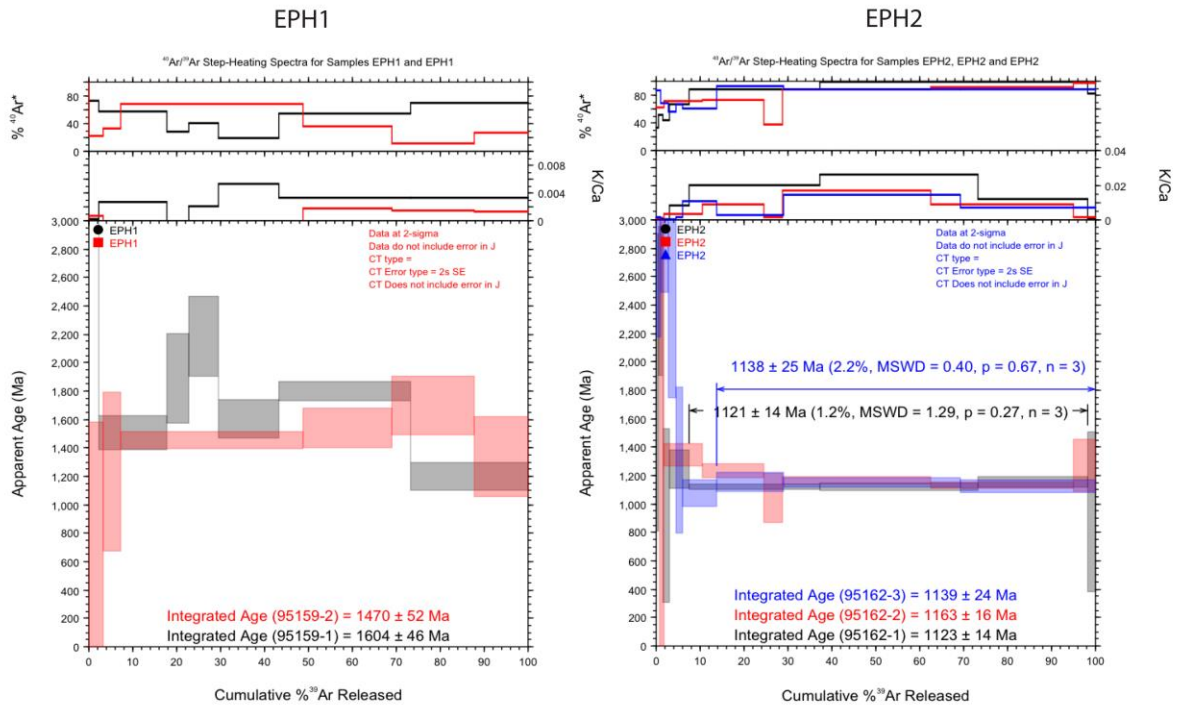

Figure 12. $^{40}Ar/^{39}Ar$ age spectra plots for ephesite samples (EPH1 & EPH2) deriving from five multigrain aliquots. Each experiment was comprised of 7-8 steps. Only integrated ages were generated from sample EPH1. Two of the three aliquots from sample EPH2 produced plateaus, which were comprised of ca. 85% and 93 % ^{39}Ar released. Saddle-like shapes and old low-T steps are taken as evidence of an extraneous argon component, potentially from a K-bearing precursor in the protore that was not fully degassed during ephesite formation. All ages are reported at 2σ.

reported from large ephesite crystals extracted from the Glosam Mine (Gutzmer and Beukes 1997b). Despite the low potassium contents, the different crystal fragments used in our analysis yielded reliable age plateaus from generally discordant age spectra (Figure 12) that provide invaluable information on the origin of ephesite.

The ephesite crystal pocket (EPH 2) in the manganese ore from the Lohatla mine yields a plateau age of 1125 ± 25 Ma (2σ, MSWD = 1,42), consistent with an isochron age 1127 ± 21 Ma (2σ, MSWD = 1,7). This age derives from two out of three analyses of multigrain aliquots and can be regarded either as the cooling or crystallization age of the mica. The relationship between the obtained ephesite age and gangue mineralization ages from the manganese ore fields of the Northern Cape (ca. 1188 to 920 Ma: chapters 2-5) and the ca. 1.2-1.0 Ga Namaqua-Natal orogeny is evident. Given that postulated temperatures in the area are generally regarded to have been well below 300°C and closure temperatures for white mica (e.g., Hames and Bowring; 1994), ephesite is likely to reflect the timing of crystallization very

closely. It is noted thought that localized regimes of higher maximum temperatures may have been also present in the Eastern Maremane dome (EMD) for a series of reasons discussed below (section 6.6).

Ephesite from the Glosam mine (EPH 1) yields much less precise integrated ages of 1470 ± 50 Ma (2σ) and 1604 ± 46 Ma (2σ) from analyses on two different aliquots, which are on average ca. 400 Ma older than that of Lohatla ephesite. These high apparent ages derive from discordant step-heating spectra with different shapes, one somewhat reminiscent of a saddle-like shape and a second more irregular spectrum characterized by significant variations in apparent age during the successive steps (Figure 12). Both saddle-like shapes (characteristic of extraneous ^{40}Ar: Kelley; 2002) and the anomalously old low-temperature steps seen in the majority of obtained spectra from both samples indicate that the measured $^{40}Ar/^{39}Ar$ ages ranging between ca. 1400 and 1600 Ma are most likely older than the true age of ephesite from the Glosam mine. Therefore, the former ages are interpreted as the result of extraneous ^{40}Ar. The possibility that some potassium is carried in inclusions or contaminants in the mineral separate can be excluded on the basis of detailed SEM investigation, which then leaves us with the scenario of extraneous ^{40}Ar having derived either from outside the system (i.e., circulating fluids) or internally, from a K-bearing precursor that was not fully degassed during ephesite formation. We favor the latter hypothesis and suggest that crystal-lattice-hosted inherited ^{40}Ar was incorporated in Glosam ephesite from a former phase in the host rock and was distributed inhomogeneously within the measured ephesite grains, thus producing the obtained step-heating spectra. The similarity of the 'old' age component in sample EPH1 (1600-1400 Ma) with older pre-Namaqua age signals from the WMD deposits (1575 ± 25 Ma) (Figure 11) could be an indication of previous related thermal events other than that of the controversial Kheis orogeny (ca. 1.9-1.8 Ga: e.g., Cornell et al; 1998, Moen; 1999) and calls for further investigation.

Considering the geology of the area and the prevailing ore genetic models, ephesite formation could have occurred by recrystallization of mostly detrital clays and earlier precipitated Al-Si components, originally concentrated in the metalliferous karst systems/continental lakes or otherwise, by metasomatic reactions of clay material within the

overlying Mapedi/Gamagara shales, the latter of which also comprise aluminous units (Gutzmer and Beukes 1997b, Schalkwyk; 2005) that satisfy the need for high amounts of aluminum present during ephesite formation (see also sections 6.3 & 6.4). Ephesite is the sodium- and lithium-rich analogue of margarite [$CaAl_2(Al_2Si_2)O_{10}(OH)_2$], therefore its formation expectedly requires special physical and compositional conditions. Margarite is commonly found in metamorphosed emery deposits (Deer et al; 1992) but it has been reported as an important rock-forming component from black shales that have undergone low-grade greenschist metamorphism (Frey and Niggli; 1972). The hypothesized reaction forming margarite in the above setting is that between pyrophyllite and calcite.

In an analogous way, the extraneous 'old' component in ephesite revealed by the $^{40}Ar/^{39}Ar$ data may indicate transformation of a silicate precursor to ephesite by addition of sodium and lithium, although direct precipitation from solution almost certainly occurs concurrently. The role of lithium during this reaction is regarded to be critical since valence compensation for the substitution of Ca by Na in margarite is possibly achieved in ephesite by introduction of Li in octahedral co-ordination (Schaller et al; 1967). What poses a significant incongruity with the simple metamorphic reaction of the above example, is that excessive requirement for sodium and lithium for ephesite formation rule out the possibility that these elements have been inherited from the postulated lateritic depositional environment of the ores but on the contrary, must have been introduced from an external source. Moreover, the Si/Al ratio in ephesite (i.e., 1/2), implies either a very low silica protolith or silica being leached out of the system. Silica depletion may occur in karst bauxites, especially the ones forming in synclines (Yang et al; 2017), but desilication processes associated with formation of margarite can also occur by metasomatic processes within amphibolite-facies metapelitic country rocks in response to contact metamorphism (Bucher et al; 2005). In the former example, paragonite and margarite are formed by progressive loss of SiO_2 from plagioclase and subsequent late-stage enrichment in Al_2O_3 leads to the production of a biotite-corundum-margarite rich rock. The nature of the protolith and possible involvement of shales and/or mobilization of aluminum are matters to which we return in a later section.

Regardless of the exact reactions taking place within the host rock, textural evidence presented earlier corroborate the geochronological results that ephesite in the ferromanganese ore can be regarded as of hydrothermal metasomatic origin, linked to the regional Namaqua tectono-thermal event. Results from this study are very encouraging regarding geochronology for this mica and emphasize that its suitability for $^{40}Ar/^{39}Ar$ dating is associated with good knowledge of the geological framework and temperatures of formation. Furthermore, low and fluctuating potassium content may be of a little consequence for dating. Our geochronological data also demonstrate that the recent supergene overprint associated with manganese oxide formation in these ores has not isotopically disturbed ephesite. The epigenetic origin of this phase is further supported by a previous attempt using step-heating $^{40}Ar/^{39}Ar$, which however failed to provide reliable plateau or integrated ages. Nevertheless, unpublished data from Gutzmer and Beukes (1998; technical report), led the researchers to tentatively infer an age of close to 1000 Ma, which is consistent with the age of the Namaqua orogeny and alkali enrichment in the Northern Cape, similar to our results. The implications of the origin of ephesite on current models is discussed later.

6.3 The unusual conditions for ephesite formation

Ephesite, $Na(LiAl_2)Al_2Si_2O_{10}(OH)_2$, is a rare sodium-lithium trioctahedral mica with only a handful of reported natural occurrences worldwide. Its wide presence in the studied ores within the aforementioned framework of documented and speculated Li-enrichment in certain ore localities is puzzling and intriguing. The scant natural occurrences of this mineral are confined on the whole to aluminum-rich and silica-deficient bulk compositions. In this regard, the first reported occurrence co-existing with corundum derives from the emery deposits of Gumuch-Dagh near Ephesus Turkey (Smith; 1851). The type-locality silicate exhibits a Si/Al ratio of 1/2 and high sodium content but differs from Postmasburg ephesite in the sense that it is described as of pearly white colour and hosts additionally CaO (up to 2.5 wt.%) and minor Fe. According to its lithium content (0.12-0.44 wt. %), the original material from Ephesus should be regarded as an ephesite but since it has not been reexamined by modern methods and in line with later reports, it is also likely that it represents a member closer to margarite.

Furthermore, confinement of natural ephesite to Al-rich environments is further supported by the paragenesis ephesite-corundum-chrysoberyl ($BeAl_2O_4$) described from greisen (Govorov; 1958), a granitic rock hydrothermally altered during its cooling by fluids containing fluorine, boron and lithium, elements that are being accommodated by Li-micas (e.g., zinnwaldite, lepidolite), topaz, tourmaline and fluorite (Pirajno; 1992). Li-mica greisens are usually peraluminous rocks (up to ca. 35 wt. % Al_2O_3) and depleted in silica (René; 2018). In yet another case, the assemblage ephesite-natrolite ($Na_2Al_2Si_3O_{10}2H_2O$)-analcime ($NaAlSi_2O_6H_2O$) has been observed as an alteration product of a nepheline-syenite pegmatite (Drits and Semenov; 1975), a rock that is likewise deficient in quartz. Besides reported natural occurrences, an ephesite-like sodium mica has been synthesized with a mixture of sodium tetraborate and topaz [$Al_2SiO_4(F,OH)_2$] at temperatures between 350 and 570°C, above which albite and corundum formed (Franke et al; 1982). The absence of lithium in the reactants emphasizes the paramount importance of a high Al/Si ratio in the formation of this mica and suggests that low lithium activity in the fluid can be compensated by introduction of aluminum in the octahedral layer. In similar fashion, thermodynamic analysis of phase relations of ephesite in the silica saturated system $NaAlSiO_4 – LiAlSiO_4 – Al_2O_3 – SiO_2 – H_2O$ showed that quartz + ephesite is always unstable down to at least 300°C and the authors concluded that the most distinctive aspect of ephesite is that it appears only in quart-undersaturated and aluminum-rich assemblages (Chaterjee and Warhus; 1984).

In light of the above, it is reasonably postulated that the primary bulk composition of the EMD ores in which ephesite develops during the Namaqua orogeny should have been anomalously high in aluminum since hydrothermal enrichment of this element would be generally considered difficult, though not improbable, due to its low geochemical mobility. Current ore genetic models do not directly address this geochemical signature but propose that sedimentary bedding textures occurred through accumulation of manganese-rich sediments in a surficial, fresh-water karst environment which gradually shifted into a depositional setting for aluminous and ferruginous shales. The silica-deficient criterion may be met if ones considers that chemical weathering of carbonate rocks generally provides minor silica and further still, if the chert-free dolomite of the Reivilo Formation was indeed the main host lithology as proposed by Gutzmer and Beukes (1996a).

The very low Si/Al ratios (<1) though, which are one of the most distinctive characteristics of these ores, are related to the presence of low silica (2.9 ± 1.6 wt.%) and high but variable aluminum (10 ± 7.1 wt.%, up to 28.6) concentrations, something that has not been sufficiently emphasized by the former authors. Similarly, little effort has been made to relate Postmasburg manganese ores to karstic bauxite deposits despite their suggested similarities as concerns the geological setting and comparable formation mechanisms. On the whole, dolomite dissolution and bauxitization are processes that could have been at play during ore formation and at first glance may explain existing geochemical signals and geological features. However, such concept should also take into account findings in the current and other recent studies which point towards a rather more complex origin involving regional tectonics and hydrothermal input. In the following section, the possibility of a bauxitic origin is being scrutinized and apparent inconsistencies are highlighted.

6.4 A bauxitic origin of primary Fe-Mn mineralization?

Bauxitic-lateritic horizons that occur in karst cavities are classified as karst bauxite and generally consist of the aluminum oxides and hydroxides gibbsite, boehmite and diaspore, common clays (e.g., illite, kaolinite) and hematite or goethite (Grubb, 1971, Bárdossy; 1982, Robb; 2004). The occurrence of the ferromanganese Postmasburg ores in an erosional setting and in particular their association with an unconformity paleosurface as emphasized by Gutzmer and Beukes (1996a), seems to overlap with the above definition in terms of general geological setting. In contrast to lateritic bauxites though, karst bauxites are not simple alteration products of exposed rock by surficial weathering but instead can be reworked chemical precipitates originally accumulated in karst solution depressions within carbonate plateaus, which can act as sediment traps for exogenous material. In this respect, introduced Al-bearing clays such as bentonitic volcanic ash can be later leached to aluminum oxide as seen for example in some Jamaican deposits (Clarke; 1966), in this way controlling bauxite composition, especially if the primary carbonate stratigraphy being leached is not particularly argillaceous. Therefore, elemental transportation could be essential in generating the geochemical signatures of the considered open-karst ores of the study area and thus their

composition should not be necessarily restricted to leaching of discrete horizons of Campbellrand dolomite.

It is worth pointing out that interactions between carbonates and karst bauxites during formation of the latter are not entirely known despite abundant research on several occurrences (e.g., MacLean et al; 1997, Mongelli; 2002) and important aspects such as the major control of terrain and elevation on aluminum, iron content and orebody thickness have been only recently made known (Yang et al; 2017). According to the latter study for example, variations in topography and drainage patterns could explain large difference in thickness (between 1 and 25 metres) observed in the EMD ferromanganese ores (Western Belt) if a karst bauxite model is invoked for primary mineralization. Regarding manganese ores associated with palaeokarsts, mechanisms of leaching of ore components show affinity with both those involving surficial meteoric waters in supergene environments where bauxite deposits are developed (Patterson; 1971) but also with processes tied with subsurface waters of elevated temperatures (100-200^{o}C) and increased activity; not differing from hydrothermal solutions in many aspects. In this context, karst manganese ores can be also characterized as having a relatively deep epigenetic nature owing to the high dissolution and migration properties of associated fluids (Varentsov; 1996).

Therefore, the envisaged setting for the Postmasburg ores in current models can be seen as one where ore components may be also extracted from other country rocks such as iron-formation, albeit primary control from Mn-bearing dolomite on composition. At the same time, clastic material filling in the karst system and subsequent reworking during sedimentation and lithification may have been likewise important for the aluminum content of the ores. An interplay of hydrothermal, sedimentary and weathering processes upon the karst surface during periodically repeated events of dissolution, break-up and re-sedimentation is thus a more likely scenario for ore accumulation, similarly to other karst deposits where interaction between oxidized alkaline water and reduced acidic fluids released from the weathering of clays drives the coevolution of bauxites and karst (e.g., Yu et al; 2016). Furthermore, depending on the timing of ore formation and/or post-depositional reworking, material from the base of the overlying Gamagara Formation and in particular the

aluminous shale of the Doornfontein Member could have also merged with the orebodies. The origin of aluminum in the aforementioned rocks is also elusive and their formation controversial.

Highly aluminous white shale beds are developed in the study area along contacts between red shales of the Sishen Member and black pyritic shales of the Doornfontein Member. These shales do not only contain high quantities of clays/micas such as pyrophyllite, kaolinite and muscovite/illite but also ubiquitous diaspore and oxides such as anatase, an assemblage which led Schalkwyk (2005) to suggest derivation from primary aluminous clays that have experienced low-grade metamorphism. The same mineralogical assemblage in these shales though has been described as replacing granular chert and interpreted as the result of hydrothermal fluid flow capable of mobilizing Al and Ti on the basis of geochemical, textural and field evidence (Cousins; 2016). The diagnostic geochemical feature of these shales is the enriched Al_2O_3 and TiO_2 values (average of ca. 1.8 times PAAS) followed by depletion in all other major elements. Despite of how aluminum-rich (avg. Al_2O_3 = 33.88 wt.%) these shales may be, their Si/Al ratio (1.42) is not below 1, as in the studied ores. Although it seems sensible to invoke a pre-existing highly aluminous protolith/protore in order to explain ephesite formation, synchronous processes of desilication and aluminum enrichment in both the Fe-Mn protolith and the overlying shales due to metasomatism associated with the Namaqua overprint event is also a possibility, which however remains speculative at the moment.

On the assumption that karstic bauxite development on certain units of the Campbellrand carbonates (for e.g., Reivilo Formation) was the chief control mechanism of ore formation, then geochemistry of the aluminum-rich ferromanganese and bixbyitic ores may be plotted in classification diagrams for bauxite deposits in an attempt to gain insight into the palaeoenvironment. As seen in Figure 13a, most available samples fall within the ferrite, bauxite ferrite and lesser laterite fields, overall highlighting the concurrent iron-rich nature of these ores. However, the above classification is based on mineralogy of bauxites (Aleva; 1994) which is entirely different than that of the EMD deposits, the latter having further experienced a metamorphic/hydrothermal overprint. Nevertheless, lateritization over bauxitization is also

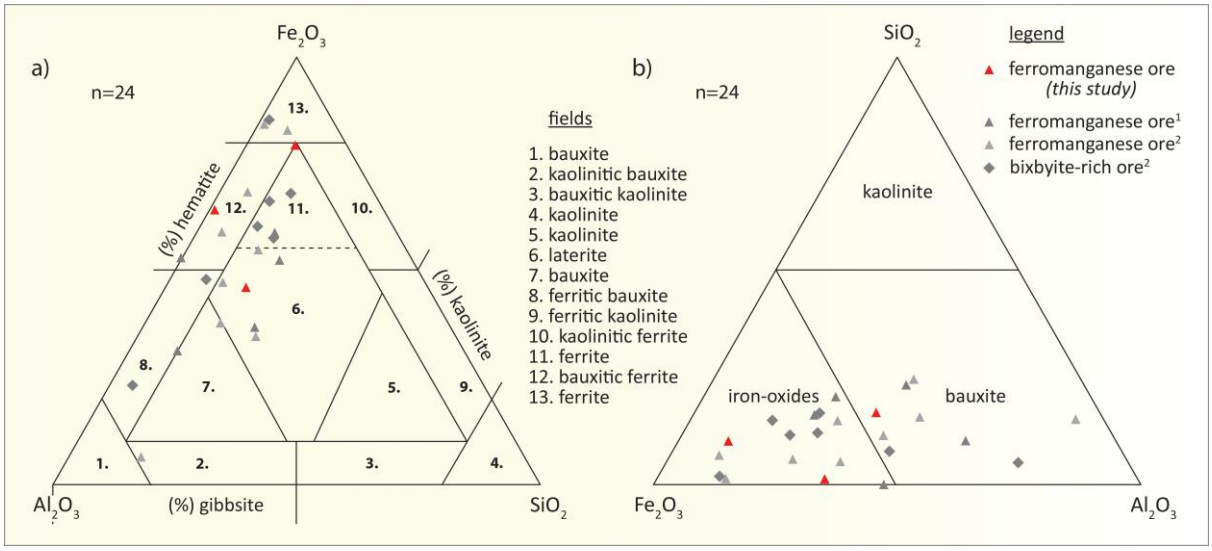

Figure 13. Plots of the PMF ferromanganese deposits of the type locality (EMD) in (a) Fe_2O_3 - Al_2O_3 - SiO_2 ternary diagram after Aleva (1994) and (b) in a SiO2 - Al_2O_3 - Fe_2O_3 ternary plot after Mutakyahwa et al (2003), both used to classify bauxite deposits. Note the suggested iron-rich character of the protore if such weathering processes are invoked for ore genesis (see also text). References: 1: Thokoa; 2020, 2: Gutzmer and Beukes (1996a).

indicated by the ternary SiO_2 - Al_2O_3 - Fe_2O_3 plots by Mutakyahwa et al; (2003) (Figure 13b), which may further stress that the origin of aluminum in these deposits is not necessarily related to similar processes of bauxite formation seen in carbonates or otherwise that iron was readily available in the original depositional environment or even introduced later on. Absolute iron enrichment in the iron cap of bauxites can reach a maximum of 50-60 wt. % Fe_2O_3 (Valeton; 1972); however, a precursor being much more iron-rich than dolomite would be needed to produce such signals. With respect to the EMD ferromanganese ores, the fact that hematite consistently alternates with manganese on the micro-scale along their whole stratigraphic extent, highlights the high availability of iron in the ore-forming environment.

Probably the most intriguing observation regarding the nature of the protolith derives from recent discoveries of ferromanganese horizons below conglomeratic iron-ore in the wider Kolomela region (WMD ores) (Fairey et al; 2019). These ores are stratigraphically and texturally equivalent to the ones from the type locality. However, compositionally, the characteristic Si/Al ratio of the latter is absent there (Si/Al = 2.16, n = 18: Fairey; 2013, Bursey; 2018), something further reflected in the mineralogy with the absence of ephesite, diaspore and other Al-rich phases and instead the presence of a large suite of Na-, Ba, K- and Ca-rich minerals. It is not easy to reckon if topographic and carbonate lithological differences can

explain this large compositional disparity and a localized accumulation of aluminum-rich residuum under apparently very similar weathering-related mechanisms of formation. This matter requires further investigation but since aluminum is in high concentrations in the overlying shales only in the EMD ores between the two localities, it is suggested that attention should be also directed on the origin of the aluminous shale units, which may be pivotal in understanding mineralization processes.

It should be also noted that spherical to subspherical pisoliths and concretionary masses of generally several millimetres or Ti-bearing oxides, typical in bauxite deposits, are seemingly absent in these ores. In contrast, the much different microconcretions present are seen being overprinted by ephesite and most likely have a different origin, related to diagenetic, metasomatic processes or even point to former oolitic shales (De Villiers; 1944). The high aluminum content of the ores is also denoted by the presence of amesite, which is rather uncommon and characterizes low-grade metamorphic rocks high in aluminum and/or magnesium, hosting also diaspore, diopside, vesuvianite and grossular among other phases (Anthony et al; 1995). Textural and paragenetic observations in this study suggest that its formation is probably related to iron-rich solutions forming hematite in the ore matrix. Several replacement-alteration textures and metasomatic veins, at least on the hand specimen scale, reflect the action of alkali-rich solutions with the protores and since ephesite is invariably associated with the above, these textures signify a certain degree of aluminum mobilization. The latter is supported by previous petrographic observations of abundant fractures filled by ephesite in the coarse-grained manganese ore and ephesite veins protruding in the overlying shales (Gutzmer and Beukes; 1996a). Thick (cm-sized) ephesite bands of probably replacive origin were also observed in this study close to the McCarthy locality. Barian goyazite, which is firstly reported here, also suggests aluminum derivation from former ephesite or diaspore, possibly during a later alteration event.

The presence of diaspore may likewise be related to aluminum mobilization processes. Apart from its association with bixbyite-rich ore, diaspore is regularly seen in assemblages with ephesite and was also noted in this study to contain gamagarite inclusions while being encompassed by ephesite. Diaspore may be a major component of bauxites, metabauxites

and some laterites (e.g., Urai and Feenstra; 2001), but it can be also found as a hydrothermal mineral, for example in alkaline pegmatites with co-existing natrolite (Sunde; 2019), a mineral that appears to be rather common in the WMD. Other examples of hydrothermal diaspore include occurrences with pyrophyllite within clay deposits in New Zealand formed at temperatures above 335^{o} C (Swindale and Hughes; 1968) or diaspore associated with, corundum, topaz, alunite and enclosing APS minerals in the advanced argillic alteration lithocap of a porphyry-epithermal system in Greece (Voudouris; 2014). Diaspore was also identified in the WMD ores in parageneses with hydrothermal Mn-carbonates and Mn-silicates (chapter 5) and moreover, the well-developed diaspore laths seen in the EMD are reminiscent to gem-quality crystals found elsewhere (e.g., Hatipoğlu; 2010) and therefore may have formed as remobilized secondary mineralization of diaspore-bearing rocks. Furthermore, it has been suggested via SEM analysis that diaspore can recrystallize into relatively coarse crystals in a weathering environment and at surface temperatures, contrary to the common belief that temperatures between 200^{o} and 300^{o}C are needed (Keller; 1978). All the above support that the origin of diaspore should not be necessarily limited to a bauxite-laterite ore protolith.

While it may be difficult to assess the primary environment of formation of these ores, the preceding detailed analysis and the solid geochronological evidence for a thermal overprint during a regional tectonic event justify a re-evaluation of the current ore genetic framework, summarized at the end of this study (section 6.7). As noted earlier, one of the key points along with the origin of aluminum, is the unusual contents of Na and particularly Li in the considered protore, both being imperative for ephesite formation. The potential origin of lithium is briefly discussed below.

6.5 Potential sources of lithium (Li)

An evaluation of the obtained whole-rock Li concentration against values from different lithologies in the literature, can potentially throw light on the source of this element and additionally put these ores into perspective in relation to economically viable Li deposits. It has been already noted (section 6.1) that since ephesite is a pervasive phase, the possibility

of finding commercially significant amounts of Li in the EMD ferromanganese ores or even the wider Northern Cape should be further examined.

The lithium content of most sedimentary rocks is very low, ranging from 0.0005 to 0.01 percent and its concentration in the upper continental crust is estimated to be 35 ± 11 ppm (Teng et al; 2004). The highest Li concentration is observed in evolved S-type granites (187 ppm), whereas clastic sediments display variable (28 to 109 ppm) but considerably lower content. On the other hand, Li-bearing granites can occasionally have concentrations of thousands of ppm and pegmatites containing true lithium micas (for e.g., spodumene, lepidolite, zinnwaldite) can host 1-2 wt. & LiO_2, which after mining and beneficiation yields a content of ca. 6-7 wt. % LiO_2 (Kundu et al; 2023). Whole-rock Li values reported here (ca. 1000-5000 ppm Li and up to 11000 ppm) for the EMD ferromanganese ores are in the range of highly enriched rocks associated with pegmatites. However, almost complete lack of igneous rocks in the Northern Cape suggests that Li has been sourced from different lithologies and was concentrated in the alkali-bearing hydrothermal fluids by other means as opposed to commercially important pegmatites.

Lithium is an incompatible element that when released from different source rocks can generally remain dissolved and enrich groundwaters/basinal brines circulating in geothermal systems associated with low-grade metamorphic terranes, oilfields, a buried heat source in sedimentary basins or increased temperature gradient due to burial or tectonics (Vine; 1976, Tomascak et al; 2003, Godfrey et al; 2013, Pfister et al; 2017). These fluids can subsequently interact with wall-rock along the flow path and Li may be taken up by silicate (mostly clay) minerals (Williams and Hervig; 2005, Tomascak et al; 2016) or under the right conditions even precipitate as Li-rich clays or lepidolite. Potentially important sources of Li to brines include high-silica volcanic rocks (felsic vitric tuffs), preexisting evaporites or evaporitic brines and clays or hydrothermally enriched clays (Price et al; 2000, Munk et al; 2016). For example, the former authors have suggested that volcanic tuffs can account for all the Li in the brines in the studied setting.

Identification of the most significant lithium contributor in the Namaqua hydrothermal system is not an easy exercise. Marine carbonates incorporate very little Li from the water from which they precipitate and furthermore, this Li is only slightly isotopically modified (2-4 ‰ lighter) (Marriott et al; 2004, Millot et al; 2010b). Therefore, water-carbonate interaction is unlikely to have played a significant role in enriching the brines. Considering that dissolution of evaporites is most likely responsible for the salinity of the regarded brines, it is reasonable to ponder the possibility that a significant Li component derived also from the same evaporitic source. However, Li is so soluble that will not precipitate by evaporative concentration and will not substitute for sodium and potassium in the common salt minerals. Hence, in a basin with marine evaporites lithium is generally restricted to very low concentrations (Pfister et al; 2017); thus, this source needs to be excluded, unless extremely concentrated marine evaporites existed in the Campbellrand stratigraphy. Contrastingly, nonmarine evaporite deposits (Type II continental evaporites) are believed to represent the most favorable trap for lithium enriched brines, with continental saline lake sequences (lacustrine evaporites, playas) containing hundreds or even thousands of ppm of Li (Smith et al; 1983, Warren; 2006, Araoka et al; 2013). The presence of continental-dominated evaporites in the study areas is highly speculative, but in absence of other propitious candidates providing Li remains a plausible scenario. Requirements for an undrained basin could have been locally and temporally met as the result of regional tectonic uplift and an arid climate, conditions that in all likelihood occurred during the protracted geological history of the Northern Cape. However, it should be also noted that tectonically active areas in contrast to stable cratons are currently regarded to be more prospective for Li brines (Benison and Bowen; 2006, Hacini et al 2008, Munk et al; 2016).

It stands to reason that the temporally and isotopically equivalent (see also section 6.6) Li-bearing sugilite in the KMF may share a common source of Li with ephesite. The same may be true for the fluid system precipitating Li-bearing micas in the WMD ores. One of the chief mineral reservoirs for continentally-derived and structurally bound lithium are silicates and particularly clay minerals, commonly found in shales. Research has shown that exchangeable Li from silicates in shales may be less than 2% of total Li in the whole rock (Phan et al; 2016) and generally Li in exchangeable/interlayer sites has poor affinity to be replaced

by competing cations in the fluid (Starkey; 1982). Therefore, for shales of the Olifantshoek Supergroup to have significantly contributed to the Li budget of the alteration fluids, considerable dissolution of primary minerals must have had occurred. However, ascribing control of Li in ephesite to an extremely Li-rich clay precursor does not explain the origin of Li in the contemporaneous sugilite in the neighboring KMF, where the geological setting rules out the possibility of pristine silicates. Continental weathering is known to lead to preferential incorporation of ^{6}Li in clays and increase of total Li content in clay-rich sediments (Phan et al; 2016). In view of that, accumulation of clays in the presumed carbonate weathering profile during protore formation may have increased Li concentration and Li oxides such as the documented lithiophorite may have locally formed. However, both matters of high Li abundance in different lithologies regionally and the profusion of sugilite in the KMF are not resolved by the former hypothesis. Furthermore, whole-rock analysis of the Gamagara/Mapedi shale from the KMF suggests almost no lithium content.

A means of investigating Li sources is the δ^{7}Li values of the regarded minerals (i.e., mainly ephesite, sugilite, lithiophorite). δ^{7}Li systematics are a sensitive tracer that has been widely used to discern the origin and evolution of groundwaters and basinal brines, weathering of silicate rocks and the effect of temperature on water-rock interactions (Bottomley et al; 1999, Millot et al; 2010, Macpherson et al; 2014, Phan et al; 2016), primarily by measuring water produced from oil and gas-bearing units and lesser whole-rock samples. It is well-recognized that ^{6}Li is preferentially incorporated into secondary minerals in different geological environments (commonly during clay formation) and that dissolution of primary minerals does not induce significant fractionation of Li isotopes (Burton and Vigier; 2012). Any overlap in δ^{7}Li values between ephesite and sugilite will provide evidence for a shared source of Li, while the range of δ^{7}Li values in conjunction with other data may illuminate gangue precipitation processes.

Even though different sources of continentally-derived Li may have contributed to the range of δ^{7}Li values of hydrothermal fluids, greater interaction for example with a terrigenous component may be identified and isotopically distinct sources further determined if future research includes whole rock samples from potential reservoir rocks. To conclude, it is

suggested that Li ultimately derived from an exogenous source, it being most likely Type II continental evaporites, the occurrence of which remains currently unknown. A priority target for further investigation is suggested to be the determination of δ^7Li values from a suite of mineral-specific and whole-rock targets. Furthermore, survey of the ephesite and Li resource estimate in the wider area as well as assessment of the feasibility of commercial extraction are highly recommended.

6.6 Isotopic evidence for regional brines and fluid constraints

The isotope ratios of oxygen and hydrogen ($^{18}O/^{16}O$ and $^{2}H/^{1}H$) hosted by the crystalline structure of diaspore, ephesite and bixbyite depend primarily on the formation temperature and isotopic composition of the fluid from which these minerals formed. Hence, combined study of the isotopic composition of these two elements can perhaps place constraints on the genesis and nature of ephesite mineralization and further allow comparisons with existing relevant isotopic information from the documented regional hydrothermal metasomatic system (chapters 3 and 5).

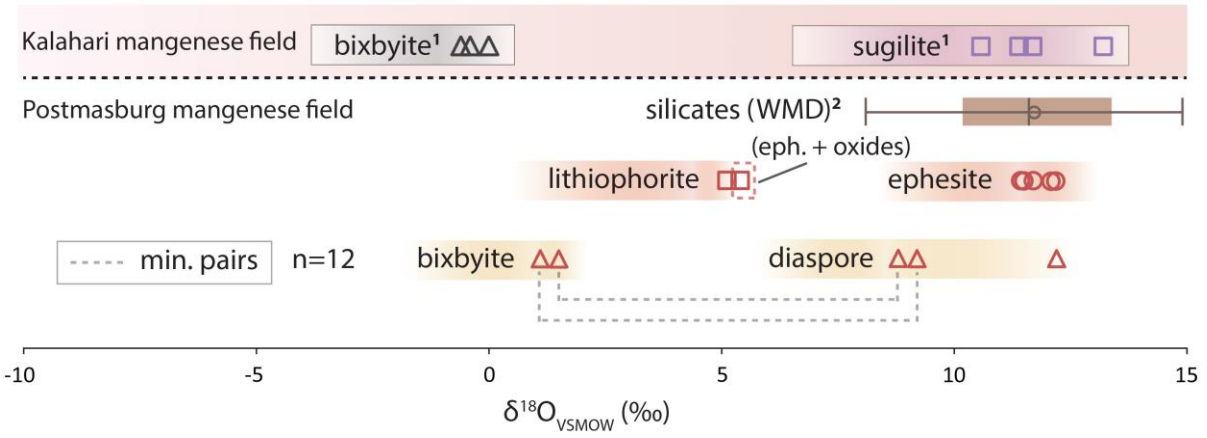

Figure 14. Oxygen isotope compositions of ephesite and oxides from Bishop, Glosam, Lohatla and McCarthy localities. Co-existing phases are connected with dashed line. Noted value within dashed square represents mixed ephesite and lithiophorite from an Al-rich band. Relevant isotopic values from 1: the KMF (sugilite, bixbyite (chapter 3) and 2: the weighted average of silicates gangues from the WMD ferromanganese ores (chapter 5) are shown for reference.

As seen in Figure 14, the inter-site isotopic similarity among the alkali-rich silicates from the KMF and the WMD deposits is expanded in this study to encompass the compositionally equivalent, i.e., sodium-rich, ephesite, but also the somewhat more

isotopically diverse diaspore from two distinct localities in the EMD. Ephesite displays an exceptionally narrow range of $\delta^{18}O$ values between +11.4 and +12.1 ‰ (average = +11.8 ± 0.3 ‰, n=5) which faithfully replicates the weighted average of silicate gangues from the WMD ferromanganese ores (+11.1 ± 1.7 ‰, n=10) and that of sugilite (+11.0 ± 1.2 ‰, n=12) and other gangues from the KMF (not shown here). Being silicate minerals, both sugilite and ephesite are expected to have positive and probably ^{18}O-enriched values in comparison to the fluid form which they have been formed. However, it is extremely intriguing that despite the significant chemical differences of the two minerals that extend to bond characteristics, possible sample or intragrain isotopic compositional heterogeneity, contamination from other phases and analytical effects, ephesite and sugilite still show an almost identical oxygen isotopic composition. Considering the previously discussed scenario of ephesite forming through metasomatism of a pre-existing phyllosilicate-rich rock, by Na- and Li-rich infiltrating fluids at the same time with hydrothermal sugilite crystallization in the KMF (ca. 1.2 Ga), a strong link between the two appears to be evident.

Determination of the temperature of the fluid being in equilibrium with the precipitating mineral is essential in order to obtain a snapshot of the fluid oxygen isotopic composition during alteration and get further insights into its origin by use of the measured $\delta^{18}O$ of different gangues. To that end, knowledge of the mineral-water fractionation factors is required, in addition to other parameters such as the extend of fluid-rock interactions and the possibility of fluid mixing, approximations that may all add limitations to $\delta^{18}O_{fluid}$ estimations using this method. Collectively, temperature estimates for bixbyite ore formation in the EMD suggest peak metamorphic conditions between 315 and 375°C, on the basis of mineral thermal stabilities, illite crystallinity applications in the overlying Gamagara shale and an empirical bixbyite geothermometer using iron content of the mineral (Plehwe-Leisen; 1985, Gutzmer and Beukes; 1996b).

However, it should be also considered that the employed geothermometer has produced a wide range of temperatures from the ores of the PMF (De Villiers; 1983), specifically from < 170° (Klipfontein) to 470°C (Gloucester), as well as unrealistic temperatures from the KMF (Black rock: 530°C) (Figure 15a); thus, there is a level of uncertainty attached

to its usage. Furthermore, existing temperature constraints may not apply to the wider braunite-rich ferromanganese ores of the PMF, since coarse-grained bixbyite ore is reported to occur as localized pods and is thought to be a product of either localized recrystallization during diagenesis/metamorphism from fluids expelled from the host rock or else the result of

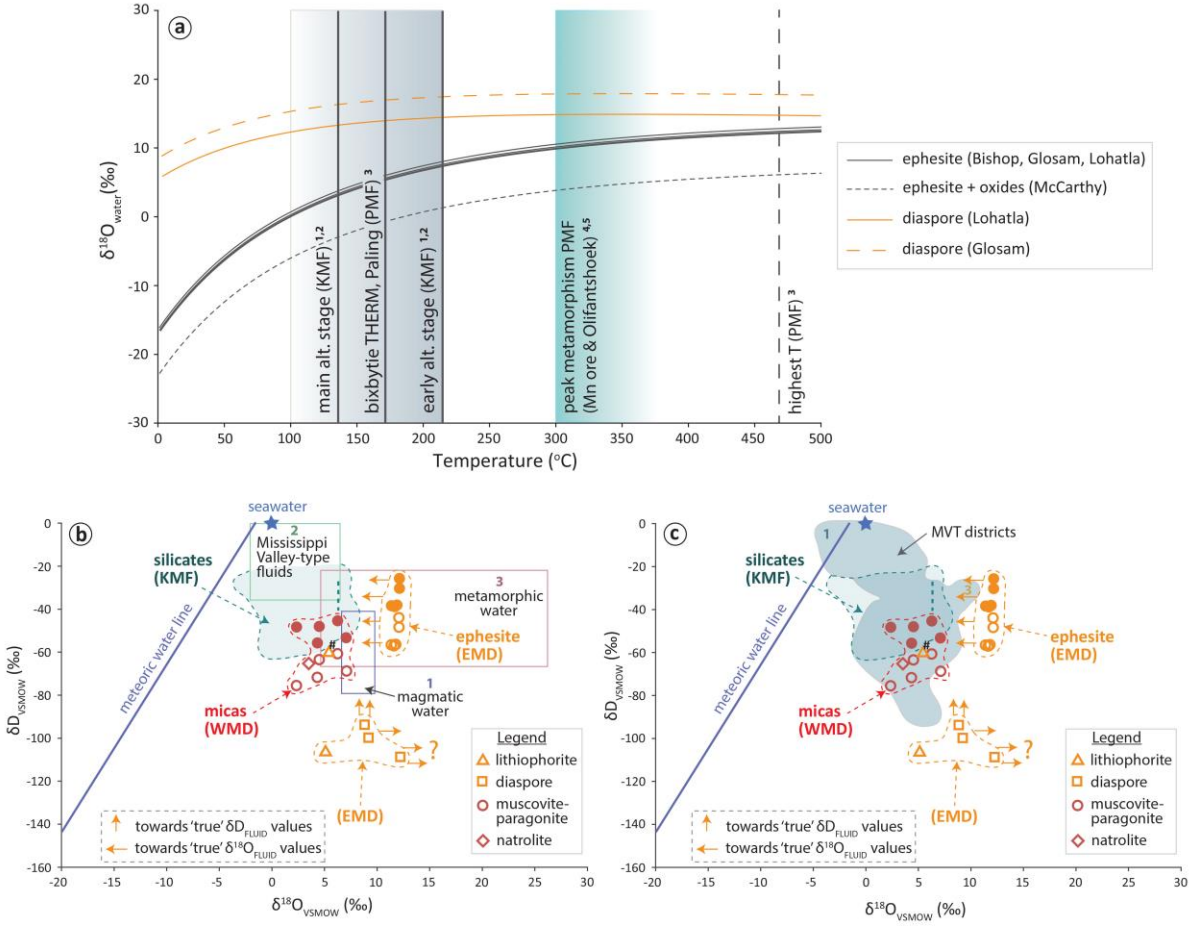

Figure 15. (a) Minera-water oxygen isotopic fractionation curves for ephesite and diaspore suggesting no coeval precipitation and/or no equilibration. Previous temperature range estimates from the Northern Cape (coloured columns) are shown for reference. 1: Lüders et al; 1999, 2: chapter 3, 3: De Villiers; 1983, 4: Plehwe-Leisen; 1985, 5: Gutzmer and Beukes; 1996b. (b & c) δD-$\delta^{18}O$ plots for gangues in the EMD ores, displaying their relationship with common water types and compositions of MVT brines. Open symbols reflect measured values and filled ones, fluid estimated values. Arrows point towards the compositional area of the expected ('true') fluid values. References: (b) 1: Taylor; 1974, 2: McLimans; 1977, 3: Sheppard; 1974. (c) 1: McLimans; 1977, Richardson et al; 1988, Kesler et al; 1977. micas (WMD): chapter 5.

post-metamorphic hydrothermal metasomatism by externally sourced fluids (Gutzmer and Beukes; 1996b). The substantiated hydrothermal mode of ephesite formation during the Namaqua orogeny further highlights the lack of knowledge with respect to associated fluid temperatures, which are more likely to have been mostly in the range between 100° and

250°C, that collectively characterizes the bulk of hydrothermal mineral formation in the rest of the Northern Cape (Lüders et al; 1999, chapters 3 and 5).

In the absence of published fractionation factors for ephesite, equations generated for its Ca-analogue margarite can be used instead as a proxy. Using the available fractionation equations of margarite and diaspore (Zheng; 1993b, Zheng; 1998) and a relatively low postulated temperature of 200°C, $\delta^{18}O$ values yielded for the metasomatic fluid range between +6.7 and +7.4 ‰ (average = +7.1 ± 0.3 ‰, n=5) for ephesite and from +14.5 to +17.8 ‰ (average = +15.7 ± 1.8 ‰, n=3) for diaspore. These estimates suggest that the two minerals have not been formed coevally and/or not in equilibrium (Figure 15a). $\delta^{18}O_{FLUID}$ values estimated from ephesite broadly reflect the ones determined for the early alteration stage of ore-upgrade in the KMF (+5.3 ± 1.4 ‰, values up to +8 ‰) and the range predicted from gangues (+2.3 to +7.1 ‰) in the PMF (WMD ores) (chapters 3 & 5). This suggests that ephesite may have formed indeed by isotopically similar brines to the presumed regional hydrothermal system, which imprinted its signature on the mineral. It can be further assumed that bonds to oxygen from a silicate precursor were broken and reformed, for complete oxygen isotope exchange and equilibration with the fluid to occur. In other words, it is probable that no intact structural units in ephesite were inherited from the hypothesized clay precursor as previously mentioned in section 6.2, something being in concern with controlled experiments between clays and water (O'Neil and Karaka; 1976).

If ephesite formed at higher temperatures (for e.g., between 300° and 350°C), as suggested in the prevailing models, the derived oxygen isotopic values of the associated fluid approach more the measured $\delta^{18}O$ ratios, i.e., ca. + 12 ‰ (Figure 15a); therefore, signifying a very ^{18}O-enriched metamorphic fluid. The likelihood of a regime of higher temperatures (> 300° and up to ca. 400°C) in the EMD than the rest of the Northern Cape, as suggested by previous authors, is not easy to explain within the framework of tectonically expelled hydrothermal brines. The ephesite-rich ores sit the farthest away from the edge of the craton, where thin-skinned tectonics apparently have had more pronounced effects. Nevertheless, these deposits are still closely associated with regional structures and unconformities that could have concentrated heated brines from the deeper strata of the basin through them.

Previously reported temperatures though, can be explained only by invoking regional thermal metamorphism or contact metamorphism. The presence of penetrating solutions emanating from emplacement of small igneous has been discounted so far and if indeed existed locally, more evidence would have appeared by now. Mica-Al-rich silicates-grossular-barite associations described from an Fe-AL-rich sample from Kolomela mine (EMD), which moreover contains an Al_2SiO_5 polymorph, are also in agreement with a higher-T regime and require further investigation. Hydrothermal andalusite has been documented along with corundum in a potassic alteration zone around an igneous intrusion, although temperatures in this setting are in the range between 450-550^oC (Outhuis; 1989). Pyrophanite, which is firstly reported here from EMD, is also associated with metamorphosed braunite-rich rocks.

Unfortunately, ephesite-diaspore pairs cannot provide any solid temperature constraints, at least with the available dataset comprising distinct diaspore and ephesite occurrences, i.e., from bixbyite and braunite-hematite ore respectively. It is noted that diaspore also occurs as inclusions in ephesite and may comprise more than one generation. The heavy $\delta^{18}O$ measured values of diaspore are not entirely surprising, since isotope fractionation between water and hydroxides results in ^{18}O-enrichment (Zheng; 1998). Also worth mentioning is the observation that the $\delta^{18}O$ ratios for Lohatla diaspore (+8.8 and +9.2 ‰) are noticeably lower than the values for Glosam diaspore (+12.2 ‰). It is theoretically possible that O-H bonds are broken and reformed more readily and that OH groups in Lohatla diaspore have been exchanged with an isotopically lighter fluid after its precipitation or else fluid(s) was depleted in ^{18}O for other reasons prior to diaspore formation. The much lower $\delta^{18}O$ values of lithiophorite (ca. +5‰) perhaps point to isotopic lighter fluids, although its precipitation could have been also controlled by a series of other factors including temperature, fractionation and temporal evolution of the fluid(s) or simply association with a temporally distinct, late-stage or more recent event. For example, evidence for later alteration is texturally provided by barian goyazite developing in the vicinity of and/or replacing diaspore. Finally, no information is available regarding oxygen isotopic fractionation in bixbyite, but intriguingly the coarse-grained EMD ores (+1.1 to +1.5‰) isotopically match bixbyite mineralization in the KMF (-0.6 to 0‰) (chapter 3).

δD measured isotopic composition for ephesite is rather homogenous (-52.3 ± 6.0 ‰, n=5), closely resembling that of silicates and micas from the WMD ores, as well as estimated δD_{FLUID} values from the former (-45.0 to -63.0 ‰) (chapter 5). δD_{FLUID} estimates from ephesite can be only based on available fractionation curves for muscovite or kaolinite (Méheut et al; 2010), the latter being preferable at low temperature settings, i.e., ca. <300°C. For a temperature of 200°C, the former fractionation curve suggests δD_{FLUID} between -29 and 41.4 ‰ (average = -37.4 ± 5.9 ‰, n=5), which is as expected notably but not remarkably different from the measured compositions (ca. 10-15 ‰), since D fractionation is generally small for these silicates at low temperatures. Close isotopic similarities between different localities/districts suggest δD fluid buffering. On the other hand, the distinct δD ratios of diaspore (-108.5 to -93.7‰), imply that considerable D exchange took place during alteration processes, if on the basis of textures, diaspore and ephesite are regarded as products of the same hydrothermal system. A crude estimate of the predicted δD_{FLUID} values from diaspore, using the fractionation equation of the hydroxide gibbsite (Méheut et al; 2010), suggests broadly similar values (-62.6, -53.8, -47.8 ‰) to that calculated from ephesite. However, this scenario is speculative and the apparent considerable variation between the isotopic compositions of ephesite and diaspore should be considered and further examined. Lithiophorite has also a distinctly lighter δD composition (-106.1 ‰) which is easier to explain invoking a different fluid source or meteoric water dilution since this can be also a supergene phase. On the other hand, the fractionation mechanism shifting the δD values by 50-60 ‰ during diaspore formation is not known, but perhaps isotopically lighter post-metamorphic/hydrothermal fluids are responsible for this signal. Interestingly, considerable variation exists between Lohatla (-93,7, -99,7‰) and Glosam diaspore (-108,5 ‰), which as mentioned earlier is also replicated in their $\delta^{18}O$ values (ca. +9.0 vs +12.0 ‰ respectively).

The origin of the fluids can be further investigated with the use of $\delta^{18}O$-δD plots (Figure 15b & c), commonly used with modern brines. Due to uncertainties in estimating $\delta^{18}O_{FLUID}$ values, data plotted from this study (open symbols, orange-coloured) are measured values, with the exception of ephesite where both measured (open symbols) and suggested δD fluid ratios (filled symbols) are shown. Compositional and other similarities between regional alkali brines and Mississippi Valley-type (MVT) Pb-Zn deposits have been extensively

presented elsewhere (chapters 3 & 5). Interestingly, ephesite overlaps with metamorphic waters (Figure 15b) and generally plots slightly outside the isotopic fields defined by most MVT deposits (Figure 15c). However, if the estimated $\delta^{18}O_{FLUID}$ ratios from ephesite are used ('true' values), data plot closer and within that of MVT ores. Explaining the compositions of diaspore and lithiophorite, which lie far from any defined field, is challenging, unless fluids with considerably lighter δD values were involved in the formation. The heavy $\delta^{18}O$ values of diaspore are compatible with hydrothermal/metamorphic fluids. If this mineral has principiated from a fluid with δD values between -50 and -60 ‰ as predicted from the gibbsite fractionation equation (true values, Figure 15), then the former and most likely origin remains the case. Overall, isotopic signatures of at least ephesite are consistent with the signals of the regional, Namaqua-related, evaporitic alkali-rich brines in the Northern Cape. A last remark regards the apparent presence of born in the fluids, an element enriched in evaporite sequences, which seems to have been imprinted on certain alkali assemblages (200 to 1500 ppm).

6.6 Insights from manganese oxides

It is apparent that weathering processes following ore formation have transformed some of the early mineral assemblages into secondary Mn-oxides, -hydroxides and -oxyhydroxides and possibly formed clays such as kaolinite. Formation of supergene manganese oxides has been attributed to recent surficial exposure, erosion and renewed karstification that also generated canga deposits in the area, something further substantiated by cryptomelane and romanechite $^{40}Ar/^{39}Ar$ dating (see also section 6.7) (Gutzmer and Beukes; 1996a, Gutzmer and Beukes; 1998, technical report). Petrographic features of the limited sample suite studied here are considerably different to that presented by previous publications, in that they lack pronounced modern weathering, showing only vague evidence for supergene enrichment. Botryoidal textures, replacements, and vug-fillings by romanechite, ramsdellite or manganite were not observed in the main ore matrix (Gutzmer and Beukes; 1996a), apart from limited occurrences of hollandite, coronadite, pyrolusite and cryptomelane, confined to localized open space fillings and replacements.

Figure 16 illustrates the chemical composition of analysed oxides, most being consistent with that of the hollandite-group Mn-oxides. These were observed more commonly in the ephesite- and bixbyite-rich ore. Relevant data from mostly veined Mn-oxides in the WMD are also displayed. Similar to other oxidized zones in Mn deposits, these minerals have been formed by weathering solutions flowing through permeable horizons, oxidizing Mn^{2+} to Mn^{+4} and also carrying Al, Fe and dissolved cations of Ba, K and Pb that readily participate in the complex tunnel structure of these oxides. Based on the predominant tunnel cation, hollandite (Ba) is more common in this study, followed by cryptomelane (K) and lastly

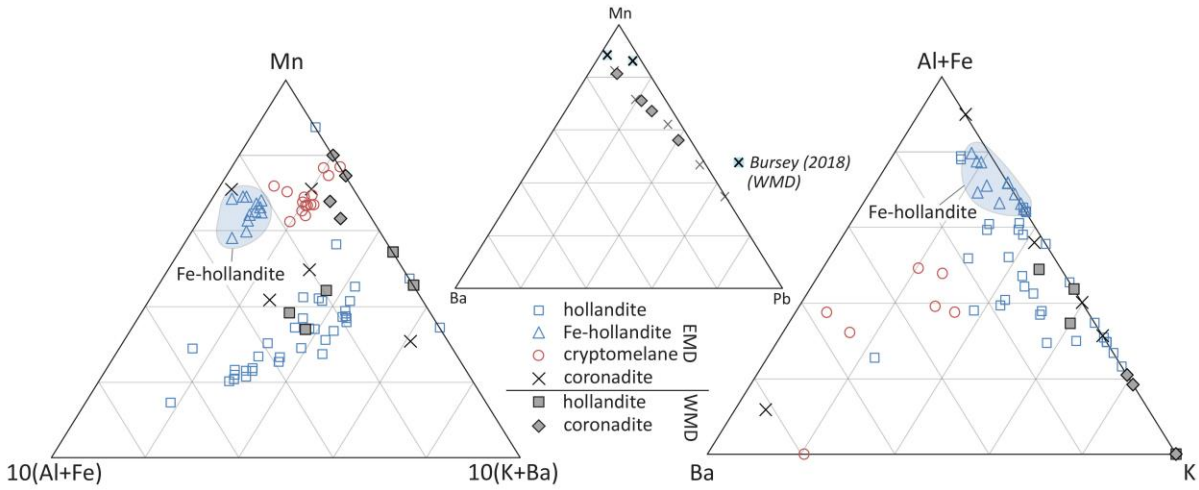

Figure 16. Ternary plots illustrating the chemical composition of tunnel structure Mn oxides analysed in this study and the wide exchanges between Al, Fe, Ba, K and Pb. In contrast to EMD, only hollandite (Ba) and coronadite (Pb) have been found in the WMD ores and attributed to hydrothermal processes. WMD data are from chapter 5 and diagrams after Spier et al (2006).

coronadite (Pb). Although the role of recent weathering processes cannot be refuted, it should be noted that the WMD occurrences lack evidence for supergene reworking and hollandite in these ores is regarded as a late-stage hydrothermal phase, in accordance to other hollandite hydrothermal vein deposits (Fairey et al; 2019, chapter 5, Post; 1999). In like manner, the origin of iron-rich hollandite (probably ferrihollandite) seen occupying space interstitially to ore laminae but also encasing and/or replacing braunite aggregates and hematite microconcretions is more elusive, since textural preservation is generally not a characteristic of supergene processes.

Later reworking of the bixbyite-rich ore is also suggested by the presence of hollandite, pyrolusite and cryptomelane which fill open space between bixbyite crystals and on the

micro-scale are seen developing growth bands together with a Mn oxide that is seemingly an alteration product of bixbyite. Extensive infills of this phase [bxb(II)] exhibit variable composition in contrast to the dominant bixbyite [bxb(I)], but show a strong relationship with the latter since they plot very close to the Mn_2O_3 - Fe_2O_3 compositional line defined by bixbyite, while also extend this line towards members containing higher Mn in relation to Fe (Figure 17). Variations in the alkali content, elements not picked up in the dominant bixbyite, do exist between these alteration-derived oxides but Al concentrations appear to be more distinctive between oxide members with contrasting brightness under EDS imaging [bxb(IIa)

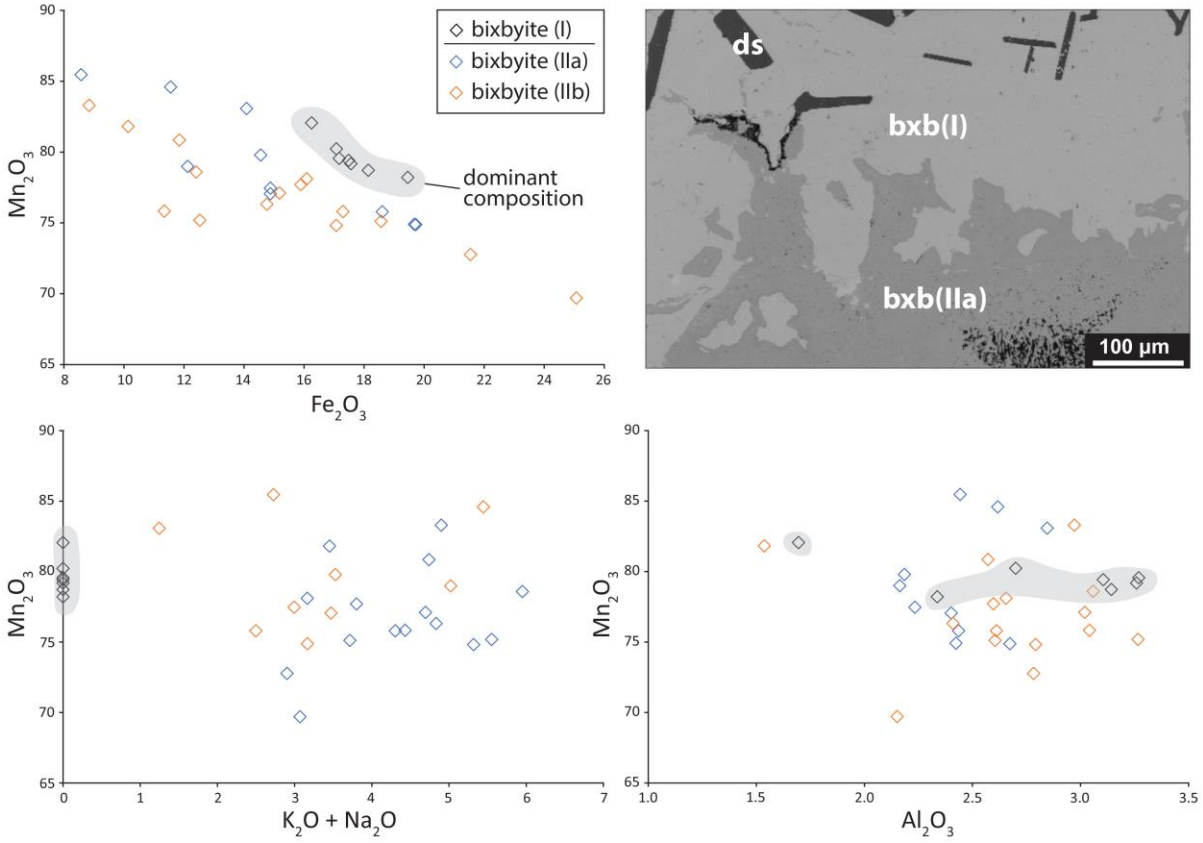

Figure 17. Compositional relationship between ore-forming bixbyite, shown as bxb(I), and a seemingly alteration product of the former [bxb(II)], which is associated with Mn oxides (hollandite, cryptomelane), filling interstitial space between bixbyite and developing growth bands. Note the similarity of bxb(II) with bxb(I) and features of the former, .i.e., its higher Mn/Fe ratio, presence of alkalis (Na, K) and Al, the latter element being higher in certain members that are also richer in Mn.

and bxb(IIb)] and in particular is higher in Mn-rich members. The origin and timing of formation of these mineral assemblages is not fully understood and identification of the involved alteration mechanisms may reveal more on the later reworking of these ores, if indeed the former are later products and not co-genetic with bixbyite.

Another Mn oxide of particular importance in these ores is lithiophorite, coarsely crystalline varieties of which are found deposited chiefly on braunite cavities (De Villiers; 1945, Gutzmer and Beukes; 1996a). These researchers emphasized its supergene origin and documented it as a notably widespread phase, forming preferential replacements of diaspore or ephesite and being dominant among other supergene oxides within bedded aluminous and ferruginous ore zones that reach up to 50 cm in thickness and are seen occasionally being crosscut by recrystallized braunite and partridgeite. The above observations raise questions about the timing of its supergene formation. Lithiophorite is only a minor constituent in the studied samples but as noted earlier, it can be seen in veinlets co-existing with equant ephesite or as inclusions within recrystallized braunite.

It is interesting to point out that compositionally, lithiophorite is a member of an isomorphous series in which the end-members have the compositions $Al_{00.5}Li_{0.5}MnO_2(OH)_2$ and $Al_{0.667}MnO_2$, therefore its name is misleading since a variety of this mineral is practically lithium-free or contains more essential components than lithium such as cobalt and nickel (Perceil; 1972, Chukhrov et al; 1985). Analyses of lithiophorite from the Gloucester and Bishop mines have shown that it has the highest Li/Al ratio among available lithiophorite analyses worldwide (De Villiers; 1945, Chukhrov et al; 1985), a fact further highlighting the particularly Al-rich geochemical environment of the EMD ores. The previous researchers have stressed that free alumina in the form of soluble organic or inorganic compounds is a necessary precondition for its formation. These agents are certainly present in lateritic weathering zones, in agreement with most natural occurrences of lithiophorite in certain acid soils and weathering zones of manganese deposits. However, low-temperature hydrothermal veins of lithiophorite or formation by Li-bearing hydrothermal solutions enriched from alkali pyroxenes and amphiboles in marine hydrothermal manganese deposits, have also been reported (Nassem et al; 1997, Post; 1999). Further research, possibly be means of lithium isotopic analysis, is needed to resolve the relationship of lithiophorite with the major hydrothermal, Li-bearing and Namaqua-related silicates (i.e., sugilite and ephesite) in the Northern Cape.

6.7 Implications for current genetic models

At present, there are significant knowledge gaps regarding the exact mechanisms of metal concentration and development of the unusual gangue mineralogy hosted by the ferromanganese ores of the Eastern Maremane dome (EMD). According to the widely accepted models, gangue mineralogical associations, including the Li-bearing ephesite, are products of fluid-rock interaction long afterwards the accumulation of ore metals in essentially fresh-water karst-related depressions (Plehwe-Leisen and Klemm; 1995, Gutzmer and Beukes; 1996a, Gutzmer and Beukes; 1997b). The mechanism of fluid generation/mobilization has been suggested to be that of compaction of the precursor sediment to the bedded ferromanganese ores during diagenetic/low-grade metamorphic recrystallization. In detail, the precursor sediment/protore is regarded to be material comprising alternations of manganese-rich wad, a term generally used for unconsolidated sediment consisting of a mix of manganese oxides of uncertain identity.

Following this hypothesis, fluids expelled progressively from the original ferromanganese succession during various degrees of diagenesis and low metamorphism, become highly concentrated in Na, Li, Ba but also other alkalis (Ca, Sr, K) if one further considers the stratigraphically and texturally equivalent WMD ores, thus ultimately leading to: i) formation of considerable amounts of ephesite, diaspore, barite and lesser other alkali-rich and gangue phases along with the ore-minerals braunite, bixbyite and hematite within both the ores and country rocks and ii) development of both fine- and coarse-grained ores, i.e., braunite-rich and bixbyite-rich ores respectively, through a complex multi-stage recrystallization, an outcome subject to fluid volume, as well as iron and silica activity. In absence of apparent geochemical differences between the various ore types, the authors of the popular models considered unlikely, although not entirely implausible, the introduction of post-metamorphic fluids and thus regarded hydrothermal fluid flow only as a means of explaining cross-cutting veins of barite, specularite and quartz.

The glaring problem with the above scenario though, is the necessity for an unusual primary chemistry of the ore precursor. A schematic model for the origin of the regarded ores redrawn from Gutzmer and Beukes (1996a) (Figure 18), facilitates understanding of the

inconsistencies between the established view and new data from the current study. Apart from manganese and iron oxides-hydroxides in the original residual sediment-wad, an amount of mixed lateritic clays would have been presumably concentrated, given the open-karst nature of this envisaged system, reminiscent more of a continental karstic lake, hollow or doline (Stage I, Figure 18A). Remnant clay/silicate material resisting dolomite dissolution and originally found interbedded with the carbonate sequence may have also been present in the original manganiferous sediments. However, apart from the presumed residual ore-enrichment, this material needs to be also enriched in the various and locally abundant alkali elements preserved in the gangues of the ferromanganese ores and specifically Na and Li in the case of EMD ores, if one attempts to explain the current ephesite-rich assemblages by only invoking post-depositional diagenetic and metamorphic processes. It is emphasized that ephesite precipitation entails a Na-bearing parental fluid with very high Li concentration and a particularly silica-depleted and aluminum-rich precursor host rock.

Determining the amount of ephesite in this metallogenic environment, and by extent also that of Na and Li, necessitates a much larger geochemical database and is beyond the scope of this study. Based on field and petrographic/textural observations, as well as on descriptions from the literature (for e.g., alternating laminae of braunite-partridgeite and ephesite-diaspore, ephesite veins extending into shales, pervasive replacement of shales by ephesite) and bulk rock analyses displaying between 1-2 wt.% Na_2O and ca. 0.4-1.1 wt.% Li, we favor that ephesite is very common and pervasive in these ores, participating in all sorts of banded and replacive metasomatic textures. Preliminary and crude mass balance calculations presented earlier suggest that ephesite is variable in the ore and apparently subject to sampling bias, ranging from 9% to 59%. In stark contrast, the authors of the original models, regarded both the ores and their precursors as being poor in Na, Mg, Cu, Ni and Co, all used as evidence for accumulation in fresh-water settings (Gutzmer and Beukes; 1996a). In our view, elemental requirements for ephesite formation rule out the possibility that these have been inherited from the postulated lateritic depositional environment, but on the contrary, they must have been introduced from an external source. Likewise, under current models, Fe and Mn are limited to dolomite dissolution; however, ore components may have

been also extracted from other country rocks such as iron-formation and furthermore, clastic material precipitating in the karst may have contributed to the aluminum budget of the ores.

Depositional sediment characteristics are thought to have gradually shifted during the postulated ore-accumulation period between 2.25 and 2.0 Ga. Specifically, the epigenetic history is believed to have been marked by infringement of a dominantly Fe-Mn depositional setting into a basin of aluminous and ferruginous shale accumulation (Stage I, Figure 18B). Continuous erosion, extensive karstification and development of the regional Transvaal-Olifantshoek angular unconformity was accompanied by local accumulation of a hematite pebble conglomerate (Doornfontein Fm) and succeeded by deposition of the shales (Gamagara Fm) and quartzites of the Olifantshoek Supergroup (Gutzmer and Beukes; 1996a). It is worth pointing out that in contrast to the BIF-clast bearing conglomerate or the chert-bearing manganiferous Wolhaarkop breccia, autochthonous ferromanganese accumulations are seemingly absent of country rock fragments, which corroborates that there is no insoluble residue from the parent rock. However, apart from the crude sedimentary bedding believed to have been inherited from the dolomites, these banded ores are in very close proximity with the Gamagara shales, the base of which also bears an aluminum-rich character; therefore, the relationship between the two requires similar attention as any investigation on the nature of the protore.

Mentions of manganese-mineralized shales or shale-bound manganese enrichment in different stratigraphic levels exist in the literature (Plehwe-Leisen and Klemm; 1995); however, these are regarded to be unrelated with the ferromanganese mineralization, them being part of the younger Gamagara Fm. Pervasive replacement of shales by ephesite, in the immediate vicinity of some of the bedded ferromanganese ores, is also noted by Gutzmer and Beukes (1996a), which essentially affirms that fluids expelled during ore-formation have altered shales, sometimes interbedded with the ores. As noted earlier, the highly aluminous Gamagara shale is interpreted by some researchers as having experienced hydrothermal alteration capable of mobilizing Al and therefore, the present Al content of the ores may be also a result of enrichment during Namaqua-induced metasomatic processes or may in fact point to replacement of former shale material in places (Stage II, Figure 18C1, see also text

below). A certain degree of aluminum mobilization can be deduced from textures of ephesite filling fractures and veins, the latter also protruding into the overlying shales, but also from diaspore and amesite which can also be of metasomatic hydrothermal origin.

The present ore assemblage comprises multiple generations of recrystallized manganese minerals that are regarded to have been developed by fluids expelled during diagenesis and low-grade metamorphism of the original sentiment between 1.9 and 1.8 Ga, i.e., during the Kheis orogeny (Stage II, Figure 18C2). In addition, Li-enriched pore fluids led to crystallization of metamorphic ephesite and diaspore, while higher fluid flow is presumably responsible for the formation of the coarsely recrystallized bixbyite-rich ores (Gutzmer and Beukes; 1996a). $^{40}Ar/^{39}Ar$ age of ephesite from this study (1125 ± 12 Ma) contends that its formation is fundamentally related to the Namaqua orogeny and consequently to the associated regional hydrothermal metasomatism impacting ore lithologies from as south as Kolomela mine, up to the northern extremity of the KMF where hydrothermal muscovite has a remarkably similar age of 1138 ± 3 Ma.

The age discrepancy between the speculated age of metamorphism and the measured age in this study provides compelling evidence for the external introduction of Na and Li by brines (Stage II, Figure 18C1) and along with age data for extraneous ^{40}Ar in ephesite, suggests a very different origin for this mineral than that in the accepted models, one that probably involves local recrystallization of a precursor aluminosilicate. Textural observations suggest the association of ephesite with alteration fronts that penetrated and locally superimposed on the precursor host rocks/protores of the EMD. A similar process partly involving metasomatic replacement of prior clays, can be inferred for the Li-uptake in hydrothermal micas of the WMD ores. Therefore, it is sensible to link the origin of Li with the passage of basinal brines through various lithologies in the basin and in addition regard that fluid transportation is facilitated primarily by permeable regional-scale structures. All things considered, the alternative scenario of Namaqua-related hydrothermal alteration being the genetic mechanism of gangue formation, as presented in Figure 18C1, is much more credible and backed by solid evidence at present.

Recent geological history of the ores (20-10 Ma) certainly involved a degree of supergene enrichment (Stage III, Figure 18D), as documented by unpublished $^{40}Ar/^{39}Ar$ dating of cryptomelane and romanechite, generally yielding discordant apparent age spectra with only some intermediate age plateaus (Gutzmer and Beukes; 1998, technical report). Erosional and renewed karstification events being at play in late Tertiary led to brecciation and slumping of ore lithologies, accumulation of romanechite crusts and pyrolusite concretions and formation of extensive canga deposits (De Villiers, 1960; Grobbelaar and Beukes, 1986, Gutzmer and Beukes; 1996a). The above suggest that karstic hollows acted as means of ore preservation until very recent times, but at the same time, present the challenge of ceased dissolution and by extent ore-forming processes according to the current models, even in the shallow ground level, for a period of ca. 2 Ga. In any case, based on petrographic observations, we presume that minerals considered to have a recent erosional origin, such as lithiophorite, are instead associated with the formation of hydrothermal ephesite. A late-stage hydrothermal origin is also attributed to certain Mn oxides, such as hollandite, coronadite and an alkali-bearing bixbyite variety [bixbyite(II)].

Based on current findings, there is no definitive answer as to whether post-depositional, Namaqua-induced hydrothermal activity was imperative for the current ore grade, for example through processes of manganese dissolution and redeposition. However, it is stressed that the origin of these deposits may be much more complex, involving an interplay between sedimentary processes, regional tectonics, hydrothermal input and weathering processes of deep epigenetic nature (i.e., elevated temperatures and increased activity) upon karstic surfaces; therefore, it should not be confined solely to supergene processes or a bauxitic/lateritic protore. The large compositional disparity between the EMD and WMD ores, owing to hypothesized local accumulation of aluminum-rich residuum only in the first, despite broadly similar weathering-related mechanisms of formation for both, requires better explanation. As previous researchers have stressed out (Fairey et al; 2019), limiting ore formation in places where a single Fe-, Mn-rich and chert free dolomite unit was exposed to surficial karstification is to disregard many hundreds of meters of the Campbellrand stratigraphy. The high iron signal in these ores, the absence of typical supergene textures in addition to of lack supergene minerals in the case of WMD ores, as well

as the remarkable enrichment in lithium and sodium are all matters signifying the strong need for revaluation of the current ore genetic models.

Figure 18. (next page)

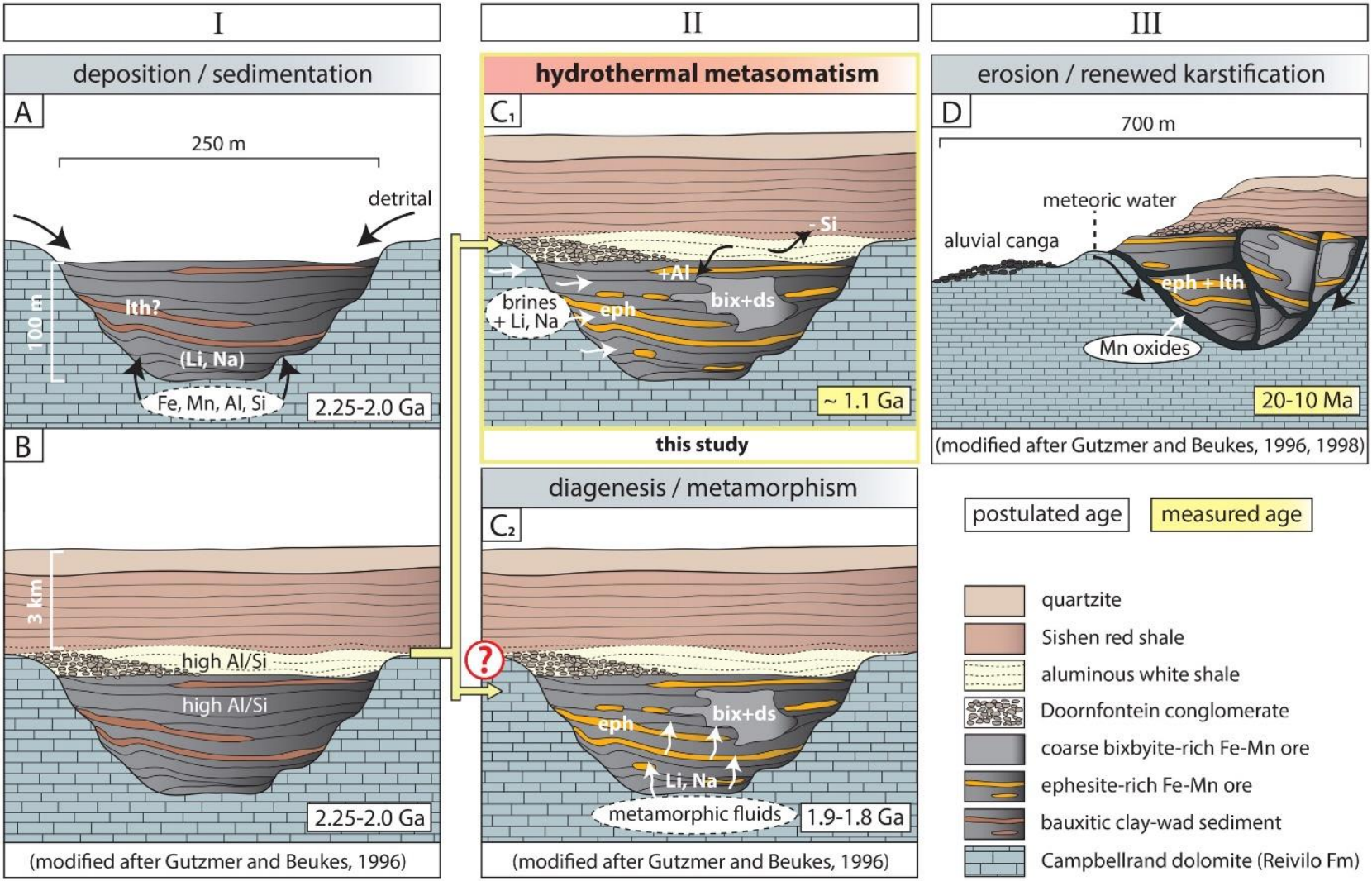

Figure 18. Schematic model illustrating the major development stages of the ephesite-rich ferromanganese ores of the PMF. According to the prevailing models, residual ore accumulation in karstic sinkholes sometime between 2.25 and 2.0 Ga (A and B) is responsible for the high Al/Si ratios and high alkali content (mainly Na, Li) of these deposits. Therefore, formation of the characteristic ephesite assemblages is explained by recrystallization and mobilization of elements (Na, Li) already present in the precursor ores, by means of metamorphic/hydrothermal fluids expelled between 1.9 and 1.8 Ga, which furthermore produced coarse and recrystallized bixbyite-rich ore (C_2). An alternative scenario (C_1-this study) explains ephesite formation as related to externally sourced Na and Li by regional-scale pervasive metasomatic basinal brines during the Namaqua orogeny (1.2-1.0 Ga), that may have further dissolved Si, mobilized Al and metasomatized shales associated with the Fe/Mn ores. Recent geological history involved a degree of localized supergene enrichment (D).

7. Summary and conclusions

The ancient supergene (ephesite-bearing) ferromanganese ores form most of the known ore reserve in the Maremane dome of the Postmasburg Manganese field. Revisiting key localities (Bishop, Lohatla, Gloucester) that provided the foundation for the existing ore genetic models, we reveal inconsistencies with respect to both the origin and diagenetic/metamorphic evolution of the ores, the latter presumably leading to pervasive ephesite formation. A reexamination of the lateritic weathering models in the broader geological context of the Northern Cape, considering geochronological, isotopic and petrographic evidence, casts doubt into the postulated supergene origin of the deposits. The main conclusions of this research can be summarized as follows:

(1) $^{40}Ar/^{39}Ar$ dating of ephesite (1125 ± 25 Ma) supports a metasomatic hydrothermal origin related to brine infiltration with $\delta^{18}O$ values between +6.7 and + 7.4 ‰ and δD between -43.8 and -56.8 ‰, during the 1.2-1.0 Ga Namaqua orogeny. The discrepancy (ca. 700 Ma) between our age and the previously hypothesized syn-metamorphic origin for ephesite during the controversial Kheis orogeny (1.8-1.9 Ga), can only be explained by external introduction of its major constituents (Na and Li), as opposed to current models ascribing alkali sources in the karstic-related protore sediments.

(2) Discordant $^{40}Ar/^{39}Ar$ step-heating spectra of ephesite (ages between 1600-1400 Ma), showing saddle-like shapes and old-low temperature steps, are best interpreted as results of inherited ^{40}Ar incorporated in ephesite from an aluminosilicate precursor in the protore and thus emphasize the need for good knowledge of the geological framework in mica $^{40}Ar/^{39}Ar$ dating. However, the precursor hypothesis conflicts with stable isotopic evidence and needs further investigation.

(3) $^{40}Ar/^{39}Ar$ results are consistent with textural observations suggesting a broadly replacive metasomatic origin for ephesite, possibly involving transformation of an older phase by addition of Na and Li. Transportation of these alkalis from alteration solutions and authigenic ephesite precipitation can also be surmised to occur, as for example in late-stage veins. The

hydrothermal origin of ephesite is further buttressed but the intriguing $\delta^{18}O$ compositional similarity between that and the contemporaneous Li-bearing sugilite in the KMF.

(3) Metasomatic processes are recorded in a series of diverse textures within hematite- and ephesite-rich layers, such as microconcretions comprising ephesite or hematite-hollandite and braunite aggregates or microconcretions overprinted by hollandite. Detailed petrographic examination further reveals previously unreported phases such as late-stage barian goyazite replacing diaspore and pyrophanite associated with ephesite. Also worth mentioning is the presence of barian muscovite, ferrihollandite, amesite, an alkali (Na, K)-bearing bixbyite generation associated with bixbyite- and diaspore- rich ore, as well as rare textural occurrences of gamagarite inclusions in diaspore, the latter emphasizing the coexistence of Na, Li, Al, Ba and V in the hydrothermal fluids.

(4) Ephesite-diaspore pairs from the produced stable isotopic dataset cannot provide solid temperature constrains and test previous estimates suggesting higher temperatures (300-400^{o}C) for the EMD. Examination of an Fe-Al-rich sample from the Kolomela mine (somewhat 40 km of the Bishop and Lohatla ferromanganese ores), revealed the presence of unidentified Al-rich silicates and an Al_2SiO_5 polymorph associated with grossular-feldspar-barite veins. Apart from the geochemical (Al-rich) resemblance of this sample with the studied EMD deposits, a high-temperature alteration regime is also implied. Pyrophanite, firstly reported here, is another possible clue for the latter scenario since traditionally is a metamorphic phase.

(5) Whole-rock lithium data from ferromanganese ores and mass-balance calculations support the presence of variable but high Li abundances (ca. 0.1-0.3 and up to 1 wt. %), controlled by their content of ephesite or lithiophorite in the EMD ores (from ca. 7 to 60 wt.% abundance) and Li-rich (0.3-0.4 wt. %) muscovite/paragonite in the WMD ores (26-40 wt. %) respectively. The high abundance of the Li-bearing species in these ores suggests an evaluation of the economic lithium potential. The source of lithium is elusive but may be dominated by dissolution of Type II continental evaporites, which however are currently unknown from the region. Whole-rock boron seems to be in the range of hundreds of ppm in

the EMD ores, but may shoot up to more than a 1000 ppm in the presence of conspicuous veining in the WMD, which renders identification of its origin critical for alteration processes.

(6) Aluminum mobilization processes can be invoked to explain diaspore-ephesite-lithiophorite associations and the distinct Si/Al ratio (<1) of the EMD ferromanganese ores, oppositely with the currently envisaged lateritic/bauxitic environment considered to solely govern the above. Textural indications such as lithiophorite-ephesite veinlets or lithiophorite inclusions in braunite, point to a possibly hydrothermal origin for lithiophorite, hollandite, and diaspore, closely associated with ephesite and markedly distinct to the documented recent supergene overprint. However, the markedly different δD values of diaspore to that of ephesite (by ca. 50-60 ‰) necessitate further explanation. The strong relationship of these ores with aluminous shales begs for further focus on possible replacement processes of clastic material being the leading ore-formation mechanism in certain cases/ore types.

(8) New models for the unique Al- and Li-rich ferromanganese ores of the PMF should incorporate new findings and place emphasis on the pervasive Namaqua-related hydrothermal processes recorded regionally in the Northern Cape. Tectonically expelled fluids have moved over long distances and reached the localities of Bishop and Lohatla, which under all new evidence represent the distal eastern arm of the Namaqua hydrothermal system.

The ferromanganese deposits have plentiful scope for future work, which should be focused on understanding the reasons for the key geochemical differences between mineralization in the eastern and western Maremane dome, as well as the relationship and origin of the Li-bearing species in the wider Northern Cape. It is suggested that attention is directed on the origin of the associated aluminous shale units, which may be pivotal in understanding mineralization processes. Future work can also involve more advanced isotopic techniques such as Li or halogen isotopes, that are potentially capable of providing insights into the origin and evolution of brines, in line with comparable studies on basinal brines from the literature. Finally, this study encourages a reexamination of the PMF ores, placing also emphasis on their Li content, especially since critical ore metals are in most cases readily available in the area through surface mining.

Synthesis & extensive synopsis

A comprehensive synopsis of the major findings and suggestions for the next steps

Introduction

This study set out initially to determine the relationship of alkali metasomatism between the two large Fe- and Mn-ore districts of the Northern Cape, namely Postmasburg and (PMF) Kalahari manganese field (KMF). Hydrothermal activity is only emphasized from the northern part of the KMF, where it is recognized as an upgrade mechanism of original (bio)chemical sedimentary manganese ores. In contrast, ore deposits in the PMF are regarded as the result of residual metal accumulation from preexisting lithologies (dolomites and BIF) during surficial karst-related and fresh-water sedimentation processes. Informed by recent findings of alkali-rich ore bodies and country lithologies in the PMF, this is the first study with clear focus on alkali gangue assemblages on a regional-scale, as well as the first to make extensive use of stable and radiogenic isotopic techniques on these hydrothermal ore-components.

Among the primary aims were to address gaps in our knowledge regarding: (1) paragenetic associations and textural occurrences of alkali-rich mineral phases, (2) dominant sources and characteristics of alteration fluids, (3) timing of mineralization events and (4) fluid-rock interactions and pathways of transportation. Taking research one step further, an attempt was made to elucidate the metallogenic implications of alkali metasomatism and put forward potential avenues for research on the basis of preliminary and upcoming results. A significant body of data acquired during the current research was not included in the previous chapters, but it is partly introduced at the end of this synthesis to stimulate and underpin the discussion on unresolved questions and future work.

Therefore, in order to avoid any confusion, this chapter is organized into **two (2) parts**. The first summarizes the major findings already presented in the main body of the thesis and

thus no new data are shown unless otherwise noted, while the second part touches on several subtopics of future research, that are however based on first-level preliminary analysis of already collected data. As a final observation, the synthesis of this thesis is rather long and repetition of material from the main body is inevitable and evident throughout the text. However, this is deliberate, since **this chapter is intended** by the author **to be read as a standalone** and broadly serve as an extensive synopsis of the entire thesis, where petrographic, radio- and stable-isotopic data are summarized in composite figures.

Part 1

Part one (1) comprises three (3) main sections and its outline is summarized as follows. The purpose of **section 1** is to marshal the most important findings from the main body of the thesis that constitute convincing evidence for a genetic link between hydrothermal alteration processes in the two major ore districts. The chronicle of the complex epigenetic history is presented in a way that: (a) catalogues all such evidence and (b) at the same time places emphasis on major outcomes that emerged during careful scrutiny of these intriguing lithologies. The chosen structure is preferred over a long and continuous geological history of the area or shorter sections based on distinct sampling sites or types of deposit, since it is regarded as easier for the reader to follow and furthermore, highlights parallels and contrasts between the whole study area, through comparisons of all petrographic and isotopic results.

Subsequently, a brief comparison between the ores located in the Eastern (type-locality) and Western Maremane dome is presented and considered to be critical for any future attempt to illuminate the genesis and evolution of these ores (**section 2**). Attention is drawn to whole-rock geochemical signals from the deposits, whereas additional petrographic observations from ongoing work in the WMD is later shown in part two (2) (**section 2.1**). Finally, a compilation of evidence and inconsistencies is provided, with an aim to build a case that the current ore genetic models for the PMF are outdated and a revision with strong focus on hydrothermal metasomatism is much needed (**section 3**).

1. A common epigenetic history for Postmasburg and Kalahari manganese fields

The recurring theme of alkali-rich gangue mineralogy seen in the Postmasburg and (PMF) Kalahari manganese fields (KMF) is not coincidental. In fact, similarities in mineralogy and mineral parageneses are unambiguously related to regional geological events that have influenced both ore districts. Metasomatic alteration is apparently quite pervasive in many orebodies of the study area and timewise postdates sedimentation of bedded manganese ores of the KMF, as well as sedimentation or protore-development, of at least some of the iron and manganese deposits contained in the PMF. The genetic link between the two ore fields is buttressed by a sufficient body of evidence that have firstly emerged from the current study and is summarized in the next pages.

1.1 $^{40}Ar/^{39}Ar$ geochronological evidence

Extent and timespan of Namaqua orogeny on the Kaapvaal Craton

The first concrete evidence linking the two ore districts are the shared Namaqua ages (ca. 1.2-1.0 Ga). The bulk of the mineralogical wealth characterizing the renowned Kalahari Manganese field is attributed to the localized residual enrichment of the sedimentary manganese beds of the Hotazel Formation by hydrothermal fluids, that are temporally linked to the late Mesoproterozoic Namaqua orogenic event (Beukes et al; 2016). This hydrothermal ore-upgrade, termed as 'Wessels event', has been related to leaching of primary manganese carbonates, development of recrystallized and coarse-grained ore minerals (braunite II, hausmannite, bixbyite, hematite), as well as redistribution and introduction of new elements (Na, K, Li, etc.) that were consumed by a staggering variety of gangue precipitates comprising silicates, borates and sulfates such as aegirine, sugilite, pectolite, andradite, richterite, gaudefroyite and barite to name a few. Age constraints on this localized enrichment are limited to $^{40}Ar/^{39}Ar$ dating of sugilite (1063 ± 18 Ma) and norrishite (1026 ± 29 Ma) and indirect palaeomagnetic dating of hematite (ca. 1250 and 1100 Ma) (Evans et al; 2001, Gnos et al; 2003).

On the basis of new $^{40}Ar/^{39}Ar$ dating results (all reported at 2σ confidence level), a similar genetic relationship between the Namaqua orogeny and hydrothermal

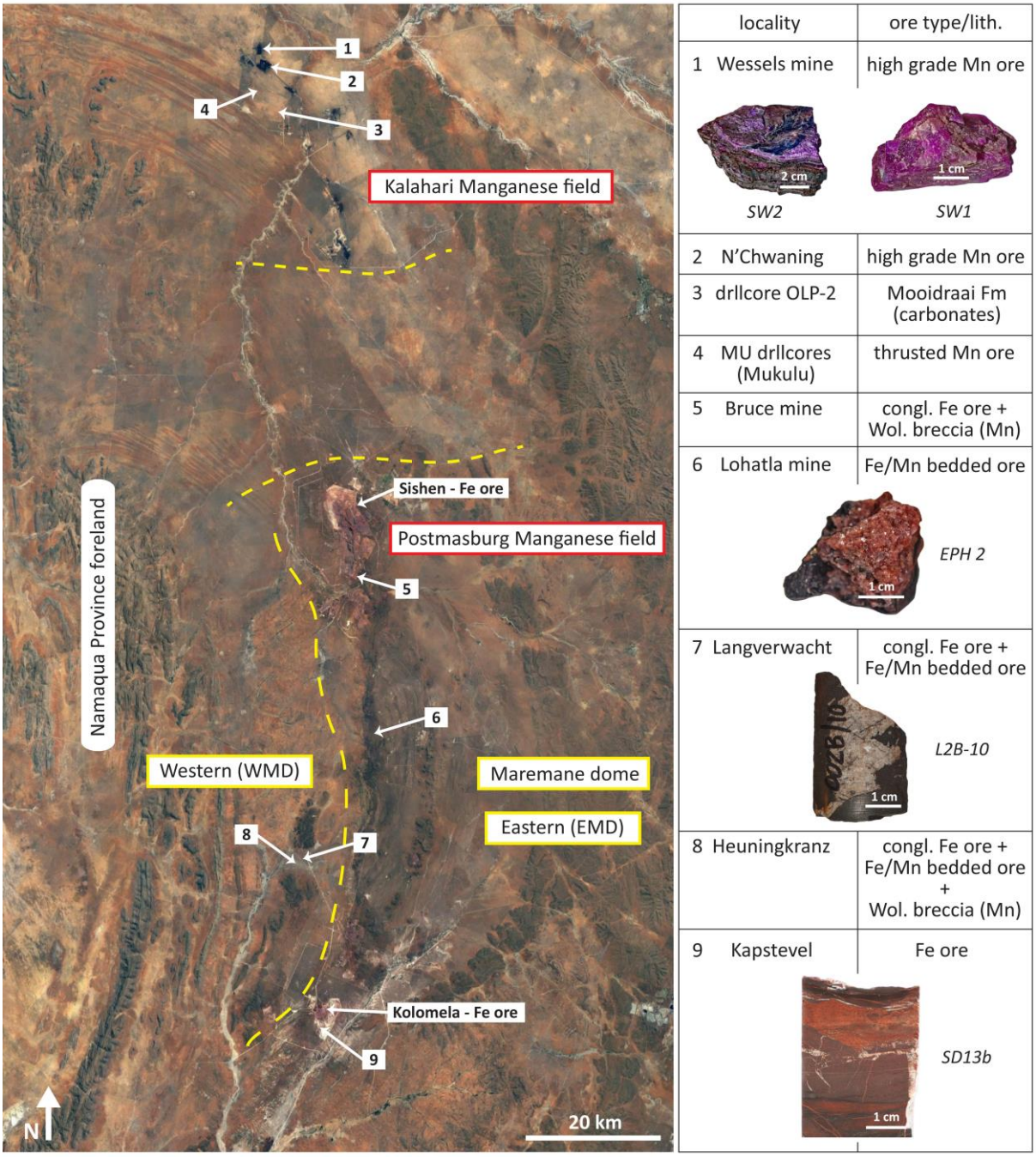

Figure 1. Geographic and lithological distribution of all dated targets from the current work and all available geochronological studies in the KMF and PMF. See also Figure 2 for age results and references.

metasomatism, as that seen in the northern part of the KMF, is also shown to exist repeatedly with respect to many localities in the PMF, hosting comparable hydrothermal assemblages. The age consistency displayed between the different localities, not only substantiates the common origin of alkali metasomatism on a regional-scale, but also gives insights into the timespan and spatial extent of tectono-thermal/alteration events associated with the

Namaqua orogeny. Figure 1 illustrates the geographic and lithological distribution of all dated minerals and Figure 2 summarizes all geochronological results and related geological and tectonic events.

A suite of in situ $^{40}Ar/^{39}Ar$ dated samples comprising three different sugilite samples (1139 ± 5, 1133 ± 2 and 1064 ± 4 Ma), muscovite (1137 ± 2 Ma), phlogopite (1037 ± 8 Ma) and potassic magnesio-arfvedsonite (1091 ± 7 Ma) from the KMF provide additional proof of the timing of hydrothermal enrichment during Namaqua orogeny and collectively suggest a refined temporal extent of hydrothermal activity in this locality spanning from 1139 ± 5 to 1037 ± 8 Ma, i.e., ca. 100 Ma in contrast to ca. 37 Ma crudely determined from previous age results. Although some caution should be exercised when interpreting the younger age signals of amphibole (1091 ± 7 Ma) and phlogopite (1037 ± 8 Ma), since they derive from a sample with clear evidence of isotopic disturbance of the Ar-system (see also next section) in other coexisting phases (sugilite and norrishite), a pattern of somewhat distinct 'older' and 'younger' ages within the 1.2-1.0 Ga period of the orogeny is also loosely replicated in the PMF. Specifically, the hydrothermal mica phlogopite (1188 ± 4 Ma), muscovite (1129 ± 4 Ma) and ephesite (1125 ± 15 Ma) from ferromanganese ore and country quartzite are believed to have formed notably earlier than paragonite (1067 ± 8 Ma) and hyalophane (1102 ± 29 and 920 ± 9 Ma) occurring in iron ore and ferromanganese deposits respectively. Again, some of the 'younger' ages should be treated cautiously, considering that the obtained age profiles suggest that loss of radiogenic ^{40}Ar may have occurred during a late thermal event and the fact that feldspars are generally prone to diffusive loss of ^{40}Ar.

However, additional age information (1020 ± 13 Ma) from an unidentified matrix-hosted silicate (termed as K1 and possibly representing either a mica/smectite or less likely an amphibole) adjacent to a late calcite-barite-feldspar vein implies that isotopic resetting and re-equilibration of preexisting gangues may have taken place during late-stage thermal events, that are distinct for example from episodes of phlogopite crystallization (1188 ± 4 Ma) in the same ores. Furthermore, textural evidence of cross-cutting relationships, as in the examples of late-infiltrating amphibole (1091 ± 7 Ma) in the KMF, or seemingly late calcite-veins with coexisting syn- or recrystallized hyalophane (920 ± 9 Ma) in the PMF ores, indicate an episodic character of hydrothermal activity. A number of replacement textures and a crude

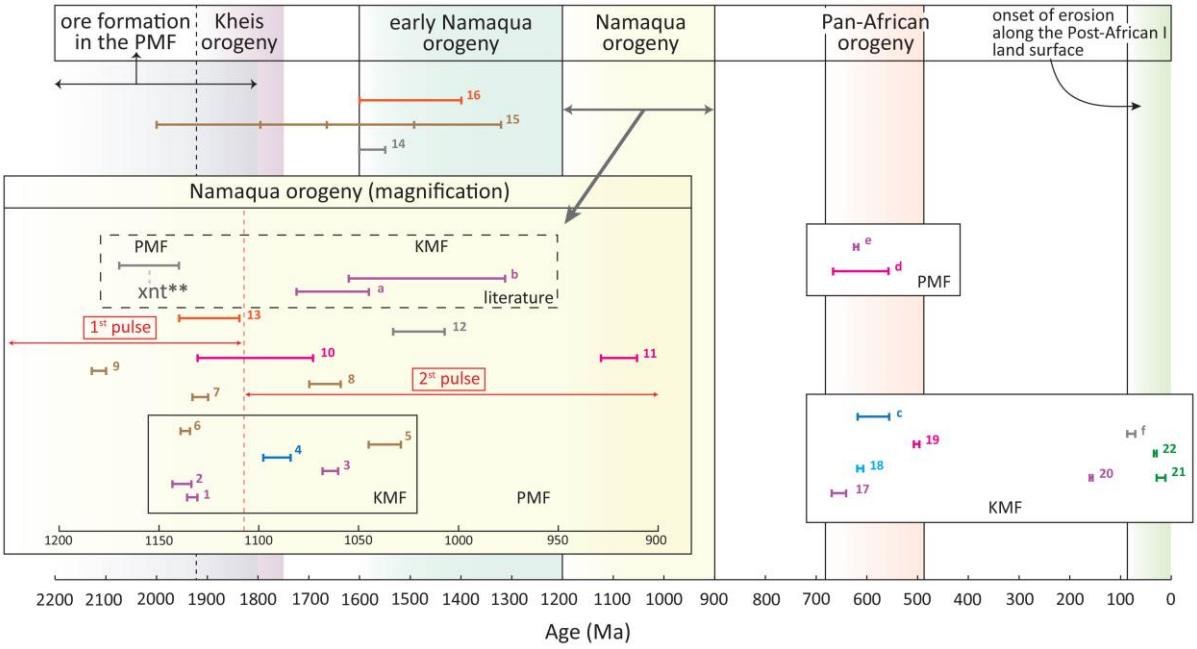

Kalahari Manganese Field (KMF)

sample ID	age (Ma)	mineral	host rock
Wessels			
SP1 SW1	1139 ± 5 1133 ± 3	1 sug 2 sug	high-grade Mn ore
SB1a+b	1064 ± 4	3	hematite lutite
—	1063 ± 18 1026 ± 29	a sug b nrs	high-grade Mn ore
SW2a+b	655 ± 14* 613 ± 5 502 ± 5 360 ± 17 # 1037 ± 8 1091 ± 7	17 sug 18 lip 19 kfs nrs 5 phl 4 Marf	hematite lutite or banded iron-formation
WBC	1138 ± 3	6 ms	hematite lutite
N'Chwaning			
SN2 N_HA N_HA2	156-158 30-32 12-28	20 sug 22 apl 21 apl	high-grade Mn ore
Mooidraai Fm			
—	588 ± 31††	c carbonates (whole rock)	
Mukulu farm			
—	77 ± 7.5†	f ap	thrusted Mn ore

Postmasburg Manganese Field (PMF)

sample ID	age (Ma)	mineral	host rock
Bruce mine			
—	620 ± 3	e sug	Wolhaarkop breccia
Lohatla			
EPH1 EPH2	ca.1500** 1125 ± 15	16 eph 13 eph	ferromanganese ore
Langverwacht			
L2B-8	1102 ± 29 1020 ± 13 1575 ± 25	10 hlp 12 K1 14 C1	ferromanganese ore
L2B-10 L537-7 BaQ2	920 ± 9 1188 ± 4 1129 ± 4	11 hlp 9 phl 7 ms	ferromanganese ore quartzite
Heuningkranz			
PM17-16	1665, 1493*	15 prg	ferromanganese ore
—	614 ± 50	d kfs	Wolhaarkop breccia
Kapstevel (Kolomela mine)			
SD13b	1067 ± 8	8 prg	iron ore

Figure 2. Compilation of geochronological data from the Northern Cape of South Africa. All are $^{40}Ar/^{39}Ar$ ages apart from the U-Pb ages from Mooidraai Fm (c) and Mukulu farm (f). Data are plotted against major geotectonic and other important events. Ages highlighted in grey colour (table) are not from this study. Coloured numbers and lowercase letters next to mineral abbreviations (table) correspond to age extents (age diagram). References for ages: Gnos et al; 2003, Moore et al; 2011, Fairey et al; 2013, 2019, Vafeas et al; 2018. References for geological events: De Paolo et al; 1991, Gutzmer and Beukes; 1996a, Cornell et al; 1998, Frimmel and Frank; 1998, Moen; 1999, Kröner and Stern; 2005, Eglington; 2006, Gutzmer et al; 2012. Mineral abbreviations: ap = apatite, apl = apophyllite, C1 = unknown matrix-hosted silicate, possibly glauconite, eph = ephesite, hlp = hyalophane, K1 = unknown matrix-hosted silicate, possibly celadonite, kfs = K-feldspar, lip = lipuite, Marf = Magnesio-arfvedsonite, ms = muscovite, nrs = norrishite, phl = phlogopite, prg = paragonite, sug = sugilite. Notes: * A second sugilite Ar/Ar age (479 ± 27 Ma) from the same sample corresponds more closely to the k-feldspar age (see also next section). ** U/Pb xenotime age (see text) # significant Ar-loss, poor age. † U/Pb apatite dating. †† lower intercept Pb/Pb age, i.e., metasomatic overprint. ★ Pronounced age peaks from Ar-Ar age distribution profile. ★★ Integrated age, obtained range 1600-1400 Ma.

paragenetic sequence suggested for the gangue mineralogy seen in ferromanganese ores of the PMF (chapter 6) are congruent with the existence of an evolving hydrothermal system comprising a series of sequential events.

In light of the above, the apparent longevity of the regarded hydrothermal system, i.e., ca. 100 Ma, is not considered to represent a continuous, evolving and prolonged event but instead episodic fluid flow that is linked to major periods of orogenic activity along the margins of the Kaapvaal Craton.

Syn-tectonic Namaqua granitoids in the external Namaqua terrains show broadly a bimodal character, with emplacement dates clustering in two periods of presumably more intense igneous activity, at 1190 ± 30 Ma and 1040 ± 30 Ma (Robb et al; 1999, Evans et al; 2001, Clifford et al; 2004, Eglington; 2006). Therefore, it is likely that both the onset and peak of the orogeny are echoed throughout the edge of the Kaapvaal Craton as distinct pulses of hydrothermal fluid flow induced by tectonic activity at ca. between 1188-1133 Ma and ca. 1102-920 Ma, in-between a relatively 'quieter' period. However, the dichotomy between these presumed periods of alteration is not conspicuous in the current dataset (Figure 2) and certainty more research is needed to understand the mode of manifestation of the Namaqua orogeny in these ore districts.

New age constraints from this study have significant geotectonic implications as regards the spatial extent of Namaqua orogeny and the so-called 'Kheis' Province.

Much debate has raged over the exact boundaries of the latter zone and interpretation of associated radioisotopic ages have been matters of considerable dispute and confusion in the literature. Some researchers have argued that evidence for an 1.9-1.7 Ga tectono-metamorphic Kheisian fabric are very scant and this distinct orogeny represents instead an early phase of the Mesoproterozoic evolution of the Namaqua Belt (Moen; 1999, Eglinton; 2006). The suite of $^{40}Ar/^{39}Ar$ ages obtained in this study demonstrates that the eastern foreland of the Namaqua Province (Kheis Province, depicted in Figure 20, chapter 6)

shows a good record of Namaqua ages in contrast to the scant available Kheisian ages. Moreover, the eastward transgression of Namaqua-related tectono-thermal activity across the Blackridge Fault system and onto the Kaapvaal Craton is corroborated by the age of alkali metasomatism in the Maremane dome (1125 ± 15 Ma, ephesite age). A U-Pb xenotime age of 1155 ± 15 Ma from Sishen iron ore mine (Rasmussen, pers. comm.), from a sample obtained and investigated by the author during his MSc research (Papadopoulos; 2016), furthers adds to the large number of Namaqua radiometric ages flanking the Blackridge Fault system; thus, reinforcing the concept of regional fluid-flow along large-scale georgical structures in the area.

To summarize, it is now well-established that the western edge of the Kaapvaal Craton is thermally disturbed from processes associated with the Namaqua orogeny, a fact that further calls into question the existence of the poorly constrained Kheis orogeny, but also highlights the possibility of this strong overprint to have potentially concealed the earlier tectonic and mineralization history of the area. In addition, by virtue of the current radioisotopic ages, the eastern foreland of the Namaqua Province, i.e., Kheis Province, should be better viewed as another tectonic zone within the extensive Namaqua Province and therefore, the revised definition of the Kheis Terrane proposed by van Niekerk and Beukes (2019) is presently more suitable.

A newly emerging regional Neoproterozoic event

The shared epigenetic history of the two ore fields and their influence by broadly coeval fluid flow is further corroborated by evidence for the existence of a regional post-Namaqua Neoproterozoic event.

$^{40}Ar/^{39}Ar$ data from banded sugilite in the KMF (Wessels mine) display ^{40}Ar-loss and partial re-equilibration of the Ar-system with regard to a heating event that is best represented by the precipitation age of coexisting lipuite (643 ± 7 Ma), a rare species firstly reported here from this mine.

The waning stages of this hydrothermal event or probably cooling below Ar-closure temperature of the associated dated minerals took place at ca. 500 Ma, as it can be deduced by the pronounced weighted mean ages of sugilite (479 ± 17 Ma) and thermally reset k-feldspar (502 ± 5 Ma) contained in the same sample. What is important though is that the 'best estimate' of the reset age of sugilite from Wessels (655 ± 14 Ma) is consistent with previously obtained ages from comparable alkali-rich assemblages in the PMF.

In particular, sugilite from manganiferous sediments in the Bruce mine (northern PMF) has yielded an age of 620 ± 3 Ma (Moore et al; 2011), interpreted as reset age on the grounds of sugilite having originally crystallized during the Namaqua orogeny, similarly to the KMF. This interpretation is in line with the new data from the KMF, which in addition hint to a separate common alteration event between the two districts, occurring later in the Neoproterozoic. Further evidence from previous studies that support this hypothesis include an $^{40}Ar/^{39}Ar$ in situ age of K-feldspar (614 ± 50 Ma) from the manganiferous Wolhaarkop breccia in the PMF and a U-Pb lower intercept age of 588 ± 31 Ma from the Mooidraai Formation in the KMF (Corfu et al; 2009, Fairey et al; 2019). However small, this number of distinct Neoproterozoic ages alludes to a disturbance of various geochronologic clocks in the Northern Cape during a thermal event occurring sometime between ca. 650-600 Ma.

Preservation of a strong Namaqua signature along with the Neoproterozoic age signals, not only in the same localities (i.e., Wessels-KMF, Heuningkranz-PMF) but also on the sample-scale, attests to the lack of complete thermal overprint, possibly owing to the low temperature of fluid circulation that for example caused partial to complete reset of sugilite and k-feldspar in places but apparently barely affected the isotopic systematics of mica or amphibole coexisting with sugilite in other alteration sites. At the same time, the regional age consistency supports shared response to a large-scale and pervasive event, akin to that earlier event in response to Namaqua orogeny, i.e., stratigraphically-restricted to the lithologies straddling regional geological boundaries such as the Blackridge Thrust belt and the regional unconformity between the Transvaal and Olifantshoek Supergroup.

The age similarity between the Neoproterozoic ages (ca. 655 - 588 Ma) and the timespan of recorded Pan-African ages (610-490 Ma) in the Gariep belt and Natal Sector of South Africa, but also with the more distal age signals of rift-related magmatism and granitoid intrusions (760 and 650-488 Ma respectively) of the Damara belt, is very intriguing.

Despite the vast distance (ca. 500 km) between the study area and the documented Pan-African orogenic belt, transportation of fluids over distances of the scale of hundreds of kilometres within extensive sedimentary basins has been demonstrated in the literature and the dynamic coupling between continental-scale groundwater fluid flow and tectonic evolution of the crust has been regularly emphasized (Kharaka et al; 1985, Oliver; 1986, Garven; 1995, Duane and Saggerson; 1995).

Whereas at present, the exact origin of the ca. 600 Ma event in the Northern Cape remains uncertain, a scenario that these ages are a far-field response to the distal Pan-African orogeny is likely, although far greater research is needed before any conclusions are reached.

In view of the foregoing, an important message deriving from all geochronological results of this study so far is that (a) alkali gangue minerals hosted by Mn- and Fe-deposits have been largely behaved as isotopically closed systems after deposition, escaping later fluid circulation and modern weathering, but (b) locally and apparently to a lesser degree, certain species have been affected by later alteration events. This asserts that caution should be exercised in future $^{40}Ar/^{39}Ar$ dating interpretations in the Northern Cape, especially as regards sugilite or k-feldspar ages (see also section 8.7 later on for young sugilite ages).

Pre-Namaqua ages in the Postmasburg manganese field

A small number of $^{40}Ar/^{39}Ar$ data are exclusively related to the PMF and in particular to the history of the deposits before the regional alkali metasomatism induced by the Namaqua orogeny. However, interpretations of these data are more open to controversy and most importantly are directly dependant on the origin of the PMF ores and the validity or not of the current models (further discussed on section 8.3).

The widely accepted surficial and karst-related mode of ore formation, is postulated to have occurred during weathering between ca. 2.2-2.0 Ga and subsequent diagenesis and low-temperature metamorphism at about 1.9-1.8 Ga, coincident with the controversial Kheis orogeny (Figure 2). If this geological framework is accepted, the following line of evidence should be interpreted: (a) a silicate $^{40}Ar/^{39}Ar$ in situ age of 1575 ± 25 Ma from ferromanganese ore matrix (WMD), reflecting Ar-contribution from an identified phyllosilicate-clay mineral (named C1, possibly glauconite) b) very scattered and 'old' pre-Namaqua $^{40}Ar/^{39}Ar$ in situ paragonite ages from a silicate-rich band in sharp contact with ferromanganese ore (WMD). The age profile of this sample comprises significant peaks at ca. 1794, 1668 and 1491 Ma. (c) Integrated step-heating $^{40}Ar/^{39}Ar$ ages of 1470 ± 50 Ma and 1604 ± 46 Ma from ephesite, being older from the plateau age of ephesite (1125 ± 15 Ma) from a mine nearby (EMD).

A number of explanations involving partial argon loss, excess argon or contamination from another unidentified mineral have been regarded for paragonite (b) (chapter 6), although no meaning has been attached to this age. As regards the phyllosilicate (C1) age (a), it has been postulated that it reflects timing of mineral formation and in particular, a preserved age of a thermal event prior to Namaqua orogeny (but succeeding 1.9-1.8 Ga Kheis), which is more closely related to the diagenetic/metamorphic evolution of the ores. To better understand this, one has to contemplate that these ores represent chemical deposits (Gutzmer and Beukes; 1996a) and clastic/phyllosilicate material precursor to the dated mineral was incorporated in the ore matrix before sediment consolidation and subsequent diagenetic/low-grade metamorphic processes.

A more robust interpretation derives from the ephesite ages (c), which can be explained as older than the 'true' age and specifically, as the result of extraneous ^{40}Ar inherited from a former phase in the host rock.

Nevertheless, whatever the mode of ore formation and exact timing of ore accumulation, the obtained $^{40}Ar/^{39}Ar$ data combined with textural evidence are believed here to support that the dated targets do not represent allochthonous material, but instead were present in the protore at the time of the 1.2-1.0 Ga Namaqua overprint. From this point on, these ages

should be regarded with caution and many interpretations tied to paragonite and phase C1 ages are purely speculative.

Emphasis should be given on the fact that Namaqua orogeny has apparently not masked ages of former geological events in the PMF, which means that certain geochronological clocks in these ores may provide more accurate estimates of these events in the future. Noteworthy is also the fact that two of the dominant peaks of paragonite (1668 Ma and 1491 Ma) overlap with the age range of mineral C1, which in turn lies within the timeframe of intrusive/volcanic activity and emplacement ages in the outer terranes of the Namaqua Province (reported ages from 1600 to 1750 Ma: Cornell et al; 1998, De Paolo et al; 1991, Eglington; 2006, Cornell et al; 2006).

It can be therefore surmised that extensional tectonics originating on the Craton during evolution of the outer terranes have contributed to heating of fluids and expulsion along the Craton margin. It is interesting that our limited Pre-Namaqua age data do not show much temporal resemblance to the controversial deformational/metamorphic Kheis event.

Whatever the case, older ages may be used as clinching evidence to suggest a relationship with the early stages of the Namaqua orogeny (ca. 1600 Ma) or at least accentuate that the age of the speculated metamorphism affecting these ores during the poorly constrained Kheis orogeny should be reappraised.

Lessons from in situ $^{40}Ar/^{39}Ar$ dating of fine-grained metasomatized Fe- and Mn-rich rocks

In the absence of other applicable radioisotopic dating techniques, employment of in situ $^{40}Ar/^{39}Ar$ dating on the extremely fine-grained Fe- and Mn-ores of the Northern Cape proved to be invaluable. First and foremost, it helped to overcome difficulties of extracting fine K-bearing minerals from the rocks. Taking into account the whole dataset, it can be said that the number of spot analyses is subject to the dating target and specific sample. However, in most cases it was found that *even less than ten spot dates can provide an age with rather good precision* for the regarded Precambrian rocks.

Excellent knowledge of the material and very detailed maps are imperative for this method and therefore in instances where uncertainties were present with respect to mineralogy and intergrown phases or mixed populations had not been previously identified, as in the case of sample PM17-16 (paragonite), the obtained age information could not be adequately evaluated. Another limitation that may have been responsible for a greater age scatter or contributions from distinct Ar reservoirs in cases of fine-grained and intricately associated mineralogy (sugilite samples and particularly SW2), is *the two-dimensional observation of the ablation spot circles*. On the other hand, identification of *distinct ways of ablation of certain phases* such as that observed for lipuite producing ellipsoidal pits on a somewhat softer material, can be used as an advantage and additional criterion for assessing mineralogical purity of the analysed spots. Low and variable potassium content of minerals (for example celsian-hyalophane) was proven to hamper in situ analyses in this study, in the sense that *large laser size* (110 and 155 μm) was needed to extract sufficient gas which *resulted in ablated cluttering the surroundings of ablated pits and blurring laser optics* for an extensive area around them. Furthermore, however small (option for 20 μm size), the size of the laser spot is not sufficient to distinguish between different grains and potentially mineral generations in such fine-grained rocks.

In certain samples, $^{40}Ar/^{39}Ar$ age results exemplify the density and importance of age information that complex targets can disclose when interrogated by high-spatial resolution UV laser ablation technique. The 1575 ± 12 Ma silicate age (C1) next to the 1020 ± 13 Ma age (K1) of another distinct K-bearing phase in the same matrix (sample L2B-8), showcases the *high $^{40}Ar/^{39}Ar$ age heterogeneity of different sample domains being only microns apart*, that can be revealed only with the aid of the laser microprobe technique. Probably the best example for the above capability of the method is the critical age information extracted from sample SW2. $^{40}Ar/^{39}Ar$ data from *six distinct mineral targets spatially confined within the limits of a normal petrographic thin section*, reveal highly variable ages between the mineral phases, ^{40}Ar-loss and the causing event (i.e., later formed minerals), the effects of thermal heating to pre-existing phases and preservation of older meaningful geological events, thus clearly *defining two separate hydrothermal events separated by ca. 500 Ma*. In yet another example from sugilite in the KMF (sample SB1), intrasample age variations coupled with textural observations, apparently disclose *distinct episodes of sugilite formation* corresponding to

succeeding hydrothermal pulses that may have been separated by an interval of ca. 60-70 Ma. This latter case also suggests that *large number of analyses* (i.e., > 25), covering different domains of sugilite bands, may be required in order to document the whole span of age information and in addition *report a meaningful weighted mean age*. It is almost certain, that other lower spatial-resolution or bulk methods involving $^{40}Ar/^{39}Ar$ laser fusion or step-heating would have obscured this age information and therefore potentially led to misinterpretation of geochronological data.

1.2 Mineralogical evidence

Regional alkali (Na,K,Ba,Ca)-rich mineral associations

Although they may not constitute hard evidence, mineralogical similarities between the two ore districts have been key clues about the possible common origin of the processes that formed them and have originally driven this hypothesis in the current and other previous studies. The repeating signal of alkalis is manifested by compositionally similar mineralogical associations that further comprise identical species and by virtue of various isotopic evidence can be safely regarded at large as having formed indeed by broadly similar and contemporaneous processes. These minerals are developed for the most part in the various manganese ore-types but Fe ores and surrounding lithologies such as quartzite may also host considerable amounts of diverse gangue species.

Distribution of alkalis in the various ore-types emphasizes control exerted by the host rock, with manganese ores, similar to other districts, exhibiting higher mineralogical variability than iron-rich or country lithologies lacking manganese, as well as more pronounced presence of Na- and Ca-rich gangue parageneses in contrast to the mainly K- and Ba-rich associations seen in the iron ores of the PMF.

As regards the PMF for instance, alkali-enrichments in quartzite are essentially characterized by simple barite-muscovite (K) associations whereas in ferromanganese ore

	mineral	chemical formula	Hotazel Fm (KMF)	Fe ore		Fe/Mn ore		Wol.breccia	
				massive	congl.	WMD	EMD	WMD	EMD
Kalahari and Postmasburg Manganese fields	albite	$Na(AlSi_3O_8)$	⬭		⬭	⬭	⬭	⬭	⬭
	aegirine	$NaFe^{3+}Si_2O_6$	⬭			⬭	⬭	⬭	⬭
	pectolite-serandite	$NaCa_2Si_3O_8(OH)$-$NaMn^{2+}{}_2Si_3O_8(OH)$	⬭			⬭		⬭	⬭
	natrolite	$Na_2Al_2Si_3O_{10}2H_2O$	⬭			⬭		⬭	
	banalsite	$Na_2BaAl_4Si_4O_{16}$	⬭			⬭	⬭		
	k-feldspar	$K(AlSi_3O_8)$	⬭			⬭		⬭	⬭
	piemontite	$Ca_2Al_2Mn^{3+}(Si_2O_7)(SiO_4)O(OH)$	⬭			⬭			
	andradite-grossular	$Ca_3Fe^{3+}{}_2(SiO_4)_3$- $Ca_3Al_2(SiO_4)_3$	⬭			⬭	⬭		
	hydroxyapophyllite	$KCa_4(Si_8O_{20})(OH,F)8H_2O$	⬭			⬭			
	sugilite	$KNa_2Fe^{3+}{}_2(Li_3Si_{12})O_{30}$	⬭						⬭
	norrishite	$KLiMn^{3+}{}_2(Si_4O_{10})O_2$	⬭						⬭
	ephesite (!)	$NaLiAl_2(Al_2Si_2O_{10})(OH)_2$	⬭				⬭		
	phlogopite	$KMg_3(AlSi_3O_{10})(OH)_2$	⬭			⬭			
	barite	$BaSO_4$	⬭	⬭	⬭	⬭	⬭	⬭	⬭
	kutnohorite	$CaMn^{2+}(CO_3)_2$	⬭		⬭	⬭		⬭	
	rhodochrosite	$Mn^{2+}(CO_3)$	⬭		⬭	⬭		⬭	
	strontianite	$SrCO_3$	⬭			⬭		⬭	⬭
	lithiophorite	$(Al,Li)MnO_2(OH)_2$	⬭				⬭		
	diaspore	$AlO(OH)$	⬭			⬭	⬭		
	hollandite	$Ba(Mn^{4+}{}_6Mn^{3+}{}_2)O_{16}$	⬭			⬭	⬭		
	kentrolite	$Pb_2Mn^{3+}{}_2(Si_2O_7)O_2$	⬭						⬭
KMF - ONLY	arfvedsonite	$[Na][Na_2][Fe^{2+}{}_4Fe^{3+}]Si_8O_{22}(OH)_2$	⬭						
	richterite	$Na(NaCa)Mg_5Si_8O_{22}(OH)_2$	⬭						
	hennomartinite	$SrMn^{3+}{}_2(Si_2O_7)(OH)_2H_2O$	⬭						
	wesselsite	$SrCuSi_4O_{10}$	⬭						
	effenbergerite	$BaCuSi_4O_{10}$	⬭						
	scottyite	$BaCu_2Si_2O_7$	⬭						
	gatehouseite	$Mn^{2+}{}_5(PO_4)_2(OH)_4$	⬭						
	gaudefroyite	$Ca_4Mn^{3+}{}_{2\text{-}3}(BO_3)_3(CO_3)(O,OH)_3$	⬭						
	ettringite	$Ca_6Al_2(SO_4)_3(OH)_{12}26H_2O$	⬭						
	shigaite	$Mn_6Al_3(OH)_{18}[Na(H_2O)_6](SO_4)_26H_2O$	⬭						
PMF - ONLY	paragonite	$NaAl_2(AlSi_3O_{10})(OH)_2$		⬭		⬭			
	Ba-muscovite	$(K,Ba)(Al,Mg)_2(AlSi_3O_{10})(OH)_2$				⬭	⬭		
	hyalophane-celsian	$(K,Ba)[Al(Si,Al)Si_2O_8]$				⬭			
	noélbensonite	$BaMn^{3+}{}_2(Si_2O_7)(OH)_2H_2O$							⬭
	armbrusterite	$K_5Na_7Mn_{15}[(Si_9O_{22})_4](OH)_{10}4H_2O$			⬭				⬭
	gamagarite	$Ba_2Fe^{3+}(VO_4)_2(OH)$					⬭		
	Ba-goyazite	$BaAl_3(PO_4)(PO_3OH)(OH)_6$					⬭		
	barytocalcite	$BaCa(CO_3)_2$				⬭		⬭	
	tamaite	$(Ca,K,Ba,Na)_{3\text{-}4}Mn_{24}(Si,Al)_{40}(OH)_{112}21H_2O$				⬭			
	As-tokyoite	$Ba_2Mn^{3+}(VO_4)_2(OH)$				⬭			
	macedonite	$PbTiO_3$				⬭			

Figure 3. A selection of minerals tabulated here highlights the many mineralogical similarities between gangues of the PMF and KMF, but also exclusive species found in each district.

barite can be associated at the same time with an abundance of Na-K and Ca-bearing species such as natrolite, albite, aegirine, serandite, calcite, hyalophane and phlogopite. Exceptions to the above exist, namely, barite with sodium-rich silicates and Mn-carbonates in conglomeratic Fe-ore (Langverwacht) or ferruginous quartzite (Heuningkranz) and barite-paragonite (i.e., sodium-rich) parageneses in the Kolomela mine (Kapstevel). The former not only demonstrate that introduction of alkalis may spread into iron-rich lithologies but also that a certain degree of manganese migration from manganese- to iron-rich entities occurs. On the other hand, sodium-depleted and K-, Ba-, Ca- CO_3-bearing associations (Mn-carbonates, calcite, barite, K/Ba feldspars) with abundant sulfur are also found in the ferromanganese ores of the PMF.

Focusing on the mineralogical similarities between the KMF and PMF, a large number of silicates, carbonates, sulfates and oxides is common in both (Figure 3). Aegirine, albite, natrolite, serandite-pectolite, banalsite, k-feldspar, piemontite, garnet (grossular, andradite), apophyllite, sugilite, ephesite, phlogopite, barite, calcite, kutnohorite, rhodochrosite, siderite, strontianite, lithiophorite, diaspore, hollandite, kentrolite, norrishite, pyrophanite are some the minerals that have been reported from both districts (Gutzmer and Beukes; 1996b, Cairncross et al; 1997, Cairncross and Beukes; 2013, this study).

The affinity between the two fields is not only restricted to comparable species but extends to mineralogical associations and their broadly replacive-type textures.

Aegirine in the KMF is commonly associated with k-feldspar, albite, sugilite, barite and the calc-silicates serandite-pectolite and in addition, it generally occurs as a layer-distributed phase and lesser as void-fillings discordant to sedimentary bedding, largely following distribution of sugilite. Likewise, in the PMF, aegirine coexists or is in close association with k-feldspar, hyalophane-celsian, albite, natrolite, serandite-pectolite and sugilite in the case of Bruce mine (Moore et al; 2011, this study). Layer-parallel development for this mineral though has been only observed within fragmented and possibly remnant clasts, whereas its

main occurrences is as void-fillings, vugs and veins. Another parallel can be drawn between carbonate associations regionally. Calcite and Mn-carbonates (manganoan calcite, kutnohorite, rhodochrosite) are typically seen in the KMF within assemblages comprising garnet, hematite, gaudefroyite, barite and other sulfates (celestine, sturmanite, etc.) (e.g., Gutzmer and Cairncross; 2002). Carbonate minerals (calcite, siderite, kutnohorite, rhodochrosite, strontianite) are apparently more restricted and broadly fine-grained in the PMF but are chiefly associated with sulfates and/or hematite (Papadopoulos; 2016, this study), although feldspars, sodium-rich silicates and garnet may also be present. Furthermore, apophyllite, firstly reported here from the PMF, is associated with calcite, natrolite and witherite, a paragenesis that is compositionally comparable with that of apophyllite, inesite and natrolite described from the KMF.

One of the principal common features displayed by the alkali-bearing assemblages is that of their metasomatic nature, manifested in the KMF by preservation of sedimentary bedding and early ovoidal structures in iron-formations, hematite-lutite and Mn ore during formation of aegirine or sugilite-bearing calc-silicate parageneses and further replicated in the PMF by replacements akin to the aforementioned.

Paragonite-hematite ooids, barite pseudomorphed carbonate rhombs in altered iron-formation, parallel laminae comprising banalsite-feldspar-natrolite or hydrothermal mica (muscovite-paragonite, ephesite) in Mn ore, replacement of concretions and common quartz-clasts replacements by associations of aegirine, albite, serandite, armbrusterite, hollandite and hyalophane are only some of the textures underlining the metasomatic character of the alteration in the PMF.

As evident from the well-studied KMF and in particular sugilite or Mn-carbonate associations, gangues may fill large cracks and vugs in host rock, but the existence of abundant feeding channels parallel to bedding, immediately below mineralization pockets, as well as lateral spread of hydrothermal minerals, highlights the layer-parallel metasomatism.

Emphasis should be also given to certain mineralogical features that according to current knowledge are unique to each district. For example, amphiboles which are present in

the KMF (arfvedsonite, namansilite, richterite) have not be found so far in the PMF. Garnet is also largely absent from the latter and when present is very fine-grained. At the same time, as documented in this study, micas (muscovite, paragonite, Ba-muscovite, phlogopite and some magnesium end-members such as celadonite appear to be common as banding constituents in the ferromanganese ores of the PMF and muscovite rather common in breccia cements and void-filling in iron ore. Additionally, they are seemingly associated to a large extent with hematite and although their origin may partly represent earlier diagenetic/metamorphic processes, clear examples of hydrothermal or recrystallized Namaqua-related mica exist. As regards the KMF, only phlogopite has been reported and here was seen mostly occurring as layer-parallel phase in aegirine-sugilite-bearing iron-formation.

The difference in abundance of micas is most likely related to the intrinsic extremely low to non-existent aluminosilicate content of the Hotazel Formation (KMF) in contrast to the much higher original concentrations presumed to have been present in the PMF protores.

A primary host rock control is also related to the occurrence of ephesite, which apart from Li, requires a particularly Al-rich environment and is thus limited to Al-rich ferromanganese ores of the PMF. Meanwhile, the Li-bearing sugilite is abundant in the KMF but in comparable alkali assemblages in the PMF, that are also hosted by Mn ore, the mineral has been only found in a handful of occurrences from a single drillcore (Moore et al; 2011) (see also section on Li species later on).

Members of the hyalophane-celsian feldspar series, present in the Bruce mine (PMF) and Heuningkranz-Langverwacht localities are unreported from the KMF, whereas common species between the two such as banalsite, seem to be particularly abundant in the PMF, i.e., in such proportions that can account for the high barium in the ferromanganese ore (Fairey; 2013, this study). Other rare Ba- or K-bearing species, such as noélbensonite or armbrusterite, have been reported only from the PMF (Figure 3). The former mineral though belongs to the lawsonite group and therefore is closely related to the equivalent Sr-bearing hennomartinite from the KFM. Other barium species exclusive to the PMF are the well-documented vanadate gamagarite and the barium phosphate (alunite) firstly reported here from the ephesite-rich

ores, namely barian goyazite. This district apparently also hosts several unidentified Ba-bearing and Mn-rich silicates as noted in the present study, as well as tamaite, a rare hydrous silicate, proxy of the whole major alkali suite of elements (Ca, Ba, Na, K) characterizing the Namaqua metasomatic event. Ba-carbonates (witherite and barytocalcite) are also found in the ferromanganese ore, growing on earlier-formed calcite and barite but apparently are not encountered in the KMF. However, the latter comprises other rare Ba/Cu silicates and phosphates such as wesselsite, scottyite, effenbergerite and gatehouseite (Giester and Rieck; 1996, Gu et al; 2019).

All things considered, mineralogical differences within the same large-scale fluid circulation system are probably related to local factors such as variability of country lithology and changes in fluid composition and its physicochemical parameters during succeeding stages/pulses and mixing with other aqueous solutions.

Complex parageneses, crosscutting textures, different solubilities of Na, K and Ba chloride complexes in aqueous fluids and geochronological evidence support the aforementioned hypothesis for successive hydrothermal pulses in both fields. A tentative paragenetic sequence based on the Langverwacht-Heuningkranz localities (chapter 5, Figure 23) broadly depicts Na-bearing silicates as early phases and K-, Ba-silicates, carbonates and sulfates as main- and late-stage phases. What is important is that the recurring theme of alkali assemblages and other associated hydrothermal species is in agreement with both the timing and origin of the metasomatic fluids (see also section 8.1.3) and such enrichments in many ores of the Northern Cape accentuate that their composition is also determined by epigenetic processes introducing comparable elements regionally.

Furthermore, although there is no argument that much higher structural- and host rock-related secondary porosity in the KMF, possibly along with differences in the physicochemical parameters of the fluids has led to the development of much coarser and well-crystallized and gem quality specimens, PMF can also claim certain mineralogical fame, not only because of the ephesite-rich ores (Lohatla, Glosam, Gloucester mines) (Cairncross; 2017), but also if all latest reports from Bruce mine and the WMD ores are taken into account.

The mineralogical heritage of the latter may be chiefly restricted to very-fine grained and intermixed assemblages but its abundance is manifested in conspicuous and metre-thick breccias or prominent veins that rarely host somewhat coarser species such as natrolite, calcite, rhodochrosite or barite. Most importantly though, important mineralogical findings such as that of sugilite, armbrusterite, As-tokyoite, noélbensonite, macedonite and pyrobelonite demonstrate that hydrothermal overprint of Fe/Mn-rich protoliths has caused the growth of remarkable minerals also in the PMF and imply that for further research will lead to new discoveries in the area.

*An updated count conducted after the findings of the present study suggests that about seventy-one **(71) species** have been found to date in the PMF.*

In comparison, over 200 declared mineral species found in vugs, veins and fault zones are reported from the KMF (Cairncross and Beukes; 2013).

Rare and newly reported Pb-, V- and As-bearing phases

A suite of intriguing Pb-, As- and V-bearing mineral species is tabulated in Figure 4. Although there is no direct evidence linking the two ore fields on the basis of these sporadic elements of low abundance, comparable rare As-, V- and Mn^{3+}-bearing species have been reported from other Mn districts, forming by late circulating and strongly oxidizing fluids

mineral	chemical formula	Mn ore	Fe/Mn ore		Wol.breccia
		KMF	WMD	EMD	EMD
As-tokyoite	$Ba_2Mn^{3+}(As,VO_4)_2(OH)$		⬭		
As-rich apatite	$Ca_5(As,PO_4)_3(Cl,F,OH)$		⬭		
As-rich hematite	Fe_2O_3 (As)		⬭		
noélbensonite	$BaMn^{3+}{}_2(Si,V_2O_7)(OH)_2(H_2O)$		⬭		
kentrolite	$Pb_2Mn^{3+}{}_2(Si_2O_7)O_2$	⬭			⬭
pyrobelonite	$PbMn^{2+}(VO_4)(OH)$		⬭		
macedonite	$PbTiO_3$		⬭		
gamagarite	$Ba_2(Fe^{3+}, Mn^{3+})(VO_4)_2(OH)$				
V-fermorite	$Ca_5(As,VO_4)_3OH$	⬭		⬭	

Figure 4. Pb-, V- and As-bearing species from the PMF and KMF. All apart from noélbensonite, which hosts only minor vanadium, have been identified during this work, some for the first time from these ores.

(Lepore et al; 2015, Kolitsch et al; 2018) and furthermore, however fine-grained, new findings in the PMF are of particular mineralogical interest.

Previous researchers have noted the co-existence of Ba-rich mineral phases with As-tokyoite and noélbensonite from the PMF and have suggested that their precipitation have occurred by interaction of a solution carrying arsenic and vanadium with pre-existing Mn-minerals (Costin et al; 2015, Fairey et al; 2019). As-tokyoite in this study was found as inclusions in banalsite veins, thus further validating previous findings and demonstrating synchronous transportation of As, V, Ba and Na in the solutions.

Other minerals in the WMD ferromanganese ores found to host appreciable arsenic (As) in their structure are fluor-apatite (5.4 wt. % As_2O_3) closely associated with albite vugs and hematite (6.6 wt. % As_2O_5) seen in hollandite-calcite associations and developing concentric layering.

The latter case of this peculiar hematite corroborates that arsenic (As) is present in Ba-bearing fluids concurrently transporting Mn and Fe and moreover, assuming that arsenic in hematite is arsenate [As(V)], a highly alkaline environment may be surmised in which As(V) sorption is increased (Di Iorio et al; 2018).

Apart from hydrothermal coronadite, two rare Pb- and/or V-bearing species are firstly reported here from the same locality, namely pyrobelonite and macedonite.

The first is hosted by hyalophane veinlets and coexists with banalsite, calcite and grossular. Noteworthily, documented pyrobelonite occurrences in the Precambrian Iron Monarch deposit (South Australia) have been attributed to late-stage alteration iron-mobilizing fluids (Pring et al; 2005). Macedonite is also found associated with banalsite, although its restricted occurrence in a silicate-band displaying sharp contact with the ore may be suggestive of the former concentration of detrital titanium. Worldwide, this rare species is seen in quartz-syenite pegmatite veins and metamorphosed Fe-Mn deposits (Burke and Kieft; 1971). Pb in the PMF is also reported from kentrolite-sugilite parageneses at Bruce mine

(Moore et al; 2011). Finally, a vanadate of particular importance, seen only in the EMD is gamagarite. This mineral firstly reported by De Villiers (1943b) as coarse-crystals in these ores, was noted in this study as inclusions within diaspore, in turn enveloped in ephesite, something that supports the coexistence of chemical reactants (Na, Al, Ba, V, Fe, Mn) in the fluids that formed these minerals. Up to this date, evidence for the presence of the regarded elements in the KMF has been limited to kentrolite, documented during this work as cross-cutting veins in banded aegirine-sugilite assemblages.

However, a new As- and V-bearing species was noted as tiny inclusions in barite, surrounded by vesuvianite crystals from N'Chwaning mine. This mineral hosts 30.7 wt. % As_2O_5 and 5.2 wt. % V_2O_5 and greatly resembles an arsenate species reported from manganese ores in India, namely fermorite (Herbert and Prior; 1911). Further research is needed to discern if maybe the vanadium-bearing fermorite from the KMF represents a distinct new species.

Li-bearing species and abundances

Parallels between the two ore fields may be further drawn on the grounds of rare Li-bearing species occurring regionally and the documented presence of this element in considerable abundances within variable ore lithologies.

It can be said that sugilite is the proxy of Li in the KMF, whereas ephesite is likewise the dominant representative of Li in the PMF,

---

since sugilite has been only found in a handful of occurrences from a single drillcore in the latter district (Moore et al; 2011). Li may be also present in trace amounts in other species of the KMF such as: (a) amphiboles, like arfvedsonite reported from this study or the recently documented potassic-mangani-leakeite [$KNa_2(Mg,Mn^{3+},Fe^{3+},Li)_5Si_8O_{22}(OH)_2$] (Gu et al; 2019), (b) other localized silicates such as lavinskyite [$K(LiCu)Cu_6(Si_4O_{11})_2(OH)_4$] (Gu et al; 2019) and (c) potentially even in aegirine, which in other metamorphosed and alkali-bearing manganiferous sediments has been reported to accommodate appreciable amounts of Li

(0.13 to 0.33 wt.% LiO_2) (Bühn et al; 1995). Overall, though, high-grade manganese ore of the KMF does not seem to contain high amounts of Li (20-80 ppm from 2 analyses).

In contrast, ferromanganese ores of the PMF which comprise higher abundances of silicate minerals host appreciable amounts of Li in: (a) micas of the muscovite-paragonite series. Li-rich micas in the WMD ores are believed to host on average 0.15-0.20 wt.% or 1500-2000 ppm Li) on the basis of whole rock abundances (ca. 1000-200 ppm Li) and estimated modal abundances of these minerals (ca. between 5 and 35 wt. %) (chapter 6). (b) ephesite, known to host between 0.12 and 0.44 wt.% Li and comprising between 9 and 59 % of the ore mineralogy in the studied samples from EMD (chapter 6) and (c) the oxide lithiophorite, which at least in the studied samples was only a minor phase.

As regards the abundance of Li in the EMD ores, further survey of the ephesite content and an economic Li resource estimate in the wider area, accompanied by assessment of the feasibility of commercial extraction, are highly recommended.

As regards the formation of the two main Li-bearing species, it can be said that ephesite precipitation in the PMF (1125 ± 25 Ma, Ar/Ar plateau age) occurred coevally to that of sugilite in the KMF (ages between 1139 ± 5 and 1064 ± 4 Ma) from very comparable fluids that imprinted their signatures on the oxygen isotopes of the two minerals (sugilite: 11.7 ± 1.1 ‰ and ephesite: +11.8 ± 0.3 ‰). Specifically, inherited ^{40}Ar in the obtained age from Glosam ephesite and the geological setting according to the prevailing models suggests possible recrystallization of ephesite from clays or earlier formed detrital aluminosilicates in the metalliferous karst system, or alternatively, formation by metasomatic reactions with former clay material within the Gamagara/Mapedi aluminous shale units overlying and being interbedded with the ore (Schalkwyk; 2005, chapter 6). However, veined ephesite suggests also direct precipitation from solution. Most importantly, involvement of shales and/or aluminum introduction satisfies the need for high amounts of this element during ephesite formation (Chaterjee and Warhus; 1984), while the role of externally derived lithium is regarded to be critical for valence compensation due to almost complete Na substitution in the structure of the Na-analogue to the Ca-bearing margarite (Schaller et al; 1967).

Likewise, sugilite has generally a metasomatic nature evidenced by its broad occurrence as layers or seams spreading laterally along conceivably compositional suitable layers (Dixon; 1985, 1988), as well as by replacement textures on the micro-scale (chapter 3). Sugilite most likely forms via mechanisms comparable to ones suggested from Tsikos and Moore (2005) for aegirine, i.e., introduction of Na, Li and probably Al from an external fluid, which then reacts with Mn released from braunite and Mn-carbonates in the host rock, as well as with Fe from BIF- or lutite-derived hematite. Its precipitation is, at least in cases, coeval to that of aegirine and

---

the most salient factor controlling its occurrence is again the availability of lithium and other fluid parameters, but perceptibly, not bulk composition of the host rock.

The above is substantiated by the apparent absence of sugilite in various Northern Cape localities with compositionally suitable host rocks and very high alkali-abundances, and furthermore, by its localized presence in quartzites at Wessels (Tsikos pers. comm.). The excessive requirement for lithium (and sodium) rules out the possibility that these elements have been inherited from the pristine immediate lithologies, but on the contrary, must have been introduced from an external source. It is noted that this conflicts with the current view of alkalis being diagenetically/metamorphically expelled from the ores themselves, in the case of ephesite formation in the EMD ores (Gutzmer and Beukes; 1996a). A brief literature survey on Li abundances in rocks and δ^7Li systematics (chapter 6, section 6.5) suggests that determination of δ^7Li values from a suite of mineral-specific and whole-rock targets can help to discern the origin of Li and identify isotopically distinct sources, which are most likely continental and involve clay minerals and chiefly Type II continental evaporites, the occurrence of the latter though being speculative and requiring further research.

1.3 Stable isotopic evidence

The case of regional barite occurrence in the Northern Cape

Barite in the Northern Cape has been extensively studied in this thesis, in terms of its textures, paragenetic associations, isotopic composition (S and Sr) and timing of formation by in situ $^{40}Ar/^{39}Ar$ dating of co-genetic micas. In this section, the major outcomes of this work are presented briefly. Barite is omnipresent in Fe-, Mn-rich lithologies and surrounding sediments such as quartzites and is always associated with Namaqua-related alkali-rich parageneses. It has a pronounced epigenetic nature (occlusion of open-space, fractures, veins, vugs, pods and lenses) and its parageneses display higher mineralogical variability in Mn-rich lithologies in comparison to Fe ores or clastic sediments, i.e., clearly indicating compositional control of the former by the host rock. Sulfur isotopic composition from texturally diverse host lithologies is remarkably constant (24.9 ± 2.5 ‰, 1σ, n= 93), implying the presence of a single and uniform sulfate pool, which by rejection of all other highly variable and lighter possible sulfur sources in the study area and due to the significant ^{34}S-enrichment in this isotopic signal, little doubt remains for the seawater or modified sweater origin of sulfur in barite.

The Neoarchean Campbellrand-Malmani carbonate platform is believed to have hosted evaporites, now evidenced by their sedimentological record (Buchanan et al; 1981, Gandin and Wright; 2007).

Therefore, barite sulfate is confidently assigned to evaporites in the carbonate stratigraphy and most likely in the Gamohaan and Kogelbeen Formations, while subtle variations in $\delta^{34}S$ values may be interpreted as reflecting dissolution of distinct evaporitic lenses with slightly different isotopic values and/or age within the stratigraphic column.

---

^{34}S-depleted values seen locally in N'Chwaning (from +18.9 to +20.7 ‰), Heuningkranz (+17.3 ‰) or Kapstevel (+17.1 ‰), may be perhaps related for example to mixing with another sulfur-bearing fluid. An exhaustive survey of the temporal sulfur isotopic fluctuations of seawater resulted in an up-to-date revised sulfur isotopic curve for the Proterozoic (chapter

2, section 5.4.2), which indicates that the approximated $\delta^{34}S$ seawater values obtained from the Northern Cape barite (i.e., +23 ± 2.5 ‰, since isotopic fractionation from sulfate solution into gypsum is around 1.65 ‰, Hanor; 2000) are at odds with the recorded range of the early Proterozoic (ca. from +8.0 to +16.0 ‰), but is comparable with seawater values displayed for most of the late Palaeo- and Meso-Proterozoic.

Hence, sulfur isotopic data are interpreted as broadly preserving a first-order evaporitic signal and not being proxies of the global marine cycle. Furthermore, the measured isotopic signal may serve as a palaeo-environmental indicator for bacterial sulfate reduction occurring in a more restricted basin, characterized by fluctuations in sulfur supply and widespread presence of microbes, in concert with conclusions from previous research on the Gamohaan Formation (Kamber and Whitehouse; 2006).

Regarding the remaining isotopic component of barite, highly radiogenic $^{87}Sr/^{86}Sr$ ratios (0.71238 - 0.73818) indicate derivation from evolved continental crust, analogous to most vein-type barite in epigenetic systems. Different crustal strontium reservoirs are suggested to have been deep-seated volcanosedimentary rocks (Ventersdorp), clastic sediments of the Olifantshoek Supergroup as strongly evidenced by the highest $^{87}Sr/^{86}Sr$ values in quartzite-hosted barite (0.72754 - 0.732308), and lesser chemical sedimentary sequences (carbonates, iron-formation). Strontium derivation from distant granitoids of the Namaqua metamorphic belt cannot be excluded since fluids are shown to have migrated over large distances. Less radiogenic values (0.70743, 0.70575) from Wessels barite perhaps reflect Sr leached directly from the Hotazel Formation or a fluid saturated in carbonate-derived Sr-isotope ratios.

However, Campbellrand carbonates directly underlying ferromanganese ore in the PMF display high $^{87}Sr/^{86}Sr$ ratios (0.719610, 0.720727), that further overlap with barite values (see also section 3 later on). In contrast, whole-rock results from the Mooidraai carbonates in the KMF (0.7029) are much less radiogenic, i.e., closer to pristine seawater, than values from prior studies used to extract information on the ancient ocean (Schneiderhan et al; 2006).

Finally, combined stable isotopic results from barite suggest that this mineral formed by mixing of: (i) deep, hot and saline basinal fluids with variable radiogenic Sr with (ii) surficial meteoric or ambient shallow groundwater introducing elevated $^{87}Sr/^{86}Sr$ ratios and dissolved Ba by leaching of siliciclastic rocks.

Oxygen-hydrogen isotopic signatures of ore and alteration minerals

The common origin of hydrothermal fluids that have influenced both ore districts has been imprinted on the O and H isotopic composition of gangue mineralogical phases. Mineral-specific stable isotopic investigations in this study were hampered by the very limited availability of pure material due to the extremely fine-grained size and intermixed nature of alteration mineralogy, particularly in the case of the Postmasburg Manganese field. Nevertheless, an inaugural step to analyse a relatively small number (O isotopes: 67, H isotopes: 56, some not shown previously in the main body of the thesis) of coarser hand-picked grains or material with minor contamination extracted from previously well-studied assemblages under optical and SEM microscopy, reveals that important results may be obtained.

The whole dataset of measured $\delta^{18}O$ mineral values is displayed in Figure 5. In general, an ^{18}O-enrichment in relation to the fluid and heavy $\delta^{18}O$ values are expected for the gangue silicate minerals due to their mere nature. However, the range of $\delta^{18}O$ ratios shown by most of the studied silicates is rather narrow (vertical black dotted lines), from +7.9 to +13.5 ‰ (average = +11.0 ± 1.6 ‰, n = 36) and the overwhelming majority of mineral phases exhibits an even tighter cluster (vertical red dotted lines) between +10.6 and +13.4 (average = +11.6 ± 1.0 ‰, n = 26). Considering sampling drawbacks and possible contaminations that are expected to reduce sample purity, this consistency in $\delta^{18}O$ values is rather surprising.

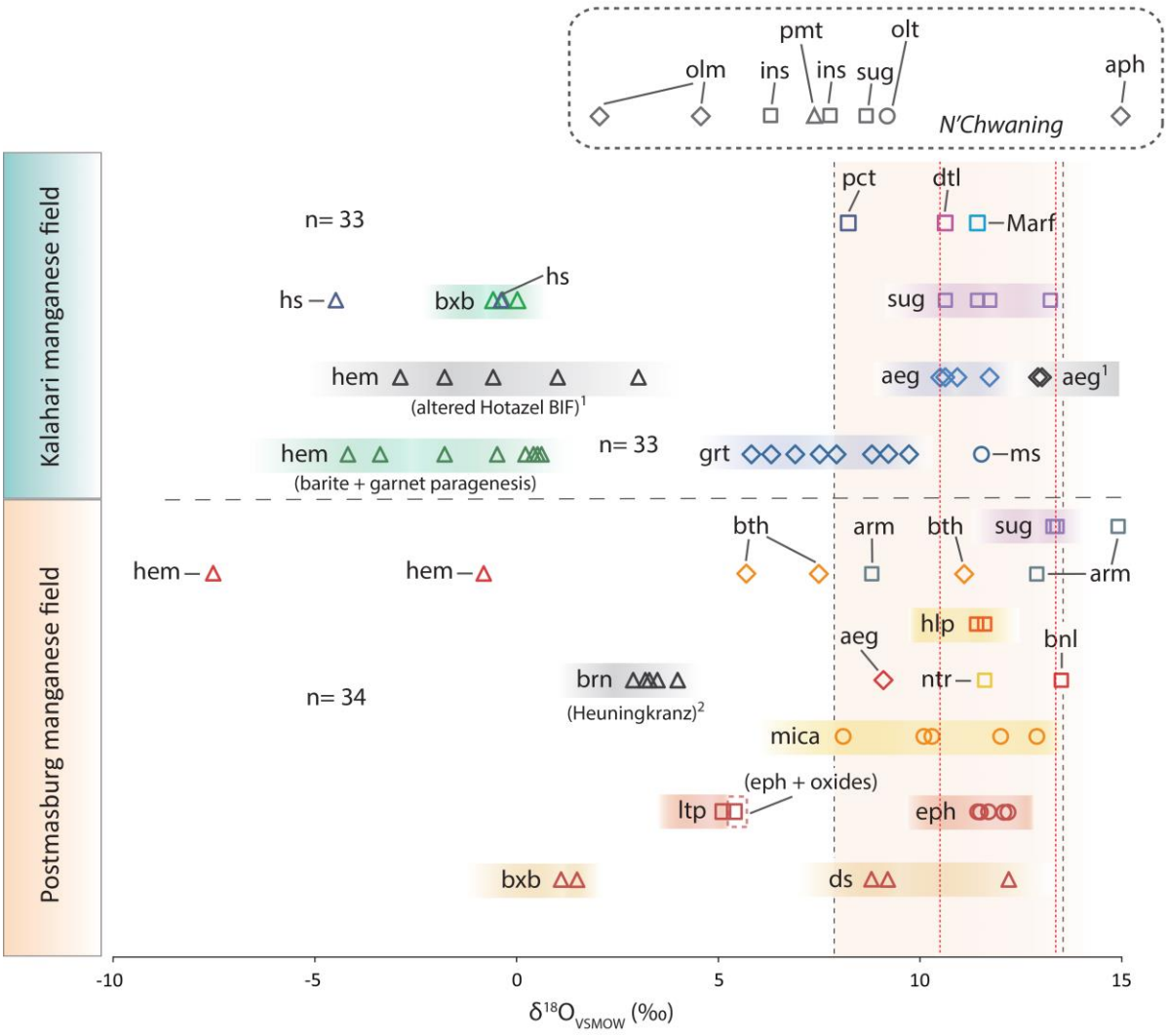

Figure 5. Oxygen isotopes from all gangue and ore minerals analysed in this study. Most silicates fall within a rather narrow range between +7.9 and +13.5 ‰ (average = +11.0 ±1.6 ‰, n = 36). Data within dotted box have not been previously shown. References: 1: Tsikos et al; 2003, 2: Fairey; 2013. Abbreviations: aeg = aegirine, aph = apophyllite, arm = armbrusterite, bnl = banalsite, brn = braunite, bth = berthierine, bxb = bixbyite, ds = diaspore, dtl = datolite, eph =ephesite, grt = garnet, hem = hematite, hlp = hyalophane, hs =hausmannite, ins = inesite, ltp = lithiophorite, Marf = magnesio-arfvedsonite, ms = muscovite, ntr = natrolite, olm = olmiite, olt = oyelite, pct = pectolite, pmt = piemontite, sug = sugilite.

The remarkable uniformity in $\delta^{18}O$ values of these silicates is attributed to relative isotopic homogeneity in the pristine mineral-forming fluid, owing to large water to rock mass ratio (w/r ratio) and precipitation within a small temperature range. In other words, oxygen isotopes appear to be buffered against isotopic change due to a large reservoir of fluid which controls the composition during mineral precipitation despite the overall fluid-rock interactions.

The alternative scenario of isotopic exchange and equilibration after extensive interaction of the fluid with the surrounding rocks immediately before precipitation, further accompanied perhaps by a lower w/r ratio, is difficult to contemplate if one takes into account sample derivation from different stratigraphic horizons and mines, as well as the compositionally inhomogeneous host lithologies that would have produced fluids with large isotopic variations, likely reflected also in the measured samples.

Therefore, it can be surmised that the isotopic signature of regional-scale fluids is largely preserved, at least in the composition of some of the hydrothermal gangue minerals in these ores.

$\delta^{18}O$ values of certain phases such as garnet, micas, armbrusterite or berthierine are possibly linked to more complex isotopic histories, also involving mixing with isotopically lighter meteoric water. For example, late-stage hydrothermal activity is known to influence oxygen isotope retentivity of micas (e.g., Bulle et al, 2020) and temporal variation in fluid composition due to wider isotopic exchange between fluids and host rock in the later alteration stages may account for the wider $\delta^{18}O$ range of garnet. Furthermore, phases like lithiophorite have been texturally shown to have more than one generation and may be also related to more recent supergene enrichment processes.

The much lighter oxygen isotopic compositions of bixbyite (-0.4 to +1.5 ‰), which also overlap between KMF and PMF, in like manner to hematite, may approach more closely that of the mineralizing fluids at the time of precipitation, a hypothesis which however needs further investigation. Coarse-grained hematite (specularite) from barite-garnet parageneses shows a broadly similar range of $\delta^{18}O$ ratios (-4.2 to + 0.6 ‰) to that previously reported from the oxidized Hotazel iron-formation and interpreted to reflect interaction with a low-$\delta^{18}O$ fluid, possibly of meteoric origin (Tsikos et al; 2003). It is worth mentioning though that depending on temperature of formation (between ca. 100-200^{o}C), hematite in this study suggests $\delta^{18}O$ fluid values up to ca. +3 or +4 ‰. Specularite (hematite) from the PMF displays very large variations (Figure 5) (from -7.5 to +4.0 ‰) (Papadopoulos et al; in prep) that are likely related to different generations/mineral-forming events or perhaps more complex precipitation mechanisms. Moreover, braunite may inherently have the lowest capacity for

^{18}O enrichment among all studied silicates (Bühn et al; 1995) and the previously determined isotopic range for braunite (+2.9 to +4.0‰) (Fairey; 2013) is likely to be nearer to the fluid isotopic composition.

Ongoing research on other uncommon silicates (Si-bonded O) in the KMF (Figure 5, dotted box), further corroborates the homogeneous and regional fluid isotopic signal but also emphasizes the possible involvement of compositionally lighter meteoric fluids or complex fractionation mechanisms during precipitation of phases such as for example inesite [$Ca_2(Mn,Fe)_7Si_{10}O_{28}(OH)25H_2O$] or olmiite [$CaMn^{2+}[SiO_3(OH)](OH)$].

$\delta^{18}O_{FLUID}$ determinations suffer from several limitations, mainly relating to the uncertainty of temperature of mineral deposition, fractionation behaviour between uncommon minerals and fluid(s) and mineral-fluid isotopic equilibrium. Despite of these limitations that cast a certain degree of doubt on the deduced temperatures and fluid calculations, the following can be inferred from the dataset of this study:

(1) Overall, calculated $\delta^{18}O$ of the mineral-forming fluids from mineral-water oxygen isotopic fractionation factors range from +3 to +8 ‰ for both ore fields and most values fall between +3.5 to +7.5 ‰.

(2) As regards the KMF, $\delta^{18}O_{FLUID}$ values may have been on average heavier (5.3 ± 1.4 ‰) during early calc-silicate precipitation than throughout main and later stages (0.2 ± 2.8 ‰ ‰), which possibly indicates dilution of isotopically heavier brines after interaction with a lighter host rock or mixing with contemporaneous meteoric water.

(3) $\delta^{18}O$ measurements of garnet-hematite, garnet-hausmannite and aegirine-natrolite pairs suggest realistic temperatures of formation (175, 120, 200 and 215°C) that are in agreement with previous fluid inclusion work from the KMF (Lüders et al; 1999: 130-210°C). Although the extent to which gangue minerals precipitate in equilibrium with the fluid is not known, these results suggest that at least some phases may be useful as potential monitors of fluid temperatures.

(4) $\delta^{18}O$ values yielded for the mineral-forming fluids from ephesite and diaspore of the EMD ores (Lohatla, Bishop, Glosam) and for a temperature range between 100° and 500°C, suggest that the two minerals have not been formed coevally and/or not in isotopic equilibrium.

The complete dataset of hydrogen (δD) isotopes from this study is illustrated in Figure 6 (data not previously shown are indicated by a black asterisk). In like manner to oxygen isotopes, there is a significant overlap between the limited δD values from micas (muscovite-paragonite, phlogopite, ephesite) and silicates (natrolite, pectolite, datolite) from the KMF and PMF, which specifically range between -28.0 and -58.5 ‰ (KMF), -60.7 and -78.7 ‰ (WMD) and from -43.8 to -56.8 ‰ (EMD), for the three distinct localities respectively. Since most rocks contain little or no molecular water, the hydrogen isotope composition of alteration minerals may be used to infer the hydrogen isotope composition of the fluid from which they formed, at least after regarding other parameters that can influence the measured hydrogen isotopic values. The effect of temperature on fractionation is apparently small, since δD_{FLUID} values calculated from all different micas and a presumed crystallization temperature of 250°C, differ on average by only 10-15 ‰ from the measured δD values. The range of the obtained δD ratios overlaps with that from metasediments (-40 to -100‰), metamorphic waters (-20 to -65‰) and generally with the broad range of values exhibited by hydrothermal waters and sedimentary basinal brines recovered from oil fields or associated with Mississippi-Valley type deposits (Ohmoto; 1986, Sheppard; 1986, Kessler et al; 1997, Shanks; 2014, Hurai et al; 2015).

This reverberating signal across the Northern Cape provides strong indications that the H-isotope composition of the infiltrating fluids dominate total hydrogen in the system and did not show major change temporally and spatially during gangue formation, at least during early alteration stages and with respect to a number of gangue species.

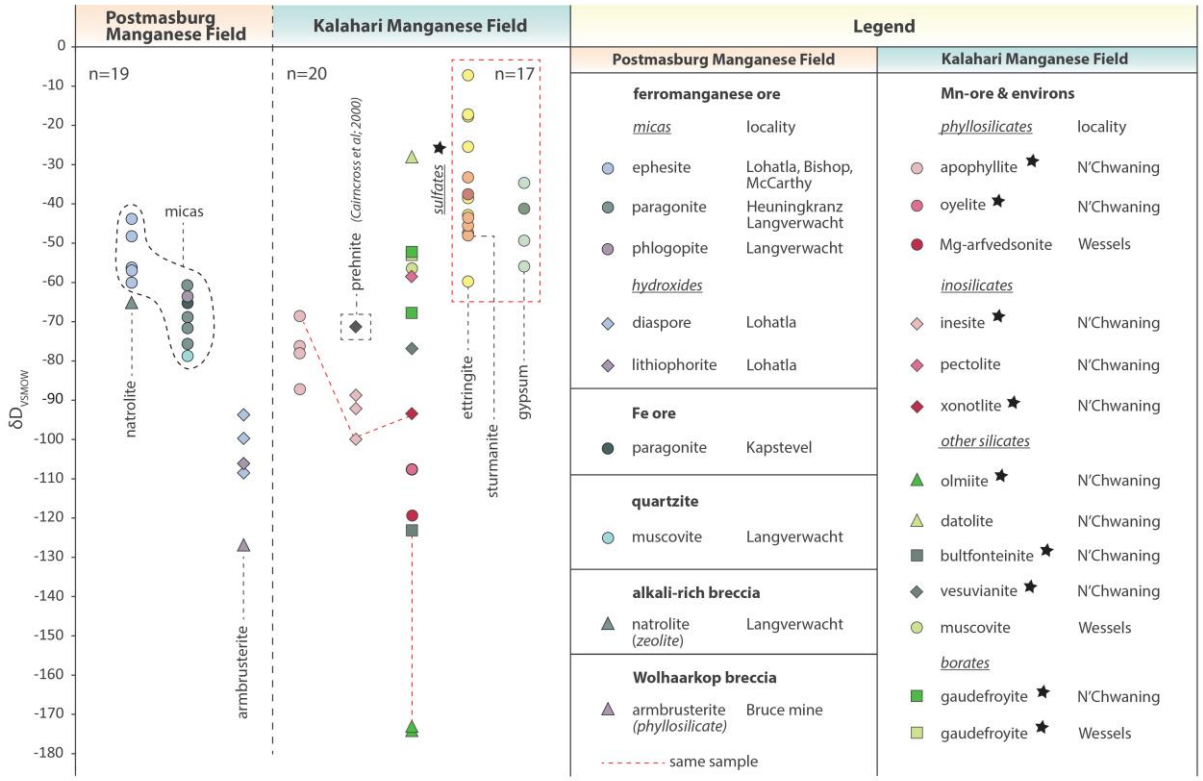

Figure 6. Complete compilation of measured hydrogen isotopes (δD) derived from this study (δD fluid values mentioned in text), apart from prehnite (Cairncross et al; 2000). Black asterisk denotes minerals that have not been previously appeared in the main body of the thesis. Red dotted line connects δD values from minerals belong to the same assemblage, i.e., same sample. A separate box is drawn for sulfate minerals of the KMF, which broadly show distinct heavier isotopic values. Colour coding for sulfates in not included in the legend but is similar to that used in Figures 15, 16, and 17 (section 2.2).

D-depleted mineral values (amphibole: -118.8 ‰, armbrusterite: -126.8‰, diaspore: -108.5 to 93.7 ‰ and lithiophorite: -106.1‰) can be only interpreted by invoking different and/or more complex modes of formation than that of hydroxyl-bearing silicates and mica. These could involve isotopic dilution of brines by contemporaneous meteoric water, later mineralogical origin related to supergene enrichment, assimilation of lighter δD values from lithologies along the flow path or significant D exchange taking place during mineral precipitation processes, if for example diaspore is, on the basis of textures and the wider geological environment, regarded coeval with ephesite, i.e., mica. However, crude δD_{FLUID} calculated values from diaspore (ca. -50 to -60 ‰ using gibbsite equation, Méheut et al; 2010) suggest that fluids in equilibrium were not that different to that of ephesite.

Hydrogen isotopic data from species not presented earlier give added insight to the problem of interpretation of the lighter δD measured ratios. Points worth mentioning from Figure 6 are:

(i) Different species display somewhat distinct groups of generally light δD values, for example, apophyllite [$KCa_4(Si_8O_{20})(OH,F)_8H_2O$] (-68.5 to -87.2‰) and inesite [$Ca_2(Mn,Fe)_7Si_{10}O_{28}(OH)_25H_2O$] (-88.7 to -99.9‰) from the KMF, minerals further known to be commonly associated and coexist with zeolites (natrolite) and other hydrous phases (Gutzmer and Cairncross; 2002). This suggests that measured isotopic compositions can be perhaps governed by the fractionation behaviour between the mineral and the fluid, while isotopic variations may be enhanced under conditions of non-isotopic equilibrium.

(ii) Interestingly, the presumed brine isotopic signature is broadly also shared by other species, such as gaudefroyite [$Ca_4Mn^{3+}{}_{2\text{-}3}(BO_3)_3(CO_3)(O,OH)_3$] (-52.2 to -67.6 ‰), vesuvianite (-76.8 ‰) and the previously published data from prehnite (-74.5 ‰) (Cairncross et al; 2020).

(iii) Isotopic fractionation between minerals in the same assemblage (couple of millimetres or centimetres distance), can be considerably high, as seen in the triplet apophyllite (-68.5 ‰), inesite (-99.5) and xonotlite [$Ca_6(Si_6O_{17})(OH)_2$] (-93.5 ‰). This again emphasizes what noted above in point (i) and is partly explained by the much later origin of apophyllite (section 2.3).

(iv) Olmiite [$CaMn^{2+}[SiO_3(OH)](OH)$] samples are anomalously light (-173 ‰, -174.1 ‰) and coexisting bultfonteinite [$Ca_2(HSiO_4)FH_2O$] is also very light (-123.1 ‰) but considerably different. Diffusional resetting and re-equilibration of isotopes in OH-bearing and hydrous phases in response to subsequent events and even groundwater fluid flow is also possible and step heating experimental work may potentially test the above by revealing distinct water sources.

(v) Finally, sulfates display distinctly enriched δD values and a rather small range (-35.4 ± 9.1 ‰, n = 14), if certain values of ettringite [$Ca_6Al_2(SO_4)3(OH)_{12}26H_2O$] (yellow circles) are excluded. This can be used as evidence that hydration water in these sulfates largely reflects

the pristine water combined into their crystal structures, which is meteoric water or evolved (and/or diluted) basinal brines during the waning stages of the Wessels-type alteration event (discussed thoroughly in section 2.2).

Unfortunately, published detailed paragenetic associations and origin of minerals such as oyelite ($Ca_{10}Si_8B_2O_{29}12.5H_2O$), olmiite and bultfonteinite are not available to further facilitate interpretations. It seems reasonable that as Gutzmer and Beukes (1996b) have stressed earlier, many of the minerals seen in this prolific district may have formed during more than one episode; therefore, both δD- and $\delta^{18}O$-information may be very difficult to decode, especially by adopting the concept of a single event of hydrothermal alteration, now further disputed by $^{40}Ar/^{39}Ar$ data (section 1.1, 2.3: apophyllite).

Insights into the likely source water are also given by $\delta^{18}O$-δD plots, commonly used in studies for various deposits and modern-day brines (Shanks; 2014). Minerals from both fields such as micas, natrolite, pectolite, datolite and ephesite (if 'true', i.e., fluid estimated values are regarded for the latter: $\delta^{18}O$: +7.1 ± 0.3 ‰, δD: -37.4 ± 5.9 ‰) plot inside the defined compositional field for a series of Mississippi Valley-type (MVT) Pb-Zn deposits and moreover partly overlap the metamorphic water box. The latter is expected, as hydrothermal fluids typically display comparable isotopic compositions, however with broader range and variable D- and O^{18}-shifts resulting from exchange reactions with different lithologies and/or fluids along their path. Generally, as also seen in MVT deposits, water-rock interactions produce higher $\delta^{18}O$ values and dilution by meteoric water causes shifts to lower $\delta^{18}O$ values. The striking isotopic homogeneity between the KMF and PMF gangues (not entirely illustrated in Figure 7 due to absence of δD and fluid isotopic estimated values), the inferred fluid buffering, the isotopic similarities with fluids from MVT deposits, the documented presence of evaporites, origination of fluids by regional compressional tectonics and a series of other evidence, lead to the following proposal for the source of the regarded fluids:

The aqueous solutions responsible for hydrothermal gangue precipitation in the ores of the KMF and PMF have probably originated as trapped meteoric and/or formation water, later heated and isotopically equilibrated with different lithologies of the Transvaal Supergroup. These deeply circulating

^{18}O-enriched fluids, had increased salinity from dissolution of an evaporite reservoir, were stored in the deeper parts of the basin or more distant lithologies before tectonic expulsion and overall can be characterized as sedimentary saline alkali-rich basinal brines.

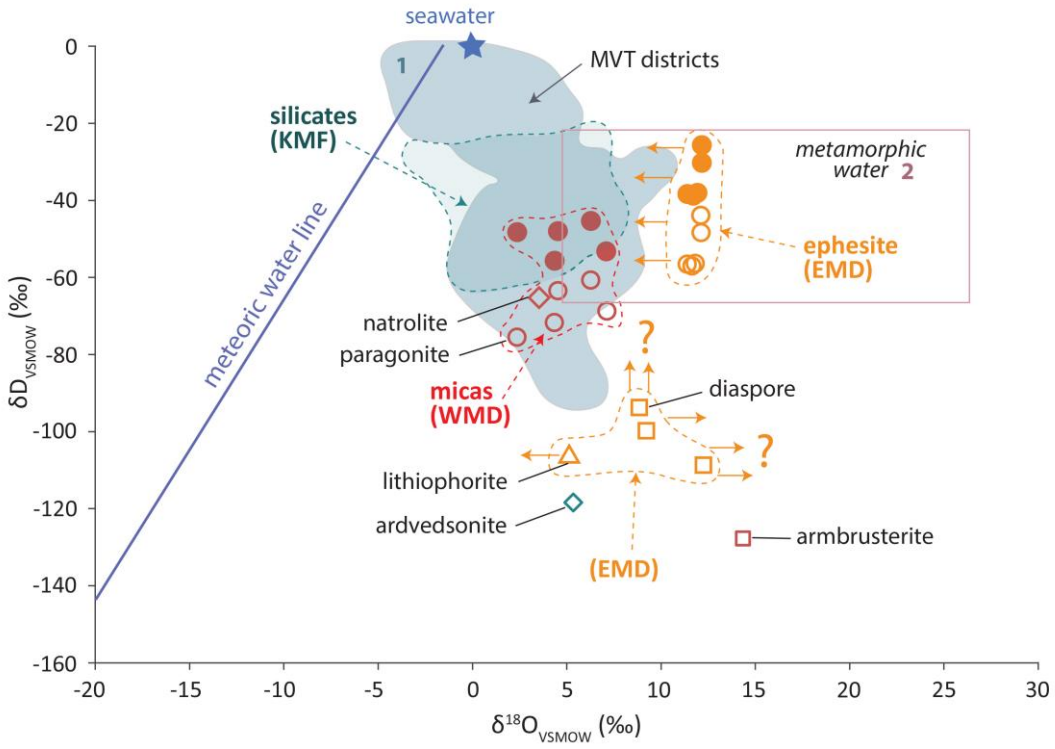

Figure 7. δD-δ^{18}O plot for gangues from the Kalahari Manganese field (KMF) and Postmasburg Manganese field (WMD and EMD)), illustrating their isotopic compositional relationship with hydrothermal basinal fluids associated with Mississippi Valley-type (MVT) Pb-Zn deposits. Typical metamorphic water is also shown. Open symbols represent measured (mineral) values and filled symbols estimated fluid composition. Arrows point towards the compositional area of the expected ('true') fluid values for ephesite, diaspore and lithiophorite of the EMD. References: 1: McLimans; 1977, Richardson et al; 1988, Kesler et al; 1997. 2: Sheppard; 1974.

Figure 7 also illustrates the potentially different formation and/or post-precipitation isotopic histories of gangues, which as stressed earlier may have assimilated lighter hydrogen isotopes from fluids or lithologies (for e.g.: arfvedsonite), may be related with fractionation mechanics leading to significant isotopic exchange (armbrusterite) or may have formed by distinct fluids during a later event (lithiophorite).

2. The ores of the Eastern and Western Maremane dome - A short comparison

Current ore models for the Postmasburg Manganese field are based on mine occurrences geographically located within the Maremane dome s.s. (EMD), in contrast to ore material on which recent studies, including this one, have focused on and derives from new explorations sites western of the type locality (WMD) and closer to the Blackridge Thrust Fault system. In an analogous way to which the commonly accepted pigeon-hole type classification into siliceous and ferruginous Mn ores has been reasonably regarded as outdated (Fairey et al; 2019), strict geographic classifications may be broadly meaningless, as for example the Khumani (Bruce mine) occurrences (EMD) of the Wolhaarkop breccia studied by Moore et al (2011) show more mineralogical affinity towards the ones from the WMD, rather than with the EMD ones used in the early ore genetic studies (Gutzmer and Beukes; 1996a). Nevertheless, pointing out notable differences between the two localities and in particular with respect to the ferromanganese ores is still instructive for understanding the origin of the ores.

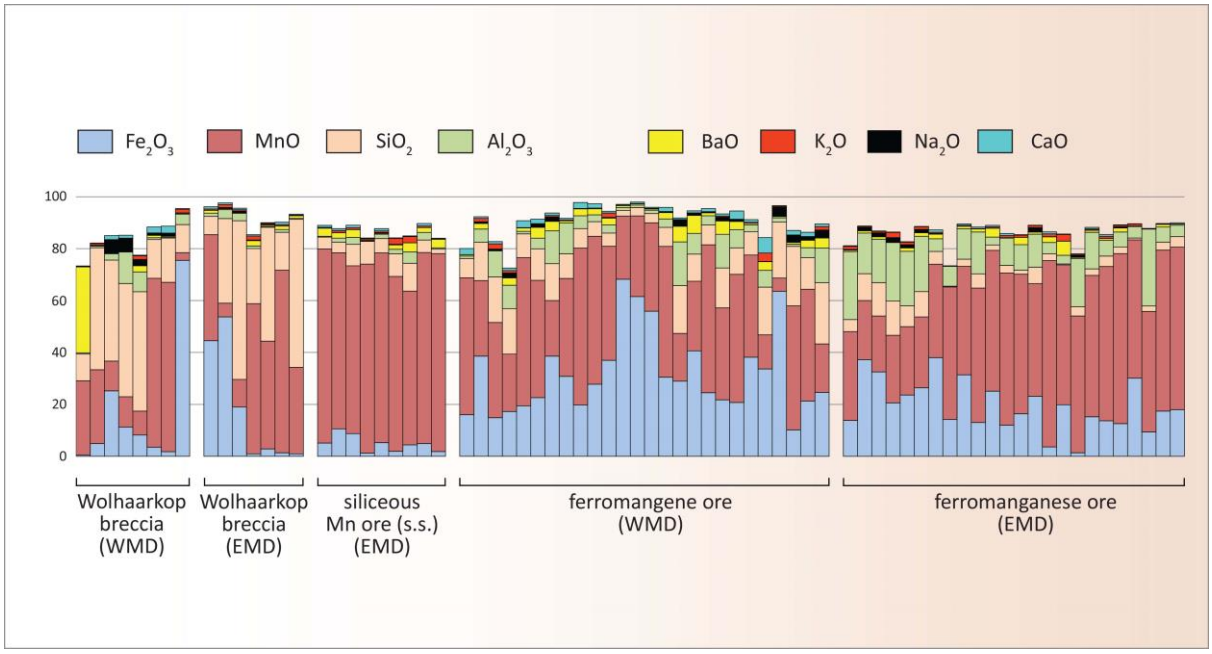

Figure 8. Geochemical comparison between different ore-types found in the type locality (EMD) and new exploration sites in the broader Kolomela mine region (WMD). Wolhaarkop breccia is the host rock of the siliceous (chert-bearing) Mn ore. Data (n=76) are from this study (Appendix IV) and Gutzmer and Beukes; 1996a, Fairey; 2013, Bursey; 2018, and Thokoa; 2020.

In addition to whole-rock Li-B geochemical analyses presented in chapter 6, twenty samples from different ore-types were analysed for their major and trace element composition (not appearing in the main body of the thesis/can be found in Appendix IV). Along with a compilation of published and unpublished geochemical data, the above are used here, in this geographic comparison between the ores.

Probably the single most critical difference between the WMD and EMD ferromanganese ores is the highly aluminous and silica-depleted nature of the latter. An overview of the chemical composition of mineralization (Figure 8) shows that EMD ferromanganese ores have a Si/Al ratio <1, which is contrastingly different than all other deposits.

As regards ore metals, WMD ores are on average more iron- (hematite)rich than the EMD ores and as a consequence less manganese-rich at the same time. Concerning major alkalis, the most evident difference is the higher CaO and BaO content of the WMD ores (> by 1.14 and 1.03 wt. % respectively), relating to abundant barite, calcite, calc-silicates and Mn- and Ba-carbonate phases being present, phases that apart from barite have not been reported from the EMD ferromanganese ores. Na_2O and K_2O are variable and broadly comparable between the two localities, but in the case of EMD these elements are mainly hosted by ephesite and Mn-oxides, whereas in the WMD they are accommodated by much more complex parageneses involving feldspars, pyroxenes, calc-silicates and zeolites.

Altogether, WMD ferromanganese ores are on average more enriched in alkalis than EMD ores of the same type and display much more mineralogical diversity with regard to silicate and carbonate species. On the other hand, restricted mineralogical variability in the ferromanganese ores is represented through particularly Al-rich minerals, reflective of the highly aluminous, silicate-depleted environment.

These include ephesite, amesite, diaspore, lithiophorite and barian goyazite. Despite its relatively poor nature in terms of gangue mineralogy, rare species such as the barium vanadate gamagarite are seen being well-developed in the EMD and have not been found in the WMD. Furthermore, abundant ephesite in the former emphasizes the high bulk Li

concentrations which are also not replicated in such abundances elsewhere in the PMF. It is reminded though, that Li in the EMD ferromanganese ores is not believed to be associated with the coincident local factor of high Al, on the basis that sugilite-bearing and Li-rich ores in the KMF have very little Al.

A comparison between the Wolhaarkop breccia of the WMD and EMD shows that possibly the only easily discernable different is that of higher alkali and specifically Na_2O (> by 2.7 wt. %) and marginally CaO content (> by 0.3 wt. %) of the first (Figure 8), undoubtedly attributed to silicates such as aegirine and albite and Mn-carbonates respectively.

High variability in Fe, Mn and Si reflects the very inhomogeneous nature of these rocks and further highlights that sample biases render geochemical comparison much more difficult than in the case of ferromanganese ores. Interestingly, siliceous Mn ores studied by Gutzmer et al (1996a) exhibit considerable BaO concentrations (up to 3.54 wt. %), in the order of values displayed by the ferromanganese ores. Data in the original publication are accompanied by whole-rock SO^3 analyses, which return zero abundance in samples with wt. % BaO. Since Ba-muscovite is the only reported Ba-species apart from barite in this study, either this mineral is rather abundant in these ores or else, other unidentified Ba-hosting species are present.

The distinctive SiO_2 / Al_2O_3 ratio (<1) of the EMD ferromanganese ores is nicely illustrated in Figure 9a, which further highlights that this feature is independent of the variable MnO content of the ores. WMD ferromanganese ores and EMD siliceous Mn ores display SiO_2 / Al_2O_3 ratios between 1 and 3, whereas SiO_2 shoots up only in the Wolhaarkop breccia and is most certainly related to gangue silicates, chert and sample bias. The negative correlation between Fe_2O_3 + MnO and Al_2O_3 + TiO_2 shown by the EMD ferromanganese ores (Figure 9b) has been interpreted by Gutzmer and Beukes (1996a) as evidence for the detrital origin of aluminum and titanium and in a similar wat the negative correlation between ore metals and SiO_2 as representing the insoluble residue (chert) of the weathered dolomite or authigenic quartz.

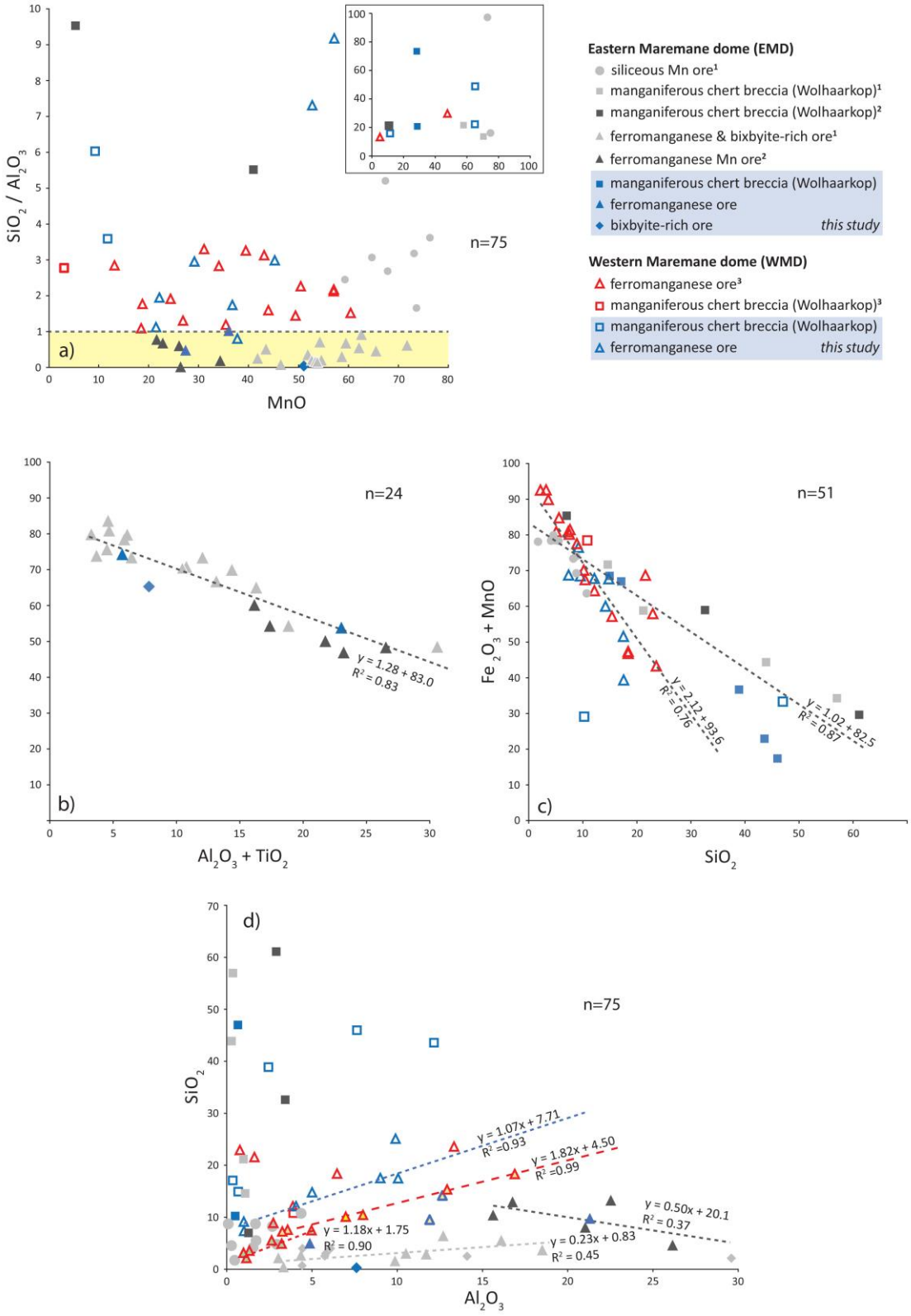

Figure 9. Major element scatterplots compare different Fe/Mn ore-types between the Eastern and Western Maremane dome (see text for discussion).

However, as seen in Figure 9c, a negative correlation between ore metals and SiO_2, but following a different trendline exists for the WMD ferromanganese ores. Coupled with petrographic observations, this trend illustrates the higher content of hydrothermal silicates in these ores and although unclear, it may not be related to residual silica at all.

A similar trend is absent from the silica-depleted EMD ferromanganese ores, but the existing correlation between ore metals and aluminum is not necessarily proof for the detrital component of this element. A closer look at distinct localities and/or drillcores reveals that different trendlines of positive correlation between SiO_2 and Al_2O_3 may occur in the WMD ferromanganese ores (Figure 9d) and these most likely reflect mineralogical control by different hydrothermal species, i.e., micas or feldspars.

Returning to the distinguishing characteristic of the EMD ferromanganese ores, as extensively discussed in chapter 6, exogenous detrital material concentrating in open-karsts or karstic continental lakes, may have been essential in generating their high aluminum geochemical signatures. However, it is not easy to contemplate that under very similar weathering-related formation mechanisms, topographic and host rock lithological differences can explain the huge compositional disparity between the EMD and WMD ferromanganese ores. Regarding EMD, attention should be pointed to the aluminous shale of the overlying Doornfontein Member, which show significant enrichment in Al_2O_3 and TiO_2 values (followed by depletion in all other major elements) and signs of hydrothermal fluid flow capable of mobilizing Al and Ti (Cousins; 2016).

In that sense, synchronous processes of desilication and aluminum enrichment in both the Fe-Mn protolith and the overlying shales due to metasomatism associated with the Namaqua overprint event, is a scenario that should also be considered.

Supporting evidence of aluminum mobilization are seen in variable textures involving ephesite, such as fracture-fillings, veins protruding in the overlying shales (Gutzmer and Beukes; 1996a) or bands of replacive origin. At least some of the diaspore present in these

ores may be likewise hydrothermal and related to aluminum mobilization processes. Diaspore was detected in the WMD, only in a single paragenesis comprising also Ba-muscovite, Mn-carbonate and an Al-rich Mn-bearing silicate. Interestingly, host rock ferromanganese ore zone is associated with apparent faulting and duplications and interbedded between shales and quartzites.

The broad stratigraphic distribution is similar for the ferromanganese ores of the two regarded localities, both developing under the Olifantshoek-Transvaal unconformity and over dolomites of the Campbellrand Subgroup. However, contrasts do exist, with the most notable being the upward grading of ores to aluminous shales in the EMD. Deposits in the WMD are unconformable overlain by red shales of the Gamagara/Mapedi Formation. EMD ores may be disconformably followed upwards by Doornfontein conglomerate (Gutzmer and Beukes; 1996a), a clastic detrital deposit formed by erosion and reworking of enriched BIF and iron ore. Although the exact thickness of this formation is not known, there is no doubt that it is considerable and specifically in the northern and southern extremities of the Maremane dome (Sishen, Beeshoek), this lithology constitutes part of the iron ore reserve (Van Schalkwyk and Beukes; 1986). An analogous clast-supported rock consisting mainly of angular to sub-rounded hematite-rich clasts is also overlies the WMD deposits in most, although not all of the studied drillcores and shows thicknesses of up to 25 metres. What is interesting though, is that the latter is enriched in alkalis, much like the Fe/Mn deposits below it.

Furthermore, the development of matrix-supported breccias, comprising alkalis and minerals such as aegirine, feldspars, hematite, muscovite and barite in very prominent in this locality and contrastingly absent in the EMD, at least under current knowledge. Finally, a noteworthy difference between the studied samples from the two localities is the lack of minerals related to supergene overprint in the WMD, a typical feature of samples from the EMD ores, on which the genetic models have been based.

---

3. Rethinking ore genesis in the Postmasburg Manganese field (PMF)

It should have been made clear by now that any attempt to project back to the original formation of these highly complex and diverse ores or provide a step-by-step model can be easily regarded as a meaningless exercise. Even if at first glance there is no need to entirely dispel the current ore genetic models for the PMF, this study stimulates new investigation on the origin and evolution of the different ore-types. In consideration of all recent findings from this and other published research, the bottom line is that the mineralization history of this region needs to be revised.

Critical gaps are embedded in the inferences made by previous authors with respect to ore genesis (Gutzmer and Beukes; 1996a, 1997b) and signals of hydrothermal activity have been omitted or not given particular attention, save for a few comments on possible syn- or post-metamorphic fluid flow evidenced by veins of barite, specularite and quartz. A starting discussion point concerns the unique Si/A ratio (<1) of the EMD ores, not seen in the equivalent WMD (wider Kolomela region), which is difficult to explain if comparable weathering mechanisms and carbonate lithologies are invoked for the formation of the ore in the whole area. The Al-rich nature of the EMD ores requires further investigation but it is possible that this is not an entirely pristine geochemical signal, but instead one related to aluminum mobilization and formation of the spatially associated aluminous shales of the Olifantshoek Supergroup, given also that the latter have presumably been affected by hydrothermal metasomatic alteration post-dating their deposition (Cousins; 2016, Land et al; 2017). The speculative nature (supergene vs hydrothermal) of gangue oxides, the total lack of minerals related to supergene enrichment in the WMD ores, the need for an exceptionally iron- (and Mn) rich dolomite being dissolved to account for the chemistry of the PMF ferromanganese ores and the abundance of replacement metasomatic alteration textures accompanied by lack of typical supergene-related textures, all stress the need for a revision of the prevailing models. The paradigm emphasizing the existing issues with the hypothesized models is that of ephesite, a mineral shown by radiogenic and stable isotopic techniques to have formed by regional and externally sourced Na- and Li-bearing hydrothermal brines as opposed to the current view of alkalis being diagenetically expelled from the ores themselves.

The core theme permeating this thesis, is that the PMF mimics to a great extent the hydrothermal findings from the KMF. Therefore, if the influence of fluids clearly belonging to the same regional system has been that of ore-upgrade in one area, it then becomes imperative to examine the effect of this hydrothermal system on preexisting Fe/Mn-rich entities and country lithologies of the PMF as well. Unfortunately, this has not been a priority research question and not a lot of textures at the hand specimen to micro-scale provide definitive snapshots of metasomatic enrichment processes. At the same time, it is evident, that lithologies do not remain inert during fluid introduction but instead small-scale mobilization of ore metals occurs through: (a) scavenging by alkali gangues and transportation prior to their precipitation, which may be also associated with redox reactions and (b) formation of hydrothermal/metasomatic oxide generations such as replacement-related braunite, vein- and breccia-related hematite associated with alkali assemblages, as well as minor other phases [braunite (II), partridgeite, hausmannite] the origin and occurrence of which require further examination.

For example, veins and vugs of Mn-bearing assemblages in conglomeratic iron ore overlying ferromanganese ore is enough proof that manganese is sourced and transported from lithologies in proximity. In the case of massive iron ore, fluids evidently permeated the ore matrix, precipitating barite and paragonite interstitially to hematite, causing development of colloform hematite textures and formation of such thoroughly intergrown assemblages that are very likely to comprise hydrothermal ore mineral generations. The high geochemical mobility of Fe and Mn encourages the former scenario. Pore-space filling and recrystallization of braunite around vugs is conspicuous in ferromanganese ore matrix. Replacements by braunite are mentioned in the prevailing models (Gutzmer and Beukes; 1996a) and furthermore, the authors commented on the origin of albite and aegirine, minerals only reported by earlier researchers (De Villiers; 1983), considering it as cogenetic with braunite.

The above examples may be far from providing a definitive answer as regards the mode of formation of the different ores or the possibility of hydrothermal overprinting having served as an enrichment factor during their extensive epigenetic history (Mesoproterozoic Namaqua orogeny and Neoproterozoic alteration event). Nevertheless, the excellent potential of the now well-documented, externally sourced alkaline brines, to leach silica and

transport ore elements over large distances mainly through chloride complexation, should be greatly considered in the ore genetic models. However vague the relationship between hydrothermal/metamorphic gangues and ore formation in other ore districts (Långban-Sweden, Liguria-Italy, Hoskins and Wood mine-Australia, etc.) may be, many of the above are characterized by a multistage geological evolution comprising for example skarn alteration units, leaching, mobilization, reprecipitation of primary elements from the ores and redeposited veined manganese mineralization. It is worth mentioning that a revised interpretation for Precambrian manganese mineralization in Australia (Manganese Group, Pilbara Craton), occurring in a comparable tectonostratigraphic setting to that of the Northern Cape, accentuates the paramount role of regional-scale hydrothermal events in ore formation within cratonic areas and specifically, associates manganese fluid 'feeders' with elemental transportation, dissolution, precipitation and replacement of different lithologies across widespread structures and unconformities (Blake et al; 2011).

Perhaps the single greatest issue with the current ore genetic models in the Northern Cape is the confinement of ore genesis to a very narrow timeframe (between ca. 2.2-2.0 Ga), a premise that does not account for regional thrust systems (Blackridge), duplications of the stratigraphic units and reactivation of normal faults caused by major orogenic events (Altermann and Hälbich; 1991, Cornell et al; 1998, Basson et al; 2018). Supergene processes may have served as ground preparation for ore formation but the complexities of the subsequent prolonged geological history are manifested in the stratigraphy and occurrence of the deposits, especially in the western edge of the craton (WMD ores), where metre-thick sections of brecciated and mineralized rock further allude to fluid expulsion by tectonic overpressure. Overall, thin-skinned tectonics have left a substantial imprint on the radiometric ages of all different deposits and are central to the new ore-genetic model presented in chapter 5 (section 6.7).

Some **key features from the suggested model** are: (a) alteration and ore-related fluids are visualized as deep buried and heated sedimentary brines that had $\delta^{18}O$ ranges between +3.5 and + 7.5 ‰, δD between -65 and -28 ‰ and temperatures mostly between 130^{o} and 250^{o}C. (b) A significant part of their salinity was acquired by leaching of former evaporites and/or evaporitic breccias presumed to have been widespread in the basin. (c) Fluid migration

was laterally forced and repeatedly focused on regional-scale lithological boundaries such as the Blackridge thrust system and the Transvaal-Olifantshoek unconformity. (d) The supracrustal successions straddling these structures have been reworked by prolonged and episodic epigenetic processes, that leached, mobilized, replaced and precipitated material, overall causing different styles of mineralization along the migration paths of fluids and (e) Finally, ore metals and alkalis may have been sourced by preexisting lithologies other than dolomites, such as the Asbestos Hills BIF (for e.g., avg. MnO = 0.8 wt. %, up to 5.9 wt. %) and the iron-rich clastic sediments of the Olifantshoek Supergroup, while fluids may also have partly originated within the Namaqua metamorphic belt, further to the west of the basin.

The chief characteristics of this model with respect to sources and mechanisms of fluid migration display significant similarities with the Mississippi Valley-type (MVT) Pb-Zn deposits. This hydrothermal style of mineralization develops likewise in non-orogenic settings, non-magmatic rocks and is associated with excretion of deep buried and heated fluids deriving mainly from evaporated seawater or dissolution of evaporites. Another relevant analogue to be considered in future research towards understanding the basic concepts of fluid genesis and interaction with the surrounding lithologies are the epigenetic sediment-hosted copper deposits, mineralization that is also associated with carbonates, shales, conglomerates, evaporites and sulfur-bearing brines in passive margins. The new findings and proposed model may only represent a stepping stone for future reconstructions that will aim to better illustrate the origin and alteration processes/stages of distinct mineralization sites. However, they provide a good foundation by emphasizing that the Northern cape deposits evolved with the possible synergy between residual/sedimentary and epigenetic tectonometamorphic/ hydrothermal processes.

A final key point concerns the dolomite underlying and/or enclosing the different manganese ore-types. On the sensible assumption that metal accumulation for manganese ore-formation in the PMF has occurred in one or more epigenetic episodes following deposition and/or diagenesis of the host-rock dolomites and country marine sediments such as BIF, it is then rationale to attribute the source of at least the bulk manganese to the immediate host lithologies, regardless of whether a strictly speaking weathering-related residual enrichment or another mode of ore-formation is invoked. Unfortunately, there is not

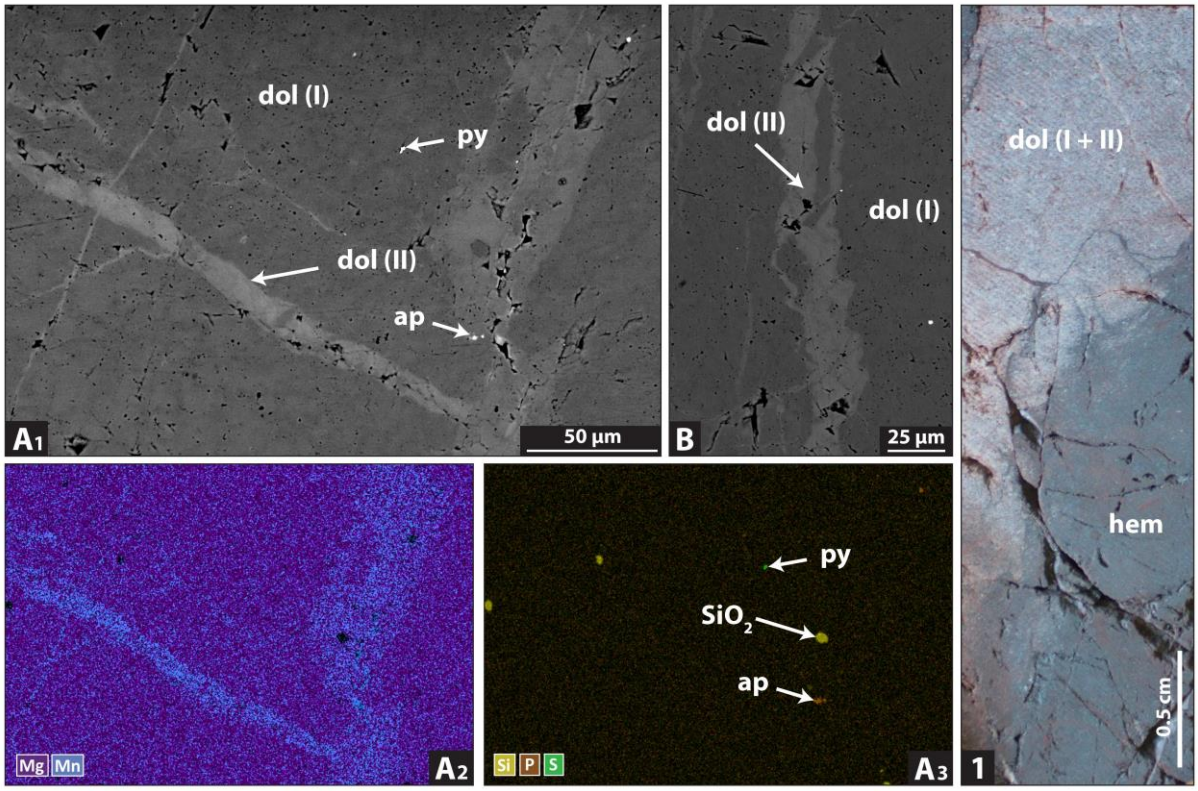

Figure 10. (1) Dolomite from the base of drillcore SLT018 (Heuningkranz), underlying ferromanganese ore (ca. depth 150 metres). Backscattered (BSE) images. (A_1 & B) Fracture-filling and manganese-rich dolomite within main dolomite matrix. (A_2) SEM map emphasizing the concentration of manganese in micro-veins and fractures. (A_3) Carbonate matrix contains traces of pyrite, apatite and quartz. ap = apatite, dol (I) = matrix dolomite, dol (II) = fracture-filling high-Mn dolomite, hem = hematite, py = pyrite.

much published knowledge with respect to the transition from dolomite to ore, the wider appearance, development and distribution of the various ferromanganese ores in space (especially regarding the more recently discovered WMD), the occurrence or not of veins, discontinuities and other notable structural features below or in the vicinity of mineralization, let alone detailed mineralogical, geochemical and isotopic data from the associated host rock dolomite. A synopsis of corresponding information relating to, for example, the ferromanganese ores, is that they are confined in the central part of the Maremane dome, they have developed by supergene weathering of the manganiferous (2-3 wt. % MnO) Reivilo Formation, they are preserved in karstic hollows and lastly are overlain or intercalated with shales in their upper stratigraphic parts.

A couple of preliminary observations are noted here with respect to a carbonate sample from the base of drillcore STL018 (figure 2, chapter 5), which allows a restricted view on dolomite immediately underlying ferromanganese ore. At the hand-specimen scale,

localized brecciation and fractures/veins apparently filled by hematite are noticeable (Figure 10.1). Optical and SEM examination of the carbonate groundmass, revealed two distinct dolomite generations: (a) a chief dolomite constituent forming a mosaic of rhombic crystals with concentrations of 26.9 wt. % MgO and 1.18 wt. % MnO (n=21) and (b) a fracture-filling and manganese-rich dolomite, precipitating mostly in domains less than 30 μm in size and having markedly different composition, with 20.6 wt. % MgO and 10.6 wt. % MnO (n=11) (Figure 10.A1 & B). Their chemical difference is also illustrated in the SEM map of Figure 10.A2. Otherwise, common micro- to submicroscopic phases in the matrix are pyrite, apatite and quartz (Figure 10.A3). Barium was identified in tiny veinlets/fractures filled by hollandite and in submicroscopic bright Ba-containing specs associated with the Mn-rich dolomite. An unidentified Mg-rich silicate, most likely product of alteration, was also noted in tiny fractures.

Intriguingly, the $^{87}Sr/^{86}Sr$ ratio of two separate dolomite samples (0.71961, 0.72073) from the aforementioned drillcore are very close to those of barite (0.71324 - 0.7278, n=9) and ephesite (0.71468) in the PMF, with the exception of couple more radiogenic values associated with quartzites. This observation corroborates that regardless of the timing of dolomitization, parts of the carbonate stratigraphy associated with mineralization may have been also hydrothermally overprinted by the regional fluid system precipitating alkalis. Petrographic observations from the single carbonate sample below ferromanganese ore indeed suggest visible signs of alteration. It is also worth mentioning that despite dolomitization or alteration which is not surprising for Palaeoproterozoic carbonates, parts of the upper Campbellrand stratigraphy are known to have unradiogenic Sr-isotope ratios that reflect dissolved Sr in the waters from which they precipitated (Kamber and Webb; 2001). On a final note, more focus should be directed towards the intimate relationship of the ores with the Campbellrand dolomites in any available stratigraphic section, since every bit of new information from such research may have profound effects on ore-genetic models.

Part 2

1. Recommendations for future work

Notwithstanding the relatively small number of end-member samples analysed during this work, if the extent and complexities of the study area are accounted for, the obtained results provide the initial steps toward establishing a more accurate picture of the epigenetic and ore-genetic processes in the Northern Cape of South Africa. A lot of fruitful avenues for future research have emerged from the current thesis, which can be broadly directed towards two paths: (A) Continuation of similar petrographic and isotopic research on both comparable and new mineralogical targets and localities (B) Implementation of new advanced analytical techniques, both well established and experimental. Some of the next steps in research may include:

(1) Further research using light stable isotope geochemistry (O, H and C) may perhaps refine the established isotopic constraints on fluid composition and origin, but more significantly further illuminate fluid-rock interactions. The latter will allow a better view into the role of hydrothermal metasomatizing fluids on the protores. Augmenting the database of the pilot study in this thesis by focusing on specific mineral suites comprising micas, carbonates, silicates or hydrous/OH-bearing phases is therefore highly recommended.

(2) $^{87}Sr/^{86}Sr$ isotopes in this study aimed to assess whether the origin of Sr in barite and by extension in the alkali metasomatic fluids can be elucidated or not. The very promising $^{87}Sr/^{86}Sr$ ratio database produced, can be supplemented by more whole-rock Sr-isotopic compositions of various host- and surrounding lithologies, which may allow for a more robust recognition of the different Sr reservoir(s). Additionally, important gangues hosting Sr such as celestine ($SrSO_4$), strontianite ($SrCO_3$) and wesselsite ($SrCuSi_4O_{10}$), or minerals bearing Ca^{2+} and CO^{3-} (gaudefroyite, sturmanite, ettringite, thaumasite) and most certainly having considerable Sr substitutions of the same or a different source as that of barite, can potentially provide similar information to that of barite as regards the composition of the mineralizing fluids.

(3) The range of geochronometers that can be used to interpret the geotectonic and mineralizing evolution of the Northern Cape may be expanded to other gangue phases characterized in this study. By means of in situ $^{40}Ar/^{39}Ar$ dating, meaningful age data regarding hydrothermal/metamorphic events can be extracted from muscovite and other mica occurrences (Ba-muscovite, phlogopite) in Fe/Mn ore and conglomeratic Fe ore. Similarly, sugilite age data from N'Chwaning mine, texturally diverse occurrences, or higher stratigraphic strata such as that in quartzite from Wessels (chapter 3), may help bolster the presence of ''younger'' alteration events or further constrain the period of hydrothermal activity.

Hydrothermal zircons or xenotime were not systematically pursued during petrographic investigation, but their presence in small quantities is very likely, akin to comparable occurrences in Sishen iron ore mine (see section 1.1, this chapter). The U/Pb system can be also attempted on apatite or even garnet from the KMF. The profusion of K-bearing armbrusterite in the WMD (ca. 3.0 wt.% K_2O, see also Part 2, section 2.1) renders it ideal for novel investigation on its suitability for $^{40}Ar/^{39}Ar$ dating. In the meantime, the most critical target for the Ar-Ar system is the sodic amphibole riebeckite (see also Part 2, section 2.4), a species which has been briefly cited in this thesis to significantly account for the alkali budget of the hydrothermal fluids permeating the ores of the Northern Cape. Modern instruments and techniques may help overcome difficulties associated with the extremely low potassium content of this phase and despite the Ar-loss issues intrinsic to amphibole dating, even low accuracy age results may still elucidate its origin and potential involvement in alteration processes.

(4) Postmasburg Manganese field (PMF) and particularly its western sector (WMD ores) are invaluable for mineralogical studies, owing to their rich and highly complex mineralogical content. This was explored in more detail in this study, something that resulted in reports of new rare minerals and lots of unidentified species. Therefore, prospects are bright for future mineral discoveries, however small their size may be. Detailed mineralogical research could further shed more light on the alteration processes and will be benefitted by integration of different tools not used here such as XRD, infrared absorption spectrometry, Raman spectroscopy and electron probe micro-analyser to name a few.

(5) Mineralogical studies can also focus on ore mineralogy [braunite (I), braunite (II) hematite, partridgeite, hausmannite], investigating both their textural and compositional characteristics in a systematic way, with an aim to further illuminate the protoliths, genetic environment and alteration/upgrade processes of the ores. In situ micro-analysis using SIMS, LA-ICP-MS and other new analytical techniques can allow to study a wide range of minor and trace elements in ore and gangue mineralogy or even determine their stable isotopic composition (i.e., $\delta^{56}/^{54}Fe$), aspects that may be important in understanding mineral formation or aid in the distinction of mineral generations (for e.g., Zhang et al; 2014, De Souza et al; 2019, Li et al; 2019).

(6) The previous work would be best supported by additional studies examining the geochemical variations of different ore-types in the PMF. The bulk rock composition of these ores can be used not only for reviewing the existing crude classification, but also potentially revealing mineralogical controls or information on the genesis of the ores if plotted in a wide set of available discrimination plots for manganese ores (Nicholson; 1992, Tumiati et al; 2010, Jones; 2017). REEs are also important in this research, since they tend to behave in a conservative way during certain fluid alteration processes and may therefore illuminate the protolith signature of the ores under examination.

(7) It is also possible that individual hydrothermal gangue phases in the PMF, such as calcite and barite, or coarse-grained ore mineral varieties such as hematite and bixbyite, are suitable for fluid inclusions studies. Considering that this is a routine technique in research associated with MVT deposits and the fact that it has been successfully used in the neighboring KMF, this method may provide reasonable temperature estimates, as well as information on the composition and salinities of the metasomatizing and/or ore-forming palaeofluids.

(8) The geochemical mechanisms of elemental transportation, redox conditions and chemistry of the fluids are aspects that can be potentially also tackled on a more theoretical basis by surveying the available literature. However speculative the outcomes of such research may be, if combined with textural, mineralogical and micro-analytical chemical data, important insights may still emerge.

(9) Isotope fingerprinting using more unique tracers such as lithium (Li), boron (B) or chlorine (Cl), may constitute a new approach on constraining fluid sources in the study area. For instance, δ^{7}Li isotopes have been widely used to decipher the origin and evolution of brines (Macpherson et al; 2014), the isotopic composition of different lithologies and magnitude of Li isotope fractionation during water-rock interactions, all burgeoning research fields (Millot et al; 2010a, Teng et al; 2014), which renders any contribution from the Li-bearing species of the Northern Cape one of high importance. Sugilite, ephesite and lithiophorite are probably the best targets for an investigatory mineral-specific essay, but a whole-rock approach on mineralogically and geochemically well-characterized ore samples can be similarly beneficial.

Boron is also a well-established tracer that can be employed to investigate the origin and evolution of fluids. Boron, was evidently saturated in the hydrothermal fluids during alteration processes in the KMF, resulting in precipitation of borates or species high in boron content (for e.g., gaudefroyite, sturmanite, charlesite, gowerite, inyoite). δ^{11}B of the aforementioned species can be compared against that of different braunite generations, which is also known to contain traces of boron, probably related to chemical sorption of this element into co-existing carbonates in the Hotazel stratigraphy, thought to have originated from hydrothermal alteration of adjacent lithologies by seawater (Varentsov and Kuleshov; 2019). It is known that halite from marine evaporites records the boron isotopic composition of contemporaneous seawater with only a slight fractionation (Paris et al; 2010) and that δ^{11}B values evolve through time. Notably though, both modern and ancient studied evaporites have varying but distinctly positive δ^{11}B values (from ca. + 20 to + 40 ‰) (Warren; 2006). Hence, for example, if an evaporitic signature is preserved in the hydrothermal minerals of the Northern Cape, it can be potentially differentiated from other sources (for e.g., magmatic/hydrothermal, non-marine evaporites) that generally show much lighter δ^{11}B values (broadly from -20 to +10 ‰) (Ranta et al; 2016).

Another 'fingerprint' of hydrothermal fluid sources and record of fluid-rock interactions may be provided by halogen isotopes (^{37}Cl and ^{81}Br). Such stable isotope surveys have been successfully utilized in ground saline waters and brines to constrain the origin of chloride and confirm Cl isotope fractionation and brine formation from evaporated palaeo-

seawater (Eggenkamp et al; 1995, Alexeeva et al; 2015). The halogen characteristics of ore-forming fluids have been also studied from hydrothermal vein minerals to identify distinct fluid signatures, i.e., mantle-derived vs low-T meteoric fluids (Graupner et al; 2006). Much like lithium (Li), both mineral-specific (separates from hydrous species in the KMF containing F, Cl, and OH) and whole-rock (ore material) isotopic analyses can be attempted, following a previous determination of the bulk halogen content. It is needless to say that interpretations would require very good knowledge of the mineralogy of the regarded samples.

(10) Finally, there is a strong need for integrated stratigraphic, tectonic and geochemical studies regarding these ores, which will incorporate any geological field and core observations that may help with the identification of structures, faults, folds, discontinuities, strata duplications and development of unconformities. The virtually complete lack of outcrop in the area can be perhaps counterbalanced with patient core studies, visits in mining outcrops, close collaboration and access to core logging data from mining companies. It is pivotal that small-scale textural, stable- and radio-isotopic observations are correlated with the wider scale geological features. All these will increase confidence in new ore genetic models and may yet finally resolve the remaining riddles associated with the alkali metasomatism in the Northern Cape.

Furthermore, a set of already obtained data allows for continuation of research on **four different topics**, all under the umbrella theme of alkali metasomatism in the Northern Cape. This work in progress is briefly presented below.

2.1 Origin of the Wolhaarkop breccia

As stated earlier in this thesis, the nature of the enigmatic brecciated lithologies playing host to or underlying the ferromanganese orebodies in the PMF should be extensively researched before any attempt to reconstruct the epigenetic history of the wider ore field. That is because: (i) studies have shown that the residual karst breccia known as Wolhaarkop breccia is geochemically and mineralogically much more complex (Moore et al; 2011, Fairey et al; 2019) than originally described and (ii) recent findings have demonstrated the presence of large-scale circulation of evaporitic brines in the region; therefore, the possibility that this

formation represents an evaporite breccia, at least it certain occasions, should be further explored. On account of the general lack of detailed petrographic studies from these rocks and particularly from the alkali-rich end-members seen in drillcore sections obtained from the WMD (for e.g., Heuningkranz locality), preliminary results from ongoing research are presented here.

Hand specimens from a thick, well-developed zone of the Wolhaarkop breccia at Heuningkranz locality (drill core SLT 1800) show large textural variability, broadly defined by clast- and matrix-dominated end-members (Figure 11.1, 11.2). The greyish black to red fine-grained matrix displays a crude layering which is occasionally replicated in the arrangement of clasts, though the majority of them is generally poorly sorted. The greyish-white sub-mm to cm-sized clasts exhibit replacement textures and micro-brecciation, macroscopically evident by rugged or serrated edges and overprints by distinct yellowish/orange or black mineralogical domains, as seen in the closeup of Figure 12.1. The visible black manganese, essentially braunite domains around clasts and within portions of the matrix, as well as the abundant vuggy textures developed in the matrix are probably the most distinctive features of the studied samples.

Thorough SEM analysis documents the elevated alkali content of these samples, hosted by the dominant association of albite, aegirine-augite and armbrusterite, a paragenesis also containing substantial manganese as braunite and manganoan calcite, besides copious barite. The abundant alkali-rich species are most commonly present in vugs, forming intricately mixed aggregates with inclusions of quartz, braunite or alkali minerals, for e.g., albite in aegirine. Euhedral elongate, scattered or aggregated aegirine crystals, range from 250 to 500 µm, but can also be over 1 mm in size and are frequently encased in manganoan calcite (Figure 11A). The latter is chief constituent of the replaced clasts and vugs and may accommodate disseminated sub-microscopic to 10 µm in size grains of barytocalcite, strontianite and REE-bearing barytocalcite, implying that forming solutions were temporarily supersaturated with respect to certain REEs, which substituted for Ca^{+} and Ba^{2+} during hydrothermal carbonate formation.

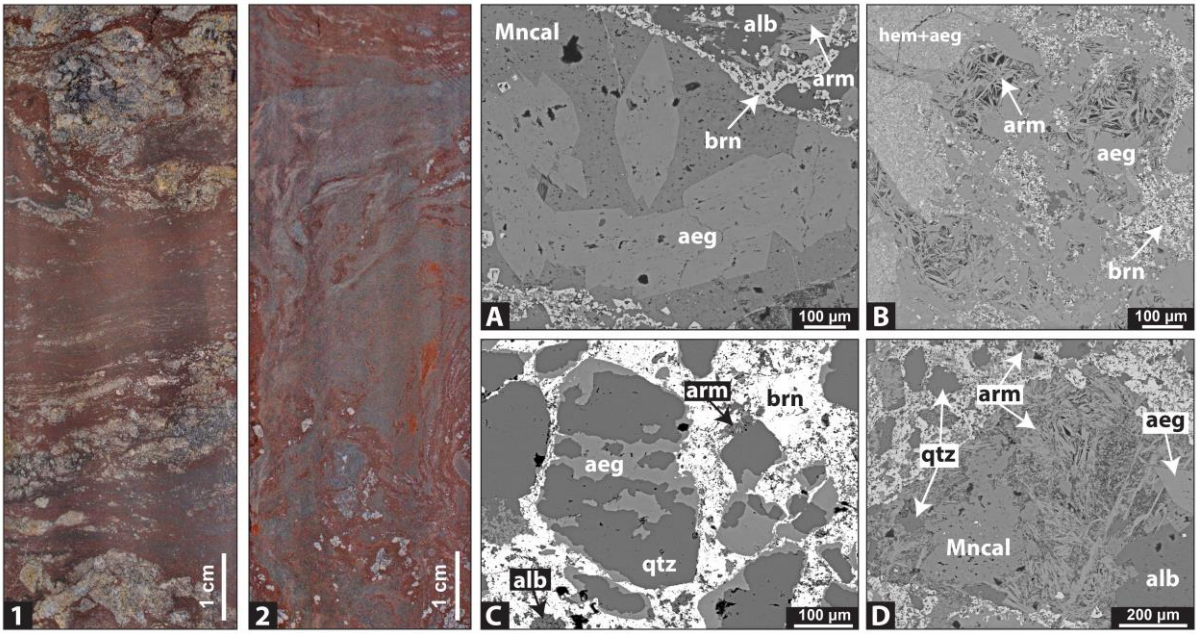

Figure 11. (1) Detail of the Wolhaarkop breccia with broadly equal proportions of matrix showing crude layering and clasts/vugs. (2) Matrix -ich portion of the breccia, displaying fine, irregular reddish lamination of most likely aegirine-rich composition, greyish hematite-rich domains, and tiny clasts/vugs floating in the matrix. (A) Euhedral aegirine in Mn-calcite, surrounded by braunite and other alkali-rich species. (B and C) Examples of quartz clasts in braunite matrix being partially or completely replaced by aegirine, albite, armbrusterite and manganoan calcite. (D) Armbrusterite veinlets with thin aegirine selvage (left) permeating braunite matrix and replacing quartz (right). aeg = aegirine, alb = albite, arm = armbrusterite, brn =braunite, hem= hematite, Mncal = manganoan calcite, qtz = quartz.

Quartz/chert clasts, diagnostic of the Wolhaarkop chert breccia, are absent in the studied samples and instead, cm-sized clasts comprise chiefly alteration minerals. Quartz grains or remnants from original clasts, between 100 and 500 µm in size and occurring in braunite-rich matrix, are seen partly to completely replaced mostly by aegirine or associations of armbrusterite, albite and Mn-carbonates (Figure 11B, 11C). Armbrusterite $[K_5Na_6Mn^{3+}Mn^{2+}{}_{14}[Si_9O_{22}]_4(OH)_{10}4H_2O]$, which otherwise is a rare species, occurs as a major component in these samples and develops largely as randomly oriented or radiating sheafs of between 100 and 500 in size (Figure 12.A). It has a composition outside the range of the average armbrusterite composition (Yakovenchuk et al; 2007), as well as that from Bruce mine (EMD, Postmasburg Manganese field; Moore et al; 2011).

Specifically, according to standardless EDS analyses, the analysed species resembling armbrusterite has an average chemical formula of $K_{2.7}Na_{3.3}Mg_{1.1}Mn_{21.1}[Si_9O_{22})_4(OH)_{10}4H_2O$, calculated on the basis of 36 Si. Apart from the much lower alkali percentages, the significant

presence of MgO (1.10 wt.%) and the much higher MnO content (35.9 versus 27 wt. % in average armbrusterite) are aspects that call for further analyses to better determine its stoichiometry and characterize this abundant species, seen paragenetically associated with the sodic alteration phases (Figure 11D). Notably, fibrous armbrusterite commonly permeates through porous and fragmented euhedral braunite and encapsulates as interlocking masses or even overprints and replaces carbonates and quartz, textures that overall suggest late precipitation for this phase.

Coarse (0.5-1.5 cm) albitized clasts surrounded by hematite- and braunite-dominated matrix display ubiquitous disseminations of euhedral braunite, microplaty hematite and clusters of rutile (100 µm) with pyrophanite inclusions and lesser hyalophane, armbrusterite, apatite and flakes of barian muscovite. Traces of yttrialite [$(Y,Th)_2Si_2O_7$] of up to 50 µm in size, intergrown with an unidentified Mg-rich silicate, as well as a distinctive Mn-bearing variety of ilmenite are present in the albite-rich clasts and vugs. Other trace components identified in the studied sample suite are As-bearing apatite, tephroite and a La-bearing silicate, the latter confined to the vicinity of braunite clusters, where it possibly develops within and preserves ghost textures of braunite. This species contains in wt. %: 35.5 SiO_2, 10.1 Al_2O_3, 28.4 MnO, 6.2 CaO and 19.9 La_2O_3, generally displaying resemblance with the mineral alexkuznetsovite-(La) [$La_2Mn(CO_3)(Si_2O_7)$], reported from an REE deposit in South Urals, Russia (Kasatkin et al; 2021).

Matrix cementing the clasts/vugs is markedly hematite rich (Fe_2O_3 up to ca. 25 wt.% from preliminary analyses) and comprises a series of fine-grained species intergrown with or precipitated in pore space, among which are aegirine, muscovite, Mn-bearing carbonates and dolomite (Figure 12B-D). Hematite is chiefly very fine-grained (cryptocrystalline), although tabular and microplaty varieties are also seen associated with euhedral braunite and the alkali-rich associations (Figure 12E). Braunite is preserved in textures suggesting replacement of former clasts by braunite, whereas in several other examples a cluster of veinlets/stockwork comprising manganoan calcite, armbrusterite and barite develops throughout braunite aggregates, pointing to a later precipitation for the former assemblages. Overall, a series of Mn-carbonates and braunite associations strikingly illustrate replacement of quartz by the former. Small fractures in remnant chert clasts filled by braunite, alkali-rich

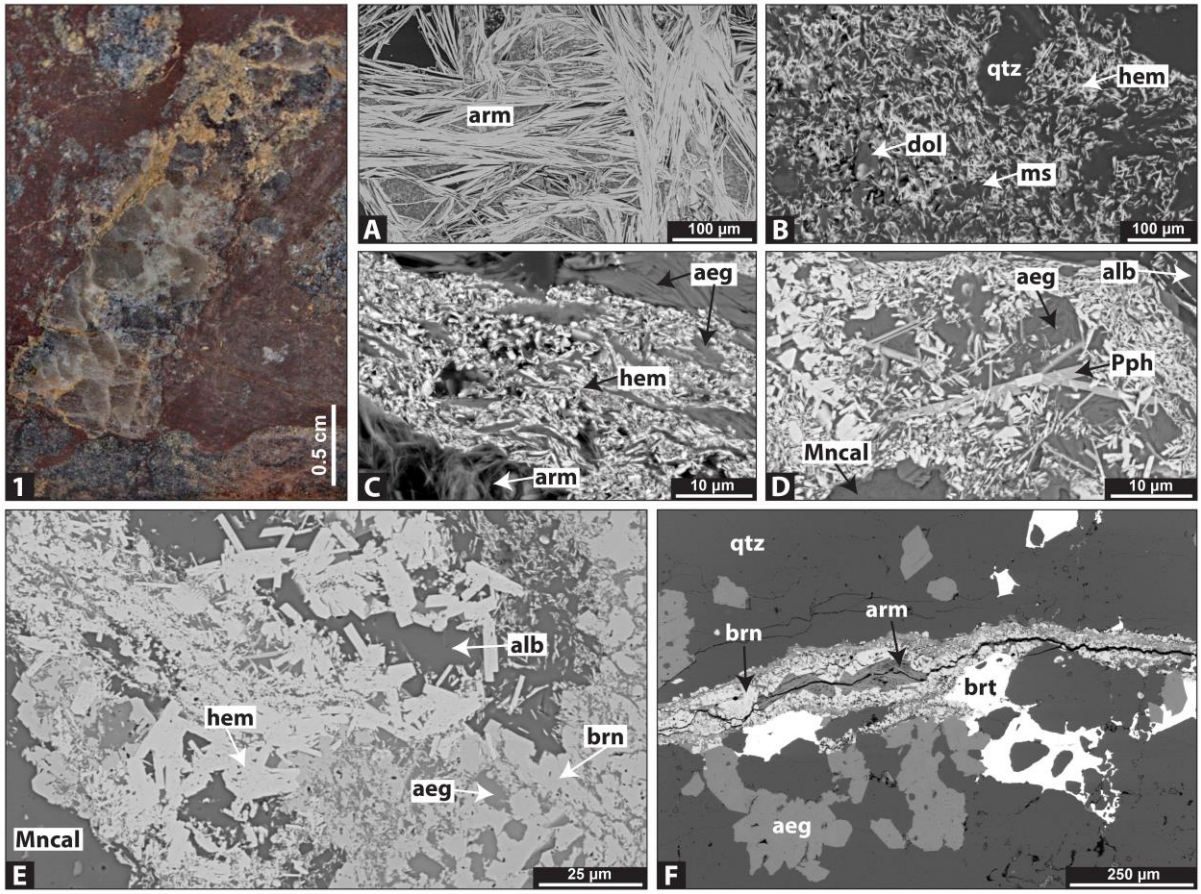

Figure 12. (1) Detail of former chert clast, having been replaced by armbrusterite (yellowish orange), calcite, braunite (greyish black), and other alteration phases. (A) Armbrusterite sheafs in altered clast. (B-D) Aegirine is quite dominant as pore space filing in hematite matrix, but in certain cases carbonates, dolomite and muscovite are also seen intergrown with cryptocrystalline hematite. Pyrophanite is apparently scarce and along with rutile controls the Ti content of the matrix. (E) Tabular hematite associated with alteration mineralogy. (F) Manganese mobilization (braunite precipitation) along micro-fracture during alkali hydrothermal alteration. aeg = aegirine, alb = albite, arm = armbrusterite, brn = braunite, brt = barite, dol = dolomite, hem = hematite, Mncal = manganoan calcite, ms = muscovite, Pph = pyrophanite, qtz = quartz.

species and barite further support manganese mobilization during hydrothermal alteration (Figure 12F). Barite is seemingly a paragenetically late phase, that overprints carbonates, occludes open space and is associated with serandite in zoned replacements.

Fairey et al (2019) reported from this locality only the presence of calcite, as subordinate phase in certain vugs. However, apart from the abundance of coarse-grained calcite filling vugs and replacing clasts, the investigated vugs and matrix also contain previously undocumented manganese-bearing carbonate species and dolomite, which develop aggregates or occur as individual rhombohedral entities of up to 200 µm in size.

Individual crystals always exhibit conspicuous zonation, characterized by a brighter manganese-rich rim and a duller interior, as seen under back-scattered imaging (Figure 13A, 13C). Extensive (several hundred mm) patches comprising carbonates display compositional zoning patterns, with variations in Ca, Mg and Mn resulting in dolomite-, Mn-rich dolomite and manganoan calcite end-members (Figure 13B, 13E). As seen in the previous figures, carbonates are found as inclusions in quartz and evidently replace it. The interiors of individual carbonate rhombs may be also filled by serandite or aegirine, which underpins the close temporal association of these alteration phases (Figure 13D).

SEM compositional line scans from different individual carbonates illustrate their common characteristics: (a) the presence of a conspicuous rim enriched in manganese and (b) interiors with lesser manganese, which show minor variations in its concentration, broadly mirrored by Mg and Ca. In the case of irregularly-shaped carbonate aggregates developing in vugs, their zoning patterns may be the result of changing fluid properties, suggesting non-equilibrium mineral growth. On the other hand, compositional zoning in individual crystals is likely to be inherent to the growth mechanism, so that abrupt shifts in chemical composition on the micro-scale are not associated with changes in the hydrothermal fluid (Reeder; 1991, Shore and Fowler; 1996). Carbonates are common constituents of hydrothermal systems and formation of secondary hydrothermal carbonates has been associated with highly saline brines in other settings (for e.g., Staude et al; 2012). Their origin has been successfully traced through stable isotope (C, O) systematics and fluid inclusions have repeatedly shed light on the temperatures of formation (Hoefs; 1997). Therefore, a similar approach on carbonates from the Wolhaarkop breccia in conjunction with fluid inclusion studies on minerals such as quartz or barite, have good chance of unraveling analogous information.

Taking into consideration the limitations of optical microscopic observations, imposed by fine-grained and broadly opaque mineralogy, the use of EDS geochemical maps is recommended to be most beneficial for discerning the distribution of both alkali- and ore-mineralogical species but also the dissemination and perhaps mobility of the critical ore metals, i.e., Fe and Mn, during alteration processes. A selection of such maps illustrates the elemental distribution of iron (red), manganese (blue), alkali-mineralogical associations (gold textbox) and alkali-rich minerals that also host Fe or Mn in their structure (white/gold textbox)

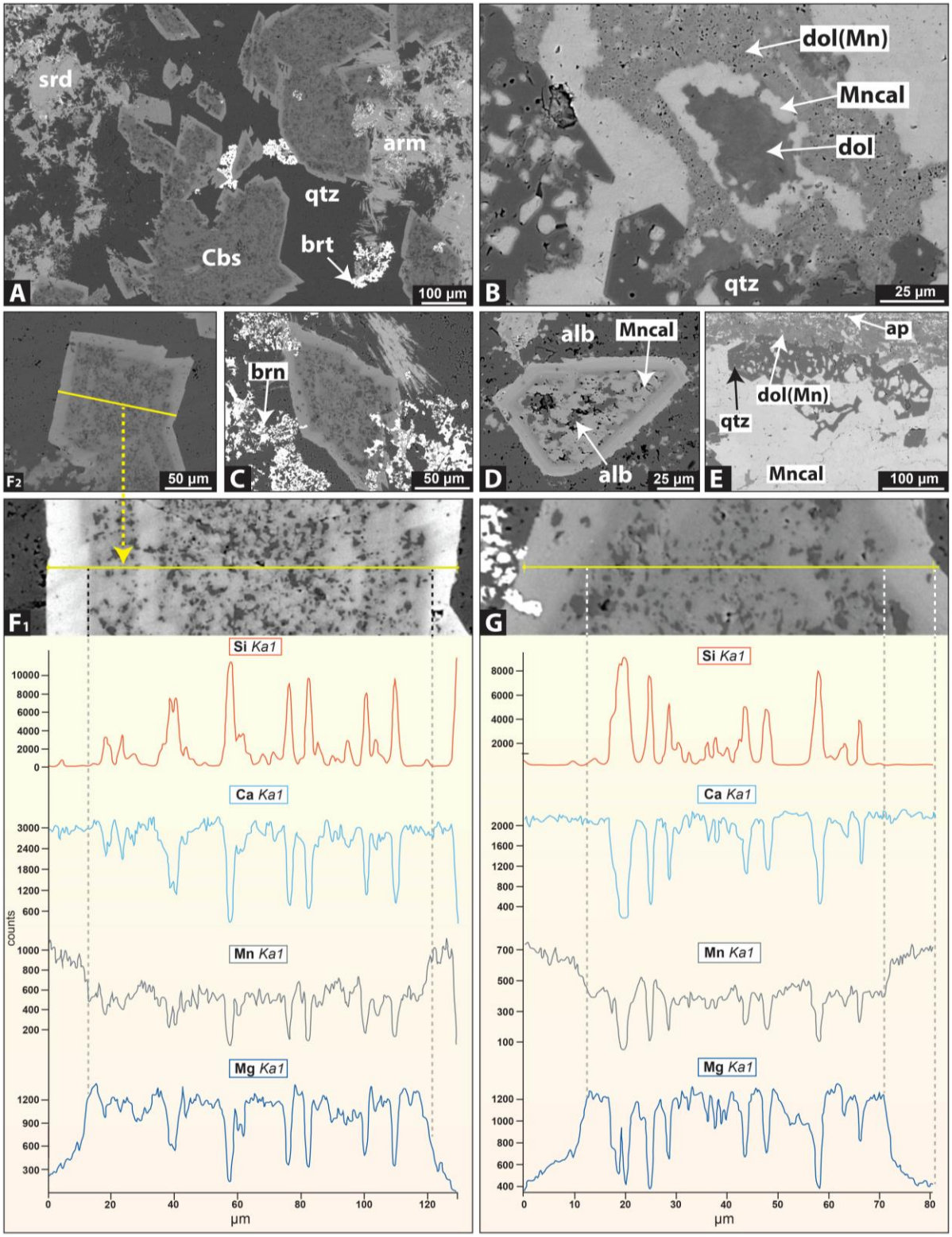

Figure 13. (A) Clusters and individual subhedral carbonate crystals within remnant quartz clast, associated with alkali phases and displaying zonation. (B) Compositional zoning in carbonates, characterized mainly by variations in dolomite composition and lesser in manganoan calcite. (C & D) Carbonate rhombs display conspicuous zoning and occasionally interiors filled by remnant quartz and alkali species, which emphasizes their close relationship with alkali metasomatism. (E) Evident replacement of former quartz by carbonates. (F1-2 & G) SEM line scans across individual carbonates demonstrate the presence of a rim higher in manganese and minor compositional variations in their interiors, with patterns apparently mirrored by Mn, Mg and Ca. alb = albite, ap = apatite, arm = armbrusterite, brn = braunite, brt = barite, Cbs = carbonates, dol = dolomite, dol(Mn) = Mn-rich dolomite. Mncal = manganoan calcite, srd = serandite, qtz = quartz.

(Figure 13). Regarding iron, the element is as to be expected particularly concentrated in the fine-grained hematite matrix, but very much also in microscopic aegirine, which as noted earlier can be seen finely intermixed with hematite in matrix surrounding minute vugs or clasts (Figure 13.C, 13.E). Locally, aegirine may be the dominant Fe-host species in the matrix (Figure 13.B) or may develop a crude layering in the hematite-rich matrix, lesser followed by braunite (Figure 13.F). Manganese appears to be thinly disseminated in the matrix as microscopic braunite, although coarser (20-50 µm) braunite grains and aggregates are locally more conspicuous (Figure 13.E, 13F). Also noteworthy, is the distribution of manganese in the form of braunite around vugs and clasts comprising alkali associations or the clustering of braunite around remnant quartz clasts (Figure 13.A, 13B). Considerable amounts of manganese are apparently also hosted by armbrusterite and Mn-bearing carbonates that develop a series of veinlets (Figure 13C, 13E) or overprint former quartz together with braunite Figure 13G). Lastly, in certain samples, the only manganese-hosts in the matrix were found to be dolomite and Mn-bearing carbonates, which become more abundant towards the contact with quartz clasts and seemingly overprint the latter (Figure 13H).

All of the above emphasize the complex features of this presumed dissolution-collapse breccia, which regardless of its original mode of formation and metal concentration, it has been most certainly overprinted by at least one and perhaps two, if one considers the pilling geochronological data (Moore et al; 2011, Fairey et al; 2019), hydrothermal events. Identification of possible pristine evaporitic breccia textures in such setting seems an arduous task, mostly suited to experts in this field. However, textures such as the observed crude layering/stratification may hint to former evaporite layers that have been dissolved (Swennen et al; 1990) and may act as guideline for tracing other textural evidence related to the origin and mechanism of brecciation.

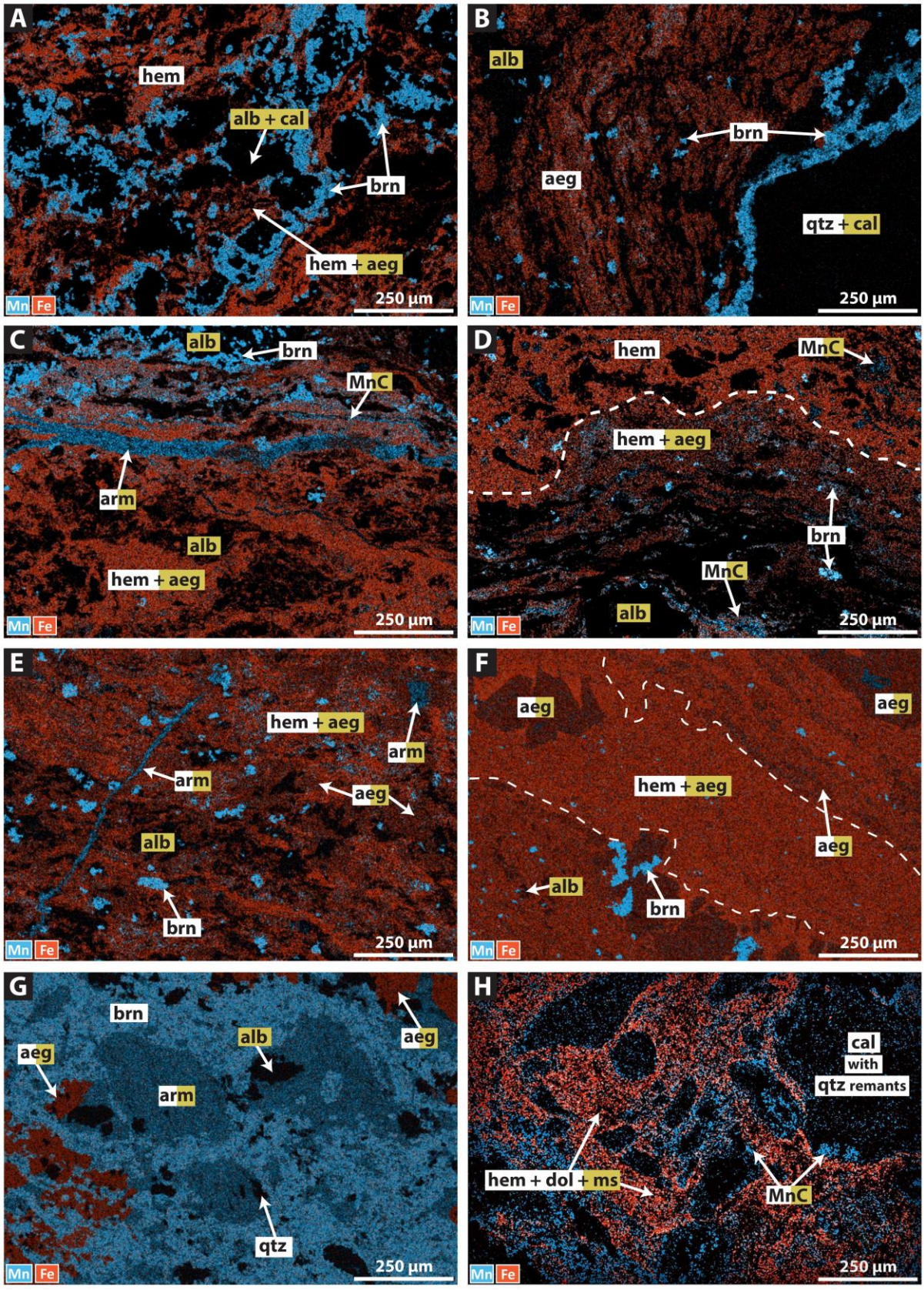

Figure 13. EDS geochemical maps from different samples of the manganiferous Wolhaarkop breccia emphasizing the distribution of Mn (blue) and Fe (red). Black areas represent remnant quartz clasts (partially or totally replace) or vugs and comprise mixtures of mainly Si, Al, Na, and lesser Ca. Alkali (sodic)-rich minerals are displayed using *gold textbox* and species/associations that also host Fe or Mn are typed within *white/gold textbox*.

2.2 The uncommon sulfates of the KMF - An overture to their isotopic composition and the waning stages of the Wessels-type hydrothermal event

During the sulfur isotopic work carried out for this research, mineral-specific isotopic analyses have been attempted on a range of sulfate minerals from the Kalahari Manganese field (KMF), including species of the unparalleled yellow to amber-coloured prismatic ettringite [$Ca_6Al_2(SO_4)_3(OH)_{12}26H_2O$] - sturmanite [$Ca(Fe^{3+},Al)_2(SO_4)_2[B(OH)]_4(OH)_{12}25H_2O$] group minerals, besides other common sulfates, i.e., gypsum and celestine. KMF is the preeminent locality worldwide for these unusual sulfates, which in N'Chwaning II mine have been found as prisms reaching 15 cm in length (Cairncross and Beukes; 2013).

Sulfates are found exclusively in the hydrothermally upgraded ore (Wessels-type) and specifically in highly variable vein- and vug-hosted mineral associations, comprising andradite, gaudefroyite, hausmannite, hematite, braunite II, kutnohorite, rhodochrosite, calcite, barite, shigaite, vonbezingite and celestine to name a few (Gutzmer et al; 1997b, Pohwat; 2012). Both their distribution mostly in secondary porosity formed during the main ore-forming event and their paragenetic associations, have been used to suggest that sulfates, along with borates and secondary carbonates, represent products of late-stage alteration. While this is a reasonable assumption, the potential that stable-isotopic fingerprinting can be applied on these unusual gangues as a means of illuminating fluid origins or composition and characteristics during the waning stages of alteration remains unexplored. Furthermore, prolonged exposure under conditions of meteoric water circulation since the Namaqua orogeny and/or other low-T hydrothermal solutions like that during the overprinting Neoproterozoic event (ca. 650-600 Ma, chapter 4, Moore et al; 2011, Fairey et al; 2019,) may have utilized discontinuities and acted upon gangue mineralogy, thus altering it, or promoting new mineral growth. For example, it is known that mineralogical diversity and locally ore-grade have increased during recent time (< 42 Ma) under supergene processes (Gutzmer et al; 1997b, Gutzmer et al; 2012). At all accounts, the rarity of these sulfates and their unique mode of occurrence in this geological environment raise questions, sought to be tackled here through introduction of more advanced analytical techniques than simple petrographic examination.

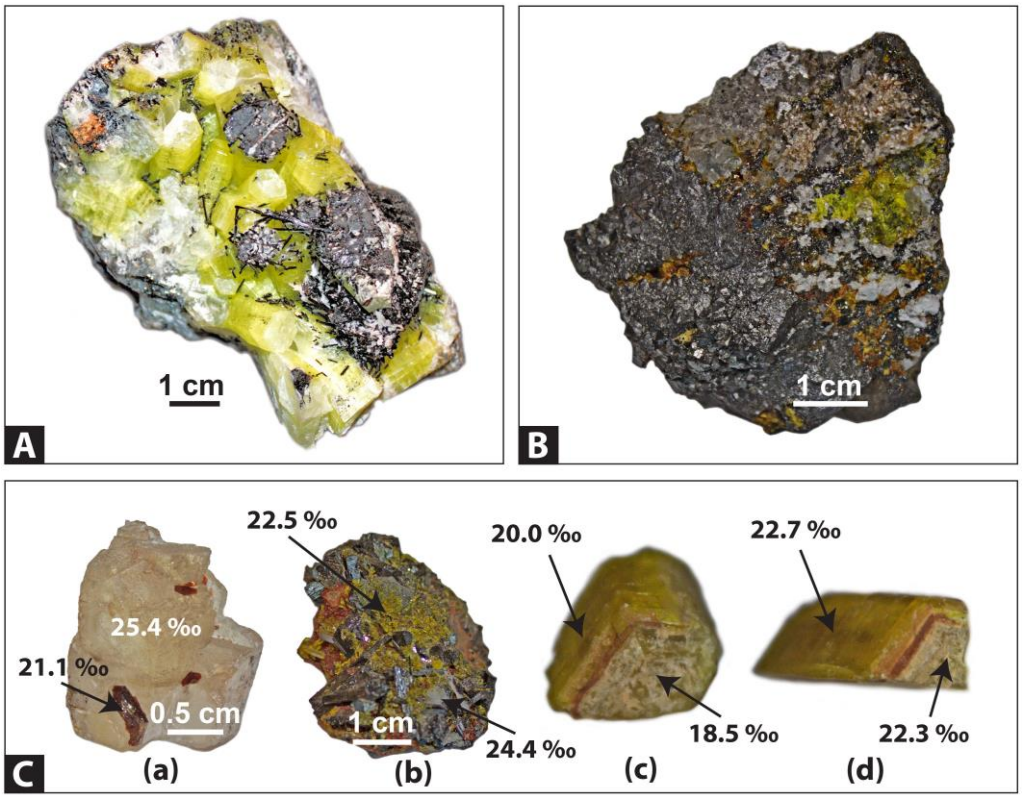

Figure 14. (A) Large and well-developed ettringite with conspicuous black gaudefroyite needles. (B) Fine grained ettringite-sturmanite species in association with calcite, hausmannite and bixbyite. (C) Intra-sample variations in $\delta^{34}S$ values in co-existing barite-shigaite (dark red) (a) and barite-ettringite (b). Small-scale sulfur isotopic variations in ettringite crystals displaying concentric growth zonation (see also text).

Most of the analysed samples in this study derive from N'Chwaning II and when their association is known, it usually comprises no more than three of four species, mainly calcite, barite, gaudefroyite and andradite, besides ore minerals such as hematite and hausmannite (Figure 14.A, 14.B). It should be noted that no analytical method was used to distinguish between these minerals apart from any done prior by mining geologists and collectors providing the samples. This is important to emphasize because as noted by Gutzmer and Cairncross (2002), visual distinction between ettringite, sturmanite and charlesite (another hydrous alumino-sulfate containing boron) is virtually impossible and the only unequivocal identification method is determination of their iron and boron content by chemical analysis. However, even in the latter case, the presence of complex concentric and compositionally variable growth zonation may lead to ambiguous results. For that reason, distinction between ettringite and sturmanite is regarded as tentative here and is essentially based on crystal habit and colour, similarly to the method used by collectors and dealers, i.e., amber-coloured

sturmanite prisms, yellow to white prismatic ettringite crystals, etc. EDS analyses on a single sample containing sturmanite associated with garnet, Sr-rich barite, microscopic diaspore and Mn-carbonates, revealed compositional variations with respect to the iron and aluminum content of the sulfate and further suggest that manganese can also substitute for iron in its structure.

Thirty-nine sulfur (n=39) and twenty-six hydrogen (n=26) isotopic analyses were carried out on selected sulfates, with the latter analyses being to a large degree experimental; therefore, comprising a step heating investigation to access water loss and hydrogen isotope variation with increasing temperature. $\delta^{34}S$ values display a rather wide range, larger than that of barite from the KMF, and a somewhat bimodal distribution (Figure 15, Appendix II). The latter broadly consists of an isotopically heavier group of celestine, sturmanite and

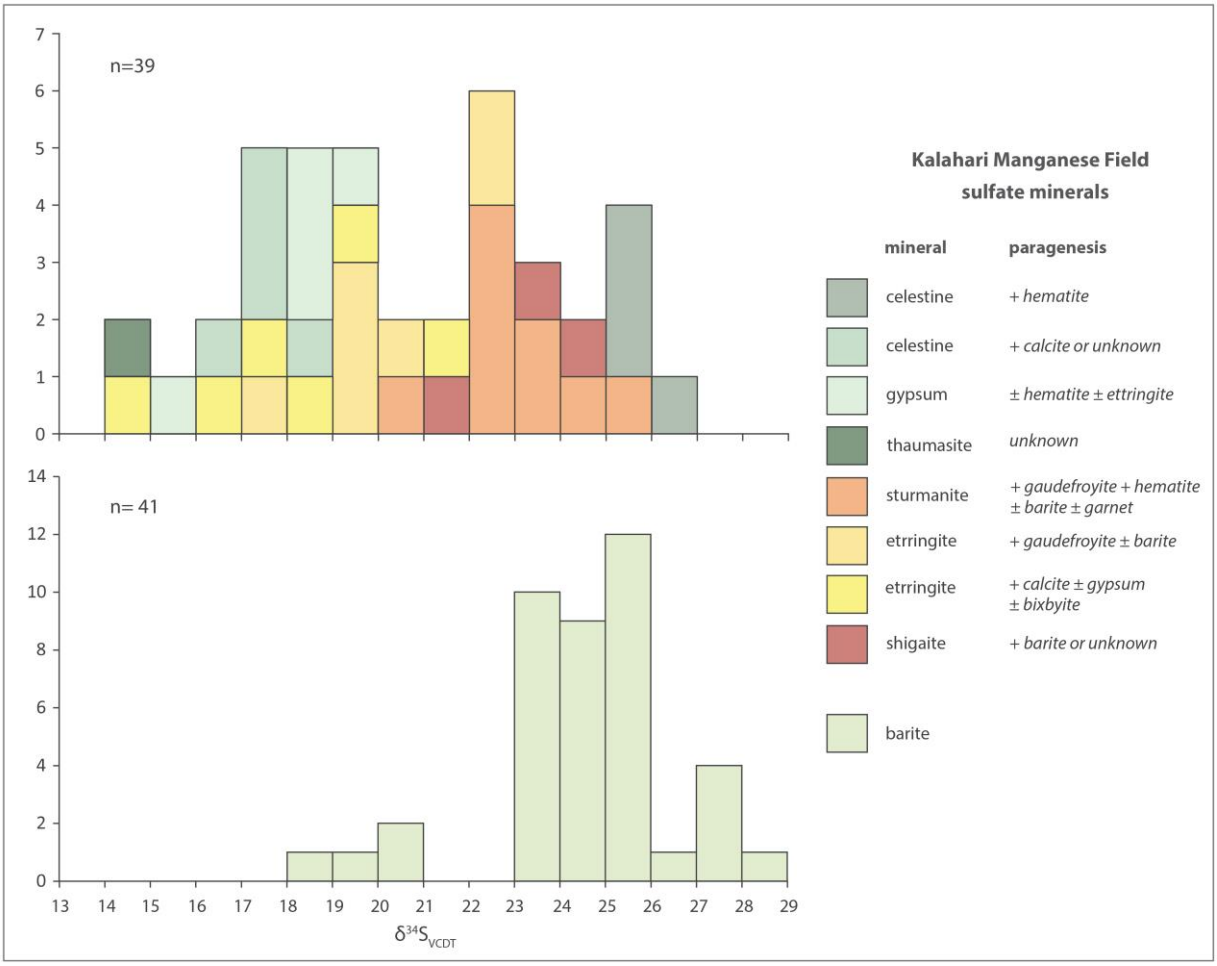

Figure 15. Histograms of sulfur isotopic compositions of sulfates from the KMF (top) and barite from the same district (bottom). Note the significant overlap between certain sulfates and barite, which can be further extended to the homogenous $\delta^{34}S$ values (24.9 ± 2.5‰) of barite mineralization in the Northern Cape; therefore, validating the association of sulfates such as sturmanite and shigaite with the waning stages of the Wessels event.

shigaite (between 20.3 and 26.0 ‰, average = 23.2 ± 1.8 ‰, n =19) and a group of lighter $\delta^{34}S$ values (between 14.3 and 19.7, average = 17.7 ± 1.7 ‰, n=20) containing again celestine, although paragenetically distinct to that of the previous group, as well as ettringite, gypsum and thaumasite. There is an obvious overlap between values of the first group and barite, which can only suggest a common origin of sulfur and a probably contemporaneous precipitation for these phases. Isotopic fractionation accompanying equilibrium chemical exchange reactions and fluid shifts during synchronous precipitation of barite and other sulfates can apparently vary significantly. For example, under closer inspection, the texturally cogenetic barite and shigaite $[Mn_6Al_3(OH)_{18}[Na(H_2O)_6](SO_4)_26H_2O]$ of Figure 14.Ca display a difference of 4.3 ‰ in their $\delta^{34}S$ values, which can be regarded as rather high for the regarded mm-scale sample context. Shigaite flakes seems to be partly enveloped by barite, possibly suggesting a slightly earlier crystallization for the former.

The pattern of isotopically heavier barite (24.4 ‰) co-existing with lighter ettringite (22.5 ‰) is repeated in another association (Figure 14.Cb) and generally, as presented above, sulfates exhibit variably but almost constantly lighter $\delta^{34}S$ values than barite in the KMF. The light isotope (^{32}S) is expected to remove preferentially over the heavy (^{32}S) from aqueous solution (e.g., Hanor; 2000), shifting the isotopic composition of the precipitating fluid towards heavier values, something that agrees with textural observations. However, other factors can control sulfur isotope fractionation such as atomic mass, ionic charge, electronic configuration of the isotopic elements and different cations (Ca and Ba, i.e., light versus heavy) in associated phases or mixing with different sulfur isotopic ratios from other sources during introduction of a distinct fluid. Analysis of such factors and scenarios is beyond the scope of the current presentation, but it should be reminded that heavier $\delta^{34}S$ barite values are regarded as more closely resembling the sulfur isotopic composition of the hydrothermal fluid, as well as of the original sulfur source (chapter 2). Consequently, it is not concluded here that sulfates generally precipitate prior to barite, although this may seem as a reasonable assumption in some cases and needs to be further explored.

A more general but rather important outcome from the current analysis is that sulfur isotopes validate the hypothesis that at least certain sulfates, along with barite, are of late-paragenetic origin with respect to the Wessels-type event. Most importantly though, these

results testify that sulfates other than barite have also preserved with satisfactory accuracy the regional isotopic signal produced during the Namaqua hydrothermal metasomatism, in that way further corroborating the presence of an evaporitic component in the sedimentary basinal brines. Accordingly, what is certain, is that physicochemical changes of the fluid(s), fluid mixing processes and/or different timings of formation need to be invoked in order to explain the lighter, i.e., < 20 ‰ $\delta^{34}S$ values recorded by many sulfates. The very nature of ettringite group minerals, them being highly hydrated calcium sulfoaluminates, casts doubt on their exclusively ''pristine'' origin in the KMF. Paragenetic associations and large crystal size may indeed point to their affiliation with late-stage alteration gangues. However, at least some gypsum, celestine and ettringite-thaumasite occurrences could very likely be precipitates of a chemically evolved alteration fluid, that has been isotopically modified after crystallization of the bulk barite and is characterized by lighter $\delta^{34}S$ ratios and saturation with respect to these phases.

It is important to also note that ettringite is an important constituent in concrete industry. In order to regulate early hydration reactions, improve strength development and reduce drying shrinkage, i.e., avoid ''sulfate attack'' and concrete failure, calcium sulfate such as gypsum is intentionally added in Portland cement concretes. Consequently, gypsum reacts with calcium aluminate in the cement to form ettringite, which contrastingly to the aesthetic mineral specimens in the KMF, develops as uniformly dispersed sub-microscopic grains (Jiahui et al; 2006, Xu et al; 2014). Interestingly, several gypsum and celestine $\delta^{34}S$ values overlap with that of ettringite and gypsum is also seen closely associated with ettringite in available samples, which may imply that hydration of gypsum and/or celestine during the waning stages of alteration drives precipitation of at least some ettringite-group species. Therefore, mixing with meteoric water and other sulfur sources may be important factors influencing the sulfur isotopic composition of these sulfates during their post-barite formation and may better explain their wider spread in $\delta^{34}S$ values. As seen in Figure 14.Cd & e, concentrically zoned ettringite apparently displays only small variations in $\delta^{34}S$ values ($\Delta\delta^{34}S$ between 0.4 and 1.5 ‰). The concentration of AlO_2^-, an element that has extremely low concentration in the pristine Hotazel Fm, has been also shown to be a critical factor influencing ettringite formation in the former presence of gypsum (Jiahui et al; 2006).

Thaumasite [$Ca_6Si_2(CO_3)_2(SO_4)_2(OH)_{12}24H_2O$], exhibits one of the lowest $\delta^{34}S$ values (14.3 ‰), along with ettringite (14.1 ‰), and is suggested here to be the latest species to crystallize among the regarded sulfates. The pale yellow thaumasite crystals sampled from N'Chwaning II mine are the best-known examples of this mineral species in the world (Gutzmer and Cairncross; 2002). Nevertheless, microscopic thaumasite forms commonly in cements like ettringite and presents a serious deterioration mechanism for the material (Dvořák et al; 2020). Conditions promoting its formation are still the subject of debate; however, research suggests that its precipitation is favoured by higher sulfate concentrations in comparison to ettringite, and generally exists in a different, low-T and low pH regime in contrast to the former (Macphee and Barnett; 2004, Rahman and Bassuoni; 2014). Although reports on its paragenesis are not available, the occurrence of ettringite in small dissolution vugs in the manganese mines of the Northern Cape, implies late precipitation much like ettringite, most likely from the reaction of the remaining sulfate in the fluid with endogenous carbonate ions and small amounts of probably exogenous aluminum.

As regards hydrogen isotopes, a small number of **step-heating experiments** was undertaken before analysing the whole suite of selected samples, in order to document the approximate temperatures of water loss for each species and assess potential isotopic changes during heating, possibly related to distinct water sources. Results are reported in Figure 16 (Appendix II in detail). Data on the thermodynamic stability of the studied minerals exist with regard to gypsum, as well as ettringite/sturmanite which have been the subject of much research due to their importance in the building industry. For example, dehydration of synthetic gypsum occurs between 95°C and 170°C, although some water is retained even at temperatures above 250°C (Strydom et al; 1995). Concerning ettringite group minerals, decomposition and dehydration are apparently more complex matters, with some existing discrepancy as regards accurate temperatures among the conclusions of various authors. In general, there is an agreement that ettringite begins to lose water molecules at 50°C and in temperatures over 90°C or mostly 100°C, ettringite is internally unstable and starts decomposing (Mehta; 1972, Taylor et al; 2001, Zhou and Glasser; 2001). However, a range of slightly higher temperatures, between ca. 110°C and 150°C, also exists in the literature as concerns thermal stability of this minerals (Fridrichová et al; 2016).

In our experiments, either three or four incremental steps were used during sample heating, with lowest temperatures starting at 200°C and then increasing at 300°C, 400°C and 550°C. The duration of each step was fifteen minutes. Although the thermal behaviour of ettringite was not examined in low temperatures, our observations suggest that this species retains significant hydrogen either as H_2O or OH^- up to 300°C and between 300°C and 400°C there is major water loss (Figure 16). The same is true for sturmanite and shigaite, while isotopic fractionations accompanying the incremental heating step from 300°C to 400°C is ca. 10 ‰ for all three previous minerals. The amount of water loss is comparable for sturmanite and shigaite at the two former temperatures (sturmanite: H_2O from 10.7% to 1.2%, shigaite: from 11.2% to 2.2%), whereas for ettringite which was also subjected to heating at 200°C for 15 minutes and lost a considerable amount of water, the shift in water percentage is much smaller between the same steps, i.e., from 3.9% to 3.2%.

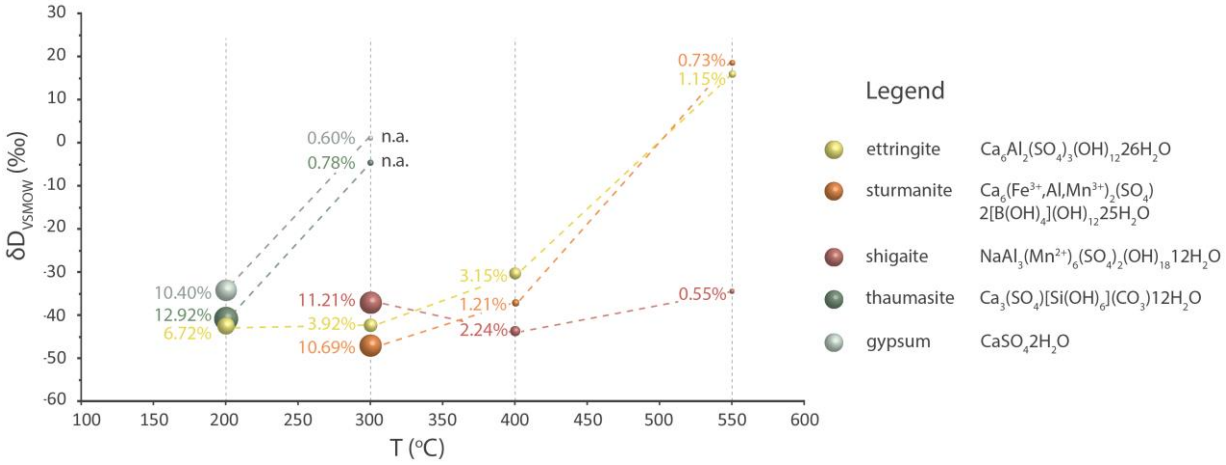

Figure 16. δD values versus temperature plot, displaying the succeeding incremental heating steps (200, 300, 400 and 550°C) applied to selected sulfates and the measured hydrogen isotopic composition for each step. The size of the coloured circles is analogous to the amount of water present in each mineral at different steps and calculated water percentages are displayed at the left of each circle.

After heating at 550°C, very little water remains in ettringite and sturmanite (1.15% and 0.73% respectively), although still measurable and showing distinctly heavier δD values (+15.6 % and 18.2 %). The significance of the latter is currently unknown but these ratios could reflect OH-bounded hydrogen being still present in the mineral structure. The remaining ettringite and sturmanite samples that were not subjected to incremental heating, but instead were heated instantly at 550°C did not display this heavier δD signal, it being apparently very weak in relation to the prevailing δD signatures. In the same respect, shigaite

submitted to all three heating steps also did not exhibit fractionation in the measured δD values. Much different is the behaviour of thaumasite, which much like gypsum, loses almost all water after the first heating step at 200^{o}C. Lower thermal stability of thaumasite in comparison to ettringite group minerals may indicate that this phase forms at even lower temperatures and is possibly the latest among the paragenetic sequence of sulfates, as also noted earlier. It is reminded that information regarding dehydration and decomposition of ettringite from the literature has been based on various experiments using cement-hosted ettringite. Step heating experiments in this study use well-crystallized natural samples, of which the effect of crystal size and habit on mineral stability is not known and furthermore, do not attempt to determine the initial temperatures of thermal decomposition of sulfates. In fact, the purpose of this investigation is to identify potential patterns of fractionation with heating and broadly test the usefulness of hydrogen isotopic applications on these uncommon sulfates.

Interestingly, variations in δD values between sulfates are not very high, especially if certain values of ettringite from calcite-bearing associations are not regarded (Figure 17). Specifically, they range between -59.7 ‰ and -7.2 ‰ and show an average of -35.4 ± 9.1 ‰ (n = 14). Three ettringite samples excluded from the previous average display δD ratios of -7.2, -17.2 and -17.7 ‰. Hydrogen isotope fractionation curves between the analysed sulfates and water in equilibrium are not available in the literature. Nevertheless, several inferences can be still drawn with respect to δD_{FLUID} values precipitating these minerals. Hydrogen isotope fractionation decreases with temperature but it has been shown that fractionation factors are not very temperature-sensitive. Even if sulfates in the KMF crystallized at very low temperatures (<100^{O}C), any shifts in the associated δD_{FLUID}, are expected to be in the range of 10-15 % in relation to the measured δD_{min} values, considering for example hydrogen fractionation behaviour in gypsum (Tan et al; 2014). Furthermore, hydrogen isotopes display the following fractionation characteristic due to kinetic effects, during which ^{1}H, i.e., the lighter isotope rather than ^{2}H enriches hydration water and hydroxyl in almost all of minerals with these groups (Satake and Matsuo; 1984, Xu et al; 1998). Therefore, it can be expected that fluid is progressively enriched in the heavy isotope during sulfate formation and the measured isotopic composition of ettringite records this process.

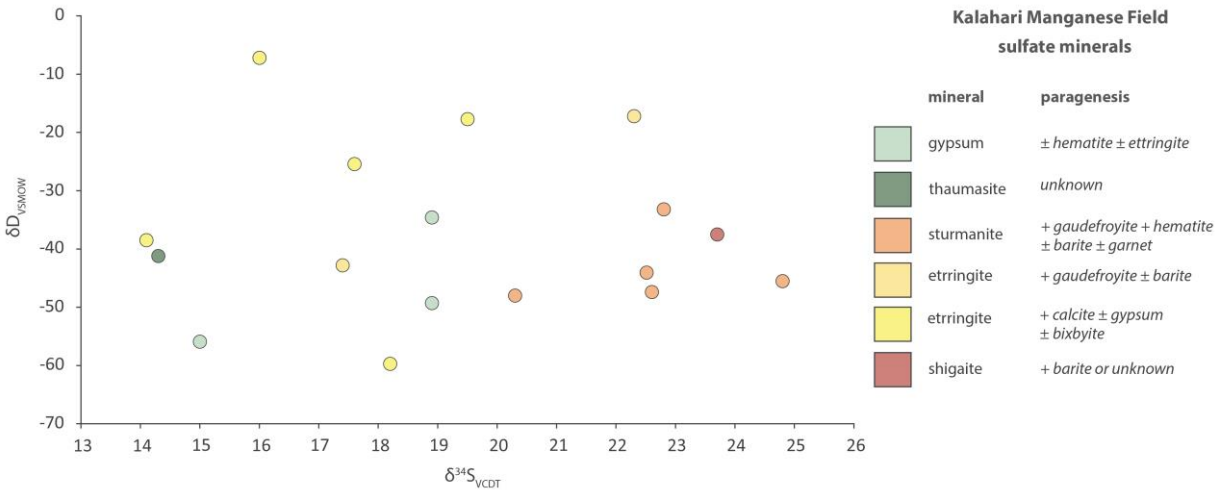

Figure 17. δD measured values versus $\delta^{34}S$ values for analysed sulfates. Colour coding is reflective of different mineralogical associations. Note the wider spread in δD ratios of measured ettringite, suggested to be related either to kinetic isotopic effects during sulfate precipitation or mixing with another sulfur source during the waning stages of mineralization.

Following the hypothesis that sulfates generally form during the waning stages of the Wessels-type alteration event and are related to the chemical evolution of infiltrating brines after fluid-rock interaction and/or fluid mixing with contemporaneous groundwater, their δD values may trace the aforementioned fluids and processes. The rather small range of δD values, may be used as evidence that hydration water in sulfates largely reflects the pristine water combined into crystal structures and that mineral dissolution, redeposition and associated kinetic isotopic effects are generally minimal among the studied sulfates. In other words, the unique sulfate mineralization in the KMF has been formed during the Mesoproterozoic and in general terms remained undisturbed since then, with the exception maybe of some ettringite and thaumasite which were either isotopically disturbed during subsequent events or even formed later. As regards the origin of the fluids precipitating these minerals, it is suggested that this was meteoric water or evolved (and/or diluted) basinal brines, consistent with the obtained δD ratios. The fact that sulfates are grouped separately and towards heavier hydrogen isotopic values than most other species analysed from the wider area (Figure 6, section 1.3) may be indicative of a distinct fluid composition during the latest stages of mineralization.

To sum up, this reconnaissance study of light stable isotopes on sulfate gangues from the KMF emphasizes the common fluid origin with regional barite mineralization in the wider basin, reveals the complexities due to kinetic isotope fractionation processes and possibly mixing with other fluid sources (i.e., groundwater), but overall shows great promise for future use of such techniques on the study area and other mineralization districts.

2.3 Timing of supergene alteration and geologically young events in the KMF

A large series of hydrated alkali- and/or manganese-bearing silicate minerals complements the large suite of aesthetic specimens in the Wessels and N'Chwaning mines. For example, minerals of the apophyllite-group [$KCa_4Si_8O_{20}(F,OH)\ 8H_2O$ - $KCa_4Si_8O_{20}(OH,F)\ 8H_2O$] are found associated with inesite [$Ca_2(Mn,Fe)_7Si_{10}O_{28(}OH)_25H_2O$], datolite, pectolite, calcite, sprays of natrolite and spheres of xonotlite [$Ca_6(Si_6O_{17})(OH)_2$] among others (Clifford; 2011). New mineral species like the first ever Sr-bearing member of the apophyllite group [Hydroxymcglassonite-(K): $KSr_4Si_8O_{20}(OH)8H_2O$] are being discovered up to this date, in associations with the common hydrothermal species sugilite, aegirine and pectolite (Yang et al; 2022). Other hydrated silicates such as bultfonteinite [$Ca_2(SiO_4)FH_2O$], which has been found apart from the KMF in xenoliths embedded in kimberlite together with apophyllite, calcite, and natrolite, also in South Africa (Biagioni et al; 2010), have been genetically related to the hydrothermal Wessels event. However, previous researchers have rightly emphasized that it is difficult to assign an accurate origin to a lot of the species observed in the KMF today, which although seen affiliated with gangues of the main Wessels alteration event, may in fact have formed subsequently to that, during several localized episodes of fluid infiltration (Gutzmer and Beukes; 1996b, Tsikos; 1999). Prehnite associated with hydroxyapophyllite, datolite, inesite, calcite and pectolite is such an example, at the moment loosely associated with a hydrothermal overprint of the Hotazel Formation that occurred at essentially low temperature (<250°C) (Cairncross et al; 2000).

Two hydroxyapophyllite specimens (or apophyllite-KOH, bearing also fluorine) from broadly similar associations from N'Chwaning II mine and comprising well-formed flaky crystals (Figure 18a-b), were used here for the first time as geochronological targets to test their significance in terms of ore genesis/upgrading or as potential tools to provide

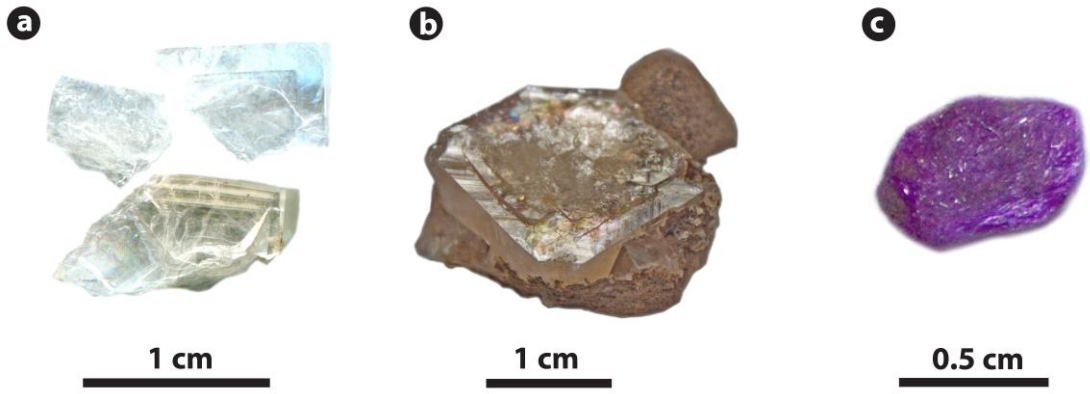

Figure 18. (a) Hydroxyapophyllite flakes separated for $^{40}Ar/^{39}Ar$ step-heating dating and (b) pseudocubic apophyllite crystals with distinctive triangular corners used in stable isotopic (O-H) and geochronological analysis. (c) Fraction of fibrous sugilite from N'Chwaning II mine used in $^{40}Ar/^{39}Ar$ dating.

geologically meaningful information as regards the timing of their formation. For this purpose, $^{40}Ar/^{39}Ar$ step-heating dating was employed (full data in Appendix I). Although none of the produced $^{40}Ar/^{39}Ar$ step-heating spectra yielded a plateau age, Ar-Ar data for sample N_HA2 (3 aliquots) are in the range of 12 to 28 Ma, and that for sample N_HA (3 aliquots) are in very good agreement, ranging between 32 and 30 Ma (Figure 19). All produced spectra display both low- and high-temperature discordances, as well as in between the high and low steps (sample N_HA). These are difficult to explain without further experiments, detailed microscopy and/or geochemical data of the analysed flakes, but it can be surmised for example that variations in K concentration may have produced ^{39}Ar recoil redistribution from higher- to lower-K regions during irradiation (e.g., Foland et al; 1993).

A pilot study on apophyllite $^{40}Ar/^{39}Ar$ dating from secondary mineralization in basalts from Antarctica has returned both plateau ages and several integrated ages due to discordant spectra similarly to our case, which have been attributed to ^{39}Ar recoil (Fleming et al; 1999). The previous study demonstrated the suitability of the mineral for $^{40}Ar/^{39}Ar$ dating by comparisons with other temporal indicators for low-T alteration in the basalts and explained age variations between samples by invoking Ar loss, alkali mobility or an extended history of mineral precipitation. Therefore, it can be reasonably suggested that apophyllite from the N'chwaning II mine is indeed young and highlights the geologically recent supergene-related mineralization overprinting parts of the KMF.

Concerning the latter, low-grade sedimentary manganese ore in the KMF has been supergene-altered along the eastern suboutcrop perimeter of the ore beds against Cenozoic sediments of the Kalahari Formation (calcretes, sands) (Kleyenstüber; 1993). As a consequence, these recent alteration processes have produced significant volumes of supergene-enriched high-grade manganese ore along the pre-Kalahari unconformity, the former comprising mainly todorokite and manganomelane (Kleyenstüber; 1985). $^{40}Ar/^{39}Ar$ dating of poorly crystalline complex mixtures of the above two K-bearing Mn^{4+} oxyhydroxides, suggests three approximate age peaks for the weathering processes below the unconformity, at around 27.8, 10.1 and 5.2 Ma ago respectively (Gutzmer et al; 2012). Furthermore, the previous researchers observed a downward younging in ages within the supergene altered zone, as would be expected in a developing weathering profile, and considered the oldest age in their dataset, i.e., 42 Ma, as a minimum estimate for the onset of the post African I cycle of weathering and erosion that followed the breakup of Gondwanaland and led to the formation of the Cretaceous to early Cenozoic African land surface. This minimum age estimate for chemical weathering has been recently placed ca. 35 Ma earlier, at 77 ± 7.5 Ma, based on U-Pb apatite dating of thrusted, supergene altered manganese ore from the Mukulu farm, an area within the Kalahari deposit containing both Wessels- (high-grade) and Mamatwan-type (low-grade) manganese ore below the Blackridge thrust fault (Vafeas et al; 2018).

In light of the above, the $^{40}Ar/^{39}Ar$ step-heating age of apophyllite from N'Chwaning II mine (between 12.2 ± 0.3 Ma and 32.2 ± 0.2 Ma), suggests that this mineral has formed during recent supergene alteration fluids circulating through the ore. This is consistent with the documented geological and paragenetic occurrences of the mineral, which usually forms in a variety of lithologies affected by low-temperature water-rock interactions and precipitates late in most paragenetic sequences (Gaines et al; 1997). In the case of continental basalts provinces where apophyllite is commonly found, late mineralization may be related either to the later stages of the magmatic event or to a temporally distinct event resulting from percolating groundwaters. Fleming et al (1999), showed that apophyllite in the Kirkpatrick Basalt precipitated in a regime of groundwater flow, with possibly increased temperatures related to normal fault movements. If such conditions and geothermal gradients were attained during the late and localized supergene overprint in the KMF requires further

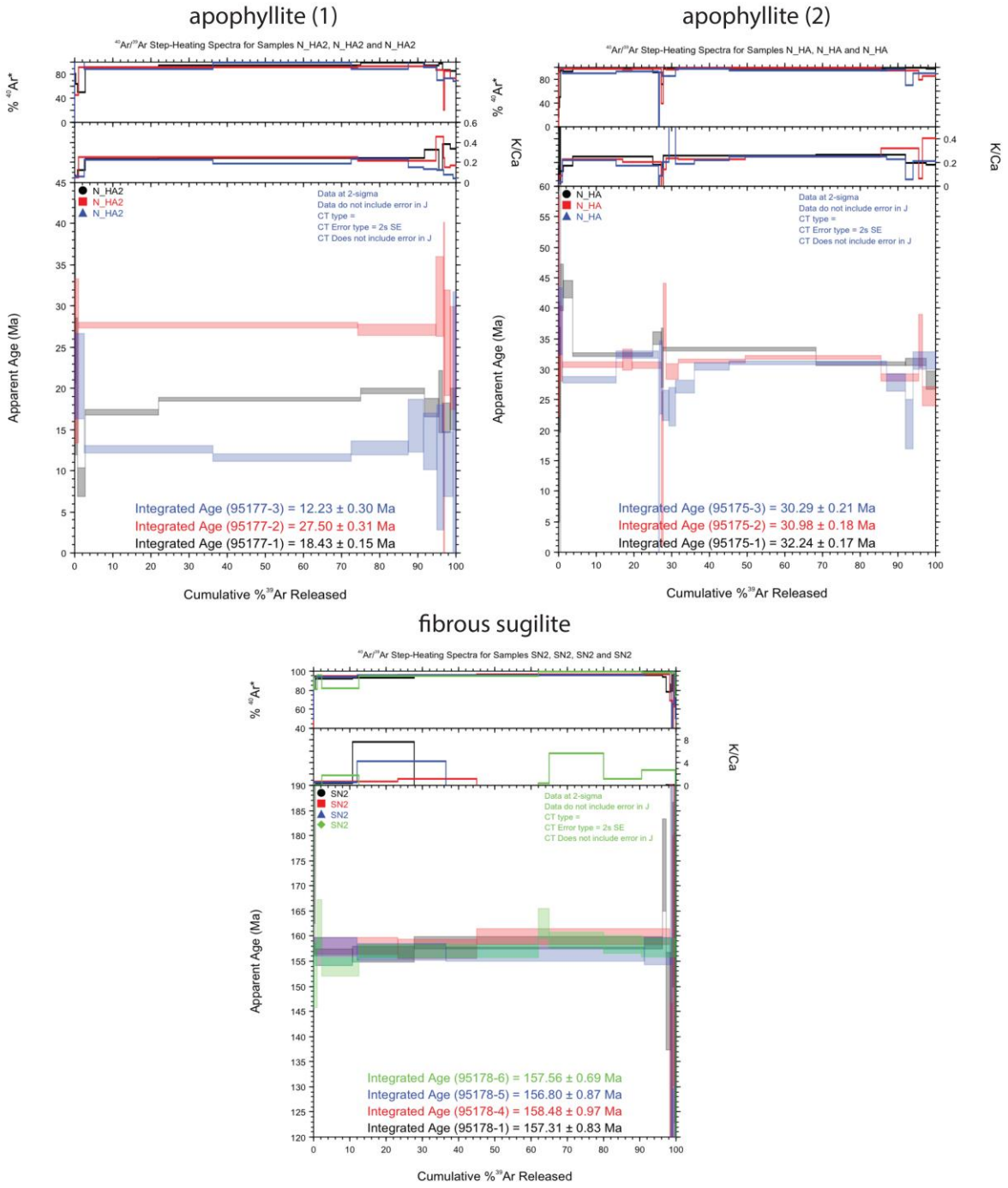

Figure 19. Plots of $^{40}Ar/^{39}Ar$ step-heating spectra for apophyllites and sugilite from N'Chwaning II mine. Ages reported at 2σ and exclude J value uncertainty. All Ar-Ar data yielded only integrated ages, that highlight the ''young'' origin of the dated material (see also text).

clarification. Minerals associated with apophyllite in other studies, such as zeolites, are usually indicative of low temperatures of formation (<100°C, extending down to ambient groundwater temperatures) (Kristmannsdóttir and Tómasson; 1978). However, conditions of

temperature, pressure, stability, fluid chemistry and characteristics promoting apophyllite formation are very poorly known at the moment.

Four apophyllite samples, certain of them associated with xonotlite and inesite, were analysed for their hydrogen isotopic composition and additionally, one sample for its oxygen isotopic signature. Sample preparation included degassing of samples under vacuum at 200^{o}C for three hours. δD values (-68.5, -76.2, -77.7 and -87.2 ‰) partly overlap with the isotopic range determined by micas and other silicates from the PMF (-78.7 to -60.7 ‰), as well as with the δD values from certain species in the KMF, such as gaudefroyite (-67.6 ‰) and vesuvianite (-76.8 ‰) (see also Figure 6, this chapter). Furthermore, apophyllite D/H ratios agree very well with that of prehnite (-71 ad -78 ‰) determined by Cairncross et al (2000) from the same mine. However, the previous authors estimated the δD_{FLUID} of the water in equilibrium with prehnite at 250^{O}C to be much lower, ca. -21‰, and suggested a most likely meteoric origin for the fluid. Hydrogen isotope fractionations between apophyllite and water are not available and attempts to calculate δD_{FLUID} ratios is beyond the scope of the current section.

In any such future effort though, temperatures used for estimations should be much lower than that used by Cairncross et al (2000) for prehnite, i.e., 250^{O}C, which seems unrealistic for the envisaged supergene formation of apophyllite. Nevertheless, it is very likely that fluids in equilibrium with apophyllite had lower δD ratios than the measured values in apophyllite, i.e., more consistent with meteoric water than metamorphic water and sedimentary basinal brines precipitating other isotopically measured species in the KMF and PMF (for e.g., PMF: δD_{FLUID} from -45.0 to -63.0 ‰, chapter 5). A single $\delta^{18}O$ value obtained for apophyllite was 15.0 ‰. The fact that this ratio is higher than all other determined $\delta^{18}O$ ratios from gangues in the wider area (averages ca. 11-12 ‰), with the only exception being that of the also hydrous armbrusterite, possibly suggests the presence of fractionation during degassing or pre-fluorination and therefore there is lack of confidence regarding these measurements. On the other hand, a calculated yield of ca. 100 % for apophyllite is intriguing and may indeed suggest a heavy $\delta^{18}O$ for this mineral. In any case, O-H isotopic data on apophyllite and paragenetically associated phases may potentially reveal more information on the apparently recent hydrologic events causing diverse mineral precipitation in the KMF.

The scene regarding recent alteration processes in the KMF is further complicated by $^{40}Ar/^{39}Ar$ step-heating data of fibrous sugilite, also obtained during the current study from the same mine (Figure 18c, Figure 19, Appendix I). Again, this samples (SN1) yielded no age plateaus, but integrated ages fall within a fairly narrow range between 155-158 Ma. Interpretation of this sugilite date is challenging since there is no geological event known from this period in the study area. Prior to these dates, consensus was that sugilite formed in both the KMF and PMF during the Namaqua orogeny (1.2-1.0 Ga), and was isotopically reset and/or recrystallized in certain localities (Wessels, Bruce mine, Heuningkranz) during the Neoproterozoic between 650 and 600 Ma (Moore et al; 2011, Fairey et al; 2019, chapters 3, 4, Synthesis section 8.1.1). The fact that sugilite is prone to ^{40}Ar-loss should be greatly taken into account and although its amenability to dating is thoroughly documented, it is imperative that obtained dates are always interpreted in relation to the geological setting and other petrographic, textural, field and available geochronological information.

Therefore, in the case of sugilite from N'Chwaning, two scenarios can be suggested: (1) The mineral has been crystallized at ca. 160 Ma ago in response to an undocumented thermal event in the area or (2) Significant ^{40}Ar-loss has occurred since the mineral precipitation and the obtained date is an artifact, reflective of a large shift from its much older original age (1.2-1.0 Ga) towards the recent supergene overprint associated with the post African I erosional cycle. According to this scenario, supergene processes had a significant impact on sugilite age, causing substantial ^{40}Ar-loss and rendering the mineral essentially undatable. The fact that almost all the available geochronological data from the KMF support retentivity of the original sugilite crystallization age, raises questions regarding the potential of supergene-related solutions, isotopically disturbing and to such great extent this mineral. On the contrary, formation of distinct sugilite generations postdating Wessels event and specifically crystallization at ca. 160 Ma ago seems also unlikely with our current knowledge. Future geochronological data from the mine will hopefully resolve the current questions regarding the thermal history subsequently to the proximal Namaqua and distal Pan-African orogenies.

To summarize, the postulated supergene origin for the ''young'' apophyllite (from 12.2 ± 0.3 Ma to 32.2 ± 0.2 Ma) cannot be directly extended to paragenetically associated minerals,

something that requires much more detailed research. Moreover, the enigmatic fibrous sugilite age (ca. 160 Ma) asks for further clarification and provides new information with respect to $^{40}Ar/^{39}Ar$ dating of this rare species.

2.4 Origin of riebeckite in the Northern Cape and its possible metallogenic role

Riebeckite [$Na_2(Fe^{2+}3Fe^{3+}_2)Si_8O_{22}(OH)_2$] is locally so abundant in the Kuruman and Griquatown iron-formations (Asbestos Hills Group) of the Transvaal Supergroup that despite its very fine-grained size, it can be seen macroscopically in massive bands (from 0.2 to ca. 15 cm), thin layers, veins or various dispersions, essentially pigmenting the rock blue (Figure 20A1-3). Under the microscope, bluish feathers or seldom coarse individual grains stand out conspicuously against chert, carbonates, magnetite and Fe-silicates of the BIF matrix (Figure 20B, 20C) (Beukes and Klein; 1990, Horstmann and Hälbich; 1995). Crocidolite, the asbestiform variety of riebeckite after which the Asbestos Hills Group is named, is also present in this lithology as distinct blue fibrous bands with sharp boundaries to the adjacent layering (Figure 20A4) and likewise riebeckite, its occurrence is similarly intriguing.

Its possible relevance with the alkali metasomatic signals surveyed in this thesis can be realized if one considers that riebeckite is the only mineral to accommodate sodium (Na) in BIFs and furthermore is locally found in such high abundances in the study area, to have allowed extensive mining in the past. The prospect that riebeckite/crocidolite-rich BIF provide an elegant source for Na during any post-depositional fluid flow events has been stated earlier in this thesis (chapters 2 & 5). As the prime alkali-mineral in the pristine lithologies of the study area, riebeckite may hold answers regarding the Namaqua hydrothermal metasomatic event and particularly on the subjects of fluid generation mechanisms, origin, pathways and fluid-rock interactions. Interrogating these questions may seem at first very challenging from an analytical point of view, but perhaps a combination of petrography, detailed mineral chemistry and mineral isotope geochemistry can provide some insight into these matters and allow a reexamination of the hypothesis that riebeckite dissolution is critical for the sodium budget of the hydrothermal brines associated with the 1.2 - 1.0 Ga Namaqua event. It must be noted that the circumstances under which this mineral forms are speculative at the moment. Based on textural analysis and resulting information regarding the relative timing of

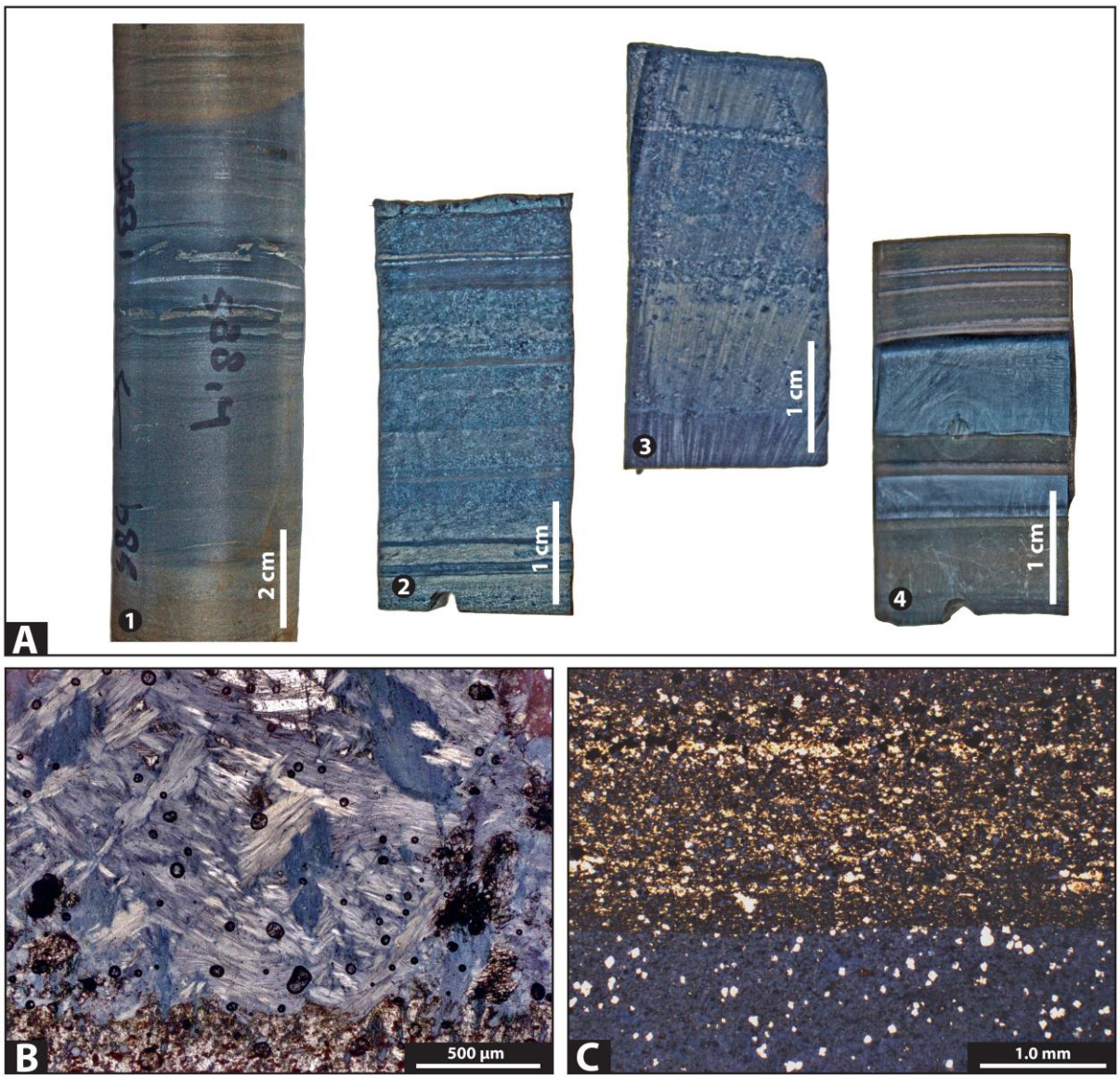

Figure 20. (A1-3) Appearance of riebeckite mesobands (cm-scale) on hand specimen, displaying also minor compositionally distinct micro-banding and disseminations of other minerals. Pure riebeckite domains (> 90% riebeckite from visual inspection under the microscope) were subsampled for isotopic analyses. (A4) Sharp contact between bands of crocidolite and BIF layering (B) Blue intergrown massive riebeckite micro-drilled for isotopic analysis. (C) Gradational contact between riebeckite (down) and chert/Fe-silicate band (up). Note the disseminated carbonate rhombs (bright spots).

its formation (grains overgrowing carbonates, aggregates and veins cross-cutting minerals), riebeckite is considered of secondary origin, related to external Na input deriving from pore-fluids during diagenesis or alkali-rich hydrothermal fluids (e.g., Trendall and Blockey; 1970). Paul Oonk (2017) argued that the localized presence of riebeckite, which is no more than a trace mineral in other parts of the stratigraphy, is better explained by invoking alkali-enrichment from hydrothermal fluids. Lateral discontinuity exhibited by riebeckite bands and lateral transition into essentially riebeckite-free rock documented in the stratigraphically

equivalent Brockman Iron Formation in Australia have also been used to support a later, possibly diagenetic origin for this species (Miyano & Klein; 1983). In general, is should be emphasized that there is a great lack of detailed studies with exclusive focus on riebeckite in BIF.

The main textures and mineralogical associations of riebeckite in pristine iron-formation have been extensively studied using optical microscopy in over thirty thin sections from five separate drill cores. The major textural generations of riebeckite and general observations originated during this meticulous work are not further discussed here. However, this formed the basis for sampling of high purity riebeckite and crocidolite (>90%) using mechanical separation and micro-drilling, with an aim to apply stable isotope fingerprinting. Further purification on selected samples was attempted by use of mild acid treatment (phosphoric acid) to remove remaining carbonate material. However, due to the associated and anticipated difficulties with evaporating this acid, this treatment was limited to very few samples. Despite that, obtained isotopic results from treated versus untreated material are apparently very similar, which can only suggest that purity as determined by detailed optical microscopy suffices for mineral-specific isotopic analyses. Moreover, treatment with HCl was not preferred in order to avoid any related isotopic fractionation.

$\delta^{18}O$ values for riebeckite range significantly from +13.2 to +18.2 ‰, but display a somewhat tight average of +15.4 ± 1.6 ‰ (n=10). This isotopic signature sits between values from quartz (ca. +20-21 ‰) and magnetite (+2 to +4.5 ‰), and is closer to carbonates (ca. +14 to 20‰) characterizing the Hotazel Iron Formation (Tsikos; 1999) and the Dales Gorge Member of the geologically equivalent Brockman Iron Formation from Australia (Becker and Clayton; 1976), which are also expected to be closely replicated in the mineralogy of the Asbestos Hills Iron Formation of the Northern Cape. Intriguingly, the so-considered late diagenetic riebeckite from the Brockman Iron Formation exhibits identical $\delta^{18}O$ values and specifically from two following textural generations: massive riebeckite textures (+14.5, +15.1, +16.9 ‰) and riebeckite dispersed (chemically extracted and purified) in magnetite mesobands (+12.8, +13.3, +13.9 ‰). Lighter riebeckite value from the Northern Cape (+13.2, +13.7, +13.8 ‰) are related with riebeckite bands with sparsely dispersed carbonates. Riebeckite from the Brockman Iron Formation is noted to have undergone isotopic exchange

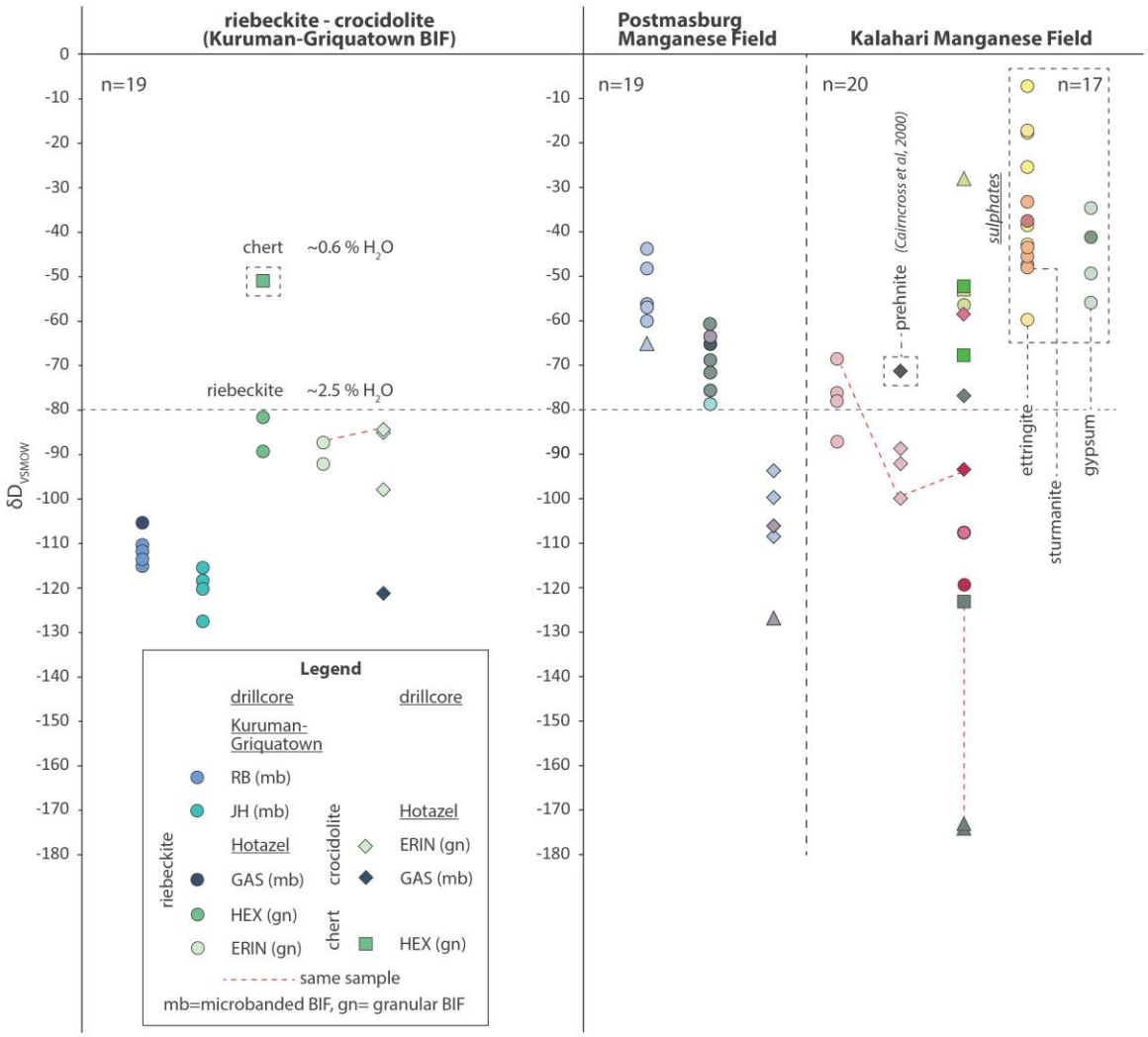

Figure 21. Hydrogen isotopic composition of riebeckite and crocidolite from different drillcores and textural occurrences of iron formation in the Northern Cape. δD values determined from a series of alkali-rich and other gangue alteration species is included for reference. See Figure 6 (this chapter) for legend regarding PMF and KMF minerals.

to some degree with the co-existing minerals, during burial metamorphism (Becker and Clayton; 1976). Interestingly, much like the other riebeckite textures, the fibrous crocidolite oxygen isotopic values are similar between the aforementioned district (+15.2 ± 0.2 ‰, n=3) and the Northern Cape (14.7 ± 0.7 ‰, n=3).

Hydrogen isotopic results from riebeckite and crocidolite are displayed in Figure 21. These values are to our knowledge the first to be ever produced by BIF-associated sodic amphiboles. Estimated water content from isotopic measurements in both riebeckite and crocidolite has an average value of 2.35 ± 0.27 ‰ (n=17). δD ratios range between -127 and -92 ‰ (n=13), but as it can also be seen from the legend in Figure 21, riebeckite from different

drill cores and/or BIF textural occurrences displays distinct groups of values. For example, riebeckite from Kuruman-Griquatown mesoband BIF (-116.5 ± 0.5 ‰, n=8) is isotopically distinct to that from granular BIF from the Hotazel (-87.6 ± 4.4 ‰, n=4). Furthermore, a value obtained from a chert mesoband comprising only carbonates, and previously treated with HCl to ensure that hydrogen reflects water associated with SiO_2, is evidently different than riebeckite (-51.2 ‰, H_2O: 0.84 %). The latter adds confidence to the hypothesis that measured riebeckite δD values represent hydrogen exclusively from the amphibole and possible contamination from minor chert is negligible. It is also worth mentioning that the hydrogen isotopic composition of crocidolite is broadly similar (from -121.2 to -84.6 ‰) and furthermore that riebeckite and crocidolite from the same locality display comparable values.

All the above generally suggest a common origin for riebeckite and crocidolite in the Northern Cape, which may be possibly comparable to that from the distal and stratigraphically correlated Brockman Iron Formation in Australia. There is also some evident overlap between riebeckite and alkali gangue δD values from the KMF and PMF, although the latter are characterized by a much heavier isotopic signal. Further and closer interrogation of the current dataset may reveal more on the possible relationship between riebeckite and alkali-rich gangue species in the PMF and KMF deposits and is underway.

References

Åberg, G., & Charalampides, G. (1988). Evolution of the mineral deposits from Långban, Sweden, as recorded from strontium isotope data. Geologiska Föreningen i Stockholm Förhandlingar, 110(4), p. 329-334.

Albaréde. F., Ferraud, G., Kaneoka. I. and Allegre, C.J. (1978). $^{40}Ar/^{39}Ar$ dating: the importance of K-feldspars in multi-mineral dating of polyorogenic areas. J. Geol. 86: p. 581-598.

Aleva, G.J.J. (1994). Laterites: concepts, geology, morphology and chemistry. International Soil Reference and Information Centre (ISRIC), Wageningen, The Netherlands. 169 p.

Alexeeva, L.P., Alexeev, S.V., Kononov, A.M., Teng, M., & Yunde, L. (2015). Halogen Isotopes (^{37}Cl and ^{81}Br) in Brines of the Siberian Platform. Procedia Earth and Planetary Science, 13, p. 47-51.

Allwood, A.C., Walter, M.R., Burch, I.W., & Kamber, B.S. (2007). 3.43-billion-year-old stromatolite reef from the Pilbara Craton of Western Australia: Ecosystem-scale insights to early life on Earth. Precambrian Research, 158(3-4), p. 198-227.

Altermann, W., & Hälbich, I. W. (1990). Thrusting, folding and stratigraphy of the Ghaap Group along the southwestern margin of the Kaapvaal Craton. South Afr Journ. of Geol. 93 (4), p. 553-566.

Altermann, W., & Hälbich, I. W. (1991). Structural history of the southwestern corner of the Kaapvaal Craton and the adjacent Namaqua realm: new observations and a reappraisal. Precambrian Research, 52(1-2), p. 133-166.

Altermann W., HaÈlbich I.W., Horstmann U.E., Ahrendt H., Fitch F.J, Miller J.A. (1992). The age of tectogenesis and metamorphism of the southwestern Kaapvaal Craton. 29th IGC, August 1992, Kyoto, Japan. Abstr vol 2-3: p. 261.

Altermann, W. (1997). Sedimentological evaluation of Pb-Zn exploration potential of the Precambrian Griquatown Fault Zone in the Northern Cape Province, South Africa. Mineralium Deposita, 32(4), p. 382-391.

Angerer, T., Duuring, P., Hagemann, S.G., Thorne, W., & McCuaig, T.C. (2014). A mineral system approach to iron ore in Archaean and Palaeoproterozoic BIF of Western Australia. Geological Society, London, Special Publications, 393(1), p. 81-115.

Anthony, J.W., Bideaux, R.A., Bladth K.W., and Nichols, M.C. (1995). Handbook of mineralogy: Volume II: Silica and Silicates. Tuscon (Mineral Data Publishing).

Araoka, D., Kawahata, H., Takagi, T., Watanabe, Y., Nishimura, K., Nishio, Y., (2013). Lithium and strontium isotopic systematics in playas in Nevada, USA: constraints on the origin of lithium. Min. Deposita 49, p. 371-379.

Armbruster, T. and Oberhänsli, R. (1988). Crystal chemistry of double-ring silicates: Structures of sugilite and brannockite, Am. Mineral., 73, p. 595-600.

Armstrong, R.A. (1987). Geochronological studies on Archaean and Proterozoic Formations of the foreland of the Namaqua Front and possible correlates on the Kaapvaal Craton. Unpubl. Ph.D. thesis, University of the Witwatersrand, 274 p.

Ashley, P. M. (1986). An unusual manganese silicate occurrence at the Hoskins mine, Grenfell district, New South Wales. Australian Journal of Earth Science 33: p. 443-56.

Avigad, D., Morag, N., Abbo, A., & Gerdes, A. (2017). Detrital rutile U-Pb perspective on the origin of the great Cambro-Ordovician sandstone of North Gondwana and its linkage to orogeny. Gondwana Research, 51, p. 17-29.

Ayora, C., Cendón, D.I., Taberner, C., Pueyo, J.J. (2001). Brine-mineral reactions in evaporite basins: implications for the composition of ancient oceans. Geology 29 (3), p. 251-254.

Bao H. & Koch P.L. (1999). Oxygen isotope fractionation in ferric oxide-water systems: Low temperature synthesis, Geochimica et Cosmochimica Acta, 63, p. 599-613.

Barbieri, M., De Vivo, B., Perrone, V., & Turco, E. (1984). Strontium geochemistry of the San Donato Unit barite mineralization (Calabria, Italy). Chemical Geology, 45(3-4), p. 279-288.

Barbieri, M., Bellanca, A., Neri, R., & Tolomeo, L. (1987). Use of strontium isotopes to determine the sources of hydrothermal fluorite and barite from northwestern Sicily (Italy). Chemical Geology: Isotope Geoscience Section, 66(3-4), p. 273-278.

Bardossy, G. (1982). Karst Bauxites, Bauxite Deposits on Carbonate Rocks, Developments in Economic Geology, Elsevier, Amsterdam, Vol. 14, 441 p.

Barton, E.S. and Burger, A.J. (1983). Reconnaissance isotopic investigations in the Namaqua mobile belt and implications for Proterozoic crustal evolution – Upington geotraverse. In: Botha, B.J.V. (Ed.), Namaqualand Metamorphic Complex. Spec. Publ. Geol. Soc. S. Afr., 10, p. 173-191.

Basso, R., Lucchetti, G., Zefiro, L., & Palenzona, A. (1992). Reppiaite, Mn5(OH)4(VO4)2, a new mineral from Val Graveglia (Northern Apennines, Italy). Zeitschrift Für Kristallographie - Crystalline Materials, 201(3-4), p. 223-234.

Basson, I.J., Thomas, S.A.J., Stoch, B., Anthonissen, C.J., McCall, M.J., Britz, J., MacGregor, S., Viljoen, S., Nel, D., Vietze, M., Stander, C., Horn, J., Bezuidenhout, J., Sekoere, T, Gous, C., Boucher, H. (2018). The structural setting of mineralization at Kolomela Mine, Northern Cape,

South Africa, based on fully-constrained, implicit 3d-modelling. Ore Geology Reviews 96, p. 306-324.

Becker, R.H., & Clayton, R.N. (1976). Oxygen isotope study of a Precambrian banded iron-formation, Hamersley Range, Western Australia. Geochimica et Cosmochimica Acta, 40(10), 1153-1165.

Bekker A., Karhu J.A., Kaufman A.J. (2006). Carbon isotope record for the onset of the Lomagundi carbon isotope excursion in the Great Lakes area, North America. Precambrian Res 148: p. 145-180.

Belkin, E.H., Cavarretta, G., De Vivo, B., Tecce, F. (1988). Hydrothermal phlogopite and anhydrite from the SH2 Well, Sabatini volcanic district, Latium, Italy; fluid inclusions and mineral chemistry. American Mineralogist 73 (7-8), p. 757-797.

Bella P., Gaál Ľ., Šucha V., Koděra P., and Milovský R., (2016). Hydrothermal speleogenesis in carbonates and metasomatic silicites induced by subvolcanic intrusions: a case study from the Štiavnické vrchy Mountains, Slovakia. International Journal of Speleology, 45 (1), p. 11-25.

Benison, K.C., and Bowen, B.B., (2006). Acid saline lake systems give clues about past environments and the search for life on Mars: Icarus, v. 183, p. 225-229.

Bennett, M.A (1987b). Genesis and diagenesis of the Cambrian manganese deposits, Harlech, North Wales. Geological Journal, 22, p. 7-18.

Bennett, E.N., Jenner, F.E., Millet, M.-A., Cashman, K.V., & Lissenberg, C.J. (2019). Deep roots for mid-ocean-ridge volcanoes revealed by plagioclase-hosted melt inclusions. Nature, 572(7768), p. 235-239.

Beukes, N.J. (1983). Palaeoenvironmental setting of iron formations in the depositional basin of the Transvaal Supergroup, South Africa. In: Trendall, A.F. & Morris, R.C. (Eds.) Iron-formation: facts and problems, p. 131-210. Elsevier, Amsterdam.

Beukes N.J. (1987). Facies relations, depositional environments and diagenesis in a major early Proterozoic stromatolitic carbonate platform to basinal sequence, Campbellrand Subgroup, Transvaal Supergroup, Southern Africa, Sedimentary Geology 54, p. 1-46.

Beukes, N.J., Smit, C.A. (1987). New evidence for thrust faulting in Griqualand West, South Africa: implications for stratigraphy and age of red beds. S. Afr. J. Geol. 90: p. 378-394.

Beukes, N.J., Klein, C., Kaufman, A.J., & Hayes, J.M. (1990). Carbonate petrography, kerogen distribution, and carbon and oxygen isotope variations in an early Proterozoic transition from limestone to iron-formation deposition, Transvaal Supergroup, South Africa. Economic Geology, 85(4), p. 663-690.

Beukes, N.J., Burger, A.M., and Gutzmer, J. (1995). Fault-controlled hydrothermal alteration of Palaeoproterozoic manganese ore in Wessels mine, Kalahari manganese Field: South African Journal of Geology, v. 98, p. 430-451.

Beukes, N.J., Gutzmer, J., & Mukhopadhyay, J. (2003). The geology and genesis of high-grade hematite iron ore deposits. Transactions of the Institute of Mining and Metallurgy B - Applied Earth Sciences 112, B18-B25.

Beukes, N. J., Edward P.W.S., and Herve W. (2016). "Manganese deposits of Africa." Episodes Journal of International Geoscience 39.2: p. 285-317.

Biagioni, C., Bonaccorsi, S., Merlino, S. (2010). Crystal structure of bultfonteinite, $Ca_4[SiO_3(OH)]_2F_2H_2O$, from N'Chwaning II mine (Kalahari Manganese Field, Republic of South Africa). Atti Soc. tosc. Sci. nat., Mem., Serie A, 115, p. 9-15.

Biagioni, C., Capalbo, C., Lezzerini, M., & Pasero, M. (2014). Ferrihollandite, BaMn4+6Fe3+2O16, from Apuan Alps, Tuscany, Italy: description and crystal structure. European Journal of Mineralogy, 26(1), p. 171-178.

Bikerman, M., Myers, T., Prout, A.A., and Smith R.C. (1999). Testing the feasibility of K-Ar dating of Pennsylvania cryptomelanes (Potassium manganese oxides). Journal of the Pennsylvania Academy of Science, vol 72. no. 3, p. 109-114.

Bhattacharyya, P. K., Dasgupta, S., Fukuoka, M., & Roy, S. (1984). Geochemistry of braunite and associated phases in metamorphosed non-calcareous manganese ores of India. Contributions to Mineralogy and Petrology, 87(1), p. 65-71.

Blake, T.S., Rothery, E., Muhling, J.R., Drake-Brockman, J.A.P., Sprigg, L.C., Ho, S.E., … Fletcher, I. R. (2011). Two episodes of regional-scale Precambrian hydrothermal alteration in the eastern Pilbara, Western Australia. Precambrian Research, 188(1-4), p. 73-103.

Blättler, C.L., Claire, M.W., Prave, A.R., Kirsimäe, K., Higgins, J.A., Medvedev, P.V., … Lepland, A. (2018). Two-billion-year-old evaporites capture Earth's great oxidation. Science, 360(6386), p. 320-323.

Blount, C.W. (1977). Barite solubilities and thermodynamic quantities up to 300°C and 1400 bars. American Mineralogist 62, p. 942-957.

Bons, P. D., & Gomez-Rivas, E. (2020). Origin of Meteoric Fluids in Extensional Detachments. Geofluids, 2020, p. 1-8.

Bottomley, D.J., Veizer, J., Nielsen, H., & Moczydlowska, M. (1992). Isotopic composition of disseminated sulfur in Precambrian sedimentary rocks. Geochimica et Cosmochimica Acta, 56(8), p. 3311-3322.

Bottomley, D.J., Katz, A., Chan, L.H., Starinsky, A., Douglas, M., Clark, I.D., Raven, K.G., (1999). The origin and evolution of Canadian Shield brines: evaporation or freezing of seawater? New

lithium isotope and geochemical evidence from the Slave craton. Chem. Geol. 155 (3-4), p. 295-320.

Bottrell, S.H., Crowley, S., & Self, C. (2001). Invasion of a karst aquifer by hydrothermal fluids: evidence from stable isotopic compositions of cave mineralization. Geofluids, 1(2), p. 103-121.

Bowers, T. S., & Taylor, H. P. (1985). An integrated chemical and stable-isotope model of the origin of Midocean Ridge Hot Spring Systems. Journal of Geophysical Research, 90(B14), 12, p. 583-606.

Brand, U. (1991). Strontium isotope diagenesis of biogenic aragonite and low-Mg calcite. Geochimica et Cosmochimica Acta, 55(2), p. 505-513.

Brandt, I. S., Rasskazov, S. V., Ivanov, A. V., Reznitskii, L. Z., & Brandt, S. B. (2006). Radiogenic argon distribution within a mineral grain: implications for dating of hydrothermal mineral-forming event in Sludyanka complex, Siberia, Russia. Isotopes in Environmental and Health Studies, 42(2), p. 189-201.

Brannon, J.C., Podosek, F.A., Viets, J.G., Leach, D.L., Goldhabe, M., & Rowan, E.L. (1991). Strontium isotopic constraints on the origin of ore-forming fluids of the Viburnum Trend, southeast Missouri. Geochimica et Cosmochimica Acta, 55(5), p. 1407-1419.

Brigatti, M.F., Kile, D.E., & Poppi, M. (2001). Crystal structure and crystal chemistry of lithium-bearing muscovite-2M1. The Canadian Mineralogist, 39(4), p. 1171-1180.

Brown, J.S. (1973). Sulfur isotopes of Precambrian sulfates and sulfides in the Grenville of New York and Ontario. Econ. Geol. 68, p. 362-370.

Brusnitsyn, A. I. (2010). Mineralogy of metamorphosed manganese deposits of the South Urals. Geology of Ore Deposits, 52(7), p. 551-565.

Buchanan, D.L., Nolan, J., Suddaby., Rouse, M.J. and Davenport, J.W.J. (1981). The genesis of sulphide mineralisation in a portion of the Potgietersrus limb of the Bushveld Complex. Economic Geology, 76, p. 568-579.

Buchanan D.L. and Rouse J.E. (1982). Role of contamination in the coprecipitation of sulphides in the Platreef of the Bushveld Complex. Proc. IGCP Projects 91 and 161; 3rd Nickel Sulphide Conference, Perth, W. Australia, p. 141-146.

Bucher, K., de Capitani, C., & Grapes, R. (2005). The development of a margarite corundum blackwall by metasomatic alteration of a slice of mica schist in ultramafic rock, Kvesjoen, Norwegian Caledonides. The Canadian Mineralogist, 43(1), p. 129-156.

Buckley, H. A., Bevan, J. C., Brown, K. M., Johnson, L. R., & Farmer, V. C. (1978). Glauconite and celadonite: two separate mineral species. Mineralogical Magazine, 42(323), p. 373-382.

Bühn, B., Okrusch, M., Woermann, E., Lehnert, K., and Hoernes, S. (1995) Metamorphic evolution of Neoproterozoic manganese formations and their country rocks at Otjosondu, Namibia. Journal of Petrology, 36, p. 463-496.

Bulle, F., Rubatto, D., Ruggieri, G., Luisier, C., Villa, I. M., & Baumgartner, L. (2020). Episodic hydrothermal alteration recorded by microscale oxygen isotope analysis of white mica in the Larderello-Travale Geothermal Field, Italy. Chemical Geology, 532, p. 119-288.

Bunch, T.E., Okrusch, M. (1973). Al-rich pargasite. American Mineralogist, Volume 58, p. 721-726.

Burger, A.J. and Coertze, F.J. (1973-74). Age determinations – April 1972 to March 1974. Ann. Geol. Surv. S. Afr., 10, p.135-141.

Burger, A. (1994). Fault-controlled hydrothermal alteration of Paleoproterozoic manganese ore in Wessels mine, Kalahari Manganese Field. Unpublished PhD thesis, 155 p.

Burke, E.A.J. and Kieft, C. (1971) Second occurrence of macedonite, PbTiO3, Långban, Sweden. Lithos: 4, p. 101-104.

Bursey R.J. (2018). A mineralogical, geochemical and metallogenic study of unusual Mn/Na/Ba assemblages at the footwall of conglomeratic iron-ore at Farm Langverwacht, Northern Cape Province of South Africa. Unpublished Msc Thesis, Rhodes University, Grahamstown, South Africa, p. 105.

Burton, K.W., Vigier, N., (2012). Lithium isotopes as tracers in marine and terrestrial environments. In: Baskaran,M. (Ed.), Handbook of Environmental Isotope Geochemistry, Advances in Isotope Geochemistry. Springer, Berlin Heidelberg, p. 41-59.

Button A. (1976). Transvaal and Hamersley basins—review of basin development and mineral deposits Miner. Sci. Eng., 8, p. 262-293.

Cabella, R., Lucchetti, G., Palenzona, A. (1990). Al-rich, Fe-poor manganoan sugilite in a pectolite-bearing assemblage from Cerchiara Mine (Northern Appennines, Italy). Neues Jahrbuch für Mineralogie, Monatshefte: 10: p. 443-448.

Cairncross, B., Dixon, R. (1995). Minerals of South Africa. Geological Society of South Africa, PO Box 44283, Linden 2104, South Africa, p. 290.

Cairncross B., Tsikos H. and Harris C. (2000). Prehnite from the Kalahari manganese field, South Africa, and its possible implications. South African Journal of Geology 103, p. 231-236.

Cairncross, B. (2011). Pocket Guide: Rocks & Minerals of Southern Africa. Penguin Random House, South Africa, p. 160.

Cairncross, B. and N. J. Beukes (2013). The Kalahari manganese field: The adventure continues. Cape Town, South Africa: Struik Nature, Random House.

Cairncross, B. (2017). Connoisseur's Choice: Sugilite, Wessels Mine, Kalahari Manganese Field, Northern Cape Province, South Africa. Rocks & Minerals, 92(6), p. 550-555.

Cairncross, B. (2017b). The Where of Mineral Names: Nchwaningite, N'Chwaning II Mine, Kalahari Manganese Field, South Africa. Rocks & Minerals, 92(3), p. 290-292.

Cairncross, B. (2019). The Where of Mineral Names: Gamagarite, Gloucester Mine, Gamagara Hills, Postmasburg Manganese and Iron-Ore Field, South Africa. Rocks & Minerals, 94(3), p. 280-285.

Cairncross, B. (2020). The Where of Mineral Names: Wesselsite, Wessels Mine, Kalahari Manganese Field, South Africa. Rocks & Minerals, 95(3), p. 282-285.

Carignan, J., Gariépy, C., & Hillaire-Marcel, C. (1997). Hydrothermal fluids during Mesozoic reactivation of the St. Lawrence rift system, Canada: C, O, Sr and Pb isotopic characterization. Chemical Geology, 137(1-2), p. 1-21.

Cartwright, & Buick. (1999). The flow of surface-derived fluids through Alice Springs age middle-crustal ductile shear zones, Reynolds Range, central Australia. Journal of Metamorphic Geology, 17(4), p. 397-414.

Cameron, E. M. (1982). Sulphate and sulphate reduction in early Precambrian oceans. Nature, 296, p. 145-148.

Cameron, E.M. (1983). Evidence from early Proterozoic anhydrite for sulphur isotope partitioning in Precambrian oceans. Nature, 304: p. 54-56.

Cerný, P. and Burt, D.M. (1984). Paragenesis, crystallochemical characteristics and geochemical evolution of micas in granitic pegmatites. In Bailey, S. W. (ed.) Micas, Vol. 13. Mineralogical Society of America Rev. Mineral, Chantily, VA, USA, p. 257-297.

Chandler, F.W. (1988). Diagenesis of sabkha-related, sulphate nodules in the early Proterozoic Gordon Lake formation, Ontario, Canada. Carbonates and Evaporites, 3(1), p. 75-94.

Chambefort, I., Dilles, J. H., & Longo, A. A. (2013). Amphibole Geochemistry of the Yanacocha Volcanics, Peru: Evidence for Diverse Sources of Magmatic Volatiles Related to Gold Ores. Journal of Petrology, 54(5), p. 1017-1046.

Chang L.L.Y., Howie R.A., Zussman J. (1996). Rock-forming Minerals, Second Edition, Vol 5B, Non-silicates: Sulfate, Carbonates, Phosphates, Halides. Longman Group, Harlow, UK, 383 p.

Chatterjee, N.D., & Warhus, U. (1984). Ephesite, Na $(LiAl_2)[Al_2Si_2O_{10}](OH)_2$: II. Thermodynamic analysis of its stability and compatibility relations, and its geological occurrences. Contributions to Mineralogy and Petrology, 85(1), p. 80-84.

Chaudhuri, S. (1978). Strontium isotopic composition of several oilfield brines from Kansas and Colorado. Geochimica et Cosmochimica Acta, 42(3), p. 329-331.

Chukhrov, F.V., Gorshkov, A.I., Sivtsov, A.V., & Berezovskaya, V.V. (1985). The Nature and Genesis Of Lithiophorite. International Geology Review, 27(3), p.348-361.

Clark, A. M., G. S. Bearne, E. E. Fejer, V. K. Din, and A. G. Couper (1980). Additional data on sugilite. Mineralogical Magazine 43: p. 947-49.

Clarke, O.M. (1966). The formation of bauxite on karst topography in Eufaula District, Alabama, and Jamaica, West Indies. Economic Geology, 61(5), p. 903-916.

Claypool, G. E., Holser, W. T., Kaplan, I. R., Sakai, H., & Zak, I. (1980). The age curves of sulfur and oxygen isotopes in marine sulfate and their mutual interpretation. Chemical Geology, 28, p. 199-260.

Clifford, T.N., Barton, E.S., Retief, E.A., Rex, D.C. and Fanning, C.M. (1995). A crustal progenitor for the intrusive anorthosite-charnockite kindred of the cupriferous Koperberg Suite, O'okiep District, Namaqualand, South Africa; new isotope data for the country rocks and intrusives. J. Petrol., 36, 231-258.

Clifford, T.N., Barton, E.S., Stern, R.A. (2004). U–Pb zircon calendar for Namaqua (Grenville) crustal events in the granulite facies terrane of the O'okiep Copper District of South Africa. J. Petrol. 45, p. 669-691.

Clifford, J.H. (2011). Connoisseur's Choice: Inesite, Wessels Mine, Northwest of Kuruman, Kalahari Manganese District, Cape Province, South Africa. Rocks & Minerals, 86(3), p. 250-260.

Coleman, M. and Moore, M. (1978). Direct reduction of sulfates to sulfate dioxide for isotopic analysis. Analytical Chemistry, 50(11), p.1594-1595.

Coombs, D. S., Dowse, M., Grapes, R., Kawachi, Y., & Roser, B. (1985). Geochemistry and origin of piemontite-bearing and associated manganiferous schists from Arrow Junction, western Otago, New Zealand. Chemical Geology, 48(1-4), p. 57-78.

Corfu, F., Polteau, S., Moore, J.M., Tsikos, H. (2009). A U-Pb discordia line for carbonate of the Mooidraai Formation, Transvaal Supergroup: Paleoproterozoic formation and Neoproterozoic fluid infiltration. Eos Transactions of the American Geophysical Union, 90(22), Joint Assembly Supplement, Abstract GA21C-03.

Cornell, D.H. (1975). Dating the Marydale Formation and the Sonama tectogenetic cycle. Abstr. Biennial Congr. Geol. Soc. S. Afr, p. 229-229.

Cornell, D.H., Hawkesworth, C.J., Van Calsteren, P. and Scott, W.D. (1986). Sm-Nd study of Precambrian crustal development in the Prieska-Copperton region, Cape Province. Trans. Geol. Soc. S. Afr., 89, p. 17-28.

Cornell, D.H., Schütte, S.S., & Eglington, B.L. (1996). The Ongeluk basaltic andesite formation in Griqualand West, South Africa: submarine alteration in a 2222 Ma Proterozoic Sea. Precambrian Research, 79(1-2), p. 101-123.

Cornell, D.H., Armstrong, R.A. and Walraven, F. (1998). Geochronology of the Proterozoic Hartley Basalt Formation, South Africa: constraints on the Kheis tectogenesis and the Kaapvaal Craton's earliest Wilson Cycle. Journal of African Earth Sciences, p. 26, 5-27.

Cornell, D.H., Thomas, R.J., Moen, H.F.G., Reid, D.L., Moore, J.M. and Gibson, R.L. (2006). The Namaqua-Natal Province. The Geology of South Africa. Geological Society of South Africa/Council for Geoscience, p. 325-379.

Corner, B. and Durrheim, R. (2018). An Integrated Geophysical and Geological Interpretation of the Southern African Lithosphere, p. 19-61.

Cortecci, G., Lattanzi, P., & Tanelli, G. (1989). Sulfur, oxygen and carbon isotope geochemistry of barite-iron oxide-pyrite deposits from the Apuane Alps (northern Tuscany, Italy). Chemical Geology, 76(3-4), 249-257.

Costin, G. Fairey, B.J. Tsikos, H. Guksik, A. (2015). Tokyoite, As-rich tokyoite and noélbensonite: new occurrences from the Postmasburg Manganese Field, Northern Cape Province, South Africa. The Can. Min., 53, p. 981-990.

Cousins, D.P. (2016). A stratigraphic, petrographic and geochemical study of the Gamagara Formation at the Maremane Dome, Northern Cape province, South Africa. Unpublished MSc Thesis, Rhodes University, Grahamstown, South Africa, p 132.

Cox, D.P., Lindsey, D.A., Singer, D.A., and Diggles, M.F. (2003, revised 2007). Sediment-hosted copper deposits of the world-Deposit models and database: U.S. Geological Survey Open-File Report 03-107 version 1.1, 50 p.

Craig H. (1961). Isotopic variations in meteoric waters. Science 133, p. 1702-1703.

Criddle, A.J., Symes, R.F. (1977). Mineralization at Tŷ Coch, Glamorgan (Mid Glamorgan), Wales: The Second Occurrence of Pyrobelonite. Mineralogical Magazine: 41(317), p. 85-90.

Dahl P.S. (1996). The crystal-chemical basis for Ar retention in micas: Inferences from interlayer partitioning and implications for geochronology. Contrib Mineral Petrol 123, p. 22-39.

Dasgupta, S., Bhattacharya, P.K., Banerjee, H., Fukuoka, M., Majumdar, N., Roy, S. (1987). Calderite-rich garnets from metamorphosed manganese silicate rocks of the Sausar Group, India, and their derivation. Mineralogical Magazine 51, p. 577-583.

Deb, M., Hoefs, J., Baumann, A. (1991). Isotopic composition of two Precambrian stratiform barite deposits from the Indian shield. Geochim Cosmochim Acta 55: p. 303-308.

Dechow, E. and Jensen, M.L. (1965). Sulphur isotopes of some central African sulphide deposits. Economic Geology 60, p. 894-941.

Deer, W.A., Howie, R.A., Zussman, J. (1992). An. Introduction to the Rock-Forming Minerals, 2nd ed., Pearson Education Limited: Harlow, UK.

Deer, W.A., Howie, R.A. and Zussman, J. (2003). Rockforming Minerals. Sheet Silicates. Micas vol. 3A, 2nd edition (M.E. Fleet, editor). The Geological Society, London, 758 p.

Delgado, A., & Reyes, E. (1996). Oxygen and hydrogen isotope compositions in clay minerals: A potential single-mineral geothermometer. Geochimica et Cosmochimica Acta, 60(21), p. 4285-4289.

DePaolo, D.J., Linn, A.M., Schubert, G. (1991). The continental crustal age distribution: methods of determining mantle separation ages from Sm–Nd isotopic data and application to the southwestern United States. J. Geophys. Res. 96, p. 2071-2088.

Derry, L.A., & Jacobsen, S.B. (1988). The Nd and Sr isotopic evolution of Proterozoic seawater. Geophysical Research Letters, 15(4), p. 397-400.

De Souza, F.R., Nalini, H.A., & de Abreu, A.T. (2019). In-situ LA-ICP-MS and EMP trace element analyses of hematite: Insight into the geochemical signature of the Neoproterozoic Urucum iron formation, Brazil. Journal of South American Earth Sciences, 102313.

De Villiers, J.E. (1943a). A preliminary description of the new mineral partridgeite: American Mineralogist, v. 28, p. 336-338.

De Villiers, J.E. (1943b). Gamagarite, a new vanadium mineral from the Postmasburg manganese deposits. American Mineralogist (1943) 28 (5): p. 329-335.

De Villiers J.E. (1944). The origin of the iron and manganese deposits in the Postmasburg and Thabazimbi areas. Transactions of the Geological Society of South Africa 47, p. 123-135.

De Villiers J.E. (1945). Lithiophorite from the Postmasburg Manganese Deposits. American Mineralogist 30 (9-10): p. 629-634.

De Villiers J.E. (1960). Manganese Deposits of the Union of South Africa. Geological Survey of South Africa: Handbook 2, Government Printer, Pretoria.

De Villiers, J.E. (1983). The manganese deposits of Griqualand West, South Africa: Some mineralogic aspects: Econ. Geol., v. 78, p. 1108-1118.

Dickin, A.P. (1995). Radiogenic isotope geology, Cambridge University Press, Cambridge.

Di Iorio, E., Cho, H. G., Liu, Y., Cheng, Z., Angelico, R., & Colombo, C. (2018). Arsenate retention mechanisms on hematite with different morphologies evaluated using AFM, TEM measurements and vibrational spectroscopy. Geoch. et Cosmoch. Acta, 237, p. 155-170.

Dill, H., & Carl, C. (1987). Sr isotope variation in vein barites from the NE Bavarian Basement: Relevance for the source of elements and genesis of unconformity-related barite deposits. Mineralogy and Petrology, 36(1), p. 27-39.

Dixon, R. (1985). Sugilite and associated minerals from Wessels mine, Kalahari manganese field: Transactions of the Geological Society of South Africa, v. 88, p. 11-17.

Dill, H.G., Pöllmann, H., & Techmer, A. (2013). 500 Million years of rift- and unconformity-related Mn mineralization in the Middle East: A geodynamic and sequence stratigraphical approach to the recycling of Mn. Ore Geology Reviews, 53, p. 112-133.

Dixon, R. (1988). Sugilite and associated metamorphic silicate minerals from the Wessels Mine, Kalahari Manganese Field. Unpublished MSc Thesis, 158 p.

Dixon, R. (1989). Sugilite and associated metamorphic silicate minerals from Wessels Mine, Kalahari manganese field. Geol. Survey S. Afr., Pretoria, Bulletin 93, 47 p.

Domagal-Goldman, S.D., Kasting, J.F., Johnston, D.T., & Farquhar, J. (2008). Organic haze, glaciations and multiple sulfur isotopes in the Mid-Archean Era. Earth and Planetary Science Letters, 269(1-2), p. 29-40.

Drits V.A., Semenov E.I. (1975). Strukturno-mineralogicheskaya kharakteristika efesita iz yuzhnoy Grenlandii. Trudy mineralogicheskogo museya imeni AYe Fersmana 24: p. 175-180.

Duane, M. J., Kruger, F. J., Roberts, P. J., & Smith, C. B. (1991). Pb and Sr isotope and origin of Proterozoic base metal (fluorite) and gold deposits, Transvaal Sequence, South Africa. Economic Geology, 86(7), p. 1491-1505.

Duane, M.J., & Saggerson, E.P. (1995). Brine expulsion, fluid transport and metallization spanning 2.0 Gyr in basins of southern and central Africa. Basin Research, 7(1), p. 97-108.

Duane, M. J., Kruger, F. J., Turner, A. M., Whitelaw, H. T., Coetzee, H., & Verhagen, B. T. (2004). The timing and isotopic character of regional hydrothermal alteration and associated epigenetic mineralization in the western sector of the Kaapvaal Craton (South Africa). Journal of African Earth Sciences, 38(5), p. 461-476.

Dugamin, E.J.M., Richard, A., Cathelineau, M. et al. (2021). Groundwater in sedimentary basins as potential lithium resource: a global prospective study. Sci Rep 11, 21091.

Dunn, P. J., J. J. Brummer, and H. Belsky. (1980). Sugilite, a second occurrence: Wessels mine, Kalahari manganese field, Republic of South Africa. Canadian Mineralogist 18: p. 37-39.

Dvořák, K., Všianský, D., Gazdič, D., Fridrichová, M., & Vaičiukynienė, D. (2020). Thaumasite formation by hydration of sulphosilicate clinker. Materials Today Communications, 101449.

Easton, A. J., Hamilton, D., Kempe, D. R. C., Sheppard, S. M. F., & Agrell, S. O. (1977). Low-Temperature Metasomatic Garnets in Marine Sediments [and Discussion]. Philosophical Transactions of the Royal Society A: Mathematical, Physical and Engineering Sciences, 286(1336), p. 253-271.

Eggenkamp H.G.M, Kreulen R., Koster Van Groos A.F. (1995). Chlorine stable isotope fractionation in evaporates. Geochimica et Cosmochimica Acta 59 (24): p. 5169-5175.

Eglington, B.M. and Armstrong, R.A. (2003). Geochronological and isotopic constraints on the Mesoproterozoic Namaqua-Natal Belt: evidence from deep borehole intersection in South Africa. Precambrian Research, 125, p. 179-189.

Eglington, B. M. (2006). Evolution of the Namaqua-Natal Belt, southern Africa - A geochronological and isotope geochemical review. Journal of African Earth Sciences, 46(1-2), p. 93-111.

Eliassen, A., & Talbot, M.R. (2005). Solution-collapse breccias of the Minkinfjellet and Wordiekammen Formations, Central Spitsbergen, Svalbard: A large gypsum palaeokarst system. Sedimentology, 52(4), p. 775-794.

Elton, N. J., Hooper, J. J., & Holyer, V. A. D. (1997). An occurrence of stevensite and kerolite in the Devonian Crousa gabbro at Dean Quarry, The Lizard, Cornwall, England. Clay Minerals, 32(02), p. 241-252.

Enami, M., & Banno, Y. (2001). Partitioning of Sr between coexisting minerals of the hollandite- and piemontite-groups in a quartz-rich schist from the Sanbagawa metamorphic belt, Japan. American Mineralogist, 86(3), p. 205-214.

Evans, D.A.D., Gutzmer, J., Beukes, N.J. and Kirschvink, J.L. (2001). Paleomagnetic constraints on ages of mineralisation in the Kalahari Manganese Field, South Africa. Economic Geology, 96, p. 621-631.

Evans, D.A.D. (2006). Proterozoic low orbital obliquity and axial-dipolar geomagnetic field from evaporite palaeolatitudes. Nature, 444 (7115), p. 51-55.

Evans, D.A.D (2007). A global survey of Precambrian evaporites: implications for Proterozoic paleoenvironments: American Geophysical Union, Fall Meeting, San Francisco, California, December 10–14, 2007, abstract #U51A-06.E.

Evans, R.K. (2014) Lithium, chap. 10 of Gunn, Gus, ed., Critical metals handbook: Hoboken, N.J., Wiley, p. 230-260.

Fairey, B.J. (2013). Genesis of karst-hosted manganese ores of the Postmasburg Manganese Field, South Africa with emphasis on evidence for hydrothermal processes. Unpublished Msc Thesis, Rhodes University, Grahamstown, South Africa, p. 158.

Fairey, B., Tsikos, H., Corfu, F., & Polteau, S. (2013). U-Pb systematics in carbonates of the Postmasburg Group, Transvaal Supergroup, South Africa: Primary versus metasomatic controls. Precambrian Research, 231, p. 194-205.

Fairey, B. J., Timmerman, M. J., Sudo, M., & Tsikos, H. (2019). The Role of Hydrothermal Activity in the Formation of Karst-Hosted Manganese Deposits of the Postmasburg Mn Field, Northern Cape Province, South Africa. Minerals, 9(7), p. 408.

Farquhar, J., Bao, H., Thiemensm M. (2000). Atmospheric Influence of Earth's Earliest Sulfur Cycle. Science, 289(5480), p. 756-758.

Faure, G. (1986). Principles of isotope geology. New York, Wiley, 464 p.

Feng, J. (1986). Sulfur and Oxygen Isotope Geochemistry of Precambrian Marine Sulfate and Chert. Northern Illinois University, Dekalb, p. 110.

Feng, X.H., Zhai, L.M., Tan, W.F., Liu, F., & He, J.Z. (2007). Adsorption and redox reactions of heavy metals on synthesized Mn oxide minerals. Environmental Pollution, 147(2), p. 366-373.

Field, C.W.; Fifarek, R.H. 1985: Light stable isotope systematics in the epithermal environment. Reviews in economic geology 2: p. 99-128.

Fleming, T.H., Foland, K.A., & Elliot, D.H. (1999). Apophyllite $^{40}Ar/^{39}Ar$ and Rb-Sr geochronology: Potential utility and application to the timing of secondary mineralization of the Kirkpatrick Basalt, Antarctica. Journal of Geophysical Research: Solid Earth, 104(B9), p.. 20081-20095.

Flude, S., & Storey, M. (2016). $^{40}Ar/^{39}Ar$ age of the Rotoiti Breccia and Rotoehu Ash, Okataina Volcanic Complex, New Zealand, and identification of heterogeneously distributed excess ^{40}Ar in supercooled crystals. Quaternary Geochronology, 33, p. 13-23.

Flude, S., Halton, A. M., Kelley, S. P., Sherlock, S. C., Schwanethal, J., & Wilkinson, C. M. (2014). Observation of centimetre-scale argon diffusion in alkali feldspars: implications for40Ar/39Ar thermochronology. Geological Society, London, Special Publications, 378(1), p/ 265-275.

Foland, K.A. (1979). Limited mobility of argon in a Metamorphic Terrain. Geochim Cosmochim Acta 43, p.793-801.

Foland, K.A., Linder J.S., Laskowski, T.E. and Grant, N.K. (1984). $^{40}Ar/^{39}Ar$ dating on glauconites: Measured 39Ar recoil loss from well-crystallized specimens. Isot. Geosci., 2: p. 241-264.

Foland, K.A., Hubacher, F.A., and Arehart, G.B. (1992). $^{40}Ar/^{39}Ar$ dating of very fine-grained samples-An encapsulated-vial procedure to overcome the problem of ^{39}Ar recoil loss: Chemical Geology, v. 102, p. 269-276.

Foland, K.A., T.H. Fleming, A. Helmann, and D.H. Elliot (1993). Potassium argon dating of fine-grained basalts with massive Ar loss: Application of the $^{40}Ar/^{39}Ar$ technique to plagioclase and glass from the Kirkpatrick Basalt, Antarctica, Chem. Geol., 107, p. 173-190.

Fontes, J.C. & Matray, J.M. (1993). Geochemistry and Origin of Formation Brines from the Paris Basin, France 1. Brines associated with triassic salts. Chem. Geol. 109, p. 149-175.

Fortier, S.M. and Giletti, B.J. (1989) An empirical model for predicting diffusion coefficients in silicate minerals. Science, 245, p. 1481-1484.

Fortier, S.M. and Giletti, B.J. (1991). Volume self-diffusion of oxygen in biotite, muscovite and phlogopite micas. Geochomica et Cosmochimica Acta, 55, p. 1319-1330.

Foster, M. (1960). Interpretation of the composition of lithium micas. U.S. Geol. Survey Prof. Paper, 354-E, p. 115-147.

Franke W., Jelinski B., Zarei M. (1982). Hydrothermal synthesis of an ephesite-like sodium mica. N Jahrb Mineral Monatsh 8: p. 337-340.

Fridrichová, M., Dvořák, K., Gazdič, D., Mokrá, J., & Kulísek, K. (2016). Thermodynamic Stability of Ettringite Formed by Hydration of Ye'elimite Clinker. Advances in Materials Science and Engineering, 2016, p. 1-7.

Frimmel, H., Frank, W. (1998). Neoproterozoic tectono-thermal evolution of the Gariep Belt and its basement, Namibia and South Africa. Precambrian Research, 90(1-2), p. 1-28.

Gaboreau, S., Cuney, M., Quirt, D., Beaufort, D., Patrier, P., & Mathieu, R. (2007). Significance of aluminum phosphate-sulfate minerals associated with U unconformity-type deposits: The Athabasca basin, Canada. American Mineralogist, 92(2-3), p. 267-280.

Gaines, R.V., H.C.W. Skinner, E.E. Foord, B. Mason, and A. Rosenzweig, (1997). Dana's New Mineralogy, John Wiley, New York.

Galindo, C., Tornos, F., Darbshire, D.P.F., Casquet, C. (1994). The age and origin of the barite-fluorite (Pb–Zn) veins of the Sierra Del Guadarrama (Spanins central system Spain): a radiogenic (Nd, Sr) and stable isotope study, Isotope geoscience section. Chem. Geol. 112, p. 351-364.

Gandin, A., Wright, D.T., Melezhik, V. (2005). Vanished evaporites and carbonate formation in the Neoarchaean Kogelbeen and Gamohaan formations of the Campbellrand Subgroup, South Africa. J. African Earth Sci., p. 1-23.

Gandin, A., & Wright, D.T. (2007). Evidence of vanished evaporites in Neoarchaean carbonates of South Africa. Geological Society, London, Special Publications, 285(1), p. 285-308.

Garcia-V.J., Orti, F., Rossel, L., Ayora, C., Rouchy, J.M. and Lugli, S. (1995). The Messinian salt of the Mediterranean: geochemical study of the salt from the Central Sicily Basin and comparison with the Lorca Basin (Spain). Bull. Soc. Géol. France, 166, p. 699-710.

Garlick, G.D. (1966). Oxygen isotope fractionation in igneous rocks. Earth and Planetary Science Letters, 1(6), p. 361-368.

Garven, G. (1995). Continental-Scale Groundwater Flow and Geologic Processes. Annual Review of Earth and Planetary Sciences, 23(1), p. 89-117.

Garvin, Paul L. (1995). Paleokarst and Associated Mineralization at the Linwood Mine, Scott County Iowa. Journal of the Iowa Academy of Science: JIAS, 102(1-2), p. 1-21.

Gaškov, M., Sepp, H., Paiste, P., Kirsimäe, K., & Pani, T. (2017). Barite mineralization in Kalana speleothems, Central Estonia: Sr, S and O isotope characterization. Estonian Journal of Earth Sciences, 66(3), p. 130-141.

Gellatly, A.M., Lyons, T.W. (2005). Trace sulfate in mid-Proterozoic carbonates and the sulfur isotope record of biospheric evolution. Geochimica et Cosmochimica Acta 69, p. 3813-3829.

Gibson, R.L., Wallmach, T., & de Bruin D. (1995). Complex zoning in vesuvianite from the Canigou Massif, Pyrenees, France. The Canadian Mineralogist (1995) 33 (1): p. 77-84.

Giester, G., & Rieck, B. (1996). Wesselsite, $SrCu[Si_4O_{10}]$, a further new gillespite-group mineral from the Kalahari Manganese Field, South Africa. Mineralogical Magazine, 60(402), p. 795-798.

Gill, B.C., Lyons, T.W., Shim, M., Hurtgen, M., Kah, L., Frank, T.D. (2005). Carbonate associated sulfate as a tracer of ancient seawater chemistry. Abstr.Pap. - Am. Chem. Soc. 229, U890.

Gill, B.C., Lyons, T.W., Frank, D.T. (2008). Behavior of carbonate-associated sulfate during meteoric diagenesis and implications for the sulfur isotope paleoproxy. Geochimica et Cosmochimica Acta 72, p. 4699-4711.

Gleeson, S. A., Yardley, B. W. D., Munz, I. A., & Boyce, A. J. (2003). Infiltration of basinal fluids into high-grade basement, South Norway: sources and behaviour of waters and brines. Geofluids, 3(1), p. 33-48.

Gnos, E., Armbruster, T., & Villa, I. M. (2003). Norrishite, $K(Mn_2^{3+}Li)Si_4O_{10}(O)_2$, an oxymica associated with sugilite from the Wessels Mine, South Africa: Crystal chemistry and ^{40}Ar-^{39}Ar dating. American Mineralogist, 88(1), p. 189-194.

Grant, N.K., Lepak, R.J., Maher, T.M., Hudson, M.R., and Carl, J.D. (1986). Geochronological framework for the Grenville rocks in the Adirondack Mountains: Geol. Soc. America Abs. with Prog., v. 18, p. 620.

Graupner, T., Niedermann, S., Kempe, U., Klemd, R., & Bechtel, A. (2006). Origin of ore fluids in the Muruntau gold system: Constraints from noble gas, carbon isotope and halogen data. Geochimica et Cosmochimica Acta, 70(21), p. 5356-5370.

Gray, D.R., Foster, D.A., Goscombe, B., Passchier, C.W., Trouw, R.A.J. (2006). $^{40}Ar/^{39}Ar$ thermochronology of the Pan-African Damara Orogen, Namibia, with implications for tectonothermal and geodynamic evolution. Precambrian Research 150, p.49-72.

Grinenko, L.N., Melezhik, V.A. and Fetisova, O.A. (1989). First discovery o barites in the Precambrian sedimentary deposits of Baltic Shield. Dokl. Akad. Nauk, 304, p. 1453-1455 (in Russian).

Grotzinger, J.P., & Kasting, J.F. (1993). New Constraints on Precambrian Ocean Composition. The Journal of Geology, 101(2), p. 235-243

Grubb P.C.L. Genesis of the Weipa bauxite deposits, N E Australia. Mineralim Deposita, 1971, 6: p. 265.

Godfrey, L.V., Chan, L.-H., Alonso, R.N., Lowenstein, T.K., McDonough, W.F., Houston, J., … Jordan, T. E. (2013). The role of climate in the accumulation of lithium-rich brine in the Central Andes. Applied Geochemistry, 38, p. 92-102.

Govorov I.N. (1958). Metasomaticheskaya zonalnost desilikatsii pri greyzenizatsii izvestnyakov. Doklady Akademii Nauk SSSR 119: p. 556-559.

Gu, X., Yang, H., Xie, X., van Nieuwenhuizen, J.J., Downs, R.T., & Evans, S.H. (2019). Lipuite, a new manganese phyllosilicate mineral from the N'Chwaning III mine, Kalahari Manganese Fields, South Africa. Mineralogical Magazine, 83(5), p. 645-654.

Guo, Q., Strauss, H., Kaufman, A.J., Schröder, S., Gutzmer, J., Wing, B., Baker, M.A., Bekker, A., Jin, Q., Kim, S., Farquhar, J. (2009). Reconstructing Earth's surface oxidation across the Archean Paleoproterozoic transition. Geology 37, p. 399-402.

Guo, J., Lu, Y., Fu., J., Qin, Z., Ning Y., and Zhang, Z. (2019). Geology and Geochronology of the Maozaishan Sn Deposit, Hunan Province: Constraints from Zircon U-Pb and Muscovite Ar-Ar Dating. Minerals 2019, 9(12), p. 773.

Gustafson, L.B. and Williams, N. (1981). Sediment-hosted stratiform deposits of copper, lead, and zinc. Econ. Geol., (75th Anniversary Volume): p. 139-178.

Gutzmer, J. (1996). Genesis and alteration of the Kalahari and Postmasburg manganese deposits, Griqualand West. South Africa. PhD thesis (unpubl.), RAU, Johannesburg, 513 p.

Gutzmer, J. and Cairncross, B. (1993). Recent mineral discoveries from the Wessels Mine, South Africa. Mineralogical Record 24: p. 365-368.

Gutzmer, J. and Beukes, N.J. (1995). Fault controlled metasomatic alteration of Early Proterozoic sedimentary manganese ores in the Kalahari manganese field, South Africa. Econ. Geol., 90, p. 823-844.

Gutzmer, J., & Beukes, N. J. (1996a). Karst-hosted fresh-water Paleoproterozoic manganese deposits, Postmasburg, South Africa. Economic Geology, 91(8), p. 1435-1454.

Gutzmer, J. and Beukes, N.J. (1996b). Mineral paragenesis of the Kalahari manganese field, South Africa. Ore geology reviews 11, p. 405-428.

Gutzmer, J. and Beukes, N.J. (1997). Effects of mass transfer, compaction and secondary porosity on hydrothermal upgrading of Paleoproterozoic sedimentary manganese ore in the Kalahari manganese field, South Africa: Mineralium Deposita, v. 32, p. 250-256.

Gutzmer, J., & Beukes, N. J. (1997b). Mineralogy and mineral chemistry of oxide-facies manganese ores of the Postmasburg manganese field, South Africa. Mineralogical Magazine, 61(405), p. 213-231.

Gutzmer, J. and Beukes, N.J. (1998). High-grade manganese ores in the Kalahari Manganese field: Characterization and dating of ore-forming events. Unpublished, final technical report, 252 p.

Gutzmer, J., Beukes, N.J., Pickard, A. and Barley, M.E. (2000). 1170 Ma SHRIMP age for Koras Group bimodal volcanism, Northern Cape Province. S. Afr. J. Geol., 103, p. 32–37.

Gutzmer, J., Pack, A., Lüders, V., Wilkinson, J., Beukes, N., & Niekerk, H. (2001). Formation of jasper and andradite during low-temperature hydrothermal seafloor metamorphism, Ongeluk Formation, South Africa. Contributions to Mineralogy and Petrology, 142(1), p. 27-42.

Gutzmer, J., & Cairncross, B. (2002). Spectacular Minerals from the Kalahari Manganese Field, South Africa. Rocks & Minerals, 77(2), p. 94-107.

Gutzmer, J., Du Plooy, A.P., & Beukes, N.J. (2012). Timing of supergene enrichment of low-grade sedimentary manganese ores in the Kalahari Manganese Field, South Africa. Ore Geology Reviews, 47, p. 136-153.

Hacini, M., Kherici, N., and Oelkers, E.H. (2008). Mineral precipitation rates during the complete evaporation of the Merouane Chott ephemeral lake: Geochimica et Cosmochimica

Acta, v. 72, p. 1583-1597.

Hanor, J.S. (1994). Origin of saline fluids in sedimentary basins. Geological Society, London, Special Publications, 78(1), p. 151-174.

Hanor, J.S., (2000). Barite-celestine geochemistry and environments of formation. Rev. Mineral. Geochem. 40, p. 193-275.

Harper, C.T., & Schamel, S. (1971). Note on the isotopic composition of argon in quartz veins. Earth and Planetary Science Letters, 12(1), p. 129-133.

Harrison, T.M. and McDougall, I. (1982). The thermal significance of potassium feldspar K-Ar ages inferred from $^{40}Ar/^{39}Ar$ age spectrum results. Geochim. Cosmochim. Acta, 46: p. 1811-1820.

Harrison, T.M., Célérier, J., Aikman, A.B., Hermann, J., Heizler, M.T. (2009). Diffusion of ^{40}Ar in Muscovite. Geochim. Cosmochim. Acta 73, p. 1039-1051.

Hartnady, C.J.H., Joubert, P., Stowe, C.W. (1985). Proterozoic crustal evolution in southwestern Africa. Episodes 8, p. 236-244.

Hatipoğlu, M. (2010). Gem-Quality Diaspore Crystals as an Important Element of the Geoheritage of Turkey. Geoheritage, 2(1-2), p. 1-13.

Hawthorne, F.C., Ungaretti, L., Oberti, R., Cannillo, E., and Smelik, E.A. (1994). The mechanism of Li incorporation in amphiboles. American Mineralogist, 79, p. 443-451.

Hawthorne, F.C., Oberti, R. Cannillo, E., Sardone, N., Zanetti, A., Grice, J.D., and Ashley, P.M. (1995). A new anhydrous amphibole from the Hoskins mine, Grenfell, New South Wales, Australia: Description and crystal structure of ungarettiite, Na $Na_2(Mn_2^{2+}Mn_3^{3+})Si_8O_{22}O_2$. American Mineralogist, 80, p. 165-172.

Hawthorne, F.C., Oberti, R., Harlow, G.E., Maresch, W.V., Martin, R.F., Schumacher, J.C., & Welch, M.D. (2012). Nomenclature of the amphibole supergroup. American Mineralogist, 97(11-12), p. 2031-2048.

Hemzacek, J.M. (1987). Replaced evaporites and the sulfur isotope age curve of the Precambrian. MSc Thesis. Northern Illinois University, Dekalb, IL, p. 77.

Herbert S., G.F., & Prior, G.T. (1911). On Fermorite, a new arsenate and Phosphate of lime and strontia, and Tilasite, from the manganese-ore deposits of India. Mineralogical Magazine

and Journal of the Mineralogical Society, 16(74), p. 84-96.

Hess, J., & Lippolt, H. (1986). Kinetics of Ar isotopes during neutron irradiation: 39Ar loss from minerals as a source of error in $^{40}Ar/^{39}Ar$ dating. Chemical Geology: Isotope Geoscience Section, 59, p. 223-236.

Hesse, R., & Schacht, U. (2011). Early Diagenesis of Deep-Sea Sediments. Developments in Sedimentology, p. 557-713.

Hilliard, P. (1999). Structural evolution and tectono stratigraphy of the Kheis Orogen and its relationship to the south western margin of the Kaapvaal Craton. Unpublished PhD thesis, 235 p.

Hiroyuki, M. (1986). The crystal structure of hollandite. Mineralogical Journal, vol 13, no. 13, p. 119-129.

Hodell, D.A., Mead, G.A., & Mueller, P.A. (1990). Variation in the strontium isotopic composition of seawater (8 Ma to present): Implications for chemical weathering rates and dissolved fluxes to the oceans. Chemical Geology: Isotope Geoscience Section, 80(4), p. 291-307.

Hodges K.V. (1991). Pressure-temperature-time paths. Ann. Rev. Earth Planet. Sci. 19, p. 207-236

Hodges, K.V. (2003). Geochronology and Thermochronology in Orogenic Systems. Treatise on Geochemistry, p. 263-292.

Hodgson, A. A. (1965). Fibrous silicates. London: Royal Institute of Chemistry.

Hoefs J., Müller G., Schuster K.A. and Walde, D. (1987). The Fe-M deposits of Urucum, Brazil: An oxygen isotope study. Chemical Geology 65, p. 311-319.

Hoefs, J. (1997). Stable Isotope Geochemistry. 4th edition, Springer-Verlag, Berlin.

Hofmann, R., & Baumann, A. (1984). Preliminary report on the Sr isotopic composition of hydrothermal vein barites in the Federal Republic of Germany. Mineralium Deposita, 19(2), p. 166-169.

Holland, H.D., (1984). The Chemical Evolution of the Atmosphere and Oceans. Princeton Univ. Press, Princeton, 582 p.

Holser, W.T. (1977). Catastrophic chemical events in the history of the ocean. Nature, 267(5610), p. 403-408.

Holtstam, D., Langhof, J. (eds.) (1999). Långban: The mines, their minerals, geology and explorers. Swedish Museum of Natural History and Raster Förlag, Stockholm & Chr. Weise Verlag, Munich: p. 216.

Horita, J. (1989a). Stable isotope fractionation factors of water in hydrated saline mineral-brine systems. Earth and Planetary Science Letters, 95(1-2), p. 173-179.

Horita, J. (1989b). Analytical aspects of stable isotopes in brines. Chemical Geology: Isotope Geoscience Section, 79(2), p. 107-112.

Horstmann, U.E., & Hälbich, I.W. (1995). Chemical composition of banded iron-formations of the Griqualand West Sequence, Northern Cape Province, South Africa, in comparison with other Precambrian iron formations. Precambrian Research, 72(1-2), p. 109-145.

Horváth, L., and R. A. Gault. (1990). The mineralogy of Mont SaintHilaire, Quebec. Mineralogical Record 21: p. 284-359.

Hughes J.M., Rakovan J.F., Bracco R., Gunter M.E. (2003). The atomic arrangement of the ganophyllite-group modulated layer silicates as determined from the orthorhombic dimorph of tamaite, with the elusive 16.8 A ganophyllite-group superstructure revealed. American Mineralogist 88, p. 1324-1330.

Huizenga, J.-M., Gutzmer, J., Banks, D., & Greyling, L. (2005). The Paleoproterozoic carbonate-hosted Pering Zn–Pb deposit, South Africa. II: fluid inclusion, fluid chemistry and stable isotope constraints. Mineralium Deposita, 40(6-7), p. 686-706.

Humphreys, H.C. and Cornell, D.H. (1989). Petrology and geochronology of low-pressure mafic granulites in the Marydale Group, South Africa. Lithos, 22, p. 287-303.

Humphreys, H.C., Schlegel, G.C-J. and Stowe, C.W. (1991). High-pressure metamorphism in garnet-hornblende-muscovite-plagioclase-quartz schists from the Kheis Belt. S. Afr. J. Geol., 94, p. 170-173.

Hurai, V., Huraiová, M., Slobodník, M., & Thomas, R. (2015). Stable Isotope Geochemistry of Geofluids. Geofluids, p. 293–344.

Jacobs, J. and Thomas, R.J. (1996). Pan-African rejuvenation of the ~1.1 Ga Natal Metamorphic Province: K-Ar muscovite and sphene fission track evidence. J. Geol. Soc. London, 153, p. 971-

78.

Jiahui, P., Jianxin, Z. & Jindong, Q. (2006). The mechanism of the formation and transformation of ettringite. J. Wuhan Univ. Technol.-Mat. Sci. Edit. 21, p. 158-161.

Johnson, C.A., Kelley, K.D., & Leach, D.L. (2004). Sulfur and Oxygen Isotopes in Barite Deposits of the Western Brooks Range, Alaska, and Implications for the Origin of the Red Dog Massive Sulfide Deposits. Economic Geology, 99(7), p. 1435-1448.

Jones, S. A. (2017). Geology and geochemistry of fault-hosted hydrothermal and sedimentary manganese deposits in the Oakover Basin, east Pilbara, Western Australia, Australian Journal of Earth Sciences, 64:1, p. 63-102.

Jonsson, E., & Broman, C. (2002). Fluid inclusions in late-stage Pb-Mn-As-Sb mineral assemblages in the Langban deposit, Bergslagen, Sweden. The Canadian Mineralogist, 40(1), p. 47-65.

Johnson, C.A., Kelley, K.D., & Leach, D.L. (2004). Sulfur and Oxygen Isotopes in Barite Deposits of the Western Brooks Range, Alaska, and Implications for the Origin of the Red Dog Massive Sulfide Deposits. Economic Geology, 99(7), p. 1435-1448.

Johnston, D.T., Farquhar, J., Habicht, K.S., & Canfield, D.E. (2008). Sulphur isotopes and the search for life: strategies for identifying sulphur metabolisms in the rock record and beyond. Geobiology, 6(5), p. 425-435.

Jonsson, E., & Hålenius, U. (2010). Mn3+-bearing pargasite from the Långban Fe-Mn oxide mineralisation, Bergslagen, Sweden. GFF, 132(3-4), p. 167-172.

Kamber, B.S., & Webb, G.E. (2001). The geochemistry of late Archaean microbial carbonate: implications for ocean chemistry and continental erosion history. Geochimica et Cosmochimica Acta, 65(15), p. 2509-2525.

Kamber, B.S., & Whitehouse, M.J. (2006). Micro-scale sulphur isotope evidence for sulphur cycling in the late Archean shallow ocean. Geobiology, 5, p. 5-17.

Kampschulte, A., & Strauss, H. (2004). The sulfur isotopic evolution of Phanerozoic seawater based on the analysis of structurally substituted sulfate in carbonates. Chemical Geology, 204(3-4), p. 255-286.

Karhu, J.A., Holland, H.D. (1996). Carbon isotopes and the rise of atmospheric oxygen. Geology 24(10): p. 867-870.

Kasatkin, A., Zubkova, N., Pekov, I., Chukanov, N., Škoda, R., Agakhanov, A., . . . Yu. Pushcharovsky, D. (2021). The mineralogy of the historical Mochalin Log REE deposit, South Urals, Russia. Part IV. Alexkuznetsovite-(La), $La_2Mn(CO_3)(Si_2O_7)$, alexkuznetsovite-(Ce), $Ce_2Mn(CO_3)(Si_2O_7)$ and biraite-(La), $La_2Fe_2(CO_3)(Si_2O_7)$, three new isostructural minerals and a definition of the biraite group. Mineralogical Magazine, 85(5), p. 772-783.

Kato, A., Matsubara, S. and Watanabe, T. (1987). Banalsite and serandite from the Shiromaru mine, Tokyo. Bulletin of the National Science Museum, series C: 13: p, 107-114.

Kawachi Y., P.M. Ashley, D. Vince, and M. Goodwin (1994). Sugilite in manganese silicate rocks from the Hoskins mine and Woods mine, New South Wales, Australia. Mineralogical Magazine 58: p. 671-77.

Kawachi, Y., Coombs, D.S., Miura, H. (1996) Noélbensonite, a new BaMn silicate of the lawsonite structure type, from Woods Mine, New South Wales, Australia. Mineralogical Magazine: 60(399): p. 369-374.

Kelley, S.P. (2002b). Excess argon in K-Ar and Ar-Ar geochronology: Chemical Geology, v. 188, p. 1-22.

Kesler, W.D. (1978). Diaspore recrystallized at low temperature. American mineralogist, vol 63, [. 326-329.

Kesler, S.E., & Jones, L.M. (1980). Sulfur- and strontium-isotopic geochemistry of celestite, barite and gypsum from the Mesozoic basins of northeastern Mexico. Chemical Geology, 31, p. 211-224.

Kesler, S.E., Jones, L.M. and Rurz, J. (1988). Strontium isotopic geochemistry of Mississippi Valley-type deposits, east Tennessee: Implications for age and source of mineralizing brines. Geol. Sot. Amer. Bull. 100, p. 1300-1307.

Kesler, S.E., Vennemann, T.W., Frederickson, C., Breithaupt, A., Vazquez, R., & Furman, F.C. (1997). Hydrogen and oxygen isotope evidence for origin of MVT-forming brines, southern Appalachians. Geochimica et Cosmochimica Acta, 61(7), p. 1513-1523.

Kessen, K.M., Woodruff, M.S., & Grant, N.K. (1981). Gangue mineral $^{87}Sr/^{86}Sr$ ratios and the origin of Mississippi Valley-type mineralization. Economic Geology, 76(4), p. 913-920.

Kharaka, Y.K., Hull, R.W. and Carothers, W.W. (1985). Water-rock interactions in sedimentary basins. SEPM (Soc. Econ. Paleontol. Mineral.), Short Course, No. 17, p. 79-176.

Kimmig, S.R., Nadeau, M.D., Swart, P.K., & Holmden, C. (2021). Mg and Sr isotopic evidence for basin wide alteration of early diagenetic dolomite in the Williston Basin by ascending crustal fluids. Geochimica et Cosmochimica Acta, 311, p. 198-225.

Kleyenstüber, A.S.E. (1984). The mineralogy of the manganese-bearing Hotazel Formation of the Proterozoic Transvaal Sequence in Griqualand West, South Africa: Transactions of the Geological Society of South Africa, v. 87, p. 257-272.

Kleyenstüber, A.S.E. (1985). A regional mineralogical study of the manganese-bearing Voëlwater Subgroup in the Northern Cape Province, Rand Afrikaans University, Johannesburg, Unpublished PhD Thesis.

Kleyenstüber, A.S.E. (1993). Significant characteristics of the manganese ores and some of the minerals occurring in the Proterozoic Kalahari Manganese Field, South Africa. Res. Geol., 17, p. 2-11.

Kodama, T., Higuchi, T., Shimizu, T., Shimizu, K., Komarneni, S., Hoffbauer, W., & Schneider, H. (2001). Synthesis of Na-2-mica from metakaolin and its cation exchange properties. Journal of Materials Chemistry, 11(8), p. 2072-2077.

Kolitsch, U., Merlino, S., Belmonte, D., Carbone, C., Cabella, R., Lucchetti, G., Ciriotti, M.E. (2018). Lavinskyite-1M, K(LiCu)Cu6(Si4O11)2(OH)4, the monoclinic MDO equivalent of lavinskyite-2O (formerly lavinskyite), from the Cerchiara manganese mine, Liguria, Italy. European Journal of Mineralogy: 30(4): p. 811-820.

Konhauser, K.O., Planavsky, N.J., Hardisty, D.S., Robbins, L.J., Warchola, T.J., Haugaard, R., … Johnson, C.M. (2017). Iron formations: A global record of Neoarchaean to Palaeoproterozoic environmental history. Earth-Science Reviews, 172, p. 140-177.

Konings, R.J.M., Boland, J.N., Vriend, S.P., and Jansen J.B.H. (1988). Chemistry of biotites and muscovites in the Abas Granite, northern Portugal. American Mineralogist 73 (7-8): p. 754-765.

Kontak, D.J. (2006). Structurally Controlled Vein Barite Mineralization in the Maritimes Basin of Eastern Canada: Geologic Setting, Stable Isotopes, and Fluid Inclusions. Economic Geology, 101(2), p. 407-430.

Köster, H.M., Ehrlicher, U., Gilg, H.A., Jordan, R., Murad, E. and Onnich, K. (1999) Mineralogical and chemical characteristics of five nontronites and Fe-rich smectites. Clay Minerals, 34, p. 579-599.

Kotov, Y. I., & Skenderov, G. M. (1988). Hydrothermal Biotite Veins. International Geology Review, 30(10), p. 1104-1113.

Kristmannsdóttir, H., and J. Tómasson. (1978). Zeolite zones in geothermal areas in Iceland, in Natural Zeolites: Occurrence Properties, and Use, edited by L.B. Sand and F.A. Mumpton, p. 277-284, Pergamon, New York.

Kröner, A., & Stern, R.J. (2005). Africa | Pan-African Orogeny. Encyclopaedia of Geology, p. 1-12.

Kundu T., Rath, S.S., Das, S.K., Parhi, P.K., Angadi, S. (2013). Recovery of lithium from spodumene-bearing pegmatites: A comprehensive review on geological reserves, beneficiation, and extraction. Powder Technlology, vol 15, 118142.

Kunzmann, M., Gutzmer, J., Beukes, N.J., & Halverson, G.P. (2014). Depositional environment and lithostratigraphy of the Paleoproterozoic Mooidraai Formation, Kalahari Manganese field, South Africa, South African Journal of Geology, 117(2), p. 173-192.

Kutoglu, A., von (1974). Structure refinement of the apatite $Ca_5(VO_4)_3(OH)$: Neues Jahrbuch für Mineralogie-Monatshefte, p. 210-218.

Land, J.S., Tsikos, H., Cousins, D., Luvizotto, G., & Zack, T. (2017). Origin of red beds and paleosols in the Palaeoproterozoic Transvaal and Olifansthoek Supergroups of South Africa: provenance versus metasomatic controls. Geological Journal, 53(1), p. 191-202.

Lange, S., Chaudhuri, S., & Clauer, N. (1983). Strontium isotopic evidence for the origin of barites and sulfides from the mississippi valley-type ore deposits in southeast Missouri. Economic Geology, 78(6), p. 1255-1261.

Laznicka, P. (1992). Manganese deposits in the global lithogenetic system: Quantitative approach: Ore Geology Reviews, v. 7, p. 279-356.

Leach, D.., Bradley, D.., Huston, D., Pisarevsky, S., Taylor, R., & Gardoll, S.J.
(2010). Sediment-hosted lead-zinc deposits in Earth history. Econ. Geol., 105, p. 593-625.

Leake, B.E., Woolley, A.R., Birch, W.D., Gilbert, M.C., Grice, J.D., Hawthorne, F.C., Kato, A., Kisch, H.J., Krivovichev, V.G., Linthout, K., Laird, J., J.C., Smith, D.C., Stephenson, N.C.N., Ungaretti, L., Whittaker, E.J.W. and Youzhi, G. (1997). Nomenclature of amphiboles - Report of the subcommittee on amphiboles of the International Mineralogical Association Commission on New Minerals and Mineral Names. European Jour. Mineral., v.9, p.623-651.

Lehmann, J., Saalmann, K., Naydenov, K.V., Milani, L., Belyanin, G.A., Zwingmann, H., … Kinnaird, J.A. (2016). Structural and geochronological constraints on the Pan-African tectonic evolution of the northern Damara Belt, Namibia. Tectonics, 35(1), p. 103-135.

Lewy, W. (2012). Banded Iron Formations (BIFs) and Associated Sediments Do Not Reflect the Physical and Chemical Properties of Early Precambrian Seas. International Journal of Geosciences 3(01): p. 226-236.

Li, D., Chen, H., Sun, X., Fu, Y., Liu, Q., Xia, X., & Yang, Q. (2019). Coupled trace element and SIMS sulfur isotope geochemistry of sedimentary pyrite: implications on pyrite growth of Caixiashan Pb-Zn deposit. Geoscience Frontiers, vol 10(6), p. 2177-2188.

Liu, W., Mei, Y., Etschmann, B., Brugger, J., Pearce, M., Ryan, C. G., … Falkenberg, G. (2017). Arsenic in hydrothermal apatite: Oxidation state, mechanism of uptake, and comparison between experiments and nature. Geochimica et Cosmochimica Acta, 196, p. 144-159.

López-Quirós, A., Sánchez-Navas, A., Nieto, F., & Escutia, C. (2020). New insights into the nature of glauconite. American Mineralogist, 105(5), p. 674-686.

Lucchetti, G., L. Cortesogno, and A. Palenzona. (1988). Low-temperature metamorphic mineral assemblages in Mn-Fe ores from Cerchiara mine (northern Appennine, Italy). Neues Jahrbuch für Mineralogie-Monatshefte 8: p. 367-83.

Lüders V., Gutzmer J, and Beukes, N.J. (1999). Fluid inclusion studies in cogenetic hematite, hausmannite and gangue minerals from high-grade manganese ores in the Kalahari manganese field, South Africa: Econ. Geol., v. 94, p. 589-596.

Lyons, T.W., and Gill, B.C. (2010). Ancient sulfur cycling and oxygenation of the early biosphere. Elements 6: p. 93-99.

Maciąg, Ł., Zawadzki, D., Kozub-Budzyń, G. A., Piestrzyński, A., Kotliński, R. A., & Wróbel, R. J. (2019). Mineralogy of Cobalt-Rich Ferromanganese Crusts from the Perth Abyssal Plain (E Indian Ocean). Minerals, 9(2), 84.

Machel, H.G. (2004). Concepts and models of dolomitization: a critical reappraisal. Geological Society, London, Special Publications, 235(1), p. 7-63.

MacLean, W.H., Bonavia, F.F., Sanna, G. (1997). Argillite debris converted to bauxite during karst weathering: evidence from immobile element geochemistry at the Olmedo Deposit, Sardinia. Mineralium Deposita 32, p. 607-616.

Macphee, D.E., & Barnett, S.J. (2004). Solution properties of solids in the ettringite-thaumasite solid solution series. Cement and Concrete Research, 34(9), p. 1591-1598.

Macpherson, G.L., Capo, R.C., Stewart, B.W., Phan, T.T., Schroeder, K., Hammack, R.W., (2014). Temperature-dependent Li isotope ratios in Appalachian Plateau and Gulf Coast Sedimentary Basin saline water. Geofluids 14, p. 419-429.

Marchesini, M. and Pagano, R. (2001). The Val Graveglia manganese district, Liguria, Italy. The Mineralogical Record, 32, p. 349-379.

Marchev, P., & Singer, B. (2002). $^{40}Ar/^{39}Ar$ geochronology of magmatism and hydrothermal activity of the Madjarovo base-precious metal ore district, eastern Rhodopes, Bulgaria. Geological Society, London, Special Publications, 204(1), p. 137-150.

Marescotti, P., Frezzotti, M.L. (2000). Alteration of braunite ores from Eastern Liguria (Italy) during syntectonic veining processes: Mineralogy and fluid inclusions. European Journal of Mineralogy, 12(2), p. 341-356.

Mark, D.F., Renne, P.R., Dymock, R.C., Smith, V.C., Simon, J.I., Morgan, L.E., … Pearce, N.J.G. (2017). High-precision $^{40}Ar/^{39}Ar$ dating of Pleistocene tuffs and temporal anchoring of the Matuyama-Brunhes boundary. Quaternary Geochronology, 39, p. 1-23.

Marriott, C.S., Henderson, G.M., Crompton, R., Staubwasser, M., Shaw, S., (2004). Effect of mineralogy, salinity, and temperature on Li/Ca and Li isotope composition of calcium carbonate. Chem. Geol. 212 (1), p. 5-15.

Martini, J.E.J., Eriksson, P.G. & Snyman, C.P. (1995). The early Proterozoic Mississippi Valley-type Pb-Zn-F deposits of the Campbellrand and Malmani Subgroups, South Africa. Mineral. Deposita 30, p. 135-145.

Master, S., Verhagen, B.T., Bassot, J.P., Beukes, N.J., Lemoine, S. (1993). Stable isotopic signatures of Paleoproterozoic carbonate rocks from Guinea, Sinegal, South Africa and Zimbabwe: constrains on the timing of the ca. 2 Ga “Lomagundi” δ13C excursion, Symposium: early Proterozoic geochemical and structural constraints–metallogeny: Publication Occasionnelle 1993/23, p. 38-41, Dacar, Sen´ egal.

Matrosov, A-G., Chebotarev, E.N., Kudryavtseva, A.J., Zyakun, A.M. and Ivanov, M.B. (1975). Sulfur isotope composition in freshwater lakes containing H_2S. Geochem. Int., 12 (3): p. 217-221.

Matsubara, S., Imai, H., Miawaki, R., and Tokiko, T. (2000). Tamaite, the Ca-analogue of ganophyllite, from the Shiromaru Mine, Okutama, Tokyo, Japan. Journal of Mineralogical and Petrological Sciences, 95, p. 79-83.

Matter, A., Peters, T., Ramseyer, K., 1987. $^{87}Sr/^{86}Sr$-Verhältnisse und Sr-Gehalte von Tiefengrundwässern. Mineralien sowie Gesteinen au dem Kristallin und der Trias der Eclogae Geologicae Helvetiae 80, p. 579-592.

Maynard, J.B., Morton, J., Valdes-Nodarse, E.L., & Diaz-Carmona, A. (1995). Sr isotopes of bedded barites; guide to distinguishing basins with Pb-Zn mineralization. Economic Geology, 90(7), p. 2058-2064.

McClung, C.R., Gutzmer, J., Beukes, N.J., Mezger, K., Strauss, H., & Gertloff, E. (2007). Geochemistry of bedded barite of the Mesoproterozoic Aggeneys-Gamsberg Broken Hill-type district, South Africa. Mineralium Deposita, 42(5), p. 537-549.

McDonald, C.S., Regis, D., Warren, C.J., Kelley, S.P., and Sherlock, S.C. (2018). Recycling argon through metamorphic reactions: The record in symplectites: Lithos, v. 300, p. 200-211.

McDougall, I., and Harrison, T.M., (1999). Geochronology and Thermochronology by the $^{40}Ar/^{39}Ar$ Method (2nd ed.): New York, Oxford University Press, 269 p.

McLaren, S., W. J. Dunlap, and R. Powell (2007). Understanding K-feldspar 40Ar/39Ar data: Reconciling models, methods and microtextures, J. Geol. Soc.,164, p. 941-944.

McLimans R.K. (1977). Geological, Fluid Inclusion, and Stable Isotope Studies of the Upper Mississippi Valley Zinc–Lead District, Southwest Wisconsin. PhD Dissertation, Pennsylvania State University, State College, Pennsylvania, p.177.

McCulloch, M.T. (1994). Primitive $^{87}Sr^{86}Sr$ from an Archean barite and conjecture on the Earth's age and origin. Earth and Planetary Science Letters, 126(1-3), p. 1-13.

McLimans R.K. (1977). Geological, Fluid Inclusion, and Stable Isotope Studies of the Upper Mississippi Valley Zinc-Lead District, Southwest Wisconsin. PhD Dissertation, Pennsylvania State University, State College, Pennsylvania, p.177.

McSwiggen, P. L., Morey, G. B., & Cleland, J. M. (1994). Occurrence and genetic implications of hyalophane in manganese-rich iron-formation, Cuyuna Iron Range, Minnesota, USA. Mineralogical Magazine, 58(392), p. 387-399.

Méheut, M., Lazzeri, M., Balan, E., & Mauri, F. (2010). First-principles calculation of H/D

isotopic fractionation between hydrous minerals and water. Geochimica et Cosmochimica Acta, 74(14), p. 3874-3882.

Mehta, P.K. (1972). Stability of ettringite on heating, J. Am. Ceram. Soc. 55, p. 55-57.

Melezhik, V.A. and Fetisova, O.A., (1989). First discovery of syngenetic barites in the Precambrian of the Baltic Shield. Dokl. Akad. Nauk, 307, p. 422-425 (in Russian).

Melezhik, V.A., Fallick, A.E., Medvedev, P.V. et al., (1999). Extreme $^{13}C_{carb}$ enrichment in ca. 2.0 Ga magnesitestromatolite-dolomite-red beds association in a global context: a case for the world-wide signal enhanced by a local environment. Earth-Sci. Rev., 48, p. 71-120.

Melezhik, V.A., Fallick, A.E., Rychanchik, D.V., & Kuznetsov, A.B. (2005). Palaeoproterozoic evaporites in Fennoscandia: implications for seawater sulphate, the rise of atmospheric oxygen and local amplification of the $\delta^{13}C$ excursion. Terra Nova, 17(2), p. 141-148.

Mertineit, M. & Schramm, M. (2019). Lithium occurrences in brines from two German salt deposits (Upper Permian) and first results of leaching experiments. Minerals 9, 766.

Millot, R., Scaillet, B., Sanjuan, B. (2010a). Lithium isotopes in island arc geothermal systems: Guadeloupe, Martinique (French West Indies) and experimental approach. Geochim. Cosmochim. Acta 74 (6), p. 1852-1871.

Millot, R., Vigier, N. & Gaillardet, J. (2010b). Behaviour of lithium and its isotopes during weathering in the Mackenzie Basin, Canada. Geochim. Cosmochim. Acta 74, p. 3897-3912.

Miyano, T., and Klein, C. (1983). Conditions of riebeckite formation in the iron-formation of the Dales Gorge Member, Hamersley Group, Western Australia, American Mineralogist 68 (5-6): 517-529.

Miyano, T., and Beukes, N.J. (1987). Physicochemical environments for the formation of quartz-free manganese oxide ores from the Early Proterozoic Hotazel Formation, Kalahari manganese field, South Africa: Econ. Geol. v. 82, p. 706-718.

Moen, H.F.G. (1980). Petrology and geological setting of the Wilgenhoutsdrif Formation, Northern Cape Province. M.Sc. thesis (unpubl.), Univ. Orange Free State, Bloemfontein, 287 pp.

Moen, H.F.G. (1999). The Kheis Tectonic Subprovince, southern Africa: a lithostratigraphic perspective. S. Afr. J. Geol., p. 102, 27-42.

Mongelli, G. (20020. Growth of hematite and boehmite in concretions from ancient karst bauxite: clue for past climate. Catena 50, p. 43-51.

Monnin, C., & Cividini, D. (2006). The saturation state of the world's ocean with respect to (Ba,Sr)SO4 solid solutions. Geochimica et Cosmochimica Acta, 70(13), p. 3290-3298.

Moore, J.M., Kuhn, B.K., Mark, D.F., Tsikos, H. (2011). A sugilite-bearing assemblage from the Wolhaarkop breccia, Bruce iron-ore mine, South Africa: Evidence for alkali metasomatism and 40Ar-39Ar dating. Eur. J. Mineral. 23, p. 661-673.

Morris, R.C. (1993) Genetic Modeling for Banded Iron-Formation of the Hamersley Group, Pilbara Craton, the Neoarchean Campbellrand-Malmani carbonate platform, Western-Australia: Precambrian Research, v. 60, n. 1-4, p. 243-286

Mortimer, N., McLaren, S., & Dunlap, W. J. (2012). Ar-Ar dating of K-feldspar in low grade metamorphic rocks: Example of an exhumed Mesozoic accretionary wedge and forearc, South Island, New Zealand. Tectonics, 31(3), n/a–n/a.

Muir M.D., Lock, D.E., Borch von der C.C. (1980). The Coorong-model for penecontemporaneous dolomite formation in the Middle Proterozoic McArthur Group, Northern Territory, Australia. In: Zenger DH (ed) Concepts and models of dolomitization - their intricacies and significance, SEPM Spec Pub128, p 51-67.

Muir, M.D., Donnelly, T.H., Wilkins, R.W.T., Armstrong, K.J. (1985). Stable isotope, petrological, and fluid inclusion studies of minor mineral deposits from the McArthur Basin: implications for the genesis of some sediment-hosted base metal mineralization from the Northern Territory. Aust. J. Earth Sci. 32, p. 239-260.

Mulch, A., Cosca, M.A., Andresen, A., and Fiebig, J. (2005). Time scales of deformation and exhumation in extensional detachment systems determined by high-spatial resolution in situ UV-laser $^{40}Ar/^{39}Ar$ dating: Earth and Planetary Science Letters, v. 233, no. 3-4, p. 375-390.

Munk, L.A., Hynek, S.A., Bradley, D.C., Boutt, D., Labay, K., Jochens H. (2016). Lithium brines: A global perspective. Revies in Economic geology, v. 18, p. 339-365.

Murakami, N., T. Kato, Y. Miúra, and F. Hirowatari (1976). Sugilite, a new silicate mineral from Iwagi Islet, southwest Japan. Mineralogical Journal 8 (2): p. 110-21.

Mutakyahwa, M.K.D., Ikingura, J.R., Mruma, A.H. (2003). Geology and geochemistry of bauxite deposits, Lushoto District, Usambara Mountains, Tanzania. Journal of African Earth Sciences 36, p. 357-369.

Nagashima M., Fukuda C., Matsumoto T., Imaoka T., Odicino G., Armellino G. (2020). Aluminosugilite, $KNa_2Al_2Li_3Si_{12}O_{30}$, an Al analogue of sugilite, from the Cerchiara mine, Liguria, Italy. Eur. J. Mineral., 32, p. 57-66.

Naseem, S., Sheikh, S.A., & Mallick, K.A. (1997). Lithiophorite and associated manganese mineralization in Lasbela area, Balochistan, Pakistan. Geosciences Journal, 1(1), p. 10-15.

Nell, J., Pollak, H., & Lodya, J. A. (1994). Intersite cation partitioning in natural and synthetic alpha-$(Fe, Mn)_2O_3$ (bixbyite) solid solutions determined from57Fe Mössbauer spectroscopy. Hyperfine Interactions, 91(1), p. 601-605.

Nicholson, K. (1992). Contrasting mineralogical-geochemical signatures of manganese oxides; guides to metallogenesis. Economic Geology, 87(5), p. 1253-1264.

Nicolaysen, L.O. and Burger, A.J. (1965). Note on an extensive zone of 1000 million-year-old metamorphic and igneous rocks in southern Africa. Sciences de la Terre, 10, p. 497-516.

Odin G.S., Fullagar P.D. (1988). Geological significance of the glaucony facies. In: Odin GS (ed) Green marine clays: developments in sedimentology. Elsevier, Amsterdam, p. 295-332.

Ohmoto, H. (1986). Stable isotope geochemistry of ore deposits. Reviews in Mineralogy, 16, p. 491-559.

Ohmoto, H., and Rye, R.O., (1979). Isotopes of sulphur and carbon, in Barnes, H.L., ed., Geochemistry of hydrothermal ore deposits, second edition: New York, John Wiley and Sons, Inc., p. 509-567.

Ojala, V. J., Groves, D., & Ridley, J. R. (1995). Hydrogen isotope fractionation factors between hydrous minerals and ore fluid at low temperatures: evidence from the Granny Smith gold deposit, Western Australia. Mineralium Deposita: international journal of geology, mineralogy, and geochemistry of mineral deposits, 30(3-4), p. 328-331.

Oliver, J. (1986). Fluids expelled tectonically from orogenic belts: their role in hydrocarbon migration and other geologic phenomena. Geology, 14, p. 99-102.

Oliver, N. H. S., McLellan, J. G., Hobbs, B. E., Cleverley, J. S., Ord, A., & Feltrin, L. (2006). 100th Anniversary Special Paper: Numerical Models of Extensional Deformation, Heat Transfer, and Fluid Flow across Basement-Cover Interfaces during Basin-Related Mineralization. Economic Geology, 101(1), p. 1-31.

O'Neil, J.R., & Kharaka, Y.K. (1976). Hydrogen and oxygen isotope exchange reactions between clay minerals and water. Geochimica et Cosmochimica Acta, 40(2), p. 241-246.

Ostwald, J. (1992). Mineralogy, paragenesis and genesis of the braunite deposits of the Mary Valley Manganese Belt, Queensland, Australia. Mineralium Deposita, 27(4), p. 326-335.

Outhuis, J.H.M. (1989). Hydrothermal andalusite and corundum in a potassic alteration zone around a proterozoic Gabbro-Tonalite-Granite intrusion NE of Persberg, Central Sweden. Mineralogy and Petrology 40, p. 1-16.

Pamić, J., Balogh, K., Hrvatović, H. *et al.* (2004). K–Ar and Ar–Ar dating of the Palaeozoic metamorphic complex from the Mid-Bosnian Schist Mts., Central Dinarides, Bosnia and Hercegovina. Mineralogy and Petrology 82, p. 65-79.

Papadopoulos, V. (2016). Mineralogical and geochemical constraints on the origin, alteration history and metallogenic significance of the Manganore iron-formation, Northern Cape Province, South Africa. Unpublished Msc Thesis, Rhodes University, Grahamstown, South Africa, p. 222.

Papadopoulos, V., Tsikos, H., Boyce, A., Mark, D. (in prep). Hydrothermal alteration of protolith iron formation and implications for associated massive iron ore genesis in the Northern Cape Province of South Africa.

Paris, G., Gaillardet, J., & Louvat, P. (2010). Geological evolution of seawater boron isotopic composition recorded in evaporites. Geology, 38(11), p. 1035-1038.

Parsons I. and Lee M. R. (2005) Minerals are not just chemical compounds. Can. Mineral. 43, p. 1959-1992.

Patterson, S.M. (1971). Investigations of ferruginous bauxite and other mineral resources on Kauai and a reconnaissance of ferruginous bauxite deposits on Maul, Hawaii. Geol. Surv. Prof. Pap., 656: 74 p.

Peacor, D.R., Rouse, R.C., and Ahn, J.-H. (1987) Crystal structure of tiptopite, a framework beryllophosphate isotypic with basic cancrinite. American Mineralogist, 72, p. 816-820.

Perceil, E. A. (1972). Quelques precisions sur la lithiophorite et "l'asbolite": C. R. Acad. Sci. Paris, t. 275, ser. D, p. 1019-1021.

Pfaff, K., Hildebrandt, L.H., Leach, D.L., Jacob, D.E., Markl, G., (2010). Formation of the Mississippi Valley-type Zn-Pb-Ag deposit in the extensional setting of the upper Rhinegraben

in the Wiesloch area, SW Germany. Miner. Deposita 45, p. 647-666.

Pfister, S., Capo, R. C., Stewart, B. W., Macpherson, G. L., Phan, T. T., Gardiner, J. B., … Hakala, J. A. (2017). Geochemical and lithium isotope tracking of dissolved solid sources in Permian Basin carbonate reservoir and overlying aquifer waters at an enhanced oil recovery site, northwest Texas, USA. Applied Geochemistry, 87, p. 122-135.

Phan, T. T., Capo, R. C., Stewart, B. W., Macpherson, G. L., Rowan, E. L., & Hammack, R. W. (2016). Factors controlling Li concentration and isotopic composition in formation waters and host rocks of Marcellus Shale, Appalachian Basin. Chemical Geology, 420, p. 162-179.

Pirajno, F. (1992). Greisen Systems. Hydrothermal Mineral Deposits, p. 280-324.

Planavsky, N.J., Bekker, A., Hofmann, A., Owens, J.D., & Lyons, T.W. (2012). Sulfur record of rising and falling marine oxygen and sulfate levels during the Lomagundi event. Proceedings of the National Academy of Sciences, 109(45), p. 18300-18305.

Plehwe-Leisen E. von and Klemm D.D. (1995). Geology and ore genesis of the manganese ore deposits of the Postmasburg manganese-field, South Africa. Mineralium Deposita 30, p. 257-267.

Pohwat, P.W. (2012). Connoisseur'S choice: Ettringite, N'Chwaning II Mine, Northern Cape Province, Republic of South Africa. Rocks & Minerals, 87(5), p. 430-438.

Polteau, S., Moore, J.M., & Tsikos, H. (2006). The geology and geochemistry of the Palaeoproterozoic Makganyene diamictite. Precambrian Research, 148(3-4), p. 257-274.

Pope M.C., Grotzinger J.P., Schreiber B.C. (2000). Evaporitic subtidal stromatolites produced by in situ precipitation: textures, facies associations, and temporal significance. Journal of Sedimentary Research 70: p. 1139-1151

Pope, M.C., & Grotzinger, J.P. (2003). Paleoproterozoic Stark Formation, Athapuscow Basin, Northwest Canada: Record of Cratonic-Scale Salinity Crisis. Journal of Sedimentary Research, 73(2), p. 280-295.

Post, J.E. (1999). Manganese oxide minerals: Crystal structures and economic and environmental significance. Proceedings of the National Academy of Sciences, 96(7), p. 3447-3454.

Price, J.G., Lechler, P.J. et al. (2000), Possible volcanic sources of lithium in brines in Clayton Valley, Nevada: Geology and Ore Deposits 2000: The Great Basin and Beyond Proceedings, v.

1, p. 241-248.

Pring, A., Francis, G., Birch, W.D. (1989). Pyrobelonite, arsenoklasite, switzerite and other recent finds at Iron Monarch, South Australia. Australian Mineralogist: 4(2), p. 49-55.

Radusinović, D. and C. Markov (1971). Macedonite - lead titanate: a new mineral. American Mineralogist: 56: p. 387-394.

Rahman, M.M., & Bassuoni, M.T. (2014). Thaumasite sulfate attack on concrete: Mechanisms, influential factors and mitigation. Construction and Building Materials, 73, p. 652-662.

Ranta, J.-P., Hanski, E., Cook, N., & Lahaye, Y. (2016). Source of boron in the Palokas gold deposit, northern Finland: evidence from boron isotopes and major element composition of tourmaline. Mineralium Deposita, 52(5), p. 733-746.

Reeder, R.J. (1991). An overview of zoning in carbonate minerals. Luminescence Microscopy and Spectroscopy: Qualitative and Quantitative Applications (SC25).

René, M. (2018). Petrology, Geochemistry and Mineralogy of Greisens Associated with Tin-Tungsten Mineralisation: Hub Stock Deposit at Krásno–Horní Slavkov Ore District, Czech Republic. Contributions to Mineralization, p. 22.

Renne, P.R.; Glen, J.M.; Milner, S.C.; and Duncan, A.R. (1996). Age of Etendeka flood volcanism and associated intrusions in southwestern Africa. Geology 24: p. 659-662.

Renne, P.R., Balco, G., Ludwig, K.R., Mundil, R., and Min, K. (2011). Response to the comment by W.H. Schwarz et al. on “Joint determination of ^{40}K decay constants and ^{40}Ar*/^{40}K for the Fish Canyon sanidine standard, and improved accuracy for 40Ar/39Ar geochronology”
by P. R. Renne et al., 2010: Geochimica et Cosmochimica Acta, v. 75, no. 17, p. 5097-5100.

Reuschel, M., Melezhik, V.A., & Strauss, H. (2012). Sulfur isotopic trends and iron speciation from the c. 2.0 Ga Pilgujärvi Sedimentary Formation, NW Russia. Precambrian Research, 196-197, p. 193-203.

Richardson C.K., Rye R.O., and Wasserman M.D. (1988). The chemical and thermal evolution of the fluids in the Cave-in-Rock fluorspar district, Illinois: Stable isotope systematics at the Deardorff mine. Economic Geology 83: p. 765-783.

Robb, L.J., Armstrong, R.A. and Waters, D.J. (1999). Nature and duration of mid-crustal granulite facies metamorphism and crustal growth: evidence from single zircon U-Pb geochronology in Namaqualand, South Africa. J. Petrol., 40, p. 1747-1770.

Robb, l. (2004). Introduction to Ore-Forming Processes. Blackwell Publishing, Oxford.

Robinson, G.W., V.T. King, J. Scovil, and F. Cureton (1995). World review of mineral discoveries 1993-1994. Mineralogical Record 26: p. 475-99.

Rosing-Schow, N., Müller, A., & Friis, H. (2018). A Comparison of the Mica Geochemistry of the Pegmatite Fields in Southern Norway. The Canadian Mineralogist, 56(4), p. 463-488.

Rudnick, R.L., Tomascak, P.B., Njo, H.B., & Gardner, L.R. (2004). Extreme lithium isotopic fractionation during continental weathering revealed in saprolites from South Carolina. Chemical Geology, 212(1-2), p. 45-57.

Rye R.O., Whelan J.F., Harrison J.E., and Hayes T.S. (1983). The origin of copper-silver mineralization in the Ravalli Group as indicated by preliminary stable isotope studies. Montana Bur. Mines Geol. Spec. Publ. 90, p. 104-111.

Saito, T., Qiu, H.-N., Shibuya, T., Li, Y.-B., Kitajima, K., Yamamoto, S., … Maruyama, S. (2018). Ar–Ar dating for hydrothermal quartz from the 2.4 Ga Ongeluk Formation, South Africa: implications for seafloor hydrothermal circulation. Royal Society Open Science, 5(9), p. 1-24.

Sangster, D.F., (1990). Mississippi valley-type and sedex lead–zinc deposits: a comparative examination. Transaction of the Institution of Mining and Metallurgy B/99, B21-B42.

Satake H., Matsuo, S. (1984). Hydrogen isotopic fractionation factor between brucite and water in the temperature range from 100 to 510^{o}C. Contributions to Mineralogy and Petrology 86, p. 19-24.

Schaen, A. J., Jicha, B. R., Hodges, K. V., Vermeesch, P., Stelten, M. E., Mercer, C. M., … Singer, B. S. (2020). Interpreting and reporting $^{40}Ar/^{39}Ar$ geochronologic data. GSA Bulletin.

Schalkwyk, G.A.C. (2005). Genesis and characteristics of the Wolhaarkop breccia and associated Manganore iron formation. Unpublished MSc Thesis, 101 p.

Scharf, A., Handy, M.R., Schmid, S.M., Favaro, S., Sudo, M., Schuster, R., & Hammerschmidt, K. (2016). Grain-size effects on the closure temperature of white mica in a crustal-scale extensional shear zone - Implications of in-situ $^{40}Ar/^{39}Ar$ laser-ablation of white mica for dating shearing and cooling (Tauern Window, Eastern Alps). Tectonophysics, 674, p. 210-226.

Schneiderhan E.A., Gutzmer, J., Strauss, H., Mezger, K., Beukes, N.J. (2006). The chemostratigraphy of a Paleoproterozoic MnF-BIF succession-the Voëlwater Subgroup of the

Transvaal Supergroup in Griqualand West, South Africa. South African Journal of Geology, 109, p. 63-80.

Schröder, S., Bekker, A., Beukes, N.J., Strauss, H., & van Niekerk, H.S. (2008). Rise in seawater sulphate concentration associated with the Paleoproterozoic positive carbon isotope excursion: evidence from sulphate evaporites in the ~2.2–2.1 Gyr shallow-marine Lucknow Formation, South Africa. Terra Nova, 20(2), p. 108-117.

Seal, R.R. (2006). Sulfur Isotope Geochemistry of Sulfide Minerals. Reviews in Mineralogy and Geochemistry, 61(1), p. 633-677.

Sha, L.-K., and Chappell, B.W. (1999). Apatite chemical composition, determined by electron microprobe and laser-ablation inductively coupled plasma mass spectrometry, as a probe into granite petrogenesis: Geochimica et Cosmochimica Acta, v. 63, p. 3861-3881.

Shanks, III, W.C. (2014). Stable Isotope Geochemistry of Mineral Deposits. In Treatise on Geochemistry, second ed. Elsevier Ltd.

Sharp, Z.D., 1990, Laser-based microanalytical method for the in situ determination of oxygen isotope ratios of silicates and oxides: Geochimica et Cosmochimica Acta, v. 54, p. 1353-1357.

Shaw D.B. & Weaver C.E. (1965). The mineralogical composition of shales. J. Sed. Pet. 35, p. 213-222.

Sheppard, S.M.F., & Taylor, H.P. (1974). Hydrogen and Oxygen Isotope Evidence for the Origins of Water in the Boulder Batholith and the Butte Ore Deposits, Montana. Economic Geology, 69(6), p. 926-946.

Sheppard, S.M.F. (1986). Characterization and Isotopic Variations in Natural Water. Reviews in Mineralogy, 16, p. 165-183.

Sherlock, S.C., Zalasiewicz, J., Kelley, S.P., & Evans, J. (2008). Excess argon ($^{40}Ar_E$) uptake during slate formation: A 40Ar/39Ar UV laserprobe study of muscovite strain-fringes from the Palaeozoic Welsh Basin, UK. Chemical Geology, 257(3-4), p. 203-217.

Shigley, J.E., J. I. Koivula, and C.W. Fryer. (1987). The occurrence and gemological properties of Wessels mine sugilite. Gems & Gemology 23: p. 78-89.

Shore, M., Fowler, A.D. (1996). Oscillatory zoning in minerals: A common phenomenon. The Canadian Mineralogist, vol 34, p. 1111-1126.

Siebert C., Kramers, J.D., Meisel, T., Morel, P., Naegler, T.F. (2005). PGE, Re-Os and Mo isotope systematics in Archean and early Proterozoic sedimentary systems as proxies for redox conditions of the early Earth. Geochimica et Cosmochimica Acta 69, p. 1787-180.

Simonson, B.M., Schubel, K.A. and Hassler, S.W. (1993). Carbonate sedimentology of the early Precambrian Hamersley Group of Western Australia. Precambrian Res., 60: p. 287-335.

Singh, D.B, Prasad, G. and Rupainwar, D.C. (1996). Adsorption technique for the treatment of As(V)-rich effluents.Colloid Surf. A 111, p. 49-56.

Smith, J.L. (1851). Emery., Amer. J. Sci., 11, p. 53-66.

Smith, G.I., Barczak, V.J., Moulton, G.F., Liddicoat, J.C., (1983). Core KM-3, a Surface-to Bedrock Record of Late Cenozoic Sedimentation in Searles Valley, California. pp. 1-73 U.S. Geol. Surv. Prof. Paper 1256.

Spier, C.A., Vasconcelos, P.M., & Oliviera, S.M.B. (2006). $^{40}Ar/^{39}Ar$ geochronological constraints on the evolution of lateritic iron deposits in the Quadrilátero Ferrífero, Minas Gerais, Brazil. Chemical Geology, 234(1-2), p. 79-104.

Starkey, H.C., (1982). The role of clays in fixing lithium. U.S. Geol. Surv. Bull. 1278-F, F1-F11.

Staude, S., Göb, S., Pfaff, K., Ströbele, F., Premo, W. R., & Markl, G. (2011). Deciphering fluid sources of hydrothermal systems: A combined Sr- and S-isotope study on barite (Schwarzwald, SW Germany). Chemical Geology, 286(1-2), p. 1-20.

Staude, S., Mordhorst, T., Nau, S., Pfaff, K., Brugmann, G., Jacob, D.E., & Markl, G. (2012). Hydrothermal carbonates of the schwarzwald ore district, southwestern Germany: Carbon source and conditions of formation using $\delta^{18}O$, $\delta^{13}C$, $^{87}Sr/^{86}Sr$, and fluid inclusions. The Canadian Mineralogist, 50(5), p. 1401-1434.

Staudt, W.J., & Schoonen, M.A.A. (1995). Sulfate Incorporation into Sedimentary Carbonates. Geochemical Transformations of Sedimentary Sulfur, p. 332-345.

Stein M., Agnon A., Katz A. and Starinsky A. (2002). Strontium isotopes in discordant dolomite bodies of the Judea Group, Dead Sea basin. Isr. J. Earth Sci. 51, p. 219-224.

Stockwell, C.H., McGlynn, J.C., Emslie, R.F., Sanford, B.V., Norris, A.W., Donaldson, J.A., Fahrig, W.F. and Currie, K.L. (1970). Geology of the Canadian Shield. In: Douglas, R.J.W. (Ed.), Geology and Economic Minerals of Canada. Econ. Geol. Rep. Geol. Surv. Can., 1, p. 43-150.

Stowe, C.W. (1986). Synthesis and interpretation of structures along the north-eastern boundary of the Namaqua Tectonic Province, South Africa. Trans. Geol. Soc. S. Afr., 89, p. 185-198.

Strauss, H. (1993). The sulfur isotopic record of Precambrian sulfates: new data and a critical evaluation of the existing record. Precambrian Research, 63(3-4), p. 225-246.

Strauss, H., & Beukes, N.J. (1996). Carbon and sulfur isotopic compositions of organic carbon and pyrite in sediments from the Transvaal Supergroup, South Africa. Precambrian Research, 79(1-2), p. 57-71.

Strauss, H., & Schieber, J. (1990). A sulfur isotope study of pyrite genesis: The mid-proterozoic Newland formation, belt supergroup, Montana. Geochimica et Cosmochimica Acta, 54(1), p. 197-204.

Strauss, H. (1997). The isotopic composition of sedimentary sulfur through time. Palaeogeography, Palaeoclimatology, Palaeoecology, 132(1-4), p. 97-118.

Strauss, H., Melezhik, V.A., Reuschel, M., Fallick, A.E., Lepland, A., Rychanchik, D.V. et al (2013). Abundant Marine Calcium Sulphates: Radical Change of Seawater Sulphate Reservoir and Sulphur Cycle. In V. Melezhik (Ed.), Reading the Archive of Earth's Oxygenation. Springer, Berlin, Heidelberg: Frontiers in Earth Sciences.

Strydom, C.A., Hudson-Lamb, D.L., Potgieter, J.H., & Dagg, E. (1995). The thermal dehydration of synthetic gypsum. Thermochimica Acta, 269-270, p. 631-638.

Sumner, D.Y. and Bowring, S.A. (1996). U-Pb geochronologic constraints on deposition of the Campbellrand Subgroup, Transvaal Supergroup, South Africa. Precambrian Research, 78, p. 25-35.

Sumner, D.Y. (2006) Sequence Stratigraphic Development of the Neoarchean Transvaal carbonate platform, Kaapvaal Craton, South Africa. South African Journal of Geology, 109 (1), p. 11-22.

Sumner, D.Y. and Grotzinger, J.P. (2004). Implications for Neoarchaean ocean chemistry from primary carbonate mineralogy of the Campbellrand-Malmani Platform, South Africa. Sedimentology, 51, p. 1-27.

Sunde, Ø. (2019). Mineralogy and geochemistry of pegmatites in the Larvik Plutonic Complex, Norway. Unpublished PhD thesis, p. 48.

Suzuoki, T., and S. Epstein (1976). Hydrogen isotope fractionation between OH-bearing minerals and water, Geochim. Cosmochim. Acta, 40, p. 1229-1240.

Swennen R., Viaene W., and Cornelissen C. (1990). Petrography and geochemistry of the Belle Roche breccia (lower Visean, Belgium): evidence of brecciation by evaporite dissolution. Sedimentology 37, p. 859-878.

Swindale, L.D., & Hughes, I.R. (1968). Hydrothermal association of pyrophyllite, kaolinite, diaspore, dickite, and quartz in the Coromandel Area, New Zealand. New Zealand Journal of Geology and Geophysics, 11(5), p. 1163-1183.

Taggart, J.E., Jr., E.E. Foord, and J.E. Shigley. (1994). Chemical composition and structural formula of manganoan sugilite from the Wessels mine, Republic of South Africa. Mineralogical Magazine 58: 679-81.

Tan, H.-B., Huang, J.-Z., Zhang, W.-J., Liu, X.-Q., Zhang, Y.-F., Kong, N., & Zhang, Q. (2014). Fractionation of hydrogen and oxygen isotopes of gypsum hydration water and assessment of its geochemical indications. Australian Journal of Earth Sciences, 61(6), p. 793-801.

Taner M.F., Laurent G. (1984). Iron-rich amesite from the Lake Asbestos Mine, Black Lake, Quebec. The Canadian Mineralogist 22 (3): p. 437-442.

Tankard, A.J., Jackson, M.P.A., Eriksson, K.A., Hobday, O.K., Hunter, D.R., Minter, W.E.L. (1982). Crustal Evolution of Southern Africa. Springer - Verlag, New York, p. 523.

Tapio, J., Ranta, J-P., Cook, N., Lahaye, Y., O'brien, H. (2021). Paleoproterozoic Rajapalot Au-Co system associated with evaporites: Chemical composition and boron isotope geochemistry of tourmaline, and sulfur isotopes of sulfates, Peräpohja belt, northern Finland. Precambrian Research, vol 365, 106410.

Taylor H.P., Jr. and Epstein S. (1962a). Relationships between O^{18}/O^{16} ratios in coexisting minerals of igneous and metamorphic rocks, Part I: Principles and Experimental Results. Bull. Geol. Soc. Amer. 73, p. 461-480.

Taylor, G.L. (1972). Stratigraphy, sedimentology, and sulfide mineralization of the Kona Dolomite. PhD Thesis, Michigan Technological Institute, Lansing, Michigan, p. 111.

Taylor H.P., Jr. (1974). The application of oxygen and hydrogen isotope studies to problems of hydrothermal alteration and ore deposition. Economic Geology 69: p. 843-883.

Taylor, H.P., Jr (1977). Water/rock interactions and the origin of H_2O in granitic batholiths: Thirtieth William Smith lecture. Journal of the Geological Society, 133(6), p. 509-558.

Taylor Jr., H.P., & Sheppard, S.M.F. (1986). Chapter 8. IGNEOUS ROCKS: I. PROCESSES of ISOTOPIC FRACTIONATION and ISOTOPE SYSTEMATICS. Stable Isotopes in High Temperature Geological Processes, p. 227-272.

Taylor, H.F.W., Famy, C., Scrivener, K.L. (2001). "Delayed ettringite formation," Cement and Concrete Research, vol. 31, no. 5, p. 683-693.

Teng, F.-Z., McDonough, W.F., Rudnick, R.L., Dalpé, C., Tomascak, P.B., Chappell, B.W., & Gao, S. (2004). Lithium isotopic composition and concentration of the upper continental crust. Geochimica et Cosmochimica Acta, 68(20), p. 4167-4178.

Teng, F.-Z., McDonough, W.F., Rudnick, R.L., & Wing, B. A.(2007). Limited lithium isotopic fractionation during progressive metamorphic dehydration in metapelites: A case study from the Onawa contact aureole, Maine. Chemical Geology, 239(1-2), p. 1-12.

Thode H.G., Monster J., Dunford H.B., (1961). Sulfur isotope geochemistry. Geochim Cosmochim Acta 25: p. 159- 174.

Thokoa, M. (2020). A comparative mineralogical and geochemical study of manganese deposits in the Postmasburg Manganese field, South Africa. Unpublished MSc Thesis, 138 p.

Thomas, R.J., De Beer, C.H. and Bowring, S.A. (1996). A comparative study of the Mesoproterozoic late orogenic porphyritic granites of southwest Namaqualand and Natal, South Africa. J. Afr. Earth Sci., 23, p. 485-508.

Thomazo, C., Pinti, D. L., Busigny, V., Ader, M., Hashizume, K., & Philippot, P. (2009). Biological activity and the Earth's surface evolution: Insights from carbon, sulfur, nitrogen and iron stable isotopes in the rock record. Comptes Rendus Palevol, 8(7), p. 665-678.

Tischendorf, G., Förster, H.-J. and Gottesmann, B. (2001a). Minor- and trace-element composition of trioctahedral micas: a review. Mineralogical Magazine, 65, p. 249-276.

Tomascak, P.B., Hemming, N.G., & Hemming, S.R. (2003). The lithium isotopic composition of waters of the Mono Basin, California. Geochimica et Cosmochimica Acta, 67(4), p. 601-611.

Tomascak, P.B., Magna, T., Dohmen, R., 2016. Advances in Lithium Isotope Geochemistry. Springer International Publishing, Cham, Switzerland, p. 195.

Tostevin, R., Craw, D., Van Hale, R., & Vaughan, M. (2016). Sources of environmental sulfur in the groundwater system, southern New Zealand. Applied Geochemistry, 70, p. 1-16.

Trendall, A.F. (1968). Three great basins of Precambrian banded iron formation deposits--a systematic comparison. Geol. Soc. Am. Bull., 79: p. 1527-1544.

Trendall, A.F., Blockley, J.G. (1970). The Iron-Formations of the Precambrian Hamersley Group, Western Australia, with Special Reference to the Associated Crocidolite, Western Australia Geological Survey Bulletin, Vol. 119, p. 1-365.

Tsikos, H., and Moore, J.M. (1997). Petrography and geochemistry of the Paleoproterozoic Hotazel iron formation, Kalahari Manganese Field, South Africa: Implications for Precambrian manganese metallogenesis: Econ. Geol. v. 92, p. 87-97.

Tsikos, H. (1999). Petrographic and geochemical constraints on the origin and post depositional history of the Hotazel Fe-Mn deposits, Kalahari Manganese Field, South Africa: Unpublished PhD thesis, Grahamstown, South Africa, Rhodes University, 217 p.

Tsikos, H., Beukes, N. J., Moore, J. M., & Harris, C. (2003). Deposition, Diagenesis, and Secondary Enrichment of Metals in the Paleoproterozoic Hotazel Iron Formation, Kalahari Manganese Field, South Africa. Economic Geology, 98(7), p. 1449-1462.

Tsikos, H., Moore, J.M. (2005). Sodic metasomatism in the Palaeoproterozoic Hotazel iron-formation, Transvaal Supergroup, South Africa: Implications for fluid-rock interaction in the Kalahari manganese field. Geofluids 5, p. 264-271.

Tucker, M.E. (2001). Sedimentary Petrology (3rd edition). Blackwell Science, Oxford.

Tulloch, A.J., & Dunlap, W.J. (2006). A Carboniferous $^{40}Ar/^{39}Ar$ amphibole emplacement age for the Au-bearing Sams Creek alkali-feldspar granite dike, west Nelson, New Zealand. New Zealand Journal of Geology and Geophysics, 49(2), p. 233-240.

Tumiati, S., Martin, S., & Godard, G. (2010). Hydrothermal origin of manganese in the high-pressure ophiolite metasediments of Praborna ore deposit (Aosta Valley, Western Alps). European Journal of Mineralogy, 22(4), p. 577-594.

Urai, J.L., & Feenstra, A. (2001). Weakening associated with the diaspore–corundum dehydration reaction in metabauxites: an example from Naxos (Greece). Journal of Structural Geology, 23(6-7), p. 941-950.

Vafeas, N.A., Viljoen, K.S., & Blignaut, L.C. (2018). Mineralogical characterization of the thrusted manganese ore above the Blackridge Thrust Fault, Kalahari Manganese Field: The footprint of the Mukulu Enrichment. Island Arc, e12280.

Vafeas, N.A., Blignaut, L.C., Viljoen, K.S., & Le Roux, P. (2019). An investigation into the $^{87}Sr/^{86}Sr$ radiogenic isotope geochemistry of the manganese ore of the Kalahari Manganese Field with a view on hydrothermal fluid flow and related rare earth element enrichments. South African Journal of Geology, 122(2), p. 237-248.

Valenza, K., Moritz, R., Mouttaqi, A., Fontignie, D., & Sharp, Z. (2000). Vein and Karst Barite Deposits in the Western Jebilet of Morocco: Fluid Inclusion and Isotope (S, O, Sr) Evidence for Regional Fluid Mixing Related to Central Atlantic Rifting. Economic Geology, 95(3), p. 587-606.

Valeton I. (1972). Bauxites: Amsterdam, Elsevier, 226 p. Chapter 6, Geochemistry of bauxite deposits, p. 183-199.

Van Niekerk, H.S. (2006). The origin of the Kheis Terrane and its relationship with the Archean Kaapvaal Craton and the Grenvillian NNMP in southern Africa. Unpublished PhD. thesis, University of Johannesburg, Johannesburg, South Africa. 402 p.

Van Niekerk, H. S., & Beukes, N. J. (2019). Revised definition/outline of the Kheis Terrane along the western margin of the Kaapvaal Craton and lithostratigraphy of the newly proposed Keis Supergroup. South African Journal of Geology, 122(2), p. 187-220.

Van Reeuwijk, L.P. (1974). The thermal dehydration of natural zeolites. Unpublished PhD thesis, p. 92.

Van Schalkwyk, J.F. and Beukes, N.J., (1986). The Sishen Iron Ore deposit, Griqualand West. In: Anhaeusser, C. R., Maske, S. (eds.) Mineral deposits of southern Africa. Geol. Soc. S. Afr., Johannesburg, p. 931-936.

Varentsov, I.M. (1996). Evolution of Manganese Ore Formation in the Earth's History. Manganese Ores of Supergene Zone: Geochemistry of Formation, p. 282-302.

Varentsov, I.M., & Kuleshov, V.N. (2019). Rare Elements-Markers of the Formation Setting of Manganese and Iron Ore Deposits in the Kalahari and Postmasburg Fields (South Africa): Communication 1. Kalahari Manganese Field. Lithology and Mineral Resources, 54(4), 333-349.

Vasconcelos, P.M., Renne, P.R., Brimhall, G.H., & Becker, T.A. (1994b). Direct dating of weathering phenomena by and K-Ar analysis of supergene K-Mn oxides. Geochimica et Cosmochimica Acta, 58(6), p. 1635-1665.

Veizer, J. (1989). Strontium isotopes in seawater through time. Ann. Rev. Earth Planet. Sci. 17, p. 141-167.

Veizer, J., Ala, D., Azmy, K., Bruckschen, P., Buhl, D., Bruhn, F., … Strauss, H. (1999). 87Sr/86Sr, δ13C and δ18O evolution of Phanerozoic seawater. Chemical Geology, 161(1-3), p. 59-88.

Velde, B. (2014). Green Clay Minerals. Treatise on Geochemistry, p. 351-364.

Velilla, N., & Jiménez-Millán, J. (2003). Origin and metamorphic evolution of rocks with braunite and pyrophanite from the Iberian Massif (SW Spain). Mineralogy and Petrology, 78(1-2), p. 73-91.

Vennemann, T. W., & O'neil, J. R. (1996). Hydrogen isotope exchange reactions between hydrous minerals and molecular hydrogen: I. A new approach for the determination of hydrogen isotope fractionation at moderate temperatures. Geochimica et Cosmochimica Acta, 60(13), p. 2437-2451.

Vermeesch, P. (2015). Revised error propagation of 40Ar/39Ar data, including covariances: Geochimica et Cosmochimica Acta, v. 171, p. 325-337.

Vine, J. D., Nonpegmatite lithium resource potential, in Lithium Resources and Requirements by the Year 2000 (1976), edited by J. D. Vine, U.S. Geol. Surv. Prof Pap., 1005, p. 54-58.

Vho, A., Lanari, P., and Rubatto, D. (2019). An internally-consistent database for oxygen isotope fractionation between minerals. J. Petrol. 60, p. 2101-2129.

Von Bezing, K.L., Dixon, R.D., Pohl, D. and Cavallo, G. (1991). The Kalahari manganese field: An Update, Mineralogical Record 22(4), p. 10-27.

Von Gehlen, K., Nielsen, H., Chunnett, I., & Rozendaal, A. (1983). Sulphur isotopes in metamorphosed Precambrian Fe-Pb-Zn-Cu sulphides and baryte at Aggeneys and Gamsberg, South Africa. Mineralogical Magazine, 47(345), p. 481-486.

Voudouris, P.C. (2014). Hydrothermal corundum, topaz, diaspore and alunite supergroup minerals in the advanced argillic alteration lithocap of the Kassiteres-Sapes porphyry-epithermal system, western Thrace, Greece. N. Jb. Miner. Abh. (J. Min. Geochem.) 191(2), p. 117-136.

Walker, R.N., Muir, M.D., Diver, W.L., Williams, N., & Wilkins, N. (1977). Evidence of major sulphate evaporite deposits in the Proterozoic McArthur Group, Northern Territory, Australia. Nature, 265(5594), p. 526-529.

Walker, J. (1983). Possible limits on the composition of the Archaean Ocean. Nature 302, p. 518-520.

Warren, J.K. (2006). Evaporites: Sediments, Resources and Hydrocarbons. Springer, Berlin. 1036 p.

Wartho, J-A. (1995a). Photo-emission electron microscopy (PEEM) heating investigations of a natural amphibole sample. Mineralogical Magazine, 59, p. 121-127.

Welin, E. (1968). Notes on the mineralogy of Sweden 6. X-ray powder data for minerals from Långban and the related mineral deposits of Central Sweden. Arkiv för Mineralogi och Geologi: 4, p. 499-541.

Wilkinson J.J., Stoffell B., Wilkinson C.C., Jeffries T.E., and Appold M.S. (2009a). Anomalously metal-rich fluids form hydrothermal ore deposits. Science 323: p. 764-767.

Wilkinson, J.J. (2014). Sediment-Hosted Zinc–Lead Mineralization. Treatise on Geochemistry, p. 219-249.

Williams-Jones, A.E., & Heinrich, C.A. (2005). 100th Anniversary Special Paper: Vapor Transport of Metals and the Formation of Magmatic-Hydrothermal Ore Deposits. Economic Geology, 100(7), p. 1287-1312.

Williams, L.B., & Hervig, R.L. (2005). Lithium and boron isotopes in illite-smectite: The importance of crystal size. Geochimica et Cosmochimica Acta, 69(24), p. 5705-5716.

Winston, D., & Roberts, S.M. (1986). Sedimentology of the Ravalli Group, middle Belt carbonate, and Missoula Group, Middle Proterozoic Belt Supergroup, Montana, Idaho and Washington. Belt Supergroup: A guide to Proterozoic rocks of western Montana and adjacent areas: Montana Bureau of Mines and Geology Special Publication, 94, p. 85-124.

Whelan, J.F., Rye, R.O., deLorraine, W., Ohmoto, H. (1990). Isotopic geochemistry of a mid-Proterozoic evaporite basin: Balmat, New York. Am. J. Sci. 290, p. 396-424.

White, J.S. (1981): Barian Goyazite from Brazil. Mineralogical Record 12: p. 379.

Whitford, D.J., Korsch, M.J., Solomon M. (1992). Strontium isotope studies of barites; implications for the origin of base metal mineralization in Tasmania. Economic Geology (1992) 87 (3): p. 953-959.

Wheatley C.J.V., Whitfield G.G., Kenny K.J., Birch A. (1986). The Pering carbonate-hosted zinc-lead deposit, Griqualand West.In: Anhaeusser CR, Maske S (eds) Mineral deposits of Southern Africa, Geological Society of South Africa, Johannesburg 1: p. 867-874.

Wohlabaugh, N. (1980). Petrology of the Big Cusp Algal Dolomite; An Informal Member of the Kona Dolomite. (Michigan Bowling Green State University, Marquette).

Xu B.L., Zheng Y.F., Zhou G.T. (1998). Experimental study on hydrogen isotope fractionation between brucite and water at low temperature. Geology-Geochemistry 26, p. 90-96.

Xu, L., Wang, P., Zhang, G. (2012). Formation of ettringite in Portland cement/calcium aluminate cement/calcium sulfate ternary system hydrates at lower temperatures. Construction and Building Materials 31, p. 347-352.

Yakovenchuk, V.N., Krivovichev, S.V., Pakhomovsky, Y.A., Ivanyuk, G.Y., Selivanova, E.A., Men'shikov, Y.P., Britvin, S.N. (2007). Armbrusterite, $K_5Na_6Mn^{3+}Mn^{2+}{}_{14}[Si_9O_{22}]_4(OH)_{10}4H_2O$, a new Mn hydrous heterophyllosilicate from Khibiny alkaline massif, Kola Peninsula, Russia. Am. Mineral., 92, p. 416-423.

Yamaguchi, K.E., Ohmoto, H. (2006). Geochemical and isotopic constraints on the origin of Paleoproterozoic red shales of the Gamagara/Mapedi Formation, Postmasburg Group, South Africa. South African Journal of Geology, 109(1-2), p. 123-138.

Yamashita, S., Mukai, H., Tomioka, N., Kagi, H., & Suzuki, Y. (2019). Iron-rich Smectite Formation in Subseafloor Basaltic Lava in Aged Oceanic Crust. Scientific Reports, 9(1).

Yang, L.-Q., Deng, J., Goldfarb, R. J., Zhang, J., Gao, B.-F., & Wang, Z.-L. (2014). $^{40}Ar/^{39}Ar$ geochronological constraints on the formation of the Dayingezhuang gold deposit: New implications for timing and duration of hydrothermal activity in the Jiaodong gold province, China. Gondwana Research, 25(4), p. 1469-1483.

Yang, L., Wang, Q., Zhang, Q., Carranza, E.J.M., Liu, H., Liu, X., & Deng, J. (2017). Interaction between karst terrain and bauxites: evidence from Quaternary orebody distribution in Guangxi, SW China. Scientific Reports, 7(1).

Yang, H., Gu, X., Scott, M.M. (2022). Hydroxymcglassonite-(K), $KSr_4Si_8O_{20}(OH)8H_2O$, the first Sr-bearing member of the apophyllite group, from the Wessels mine, Kalahari Manganese Field, South Africa. Amer. Mineral. 107 (9), p. 1818-1822.

Yapp, C.J. (1990). Oxygen isotopes in iron (III) oxides. 1. Mineral-water fractionation factors, Chemical Geology 85, p. 329-335.

Yasuyuki, B. (1996). Strontian hollandite in a quartz schist from the Saruta-gawa area in the Sanbagawa metamorphic terrain, central Shikoku, Japan. Mineralogical Journal, 18 (1), p. 23-30.

Yu, W.C., Algeo, T.J., Du, Y.S., Zhang, Q.L. & Liang, Y.P (2016). Mixed volcanogenic–lithogenic sources for Permian bauxite deposits in southwestern Youjiang Basin, South China, and their metallogenic significance. Sedimentary Geology 341, p. 276-288.

Yu, D., Cui, F., Cong, Y., Zhang, C., Tian, Q., & Guo, X. (2019). Simultaneous Selective Chlorination and Carbothermic Reduction of High-Iron Manganese Ore for the Recovery of Manganese Chloride and Metallic Iron. Metals, 9(10), 1124.

Zhang, J., Li, L., Gilbert, S., Liu, J.-J., & Shi, W.-S. (2014). LA-ICP-MS and EPMA studies on the Fe-S-As minerals from the Jinlongshan gold deposit, Qinling Orogen, China: implications for ore-forming processes. Geological Journal, 49(4-5), p. 482-500.

Zhang, J., Li, Y., Wang, L., Zhang, C., & He, H. (2015). Catalytic oxidation of formaldehyde over manganese oxides with different crystal structures. Catalysis Science & Technology, 5(4), p. 2305-2313.

Zheng, Y.F. (1991). Calculation of oxygen isotope fractionation in metal oxides. Geochim Cosmochim Acta 55: p. 2299-2307.

Zheng, Y.F. (1993a). Calculation of oxygen isotope fractionation in anhydrous silicate minerals. Geochimica et Cosmochimica Acta, 57 (5), p. 1079-1091.

Zheng, Y.F. (1993b). Calculation of oxygen isotope fractionation in hydroxyl-bearing silicates. Earth Planet Sci Lett 120: p. 247-263.

Zheng, Y.F. (1998). Oxygen isotope fractionation between hydroxide minerals and water. Phys Chem Min 25, p. 213-221.

Zhou, Q., Glasser, F.P. (2001). “Thermal stability and decomposition mechanisms of ettringite at <120°C,” Cement and Concrete Research, vol. 31, p. 1333-1339.

Zou, H., Li, M., Santosh, M., Zheng, D., Cao, H., Jiang, X.-W., … Li, Z. (2022). Fault-controlled carbonate-hosted barite-fluorite mineral systems: The Shuanghe deposit, Yangtze Block, South China. Gondwana Research, 101, p. 26-43.